

**Kathrin Valerius**

**Spektrometeruntergrund  
und seine Unterdrückung  
beim KATRIN Experiment**

**Spectrometer-related background processes  
and their suppression  
in the KATRIN experiment**

**– 2009 –**



Experimentelle Physik

Dissertationsthema

Spektrometeruntergrund und seine Unterdrückung  
beim KATRIN Experiment

Inaugural-Dissertation  
zur Erlangung des Doktorgrades der Naturwissenschaften  
im Fachbereich Physik  
der Mathematisch-Naturwissenschaftlichen Fakultät  
der Westfälischen Wilhelms-Universität Münster

vorgelegt von  
Kathrin Valerius  
aus Wittlich

– 2009 –

<b>Dekan:</b>	<b>Prof. Dr. J. P. Wessels</b>
<b>Erster Gutachter:</b>	<b>Prof. Dr. Ch. Weinheimer</b>
<b>Zweiter Gutachter:</b>	<b>Prof. Dr. J. P. Wessels</b>
<b>Tag der mündlichen Prüfung:</b>	<b>20.03.2009</b>
<b>Tag der Promotion:</b>	<b>20.03.2009</b>

## Zusammenfassung

Die bislang ungeklärte Frage nach der absoluten Massenskala der Neutrinos hat große Relevanz für die Teilchenphysik, sowie auch für die Kosmologie und die Astrophysik. Eine Möglichkeit zur direkten Neutrinomassenbestimmung bietet die präzise Vermessung des Tritium- $\beta$ -Spektrums. Die Signatur einer endlichen Neutrinomasse ist nur mit hochauflösenden Elektronenspektrometern zugänglich, welche gleichzeitig eine Messung mit sehr geringem Untergrund erlauben. Bei dem momentan am Forschungszentrum Karlsruhe im Aufbau befindlichen KATRIN-Experiment, welches eine Sensitivität von  $m(\nu_e) < 0,2 \text{ eV}/c^2$  (90% C. L.) anstrebt, kommt hierzu eine Kombination aus zwei elektrostatischen Retardierungsspektrometern mit magnetischer adiabatischer Kollimation („MAC-E-Filter“) zum Einsatz.

In dieser Arbeit wurden verschiedene spektrometerbezogene Untergrundquellen im KATRIN-Experiment sowie Methoden zu ihrer Unterdrückung untersucht. Sekundärelektronen aus den Retardierungselektroden bilden eine wesentliche Untergrundkomponente, welche durch eine Innenelektrode aus Drähten auf negativerem Potential abgeschirmt werden kann. Im Rahmen dieses Dissertationsprojektes wurde ein komplexes, doppelagiges Drahtelektrodensystem für das KATRIN-Hauptspektrometer entworfen und mit Hilfe von detaillierten Computersimulationen optimiert. Ebenso können Fallen für geladene Teilchen, welche im Experimentaufbau an verschiedenen Stellen auftreten, zur Untergrundrate beitragen. Die Möglichkeit, solche Fallen durch geeignetes Elektrodendesign zu unterdrücken, wurde in dieser Arbeit am Beispiel des Vorspektrometers untersucht. Auch die Schnittstelle zwischen den beiden KATRIN-Spektrometern bildet prinzipbedingt eine Penningfalle für Elektronen. Ein wesentliches Ziel dieser Arbeit war es, das System mit einem Testaufbau nachzustellen und die Funktionsweise eines Mechanismus zur periodischen Entleerung der Falle zu erproben. Hierzu wurde ein periodisch durch das Fallenvolumen bewegter Metalldraht verwendet, welcher prinzipiell auch für einen Einsatz im realen KATRIN-Aufbau geeignet ist. Zur künstlichen Füllung der Falle im Testaufbau wurde u. a. eine Kathode aus Edelstahl mit UV-Licht aus einer Leuchtdiode bestrahlt, um Photoelektronen zu erzeugen. Dabei konnte auch gezeigt werden, dass sich eine solche schnell pulsare Photoelektronenquelle (mit Leuchtdiodenpulsbreiten von  $\tau \gtrsim 40 \text{ ns}$  bei Wiederholraten von  $1 - 10 \text{ kHz}$ ) aufgrund der geringen Breite der gemessenen Elektronen-Energieverteilung ( $\sigma \approx 0,2 \text{ eV}$ ) in Verbindung mit Flugzeitmessungen auch zur Charakterisierung der elektromagnetischen Eigenschaften von MAC-E-Filtern, insbesondere für Kalibrationsmessungen des KATRIN-Hauptspektrometers, nutzen ließe. Zusätzlich kann die Winkelverteilung der emittierten Elektronen durch geeignete Wahl der elektromagnetischen Felder gesteuert werden. Ein Prototyp einer solchen winkelselektiven Photoelektronenquelle wurde ebenfalls erfolgreich am Mainzer MAC-E-Filter getestet und soll in detaillierten Studien im Hinblick auf eine Anwendung am KATRIN-Hauptspektrometer weiterentwickelt werden.

## Abstract

Despite the impressive progress the field of neutrino physics has seen over the past decade, the absolute scale of neutrino masses remains an open question with a large impact on particle physics, astrophysics, and cosmology. One way of direct neutrino mass determination with a laboratory experiment consists in the precise measurement of the tritium  $\beta$ -decay spectrum. The imprint of a non-zero neutrino mass on the spectrum is discernible only with high-resolution electron spectroscopy methods which at the same time allow to achieve a very low background level. In the upcoming KATRIN experiment, aiming for a sensitivity of  $m(\nu_e) < 0.2 \text{ eV}/c^2$  (90% C. L.), two successive electrostatic retardation filters with magnetic adiabatic collimation (“MAC-E filters”) will be used.

In this work, various spectrometer-related background sources and methods to suppress them were investigated. Secondary electrons created at the surface of the retardation electrodes form a major source of background in MAC-E filters. This background component can be suppressed significantly by means of an inner wire electrode at a more negative electric potential than the one supplied to the solid retardation electrodes. In the course of this dissertation project a complex double-layer wire electrode system for the KATRIN main spectrometer was designed and optimized based on detailed computer simulations. Furthermore, traps for charged particles, which occur in several places throughout the experimental setup, can contribute to the background rate. The possibility to suppress such traps by a suitable design of the electrode system was investigated in this work for the example of the KATRIN pre-spectrometer. Likewise, the interface between pre- and main spectrometer forms an unavoidable Penning trap for electrons. A central aim of this thesis was to simulate this system in a mockup experiment and to devise and test a mechanism to periodically empty the trap. To this end, a metallic wire was scanned through the trapping volume periodically. This concept was found to be suitable for an application at the real KATRIN setup.

Among other methods, photoelectrons created by irradiating a cathode with UV light from a light emitting diode (LED) were used as an artificial mechanism to fill the trap. In the course of the measurements, it was also demonstrated that such a fast-pulsed photoelectron source (LED pulse width  $\tau > 40 \text{ ns}$ , repetition rate  $1 - 10 \text{ kHz}$ ) with a small measured energy spread ( $\sigma \approx 0.2 \text{ eV}$ ) may be used to characterize the electromagnetic properties of MAC-E filters. In particular, it might serve as a calibration source to be used in a time-of-flight measurement mode at the KATRIN main spectrometer. As an additional feature, angular definition of the photoelectrons can be obtained by a suitable choice of the electromagnetic field configuration. A prototype of such an angular-selective electron source was successfully tested in the scope of this work, and studies are under way to further develop the concept in view of a potential application at the KATRIN main spectrometer.



*Experimental science is continually revealing to us new features of natural processes and we are thus compelled to search for new forms of thought appropriate for their description.*

— James Clerk Maxwell



# Contents

<b>1</b>	<b>Introduction</b>	<b>1</b>
1.1	A brief historical outline of neutrino physics . . . . .	1
1.2	Neutrinos as a probe of physics beyond the Standard Model . . . . .	4
1.3	The role of neutrinos in astrophysics and cosmology . . . . .	9
1.4	Methods to determine the absolute neutrino mass scale . . . . .	11
1.4.1	Cosmological bounds on neutrino mass . . . . .	11
1.4.2	Direct kinematic methods . . . . .	12
1.4.3	Neutrinoless double beta decay . . . . .	16
<b>2</b>	<b>The KATRIN experiment</b>	<b>21</b>
2.1	Tritium beta-decay . . . . .	21
2.2	The MAC-E filter technique . . . . .	24
2.2.1	General working principle . . . . .	24
2.2.2	Energy resolution and transmission function . . . . .	26
2.3	Overview of the components of the KATRIN setup . . . . .	31
2.3.1	Basic parameters of the KATRIN experiment . . . . .	31
2.3.2	Tritium source and pumping sections . . . . .	32
2.3.3	Spectrometer section . . . . .	34
2.3.4	Electron detector system . . . . .	36
2.4	Systematic and statistical uncertainties . . . . .	38
2.5	Sources of background in the KATRIN experiment . . . . .	42
<b>3</b>	<b>Background suppression in MAC-E filters by electrostatic screening</b>	<b>47</b>
3.1	Concept of background reduction by a screening wire electrode . . . . .	47
3.2	Development of the concept and tests at the Mainz MAC-E filter . . . . .	49
3.3	Implementation of the concept at the KATRIN pre-spectrometer . . . . .	50
3.4	Transfer of the concept to the KATRIN main spectrometer . . . . .	52
3.4.1	Parameters of a double-layer wire electrode system . . . . .	56
<b>4</b>	<b>Design studies for the wire electrode of the KATRIN main spectrometer</b>	<b>61</b>
4.1	Technical requirements . . . . .	61
4.2	Design criteria . . . . .	62
4.2.1	Homogeneity of electric retardation potential and magnetic field in the analyzing plane . . . . .	62
4.2.2	Transmission properties . . . . .	64
4.2.3	Adiabaticity . . . . .	65
4.2.4	Avoidance of traps for charged particles . . . . .	65
4.3	Simulation tools . . . . .	67
4.3.1	Calculation of magnetic fields . . . . .	67
4.3.2	Calculation of electric fields . . . . .	68
4.3.3	Trajectory calculation for charged particles in electromagnetic fields . . . . .	72
4.3.4	Auxiliary programs . . . . .	75

4.4	Implementation of the wire electrode design as a computer model . . . . .	76
4.4.1	General layout of the wire electrode system . . . . .	76
4.4.2	Modification of relevant parameters . . . . .	78
4.5	Estimation of tolerances for fabrication and mounting of the electrode system . . . .	80
4.5.1	Tolerance estimates regarding the bending of wires . . . . .	81
4.5.2	Tolerance estimates for the radial displacement of modules . . . . .	86
4.5.3	Tolerance estimates for the shape of the spectrometer vessel . . . . .	87
4.5.4	Technical implications of the tolerance simulations . . . . .	87
4.6	Measures to improve the homogeneity of the electric field . . . . .	90
4.6.1	Simple model using full rotational symmetry . . . . .	91
4.6.2	Enhanced model using discrete rotational symmetry . . . . .	93
4.7	Further design details obtained with a model using discrete rotational symmetry . .	103
4.8	Overview of final parameters of the wire electrode system for the KATRIN main spectrometer . . . . .	105
4.9	Assembly of the modules and quality assurance procedures . . . . .	107
4.10	Summary and status . . . . .	110
<b>5</b>	<b>Penning traps in the KATRIN setup as a potential background source</b>	<b>113</b>
5.1	Discharge mechanisms . . . . .	114
5.1.1	Townsend discharge . . . . .	114
5.1.2	Vacuum breakdown . . . . .	116
5.1.3	Penning trap and Penning discharge . . . . .	116
5.1.4	Methods to counteract discharge problems due to particle traps . . . . .	122
5.2	The Penning trap inside the pre-spectrometer . . . . .	123
5.2.1	Location of the Penning trap . . . . .	126
5.2.2	Modification of the electrode system to remove the Penning trap in the cone region . . . . .	129
5.2.3	Operational modes of the KATRIN pre-spectrometer . . . . .	130
5.2.4	Proposal for an additional pair of electrodes . . . . .	132
5.2.5	Electric field strength: original versus modified setup . . . . .	138
5.2.6	Behavior of the system after installation of the new electrodes . . . . .	142
5.3	The Penning trap inside the main spectrometer . . . . .	143
5.4	The Penning trap between pre- and main spectrometer . . . . .	144
5.4.1	Trapping mechanisms and relevance for background concerns . . . . .	144
5.4.2	Validity of the simulation results in view of the new KATRIN reference design	149
5.4.3	Countermeasures . . . . .	151
5.5	Effects of Penning discharges in other experiments . . . . .	153
<b>6</b>	<b>Experimental tests of a method to empty the Penning trap between pre- and main spectrometer</b>	<b>155</b>
6.1	Aim and requirements of the experimental test . . . . .	155
6.2	Setup and field configurations at the Mainz MAC-E filter . . . . .	156
6.2.1	Pre-spectrometer mockup: vacuum chamber and “backplate” . . . . .	156
6.2.2	Mechanical device to sweep a wire through the beam line: the “wire scanner”	158
6.2.3	Configuration of electric and magnetic fields . . . . .	165
6.2.4	Methods of filling the trap . . . . .	168
6.2.5	Electron detection, data acquisition, and high-voltage system . . . . .	170
6.3	First measurement phase: proof of principle . . . . .	175
6.3.1	Increased background rate caused by backplate on high voltage . . . . .	175

6.3.2	Characteristics of the Penning effect without extra filling of the trap . . . . .	175
6.3.3	Characteristics of the Penning effect with injection of photoelectrons . . . . .	184
6.4	Second and third measurement phases: ignition and specific quenching of Penning discharges . . . . .	192
6.4.1	Observations from the second measurement phase . . . . .	192
6.4.2	Results of the third measurement phase . . . . .	198
6.5	Discussion of results and application to KATRIN . . . . .	203
<b>7</b>	<b>Tests of a UV LED-based photoelectron source</b>	<b>207</b>
7.1	Motivation . . . . .	207
7.1.1	Time-of-flight simulations for the KATRIN main spectrometer . . . . .	208
7.1.2	Details of the transmission function and proposal of an enhanced time-of-flight mode . . . . .	211
7.2	Suitable light sources for fast-pulsed photoelectron production . . . . .	217
7.3	Pulsed photoelectron production from a stainless steel cathode . . . . .	220
7.3.1	Timing properties, photoelectron yield and photoelectron multiplicities . . .	220
7.3.2	Energy scan of photoelectrons at 18 keV . . . . .	228
7.3.3	Time-of-flight spectrum of photoelectrons at 18 keV . . . . .	233
7.4	Prototype studies of a pulsed photoelectron source with angular selectivity . . . . .	238
7.4.1	Mechanical construction of the fiber-coupled photoelectron gun . . . . .	242
7.4.2	Measurement of integrated energy spectra: comparison between outer and inner fiber . . . . .	247
7.5	Evaluation of results and outlook . . . . .	251
7.5.1	Summary of simulation studies for time-of-flight measurements at the KATRIN main spectrometer and experimental tests at the Mainz spectrometer .	251
7.5.2	Upgraded design of an angular-selective photoelectron gun . . . . .	255
<b>8</b>	<b>Conclusions and outlook</b>	<b>257</b>
<b>A</b>	<b>Electric screening factor of a single-layer cylindrical wire electrode</b>	<b>265</b>
<b>B</b>	<b>Technical drawings</b>	<b>269</b>
B.1	Pre-spectrometer shielding electrode . . . . .	269
B.2	Disc-shaped high voltage electrode for Penning trap experiments at Mainz . . . . .	271
B.3	Scanning wire device to disturb the trapping conditions of charged particles . . . . .	272
B.4	Prototype of a fiber-coupled photoelectron source . . . . .	274
<b>C</b>	<b>Technical data of the electron detector and the UV LEDs</b>	<b>277</b>
C.1	Silicion PIN diode Hamamatsu S3590-06 . . . . .	277
C.2	UV LED 265 nm and 255 nm . . . . .	277
<b>D</b>	<b>Run descriptions (phase II of wire scanner measurements)</b>	<b>281</b>
<b>E</b>	<b>Operation and control of UV LEDs</b>	<b>285</b>
E.1	First measurement phase (2007) . . . . .	285
E.2	Second and third measurement phases (2008) . . . . .	285
<b>F</b>	<b>Photoelectron current and quantum efficiency</b>	<b>289</b>
F.1	Measurement of the current of photoelectrons . . . . .	289
F.2	Determination of the quantum efficiency . . . . .	290

*Contents*

List of figures	293
List of tables	299
References	301

# 1 Introduction

Although today neutrinos are well-established in the framework of the Standard Model of elementary particle physics, essential questions regarding their fundamental properties have remained unanswered. Attempts to explain some of these characteristics even lead to physics beyond the Standard Model, and the past years have seen a flourishing research activity both in theoretical and in experimental neutrino science. The abounding evidence from recent neutrino flavor oscillation experiments confirming that neutrinos have non-vanishing masses marks an important milestone, which provides further motivation for the ongoing hunt for the absolute neutrino mass scale that has up to now not been uncovered.

This chapter gives an introduction to neutrino physics with a special emphasis on the topic of neutrino masses, which not only have a natural impact on particle physics but are also closely linked to modern cosmology and astrophysics. Different methods to determine the absolute neutrino mass scale are discussed.

## 1.1 A brief historical outline of neutrino physics

### The beta decay puzzle

The discovery of radioactivity at the end of the 19<sup>th</sup> century started a wealth of investigations concerned with the structure of atoms and nuclei. Soon, three types of radiation were distinguished, which were classified according to their penetrating power as  $\alpha$ ,  $\beta$  and  $\gamma$  rays. While  $\alpha$ -particles were identified with helium nuclei [Rut08],  $\beta$ -rays were found to be composed of electrons [Kau02]. Lastly,  $\gamma$ -rays were shown [Rut14] to be electromagnetic radiation with energies higher than those known from X-rays. Guided by the experimental observation that both in  $\alpha$ - and  $\gamma$ -decay particles with discrete energies are ejected from the nucleus, the common expectation at that time was that such a behavior should also be found in  $\beta$ -radioactivity. Early experiments on  $\beta$ -spectroscopy made use of magnetic momentum separation and subsequent photographic detection (see, for example, [Bae10, Bae11]). These studies indeed indicated a discrete energy distribution of  $\beta$ -particles, but the results remained inconclusive.

In 1914, J. Chadwick [Cha14] used a new approach, replacing the photographic plate by an ionization counter. In contrast to previous experiments, his measurements<sup>1</sup> revealed a continuous  $\beta$ -spectrum (see figure 1.1).

Chadwick's experimental findings were met with astonishment and scepticism. Not only was the observed spread of  $\beta$ -energies over such a wide – and continuous – range at odds with the concept of a “quantized” nucleus with well-defined energy levels, but, more importantly, it seemed to violate energy and momentum conservation for the radioactive disintegration which was thought

---

<sup>1</sup>In the same work, Chadwick was able to show that the photographic method was misleading because the relative intensity of lines was strongly exaggerated as compared to a continuous contribution and the development process of the plate had considerable influence on the resulting photographic picture. Chadwick's spectra actually contained a few sharp lines – much weaker and fewer in number than in the photographic measurements – on top of a continuous “background”. However, Chadwick concluded that the main component was formed by the continuum rather than by the discrete lines. See reference [Pai86] for details.

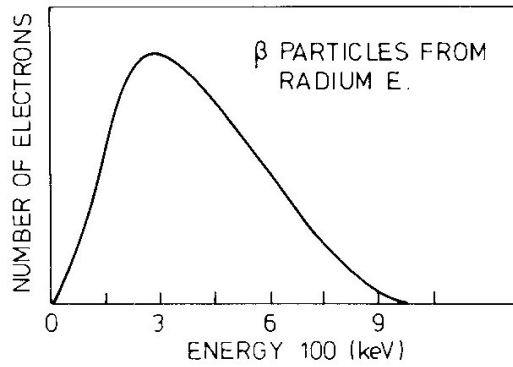


**Figure 1.1:** Continuous  $\beta$ -spectrum of Radium E, measured with an ionization counter and using magnetic separation of electron momenta (after [Ell27], reprinted in [Hey04]). The relative intensity is highest at energies around 300 keV and the maximum energy reached is close to 1 MeV.

of as a two-body process. For several years, nuclear physicists were considering the possibility that the continuous  $\beta$ -spectra could be due to secondary effects modifying the energies of the  $\beta$ -particles after they emerged from the nucleus with definite characteristic energies (see, for example, [Mei22]), or that maybe the conservation laws might only hold in the statistical limit.

By the end of the 1920s, the long-lasting controversy could finally be considered as settled, when calorimetric measurements of the mean amount of heat liberated in the  $\beta$ -decay of Ra E ( $^{210}\text{Bi}$ ), which were carried out by C. D. Ellis and W. A. Wooster [Ell27] and later confirmed and refined by L. Meitner and W. Orthmann [Mei30], cleared out any doubts about the continuous shape of the primary  $\beta$ -spectrum. Still, the fundamental question remained unanswered: How could these experimental findings be explained?

Eventually, W. Pauli proposed a way out in his famous letter [Pau30] dating from 1930, in which he postulated the existence of electrically neutral spin 1/2 particles with a mass “of the same order of magnitude as the electron mass and in any event not larger than 0.01 proton masses” in the nucleus. The hypothesis that such a neutral particle is emitted in  $\beta$ -decay together with the electron, forming a three-body process, would then indeed allow to understand the puzzling experimental results.

By 1934, E. Fermi had succeeded in setting up a theoretical description of  $\beta$ -decay including the new particle [Fer34], which was from then on called the “neutrino” to distinguish it from the much more massive neutral nucleon, the neutron, that had in the meantime been discovered by Chadwick [Cha32]. In contrast to Pauli’s original conception, Fermi did not assume the neutrino and the electron to be present inside the nucleus prior to the decay. Instead, in his model the two particles were supposed to be created at the instant of their emission. Modelled on the well-established theory of electromagnetic interactions, Fermi’s approach proved useful in describing not only  $\beta$ -decay, but also several related processes which are due to the weak force. Therefore, it has been termed the “universal Fermi interaction”. Despite some modifications, the basic framework of Fermi’s theory is still valid today in the low-energy limit of the weak interaction. R. P. Feynman and M. Gell-Mann [Fey58], E. C. G. Sudarshan and R. E. Marshak [Sud58], and J. J. Sakurai [Sak58] independently proposed to expand Fermi’s vector current (“V”-type) interaction by adding an axial vector current (“A”-type) contribution. The “V – A” structure chosen for the description of the weak interaction is not symmetric with respect to spatial reflection (*i. e.*, under the parity transformation). In fact, parity is maximally violated in weak interactions, as was demonstrated in classic experiments by C. S. Wu *et al.* [Wu57] and M. Goldhaber *et al.* [Gol58].

### The experimental search for neutrinos

In spite of Pauli's conviction that the particle he had introduced would probably never be detected due to its extremely weak interaction, the hunt for experimental evidence started soon after the neutrino hypothesis became known. Further indirect hints came from experiments on momentum conservation in  $\beta$ -decay [Lei36, Cra38, Cra39], where the recoil of the daughter nucleus was observed together with the emitted electron, for example in pictures taken with a cloud chamber. Clearly, the emission of a third – “invisible” – partner was required to explain the cases in which electron and recoiling nucleus were not emitted in exactly opposite directions.<sup>2</sup> By the end of the 1940s, the neutrino was generally believed to be “real” due to its usefulness in explaining a wealth of experimental data. However, what was still missing was a detection of neutrinos separately from the process in which they are born, and so, in 1951, F. Reines and C. L. Cowan set out to plan an experiment to “demonstrate the existence of the neutrino in the free state (...) by an observation at a remote location” [Rei96]. They chose to look for the reaction<sup>3</sup>

$$\bar{\nu} + p \rightarrow n + e^+, \quad (1.1)$$

with a large-volume, segmented liquid-scintillator detector and a nuclear reactor as a high-intensity source of antineutrinos. Two reservoirs of target material ( $\text{CdCl}_2$  dissolved in water) were sandwiched between three tanks filled with liquid scintillator and instrumented with photomultiplier tubes. The strategy to use a delayed coincidence formed by the photons created in the annihilation of the positron with an electron and the gamma rays emitted upon the capture of the decay neutron on a Cd nucleus proved essential in overcoming the large background. Nevertheless, it took several years and various improvements of the experimental setup before the results were sufficient to support a confident claim that, more than 25 years after its “invention”, the neutrino had finally been detected. Furthermore, Cowan and Reines were able to give a value [Rei59] for the measured cross section of the reaction (1.1):

$$\sigma = (11 \pm 2.6) \cdot 10^{-44} \text{ cm}^2 \quad (1.2)$$

(at  $E_\nu \leq 8 \text{ MeV}$ ).

Just a few years later, M. Schwartz, L. M. Lederman and J. Steinberger were able to demonstrate that there is more than only one type of neutrinos [Dan62]. In their experiment they used a proton accelerator to produce a shower of pions which subsequently decayed into muons and neutrinos:

$$\pi^+ \rightarrow \mu^+ + \nu, \quad \pi^- \rightarrow \mu^- + \bar{\nu}. \quad (1.3)$$

When interacting with matter, the neutrinos from the reaction (1.3) were found to produce  $\mu^\pm$ , but not  $e^\pm$ , which led to the conclusion that there must be at least two different types of neutrinos: one (namely  $\nu_e, \bar{\nu}_e$ ) is associated with the production of  $e^\pm$ , the other one ( $\nu_\mu, \bar{\nu}_\mu$ ) is related to  $\mu^\pm$ .

These two neutrino flavors fitted smoothly into the Standard Model of elementary particle physics, which emerged in the early 1960s and gradually evolved into the extensive and successful concept we know today. The Standard Model distinguishes 12 fundamental fermions (quarks and leptons, see table 1.1) plus their corresponding antiparticles. Bosons ( $\gamma, W^\pm, Z^0, g$ ) mediate the interactions. Quarks and leptons are grouped into doublets which form three families (or generations). For the quarks this makes six flavors which come in three colors. Their electric charges are  $\pm \frac{1}{3}e$  and  $\pm \frac{2}{3}e$ . Until the early 1970s, the quark model only incorporated the four lightest ones (u, d,

<sup>2</sup>Similar evidence came from experiments detecting nuclear recoil in the electron capture process (see, for example, [All42]), which was likewise attributed to the emission of a neutrino. For reviews of the experimental evidence for the existence of neutrinos from recoil studies, see, for example, references [Pon47, Cra48].

<sup>3</sup>At the time of the experiment, no distinction was made between the neutrino flavors  $\nu_e, \nu_\mu$  and  $\nu_\tau$ .

c, s), *i. e.*, two families in perfect symmetry to the two known lepton doublets,  $(\nu_e, e)$  and  $(\nu_\mu, \mu)$  (with the neutrinos being electrically neutral and the charged leptons carrying one elementary charge  $\pm e$ ). However, in 1973 M. Kobayashi and T. Maskawa [Kob72] predicted the existence of a third family of quarks as this yields a mechanism for the generation of CP violation.<sup>4</sup> Hence, it seems natural that there should also be a third lepton family. Indeed, the charged component  $\tau$  of the missing doublet was discovered in 1975 by M. L. Perl *et al.* [Per75], but it took 25 more years until also the partner-neutrino  $\nu_\tau$  was found [Kod01].<sup>5</sup>

**Table 1.1:** The 12 fundamental fermions of the Standard Model of elementary particle physics.

quarks			leptons		
u	c	t	$\nu_e$	$\nu_\mu$	$\nu_\tau$
d	s	b	$e^-$	$\mu^-$	$\tau^-$

## 1.2 Neutrinos as a probe of physics beyond the Standard Model

Aside from being electrically neutral, neutrinos are in the Standard Model assumed to have no electric or magnetic dipole moment (and hence they cannot interact electromagnetically). Furthermore, neutrinos are considered as being massless. Generally, fermions in the Standard Model acquire mass via Yukawa couplings between left- and right-handed components of the fermion fields. The values of the masses, however, are not predicted by the model and have to be inserted as free parameters. Because of the maximum parity violation of the weak interaction, the Standard Model only includes left-handed neutrinos  $\nu_L$  and right-handed antineutrinos  $\bar{\nu}_R$ ; therefore, it is not possible to form a standard fermion mass term.

Over the past decade, evidence for non-vanishing neutrino masses has been collected in a large number of experiments observing neutrino flavor oscillations.

There are two general prerequisites for neutrinos to be able to change their flavor over a certain distance of propagation from the point of creation to their detection:

1. Neutrinos mix, *i. e.*, the flavor states  $|v_\alpha\rangle$  ( $\alpha = e, \mu, \tau$ ) are not identical to the eigenstates  $|v_i\rangle$  ( $i = 1, 2, 3$ ) of the mass operator  $M$ . These two sets of states are connected by a unitary mixing matrix  $U$  according to

$$|v_\alpha\rangle = \sum_i U_{\alpha i} |v_i\rangle, \quad (1.4)$$

$$|v_i\rangle = \sum_\alpha U_{i\alpha}^\dagger |v_\alpha\rangle = \sum_\alpha U_{\alpha i}^* |v_\alpha\rangle. \quad (1.5)$$

2. At least one of the mass eigenvalues  $m_i$  associated to the states  $|v_i\rangle$  is non-zero.

<sup>4</sup>M. Kobayashi and T. Maskawa shared a part of the 2008 Nobel Prize in Physics "for the discovery of the origin of the broken symmetry which predicts the existence of at least three families of quarks in nature" [http://nobelprize.org/nobel\\_prizes/physics/laureates/2008/](http://nobelprize.org/nobel_prizes/physics/laureates/2008/). The b and t quarks were both experimentally discovered at Fermilab (see [Her77] and [Aba95, Abe95], respectively).

<sup>5</sup>The question whether there actually exist more than three lepton families can be reduced to determining the number  $N_\nu$  of weakly interacting neutrino flavors.  $N_\nu$  (defined as the number of light weakly interacting neutrino flavors satisfying  $m_\nu < \frac{m_{Z^0}}{2}$ ) is accessible via precision measurements of the total decay rate  $\Gamma_{Z^0}$  of the  $Z^0$  boson. A combined analysis of all four experiments at the Large Electron-Positron collider (LEP) yields  $N_\nu = 2.984 \pm 0.008$  [PDG08], in agreement with the number of lepton families present in the Standard Model.

In the following, the theoretical framework of neutrino flavor oscillations in vacuum shall be introduced.

A neutrino of flavor state  $|v_\alpha\rangle$  ( $\alpha = e, \mu, \tau$ ) is created in a weak interaction process together with its corresponding charged lepton partner  $\ell_\alpha$ . This flavor state is not an eigenstate of the mass operator  $M$ , but can be expressed as a linear superposition of the mass eigenstates  $|v_i\rangle$  with the eigenvalues  $m_i$  ( $i = 1, 2, 3$ ) via the unitary mixing matrix  $U$  (compare, e. g., [Zub04]):

$U$ , which forms an analogon to the CKM matrix known in the quark sector of the Standard Model, is often referred to as the PMNS matrix (acknowledging important contributions by B. Pontecorvo [Pon67], Z. Maki, M. Nakagawa and S. Sakata [Mak62]). The  $(n-1)^2$  independent parameters of a unitary  $n \times n$  matrix can be expressed by  $\frac{1}{2}n(n-1)$  mixing angles of an  $n$ -dimensional rotation matrix and by  $\frac{1}{2}(n-1)(n-2)$  phases. For  $n = 3$  one thus obtains three mixing angles  $\theta_{ij}$  and one phase  $\delta$ :

$$U = \begin{pmatrix} 1 & 0 & 0 \\ 0 & \cos \theta_{23} & \sin \theta_{23} \\ 0 & -\sin \theta_{23} & \cos \theta_{23} \end{pmatrix} \begin{pmatrix} \cos \theta_{13} & 0 & \sin \theta_{13} e^{i\delta} \\ 0 & 1 & 0 \\ -\sin \theta_{13} e^{-i\delta} & 0 & \cos \theta_{13} \end{pmatrix} \times \begin{pmatrix} \cos \theta_{12} & \sin \theta_{12} & 0 \\ -\sin \theta_{12} & \cos \theta_{12} & 0 \\ 0 & 0 & 1 \end{pmatrix} \quad (1.6)$$

Although  $\delta$  has up to now not been measured in neutrino oscillation experiments, it is possible that it introduces a violation of CP symmetry similar to that observed in the quark sector. For Majorana-type neutrinos ( $\nu = \bar{\nu}$ ), two additional phases  $\alpha_{1,2}$  have to be included, and the mixing matrix (1.6) is modified accordingly:

$$U_{\text{Majorana}} = U \text{diag}(1, e^{i\alpha_1/2}, e^{i\alpha_2/2}). \quad (1.7)$$

$\alpha_1$  and  $\alpha_2$  cannot be detected in neutrino oscillations.

Assuming their mass eigenvalues are different ( $m_i \neq m_j$  for  $i \neq j$ ), the eigenstates  $|v_i\rangle$  will exhibit a different time evolution, which follows from applying the Schrödinger equation (using  $\hbar = 1$  and  $c = 1$ ):

$$|v_i(t)\rangle = e^{-iE_i t} |v_i\rangle, \quad (1.8)$$

$$\text{with } E_i = \sqrt{p_i^2 + m_i^2} \approx p + \frac{m_i^2}{2p} \approx E + \frac{m_i^2}{2E} \text{ for } p \gg m_i, \quad (1.9)$$

Due to these different phase factors, after a time  $t$  a formerly pure flavor eigenstate has evolved into

$$|v(t)\rangle = \sum_i U_{\alpha i} e^{-iE_i t} |v_i\rangle \stackrel{(1.5)}{=} \sum_{i,\beta} U_{\alpha i} U_{\beta i}^* e^{-iE_i t} |v_\beta\rangle. \quad (1.10)$$

At the distance  $L$  from its origin, the neutrino is detected in another weak interaction process, in which a charged lepton of type  $\ell_\beta$  is produced. The probability  $P(\alpha \rightarrow \beta; t) \equiv |\langle v_\beta | v(t) \rangle|^2$  of finding the neutrino which started in a particular flavor  $\alpha$  after a time  $t$  in the flavor  $\beta$  is given by

$$P(\alpha \rightarrow \beta; t) = \left| \sum_i U_{\alpha i} U_{\beta i}^* e^{-iE_i t} \right|^2 \quad (1.11)$$

$$= \sum_i |U_{\alpha i} U_{\beta i}^*|^2 + 2 \text{Re} \sum_{j>i} U_{\alpha i} U_{\alpha j}^* U_{\beta i}^* U_{\beta j} e^{-i(E_i - E_j)t}. \quad (1.12)$$

## 1 Introduction

For ultra-relativistic neutrinos, the flight time  $t$  corresponds to a distance  $L \approx t$ . Using eq. (1.9) the following relation can be derived:

$$(E_i - E_j)t \approx \frac{m_i^2 - m_j^2}{2} \cdot \frac{L}{E} \equiv \frac{\Delta m_{ij}^2}{2} \cdot \frac{L}{E}. \quad (1.13)$$

The first term in eq. (1.12) yields a time-averaged transition probability, while the second term varies periodically with  $t$  (or, correspondingly, with  $L/E$ ). Equation (1.13) shows that this oscillating behavior is possible only if at least one of the mass eigenvalues is non-zero. Since eq. (1.12) was derived under the premise of neutrino mixing, it implies that the lepton flavor number  $L_\alpha$  is not conserved.<sup>6</sup>

It is instructive (and useful for the analysis of many experimental results) to break down the above  $3 \times 3$  formalism to the  $2 \times 2$  case (*i. e.*, only one mixing angle  $\theta$  and no phase required):

$$\begin{pmatrix} \nu_\alpha \\ \nu_\beta \end{pmatrix} = \begin{pmatrix} \cos \theta & \sin \theta \\ -\sin \theta & \cos \theta \end{pmatrix} \begin{pmatrix} \nu_1 \\ \nu_2 \end{pmatrix}. \quad (1.14)$$

This gives an oscillation probability of

$$P(\alpha \rightarrow \beta) = \sin^2(2\theta) \sin^2\left(\frac{\Delta m^2 L}{4E}\right), \quad (1.15)$$

with  $\Delta m^2 := m_2^2 - m_1^2$ . The mixing angle  $\theta$  defines the amplitude of the oscillation, whereas  $\Delta m^2$  determines the oscillation frequency.

It should be noted that, different from the vacuum case discussed above, the propagation of neutrinos in matter is affected by elastic, coherent forward scattering. Neutrinos passing regions of variable electron density can therefore be subject to a resonant enhancement of the transformation probability. This is generally subsumed under the term ‘‘MSW effect’’, named after S. P. Mikheyev, A. Yu. Smirnov [Mik86] and L. Wolfenstein [Wol78]. It is particularly relevant for the description of solar neutrinos and their flavor oscillations. The associated processes can however not be treated in detail here.

Experiments searching for neutrino flavor oscillations make use of natural as well as of man-made neutrino sources:

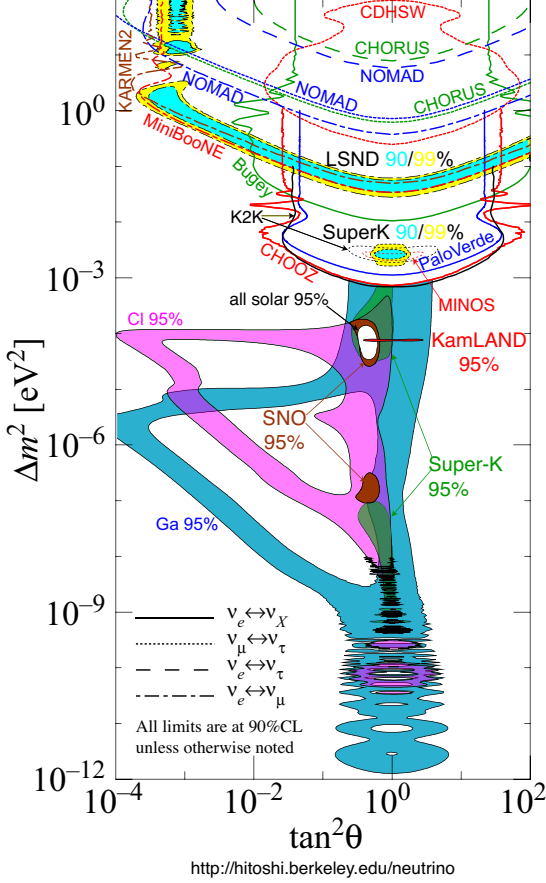
- $\nu_e/\bar{\nu}_e, \nu_\mu/\bar{\nu}_\mu$  created in collisions of high-energy cosmic rays with nuclei in the Earth’s atmosphere: Super-Kamiokande experiment [Fuk98a, Fuk98b, Ash04, Ash05];
- $\nu_e$  originating in nuclear fusion processes in the Sun’s interior: many radiochemical experiments since the late 1960s (for early results of the pioneering Homestake experiment see [Dav68, Bah68]), final confirmation of oscillations by the SNO experiment [Ahm02, Ahm04, Aha07];
- $\bar{\nu}_e$  emitted in  $\beta$ -decays of fission products in nuclear power reactors: *e. g.*, KamLAND experiment [Ara05];
- $\nu_\mu$  produced by directing a proton beam from a particle accelerator at a target: *e. g.*, K2K experiment [Ahn06].

Figure 1.2 presents an overview of a wealth of experimental results, covering various oscillation channels. A combined analysis of present data [PDG08] yields the following oscillation param-

<sup>6</sup>Lepton flavor conservation is not strictly demanded in the framework of the Standard Model, as no corresponding symmetry principle is known.

ters:

$$\begin{aligned}
 \sin^2(2\theta_{12}) &= 0.86_{-0.04}^{+0.03}, & \frac{\Delta m_{12}^2}{10^{-5} \text{eV}^2/c^4} &= 8.0 \pm 0.3, \\
 0.92 < \sin^2(2\theta_{23}) &\leq 1, & 1.9 < \frac{\Delta m_{23}^2}{10^{-3} \text{eV}^2/c^4} &< 3.0, \\
 \sin^2(2\theta_{13}) &< 0.19. & &
 \end{aligned} \tag{1.16}$$



**Figure 1.2:** Overview: current status of neutrino oscillation parameters (compiled by H. Murayama and published in [PDG08]). Results of experiments covering various channels ( $\nu_e \leftrightarrow \nu_x$ ,  $\nu_\mu \leftrightarrow \nu_\tau$ ,  $\nu_e \leftrightarrow \nu_\tau$ ,  $\nu_e \leftrightarrow \nu_\mu$ ) allow to address the different parameters of the mixing matrix  $U$ . A consistent overall picture emerges.

These results indicate that neutrinos have a small, but definitely non-zero rest mass, which means that the present description of neutrinos in the Standard Model is incomplete. The splittings between the masses are small, and  $m_3$  is clearly set off from the more closely spaced pair ( $m_1, m_2$ ). However, the relative ordering of ( $m_1, m_2$ ) and  $m_3$  remains to be determined.<sup>7</sup> At present, two scenarios usually denoted as normal and inverted hierarchy are possible (see figure 1.3). In case the smallest of the neutrino mass values is larger than about  $0.1 - 0.2 \text{ eV}/c^2$ , the splittings become negligible and one speaks of degenerate neutrino mass values  $m_1 \approx m_2 \approx m_3$  (compare also figure 1.4(a) further below).

Furthermore, the measured neutrino oscillation parameters demonstrate that, due to the strong mixing<sup>8</sup> of the mass eigenstates, the structure of the PMNS matrix differs from that of the CKM matrix for quarks.

<sup>7</sup>The ordering within the doublet ( $m_1, m_2$ ) can be fixed by an analysis of the solar neutrino oscillation data when taking into account the matter-induced MSW effect.

<sup>8</sup> $\theta_{12} \approx 32^\circ$  is large, and  $\theta_{23} \approx 45^\circ$  is even maximal.  $\theta_{13}$ , on the other hand, appears to be quite small.

## 1 Introduction

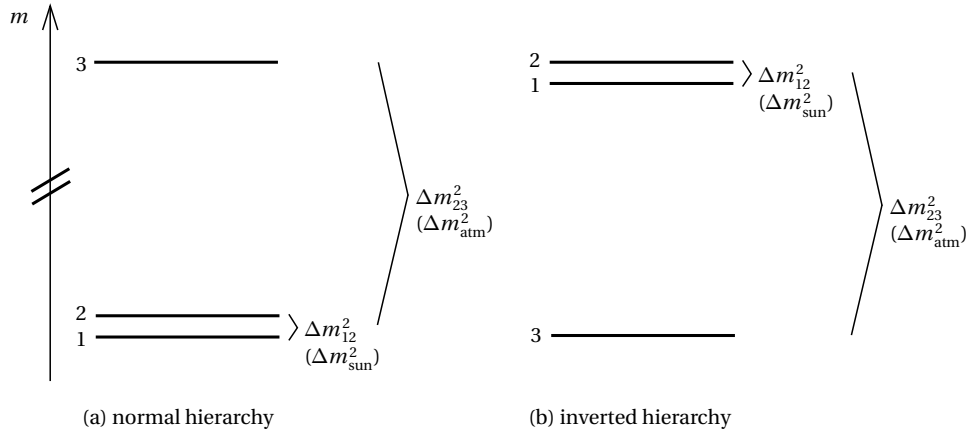


**Figure 1.3:** Sketch showing the arrangement of neutrino mass eigenvalues  $m(\nu_i)$  in normal (a) and inverted (b) hierarchy. The large splitting  $\Delta m_{23}^2$  (mainly from atmospheric neutrino oscillations) and the much smaller  $\Delta m_{12}^2$  (mainly from the solar neutrino oscillations) are also indicated.

Many different ways of accommodating non-zero neutrino masses in extensions of the Standard Model are being explored. The attempts of finding a suitable model are challenged by the need to explain the smallness of neutrino masses as compared to those of the other fermions.

A straightforward way to generate neutrino masses is to add right-handed neutrinos to the Standard Model, which yields a so-called Dirac mass term based on the Yukawa couplings mentioned above:

$$\mathcal{L}_D = -m_D \bar{\nu}_R \nu_L + h.c. \quad (1.17)$$

However, this method is rather unsatisfactory, as the parameter  $m_D$  can be freely chosen and is not constrained by any mechanism forcing the neutrino masses to be so tiny.

Should neutrinos turn out to be their own antiparticles (*i. e.*, Majorana-type neutrinos: see [Maj37]), which is in principle allowed since no quantum numbers would be violated, additional mass terms are available:

$$\mathcal{L}_M = -M_R \bar{\nu}_R^c \nu_R + h.c., \quad (1.18)$$

where the constant  $M_R$  can be chosen to be very large (*e. g.*, of the order of  $10^{15}$  eV/ $c^2$ ). In the so-called *seesaw mechanism* of type I, the combination of Dirac and Majorana mass terms allows to construct a scenario in which a super-massive Majorana neutrino with  $m_{\nu 1} \approx M_R$  and a light species with  $m_{\nu 2} \approx m_D^2/M_R$  exist. Predictions for the light neutrino masses from the seesaw mechanism of type I are rather model-dependent, but generally favor hierarchical neutrino mass scenarios. In the seesaw mechanism of type II the small neutrino masses are generated by introducing a Higgs-triplet  $\Delta$  (see for example [Ott08]) in addition to the Higgs-doublet  $\phi$  which is usually employed to generate fermion masses by spontaneous symmetry breaking. This second kind of mechanism favors degenerate neutrino masses  $m_1 \approx m_2 \approx m_3$ . Neutrino mass measurements with sufficient sensitivity to discriminate between the hierarchical and the degenerate case (like for example anticipated for the the upcoming KATRIN experiment) would thus allow to distinguish various theoretical concepts and even rule out a certain fraction of models.

## 1.3 The role of neutrinos in astrophysics and cosmology

The cosmic microwave background (CMB) radiation, which was discovered by A. A. Penzias and R. W. Wilson in 1965 [Pen65], forms one of the pillars of evidence for the so-called “Big Bang” model of cosmology. It states that the Universe had a very hot and dense origin, from which it cooled and expanded into its present state. One prediction of the Big Bang theory is that a large number of neutrinos should have been created by frequent weak interactions at high temperatures in the early Universe. These primordial neutrinos ceased to be in thermal equilibrium with the other particle species when their interaction rate  $\Gamma_\nu(T)$  became smaller than the expansion rate of the Universe, which is given by the Hubble parameter  $H(T)$ . This happened at a temperature of  $T \approx 10^{10}$  K ( $E \approx 1$  MeV), reached after about 1 s. The present-day density  $n_{\nu 0}$  of these *relic neutrinos* is related to the photon density  $n_{\gamma 0}$  of the cosmic microwave background:

$$\begin{aligned} n_{\nu 0} &= \frac{3}{4} \frac{g_\nu}{g_\gamma} \frac{4}{11} n_{\gamma 0}, \\ &\approx \frac{9}{11} \cdot 411 \text{ cm}^{-3} \approx 336 \text{ cm}^{-3} \end{aligned} \quad (1.19)$$

which makes neutrinos the second-most abundant particle species in the Universe right after the photons. Here,  $g_\nu = 6$  and  $g_\gamma = 2$  denote the relativistic degrees of freedom for three flavors of neutrinos and for photons, respectively.

Likewise, the present-day temperature of this “cosmic neutrino background” can be calculated:

$$T_{\nu 0} = T_{\gamma 0} \left( \frac{4}{11} \right)^{1/3}. \quad (1.20)$$

Inserting the measured value of the CMB temperature,  $T_{\gamma 0} = (2.725 \pm 0.001)$  K [Fix02], one arrives at  $T_{\nu 0} \approx 1.95$  K, which corresponds to thermal energies in the sub-meV range. At such low energies, the neutrino interaction cross sections are extremely small<sup>9</sup>, and therefore the chances of a direct experimental detection of the cosmic neutrino background are dismal.

However, neutrinos contribute to the total energy density  $\Omega_{\text{tot}}$  of the Universe. In the current Standard or Concordance Model of cosmology,  $\Omega_{\text{tot}}$  is composed of the following components:

$$\begin{aligned} \Omega_{\text{tot}} &= \Omega_\Lambda + \Omega_m + \Omega_r + \Omega_k \\ &\quad \text{dark energy} \quad \text{matter} \quad \text{radiation} \quad \text{curvature} \\ &\approx 0.76 + 0.24 + \mathcal{O}(10^{-5}) + 0 \end{aligned} \quad (1.21)$$

where the matter contribution  $\Omega_m$  contains cold dark matter ( $\Omega_{\text{cdm}} \approx 0.20$ ), baryonic matter ( $\Omega_b \approx 0.04$ ) and neutrinos ( $\Omega_\nu$ ). Modern cosmology and astrophysics allow to determine most parameters of the Concordance Model to a good accuracy (see table 1.2). In particular, recent precise measurements of the absolute temperature of the cosmic microwave background and of its small anisotropies with the COBE and WMAP satellites<sup>10</sup>, together with a wealth of other observational data, caused a boost in this field of research.

A big handicap of the Concordance Model, however, is that so little is known about the nature of its constituents. The origin of dark energy, which is supposed to fill up about 3/4 of  $\Omega_{\text{tot}}$  today, is completely open. The composition of dark matter has also remained a field of speculation, with

<sup>9</sup>For example,  $\sigma \approx 10^{-54}$  cm<sup>2</sup> both for the charged current reaction  $\nu_e + n \rightarrow p + e^-$  and for scattering  $\nu + e \rightarrow \nu + e$ .

<sup>10</sup>A future satellite mission, PLANCK, will reach an even higher precision than its predecessors COBE (Cosmic Microwave Background Explorer, see <http://lambda.gsfc.nasa.gov/product/cobe/>) and WMAP (Wilkinson Microwave Anisotropy Probe, see <http://map.gsfc.nasa.gov/>).

## 1 Introduction

**Table 1.2:** Key parameters of the Concordance Model of cosmology. All values are taken from [Dun09], except for  $\Omega_r h^2$  which stems from [PDG08]. While the radiation energy density gives a small, but measurable contribution, the curvature term  $\Omega_k$  included in eq. (1.21) is very close to zero, and in many models it is assumed to be exactly zero. Precise measurements of the position of the first peak in the CMB anisotropy power spectrum combined with constraints on the Hubble parameter from other measurements allow to determine the total energy density as  $\Omega_{\text{tot}} = 1.011 \pm 0.012$  [PDG08], which means that the Universe is indeed flat.

parameter	value
$H_0$	$71.9^{+2.6}_{-2.7} \frac{\text{km}}{\text{s}\cdot\text{Mpc}}$
$\Rightarrow h^2$	$\approx 0.5$ (see eq. (1.23))
$\Omega_\Lambda$	$0.742 \pm 0.030$
$\Omega_m$	$0.258 \pm 0.030$
$\Omega_b h^2$	$0.0227 \pm 0.0006$
$\Omega_r h^2$	$2.47 \cdot 10^{-5}$

several theoretical models in place, but none of them experimentally confirmed up to now. Together with the small amount of baryonic matter and the photons forming the cosmic microwave background radiation, neutrinos make up the part of the energy density that can be identified with known particles (compare figure 1.4).

For neutrinos of masses in the range between  $\sim 5 \cdot 10^{-4} \text{ eV}/c^2$  and  $1 \text{ MeV}/c^2$  the neutrino energy density is usually parameterized [Les06] as

$$\Omega_\nu = \frac{\rho_\nu}{\rho_{\text{crit}}} = \frac{\sum_i m(\nu_i)}{93.1 h^2 \text{ eV}/c^2}, \quad (1.22)$$

with the reduced Hubble parameter

$$h = \frac{H_0}{100 \frac{\text{km}}{\text{s}\cdot\text{Mpc}}} \quad \text{with } h^2 \approx 0.5 \quad (\text{see table 1.2}) \quad (1.23)$$

and the critical density

$$\rho_{\text{crit}} = \frac{3H_0^2}{8\pi G_N} = 1.88 \cdot 10^{-29} h^2 \frac{\text{g}}{\text{cm}^3} = 10.5 h^2 \frac{\text{keV}}{\text{cm}^3}. \quad (1.24)$$

Assuming degenerate neutrinos with  $\sum m(\nu_i) = 6 \text{ eV}/c^2$  (according to the present upper limits on  $m(\nu_e)$  from laboratory experiments, compare eq. (1.31)) yields an upper limit of  $\Omega_\nu < 0.13$ . Combining this with the lower limit of  $\Omega_\nu \gtrsim 0.001$  which can be derived from the Super-Kamiokande results on atmospheric neutrino oscillations (see eq. (1.16)), the experimentally allowed range of  $\Omega_\nu$  stretches over two orders of magnitude. For comparison, the sensitivity aimed for with the KATRIN experiment corresponds to  $\Omega_\nu \approx 0.013$  (again, assuming degenerate neutrinos with  $m_1 \approx m_2 \approx m_3 = 0.2 \text{ eV}/c^2$ ).

On the other hand, astrophysical observations now reach a level of precision that permits to deduce limits on the neutrino mass from their data. Such cosmological bounds on neutrino masses, however, are strongly coupled to other parameters used for the fine-tuning of the cosmological models, as will be discussed in section 1.4.1. Therefore, improving the results of laboratory measurements of the neutrino mass would provide an important feedback to astrophysics, with the possibility to break the degeneracy which presently exists for example between  $M_\nu = \sum m(\nu_i)$  and the equation of state parameter  $w$  of the dark energy (see, *e. g.*, [Han05, Ser07, Kri08]).

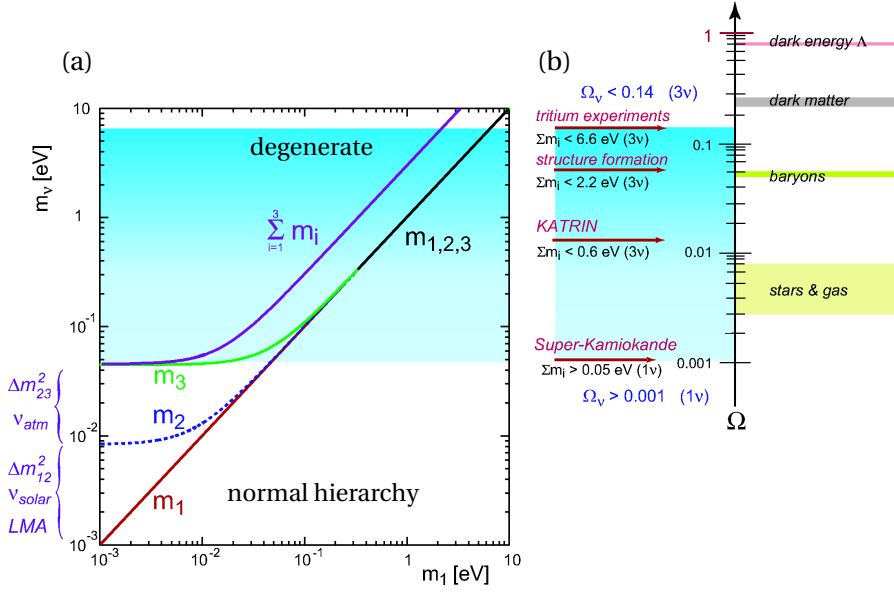


**Figure 1.4:** (a) Neutrino mass eigenvalues  $m_1$ ,  $m_2$  and  $m_3$  as a function of  $m_1$  in the hierarchical and the degenerate scenario. The neutrino mixing parameters according to eq. (1.16) obtained from oscillation experiments are taken into account. The KATRIN sensitivity roughly marks the border between the hierarchical and the degenerate case. (b) Composition of the total energy density  $\Omega_{tot}$  of the Universe according to the Concordance Model of cosmology. Present bounds on the neutrino contribution  $\Omega_\nu$ , from laboratory experiments (upper limit) and from neutrino oscillations (lower limit) cover two orders of magnitude (cyan band).

## 1.4 Methods to determine the absolute neutrino mass scale

In the following sections, principal methods to address the absolute neutrino mass scale shall be introduced. Apart from the cosmological limits, direct kinematic measurements and the search for neutrinoless double  $\beta$ -decay will be discussed.

### 1.4.1 Cosmological bounds on neutrino mass

Cosmological observations allow to constrain the sum  $M_\nu = \sum m(\nu_i)$  of neutrino masses, which are generally assumed to be degenerate. There are two principal ways of deducing  $M_\nu$  from cosmological data:

- Massive neutrinos modify the CMB temperature anisotropy spectrum. The effect is an indirect one and rather weak. Usually, a combination of several data sets is necessary to circumvent a degeneration with the values of other cosmological parameters. With the enhanced sensitivity of the WMAP 5-year data, it was possible to give an upper limit of  $M_\nu < 1.3 \text{ eV}/c^2$  (95% C. L.) [Kom09] based on the CMB temperature anisotropy spectrum alone, which improves by a factor of 2 by adding data from supernovae redshift surveys and from observations of baryon acoustic oscillations in large-scale structure surveys to the analysis.
- Finite neutrino masses also influence the power spectrum of the matter distribution in the Universe. This can be explained by the so-called “free-streaming” of neutrinos: they do not contribute to the formation and enhancement of structure on scales smaller than their

## 1 Introduction

particle horizon<sup>11</sup> at the time they turn non-relativistic. It can be shown [Hu98, Teg04b, Les06] that at small scales (*i. e.*, large wavenumbers  $k$ ) a non-vanishing neutrino fraction

$$f_\nu = \frac{\Omega_\nu}{\Omega_m} = \frac{\rho_\nu}{\rho_{\text{cdm}} + \rho_b + \rho_\nu}, \quad (1.25)$$

which depends on the neutrino mass, produces a damping of the matter power spectrum  $P(k; f_\nu)$  with respect to the  $f_\nu = 0$  case  $P(k; 0)$  of approximately

$$\frac{P(k; f_\nu)}{P(k; 0)} \approx e^{-8f_\nu}. \quad (1.26)$$

The sensitivity of this method is illustrated in figure 1.5. Measurements of the matter power spectrum can be obtained by galaxy redshift surveys, like for example the Sloan Digital Sky Survey (SDSS), and by several other observations (*e. g.*, galaxy cluster abundance, weak gravitational lensing, Lyman- $\alpha$  forest). The neutrino mass is then deduced from a comparison with computer models of structure formation (see figure 1.6). Present upper limits cover the range between  $M_\nu < 0.2 \text{ eV}/c^2$  and  $1 \text{ eV}/c^2$  [PDG08, Les06], and a sensitivity of  $M_\nu = 0.1 \text{ eV}/c^2$  or even below is expected for refined measurements<sup>12</sup> in the near future.

### 1.4.2 Direct kinematic methods

Direct methods to determine neutrino masses are essentially model-independent, since they are mainly based on the relativistic energy-momentum relation

$$E^2 = p^2 c^2 + m^2 c^4 \quad (1.27)$$

and other well-known principles of kinematics.<sup>13</sup>

Usually, the kinematic variables of charged leptons created in weak interactions involving neutrinos are measured. Therefore, the observable in such experiments is a weighted sum over the squared neutrino mass eigenvalues, according to the mixing matrix  $U$  (eq. (1.6)):

$$m^2(\nu_\ell) := \sum_j |U_{\ell j}|^2 m^2(\nu_j), \quad \ell = e, \mu, \tau \quad (1.28)$$

So far only upper bounds have been found. For  $m(\nu_\mu)$  and  $m(\nu_\tau)$ , these were derived from pion and tau decay, respectively:

$$m(\nu_\mu) < 0.19 \text{ MeV}/c^2 \quad (90\% \text{ C.L.}) \quad [\text{Ass96, PDG08}] \quad (1.29)$$

$$m(\nu_\tau) < 18.2 \text{ MeV}/c^2 \quad (95\% \text{ C.L.}) \quad [\text{Bar98}] \quad (1.30)$$

In comparison, the present upper limit on  $m(\nu_e)$  derived from the precise measurement of the highest electron energies in the tritium  $\beta$ -spectrum is more stringent by about five (resp. seven) orders of magnitude [PDG08]:

$$m(\nu_e) < 2 \text{ eV}/c^2. \quad (1.31)$$

<sup>11</sup>Here, the ‘‘horizon’’ is defined as the distance a particle can travel between given times  $t_i$  and  $t_f$ .

<sup>12</sup>Upcoming observational tools are the PLANCK satellite (<http://www.rssd.esa.int/index.php?project=PLANCK>) and the Large Synoptic Survey Telescope (LSST, <http://www.lsst.org/>).

<sup>13</sup>This distinguishes the direct measurements from the sensitive, but rather model-dependent methods (cosmological observations, search for  $0\nu\beta\beta$ ) presented in sections 1.4.1 and 1.4.3.

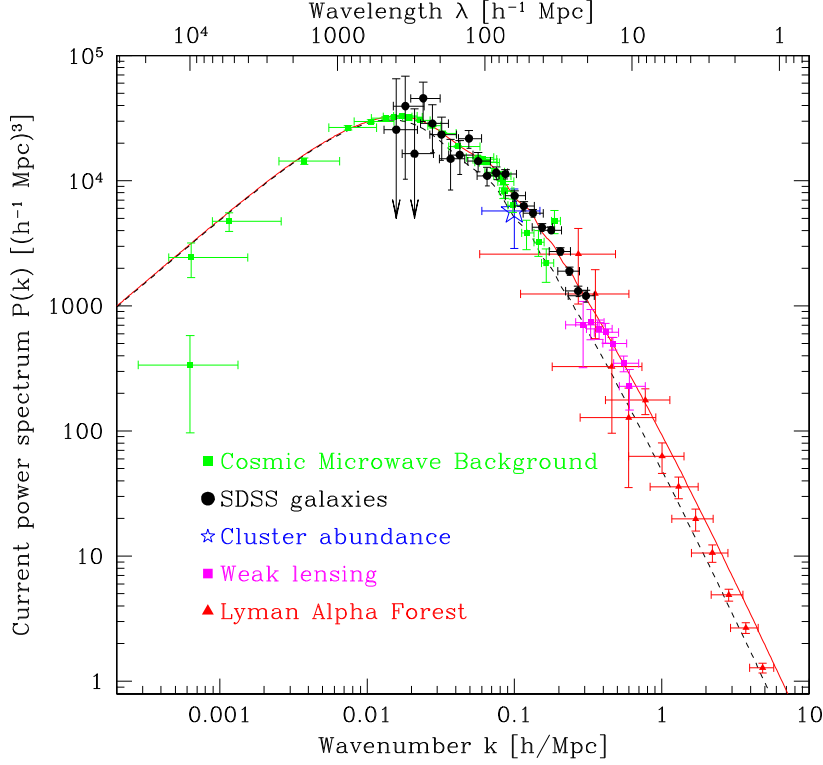


**Figure 1.5:** Power spectrum  $P(k)$  of the matter distribution in the Universe (from [Teg04a]). This plot spanning five decades in the wavenumber  $k$  (or the length scale  $\lambda$ ) comprises data from various observations. The solid curve indicates a model with matter density  $\Omega_m = 0.28$  and baryon fraction  $f_b = \Omega_b/\Omega_m = 0.16$ . The dashed curve incorporates non-zero neutrino masses. Here,  $M_\nu \equiv \sum m(\nu_i) = 1 \text{ eV}/c^2$  was chosen, which according to eqs. (1.22), (1.25) and (1.26) roughly halves the power  $P(k)$  at the small scales  $\lambda$  where neutrinos most strongly influence the matter distribution.

This evaluation is based on the results of the neutrino mass experiments at Troitsk and Mainz, which both use the MAC-E filter technology (see section 2.2) that will also be employed at the KATRIN experiment. In detail, their findings are:

$$\begin{aligned} m^2(\nu_e) &= (-0.6 \pm 2.2 \pm 2.1) \text{ eV}^2/c^4, \\ m(\nu_e) &< 2.3 \text{ eV}/c^2 \end{aligned} \quad (\text{Mainz, [Kra05]}) \quad (1.32)$$

$$\begin{aligned} m^2(\nu_e) &= (-2.3 \pm 2.5 \pm 2.0) \text{ eV}^2/c^4, \\ m(\nu_e) &< 2.1 \text{ eV}/c^2 \end{aligned} \quad (\text{Troitsk}^{14}, [\text{Lob03}]) \quad (1.33)$$

Out of the three cases mentioned above, the electron-based neutrino mass search has the highest potential for development. Apart from tritium,  $^{187}\text{Re}$  qualifies as a suitable  $\beta$ -emitter for neutrino mass measurements. It possesses an extremely low endpoint energy of 2.47 keV, which

<sup>14</sup>The measurements of the Troitsk experiment exhibit an anomalous feature in the form of a step-like increase in the integrated energy spectrum, which can be interpreted as an additional line on top of the tritium  $\beta$ -spectrum a few eV below its endpoint. Physically meaningful results for  $m^2(\nu_e)$  can only be obtained by taking this anomaly into account on a run-by-run basis via two additional parameters of the fit function. The origin of this anomaly, which did not occur in the measurements of the Mainz group, is still unclear. Therefore, a direct comparison of the two results is difficult.

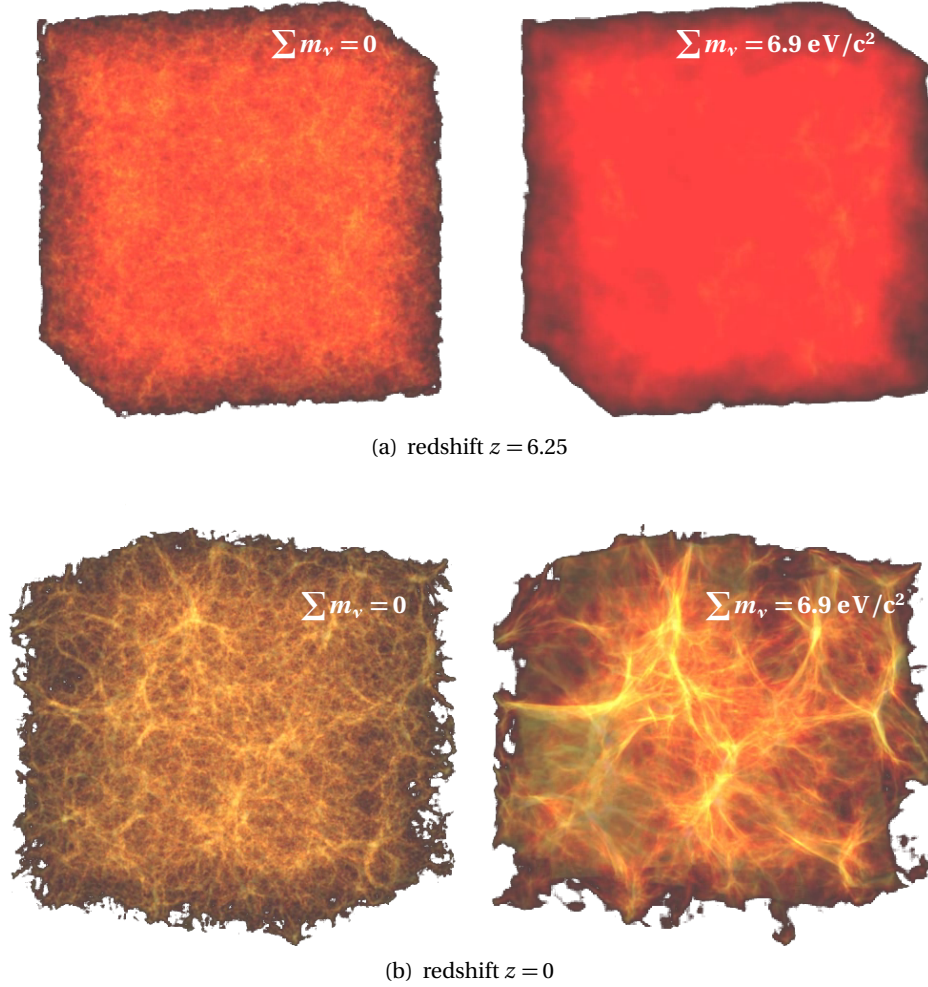


**Figure 1.6:** Computer simulations: neutrino mass and structure formation (T. Haugbølle, [Hau08]). Left-hand panel: dark matter density field in a  $\Lambda$ CDM model with zero neutrino mass. Right-hand panel: same model, however with  $\sum m_\nu = 6.9 \text{ eV}/c^2$ , corresponding to the present upper limit from tritium  $\beta$ -decay experiments. The pictures show one octant of a simulation done for a box size of 512 Mpc. The differences in the evolution of structures on smaller scales for massless and massive neutrinos is clearly visible between the snapshots taken at a redshift of (a)  $z = 6.25$  and (b)  $z = 0$ . Due to their free-streaming, massive neutrinos contribute to a smearing of small-scale structure, manifested in the pictures on the right-hand side in a softening of the filaments and an enhancement of the size of voids. By comparing these numerical results with observations the neutrino mass can be deduced.

helps to maximize the relative fraction of interesting events close to the endpoint of the spectrum (where the sensitivity on  $m(\nu_e)$  is highest). Due to its half-life of  $4.3 \cdot 10^{10} \text{ a}$  it can only be used with the bolometer technique, which combines source and detector. With a present upper limit of  $m(\nu_e < 15 \text{ eV}/c^2)$  (90% C. L.) [Sis04], microbolometer-based results are not yet competitive with what has been achieved in tritium  $\beta$ -decay studies. However, the two-staged MARE project [Mon06] aims for a sensitivity corresponding to that of present tritium experiments (eq. 1.31), with the prospect of further improvement by scaling up the number of bolometer crystals and optimizing the experimental technique in future developments.

For tritium  $\beta$ -decay, a sub-eV sensitivity is now within reach. A detailed description of the mea-

surement method and its realization at KATRIN is given in chapter 2.

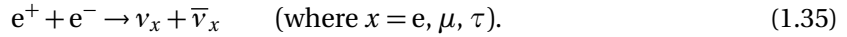
### Supernova neutrinos: time of flight measurements

Another method to study neutrino masses based on purely kinematic grounds consists of the observation of energy-dependent time-of-flight differences for neutrinos emitted in a nearby supernova explosion. Figure 1.7 presents collected neutrino events measured with three experiments (Kamiokande II, IMB and Baksan) for SN 1987A at a distance of about  $d \approx 168\,000$  ly in the Large Magellanic Cloud. To date, this represents the only occasion such a neutrino burst from a supernova was detected.

Supernovae of type II are extremely powerful neutrino sources. If a neutron star is formed in the process<sup>15</sup>, the neutronization of the core matter creates neutrinos through the reaction



However, the bulk part stems from the subsequent cooling of the neutron star, which dominantly takes place via thermal pair production processes<sup>16</sup> of the type



Although a huge number of about  $10^{57}$  neutrinos are emitted, even the neutrino signal from a supernova explosion in the direct vicinity of our Milky Way is hard to detect since the total flux is distributed on the surface of a sphere, and it is therefore continuously diluted by the expansion of the shell. Once this shell with a thickness of a few light seconds reaches a radius of 168 000 light years, “only”  $10^{14}$  neutrinos per square meter remain. Out of these, about 25 caused an event measured in one of the three detectors. They represent the first neutrinos to be observed from an astrophysical source other than the Sun.<sup>17</sup>

Assuming that neutrinos with an energy bandwidth  $[E_{\nu \text{ min}}, E_{\nu \text{ max}}]$  are emitted from a source at a distance  $d$ , a neutrino rest mass can thus be inferred from the spread of arrival times (see, for example, [Zub04]). The time of flight  $T_{\text{flight}}$  corresponds to the difference between the time of emission,  $t_{\text{emis}}$ , and the time of observation at Earth,  $t_{\text{obs}}$ , and can be expressed in terms of the neutrino mass and energy in the following way:

$$\begin{aligned} T_{\text{flight}} = t_{\text{obs}} - t_{\text{emis}} &= \frac{d}{v} = \frac{d}{c} \frac{E_\nu}{p_\nu c} \\ &= \frac{d}{c} \frac{E_\nu}{\sqrt{E_\nu^2 - m_\nu^2 c^4}} \approx \underbrace{\frac{d}{c}}_{=: t_0} \left( 1 + \frac{m_\nu^2 c^4}{2E_\nu^2} \right). \end{aligned} \quad (1.36)$$

For  $m_\nu = 0$ , this reduces to  $T_{\text{flight}} = t_0 = d/c$ . If  $m_\nu > 0$ , however, neutrinos with higher energies are expected to arrive marginally earlier than those with lower energies.

<sup>15</sup>About two years after the observation of SN 1987A, a neutron star was indeed found at the corresponding location in the form of a pulsar (see, for example, [Kri89]).

<sup>16</sup>The efficiency of cooling by photon emission is very low due to the very short mean free path of photons in the dense matter of the neutron star.

<sup>17</sup>Certainly, this has to be counted among one of the highlights in observational astrophysics (particularly in neutrino astrophysics), and the experimental efforts which led to the observation were appreciated by awarding part of the 2002 Nobel Prize in physics to M. Koshiba (Kamiokande/SuperKamiokande) for “for pioneering contributions to astrophysics, in particular for the detection of cosmic neutrinos” (see [http://nobelprize.org/nobel\\_prizes/physics/laureates/2002/](http://nobelprize.org/nobel_prizes/physics/laureates/2002/) for further information).

## 1 Introduction

The difference in arrival time on Earth for two neutrinos with energies  $E_1$  and  $E_2$  is given by

$$\begin{aligned} \Delta t_{\text{obs}} &= t_{\text{obs},2} - t_{\text{obs},1} = T_{\text{flight},2} - T_{\text{flight},1} + \underbrace{\Delta t_{\text{emis}}}_{\text{unknown, model dependent}} \\ &= \frac{d}{2c} m_{\nu}^2 c^4 \left( \frac{1}{E_2^2} - \frac{1}{E_1^2} \right) + \Delta t_{\text{emis}}. \end{aligned} \quad (1.37)$$

$\Delta t_{\text{obs}}$ ,  $d$  and  $E_{1,2}$  are measured, while  $\Delta t_{\text{emis}}$  and  $m_{\nu}$  are unknown.

Present experimental data are consistent with zero neutrino mass. Figure 1.7 shows that the detection interval of neutrinos associated with SN 1987A was about 13 s long<sup>18</sup>, and that the measured energies ranged between 10 and 40 MeV. A naive estimate using eq. (1.37) and  $\Delta t_{\text{emis}} = 0$  gives<sup>19</sup>  $m_{\bar{\nu}_e} \lesssim 20 \text{ eV}/c^2$ . The obtained upper bounds are influenced by the assumptions regarding reasonable emission intervals  $\Delta t_{\text{emis}}$  and furthermore depend on the neutrino events selected for the evaluation. In a refined analysis [Lor02] the upper limit on  $m_{\bar{\nu}_e}$  was improved to

$$m_{\bar{\nu}_e} < 5.7 \text{ eV}/c^2 \quad (95\% \text{ C.L.}). \quad (1.38)$$

It is anticipated that a future nearby core-collapse supernova explosion seen by today's detectors with better sensitivity (*e. g.*, SuperKamiokande, SNO+) would yield a wealth of further information – not only regarding the rest mass of the neutrino, but also concerning other properties like for example its lifetime, magnetic moment or electric charge.

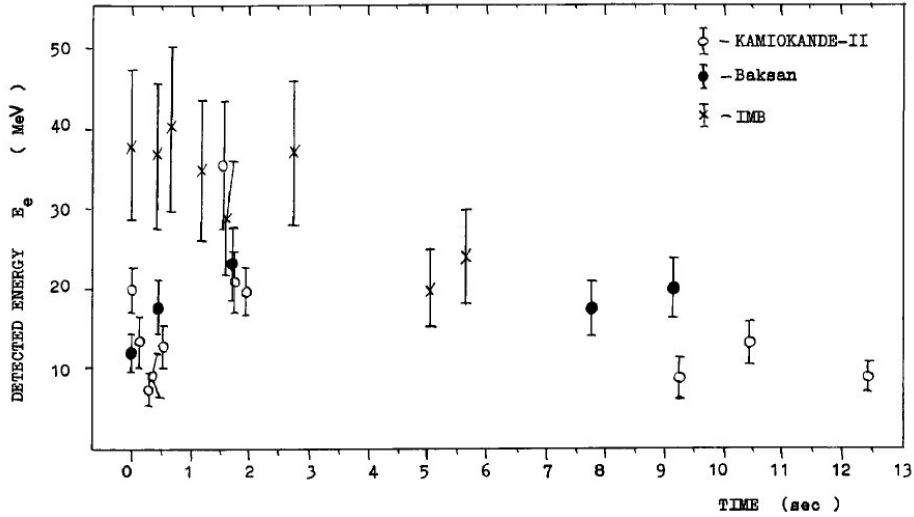


**Figure 1.7:** Neutrino burst from the supernova SN 1987A [Ale88]. The plot includes data from three experiments: the two water Cherenkov detectors Kamiokande II (Kamioka mine, Japan) and Irvine-Michigan-Brookhaven (IMB, Ohio, USA), and the Baksan underground scintillation telescope.

### 1.4.3 Neutrinoless double beta decay

The possibility that a nucleus might be subject to a double  $\beta$ -decay was first proposed by M. Goeppert-Mayer in 1935 [Goe35]. Since this represents a second-order process of the weak inter-

<sup>18</sup>When compared to the overall time of flight  $t_0 = \frac{d}{c} \approx 5 \cdot 10^{12} \text{ s}$  determined by the distance of  $d \approx 1.68 \cdot 10^5 \text{ ly}$  travelled by the neutrinos, the smallness of the observed spread of arrival times  $\Delta t_{\text{obs}}$  thus impressively underlines the subtlety of neutrino masses.

<sup>19</sup>As the detected neutrinos were predominantly of the type  $\bar{\nu}_e$ , the estimate yields an upper limit on the mass of the electron antineutrino.

action, half-lives are expected to be very long (of the order of  $10^{20}$  a or even more). In the so-called two-neutrino double  $\beta$ -decay, the nucleus undergoes two  $\beta$ -disintegrations at a time and emits two electrons and two neutrinos. This form of double  $\beta$ -decay ( $2\nu\beta\beta$ ) does not carry information on the neutrino mass and conserves lepton number. The process was first observed for the isotope  $^{82}\text{Se}$  [Ell87].

However, in a special case of double  $\beta$ -decay, a virtual neutrino is exchanged and no neutrino is emitted ( $0\nu\beta\beta$ , first mentioned by W. H. Furry in 1939 [Fur39]). This process violates lepton number by two units. The decay scheme of  $0\nu\beta\beta$  can be decomposed into two steps (Racah sequence):

$$\begin{aligned} (Z, A) &\rightarrow (Z-1, A) + e^- + (\bar{\nu}_e)_R, \\ (Z-1, A) &+ (\nu_e)_L \rightarrow (Z-2, A) + e^- \end{aligned} \quad (1.39)$$

Since the right-handed antineutrino  $(\bar{\nu}_e)_R$  emitted in the first interaction step has to be absorbed in the second step as a left-handed neutrino  $(\nu_e)_L$ , for  $0\nu\beta\beta$  to occur neutrinos are required to be of Majorana type. Furthermore, only massive neutrinos can change helicity<sup>20</sup>, with the probability of the neutrino to be found in the “wrong” helicity state being proportional to  $(m_\nu/E_\nu)^2$ .

The half life  $T_{1/2}^{0\nu}$  of neutrinoless double  $\beta$ -decay is related to the so-called effective Majorana neutrino mass  $m_{ee}^\nu$  (see eq. (1.43) below) via

$$\left(T_{1/2}^{0\nu}\right)^{-1} = G^{0\nu} |\mathcal{M}^{0\nu}|^2 \left(\frac{m_{ee}^\nu}{m_e}\right)^2, \quad (1.40)$$

where  $G^{0\nu}$  is the phase space integral for the two electrons and  $\mathcal{M}^{0\nu}$  is the nuclear matrix element. Provided that the latter can be calculated with sufficient accuracy using theoretical models, the value of  $m_{ee}^\nu$  can thus be derived from a measured decay rate for  $0\nu\beta\beta$ . In the absence of a detected signal, a lower limit on the half life  $T_{1/2}^{0\nu}$  transforms into an upper limit on the neutrino mass.

The highest sensitivity to date has been achieved by the Heidelberg-Moscow experiment searching for  $0\nu\beta\beta$ -decay in  $^{76}\text{Ge}$ . In 2001, the collaboration published an upper bound on the effective Majorana neutrino mass [Kla01] of

$$m_{ee}^\nu < 0.35 \text{ eV}/c^2 \quad (90\% \text{ C. L.}). \quad (1.41)$$

Using additional data, a new calibration and a refined analysis, a subgroup of the collaboration found evidence [Kla04] for a signal at the right decay energy with  $4.2\sigma$  significance, from which they deduced an effective Majorana neutrino mass in the range of

$$0.1 \text{ eV}/c^2 \leq m_{ee}^\nu \leq 0.9 \text{ eV}/c^2, \quad (1.42)$$

with a best-fit value of  $m_{ee}^\nu = 0.44 \text{ eV}/c^2$ . The large uncertainties are mainly due to differing values of the nuclear matrix element obtained from various calculations. Although the significance could in the meantime be increased to  $6\sigma$  [Kla06], the claim failed to convince parts of the community, and the test of the present evidence by forthcoming experiments<sup>21</sup> is eagerly awaited.

<sup>20</sup>In principle, contributions of right-handed currents “ $V+A$ ” in addition to the standard “ $V-A$ ” interaction might also provide helicity matching. This scenario shall however not be treated here. Likewise, alternative decay schemes associated for example with the emission of a majoron particle (see for example [Zub04]) cannot be discussed here.

<sup>21</sup>For example, GERDA, CUORE, Nemo/SuperNemo, EXO, Majorana and SNO+ are among the next generation of  $0\nu\beta\beta$  experiments expected to probe Majorana neutrino masses with increased sensitivity.

### Complementarity of neutrino mass determinations using single and double $\beta$ -decay

The observable  $m_{ee}^{\nu}$  in  $0\nu\beta\beta$ -decay is given by a coherent sum over all neutrino mass eigenvalues  $m_j$  and can be expressed [Ott08] in terms of the mixing parameters  $\theta_{12}$ ,  $\theta_{23}$ ,  $\theta_{13}$ ,  $\delta$  and  $\alpha_{1,2}$  from eq. (1.6):

$$\begin{aligned} m_{ee}^{\nu} &:= \left| \sum_j U_{ej}^2 m_j \right| \\ &= \left| |U_{e1}|^2 m_1 + |U_{e2}|^2 e^{i\alpha_1} m_2 + |U_{e3}|^2 e^{i\alpha_2} m_3 \right| \\ &= \left| (m_1 \cos^2 \theta_{12} + m_2 e^{i\alpha_1} \sin^2 \theta_{12}) \cos^2 \theta_{13} + m_3 e^{i(\alpha_2+2\delta)} \sin^2 \theta_{13} \right| \end{aligned} \quad (1.43)$$

This parameterization shows that the Majorana phases  $\alpha_{1,2}$  entering the summation can lead to a (partial) cancellation of terms in  $m_{ee}^{\nu}$ , a feature that yields the key difference to the observable  $m(\nu_e)$  in kinematical neutrino mass searches (see section 1.4.2 and compare figure 1.8). In particular, the term containing  $m_3$  can be neglected for degenerate masses or inverse hierarchy (*i. e.*,  $m_3 \ll m_1, m_2$ ) since  $\theta_{13}$  is small. In either of the two scenarios,  $m_1$  and  $m_2$  are about equal, and a destructive phase  $\alpha_1 \approx \pi$  might yield a strong cancellation effect.

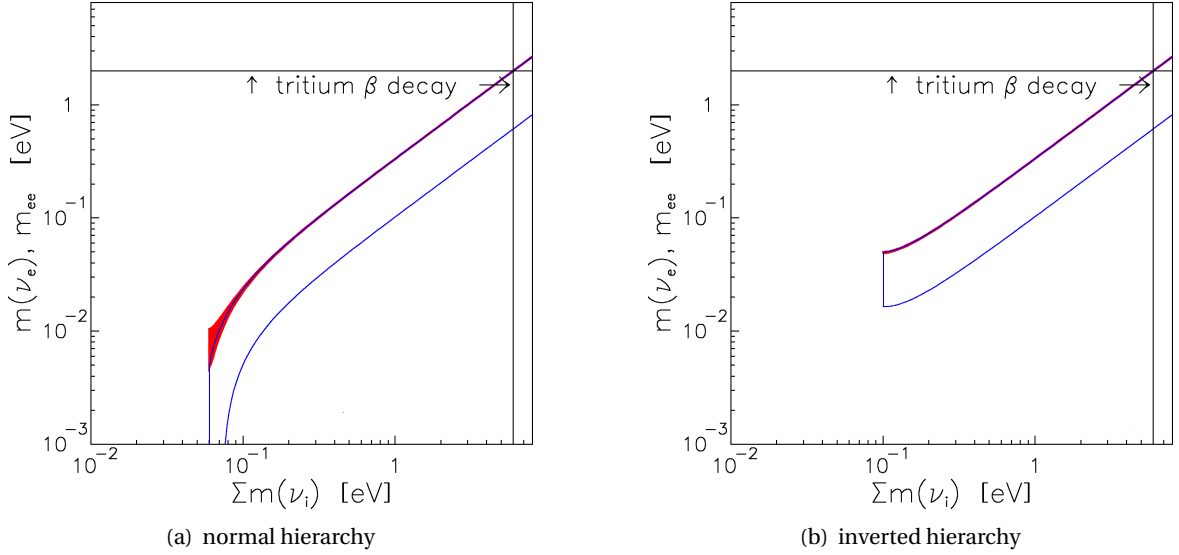


**Figure 1.8:** Comparison of the neutrino mass observables  $m_{ee}^{\nu}$  (neutrinoless double  $\beta$ -decay, blue open band) and  $m(\nu_e)$  (single  $\beta$ -decay, red solid band) [Ott08]. Two scenarios are considered: (a) normal hierarchy and (b) inverted hierarchy. The correlation of both observables with the cosmologically relevant sum of neutrino mass eigenvalues  $\sum m(\nu_i)$  is shown together with the present upper limit from the Mainz and Troitsk tritium  $\beta$ -decay experiments. The width of the bands reflects experimental uncertainties of the mixing angles as well as the unknown phases  $\alpha_1$ ,  $(\alpha_2 + 2\delta)$  in entering the expression for  $m_{ee}^{\nu}$  (eq. (1.43)). Further uncertainties regarding  $m_{ee}^{\nu}$  which arise from the model-dependent values of the nuclear matrix elements are not taken into account.

## Thesis outline

This work is organized as follows:

Chapter 2 introduces the method of neutrino mass determination from tritium  $\beta$ -decay. The setup of the KATRIN experiment and, in particular, the principle of the MAC-E filter are presented. In view of their relevance to the chapters to follow, a general overview of the background components expected in KATRIN is given in the last section.

The concept of a wire electrode system for background suppression in MAC-E filters by electrostatic shielding of secondary electrons originating from electrode surfaces is the central topic of chapter 3. After working out details of the underlying principle, previous implementations and tests at the Mainz neutrino mass experiment and the KATRIN pre-spectrometer are outlined. Finally, the requirements for an application to the large KATRIN main spectrometer are defined.

Chapter 4 covers the computer simulations that have been carried out within this work in order to conceive and optimize the design of a two-layer wire electrode system for the KATRIN main spectrometer. It starts out with a description of the tools used to perform the calculations and lists the requirements to be observed from the technical point of view as well as regarding the electromagnetic design of MAC-E filters. The evolution of the computer model is traced along with the obtained results concerning several design parameters, technical implementation and tolerance estimates for fabrication and mounting of the electrode parts. The chapter concludes with a discussion of the stringent technical requirements the production process is subject to.

Chapter 5 again picks up the topic of background in setups involving the MAC-E filter technique, albeit with a different emphasis: here, the potentially harmful influence of traps for charged particles and the associated background generated by long storage times and multiple ionization processes is examined. Several mechanisms that can lead to strong electric discharges are discussed. Three sections within the KATRIN setup are identified as hosts of charged particle traps of the Penning type, namely inside the pre- and main spectrometers as well as at the interface between the two successive MAC-E filters. These three trapping scenarios are treated in separate sections.

Within the scope of this work, experimental studies to investigate the Penning trap situation between the two spectrometers were carried out with a test setup at the Mainz MAC-E filter. The aim was to construct and test a mechanical device („wire scanner“) that allows to empty the trap in periodic intervals, but otherwise leaves the tritium spectroscopy to be performed with the KATRIN setup undisturbed. The results of these investigations are described in chapter 6.

In the course of the abovementioned tests the Mainz MAC-E filter was also used to perform spectroscopy measurements with a photoelectron source consisting of a stainless steel cathode irradiated by UV light from a light emitting diode (chapter 7). By virtue of the fast switching capabilities of the LED, very short photoelectron pulses were produced and a time-of-flight spectrum was recorded. Aside from this simple setup, a novel design of a photoelectron gun with the additional feature of angular selectivity was also prototyped and tested. An upgraded version of such an electron source and the systematic position-sensitive investigation of the transmission function might be very useful for calibration measurements of the KATRIN main spectrometer.

Conclusions of this work and an outlook are presented in chapter 8.



## 2 The KATRIN experiment

Building on the experience gained in many previous experiments studying tritium  $\beta$ -decay with the aim of determining the value of the electron neutrino mass, the Karlsruhe Tritium Neutrino experiment (KATRIN) is designed to reach a sensitivity of  $200 \text{ meV}/c^2$ .

This chapter presents the physical foundations of the measurement method (sections 2.1 and 2.2) and the major components of the experimental setup (section 2.3). Furthermore, systematic and statistical uncertainties (section 2.4) as well as the main sources of background (section 2.5) expected at KATRIN are discussed.

### 2.1 Tritium beta-decay

In the process of  $\beta^-$ -decay an electron and an electron-antineutrino are emitted:

$$(A, Z) \rightarrow (A, Z + 1)^+ + e^- + \bar{\nu}_e + Q, \quad (2.1)$$

where  $A$  and  $Z$  are the atomic mass number and nuclear charge of the mother isotope and  $Q$  is the total energy released in the decay.

This surplus energy is passed on to the decay products in various forms:

- In addition to their rest energies  $m_e c^2$  and  $m(\nu_e) c^2$ , both electron and neutrino receive a certain amount of kinetic energy.
- A small recoil energy  $E_{\text{rec}}$  is transferred to the daughter  $(A, Z + 1)^+$ .
- In addition, the decay can lead with a probability  $P_k$  to an excited state of the daughter at an excitation energy  $V_k$ .

Fermi's golden rule can be used to calculate<sup>1</sup> the rate  $\dot{N}$  of electrons emitted into the energy interval between  $E$  and  $E + dE$ :

$$\frac{d\dot{N}}{dE} = \frac{d^2 N}{dE dt} = \frac{2\pi}{\hbar} |\mathcal{M}|^2 \rho(E_{\text{tot}}, E_{\text{tot}, \nu}), \quad (2.2)$$

where  $\mathcal{M}$  is the transition matrix element and  $\rho(E_{\text{tot}}, E_{\text{tot}, \nu})$  is the two-particle phase space density of the antineutrino–electron pair in the final state. The former is usually expressed as a decomposition into a leptonic and a hadronic (or nuclear)<sup>2</sup> part:

$$\mathcal{M} = G_F \cos \theta_C \mathcal{M}_{\text{nuc}} \mathcal{M}_{\text{lep}}. \quad (2.7)$$

Here,  $G_F$  denotes the Fermi coupling constant and  $\theta_C$  the Cabibbo angle.

$|\mathcal{M}_{\text{lep}}|^2$  is essentially determined [Zub04, Ott08] by the probability to find the two emitted leptons at the location of the nucleus, which in the simplest case is for each lepton inversely proportional to the normalization volume  $V$ . In addition, the Coulomb interaction between the emitted charged lepton and the nucleus must be taken into account by including the Fermi function

<sup>1</sup>For the moment, the nuclear recoil and the excited final states shall be neglected.

<sup>2</sup>The nuclear matrix element contains a Fermi part  $\mathcal{M}_F$  and a Gamow-Teller part  $\mathcal{M}_{GT}$ , which contribute according

## 2 The KATRIN experiment

$F(Z+1, E)$ :

$$|\mathcal{M}_{\text{lep}}|^2 = \frac{1}{V^2} F(Z+1, E). \quad (2.8)$$

The momenta of electron and neutrino are not directly correlated (as the nucleus balances all momenta) and hence the phase space factors for neutrino and electron may be treated separately and expressed as a function of the kinetic energy  $E$  of the electron (compare [Wei03, Zub04]):

$$\begin{aligned} \rho(E_{\text{tot}}, E_{\text{tot},\nu}) &= \frac{dn_e}{dE_e} \frac{dn_\nu}{dE_\nu} = \frac{V^2 p E_{\text{tot}} p_\nu E_{\text{tot},\nu}}{4\pi^4 \hbar^6} \\ &= \frac{V^2}{4\pi^4 \hbar^6} p (E + m_e c^2) (E_0 - E) \cdot \sqrt{(E_0 - E)^2 - m^2(\nu_e) c^4}. \end{aligned} \quad (2.9)$$

$V$  is again the normalization volume. Assembling all ingredients, one thus gets

$$\frac{dN}{dE dt} = R(E) \cdot \sqrt{(E_0 - E)^2 - m^2(\nu_e) c^4} \Theta(E_0 - E - m(\nu_e) c^2), \quad (2.10)$$

with

$$R(E) = \frac{G_F^2 \cos^2 \theta_C}{2\pi^3 \hbar^7} |\mathcal{M}_{\text{nuc}}|^2 F(Z+1, E) p (E + m_e c^2) (E_0 - E). \quad (2.11)$$

The inclusion of the  $\Theta$  function in eq. (2.10) ensures that  $E_0 - E - m(\nu_e) c^2 > 0$ . After incorporating the excited final states  $V_k$  and the incoherent sum

$$m^2(\nu_e) := \sum_j |U_{ej}|^2 m^2(\nu_j). \quad (2.12)$$

introduced in eq. (1.28) as the neutrino mass observable<sup>3</sup>, the final result reads

$$\begin{aligned} \frac{dN}{dE dt} &= \text{const.} \cdot |\mathcal{M}_{\text{nuc}}|^2 F(Z+1, E) p (E + m_e c^2) \\ &\quad \cdot \sum_j \sum_k |U_{ej}|^2 P_k \epsilon_k \sqrt{\epsilon_k^2 - m^2(\nu_j) c^4} \Theta(\epsilon_k - m(\nu_j) c^2), \end{aligned} \quad (2.13)$$

$$\text{with } \epsilon_j := E_0 - E - V_k. \quad (2.14)$$

Evidently, a finite neutrino mass modifies the shape of the  $\beta$ -spectrum most strongly in the region close to the endpoint  $E_0$ , which is illustrated in figure 2.1. It is also clear that the relative influence of an  $m(\nu_e) \neq 0$  will be more pronounced for a  $\beta$ -emitter with a low endpoint energy. Tritium possesses a very low endpoint energy and is thus particularly suitable for neutrino mass searches. In principle the neutrino mass is detectable as a shift of the endpoint towards a slightly lower energy  $E_0 - m(\nu_e c^2)$ . However, this method is difficult to realize for two main reasons:

---

to the weak vector coupling  $g_V$  and the axial vector coupling  $g_A$ , respectively:

$$|\widetilde{\mathcal{M}}_{\text{nuc}}|^2 = g_V^2 |\mathcal{M}_F|^2 + g_A^2 |\mathcal{M}_{GT}|^2 = g_V^2 \left[ |\mathcal{M}_F|^2 + \frac{g_A^2}{g_V^2} |\mathcal{M}_{GT}|^2 \right] \quad (2.3)$$

$$= G_F^2 \cos^2 \theta_C |\mathcal{M}_{\text{nuc}}|^2, \quad (2.4)$$

$$\text{with } g_V = G_F \cos \theta_C, \quad |\mathcal{M}_{\text{nuc}}|^2 := |\mathcal{M}_F|^2 + \frac{g_A^2}{g_V^2} |\mathcal{M}_{GT}|^2, \quad (2.5)$$

$$\text{and } \frac{g_A}{g_V} = -1.259 \pm 0.004 \quad ([\text{Hey04}], \text{ sec. 5.3.3}). \quad (2.6)$$

Equation (2.4) was used to obtain the factorized relation displayed in eq. (2.7).

<sup>3</sup>Due to the smallness of the neutrino mass splittings it will not be able to discern individual steps corresponding to the neutrino mass eigenstates in the shape of the  $\beta$ -spectrum measured with KATRIN. Therefore, it is justified to use eq. (2.12) as an effective observable.

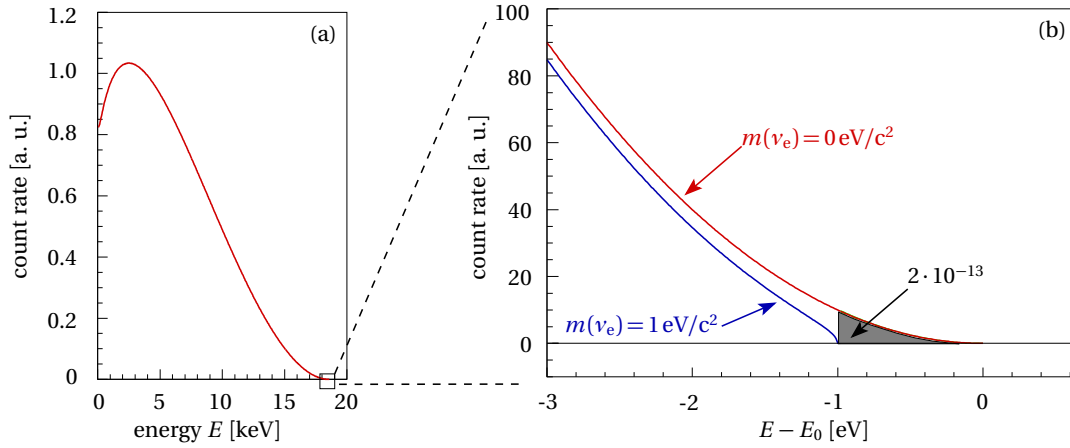


**Figure 2.1:** Continuous shape of the full tritium  $\beta$ -spectrum up to the endpoint at  $E_0 \approx 18.6$  keV (a), and close-up on the last 3 eV below the endpoint (b). Two calculated  $\beta$ -spectra for zero neutrino mass (red) and for a small non-vanishing neutrino mass (blue) are shown. The imprint of  $m(\nu_e) \neq 0$ , seen as an offset throughout the entire spectrum and via a shift of the endpoint  $E_0$  towards a slightly lower energy, is tiny: For a hypothetical neutrino mass of  $m(\nu_e) = 1 \text{ eV}/c^2$  the “missing count rate” in the energy interval between  $E = E_0 - m(\nu_e)c^2$  and  $E = E_0$  amounts to a fraction of only about  $2 \cdot 10^{-13}$  of all decays (gray-shaded area).

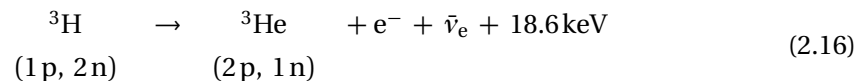
- It is hard to pin down the actual position of the endpoint in the measured tritium  $\beta$ -spectrum since it will be covered by a considerable background.
- The most recent determination of the (T,  $^3\text{He}$ ) mass difference [Nag06] leads<sup>4</sup> to an endpoint energy of

$$E_0(\text{T}_2) = (18571.8 \pm 1.2) \text{ eV} \quad (2.15)$$

for molecular  $\text{T}_2$  [Ott08]. Owing to the high sensitivity that KATRIN aims for, even the very good accuracy of this measurement is not sufficient to use this value as an input parameter for the determination of the neutrino mass. Instead,  $E_0$  will be extracted from the measured shape of the  $\beta$ -spectrum as one of the free parameters<sup>5</sup> in the fit function.

Aside from the low  $E_0$  value, tritium is also advantageous in several other regards:

- The decay



represents a super-allowed transition between mirror nuclei. The strong overlap between the nucleon wave functions helps to achieve a large nuclear matrix element and hence favors a large decay amplitude. The half-life of tritium is 12.3 a. Therefore, high count rates can be obtained even with a comparatively small density of the source material, which is important in view of reducing systematic uncertainties related to inelastic scattering of electrons on their way through the source.

<sup>4</sup>When deducing the endpoint energy for molecular  $\text{T}_2$  from the measured mass difference  $\Delta m(\text{T}, {}^3\text{He})$ , the difference of the molecular binding energies  $E_B(\text{T}_2)$  and  $E_B({}^3\text{HeT}^+)$  as well as the ionization energy  $E_{\text{ion}}(\text{T}_2)$  have to be taken into account. The electron mass is already included in  $\Delta m(\text{T}, {}^3\text{He})$ , since by definition neutral mother and daughter atoms are considered. Furthermore, the recoil energy  $E_{\text{rec}} = 1.72 \text{ eV}$  of the daughter molecule gives a significant correction of the endpoint energy  $E_0$ .

<sup>5</sup>In general, there are four free parameters: the signal and background rates  $s$  and  $b$ , the endpoint energy  $E_0$  and the neutrino mass square  $m^2(\nu_e)$ .

- The Fermi function  $F(Z+1, E)$  for the daughter nucleus is nearly constant over a wide range of electron energies and can be approximated with  $F(Z+1, E) \approx 1$  in the interesting region just below  $E_0$  (compare [KAT04]).
- Molecular tritium as well as its daughter possess a simple electronic structure which permits to quite accurately calculate the final state distribution and to model its influence on the theoretical  $\beta$ -spectrum.

## 2.2 The MAC-E filter technique

To cope with the low signal rates in the small region of interest at the high-energy tail of the tritium  $\beta$ -spectrum, a high-resolution spectroscopy technique which allows to collect electrons over a large solid angle while also providing a good background reduction is required. In most instruments the energy resolution deteriorates with increasing angular acceptance. For example, typical electrostatic spectrometers only analyze the energy component parallel to the electrostatic retardation field, but are insensitive to a potential transverse component.<sup>6</sup> A way out consists in combining an electrostatic spectrometer with an inhomogeneous magnetic guiding field, which reaches its minimum at the point of maximum electrostatic retardation. This principle was first introduced in the 1970s and early 1980s in the fields of plasma physics [Hsu76] and low-energy electron spectroscopy [Bea80, Bea81, Kru83], and later adopted for a very successful use in the neutrino mass experiments at Troitsk [Lob85] and Mainz [Pic92a]. Today, the working principle is usually subsumed under the expression “magnetic adiabatic collimation with an electrostatic filter” (short: MAC-E filter). In an early publication, Kruit and Read [Kru83] used the term “magnetic field parallelizer”, which quite graphically describes the key feature of this kind of spectrometer to be discussed in some more detail in the following.

### 2.2.1 General working principle

The basic constituents of a MAC-E filter are shown in figure 2.2. Two superconducting solenoids at the entrance and exit of the spectrometer generate the magnetic field guiding the electrons along the magnetic field lines from their origin in the source (shown on the left side in figure 2.2) to the detector (on the right side). The magnetic field is symmetrical with respect to the central plane of the spectrometer, but it is highly inhomogeneous: The minimum field strength  $B_{\min}$  at the central plane is suppressed by several orders of magnitude with respect to the maximum  $B_{\max}$  occurring at the center of the solenoids. The second important ingredient of the MAC-E filter is the retardation of the electrons by an electrostatic field, which at the center of the spectrometer is nearly parallel to the magnetic field lines.

Depending on the angle  $\theta = \angle(\mathbf{B}, \mathbf{p})$  between the electron momentum  $\mathbf{p}$  and the magnetic field  $\mathbf{B}$  at the starting point, the electron will possess a certain amount of cyclotron energy and perform a gyration motion about the magnetic field line. Thus, the total kinetic energy  $E_{\text{kin}}$  is split between

---

<sup>6</sup>In the 1950s, Hamilton *et al.* [Ham50, Ham53] already conceived a hemispherical electrostatic  $\beta$ -spectrometer providing a large usable solid angle at a reasonable energy resolution. However, this technique cannot be easily scaled to a sensitivity required in modern neutrino mass experiments (see ref. [Ott08] for details).

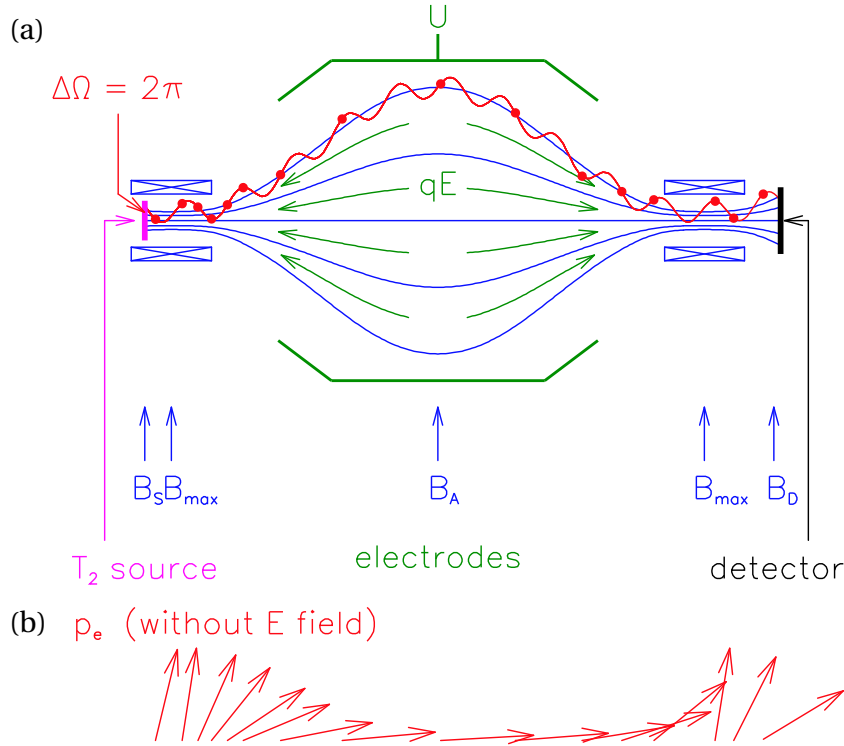


**Figure 2.2:** (a) Schematic view of an electrostatic spectrometer with magnetic adiabatic collimation (MAC-E filter). The electrons starting from the source are guided along magnetic field lines towards the detector. Only those electrons with sufficient longitudinal energy can overcome the electrostatic retardation barrier and get reaccelerated onto the detector. (b) Adiabatic change of the momentum direction with respect to the (axial) magnetic field. For this illustration, the electrostatic retardation is left out and only the magnetic gradient force is considered.

the transverse component  $E_{\perp}$  and the longitudinal<sup>7</sup> component  $E_{\parallel}$ :

$$\begin{aligned} E_{\parallel} &= E_{\text{kin}} \left( \frac{\mathbf{B} \cdot \mathbf{p}}{|\mathbf{B}| |\mathbf{p}|} \right)^2 = E_{\text{kin}} \cdot \cos^2 \theta, \\ E_{\perp} &= E_{\text{kin}} - E_{\parallel} = E_{\text{kin}} \cdot \sin^2 \theta. \end{aligned} \quad (2.17)$$

The cyclotron motion defines an orbital magnetic moment  $\mu$ , which can be expressed in non-relativistic notation as

$$\mu = |\boldsymbol{\mu}| = \frac{q}{2m_e} |\mathbf{l}| = \frac{E_{\perp}}{B}, \quad (2.18)$$

where  $\mathbf{l}$  denotes the orbital angular momentum.

As the electron passes through the strong gradient of the magnetic field strength between the starting point and the central plane of the spectrometer, the magnetic gradient force

$$\mathbf{F}_{\nabla} = \nabla(\boldsymbol{\mu} \cdot \mathbf{B}) \quad (2.19)$$

(again, the non-relativistic expression is used) causes an acceleration of the electron parallel to the magnetic field lines, in the direction of the minimum magnetic field strength. Since in the

<sup>7</sup>Throughout this thesis, the pairs of terms *axial/longitudinal energy* and *cyclotron/transverse energy* will often be used synonymously.

static magnetic field the total energy is conserved, this increase of  $E_{\parallel}$  has to take place at the expense of  $E_{\perp}$ , which is decreased accordingly.

At this point it should be noted that, aside from its obvious role regarding the energy analysis of the electrons, the electrostatic field fulfills another important task: the early onset of the deceleration of the electrons ensures that the energy transformation takes place *adiabatically* by keeping the relative change of the magnetic field strength along one cyclotron loop sufficiently low. In the so-called adiabatic limit<sup>8</sup> the product of the relativistic Lorentz factor  $\gamma = [1 - \frac{v^2}{c^2}]^{-1/2}$  and the absolute value of the orbital magnetic moment,  $|\mu|$ , is a constant of the motion:

$$\gamma\mu = \text{const.} \quad (2.20)$$

Since electrons generated in tritium  $\beta$ -decay reach a maximum value of  $\gamma = 1.04 \approx 1$ , the non-relativistic approximation may be applied, in which case the conserved quantity is the orbital magnetic moment itself:

$$\mu = \frac{E_{\perp}}{B} = \text{const.} \quad (2.21)$$

The transverse kinetic energy component  $E_{\perp}$  and hence the angle  $\theta$  generally transform as follows between a starting point  $(z_i, r_i)$  and a final point  $(z_f, r_f)$ :

$$\begin{aligned} (E_{\perp})_f &\stackrel{\text{eq. (2.21)}}{=} (E_{\perp})_i \cdot B_f/B_i \\ \Rightarrow \sin^2(\theta_f) &\stackrel{\text{eq. (2.17)}}{=} \sin^2(\theta_i) \cdot B_f/B_i \end{aligned} \quad (2.22)$$

In the first half of the MAC-E filter up to the analyzing plane,  $B_f/B_i$  is smaller than 1, and hence the transformation takes place in the direction  $E_{\perp} \rightarrow E_{\parallel}$ . Thus, for sufficiently small  $B_f/B_i$  nearly all of the kinetic energy of the particle has been converted to longitudinal energy in the analyzing plane and can be probed by the retardation potential. After passing the analyzing plane, however,  $B_f/B_i > 1$  and the transformation is inverted to  $E_{\parallel} \rightarrow E_{\perp}$ . This smooth variation of the angle of the momentum vector  $\mathbf{p}$  with respect to the magnetic field vector  $\mathbf{B}$  is indicated in figure 2.2(b).

### 2.2.2 Energy resolution and transmission function

The energy resolution of a MAC-E filter immediately follows from eq. (2.22): in the extreme case where the total kinetic energy of the electron at the starting point,  $E_{\text{start}}$ , is given in the form of transverse energy ( $(E_{\perp})_i = E_{\text{start}}$ ), the adiabatic transformation according to eq. (2.22) will result in a small remainder of transverse energy left over at the analyzing plane. This maximum amount of non-analyzable energy defines the theoretical resolution  $\Delta E$ :

$$\Delta E \equiv (E_{\perp})_{\text{max}} = E_{\text{start}} \cdot \frac{B_{\text{min}}}{B_{\text{max}}}. \quad (2.23)$$

The resolution is therefore in principle only limited by the minimum ratio  $\frac{B_{\text{min}}}{B_{\text{max}}}$  of the magnetic fields that can be realized experimentally.

<sup>8</sup>The adiabaticity criterion may be cast into the following mathematical form:

$$\left| \frac{1}{B} \frac{d\mathbf{B}}{dt} \right| \ll \omega_{\text{cyc}} = \frac{qB}{\gamma m_e}.$$

A detailed account of the adiabatic motion of charged particles in electromagnetic fields can be found in ref. [Nor63]. The trajectory of adiabatic motion can be simplified by using the guiding center approximation (see [Nor61]), which for example allows to significantly reduce the computational efforts of numerical simulations.

This energy resolution is imprinted on the shape of the transmission curve of a MAC-E filter for an isotropically emitting source, as can be seen by first writing down the condition for an electron to surpass the electrostatic filter:

$$E_{\parallel}(\mathbf{r}) - qU(\mathbf{r}) = E_{\text{start}} - E_{\perp}(\mathbf{r}) - qU(\mathbf{r}) > 0, \quad (2.24)$$

*i. e.*, the longitudinal component of the kinetic energy has to remain larger than the potential energy at each point  $\mathbf{r}$  along the trajectory. According to eq. (2.17) the expression in eq. (2.24) contains a dependence on the angle  $\theta$ , and the transmission condition for an electron to pass the analyzing plane at the center of the spectrometer takes the following form:

$$(E_{\parallel})_{\text{ana}} - qU_0 = E_{\text{start}} \left( 1 - \sin^2 \theta_{\text{start}} \cdot \frac{B_{\text{ana}}}{B_{\text{source}}} \right) - qU_0 > 0, \quad (2.25)$$

where

- $E_{\text{start}}$  is the starting kinetic energy of the electron in the source,
- $B_{\text{source}}$  is the magnetic field strength in the source,
- $B_{\text{ana}}$  is the magnetic field strength in the analyzing plane,
- $(E_{\parallel})_{\text{ana}}$  is the longitudinal kinetic energy in the analyzing plane,
- $\theta_{\text{start}}$  is the angle between magn. field lines and electron momentum at the starting point, and
- $U_0$  is the maximum retardation potential reached in the analyzing plane.

This relation can be used to define the opening angle of the cone of emission in which all electrons fulfill the transmission condition, provided that their starting energy is larger than  $qU_0$ :

$$\theta \leq \theta_{\text{start}} = \arcsin \left( \sqrt{\frac{E_{\text{start}} - qU_0}{E_{\text{start}}} \cdot \frac{B_{\text{source}}}{B_{\text{ana}}}} \right). \quad (2.26)$$

The angular acceptance of the spectrometer relative to the full forward solid angle of  $2\pi$  can then be obtained by inserting eq. (2.26) into

$$\frac{\Delta\Omega}{2\pi} = 1 - \cos \theta_{\text{start}}, \quad (2.27)$$

which yields the transmission function of the MAC-E filter:

$$T(E_{\text{start}}, qU_0) = \begin{cases} 0 & \text{for } E_{\text{start}} < qU_0 \\ 1 - \sqrt{1 - \frac{(E_{\text{start}} - qU_0) B_{\text{source}}}{E_{\text{start}} B_{\text{ana}}}} & \text{for } E_{\text{start}} \left( 1 - \frac{B_{\text{ana}}}{B_{\text{source}}} \right) \leq qU_0 \leq E_{\text{start}} \\ 1 & \text{for } qU_0 \leq E_{\text{start}} \left( 1 - \frac{B_{\text{ana}}}{B_{\text{source}}} \right). \end{cases} \quad (2.28)$$

(It is useful to exploit the relation  $\cos(\arcsin(\sqrt{x})) = \sqrt{1-x}$ .)

$T(E_{\text{start}}, qU_0)$  describes the fraction of electrons emitted with a starting energy  $E_{\text{start}}$  into the forward solid angle which are actually able to pass the electrostatic filter at a particular setting  $qU_0$  of the retardation energy.

In a realistic experiment containing a MAC-E filter, another factor limiting the transmission probability will usually be present: The magnetic field strength  $B_{\text{source}}$  at the source will typically be

## 2 The KATRIN experiment

lower than the maximum magnetic field strength  $B_{\max}$  occurring in the setup. This measure serves the purpose of cutting off electrons with very large starting angles, since due to the prolonged flight path these electrons have a larger probability of undergoing scattering collisions (and therefore potential energy loss processes) inside the source.

Hence, magnetic reflection can be employed to reject all electrons with starting angles exceeding the maximum value of

$$\theta_{\text{start}}^{\max} = \arcsin \left( \sqrt{\frac{B_{\text{source}}}{B_{\max}}} \right) \quad (2.29)$$

from the analysis. Technically, this can be achieved by a so-called pinch magnet placed at some point upstream of the electron detector. The pinch magnetic field then defines the maximum magnetic field strength inside the experimental setup.

Under these conditions, the expression for the transmission function is modified [Pic92a] to

$$T(E_{\text{start}}, qU_0) = \begin{cases} 0 & \text{for } E_{\text{start}} < qU_0 \\ \frac{1 - \sqrt{1 - \frac{(E_{\text{start}} - qU_0) B_{\text{source}}}{E_{\text{start}} B_{\text{ana}}}}}{1 - \sqrt{1 - \frac{B_{\text{source}}}{B_{\max}}}} & \text{for } qU_0 \leq E_{\text{start}} \leq qU_0 \frac{B_{\max}}{B_{\max} - B_{\text{ana}}} \\ 1 & \text{for } E_{\text{start}} > qU_0 \frac{B_{\max}}{B_{\max} - B_{\text{ana}}} \end{cases} \quad (2.30)$$

This normalized transmission function is plotted in figure 2.3 for the example of the KATRIN main spectrometer ( $\Delta E = 0.93$  eV at  $E = 18.6$  keV,  $\theta_{\text{start}}^{\max} = 50.77^\circ$ ). By gradually stepping the retardation voltage and counting the number of electrons arriving at the detector for each step, the MAC-E filter works as a sharp high-pass filter (as the ideal transmission function has no tails towards high or low energies), and the measured spectrum is thus an integrated one.

Several characteristics of the MAC-E filter – again for the example of the KATRIN main spectrometer – are plotted in figure 2.4 as a function of the axial position  $z$ . The top panel shows the track of an electron through the KATRIN main spectrometer, from the starting point in the center of the entrance solenoid at  $z = -12$  m to the analyzing plane at  $z = 0$ . The electron was simulated with the largest accepted component of initial transversal energy (*i. e.*, with the maximum starting angle  $\theta_{\text{start}}^{\max} = 50.77^\circ$ ), and with the largest accepted radial starting position (*i. e.*, at the outer border of the transported magnetic flux tube). The total kinetic energy at the starting point was 18.6 keV. Since the magnetic flux

$$\Phi = \int B \, dA \quad (2.31)$$

is a conserved quantity, the diameter of the flux tube widens as the magnetic field strength drops (see second panel from top). Hence, the electron reaches its maximum radial position at the location of the minimum magnetic field, *i. e.*, in the analyzing plane of the main spectrometer. This illustrates the need for a large diameter of the main spectrometer vessel (compare section 2.3.1). The third and fourth graphs trace the characteristic evolution of the electrostatic potential and the longitudinal kinetic energy along the track, respectively. The absolute value of the electric potential quickly rises to its maximum value and then stays almost constant over most of the distance. In contrast, the behavior of  $E_{\parallel}$  looks a little more complicated. The initial rise of the longitudinal kinetic energy within about the first meter of its trajectory mirrors the adiabatic conversion of  $E_{\perp} \rightarrow E_{\parallel}$  due to the rapid decrease of the magnetic field strength, which happens while the electron is still in the grounded beam tube, where the electric potential gradually starts to build

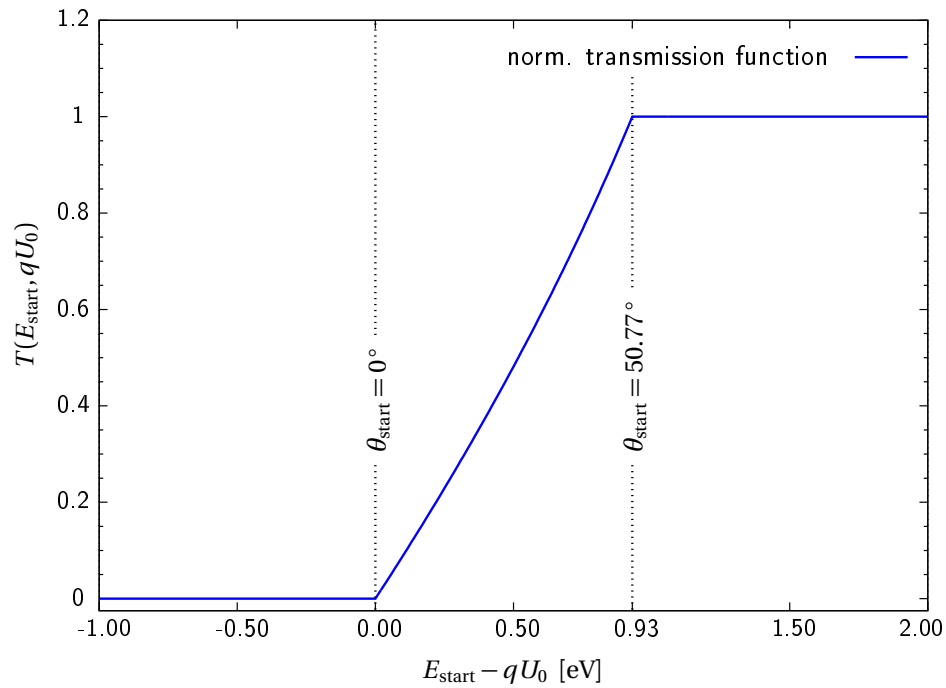


**Figure 2.3:** Typical transmission function of a MAC-E filter. The graph shows the normalized transmission function  $T(E_{\text{start}}, qU_0)$  of the KATRIN main spectrometer. According to equation (2.30), the magnetic field parameters (here:  $B_{\text{source}} = 3.6\text{ T}$ ,  $B_{\text{ana}} = 0.3\text{ mT}$  and  $B_{\text{max}} = 6\text{ T}$ ) enter the analytical expression for  $T(E_{\text{start}}, qU_0)$ .

up. As soon as the electron enters the strong retardation potential, its longitudinal kinetic energy is gradually reduced and assumes a minimum value as the electron finally reaches the analyzing plane.

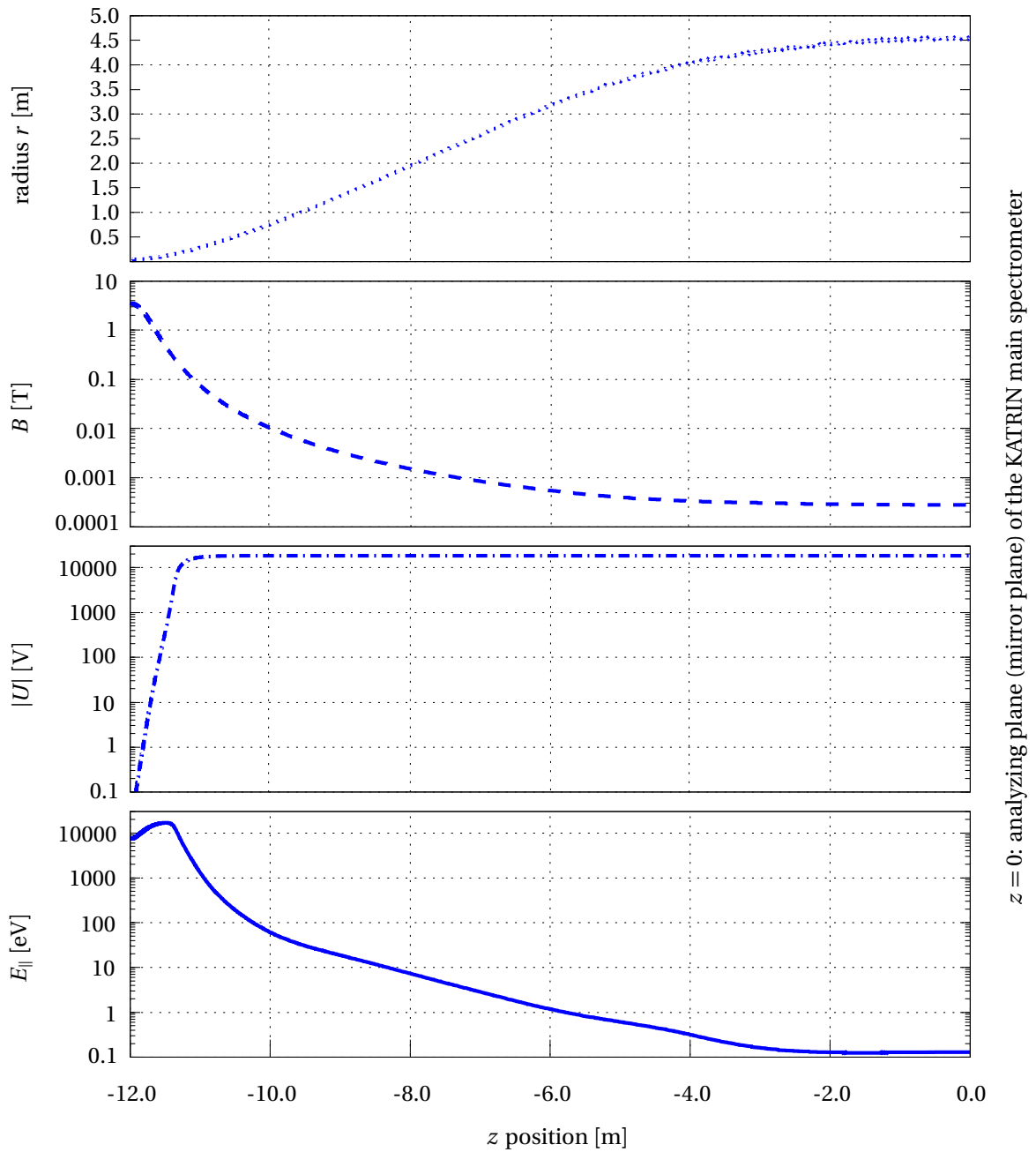


**Figure 2.4:** Characteristics of a MAC-E filter (here: the KATRIN main spectrometer as an an example). From top to bottom: trajectory of an electron in the  $rz$ -plane (dotted curve), magnetic field strength  $B(z)$  (dashed curve), electric potential  $|U(z)|$  (dash-dotted curve) and longitudinal kinetic energy  $E_{||}(z)$  (solid curve).

## 2.3 Overview of the components of the KATRIN setup

KATRIN is presently being set up at Forschungszentrum Karlsruhe, where the expertise and infrastructure of the Tritium Laboratory (TLK) allow to handle and process the amount of gaseous  $T_2$  necessary<sup>9</sup> to achieve the high luminosity required by the experiment.

Figure 2.5 presents the main components of the KATRIN experiment<sup>10</sup>, starting with the tritium source on the left of the drawing and continuing via the pumping sections and the two spectrometers to the electron detector system on the right side. All parts of the setup are linked by a magnetic field which ensures efficient guiding of the electrons emerging from  $\beta$ -decay processes in the source. This magnetic guiding field is provided by a chain of superconducting solenoids distributed along the whole beam line with a total length of approximately 70 m.

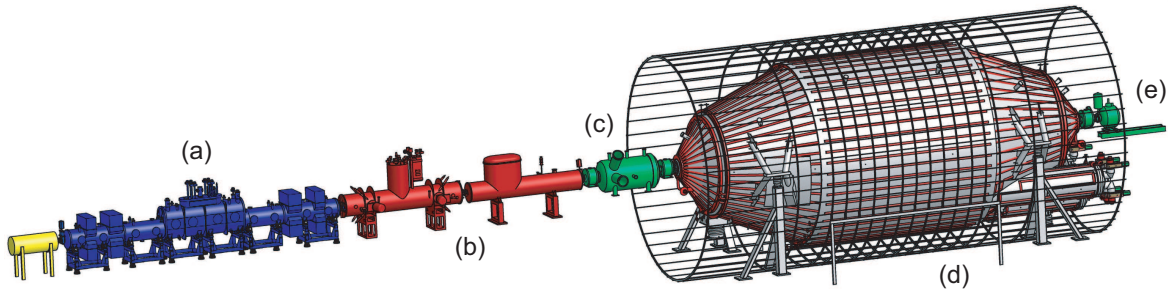


**Figure 2.5:** Overview of the KATRIN experiment. The length of the total setup amounts to about 70 m. The main components are (from left to right): (a) calibration and monitoring system (CMS) and windowless gaseous tritium source (WGTS), (b) transport and pumping section (differential pumping section, DPS, and cryogenic pumping section, CPS), (c) pre-spectrometer, (d) main spectrometer, and (e) detector system. The monitor spectrometer is not shown.

### 2.3.1 Basic parameters of the KATRIN experiment

Before describing the main components of the setup, the choice of the basic parameters of the KATRIN experiment shall briefly be motivated.

The luminosity  $L$  of the experimental setup can be defined as the product of the source strength  $S$ , the usable fraction  $\Delta\Omega/4\pi$  of the solid angle accepted by the spectrometer and the detection efficiency  $\eta$ :

$$L = S \frac{\Delta\Omega}{4\pi} \eta. \quad (2.32)$$

Together with the resolving power  $E/\Delta E$ , the luminosity forms a “figure of merit”, which should be optimized in order to achieve a high sensitivity on the neutrino mass:

$$P = S \frac{\Delta\Omega}{4\pi} \eta \frac{E}{\Delta E}. \quad (2.33)$$

- The sensitivity aim of  $0.2 \text{ eV}/c^2$  requires a resolving power of  $E/\Delta E = 20000$ , which, according to eq. (2.23), defines the magnetic field ratio of  $B_{\max}$  over  $B_{\min} = B_{\text{ana}}$ . The minimum field strength  $B_{\min}$ , on one hand, is constrained by the necessity to minimize the influence

<sup>9</sup>A quantity of 40 g of gaseous  $T_2$  will have to be cycled through KATRIN’s tritium source per day, which corresponds to an injection rate of 4.7 Ci/s.

<sup>10</sup>In fall 2006 the overall setup underwent several significant modifications as compared to the KATRIN Design Report of 2004 [KAT04]. Figure 2.5 shows the new reference configuration of the experiment incorporating these changes.

## 2 The KATRIN experiment

of the Earth magnetic field and other stray fields, and to maintain an adiabatic motion of the electrons. The scale of  $B_{\max}$ , on the other hand, is set by the typical field strengths achievable with superconducting magnets at a reasonable technical effort. On the basis of these considerations [KAT04], the following magnetic field strengths were chosen for KATRIN:

$$B_{\min} = B_{\text{ana}} = 0.3 \text{ mT}, \quad B_{\max} = B_{\text{pinch}} = 6 \text{ T}. \quad (2.34)$$

The pinch magnet will be located at the exit of the main spectrometer, right5 upstream of the detector.

- The source strength  $S$  depends on the effective area  $A_{\text{source}}$ . In order to achieve a high signal rate at a given column density of the source gas, the area should be as large as possible. However, due to the conservation of the magnetic flux (eq. (2.31)) the effective area of the source is proportional to the area of the analyzing plane of the main spectrometer. In view of the difficult transportation of a large stainless steel vessel from its production site to the location of the experiment, a diameter larger than 10 m was not feasible. Including some safety margin and allocating additional space for the installation of an inner electrode system, the diameter of the usable magnetic flux is determined to be  $r_{\text{ana}} = 9 \text{ m}$ , which yields a geometrical area of  $A_{\text{ana}} = 63.6 \text{ m}^2$ . Together with the proposed value of  $B_{\text{ana}}$  given in eq. (2.34), this results in a nominal transported magnetic flux of

$$\Phi = B_{\text{ana}} \cdot A_{\text{ana}} = 191 \text{ T cm}^2. \quad (2.35)$$

- As can be seen from eq. (2.29), the accepted forward solid angle  $\Delta\Omega$  is determined by the ratio of the magnetic field strength  $B_{\text{source}}$  at the source and the pinch magnetic field  $B_{\text{pinch}} = B_{\max}$ . To achieve a high acceptance relative to the full forward solid angle of  $2\pi$ ,  $B_{\text{source}}$  should be large. However, there are two opposing arguments:
  - The ratio  $B_{\text{source}}/B_{\max} < 1$  is necessary to limit the accepted starting angle in order to suppress systematic uncertainties due to electron energy losses inside the source.
  - The magnetic field at the source should not be too strong, otherwise the transported magnetic flux will be confined to a very small diameter, which in turn cuts down on the effective source area and hence on the signal strength  $S$ .

In view of these requirements,  $B_{\text{source}} = 3.6 \text{ T}$  (thus,  $\theta_{\text{start}}^{\max} = 50.77^\circ$ ) was picked for KATRIN. Using eq. (2.35), the geometrical area of the magnetic flux tube in the tritium source is therefore  $A_{\text{source}} = 53 \text{ cm}^2$ . Taking into account the rejection of the electrons with highest angles, however, this is reduced to an effective source area  $A_{\text{source}}^{\text{eff}} = A_{\text{ana}} \cdot \Delta E/E \approx 31.8 \text{ cm}^2$ .

- Finally, a high detection efficiency  $\eta$  can be achieved by choosing a suitable detector technology (see section 2.3.4).

### 2.3.2 Tritium source and pumping sections

All tritium-related parts of the KATRIN setup (see figure 2.6) are housed within the safety barriers of the Tritium Laboratory, which had to be enlarged in order to accommodate the extensive installations of the KATRIN source and transport system.<sup>11</sup> The central piece is the windowless gaseous tritium source (WGTS) consisting of a 10 m long beam tube of  $\varnothing 90 \text{ mm}$ . Cold molecular tritium gas ( $\text{T}_2$ , temperature  $T = 27 \text{ K}$ ) is injected through a port in the middle of the tube and

<sup>11</sup>Next to the TLK building, dedicated halls for the remaining components (spectrometers and detector setup, monitor spectrometer) and the related infrastructure (*e. g.*, cryogenics supply) were built.

### 2.3 Overview of the components of the KATRIN setup

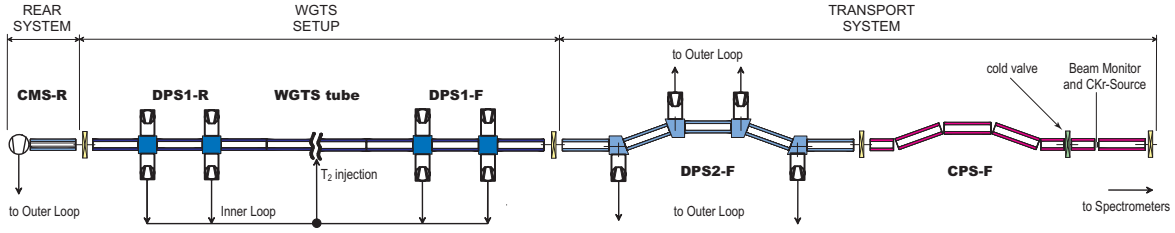


**Figure 2.6:** Schematic view of the tritium-related parts of the KATRIN setup. From left to right, the drawing shows the rear calibration and monitoring system (CMS-R), the long WGTS tube with the rear and front differential pumping sections (DPS1-R, DPS1-F and DPS2-F), and the cryogenic pumping section (CPS-F). The latter forms the interlink between the source and transport system and the spectrometer section.

continuously pumped at both ends. The recovered gas is processed in a closed cycle in order to maintain an isotopic purity of  $> 95\%$ . The isotopic composition is monitored in-line by laser Raman spectroscopy [Lew08]. The magnetic guiding field of  $B_{\text{source}} = 3.6\text{ T}$  needs to be kept up along the full extent of the source with a high degree of homogeneity ( $< 0.2\%$ ).

The column density  $\rho d$ , among other parameters, defines the signal rate of  $\beta$ -electrons. It can be controlled via the injection pressure  $p_{\text{inj}}$ . The maximum signal rate (and hence the choice of  $\rho d$ ) is limited by inelastic scattering of electrons inside the gaseous source. For KATRIN, an optimum working point of  $\rho d = 5 \cdot 10^{17} \text{ cm}^{-2}$  was determined, corresponding to  $p_{\text{inj}} = 3.4 \cdot 10^{-3} \text{ mbar}$  or about  $5 \cdot 10^{19}$  molecules per second. KATRIN's sensitivity goal demands a stabilization of the column density to a level of  $0.1\%$ . This implies stabilizing the source temperature and the injection pressure to better than  $30 \text{ mK}$  and  $10^{-6} \text{ mbar}$ , respectively.

To reduce the tritium flow into the spectrometer section to  $< 10^{-14} \text{ mbar l/s}$  as necessitated by the background requirements (compare section 2.5), a combination of differential pumping with strong turbomolecular pumps (two stages: DPS1-F and DPS2-F, compare figure 2.6) and cryogenic pumping is employed. Considering that the flow from the WGTS towards the pumping sections amounts to about  $2 \text{ mbar l/s}$ , a suppression factor of  $10^{14}$  is required, with about equal contributions of  $10^7$  each to be reached by the differential and the cryogenic pumping. The latter relies on the concept of cryotrapping at cold surfaces: the inner walls of the CPS beam tube will be covered with argon frost at a temperature of  $4.5 \text{ K}$  to enhance the pumping rate by increasing the effective surface area (see [Eic09]). From figure 2.6 it can also be seen that the beam line inside the front pumping section is bent into several kinks to suppress the so-called “beaming” effect by impeding the direct axial motion of neutral molecules from the source towards the spectrometers.

The maximum magnetic field strength inside the transport and pumping section amounts to  $5.6 \text{ T}$ . In order to avoid non-adiabatic energy losses of the electrons it is necessary to keep a minimum magnetic field strength of  $0.3 \text{ T}$  in those regions with a necessarily lower magnetic field, *e. g.*, close to the pump ports [Thü03].

On the opposite side of the WGTS a calibration and monitoring system (CMS-R) contains instruments to measure important operational parameters like the activity of the source. It provides access for an electron gun to determine the response function of the overall system and to monitor the column density of the source. Furthermore, the rear wall of the CMS-R can serve as a means to detect the influence of plasma effects and to compensate variations of the electric potential of the source.

### 2.3.3 Spectrometer section

The spectrometer section comprises two successive MAC-E filters serving different purposes in the main beam line and a third one in a separate “monitor beam line”. In the pre- and main spectrometers, a new electrode concept is employed: in contrast to the previous experiments at Mainz and Troitsk, these two spectrometers possess a vacuum vessel which at the same time is used as a high-voltage electrode to generate the retardation potential. Furthermore, this vessel electrode is complemented by an inner electrode system made of wires, which fulfills the dual task of

- reducing the background component of secondary electrons ejected from the solid retardation electrodes, which is typical of MAC-E filters, and of
- fine-tuning the electrostatic potential in the interior of the spectrometer.

This concept will be discussed in detail in chapters 3 and 4 of this work.

#### The main spectrometer

The main spectrometer is designed to provide the high energy resolution of 0.93 eV at electron energies around 18.6 keV which is required for KATRIN (see section 2.3.1). Its huge dimensions, summarized in table 2.1 and seen in figure 2.7, are a consequence of the high sensitivity aimed for with the KATRIN experiment.

In order to reach a residual gas pressure of  $p < 10^{-11}$  mbar needed for a low background, the vessel will be equipped with a powerful vacuum system comprising turbomolecular pumps and over 3 km of non-evaporable getter material (with a combined pumping speed of about 250 000 l/s).

As can be seen in figure 2.5, the main spectrometer vessel is enclosed by a complex air coil system which consists of two components with different purposes:

- EMCS: The Earth Magnetic field Compensation System (axial loops in figure 2.5) is necessary to obtain a symmetric shape of the magnetic flux tube and to confine it within the dimensions of the spectrometer vessel. Without such corrections, the Earth magnetic field yields an intolerable distortion of the flux tube.
- LFCS: The Low Field Correction System (circular loops in figure 2.5) compensates for the axial component of the Earth magnetic field. More importantly, it allows to compensate for harmful effects of the stray fields of the powerful superconducting magnets, to homogenize the magnetic field strength and to tune it to the value of 0.3 mT at the analyzing plane, thus ensuring the required energy resolution of the main spectrometer.

Having arrived on site in November 2006, the main spectrometer vessel has passed first high-voltage tests and a baking cycle to 350 °C. Initial vacuum tests of the vessel after baking (with only

**Table 2.1:** Characteristics of the main spectrometer vessel.

overall length of vessel	23.28 m
inner diameter of cylindrical part	9.8 m
wall thickness	32 mm (cylinder) / 25 mm (cones)
inner surface area of vessel	about 650 m <sup>2</sup>
volume	about 1250 m <sup>3</sup>
weight	about 190 t



**Figure 2.7:** Photograph of the KATRIN main spectrometer vessel during transportation to the spectrometer building on site of Forschungszentrum Karlsruhe in November 2006. A comparison with the height of the person depicted in the lower right corner of the image demonstrates the dimensions of the spectrometer.

a part of the final pumping speed implemented, and without the inner electrode system installed) were also successful. The mounting of the inner electrode system and electromagnetic test measurements form the next major steps in the commissioning process of the main spectrometer.

### The pre-spectrometer

The task of the pre-spectrometer is to reject the large low-energy part of the tritium  $\beta$ -spectrum (for example, by setting the filter energy to  $qU_{\text{prespec}} \approx E_0 - 300 \text{ eV}$ ) which does not carry significant information for the determination of  $m(\nu_e)$ . This will cut down the flux of  $\beta$ -electrons into the main spectrometer from about  $10^{10}$  to only  $10^3$  electrons per second, thereby reducing the probability of ionizing collisions between  $\beta$ -electrons and residual gas molecules inside the main spectrometer, which might cause background.

With a magnetic field strength of  $B_{\text{solenoid, prespec}} = 4.5 \text{ T}$  in the two superconducting solenoids and  $B_{\text{ana, prespec}} \approx 20 \text{ mT}$  at the central plane, the relative energy resolution of the pre-spectrometer is  $\Delta E/E \approx 1/225$  in the isolated test operation without pinch magnet and  $\Delta E/E \approx 1/300$  when incorporated into the KATRIN beamline with  $B_{\text{pinch}} = 6 \text{ T}$ . Compared to the resolution of the main spectrometer, this value appears quite modest. However, the function of the pre-spectrometer does not require a superior energy resolution.

As a smaller version (length about 4 m, diameter 1.7 m) of the main spectrometer, the pre-spectrometer forms an important testbed for various techniques to be used in the KATRIN experiment. The pre-spectrometer been available on-site of Forschungszentrum Karlsruhe since 2003.

### The monitor spectrometer

Parallel to the main KATRIN beam line, the MAC-E filter of the former Mainz neutrino mass experiment will be operated using the same high-voltage source as the main spectrometer in order



**Figure 2.8:** Photograph of the KATRIN pre-spectrometer. The stainless steel vessel is encased in the heating/cooling system. A superconducting magnet is placed at either end of the spectrometer.

to continuously check the stability of its retardation potential with calibration sources based on atomic and nuclear energy standards. The setup of the monitor spectrometer includes two superconducting magnets and a grounded vacuum vessel equipped with an inner electrode system to produce the electrostatic retardation field and an air coil system to shape and optimize the magnetic field in the analyzing plane. A simple electron detector will be installed. Compared to the settings used for the neutrino mass measurements at Mainz, the resolution of this MAC-E filter is increased to match that of the KATRIN main spectrometer, which has to be paid for by a lower acceptance.<sup>12</sup> The setup of the monitor spectrometer (resp. the former Mainz spectrometer) will be discussed in more detail in chapter 6, where measurements carried out in the scope of this thesis with the help of this instrument are presented.

### 2.3.4 Electron detector system

Those electrons that pass the energy filter at the analyzing plane of the main spectrometer will be reaccelerated to their original energy of around 18.6 keV and magnetically guided onto the detector. The following list defines the requirements for the detector system<sup>13</sup>:

- High detection efficiency for electrons with energies up to 50 keV.<sup>14</sup>
- Good energy resolution of  $\lesssim 1$  keV and a low dead layer thickness (required for background studies and background discrimination).
- The detector and data acquisition system must be able to withstand high electron rates of the order of  $10^5 \frac{1}{s}$  (e. g., from an electron gun or from a  $^{83m}\text{Kr}$  conversion electron source) during calibration measurements.
- The timing resolution must comply with the requirements for a time-of-flight measurement mode ( $\sigma_{\text{time}}$  of the order of 100 ns, compare simulation studies for time-of-flight values at the main spectrometer in this work: sections 7.1.1 and 7.1.2).

<sup>12</sup>The increased energy resolution requires a reduction of the magnetic field strength in the analyzing region, thus causing a widening of the magnetic flux tube and consequently a limitation of the transported magnetic flux  $\Phi$ . Details concerning the modifications can be found in [Thü07].

<sup>13</sup>In order to distinguish between the electron detector at the exit of the main spectrometer and several other detectors to be used for monitoring and calibration tasks in various locations throughout the experimental setup, the former is often referred to as the “KATRIN final plane detector”.

<sup>14</sup>In addition to the nominal signal range of about 18.6 keV during tritium runs, electrons at higher energies of up to 32 keV will be used for calibration purposes. Furthermore, the option of shifting the region of interest for the neutrino mass measurements to the 50 keV range by post-acceleration of the transmitted electrons in order to obtain a lower intrinsic detector background in the analyzing window is being considered (compare section 2.5).

- The detector-related background should be smaller than the spectrometer-related background component (see section 2.5).
- A good position sensitivity is necessary in order to
  - map the source profile,
  - determine the radial position of the particle track within the spectrometer to compensate inhomogeneities of the electric potential ( $\Delta U_{\text{ana}}(r)$ ) and the magnetic field ( $\Delta B_{\text{ana}}(r)$ ) in the analyzing plane<sup>15</sup>, and to
  - reject background events originating outside of the analyzed magnetic flux.

Furthermore, the electron detector will be situated at a magnetic field of 3 – 5.6 T, which is created by a dedicated detector solenoid. Therefore, the hardware needs to be compatible with the operation in strong magnetic fields.

A detector setup based on a large-area silicon PIN diode, which is designed to fulfill the aforementioned requirements, is presently under construction. As shown in figure 2.9, the position sensitivity is achieved by a radial and azimuthal segmentation on a circular chip.

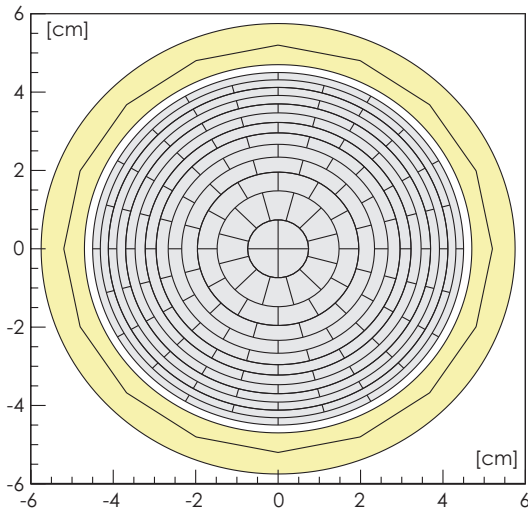


**Figure 2.9:** Pixel layout of the KATRIN final plane detector. Segmentation into 12 concentric rings (plus a central four-pixel “bull’s eye”) in radial direction and 12 parts in azimuthal direction yields 148 pixels of equal area, which are arranged in a staggered alignment. The total sensitive area of the monolithic Si-PIN diode amounts to about 63.6 cm<sup>2</sup>, corresponding to the area covered by the nominal magnetic flux of  $\Phi = 191 \text{ T cm}^2$  at a magnetic field strength of  $B = 3 \text{ T}$ .

<sup>15</sup>A detailed account of the effects of such inhomogeneities on the transmission function of the main spectrometer is given in section 4.2.1.

## 2.4 Systematic and statistical uncertainties

Clearly, the identification and careful control of systematic uncertainties is essential in a precision experiment like KATRIN. In detailed studies described in [KAT04], a number of contributions were identified and possible solutions to keep the individual contributions small were proposed. Here, six main contributions shall be listed:

1. *Elastic and inelastic scattering* inside the source will cause an energy loss  $\delta E$  of the electrons. Elastic collisions may change the angle  $\theta$  of the electron momentum with respect to the magnetic field and hence
  - cause electrons to lose a fraction of their longitudinal kinetic energy by an increase of  $\theta$ , which might affect the transmission condition, or
  - bring electrons which were originally emitted at large angles above the maximum accepted angle of  $\theta = 50.77^\circ$  into the transmitted angular range.

Inelastic processes involving an excitation of the gas molecules start playing a significant role above  $\delta E \approx 10$  eV. The energy loss function  $f(\delta E)$  has to be determined precisely by electron gun measurements and will be used as an input for the analysis of the measured  $\beta$ -spectrum (for more information on the procedure see [Wol08]).

2. Fluctuations of the *column density of the windowless gaseous tritium source* will directly influence the signal rate and the abovementioned energy loss of electrons by scattering. Therefore, a stabilization of the column density and a monitoring of fluctuations with high accuracy are needed. The latter can for example be achieved by repeated measurements with an electron gun in breaks between successive neutrino mass measurement runs, or even during the runs by continuously checking for short-term variations of the count rate with a monitor detector located at the outer border of the flux tube [Schm08].
3. *The final state distribution* of the  $(^3\text{HeT})^+$  daughter molecule also influences the shape of the measured  $\beta$ -spectrum. While the lowest excited electronic state of this molecule occurs at an energy of 27 eV and may thus be cut out by an appropriate choice of the analyzing interval, the electronic ground state, which is populated in about 57% of the decays, possesses rotational and vibrational excitations (with a mean excitation energy of 1.7 eV and a width of  $\Gamma \approx 0.36$  eV, which ultimately defines the energy resolution which can be accomplished with  $\beta$ -decay experiments using molecular tritium sources). A modelling of the final state distribution must take into account parameters like the source temperature, the isotopic composition (*i. e.*, the admixture of DT and HT molecules in the source gas) and the ratio of para- and ortho-tritium (see [Dos06]).
4. Positive ions like  $\text{T}^+$ ,  $\text{T}_2^+$  and  $\text{T}_3^+$  can be produced in the source. Moreover, electrons colliding with  $\text{T}_2$  molecules can form  $\text{T}_2^-$  ions. These can introduce further systematic uncertainties, as their individual  $\beta$ -spectra exhibit *different endpoint energies* and contribute to the total decay rate. However, the endpoint energies of all ions except that of  $\text{T}^-$  are lower than and sufficiently far away from that of  $\text{T}_2$  in order to become negligible in view of the cubic rise  $(E_0 - qU)^3$  of the count rate and the small analysis interval of KATRIN. The concentration  $n(\text{T}^-)/n(\text{T}_2)$  is determined by the production rate and the storage time of the ions. For a concentration of  $< 2 \cdot 10^{-8}$  (as estimated in [KAT04]), the expected systematic uncertainty will only give a minor contribution.
5. *Fluctuations of absolute energy scale* defined by the difference between the source potential and the analyzing potential of the main spectrometer have a direct effect on the measured  $\beta$ -spectrum. Aside from a continuous measurement of the high voltage using a custom-

built precision divider and a precision voltmeter [Thü07], the energy scale will also be monitored with stable calibration sources in the monitor beam line [Ost09, Kas08, Zbo10] (cf. section 2.3.3).

6. Due to various influences which will be further discussed in this thesis, the *transmission function of the main spectrometer* deviates from the sharp analytical form presented in figure 2.3. Inhomogeneities of the electric potential and the magnetic field of the main spectrometer, as well as the effect of an early retardation of the electrons (see sections 4.2.1 and 4.2.2), will lead to a broadening and smearing of the transmission function. Using a segmented detector helps to reduce the influence of these effects, but nevertheless extensive calibration measurements (performed for each pixel of the detector) need to be carried out to achieve a detailed understanding of the transmission properties of the main spectrometer.

None of the individual systematic effects on the above list is expected to give a contribution of more than about  $\sigma_{\text{syst},i} = 0.007 \text{ eV}^2/c^4$  (for a detailed discussion of the estimated values see [KAT04]). Thus, as a working hypothesis, an error budget of this size can be attributed to each of the independent groups, and the total systematic uncertainty with respect to the observable  $m^2(\nu_e)$  amounts to

$$\Delta m_{\text{syst}}^2 = \sqrt{\sum \sigma_{\text{syst},i}^2} = 0.017 \text{ eV}^2/c^4. \quad (2.36)$$

Aside from the items mentioned above, several other effects will give further contributions (which are also included in the general estimate (2.36)). These are

- energy-dependence of the background,
- variations of the electric potential (in particular, build-up of space charges) and of the magnetic field strength inside the source,
- Doppler shift of electron energies due to the motion of the  $T_2$  molecules, and
- energy loss of electrons via synchrotron radiation.

While the systematic uncertainty can be reduced by choosing a smaller analyzing interval, the statistical uncertainty rises due to the rapid loss of signal rate. This is due to the cubic term in the expression [Ott08] for the total count rate  $r$  at a given filter setting  $qU = E_0 - \epsilon$ :

$$\begin{aligned} r(\epsilon) &= s + b \\ &\approx A \left( \epsilon^3 - \frac{3}{2} \epsilon \sum_i |U_{ei}|^2 m_i^2 \right) + b, \end{aligned} \quad (2.37)$$

where

- $\epsilon$  is the width of the measurement interval below the endpoint of the tritium  $\beta$ -spectrum,
- $A$  is the characteristic amplitude of the  $\beta$ -spectrum,
- $b$  is the overall background rate, and
- $s$  is the integral signal rate.

Based on eq. (2.37) it is possible to find a filter setting  $\epsilon_{\text{opt}}$  (see [Ott08]) yielding a signal-to-background ratio of 2 which defines a region of optimal sensitivity on the neutrino mass:

$$s(\epsilon_{\text{opt}}) = 2b. \quad (2.38)$$

These considerations suggest a division of the measuring interval into three principal regions:

## 2 The KATRIN experiment

1. The measurements at  $qU \ll E_0$  (*i. e.*, with high count rate) allow to determine the position of the endpoint by extrapolating the  $\beta$ -spectrum.
2. The background rate can be fixed by measuring the count rate at retardation energies above the tritium endpoint:  $qU > E_0$ .
3. Finally, the region shortly below the endpoint (at  $\epsilon_{\text{opt}} \approx 3 \text{ eV}$ ) bears the highest sensitivity to  $m^2(\nu_e)$ . Therefore, the largest part of the measurement time should be spent on this region.

Hence, it is possible to find a distribution of measuring time spent at various settings of the retardation energy which optimizes the statistical uncertainty, as illustrated in figure 2.10. Figure 2.11 shows that the dependence of the statistical uncertainty on the lower limit of the measuring interval for the KATRIN reference setup becomes flat at  $\epsilon \gtrsim 35 - 30 \text{ eV}$ , and thus increasing the interval would not contribute significantly to the reduction of the statistical error. For an interval of  $[E_0 - 30 \text{ eV}, E_0 + 5 \text{ eV}]$  and three years of effective measurement time at a total background rate of  $0.01 \frac{1}{\text{s}}$ , a statistical uncertainty of similar size as the total systematic uncertainty will be reached:

$$\Delta m_{\text{stat}}^2 = 0.018 \text{ eV}^2/\text{c}^4 \quad (2.39)$$

Quadratically adding the values of the systematical and the statistic uncertainties according to eqs. (2.36) and (2.39), one obtains a total uncertainty of

$$\sigma_{\text{tot}} = 0.025 \text{ eV}^2/\text{c}^4, \quad (2.40)$$

which leads to a discovery potential of

$$\begin{aligned} m(\nu_e) &= 0.30 \text{ eV}/\text{c}^2 & (3\sigma) \\ \text{or } m(\nu_e) &= 0.35 \text{ eV}/\text{c}^2 & (5\sigma). \end{aligned} \quad (2.41)$$

Should no neutrino mass signal be found, KATRIN's sensitivity will allow to set an upper limit of

$$m(\nu_e) < 0.2 \text{ eV}/\text{c}^2 \quad (90\% \text{ C.L.}). \quad (2.42)$$

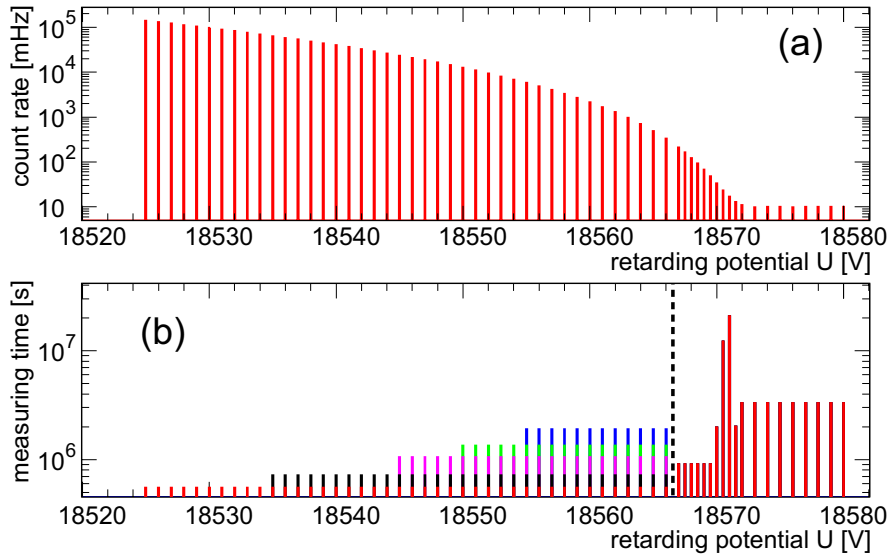


**Figure 2.10:** Optimized distribution of measurement points (from [KAT04]). (a) Simulated count rate at various settings of the retardation potential at a constant background rate of  $0.01 \frac{1}{s}$ . (b) Measuring time to be spent at individual settings of the retardation potential. The proposed scheme is the outcome of an optimization study to distribute a total measurement time of three years over the full analyzing interval. The colors indicate different lower limits of the measuring interval from 50 eV (red) to 20 eV (blue) below  $E_0$ ; the height of the entries represents the integrated time over many scans. At  $qU_0 > 18566$  eV the measurement time is not influenced by the lower limit of the energy interval. This optimization allows to improve the statistical accuracy by about 40 – 50% as compared to a uniform distribution of the measuring time.

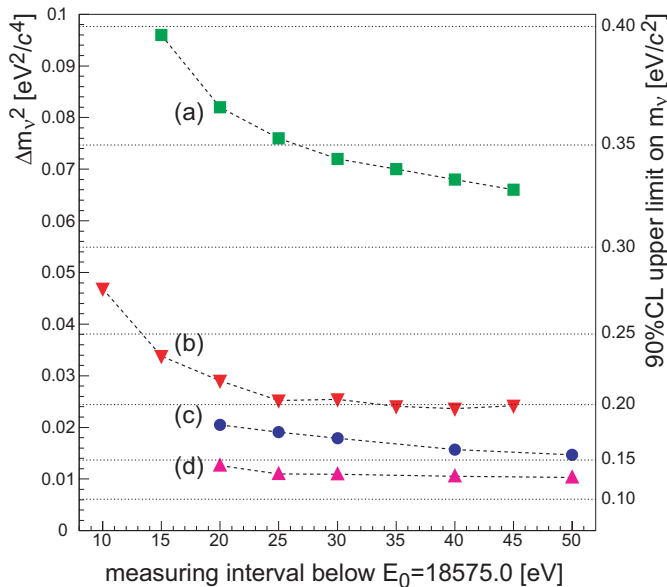


**Figure 2.11:** Statistical uncertainty  $\sigma$  (for three years of measurement time) as a function of the lower limit of the measuring interval below  $E_0$  (from [KAT04]). Different experimental configurations and background levels are compared: (a) configuration as of 2001 [KAT01] with a  $\varnothing$  7 m main spectrometer and a lower luminosity of the source. (b) Updated values of source strength and spectrometer diameter, combined with a higher isotopic purity of the  $T_2$  gas. (c) Same parameters as in (b), but taking into account the optimized measurement point distribution presented in fig. 2.10. (d) Reduction of the background rate from  $0.01 \frac{1}{s}$  as in (a) to (c) to  $0.001 \frac{1}{s}$ .

## 2.5 Sources of background in the KATRIN experiment

A comprehensive treatise of the variety of backgrounds arising from different sources throughout the experimental setup of KATRIN can be found in chapter 8 of reference [KAT04]. The following brief overview introducing the main sources of background and the measures taken to suppress them is intended to lead over to later parts of this work dealing with two of the major background contributions (chapters 3 and 4, 5 and 6).

### Background from the detector system

Contributions to the detector-related background are expected from three principal sources:

- environmental background (mainly thorium and uranium decay chains and  $^{40}\text{K}$ ),
- cosmogenic background (atmospheric gammas, muons and cosmogenic neutrons), and
- radionuclides in the detector materials.

A total detector-related background rate of  $b_{\text{det}} \leq 1 \cdot 10^{-3} \frac{1}{\text{s}}$  in the region of interest around 18.6 keV is aimed for. This value is similar to the one reached for example with a segmented Si-PIN diode at the Mainz experiment; however, the KATRIN final plane detector consists of a much larger support system and has a more than 20 times larger active area than the detector used at Mainz. Therefore, additional measures to reduce the intrinsic background are necessary. Materials for all parts in the detector environment will be carefully selected with respect to low-level activity and vacuum compatibility (the reference value of the residual gas pressure in the detector system is  $p < 10^{-10}$  mbar). Furthermore, passive and active (veto) shields will be installed (compare figure 2.12). Nevertheless, in order to achieve the required background level post-acceleration of the  $\beta$ -electrons by about 30 keV could be necessary in addition to the shielding. Simulations indicate that the detector backgrounds might be reduced by as much as a factor of two by shifting the signal to a higher energy region around 50 keV [Leb08].

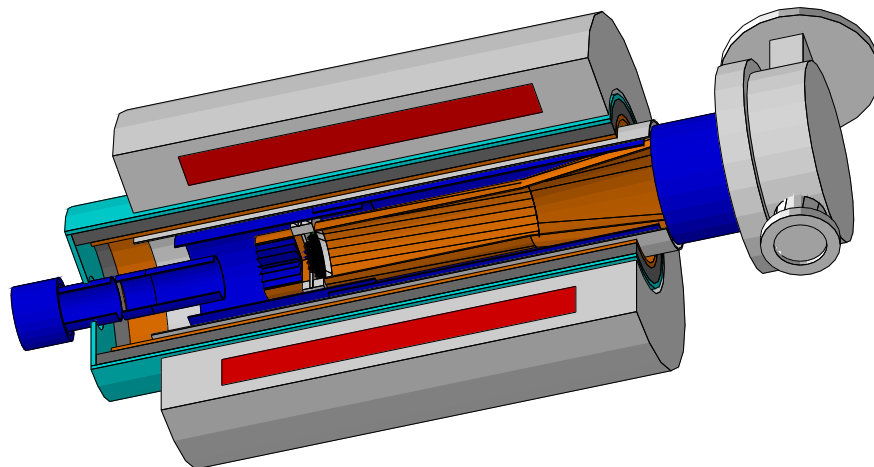


**Figure 2.12:** KATRIN final plane detector: general layout including detector magnet, shields and post-acceleration electrode [Leb09]. Starting with the outermost layer, the following components are shown: superconducting magnet: cryostat (grey) and coil (red), plastic scintillator (cyan) as active veto shield, lead (dark grey) and copper (orange) as passive shielding, beam line vacuum tube (light grey), ceramics HV insulator (blue) and post-acceleration electrode (orange).

### Tritium decay inside the analyzing volume of the main spectrometer

Any low-energy electrons born inside the analyzing volume of the main spectrometer (*i. e.*, at strong negative potential) represent a potential background source. Depending on their place of origin, they may either be guided and accelerated onto the detector, which they will hit with a kinetic energy similar to that of the signal electrons, or else be accelerated towards the upstream end of the spectrometer. Such low-energy electrons can for example be liberated in shake-off processes accompanying the  $\beta$ -decay of  $T_2$  molecules inside the spectrometer in about 15% of the cases. To keep this background component below a rate of about  $1 \cdot 10^{-3} \frac{1}{s}$ , the tritium partial pressure inside the spectrometer has to be limited to  $p(T_2) < 10^{-20}$  mbar (compare the requirements regarding tritium retention in the pumping system described in section 2.3.2).

### Electrons originating from solid high-voltage electrodes of the main spectrometer

Aside from the aforementioned electrons born inside the spectrometer volume, a significant background rate can also be caused by electrons created at the high-voltage electrodes of a MAC-E filter. This can happen through various processes:

- Emission of  $\delta$ -electrons due to *environmental  $\gamma$ -radiation* or *atmospheric muons* crossing the electrode material. As KATRIN cannot be built in the shielded environment of an underground laboratory, this background component can in principle not be avoided. Given its large surface area of about  $650 \text{ m}^2$ , the flux of atmospheric muons of  $\Phi_\mu \approx 190 \text{ s}^{-1} \text{ m}^{-2}$  [Bog06] is expected to affect the KATRIN main spectrometer more severely than the smaller spectrometers at Troitsk and Mainz. Simulations and experimental studies (see for example [Arl09]) are necessary to examine these background processes in more detail and to obtain an estimate of the expected rates. In particular, the presently poor understanding of the yield of  $\delta$ -electrons per incident  $\gamma$  or muon and of the transfer efficiency of the electrons from the electrodes towards the inner spectrometer volume (compare the discussion below) should be improved.
- *Decay of radionuclides* in the electrode material. This contribution can be suppressed by applying stringent purity demands for the employed materials. For the main spectrometer vessel, for example, the stainless steel was selected according to the requirement that a total activity of 4 Bq/kg should not be exceeded.
- *Field emission* from small-scale irregularities (“microtips”) on the surfaces or at sharp edges of electrodes. This component may be minimized by a careful preparation of all parts of the electrode system.

Having identified the potential background sources listed above, the question remains how these electrons starting from the electrode surfaces outside of the transported magnetic flux can travel inwards and eventually find their way onto the detector at all. In principle, this radial transport of electrons should be strictly prohibited by an intrinsic feature of the MAC-E filter: the magnetic shielding. One distinguishes two scenarios, depending on the direction of motion of electrons originating from the solid-metal electrodes outside of the transported magnetic flux tube:

- a) Electrons with a dominant radial component of motion (*i. e.*, perpendicular to the magnetic field lines) will be deflected back towards the electrodes by virtue of the Lorentz force and hence cannot reach the sensitive inner volume.
- b) Electrons with a large component of motion parallel to the magnetic field lines will be guided magnetically towards the ends of the spectrometer. Those electrons leaving the central volume towards the source side (“upstream” half of the spectrometer) are not harmful at all. On the other hand, those electrons originating in the “downstream” half can be accel-

erated in the direction of the detector and gain a significant amount of energy in the electrostatic field. In fact, if they are emitted from the hull with a small kinetic energy  $E_{\text{secondary}}^{\text{start}}$  of up to a few 100 eV at maximum<sup>16</sup>, they can be accelerated to a final energy

$$E_{\text{secondary}}^{\text{final}} = E_{\text{secondary}}^{\text{start}} + qU \approx E_{\text{signal}} \quad (2.43)$$

which is close to the energy  $E_{\text{signal}}$  of the electrons from tritium  $\beta$ -decay. In this case the energy resolution of the detector does not permit to separate the signal from the background. However, the important point is that the secondary electrons from the walls should not be able to hit the sensitive area of the detector at all, since the latter only covers the part of the magnetic flux tube which does not touch any electrode surfaces.

These considerations show that – in theory – the direct transport of electrons from the hull to the detector should indeed be ruled out. Nevertheless, experimental evidence gathered at the MAC-E filter of the former Mainz neutrino mass experiment [Scha09] demonstrates that electrons from high-voltage electrodes form a major background. This proof was established in several tests, for example by imaging parts of the electrodes onto the detector via a particular setting of the magnetic field lines, or by investigating the timing correlation between traversing muons and electron events on the detector (see [Scha01, Schw04, Fla04]).

The question thus arises why this magnetic shielding is not perfect. At Mainz, the fraction of electrons penetrating the magnetic shield and making their way to the detector was experimentally determined to be of the order of  $10^{-5}$ , whereas at Troitsk a value of about  $10^{-6}$  was found.

In principle, a radial motion of the electrons perpendicular to the magnetic field lines can be caused by diffusion processes due to elastic collisions with rest gas molecules. However, a simple estimate [KAT04] of the radial diffusion time  $t_{\text{rad}}$  based on an upper limit of the radial diffusion coefficient

$$D_{\perp} \leq \rho_{\text{cyc}}^2 / \tau_{\text{coll}}, \quad (2.44)$$

where  $\rho_{\text{cyc}}$  is the cyclotron radius of the electron and  $1/\tau_{\text{coll}}$  is the mean collision rate, yields values many orders of magnitude larger [Glü05c] than for example the empirical time scale of the prompt background of  $\lesssim 10 \mu\text{s}$  [Schw04] observed at the Mainz spectrometer.<sup>17</sup>

An attempt to understand the radial transport phenomena of background electrons from the electrodes was made in reference [San03], where trajectory calculations were carried out to investigate details of the electron motion. For this purpose, it is necessary to decompose the adiabatic motion of an electron in an electromagnetic field into three components: 1) the gyration around a “guiding center” (*i. e.*, a fictive point on a magnetic field line), 2) the translational motion of the guiding center along the magnetic field line, and 3) the magnetron drift motion, which is directed perpendicularly to the magnetic field line. The transverse drift velocity  $\mathbf{u}_{\perp}$  is the sum of two components, which arise from the motion of the charged particle in crossed electric and magnetic fields (so-called  $\mathbf{E} \times \mathbf{B}$  drift) and the second is caused by the curvature of the magnetic field (gradient  $B$  drift). Combining these two terms, the total magnetron drift velocity can be expressed [Ott08] as

$$\begin{aligned} \mathbf{u}_{\perp} &= \mathbf{u}_{\mathbf{E} \times \mathbf{B}} + \mathbf{u}_{\nabla_{\perp} B} \\ &= \frac{\mathbf{E} \times \mathbf{B}}{B^2} + \frac{2E_{\parallel} + E_{\perp}}{q} \frac{\nabla_{\perp} B}{B^3} \times \mathbf{B}. \end{aligned} \quad (2.45)$$

<sup>16</sup>The shape of the energy spectrum of the secondary electrons is not known precisely. Yet there are experimental hints from tests of a screening wire electrode at the Mainz spectrometer that the bulk of the secondary electrons are emitted at much lower energies. These results will be discussed in section 3.2.

<sup>17</sup>Although at least a part of the background electrons seem to use a fast transfer channel, it is likely that another part may not be able to reach the detector directly, but only via intermediate processes like trapping, scattering, and subsequent release from the trap onto the detector.

It is important to note that, given perfect axial symmetry of the electromagnetic fields, the drift motion is purely azimuthal and does not contain a radial or axial component. However, in the more realistic case of a small deviation<sup>18</sup> from axial symmetry, the magnetron motion may acquire a radial component which can provide a migration of the electron from the outer walls of the spectrometer to its interior. This notion was confirmed in further simulation-based investigations (see [Alc03, Glü05c]). For the radial drift motion to become significant, it is necessary that the ordinary azimuthal component is small (for example due to an inverse sign of the two additive components given in eq. (2.45)).

Lastly, it should be mentioned that non-adiabatic motion (for example of electrons with higher energies) may enhance the probability of inward migration. The 10 times stronger intrinsic background suppression observed by the Troitsk group might thus be related to the higher adiabaticity provided by their spectrometer.

Hence, the strategy to suppress background electrons originating from the vessel hull at the KATRIN main spectrometer is threefold:

1. provide good adiabaticity conditions (this can for example be achieved by a long spectrometer, compare [Val04]),
2. provide good axial symmetry of electromagnetic fields (*e. g.*, by reducing distortions due to geomagnetic field with compensation coils (EFCS, see section 2.3.3) and by using non-magnetic construction materials at least in the part of the spectrometer building surrounding the analyzing plane), and
3. support the intrinsic magnetic screening ( $\mathcal{O}(10^{-6}) - \mathcal{O}(10^{-5})$ ) by the additional implementation of electrostatic screening with a wire electrode, which should enhance the overall suppression by another factor of order 10 – 100 (see chapters 3 and 4 of this work).

### Ionizing collisions of trapped electrons with residual gas molecules

As will be discussed in later parts of this work (mainly in chapter 5), trapped electrons can be a troublesome source of background. In view of the artificially prolonged flight path of the stored particles, even the long mean time between ionizing collisions at the extreme vacuum conditions at KATRIN may not be sufficient to prevent the creation of a significant amount of positive ions and secondary electrons. The ionization chain will proceed until the electron energy drops below the ionization threshold or the trapping conditions are broken. Considering that the electrons may be born in a strong negative potential, the length of the ionization chain can be considerable. Electron trapping inside the main spectrometer might for example occur

- a) by the “magnetic bottle” effect (*i. e.*, the electron is magnetically reflected when approaching the strong solenoids at both ends of the main spectrometer);
- b) via electrostatic reflection at the negative potential of the analyzing plane and by magnetic reflection at either end of the spectrometer;
- c) in localized Penning-type traps which are known to exist in various places in the experimental setup – not only inside the main spectrometer or the pre-spectrometer, but also in between the two joined MAC-E filters.

The Penning-like traps can even lead to the build-up of a plasma, with disastrous effects on the background rate (as for example observed in early stages of the Troitsk and Mainz experiments as

---

<sup>18</sup>Such non-axisymmetric fields may for example be caused by an electric dipole component, by a misalignment of magnets, or by the presence of magnetic materials in the vicinity of the spectrometer (*e. g.*, normal steel used in the construction of buildings).

## 2 *The KATRIN experiment*

well as at the KATRIN pre-spectrometer).

Aside from a careful electromagnetic design, which helps to avoid particle traps in the first place, active measures might be necessary to (periodically) break the storage conditions in traps which cannot principally be avoided. For example, the use of electric dipole fields  $\mathbf{E}_{\text{dip}}$  to stimulate an enhanced  $\mathbf{E} \times \mathbf{B}$  drift motion of the trapped particles (compare eq. (2.45)) is envisioned at KATRIN. Such strong dipole fields can for example be realized by separate halves of an inner electrode system (compare the discussion in chapter 3).

Further measures to prevent the harmful effects of Penning traps are presented in section 5.1.4.

# 3 Background suppression in MAC-E filters by electrostatic screening

In the previous chapter secondary electrons from cathode surfaces were identified as one of the major sources of background expected for the KATRIN experiment. The following considerations are devoted to a method of suppressing this particular background component in MAC-E filters: the concept of electrostatic shielding by a quasi-massless grid<sup>1</sup> of wires. The discussion starts with a phenomenological description of this technique in section 3.1. Section 3.2 briefly reviews successful tests of the method at the Mainz MAC-E filter, while section 3.3 gives a short overview of the wire electrode system of the KATRIN pre-spectrometer. This experience provides a basis for the transfer of the concept to the large KATRIN main spectrometer (section 3.4), which was one of the tasks of this work (for details see also chapter 4).

## 3.1 Concept of background reduction by a screening wire electrode

The basic idea of the screening concept to suppress secondary electrons from the vessel material is to make the electric potential in the inner volume of the MAC-E filter more negative than that of the large-area vessel electrode by installing a wire grid at a voltage

$$U_{\text{grid}} = U_{\text{vessel}} - \Delta U \quad (\Delta U > 0) \quad (3.1)$$

between vessel and inner volume. As an example, the sketch in figure 3.1 illustrates the case of an electron emerging with low initial kinetic energy from the vessel hull after the passage of an atmospheric muon through the hull. The trajectory of the electron is deflected back towards the hull, and thus the electron is kept from penetrating the sensitive spectrometer volume.<sup>2</sup> The distribution of the initial kinetic energy  $E_{\text{kin}}^{\text{start}}$  of those secondary electrons generated at the surface of the vessel sets the scale for the voltage difference  $\Delta U$  (also called “screening voltage” hereafter) to be applied between vessel and grid electrode: only electrons with energies satisfying

$$E_{\text{kin}}^{\text{start}} \lesssim q \Delta U \quad (3.2)$$

will be rejected by the grid.

For this idea to work it is of course necessary to keep the amount of additionally installed material at a minimum. In general, this is expressed through the so-called geometrical coverage factor,  $f_{\text{gc}}$ , which is also referred to in the literature as the “opacity” of the grid [Rea98]. Neglecting for the moment any solid material needed in a realistic setup for the mounting structures, the opacity can be defined solely through the characteristic parameters of the wire grid. It is determined by

---

<sup>1</sup>Here and in the following, the term “grid” is meant to denote an assembly of parallel, but not crossed, wires.

<sup>2</sup>This is in fact a simplified picture; in reality, the motion of the electron is not only determined by the electric field but also by the magnetic field not shown here. For details see section 2.5.

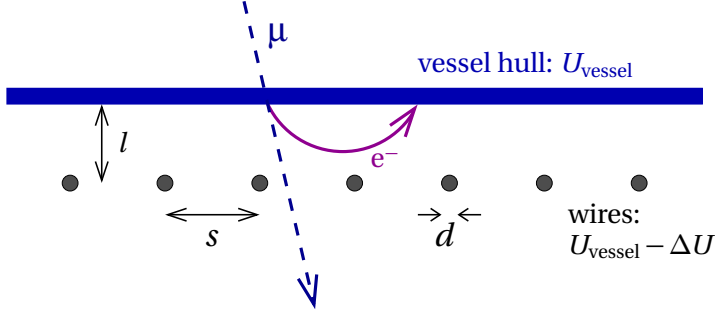


**Figure 3.1:** Principle of background suppression by electrostatic screening with a wire grid placed on a negative voltage relative to the vessel electrode. Low-energy secondary electrons originating from the vessel hull are electrostatically reflected due to the negative gradient of the electric potential along their way from the hull towards the inner volume of the vessel.

the ratio of the wire diameter  $d$  and the pitch  $s$ :

$$f_{gc} = \frac{d}{s}. \quad (3.3)$$

Keeping the opacity low thus means that, at a given wire diameter  $d$ , the wires cannot be too closely spaced – otherwise they can become a significant source of background themselves. Therefore, a suitable ratio of wire diameter  $d$  and wire spacing  $s$  needs to be found.

How does this requirement of a small diameter or a large spacing  $s$  relate to the electrostatic screening properties of the grid?

Between neighboring wires, the potential drops due to the influence of the potential of the vessel electrode  $U_{\text{vessel}}$ . Averaging over the potential in the plane of the grid gives an equivalent potential  $U_{\text{equiv}}$ , which in our case is more positive than the potential  $U_{\text{grid}}$  applied to the wires. This effect reduces the screening efficiency of the grid because the electrostatic repulsion of an electron crossing the relatively large gap between two wires is weaker than that felt by an electron incidentally headed straight towards one of the wires. The concept of an equivalent potential is discussed in the literature<sup>3</sup>, for example in [Rea98, Rea99]. It leads to a convenient way of expressing the effective potential  $U_{\text{eff}}$  in the inner volume of a cylindrical system of electrodes, which corresponds to good approximation to the equivalent potential, in terms of the voltages  $U_{\text{grid}}$  and  $U_{\text{vessel}}$ :

$$U_{\text{eff}} \approx U_{\text{equiv}} = U_{\text{grid}} + \delta U. \quad (3.4)$$

An motivation for an analytical expression of the equivalent potential is given in appendix A. In the case of a MAC-E filter,  $U_{\text{eff}}$  essentially represents the retardation potential. The aim is to achieve an effective potential  $U_{\text{eff}}$  close to that of the wires, *i. e.*, the influence of the more positive potential of the vessel should be suppressed.<sup>4</sup> This suppression can be measured by the so-called electrostatic screening factor  $S$ , which is defined by the following relation:

$$\delta U = \frac{U_{\text{vessel}} - U_{\text{grid}}}{S} = \frac{\Delta U}{S}. \quad (3.5)$$

<sup>3</sup>In general the charge density and therefore also the potential  $\phi_1$  at the side of the wire facing the solid electrode will be different from the potential  $\phi_2$  at the side pointing away from the electrode. According to ref. [Rea98], the equivalent potential can be understood as the average of the potentials  $\phi_1$  and  $\phi_2$ . The equivalent potential allows to simplify the numerical calculation of the potential far away from the grid, as for this purpose the wires can be replaced by a continuous sheet electrode placed at the equivalent potential.

<sup>4</sup>Concerning fluctuations of the electrostatic potentials, a large screening factor is advantageous as the influence of  $U_{\text{vessel}}$  on  $U_{\text{eff}}$  is proportional to  $1/S$  (compare also the discussion in section 3.4). It is easier to stabilize the grid potential to a high level, since it is placed within the “Faraday cage” formed by the vessel hull.

For a cylindrical electrode system made of a solid outer electrode of radius  $R$  and an inner wire electrode with radius  $r = R - l$ , equispaced wires with pitch  $s = \frac{2\pi r}{N_{\text{wires}}}$  and wire diameter  $d$ , the screening factor is in good approximation given by

$$S \approx 1 + \frac{2\pi l}{s \ln\left(\frac{s}{\pi d}\right)} \quad (3.6)$$

(compare appendix A). This relation holds for thin wires ( $\pi d \ll s$ ) and large radii  $R \gg l$ .

It can be seen from equation (3.6) that for the electric screening factor to become large

- $l$  and  $d$  should be large and
- $s$  should be small.

## 3.2 Development of the concept and tests at the Mainz MAC-E filter

Background processes at the Mainz MAC-E filter have been the subject of various extensive studies. After the neutrino mass measurements had been concluded, several modifications of the electrode system were effected with the aim of finding an efficient mechanism of background reduction. In view of the planned realization at the KATRIN spectrometers, the electrostatic screening method was tested at Mainz, resulting in the lowest background level ever achieved at a MAC-E filter. In a first step, a cylindrical wire electrode with radius  $r = 450$  mm, length  $L = 930$  mm, wire pitch  $s = 10$  mm and wire diameter  $d = 0.2$  mm was installed in the central part of the spectrometer [Mül02].<sup>5</sup> This configuration is usually denoted as “Mainz III”. The wire grid covers about 40% of the total electrode surface of the Mainz spectrometer, with a geometrical coverage of  $f_{\text{gc}} = \frac{d}{s} = 2\%$ . However, taking into account the unshielded mounting structures of the electrode, the geometrical coverage increases to about 5%. With a spacing of  $l = 25$  mm between wire grid and solid electrodes the electric screening factor for this system can be calculated to be  $S_{\text{Mainz III}} \approx 6.7$ . Measurements carried out with this setup showed already a significant decrease of the spectrometer-induced background rate at comparatively low screening voltages<sup>6</sup>  $\Delta U = U_{\text{solid}} - U_{\text{grid}}$  of up to 175 V: while during the neutrino mass measurements without any wire grids (“Mainz II” setup) the average background rate was of the order of  $1.5 \cdot 10^{-2} \frac{1}{s}$ , the central grid electrode allowed a background suppression by about a factor of 3 down to  $\approx 5 \cdot 10^{-3} \frac{1}{s}$ .

In the next step (“Mainz IV”), a second wire electrode covering even larger parts of the solid high-voltage electrode system was constructed and installed [Fla04]. In addition to the cylindrical section, this electrode also possesses two conical parts (see figure 3.2). It was meant as a prototype of the inner electrode system later to be installed at the pre-spectrometer (compare section 3.3).

These actions allowed to suppress the overall background rate considerably. Figure 3.3 presents the measured background rate in the “Mainz V” configuration<sup>7</sup> as a function of the screening

<sup>5</sup>The electrode is divided into four sectors that can be supplied with independent electric potentials. This allowed to study for example the influence of electric dipole fields on the background rate.

<sup>6</sup>In the previous notation,  $\Delta U$  was defined as the difference between the vessel voltage  $U_{\text{vessel}}$  and the grid voltage  $U_{\text{grid}}$  (see eq. (3.1)). Since in the Mainz spectrometer the vessel is on ground potential and the retardation potential is defined instead by a set of inner solid-metal electrodes on high voltage, the notation is altered for the sake of the discussion to  $\Delta U = U_{\text{solid}} - U_{\text{grid}}$ .

<sup>7</sup>“Mainz V” essentially consists of the wire electrode configuration of “Mainz IV” with an improved shielding of the wires in the conical part where the electric field strength is highest. Protective aluminium tubes of 5 mm diameter were employed in order to prevent field emission at the ends of the wires. Furthermore, a set of field-shaping solid conical electrodes was added.

voltage  $\Delta U$ . The two datasets shown in this figure were measured with different magnetic field strengths ( $B_{\text{solenoid}} = 1.7\text{T}$  or  $5.1\text{T}$  in the two superconducting solenoids). Due to the stronger magnetic shielding for higher magnetic field values, the background rate for the  $1.7\text{T}$  setting is higher, in particular at  $\Delta U = 0$ . In comparison to the shielding by the central cylindrical grid electrode of the “Mainz III” configuration, the new setup allowed to further reduce the background rate to  $2.8 \cdot 10^{-3} \frac{1}{\text{s}}$  at  $B_{\text{solenoid}} = 5.1\text{T}$  and  $\Delta U = 200\text{V}$ . Subtracting the intrinsic detector background rate of  $b_{\text{det}} = 1.6 \cdot 10^{-3} \frac{1}{\text{s}}$ , one thus obtains a record residual background rate of  $1.2 \cdot 10^{-3} \frac{1}{\text{s}}$  originating from the spectrometer.

Further tests of the electrostatic screening were done, for example:

- Tests with a  $^{22}\text{Na}$  source placed on top of the spectrometer vessel [Scha01, KAT04]. 511 keV gamma rays from the source produce electrons at the solid electrodes via Compton- or photoelectric processes.
- Tests with a collimated X-ray beam directed from outside the vessel at various parts of the electrode system [Fla04] (see figure 3.4).
- Background measurements in coincidence with muon detection [Schw04, KAT04] to determine the rate of muon-induced background.

In all cases, a significant reduction of the respective background component under investigation was observed due to the influence of the wire electrode.



**Figure 3.2:** Photograph showing the wire electrode of the “Mainz IV” setup before insertion into the spectrometer (photo taken from [Fla04]). The grid is segmented into three parts: besides the central cylindrical section, two conical wire segments were added in order to cover a larger fraction of the solid electrodes as compared to the “Mainz III” setup.

### 3.3 Implementation of the concept at the KATRIN pre-spectrometer

The KATRIN pre-spectrometer, which has been operated in test mode since 2004 at Forschungszentrum Karlsruhe, also is equipped with a wire electrode system.<sup>8</sup> Taking a lesson from the initial field emission problems at the wires in the conical section of the “Mainz IV” electrode, the conical end parts of the pre-spectrometer inner electrode were made of sheet metal.<sup>9</sup> To this, a grid

<sup>8</sup>Following a basic design conceived in [Fla04], the mechanical concept and fabrication of the inner electrode of the pre-spectrometer were done at the University of Washington at Seattle (T. Burritt *et al.*).

<sup>9</sup>A continuous electrode surface is much less sensitive to field emission because, unlike for thin wires, there is no enhancement of the field strengths.

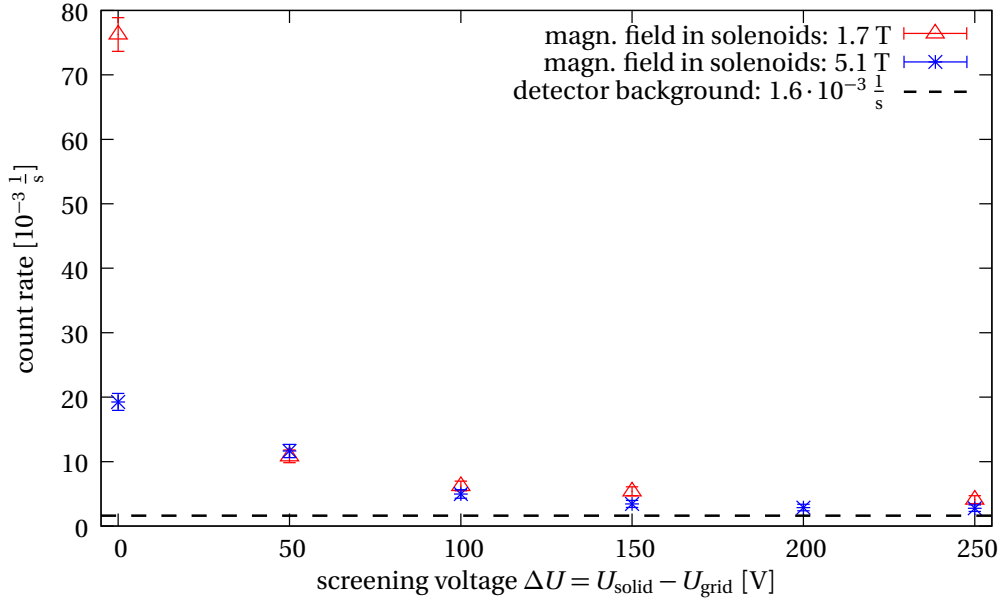


**Figure 3.3:** Background reduction by screening wire grids at the Mainz MAC-E filter (configuration “Mainz V”): dependence of the background count rate on the electrostatic screening potential. Measurements for two settings of the central magnetic field inside the spectrometer solenoids are shown ( $\triangle$ :  $B = 1.7 \text{ T}$  and  $*$ :  $B = 5.1 \text{ T}$ ). For comparison, the average background rate during neutrino mass measurements (without any wire grid) was of the order of  $1.5 \cdot 10^{-2} \text{ s}^{-1}$ . Figure adapted from [Fla04].

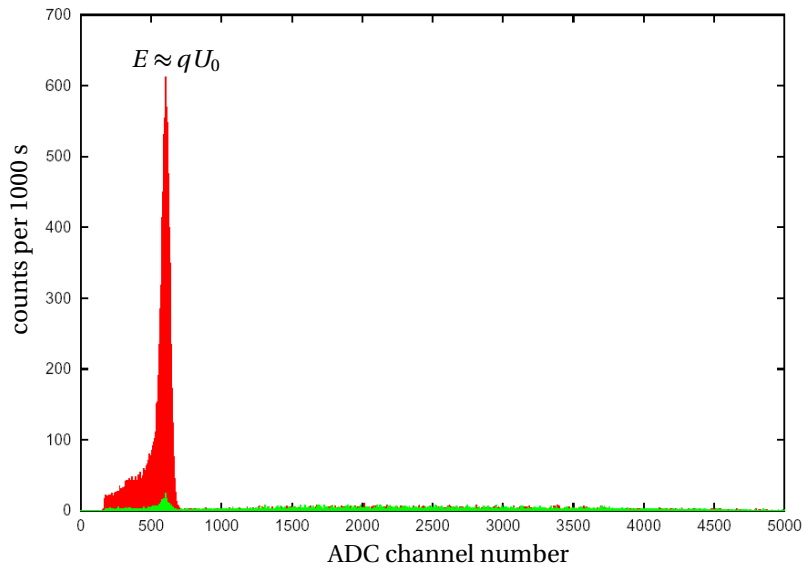


**Figure 3.4:** X-ray-induced background at the Mainz spectrometer (configuration “Mainz III”) without screening voltage (red) and with active screening grid ( $\Delta U = 100 \text{ V}$ ) (green). The largest reduction of background was observed when directing the X-rays at the central region of the spectrometer, where the magnetic field strength is minimal and therefore the intrinsic magnetic shielding is comparatively weak. The count rate in the peak corresponding to the retardation energy  $qU_0$  measured at the outermost detector segment was reduced by a factor of about 30. These measurements are described in [Fla04]; the picture was taken from [KAT04].



**Figure 3.5:** Photograph showing the wire electrode system of the pre-spectrometer before installation. Apart from three sections (two cones, one cylindrical part) equipped with a single layer of wires fixed to a mounting structure, the electrode consists of two conical sections made of sheet metal in order to cope with the high electric field strengths in the vicinity of the ground electrodes at the entrance and exit of the spectrometer. A cradle-like support system resting on the bottom of the vessel is used. Electrical decoupling between vessel and inner electrode is provided by a set of glass insulator tubes.

electrode consisting of two conical sections and a central cylindrical section, much like the ones at Mainz, are added (see figure 3.5). With a wire diameter of  $d = 0.5$  mm, a pitch of  $s \approx 22$  mm and a spacing to the solid electrode of  $l \approx 60$  mm, the central part possesses a geometrical coverage of  $f_{gc} \approx 2.3\%$  and an electric screening factor of  $S_{\text{pre-spec}} \approx 7.5$ . All parts of the inner electrode are split into halves that are insulated against each other. Potential differences up to a few kV can be applied to the two segments in order to produce an electric dipole field.

It should be noted here that the purpose of installing a wire electrode at the pre-spectrometer is different from that of having a wire electrode inside the main spectrometer. While background reduction is vital in the main spectrometer, its significance is not as large in the case of the pre-spectrometer: As the retardation voltage of the pre-spectrometer is about 300 V more positive than that of the main spectrometer, background electrons produced in the pre-spectrometer and accelerated by the retardation potential in the direction of the main spectrometer will be rejected by the main energy filter. (They might still contribute to filling the Penning trap between the two MAC-E filters, which will be discussed in chapters 5 and 6). However, detailed tests of the efficiency of background reduction (normal screening grid operation and dipole mode) are planned to be carried out with the pre-spectrometer setup, as it in general resembles the main spectrometer system more closely than the Mainz spectrometer. Unfortunately these measurements had to be delayed due to ongoing investigations of Penning traps inside the pre-spectrometer and the installation and testing of a modified electrode system in the cone regions (see section 5.2). Therefore, the screening test measurements at Mainz remain the most comprehensive and conclusive ones to date. Presently the pre-spectrometer is being prepared for the start of background tests with the screening grid. An X-ray source has recently been installed which will be used to perform measurements similar to those done at Mainz.

### 3.4 Transfer of the concept to the KATRIN main spectrometer

First studies regarding an implementation of the screening concept for the main spectrometer were carried out in the work described in [Val04]. The basic parameters of the wire electrode design were laid down there (see tables 3.1 and 3.2 and figure 3.6). As a novel feature compared to the earlier wire electrode “prototypes” built for the Mainz MAC-E filter and the KATRIN pre-spectrometer, the main spectrometer wire electrode is conceived as a double-layer system.

The main motivation for using a two layers of wires results from the conflicting requirements

regarding the geometrical parameters  $s$  and  $d$  of the grid, which were already encountered in section 3.1. On the one hand, the surface area of the high-voltage electrodes in the KATRIN main spectrometer exceeds that of previous MAC-E filters by about two orders of magnitude, and thus a low geometrical coverage  $f_{\text{gc}}$  of the grid is of key importance in order to maintain a background level of  $\lesssim 10^{-2} \frac{1}{s}$  reached with the smaller spectrometers. The background suppression factor due to the wire grid is approximately given by  $1/f_{\text{gc}}$  (which follows from geometrical arguments), and hence one finds that  $f_{\text{gc}} \lesssim 1\%$  needs to be achieved for the KATRIN main spectrometer. Therefore, a small wire diameter  $d \ll s$  is required.

On the other hand, there are two arguments opposing this demand:

- The electric field strength at the surface of a wire in the grid can be approximated by

$$E_{\text{surf,wire}} \approx \frac{\Delta U}{l} \frac{s}{\pi d} = \frac{\Delta U}{l} \frac{1}{\pi f_{\text{gc}}}, \quad (3.7)$$

where  $\Delta U$  is again the difference between the electric potentials of the solid and the wire electrode in the case of a single-layer grid (compare eq. (A.12) in appendix A). Experience from the Mainz experiment shows that field emission at the wires starts at around  $E_{\text{surf,wire}} \approx 0.4$  to  $0.7 \frac{\text{MV}}{\text{m}}$  [Mül02, Fla04, KAT04]. Thus, the wire diameter  $d$  (or, more generally, the factor  $ld/s$ ) should be large in order to prevent field emission. This is particularly important since it is planned to use the wire electrode of the main spectrometer also in the dipole mode, where high electric potential differences of the order of 1 to 2 kV relative to the vessel wall will be applied to the wires. The electric dipole field serves the purpose of removing charged particles, which are trapped in isolated regions inside the spectrometer, from the sensitive analyzing volume by virtue of the  $\mathbf{E} \times \mathbf{B}$  drift motion. First studies applying this method to the MAC-E filter of the former Mainz neutrino mass experiment were carried out in [Thü02, Mül02].

It is immediately clear from eq. (3.7) that, for a fixed range of  $l$  and  $\Delta U$ , the requirement of a small geometric coverage conflicts with the aim of obtaining a low electric field strength  $E_{\text{surf,wire}}$ .

- The high voltage on the main spectrometer vessel electrode will unavoidably be affected by a considerable ripple  $\Delta U_{\text{vessel}}$ . Part of it stems from instruments (like for example vacuum pumps) connected to the tank, but the high voltage supplies themselves will also give a contribution typically of  $\mathcal{O}(100 \text{ mV})$ . For the purpose of reducing the influence of the low-frequency part of this ripple on the retardation potential inside the spectrometer, a large electric screening factor  $S$  is helpful. This can be seen from eqs. (3.4) and (3.5):

$$\Delta U_{\text{ana}} \equiv \Delta U_{\text{eff}} \approx \left(1 - \frac{1}{S}\right) \cdot \Delta U_{\text{grid}} + \frac{1}{S} \cdot \Delta U_{\text{vessel}}, \quad (3.8)$$

with  $\Delta U_{\text{grid}}$  being the ripple on the wire electrode high voltage and  $\Delta U_{\text{ana}}$  denoting the fluctuations of the retardation potential.  $\Delta U_{\text{grid}} \ll \Delta U_{\text{vessel}}$  can be achieved by using special high-precision and high-stability power supplies (e. g.,  $\Delta U_{\text{grid}}$  of  $\mathcal{O}(10 \text{ mV})$  peak-to-peak [FuG08]). Hence, eq. (3.8) indicates that  $\Delta U_{\text{vessel}}$  is suppressed by a factor of  $1/S$ .

According to eq. (3.6), a large value of  $S$  (at a given  $l$ ) translates into a small value of the background screening factor  $1/f_{\text{gc}}$ :

$$S \approx 1 + \frac{2\pi l}{s \ln\left(\frac{s}{\pi d}\right)} = 1 + \frac{2\pi l}{s \ln\left(\frac{1}{\pi f_{\text{gc}}}\right)}. \quad (3.9)$$

### 3 Background suppression in MAC-E filters by electrostatic screening

The parameter  $l$  representing the radial distance between the wires and the solid electrode forms a lever arm which helps to relieve some of the tension. However,  $l$  can only be enlarged within certain limits, as the physical margin in radial direction between the vessel hull of the spectrometer and the outer border of the transported magnetic flux is only  $\approx 0.4$  m. Another method to resolve the conflict is indeed the use of two wire layers with different wire diameters. This is also supported by a third argument: For the retardation potential  $U_{\text{eff}}$  to be homogeneous, a constant value of  $l$  is required. Since the shape of the central section of the vessel deviates from a perfect cylinder, whereas the wire electrode is supposed to define a nearly ideal cylinder (within very tight tolerances, compare section 4.5),  $l$  cannot be expected to be uniform over the full extent of the wire electrode. With the inclusion of a second wire layer, this problem is reduced to controlling the relative distance  $l_2$  between the wire layers with high precision<sup>10</sup>, while the distance  $l_1$  between the vessel and the first (outer) layer becomes less relevant.

In the light of the arguments presented above, the following section therefore summarizes the most important characteristics of a two-layer wire electrode for the KATRIN main spectrometer.

**Table 3.1:** Parameters of the wire electrode for the KATRIN main spectrometer in an early design stage (according to [Val04]). During the course of the design studies described in chapter 4 of the present work, most of the parameters were modified, *e. g.*, the wire diameters and the layer spacing. The voltage differences given here are to be understood as reference values, since the voltages applied to different sections of the wire electrode may vary slightly (see figure 3.6 and table 3.2).

	first (outer) layer	second (inner) layer
distance to vessel hull	150 mm	200 mm
wire diameter $d$	0.5 mm	0.15 mm
circumferential wire pitch $s$	$\approx 25$ mm	$\approx 25$ mm
voltage difference $U_{\text{vessel}} - U_{\text{wire}}$	-100 V	-200 V

**Table 3.2:** Electric potentials assigned to different parts of the electrode system in an early design stage [Val04] (compare figure 3.6).

segment	type	potential [kV]		# of wires
		first (outer) layer	second (inner) layer	
A	solid (ground electrode)	0	—	—
B, C, D	solid (vessel electrode)	-18.400	—	—
E	solid (inner electrode)	-18.400	—	—
a	wires (inner electrode)	-18.470	-18.570	1194
b	wires (inner electrode)	-18.490	-18.590	1194
c	wires (inner electrode)	-18.497	-18.597	1194
d, e, f	wires (inner electrode)	-18.500	-18.600	1194

<sup>10</sup>The meaning of  $l_1$  and  $l_2$  is explained in figure 3.7 further below.

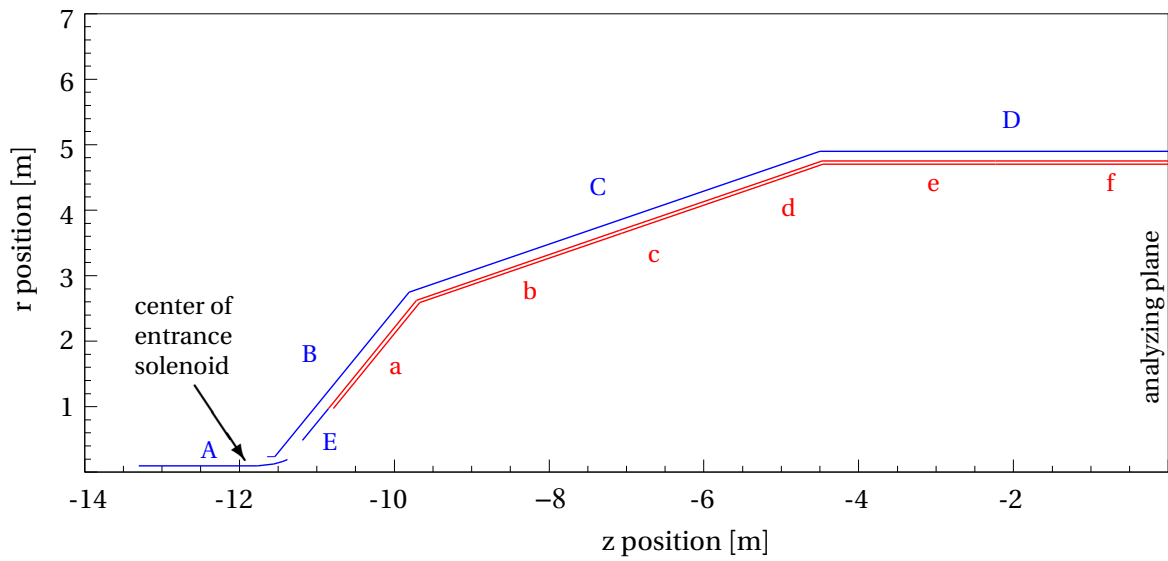


**Figure 3.6:** Early conceptual design of the two-layer main spectrometer wire electrode (according to [Val04]). Contours of the wire layers (equidistant spacing to the vessel hull:  $l_1 = 150\text{mm}$  and  $l_1 + l_2 = 200\text{mm}$ , respectively) are marked in red, while all solid parts of the electrode system are drawn in blue colour. The latter category comprises vessel and ground electrodes as well as certain parts of the inner electrode which are placed in regions of high electric fields and were thus intended to be made of solid metal rather than thin wires in the early stages of the development of the wire electrode. For the electric potentials in this configuration see table 3.2.

### 3.4.1 Parameters of a double-layer wire electrode system for the main spectrometer

Although the overall concept of the wire electrode for the KATRIN main spectrometer has in the meantime undergone major revisions regarding several aspects (see chapter 4), the basic features were established already in the early drafts:

- The wires of the two layers should be arranged in a staggered configuration, as illustrated in figure 3.7. Hence both layers must include the same number of wires:  $N_{\text{wire},1} = N_{\text{wire},2} \equiv N_{\text{wires}}$ . Due to the different circumferential length of the two wire layers, which are placed on cylinders of slightly different radii, this means that the pitch  $s$  between the wires is only approximately the same in the two layers:

$$\frac{2\pi(R-l_1)}{N_{\text{wires}}} = s_1 \approx s_2 = \frac{2\pi(R-(l_1+l_2))}{N_{\text{wires}}}. \quad (3.10)$$

For example, with  $R = 4900$  m,  $l_1 = 150$  mm,  $l_2 = 50$  mm and  $N_{\text{wires}} = 1194$  one obtains  $s_1 = 25.0$  mm and  $s_2 = 24.73$  mm.

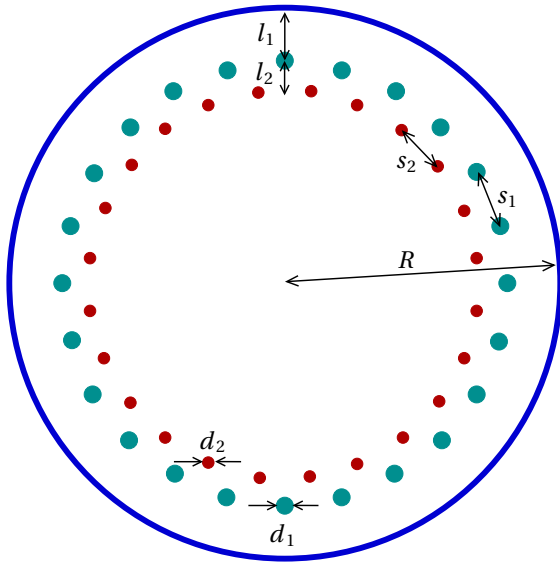


**Figure 3.7:** Schematic illustration: parameters of a double-layer wire electrode. The solid cylindrical electrode of radius  $R$  encloses two concentric cylinders of radii  $R-l_1$  and  $R-(l_1+l_2)$  (with  $l_2 < l_1$ ) along which the wires are distributed in a staggered arrangement: one wire of the inner layer fills the gap between two neighboring wires of the outer layer. In the outer and inner layer the wire diameters are  $d_1$  and  $d_2 < d_1$ , respectively. Since both  $l_2$  and  $l_1$  are much smaller than  $R$ , the wire pitch in the two layers is approximately the same ( $s_2 \approx s_1$ ).

- The spacing of the inner wire layer with respect to the vessel hull,  $l_1 + l_2$ , should allow for a margin  $\delta r$  of at least a few centimeters between the border of the nominal magnetic flux and the wire electrode. This holds in particular for the region close to the analyzing plane, where the diameter of the flux tube assumes its maximum value:

$$4.5 \text{ m} = r_{\text{flux,ana}} = R_{\text{vessel}} - (l_1 + l_2) - \delta r. \quad (3.11)$$

For example, the choice  $l_1 + l_2 = 150 \text{ mm} + 50 \text{ mm}$  leaves a clearance of  $\delta r \approx 150 \text{ mm}$ . The safety margin is necessary in order to

- impede by virtue of magnetic screening the direct migration of electrons from the cathode surfaces – especially from the wire electrode itself – towards the inner volume of the spectrometer, and to
- achieve a homogeneous effective potential seen by the electrons out of reach of the ripple structure caused by the wires (*i. e.*,  $\delta r \gg s/(2\pi)$ , compare appendix A).

- Previous experience from the tests of the wire electrode concept at the Mainz MAC-E filter indicates that a staged screening potential of  $2 \times 100\text{V}$  (*i. e.*, 100V difference between vessel hull and outer wire layer and another 100V between the two wire layers) should be sufficient to intercept the majority of the secondary electrons from the solid electrodes (see figure 3.3).
- Wire diameters of  $d_1 = 0.5\text{ mm}$  and  $d_2 = 0.15\text{ mm}$  for the outer and inner layer, respectively, yield the following values for the opacity and the electric screening factor of the grid:

$$\begin{aligned} \text{outer layer: } f_{\text{gc},1} &\approx 2\%, & S_1 &\approx 14.6, \\ \text{inner layer: } f_{\text{gc},2} &\approx 0.6\%, & S_2 &\approx 4.2. \end{aligned} \quad (3.12)$$

Hence, the outer layer is responsible for the bulk part of the electric screening while possessing a comparatively large geometrical coverage. Therefore, it is advisable to mask it with a second layer of lower screening and, in return, reduced coverage.  $S_1$  and  $S_2$  can be used in order to approximately relate the applied potentials  $U_{\text{vessel}}$ ,  $U_{\text{grid},1}$  and  $U_{\text{grid},2}$  to the effective retardation potential  $U_{\text{eff},2}$  in the far-field region at large radial distance from the inner wire layer. Combining eqs. (3.4) and (3.5) one finds that the effective potential resulting from the outer layer of wires reads

$$U_{\text{eff},1} = U_{\text{grid},1} + \frac{U_{\text{vessel}} - U_{\text{grid},1}}{S_1}. \quad (3.13)$$

Assuming that the radial distance between the two layers is large compared to the wire pitch, the effective potential resulting from the inner layer can be computed using  $U_{\text{eff},1}$  as a point of reference instead of the potentials  $U_{\text{vessel}}$  or  $U_{\text{grid},1}$ :

$$U_{\text{eff},2} = U_{\text{grid},2} + \frac{U_{\text{eff},1} - U_{\text{grid},2}}{S_2}. \quad (3.14)$$

Inserting eq. (3.13) into (3.14) yields

$$U_{\text{eff},2} = U_{\text{grid},2} + \frac{1}{S_2} \left( U_{\text{grid},1} + \frac{U_{\text{vessel}} - U_{\text{grid},1}}{S_1} - U_{\text{grid},2} \right). \quad (3.15)$$

However, the value obtained by inserting the relevant parameters into eq. (3.15) can only be used for an illustrative (toy) model since it neither takes into account the influence of mounting structures nor the graded values of the potentials on different parts of the wire electrode. Furthermore, the expression (3.6) for the analytical form of the screening factor is valid strictly only for infinite planar or, at best, cylindrical electrodes. Nevertheless, it is instructive to get an estimate of the effective potential resulting from the electrode configuration. Inserting the values  $U_{\text{vessel}} = -18.4\text{ kV}$ ,  $U_{\text{grid},1} = -18.5\text{ kV}$  and  $U_{\text{grid},2} = -18.6\text{ kV}$  together with  $S_1$  and  $S_2$  from eq. (3.12) one thus obtains

$$\begin{aligned} U_{\text{eff},2} &\approx -18574.6\text{ V} \\ &= U_{\text{grid},2} + 25.4\text{ V}. \end{aligned} \quad (3.16)$$

The effective retardation potential is thus appreciably more positive than the voltage applied to the innermost wire layer. Despite all limitations of the model, the computer simulations qualitatively reproduce the value obtained in eq. (3.16).

- The azimuthal division of the wire electrode into two electrically independent halves, although not visible in the  $rz$ -cut in figure 3.6, is implicitly included in all design considerations. It allows to operate the inner electrode in the aforementioned dipole mode during

### 3 Background suppression in MAC-E filters by electrostatic screening

short measurement intervals. Since the azimuthal (circumferential) distribution of wires should form a closed circular contour without any distinguished direction introduced by a particular “dipole separation gap”, the nominal uniform spacing  $s$  of the wires must be sufficient to sustain the full dipole potential difference in the low kV range. A pitch of  $s \approx 25$  mm seems suitable to fulfill this condition.

- The field strength at the surface of the grid needs to be considered separately for the normal mode with both halves of the electrode at the same potential and for the dipole operation with large potential differences. In the normal mode, the inner wire layer with the smaller wire diameter is more critical (compare eq. (3.7)):

$$E_{\text{surf, wire1}} \approx \frac{100 \text{ V}}{50 \text{ mm}} \frac{25 \text{ mm}}{\pi \cdot 0.15 \text{ mm}} \approx 110 \frac{\text{V}}{\text{mm}}. \quad (3.17)$$

From the geometrical factor  $l_1 d_1 = 10 \cdot l_2 d_2$  one sees that for the same value of  $\Delta U$  the electric field strength at the outer wire layer should be a factor of 10 lower than at the inner layer. It can therefore only become critical in the dipole mode, where both wire layers are short-circuited and the potential difference  $\Delta U_1$  to the vessel hull is large. If one assumes a dipole voltage of  $\Delta U_{\text{dipole}} = 1$  kV, the factor of 10 cancels and one obtains the same approximate value of the electric field strength as for the inner layer:

$$E_{\text{surf, wire2}} \approx \frac{1000 \text{ V}}{150 \text{ mm}} \frac{25 \text{ mm}}{\pi \cdot 0.5 \text{ mm}} \approx 110 \frac{\text{V}}{\text{mm}}. \quad (3.18)$$

Although both values are well below the critical value of  $400 \frac{\text{V}}{\text{mm}}$  determined experimentally at the Mainz setup, it has to be kept in mind that a significantly higher electric field strength can arise at particular points of the geometry that are not included in the simplified estimate above. For example, sharp bends of the wire in the vicinity of the mounting structures might become critical. Therefore, an experimental investigation was started to validate the technical concept [Zac09].

In the original draft, the parts of the inner electrode closest to the ground electrodes were conceived as sheet-metal cones as an additional precautionary measure. This concept was inspired by the experience at Mainz and the inner electrode concept of the pre-spectrometer (compare figure 3.5). It had to be abandoned later due to technical constraints (see next chapter).

**Table 3.3:** Comparison of geometrical coverage  $f_{gc}$  and electrostatic screening factor  $S$  for the wire electrodes of the configurations III and IV/V of the Mainz MAC-E filter, the KATRIN pre-spectrometer and the *first draft* for the KATRIN main spectrometer. (Note that the parameters for the wire electrode of the main spectrometer were changed in the course of the design studies described in chapter 4.) The numbers given for  $f_{gc}$  and  $S$  apply for the cylindrical sections of the wire electrodes; both values change for the conical sections where the wire spacing  $s$  varies with the axial position. For the two-layer system of the KATRIN main spectrometer, the wires of the inner layer determine the geometrical coverage ratio  $f_{gc}$ , while the bulk part of the electrical screening factor is due to the outer layer with larger  $l$  and  $d$  (compare eq. (3.12)). The background reduction is indicated by giving the approximate background count rates (in units of  $10^{-3} \frac{1}{s}$ ) without and with screening as well as the resulting suppression factors. It is not yet clear what the actual unshielded background rate at the main spectrometer will be, but probably a suppression factor of the order of  $10 - 100$  will be needed to achieve the desired range of  $10^{-2} \frac{1}{s}$ .

setup	$f_{gc} = \frac{d}{s}$	S	coverage of solid electrodes by wires	background reduction (approx. rates in $10^{-3} \frac{1}{s}$ )	suppression factor
<i>Mainz III</i> wires only: incl. unshielded mounting rods:	$\frac{0.2 \text{ mm}}{10 \text{ mm}} = 2\%$ $\approx 5\%$	6.7	ca. 40%	$(10 - 15) \xrightarrow{\Delta U = 100 - 200 \text{ V}} 5$ (experimentally determined)	3
<i>Mainz IV/V</i> support structure partly shielded	$\frac{0.2 \text{ mm}}{20 \text{ mm}} = 1\%$	6	full	$(10 - 15) \xrightarrow{\Delta U = 100 - 200 \text{ V}} 1.2$ (experimentally determined)	10
<i>KATRIN pre-spectrometer</i> wires only:	$\frac{0.5 \text{ mm}}{22 \text{ mm}} \approx 2.3\%$	7.5	full (but with solid-metal cones)	under investigation	
<i>KATRIN main spectrometer</i> wires only:	$\frac{0.15 \text{ mm}}{25 \text{ mm}} = 0.6\%$	14.6	full	? $\xrightarrow{\Delta U \approx 2 \times 100 \text{ V}} \lesssim 10$ (aim, 2 layers)	10 - 100

### *3 Background suppression in MAC-E filters by electrostatic screening*

## 4 Design studies for the wire electrode of the KATRIN main spectrometer

Starting from the basic parameters of the wire electrode for the KATRIN main spectrometer described in the last section of the previous chapter, detailed simulation-based design studies were needed to refine the concept and elaborate technical details. In some points disparate physical and technical requirements needed to be balanced in close collaboration with the engineers.

The account of the investigations carried out in the scope of this work is divided into the following parts: Sections 4.1 and 4.2 define the technical requirements and important design criteria in view of the electromagnetic properties of a MAC-E filter. An overview of the tools and numerical methods used for the computer simulations is given in section 4.3. The step-wise implementation of the computer model and the main results of the investigations are described in sections 4.4 through 4.8. Finally, section 4.9 summarizes the production and quality assurance steps, while section 4.10 contains concluding remarks and briefly reviews the hardware status of the project.

### 4.1 Technical requirements

Several technical requirements set the framework for the concept and realization of a wire electrode system of the KATRIN main spectrometer.

- Compliance with the ultra-high vacuum demands of the KATRIN spectrometer section is a vital issue:
  - In order to meet the specified outgassing rate of  $< 10^{-12} \text{ mbar l s}^{-1} \text{ cm}^{-2}$ , only a limited selection of materials (*e. g.*, stainless steel, ceramics (Frialit) and gold) may be used for the construction of the wire electrode. The requirements are quite different from those of wire chambers typically used in the large detector systems known in particle physics, as for example the usage of glue to fix the wires is strictly prohibited.
  - All pieces to be installed inside the main spectrometer must be cleaned according to the ASTeC procedure<sup>1</sup>, which includes degreasing with a detergent in an ultrasonic bath and subsequent rinsing with demineralized water.
  - Vacuum compatibility also implies the venting of screws and other pieces that might house air enclosures, which causes a considerable additional work load during production.
  - Minimizing the the surface area introduced by the inner electrode (in particular by the solid mounting structures) is one of the criteria to be kept in mind during the design stage.<sup>2</sup>
  - Finally, the assembly of the modules needs to take place in a cleanroom environment.

---

<sup>1</sup>Guidelines for UHV-compatible preparation and cleaning of stainless steel surfaces were released by the Accelerator Science and Technology Centre, ASTeC (see website <http://www.astec.ac.uk/>).

<sup>2</sup>This point is of course not only important with regard to vacuum issues, but also essential for the efficiency of the achieved background suppression.

- The abovementioned vacuum demands require a bakeout of the whole spectrometer including the inner electrode system at temperatures up to 350°C. In order to avoid any mechanical stress and potential permanent deformation of the electrode system, the material of the wire electrode must possess a thermal expansion coefficient compatible with that of the stainless steel (1.4429 DIN) of the spectrometer vessel. This can be achieved by using a suitable stainless steel grade (*e. g.*, 1.4429 DIN or 1.4435 DIN (for plates), 1.4404 DIN (for wires)) as the only working material for the wire electrode, which is also favored from the point of view of vacuum compatibility.
- Only non-magnetic materials can be used. The aforementioned stainless steel grades also fulfill this demand.
- Furthermore, all material has to be carefully screened for radioactive contamination. This not only holds for the stainless steel wires and sheet metal, but also for the welding seams of the mounting structures which often contain radionuclides related to the thorium chain (see refs. [Geb07, Ben09]).
- In addition, the wire material was selected with respect to elasticity and thermal properties [Rei07], as well as in view of the surface quality [Geb07], which plays an important role in avoiding field emission. Of course all parts of the mounting structures (those belonging to the modules as well as those for the rail system) must be electropolished to round off sharp edges and microtips.
- The necessity to handle and mount the parts of the wire electrode inside the spectrometer calls for a modular design with a maximum weight of the individual parts of about 20 kg.

## 4.2 Design criteria

The design criteria regarding the inner electrode system of the main spectrometer are strongly coupled to those applied to the design of the vessel electrode (see reference [Val04]). Four of the key points regarding the electromagnetic design of the main spectrometer will be introduced in the following.

### 4.2.1 Homogeneity of electric retardation potential and magnetic field in the analyzing plane

In an ideal MAC-E filter both the electrostatic retardation potential  $U_{\text{ana}}$  and the minimum magnetic field strength  $B_{\text{ana}}$  are invariable along the full extent of the analyzing plane, which in the case of the KATRIN main spectrometer covers a diameter of 9 m. Equation (2.28) reflects these idealized characteristics of the spectrometer: constant values enter the analytical expression for the transmission function, irrespective of any radial dependencies of the fields.

In reality, however, inhomogeneities both in the electric and the magnetic field will be introduced due to various influences (finite-size effects as well as local distortions of the field configuration). The magnitude of the inhomogeneities in the analyzing plane can be estimated by the two quantities

$$\begin{aligned} \Delta U_{\text{ana}} &= |U_{\text{ana}}(r=0) - U_{\text{ana}}(r=r_{\text{ana,max}})| \\ \text{and} \quad \Delta B_{\text{ana}} &= |B_{\text{ana}}(r=0) - B_{\text{ana}}(r=r_{\text{ana,max}})|. \end{aligned} \quad (4.1)$$

The radius of the magnetic flux tube at the analyzing plane of the main spectrometer is  $r_{\text{ana,max}} = 4.5$  m. Typically, the retardation potential is about 0.5 – 1 V more negative and the magnetic field

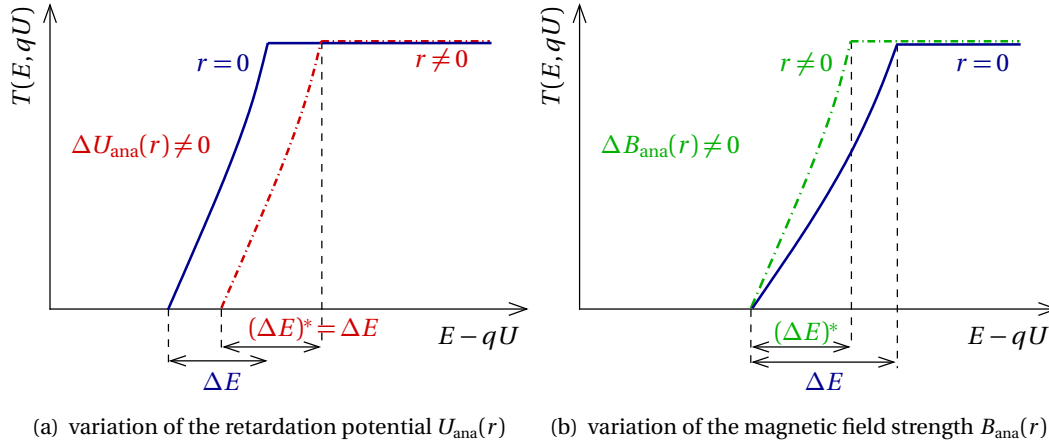


**Figure 4.1:** Influence of field inhomogeneities on the shape of the transmission function. In this sketch the cases  $\Delta U_{\text{ana}}(r) \neq 0$  (a) and  $\Delta B_{\text{ana}}(r) \neq 0$  (b) are treated separately in order to disentangle both effects. In practice, however, they will usually be present simultaneously, and a continuous distribution of radii instead of a single value needs to be considered (compare figure 4.2).

strength reduced by 12 – 15% at the outer border of the flux tube.

Figure 4.1 illustrates the influence of radial variations of the fields on the transmission function. Depending on the radius at which the electrons pass the analyzing plane, they experience a different retardation potential. This leads to a shift of the onset of transmission relative to the nominal value, while the width of the rise is left unchanged:  $(\Delta E)^* = \Delta E$  (fig. 4.1(a)). In contrast, a radial variation of the magnetic field across the analyzing plane will affect the width of the transmission function (fig. 4.1(b)).

As a result, the real transmission function, which integrates over all radii  $r \leq r_{\text{ana,max}}$ , is broadened significantly and the sharp edges of the analytical shape are smeared out. Both effects are of course undesirable. On the basis of preliminary values for the potential depression  $\Delta U_{\text{ana}}(r)$  and the variation of the magnetic field  $\Delta B_{\text{ana}}(r)$  obtained in this work, a Monte Carlo study of their effects on the transmission function was carried out by J. Dunmore (Univ. of Washington, Seattle) [Dun07]. As expected, the outcome of the simulation (figure 4.2) shows a considerable deterioration of the properties of the transmission function. The largest influence stems from the potential depression  $\Delta U_{\text{ana}}$ .

To reach the sensitivity on the neutrino mass envisaged for KATRIN, measures to reduce this effect need to be taken:

- The electromagnetic design of the main spectrometer should be optimized such as to minimize the amount of inhomogeneity. For example, the shape and potential distribution of the inner electrode system can be adjusted to reduce the potential depression in the analyzing plane.<sup>3</sup> The homogeneity of the magnetic field can be improved by choosing an appropriate configuration of the air coils.
- The effective magnitude of the radial inhomogeneities is reduced by using a radially segmented detector. Since the number of independent pixels is limited due to technical rea-

<sup>3</sup>In fact, as will be seen in section 4.6, the implementation of realistic wire electrodes with solid mounting structures results in a higher inhomogeneity of the retardation potential compared to the case without wire electrode. However, the effect can be lessened by carefully choosing a suitable layout of the wire electrode geometry, by tuning the distribution of electric potentials to various parts of the electrode system and by introducing dedicated compensation structures (see section 4.6).

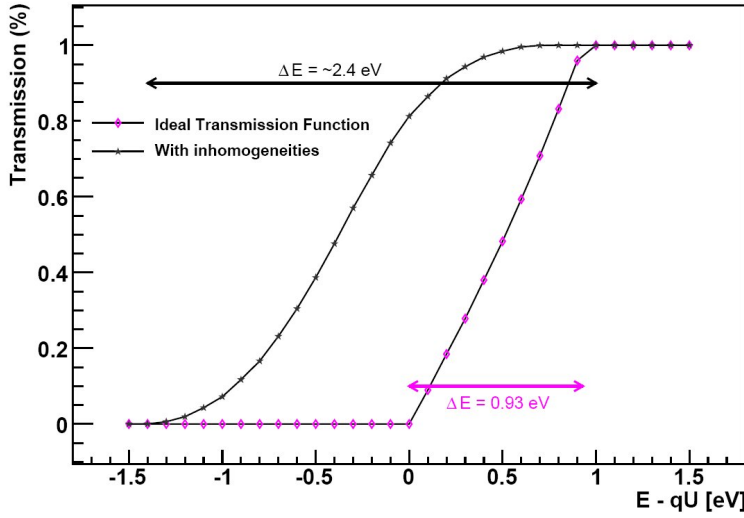


**Figure 4.2:** Simulated transmission function including inhomogeneities of the retardation potential ( $\Delta U_{\text{ana}} \approx 1.2\text{V}$ ) and of the magnetic field ( $\Delta B_{\text{ana}} \approx 4 \cdot 10^{-5}\text{T}$ ). If the segmentation of the detector area into radial pixels is not considered, the width of the transmission function will thus be increased from the nominal value of  $\Delta E = 0.93\text{eV}$  to about  $2.4\text{eV}$ . Figure taken from [Dun07].

sons, a residual effect on the transmission function remains. A radial discretization into 12 concentric rings and a central four-piece bull’s eye has been established as a viable compromise for the KATRIN final plane detector<sup>4</sup> (see figure 2.9). The arrangement of the pixel rings approximately matches the gradient of the potential depression imaged from the  $\varnothing 9\text{m}$  analyzing plane onto the  $\varnothing 90\text{mm}$  detector chip. In order to be able to fully exploit the benefits of the segmentation of the detector in the analysis of the tritium runs, each pixel needs to be calibrated separately and the individual transmission function has to be determined. This requires extensive and rather time-consuming calibration runs with a high-precision electron source that allows to spatially scan the full cross section of the magnetic flux tube (see discussion in section 7.1).

#### 4.2.2 Transmission properties

The working principle of the MAC-E filter requires an electron traversing the spectrometer to reach its minimal longitudinal kinetic energy at the plane where maximum electrostatic retardation and minimum magnetic field coincide. By convention, this analyzing plane is situated at an axial position  $z = 0$  (it corresponds to the mirror plane of the spectrometer in axial direction). If the minimum of the longitudinal kinetic energy occurs at an axial position  $z_m \neq 0$ , an effective analyzing plane is created. This phenomenon, which is also characterized quite graphically as “too early retardation”, deteriorates the energy resolution of the spectrometer: the magnetic field strength  $B_m$  at  $z_m$  will be higher than at  $z = 0$ , therefore the electron will pass the shifted effective analyzing plane with a higher amount of residual transversal kinetic energy  $E_{\text{trans}}$ .

To quantify the effect it is instructive to define a parameter  $\delta E_{\parallel}$  as

$$\delta E_{\parallel} = E_{\parallel, \text{ana}} - E_{\parallel, \text{min}}, \quad (4.2)$$

where  $E_{\parallel, \text{ana}}$  denotes the value of the longitudinal kinetic energy at the nominal location of the analyzing plane ( $z = 0$ ) and  $E_{\parallel, \text{min}}$  is the global minimum of the longitudinal kinetic energy reached along the trajectory.

It is therefore important to control the evolution of the longitudinal kinetic energy of electrons from their starting point at the entrance of the spectrometer until they reach the analyzing plane.

<sup>4</sup>In addition, the detector is also divided into 12 azimuthal sectors.

Along with the inspection of the homogeneity of the electrostatic and magnetic fields, this step needs to be repeated for each modification of the electromagnetic configuration of the spectrometer. For this purpose, either a microscopic tracking routine or an approximative adiabatic tracking can be used (both programs are described in section 4.3.3). Electrons passing the analyzing plane at the outer border of the magnetic flux tube with small surplus energies of the order of  $\lesssim 1$  eV, which additionally possess a large cyclotron component of the motion (*i. e.*, large starting angles of  $\theta_{\text{start}} \lesssim \theta_{\text{start,max}} \approx 51^\circ$  at the source), represent the most critical group since

1. they cross the analyzing plane at large radii, where the electrostatic retardation is strongest (due to the potential depression mentioned in the previous section), and
2. a large part of their initial kinetic energy resides in the transversal component  $E_{\perp}$ .

### 4.2.3 Adiabaticity

The adiabatic conversion of kinetic energy between the transversal and longitudinal components, which is the key to the superior energy resolution that can be reached with a MAC-E filter, is not a predisposed feature that can be taken for granted. Rather the adiabatic properties can be impaired by various influences, for example by a faulty configuration of the electric and magnetic fields. The entrance region of the spectrometer, in particular, is prone to conditions departing from adiabaticity as here a sudden transition between zero potential (inside the ground electrode) and strong retardation takes place in a highly inhomogeneous magnetic field. The second region where non-adiabatic conditions can occur is the large central part of the spectrometer, where the electrons are guided only by a weak magnetic field. Electrons crossing the analyzing plane with high kinetic energy (*i. e.*, with large surplus energies with respect to the electric filter potential) will not be guided efficiently.

In general, a careful adjustment of the electric and magnetic fields during the design phase helps to produce good adiabaticity conditions. These can be checked by looking for changes in the adiabatic invariant

$$\gamma\mu = \frac{p_{\perp}^2}{2mB}, \quad (4.3)$$

for example along the trajectory of an electron through a MAC-E filter. Any sizeable deviation from  $\gamma\mu = \text{const.}$  which cannot be attributed to numerical inaccuracies indicates a limited adiabatic energy transfer. In this case a broadening of the transmission function occurs, which is rather difficult to assess. Therefore, non-adiabatic behavior should be avoided and controlled by computer simulations.

A study of the adiabaticity characteristics of the main spectrometer (vessel electrode only) was carried out in [Val04]. Since no severe changes are expected to be caused by the inclusion of the wire electrode, the reinvestigation of adiabaticity was deferred in favor of the more immediate difficulties regarding field homogeneity and transmission properties.

### 4.2.4 Avoidance of traps for charged particles

A further design criterion to be taken into account is related to the incidental trapping of charged particles. As pointed out in various places throughout this work, the configuration of electromagnetic fields present in a MAC-E filter naturally gives rise to particle traps which can cause an increase of background through secondary effects like ionizing collisions with residual gas molecules.

There are three main mechanisms by which charged particles can be stored in MAC-E filters:

- **Magnetic trapping** follows the principle of the “magnetic bottle”. A particle which starts from some position within the MAC-E filter at a relatively low magnetic field strength and propagates towards the regions of higher magnetic field strength at either end of the spectrometer will experience a transformation of the longitudinal component  $E_{\parallel}$  of the kinetic energy into the transversal component  $E_{\perp}$  by virtue of the magnetic gradient force. If the relative fraction of transversal kinetic energy of the particle at the starting point is sufficiently large, the magnetic mirror effect will eventually extract all of the longitudinal energy and cause the particle to reverse its direction of motion at some point of reflection, which can easily be seen by applying equation (4.20). In the case where reflection occurs at both ends of the spectrometer the trapping mechanism is said to be purely magnetic.
- **Electrostatic trapping with magnetic guiding** occurs when a charged particle follows a magnetic field line that intersects a particular electrostatic equipotential line twice.<sup>5</sup> This kind of field configuration resembles that of the Penning trap and is the most relevant one for the studies that are described in the following.
- **Electromagnetic trapping** forms a combination of the two abovementioned effects: the charged particle is for example reflected by the strongly negative electric potential in the analyzing plane and by the magnetic mirror effect at one of the ends of the spectrometer.

Chapter 5 is devoted to the complex of problems associated with Penning-type traps. For example, deep Penning-like traps are located at the conical entrance and exit regions of the pre- and main spectrometer, and another trap exists between the two spectrometers. While the former type of trap can largely be suppressed by a suitable design of the electrode system (see sections 5.2 and 5.3), the latter cannot be avoided and a dedicated mechanism is needed to prevent the build-up of a charged plasma (compare section 5.4 and chapter 6).

---

<sup>5</sup>In the case of a MAC-E filter with negative electric potentials this applies for negatively charged particles, *i. e.*, mainly for electrons and in rarer cases also for negatively charged molecules.

## 4.3 Simulation tools

The program package used for the electromagnetic design studies of the main spectrometer and its inner electrode system was written by F. Glück (Forschungszentrum Karlsruhe) [Glü05a, Glü06a, Glü09a] and maintained by S. Vöcking (Univ. Münster, see also [Vöc08]). It consists of a number of routines, written in the programming language C, that can be grouped into the following categories:

- computation of static magnetic fields from a given coil configuration,
- computation of electrostatic fields from a given electrode configuration,
- trajectory calculation for charged particles moving in electromagnetic fields,
- auxiliary programs (for example magnetic field line calculation, creation of geometry input files or visualization of geometries).

The methods and basic working principles of the programs representing each of these tasks will be briefly outlined in the following.<sup>6</sup>

### 4.3.1 Calculation of magnetic fields

The magnets included in the KATRIN setup can be described as cylindrical inductor coils. Both superconducting magnets (for the high-field coils with magnetic field strengths up to 6 T) and normal-conducting air coils (mostly for the field-shaping in low-field regions) are used. In most applications the coils are aligned to a common axis of rotational symmetry, which simplifies the calculation.<sup>7</sup> However, considering the global arrangement of coils also the tilted magnets in the cryogenic pumping section (CPS) need to be taken into account. In addition, the implementation of (small) tilt angles is necessary for the estimation of tolerances with regard to placement and alignment of the magnets. Therefore, a general method to compute the magnetic field from an assembly of cylindrical coils with individual symmetry axes is needed. This is realized in the program `magfield3`, which expects as an input the following coil parameters:

<code>Ncoil</code>	number of coils,
<code>I [k]</code>	current density (number of windings times current divided by cross section of the coil in the $rz$ -plane, in A/m <sup>2</sup> ),
<code>A [k] [1], B [k] [1]</code>	Cartesian coordinates ( $l = x, y, z$ ) of the two axial endpoints of the coil, defining the local symmetry axis (in m),
<code>Rmin [k], Rmax [k]</code>	minimum and maximum radius of the coil winding (in m),
<code>n [k]</code>	discretization parameter: number of radial segments of the coil.

Here,  $k = 1, \dots, Ncoil$  represents the coil index. For applications that only involve a single global symmetry axis the simplified program `magfield2` (with slightly different input parameters) can be used.

Both programs use a similar approach. The body of a coil can be decomposed into a number of thin current loops, for which the magnetic field is given by Biot-Savart's law:

<sup>6</sup>Details concerning the simulation software are documented for example in references [Hug08], [Vöc08] and [Val04].

<sup>7</sup>The main spectrometer subsystem for example, with three superconducting coils (including pinch and detector magnets) and the set of 14 field-shaping air coils, contains only a single symmetry axis.

$$d\mathbf{B} = \frac{\mu_0 I}{4\pi} \frac{d\mathbf{l} \times \mathbf{r}}{r^3}, \quad (4.4)$$

where  $d\mathbf{B}$  is the magnetic field induced at a fieldpoint  $\mathbf{r}$  by a current  $I$  through an infinitesimal piece of conductor (direction and length determined by  $d\mathbf{l}$ ).

Starting from eq. (4.4) the components  $B_r$  (radial),  $B_\phi$  (azimuthal) and  $B_z$  (axial) of the magnetic field can be calculated analytically by using complete elliptical integrals (see for example chapter 2.2 of reference [Kno00]). This powerful method allows to compute  $\mathbf{B}$  in any arbitrary field point (even within the coil winding itself) to high accuracy. However, the computation is rather time-consuming. Therefore, an approximative but faster method can be applied, which is based on an expansion of the field components in terms of Legendre polynomials (see for example [Gar51]). The series does not converge for arbitrary fieldpoints but only for those within a certain convergence area defined by the coil configuration. Depending on the distance between fieldpoint and coil, either the “central” or “remote” Legendre polynomial expansion can be employed.

### 4.3.2 Calculation of electric fields

Two techniques traditionally used for the numerical solution of electrostatic problems are the *finite difference method (FDM)* and the *finite element method (FEM)*. Since the achievable accuracy strongly depends on the granularity of grids or meshes subdividing the full volume taken up by the input geometry, these methods are not very well suited for electrode geometries which comprise both very large and tiny dimensions.<sup>8</sup> Therefore, the routines used for the studies presented here are based on a different approach.

Introduced in the 1960s, the *boundary element method (BEM)*<sup>9</sup> (see for example [Har76, Ren82]) has by now become well established. In early developmental stages it was mainly used for the computation of electrostatic lenses [Cru63, Rea71], but a wide range of further applications soon followed and a number of program packages (such as the Charged Particle Optics codes CPO2d and CPO3d [CPO08]) became commercially available.

The main advantage of the boundary element method is that it provides continuous field and potential distributions [Ren82] while using a smaller amount of computational resources as compared to the FDM or FEM methods. Reference [Cub99] presents a comparison of these three techniques on the basis of benchmark tests.

The charge density method replaces conducting electrodes in a vacuum environment by charged surfaces which are then subdivided into a number of  $N$  small elements with a homogeneous charge density  $\sigma_i$  ( $i = 1, \dots, N$ ). An element with surface area  $a_i$  thus has a total charge  $q_i = a_i \sigma_i$ . The charges give rise to a potential distribution which can be determined in the following way.

In the first step, the potential contribution of the element  $j$  at the center of element  $i$  is evaluated:

$$\phi_{ij} = \frac{\sigma_j}{4\pi\epsilon_0} \int_{a_j} \frac{d^2\mathbf{r}_j}{|\mathbf{r}_i - \mathbf{r}_j|}. \quad (4.5)$$

Since in this version of the boundary element method the charge density on each element is assumed to be constant, the integral only depends on the geometry of the two elements  $i$  and  $j$ . The

<sup>8</sup>Any solely FDM- or FEM-based attempt to calculate for example the potential inside the large KATRIN main spectrometer with the small details introduced by the wire electrode will encounter this discretization problem (compare initial studies in [Val04]). A possible workaround is to replace the geometry details of the wire electrode by a solid electrode placed on the corresponding equivalent potential, see section 3.1.

<sup>9</sup>Other terms describing the same method include *charge density*, *surface charge* or *integral equation method*.

fact that only the potential at the center of the element is computed introduces an error, which is however of no concern as long as the elements are chosen to be small enough.<sup>10</sup>

Next, the collective contribution of all the elements is considered. Summation over all elements yields the resulting potential  $U_i$  at the center of element  $i$  :

$$U_i = \sum_{j=1}^N \phi_{ij} = \sum_{j=1}^N C_{ij} \sigma_j, \quad (4.6)$$

where the coefficients  $C_{ij}$  contain the geometry information:

$$C_{ij} = \frac{1}{4\pi\epsilon_0} \int_{a_j} \frac{d^2 \mathbf{r}_j}{|\mathbf{r}_i - \mathbf{r}_j|}. \quad (4.7)$$

The vector  $\mathbf{U}$  is generated from the potentials applied to the electrodes and used as an input.<sup>11</sup> Hence, the problem is essentially reduced to finding the coefficients  $C_{ij}$  and solving the set of linear equations defined by (4.6) for the vector  $\boldsymbol{\sigma}$  of charge densities on all the elements.

Special care needs to be taken for electrodes with sharp edges or at joints of two neighboring electrodes that form a narrow angle, in which cases singularities in the charge density can occur. Such difficulties can at least be amended by choosing an appropriate distribution of elements along the electrode, for example by increasing the number of elements towards the ends of long electrodes.

Usually, one is interested in the potential at any fieldpoint  $\mathbf{r}$  outside the electrodes rather than in the charge densities. Therefore, the last step is the superposition of all individual charge densities  $\sigma_k$  (with  $k = 1, \dots, N$ ) which were calculated before:

$$U(\mathbf{r}) = \frac{1}{4\pi\epsilon_0} \sum_{k=1}^N \sigma_k \int_{a_k} \frac{d^2 \mathbf{r}_k}{|\mathbf{r} - \mathbf{r}_k|}. \quad (4.8)$$

The computation of the coefficients  $C_{ij}$  becomes significantly more simple if certain symmetries of the electrode configuration can be exploited. For the applications discussed in this work, axially-symmetric objects are of particular relevance. In this case the geometry can be decomposed into thin rings of charge for which the potential can be computed analytically using the complete elliptical integral of the first kind (see, *e. g.*, [Ren82]). Similar to the calculation of magnetic fields described above, Legendre polynomials are also useful for the computation of electric potentials and fields.

Both methods are employed in two programs, `e1cd3_2` and `e1cd3_3`, which use varying degrees of rotational symmetry.<sup>12</sup> Mirror symmetry provides an (optional) additional simplification. The electrode configuration of the main spectrometer, for example, is mirrored with respect to the central plane (analyzing plane, usually placed at  $z = 0$ ).

- In `e1cd3_2` solid-metal electrodes can take the shape of either cylindrical or conical segments, *i. e.*, full rotational symmetry is used. Wires can also be implemented. Each wire segment is defined by a straight line replicated with an  $n$ -fold discrete rotational symmetry.

<sup>10</sup>This is in fact the major limitation to any large-scale application of the charge density method, see for example the extension of the boundary element method using multipole expansions developed in reference [Vöc08].

<sup>11</sup>Electrode surfaces are equipotential surfaces; therefore, a voltage  $U$  applied to a specific segment of the electrode system also represents the potential  $U_i$  for all elements of this segment.

<sup>12</sup>In fact, the files `elcd3_2.c` and `elcd3_3.c` are function libraries that contain the algorithms called from the executable programs. The main programs, or executables, are named `e1main2` and `e1main3`, respectively.

Wires as well as solid shapes are thus determined by line elements in the  $rz$ -plane. The following parameters are therefore needed as input:

**for solid and wire electrodes:**

$N_{el}$	number of electrode segments
$zA[k], zB[k]$	$z$ -positions of the two endpoints of the straight line defining the segment with index $k$ ( $k = 1, \dots, N_{el}$ )
$rA[k], rB[k]$	$r$ -position of the two endpoints of the straight line
$U[k]$	electric potential applied to the segment with index $k$
$disc[k]$	discretization parameter for segment with index $k$

**additional parameters for wire electrodes:**

$d[k]$	wire diameter of the segment with index $k$
$\phi_i[k]$	relative azimuthal angle of the segment with index $k$
$n[k]$	discrete rotational symmetry for the segment with index $k$ ( <i>i. e.</i> , number of wires in azimuthal direction)

Figure 3.6 shows an example of an input geometry for a calculation using `elcd3_2`.

- `elcd3_3` was developed as an extension of `elcd3_2`. It accepts either rectangles or wires as electrode segments. By abandoning the geometry input via fully-rotated line elements the usage of objects with partial rotational symmetry becomes possible. In fact, the rectangles and wires can have any orientation in space, which in principle allows the modeling of arbitrary three-dimensional geometries.<sup>13</sup> This is necessary for more realistic simulations of the wire electrode for the KATRIN main spectrometer, in particular regarding the details of the mounting structures (see following sections). The implementation of more complex geometries using discrete rotational symmetry also for solid electrode parts allows to study the influence of these details on the shape of the electric field.

An input file for `elcd3_3` must contain the following parameters (see illustration in figure 4.3):

**for solid electrode parts:**

$i$	global index of the element
$i\_sigma$	index of the charge density group the element belongs to
$type[i]$	$type=1$ identifies an object as being a solid piece of electrode
$rot[i]$	parameter for discrete rotational symmetry
$Px[i], Py[i], Pz[i]$	Cartesian coordinates of the corner point
$n1x[i], n1y[i], n1z[i]$	Cartesian coordinates of the first unit vector
$n2x[i], n2y[i], n2z[i]$	Cartesian coordinates of the second unit vector
$a1[i], a2[i]$	side length in direction of first and second unit vector, respectively
$U[i]$	electric potential applied to the element with index $i$

<sup>13</sup>In practice, the fully three-dimensional approach cannot be realized for large objects such as the KATRIN main spectrometer due to the huge number of elements that would be needed. Instead, several groups of identical parts are implemented, which are multiplied and rotated with a discrete rotational symmetry.

**for wires:**

$i$	global index of the element
$i\_sigma$	index of the charge density group the element belongs to
$type[i]$	$type=2$ identifies an object as being a wire
$rot[i]$	parameter for discrete rotational symmetry
$P1x[i], P1y[i], P1z[i]$	Cartesian coordinates of one end of the wire
$P2x[i], P2y[i], P2z[i]$	Cartesian coordinates of the second end of the wire
$d[i]$	wire diameter
$U[i]$	electric potential applied to the element with index $i$

The use of two independent indices  $i$  and  $i\_sigma$  allows to group the electrode elements into subsets with common charge density, which can help to save computational resources in geometries with discrete rotational symmetry. The unit vectors  $n_1$  and  $n_2$  are expected to be orthonormal. To make the length of a line of input for a wire equal to that of a rectangle, a set of four arbitrary numbers needs to be inserted between the  $d$  and  $U$  parameters of a wire. These four parameters are ignored during readout.

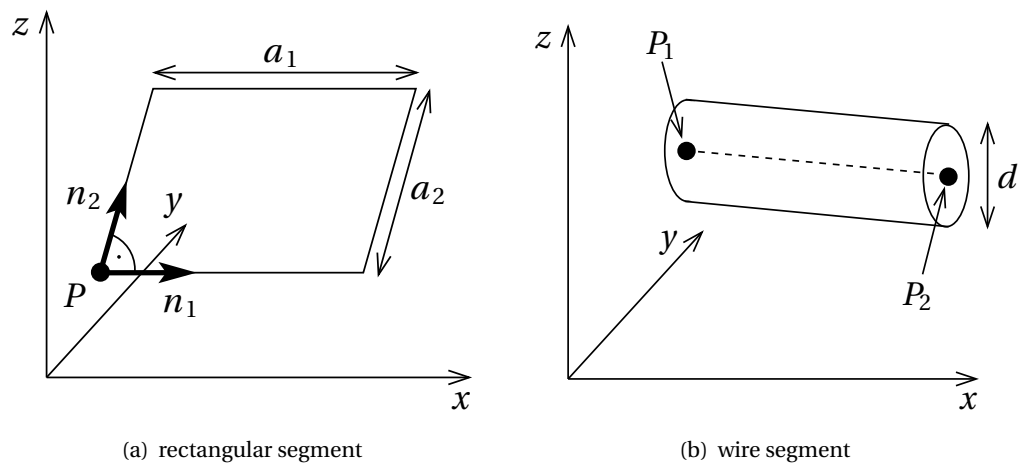


**Figure 4.3:** Definition of input parameters for `e1cd3_3`: (a) solid electrode geometry with rectangular elements, (b) wire geometry.

### 4.3.3 Trajectory calculation for charged particles in electromagnetic fields

The program `traj` performs a detailed calculation of the trajectory of a charged particle in electromagnetic fields. The calculation is referred to as being “microscopic” since it follows the loops of the cyclotron motion instead of employing the adiabatic approximation to track the particle along a specific magnetic field line and neglecting the gyration. The latter approach is chosen in the `transmission` code. These two programs and their respective uses are introduced in the following paragraphs.

#### Microscopic trajectory calculation with `traj`

The motion of a charged particle in combined electric and magnetic fields can be described by six differential equations of first order:

$$\begin{aligned}\dot{\mathbf{x}} &= \mathbf{v}, \\ \dot{\mathbf{p}} &= \mathbf{F}_L,\end{aligned}\tag{4.9}$$

where  $\mathbf{F}_L = q(\mathbf{E} + \mathbf{v} \times \mathbf{B})$  is the Lorentz force.  $\mathbf{x}$  represents the vector of Cartesian coordinates in each point of the trajectory,  $\mathbf{v}$  is the velocity and  $\mathbf{p}$  the momentum vector of the particle. A fully relativistic formulation is used.

The tracking routine evaluates the fields  $\mathbf{E}$  and  $\mathbf{B}$  in every point before solving the system of equations (4.9), and uses the 4<sup>th</sup> or 8<sup>th</sup> order Runge-Kutta algorithm for stepping. Employing the higher order algorithm is recommended since it offers better accuracy of the calculation.

Each cyclotron turn with a period  $T$  of

$$T = \frac{2\pi}{\omega_{\text{cyc}}} = 2\pi \frac{\gamma m}{qB}\tag{4.10}$$

is divided into a number of `ntimestep` calculation steps, which allows a flexible adjustment of the tracking routine to a particle traversing regions with strongly varying field strengths. It provides a simple way to implement an adaptive determination of the step size

$$h = \frac{T}{n_{\text{timestep}}}\tag{4.11}$$

which is tailored to the specific problems to be solved in different places within the KATRIN setup. The user can influence computation time on the one hand and accuracy on the other hand by tuning the `ntimestep` parameter.

To start the computation the following input parameters are needed:

<code>E_start</code> [eV]	total kinetic energy of the particle at the start of the calculation,
<code>z_start</code> [m]	$z$ coordinate of the starting point,
<code>r_start</code> [m]	$r$ coordinate of the starting point,
<code>theta</code> [deg]	angle defined by $\theta = \angle(\mathbf{B}, \mathbf{p})$ at the starting point,
<code>phi</code> [deg]	azimuthal angle with respect to the magnetic field line at the starting point,
<code>z_end</code> [m]	$z$ coordinate at which the calculation will be stopped.

Many useful parameters of the trajectory are available as output after each step of the calculation:

$z$ [m]	$z$ -coordinate,
$r$ [m]	$r$ -coordinate,
$B$ [T]	absolute value of the magnetic field strength,
$\Phi$ [V]	value of the electric potential,
$\text{err1} = \frac{E_{\text{total}} - E_{\text{total,start}}}{E_{\text{total}}}$	(dimensionless) parameter to estimate numerical errors of the calculation by checking the conservation of total energy,
$\text{err2} = \frac{L - L_{\text{start}}}{L}$	(dimensionless) parameter to estimate numerical errors of the calculation by checking the conservation of total angular momentum,
$\Gamma = \frac{(\gamma\mu) - (\gamma\mu)_{\text{start}}}{(\gamma\mu)}$	parameter to check for a relative deviation from adiabatic motion,
$\cos(\mathbf{B}, \mathbf{p})$	cosine of the angle between the magnetic field vector and the momentum vector of the particle,
$E_{\parallel}$ [eV]	longitudinal component of the kinetic energy,
$E_{\perp}$ [eV]	transversal component of the kinetic energy,
$t_{\text{of}}$ [ $\mu\text{s}$ ]	time of flight elapsed since the start of the trajectory.

An extension of the trajectory calculation allows to include collisions with gas molecules for given values of the residual gas pressure and ambient temperature. However, this part of the routine is typically deactivated for the calculations regarding the electromagnetic design.

In most applications the microscopic tracking routine is used in combination with a fully rotational-symmetric electric field configuration generated with `e1cd3_2`. The usage together with `e1cd3_3` is in principle also possible, but practically inconvenient because of the significantly increased amount of computation time for the electric field from a partially rotational-symmetric geometry.<sup>14</sup> For such applications the microscopic trajectory calculation is discarded in favor of the `transmission` program (see next paragraph), which is in general much faster.

### Calculation of the longitudinal energy in the adiabatic approximation with `transmission`

An alternative algorithm is based on the assumption that the transversal component  $E_{\perp}$  of the relativistic kinetic energy<sup>15</sup> transforms adiabatically according to

$$(E_{\perp})_f = (E_{\perp})_i \cdot \frac{B(r_f, z_f)}{B(r_i, z_i)} \cdot \frac{\gamma_i + 1}{\gamma_f + 1} \quad (4.12)$$

<sup>14</sup>If the geometry possesses a discrete rotational symmetry, the electrodes can be approximated by a number of circular rings. In this case the calculation of fields and thus also the microscopic tracking routine can be sped up by using the zonal harmonic (Legendre polynomial) approximation. The calculation of the source constants needed for this method is implemented in `e1cd3_3`.

<sup>15</sup>The “relativistic kinetic energy”  $E_{\text{kin}} = E_{\perp} + E_{\parallel}$  is additive because of the Pythagorean relation,  $p^2 = p_{\perp}^2 + p_{\parallel}^2$ . It can be written as

$$\begin{aligned} E_{\text{kin}} &= E - mc^2 = (\gamma - 1)mc^2 \\ &= \frac{(\gamma - 1)(\gamma + 1)mc^2}{\gamma + 1} \\ &= \frac{(\gamma^2 - 1)mc^2}{\gamma + 1} = \frac{\beta^2\gamma^2 mc^2}{\gamma + 1} \\ &= \frac{1}{\gamma + 1} \frac{p^2}{m}, \end{aligned}$$

with  $p = \beta\gamma mc$  and  $(\beta\gamma)^2 = \gamma^2 - 1$ .

when the particle propagates from a starting point  $(r_i, z_i)$  to an arbitrary point  $(r_f, z_f)$ . The adiabatic invariant

$$\frac{p_{\perp}^2}{B} = \text{const.} \quad (4.13)$$

was used to obtain eq. (4.12). The longitudinal kinetic energy in any point along the trajectory can then be determined from eq. (4.12) through  $E_{\parallel} = E_{\text{kin}} - E_{\perp}$ .

By relying on the adiabatic energy transformation the time-consuming microscopic trajectory calculation can be avoided. Instead, the particle is tracked along a magnetic field line and the values of  $r$ ,  $z$  and  $E_{\parallel}$  are computed in a specified number of points and written to the output file. The intended use of the program `transmission` is to test whether the transmission condition is fulfilled for a particle trajectory with given starting parameters. In principle, the calculation can be started at any point  $(r, z)$  within the magnetic flux tube. It is, however, reasonable to choose such starting conditions for which the transmission condition is most critical, namely

- large starting radii  $r_{\text{start}}$  (the retardation potential in the analyzing plane is highest at large radii) and
- large starting angles  $\theta_{\text{start}}$  close to the maximum accepted angle defined by the magnetic field at the pinch magnet,  $B_{\text{pinch}} = 6 \text{ T}$  (see eq. (2.29)).

Furthermore, the starting point should be located in a region with rather homogeneous magnetic field (for example at the center of a superconducting solenoid) in order to justify the approximation

$$\Phi = \int B \, dA \approx B \cdot A \quad (4.14)$$

used to calculate the magnetic flux  $\Phi$ .

The program is divided into two parts:

### 1. Calculation of the starting parameters

For a given axial starting position  $z_{\text{start}}$  determined by the user and a magnetic field strength  $B_{\text{start}}$ , the maximum starting radius within the magnetic flux tube is determined by the radius of the flux tube inside the (homogeneous) magnetic field of the source:

$$r_{\text{start, max}} = r_{\text{source, max}} \cdot \sqrt{\frac{B_{\text{source}}}{B_{\text{start}}}}. \quad (4.15)$$

For KATRIN's tritium source, the WGTS, the relevant parameters are

$$\begin{aligned} B_{\text{source}} &= 3.6 \text{ T}, \\ r_{\text{source, max}} &= 0.041 \text{ m}, \\ \theta_{\text{source, max}} &= 50.8^{\circ}. \end{aligned} \quad (4.16)$$

At the center of the entrance solenoid of the main spectrometer, for example, the magnetic field strength is  $B_{\text{solenoid}} = 4.5 \text{ T}$ , resulting in a maximum starting radius of

$$r_{\text{start, max}} = 0.041 \text{ m} \cdot \sqrt{\frac{3.6 \text{ T}}{4.5 \text{ T}}} \approx 0.037 \text{ m} \quad (4.17)$$

and a maximum starting angle of

$$\theta_{\text{start, max}} = \arcsin \left( \sqrt{\frac{4.5 \text{ T}}{6.0 \text{ T}}} \right) \approx 60^{\circ}. \quad (4.18)$$

Once  $z_{\text{start}}$  (user-defined),  $r_{\text{start}} = r_{\text{start,max}}$  and  $\theta_{\text{start}} = \theta_{\text{start,max}}$  are known, the program calculates the amount of initial kinetic energy necessary for the particle to reach the analyzing plane at  $z = 0$  with zero longitudinal kinetic energy (compare eq. (2.24)):

$$E_{\text{kin,transmission}} = q(U_{\text{ana}} - U_{\text{start}}) \cdot \left[ 1 - \sin^2(\theta_{\text{start}}) \cdot \frac{B_{\text{ana}}}{B_{\text{start}}} \cdot \frac{\gamma_{\text{start}} + 1}{\gamma_{\text{ana}} + 1} \right]^{-1}. \quad (4.19)$$

Both the electric and magnetic field maps are needed to evaluate  $(U_{\text{start}}, B_{\text{start}})$  at the starting coordinates and  $(U_{\text{ana}}, B_{\text{ana}})$  at the analyzing plane, respectively.

## 2. Calculation of the longitudinal kinetic energy at regular intervals along a magnetic field line

In the next step, the simulation of a particle with a total kinetic energy  $E_{\text{kin,start}}$  equal to that defined by eq. (4.19) is started. The program follows the magnetic field line going through  $(r_{\text{start}}, z_{\text{start}})$  and calculates the longitudinal kinetic energy in a number of intermediate points  $m$  until reaching the final  $z$ -coordinate (e. g., at  $z = 0$ ):

$$\begin{aligned} E_{\parallel,m} &= E_{\text{kin,start}} - E_{\perp,m} - q(U_m - U_{\text{start}}) \\ &= E_{\text{kin,start}} \left( 1 - \sin^2(\theta_{\text{start}}) \cdot \frac{B_m}{B_{\text{start}}} \cdot \frac{\gamma_{\text{start}} + 1}{\gamma_m + 1} \right) - q(U_m - U_{\text{start}}) \end{aligned} \quad (4.20)$$

The transmission condition is satisfied if for any electron started with an energy

$$E_{\text{start}} \geq E_{\text{start,transmission}} \quad (4.21)$$

the longitudinal kinetic energy  $E_{\parallel,m}$  remains positive in all points throughout the trajectory until the analyzing plane is reached. This should be fulfilled if the MAC-E filter works correctly. If at any point  $E_{\parallel,m}$  becomes smaller than zero due to a faulty field configuration, the electron is considered as being reflected; it therefore cannot pass the analyzing plane.

### 4.3.4 Auxiliary programs

In the following, three of the peripheral programs used for electromagnetic design studies will be introduced.

- `fieldlinepot` is an auxiliary program which evaluates the electric potential along magnetic field lines for a given coil configuration in a volume specified by the user. Two separate versions for electric charge density maps generated with either `e1cd3_2` or `e1cd3_3` exist. The program is particularly helpful for finding local traps for charged particles; it has been used extensively for the design of shielding electrodes to suppress Penning traps both in the pre- and main spectrometer (compare section 5.2 in this work and references [Hug08, Zac09]).
- The visualization tool `ROOTsim` helps to validate a modified or newly generated geometry before starting the process of field calculation. It is an important tool to detect errors, particularly in complex electrode configurations, and to generate more plastic views of the geometry, which is expedient during the design phase. A first version of `ROOTsim` was written by M. Prall on the basis of the `ROOT` framework [ROOT]. Its main purpose was to generate a visualization of the wire electrode details implemented with the discrete rotational symmetry of the `e1cd3_3` code. S. Vöcking enlarged the functionalities of the tool and prepared it for a more universal use [Vöc08], for example by implementing reading capabilities for all common input formats used for the field calculation programs described above, including not only the electrodes, but also the magnet system.

- Due to the rising complexity of geometry details to be considered, eventually a powerful tool to automatically generate the increasingly voluminous input files for the (electric) field calculation routines became indispensable. For this purpose, a modular and highly flexible tool called `MainSpec` was provided by S. Vöcking [Vöc08]. Based on the *Python* programming language, it possesses a graphical user interface and incorporates `ROOTsim` to allow direct inspection of a new configuration. Parts of the geometry that are already fixed (most importantly, the geometry of the main spectrometer vessel) can be read from external files and used as constraints to define the details of the inner electrode and its complex mounting structure.

## 4.4 Implementation of the wire electrode design as a computer model

Numerical calculations of the main spectrometer and its wire electrode system are challenging, not only from the point of view of the electric field algorithms described in section 4.3.2, but also regarding the process of creating a realistic input model geometry. A step-wise approach was chosen, with gradual refinements of the details from stage to stage as more sophisticated programs allowed to increase the complexity of the model. The process of implementing an increasing level of detail is outlined in table 4.1. In parallel, engineering concepts for a technical realization became more and more elaborate. This naturally led to a dismissal of some of the original ideas, while new ones were being introduced. The following remarks therefore represent an attempt to trace the growth of the computer model on the one hand and the evolution of technical concepts on the other, both of which are strongly interrelated.

### 4.4.1 General layout of the wire electrode system

Based on the initial ideas described in section 3.4, possibilities for a technical implementation of such a complex wire electrode system were evaluated. A modular setup involving external fabrication of a large number of individual electrode parts, transportation to the main spectrometer and subsequent installation was favored over the alternative scenario of in-situ construction. In the former approach the size of each module is limited in the first instance by the dimensions of the three large pumping ports of the main spectrometer vessel ( $\varnothing 1.7$  m each) which form the only access for inserting large parts from outside once the assembly of the vessel is completed.

Each module consists of a specified number of wires attached to solid holding structures whose form matches the curvature of the vessel. Therefore, the shape of the modules in the cylindrical part will be different from that of the modules in the conical sections of the spectrometer. In addition to the wire holders in azimuthal direction, spacer rods running in axial direction will be inserted to span the wires and keep up the mechanical tension (see figure 4.4). A “C-shaped” profile was chosen for the spacer rods because it offers a favorable compromise regarding weight and stability. Typically, three or four of such spacers will be integrated in a module.

The azimuthal holders require particular consideration. On the one hand, they should be stable enough not to be mechanically deformed by the forces of a large number of tensioned wires attached to them; on the other hand, they should be “quasi-massless”.<sup>16</sup> Eventually, a comb-shaped

---

<sup>16</sup>There are essentially two arguments calling for a low mass and small spatial extent of the holding structures: 1) the amount of material to be installed inside the main spectrometer vessel should be as low as possible in order to prevent it from becoming a source of background electrons by virtue of the same mechanisms that cause background

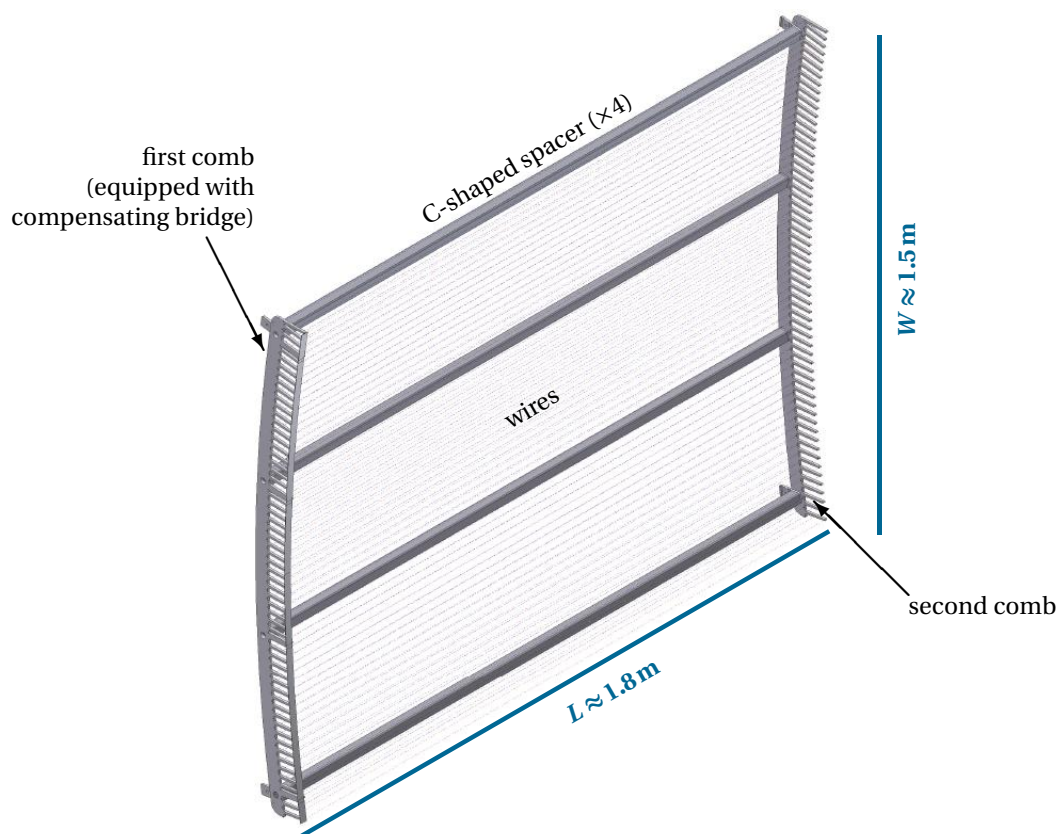


**Figure 4.4:** Drawing of a wire electrode module from the cylindrical part of the main spectrometer. The purpose of the compensating bridge is explained in section 4.6.

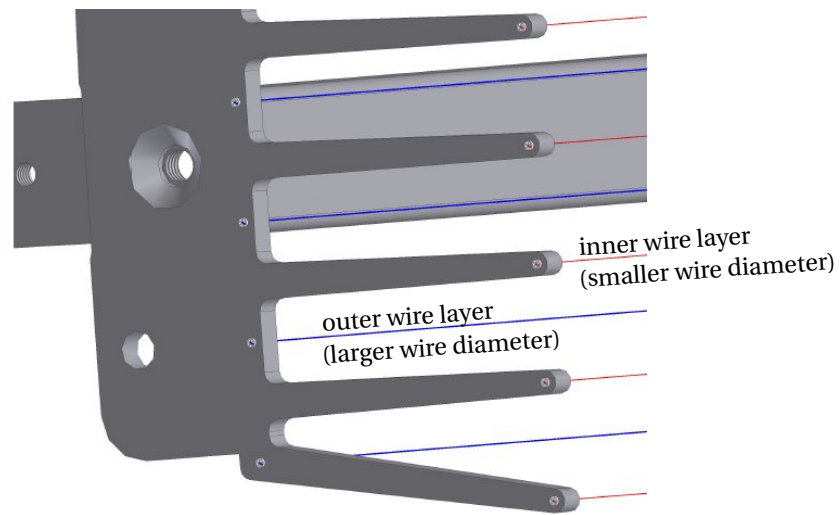
form (also shown in figure 4.4) with the “teeth” of the comb oriented along radial beams, emerged as a viable solution.

Small tubes made of ceramics are employed to keep the wires in place. This mechanism is illustrated in figure 4.5. Apart from facilitating a precise positioning of each wire, the ceramics also provide electrical insulation such that different potentials can be applied to the wires and to the solid mounting structures.

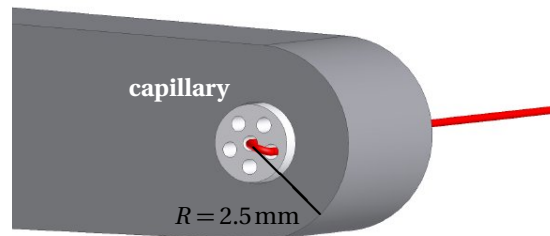
Originally, wire modules with approximate dimensions  $L \approx 3$  m (length) and  $W \approx 1.5$  m (width) were envisioned. However, weight and handling of such large parts turned out to be a problem. The length of the modules was thus reduced to  $\approx 1.8$  m in the second stage of the design (see table 4.1). The parameters regarding axial and circumferential segmentation had to be fixed at an early time because provisions to arrange for mounting points for the inner electrode had to be taken already during the construction phase of the spectrometer vessel. For this purpose, threaded stainless steel bolts (M10) were attached to the inner surface of the vessel, and their number as well as the positions had to be finalized due to the time constraints of the construction plan for the main spectrometer tank.

---

from the hull of the vessel, and 2) their disturbing influence on the electric potential generated by the wire electrode should be as small as possible.



(a)



(b)

**Figure 4.5:** Realization of a mechanism to mount the wire electrode via comb-like structures. (a) The spacing in radial direction is achieved by inserting solid-metal parts with the wires of the first layer attached at the outer rim and the wires of the second layer at the inner rim. (b) The wires are kept in place by small insulator tubes (capillaries) made of ceramics, with the centers placed at a distance of 2.5 mm from the tip of the tooth. The capillaries have a diameter of 2 mm and possess six drill holes of 0.4 mm diameter. The wire enters through the central hole and is fixed by bending it (“U-bend”) and feeding the short end of the wire back into one of the remaining drill holes.

#### 4.4.2 Modification of relevant parameters

The following list points out the most important developments of the technical design with respect to the first draft introduced in section 3.4.

- For the cylindrical part with a total length of 9 m the reduction of the module length  $L$  from 3 m to 1.8 m leads to an increase of the number of module rings from three to five. An odd number of module rings was chosen so as to keep the most sensitive region close to the analyzing plane clear of a junction of rings. The intention was to keep the distortions of the electric potential that are naturally introduced by such a junction (see later sections) as low as possible at the location of the analyzing plane.

**Table 4.1:** Progressive stages of the computer model of the wire electrode for the main spectrometer.

<b>First stage</b>	fully rotational-symmetric model using <code>e1cd3_2</code> : only wires, no mounting structures yet, no gaps either in $z$ - or in azimuthal direction
<b>Second stage</b>	major review of the design: modification of key parameters $d_1$ , $d_2$ , $l_2$ and $L$ (see table 4.2), still no mounting structures implemented (continued use of <code>e1cd3_2</code> )
<b>Third stage</b>	mounting structures in all parts of the spectrometer implemented as solid belts, using full rotational symmetry (continued use of <code>e1cd3_2</code> )
<b>Fourth stage</b>	transition to <code>e1cd3_3</code> : cylindrical part equipped with combs, no mounting structures in conical parts, introduction of compensating structures in cylindrical part
<b>Fifth stage</b>	“hybrid model”: cylindrical part equipped with combs, conical parts with continuous belts (no teeth) taken over from former <code>e1cd3_2</code> model, further development of compensating structures for the cylindrical section
<b>Sixth stage</b>	automated creation of input files using <code>MainSpec</code> , full implementation of mounting structures with <code>e1cd3_3</code> , modified design of ground electrodes and wire modules in the steep cone, inclusion of additional conical electrodes to avoid Penning traps at the exit and entrance regions of the spectrometer [Hug08, Zac09]

- The radial distance between the two wire layers was increased by 20 mm. The length of the “teeth” acting as spacers in radial direction was thus enlarged from 50 mm to 70 mm. At the same time, the wire diameter  $d_1$  of the outer layer was reduced from 0.5 mm to 0.3 mm, while the wire diameter  $d_2$  of the inner layer was increased from 0.15 mm to 0.2 mm. These modifications were mainly motivated by the outcome of tolerance simulations regarding the sag of the wires, and the arguments leading to this step will be laid out in section 4.5.1.
- The number of wires per layer in the cylindrical part was adjusted from 1194 to 1200 to allow a division into 20 modules per ring.<sup>17</sup> The same argument led to a modification of the number of wires in the conical sections (see table 4.6 for details).
- The sheet-metal parts that were usually planned to be installed at the section of the inner electrode system closest to the ground electrodes were replaced by wire electrode modules for two main reasons:
  1. The weight of a solid-metal electrode of this size is rather large. Furthermore, construction and mounting of such pieces would be more difficult than extrapolating the design of a wire electrode.
  2. Without a wire grid, no shielding against background electrons coming from the sheet-metal electrodes is available. This could be dangerous in particular in the case of the cone at the downstream end of the spectrometer, as electrons here can directly reach the detector.

However, only one layer of wires will be used in the modules belonging to the steep conical section.

<sup>17</sup>The change in the wire pitch  $s_1$  and  $s_2$  resulting from this update is marginal.

Because of the constraints mentioned in section 4.3.3, the program `traj` for microscopic trajectory calculation could only be used up to the third stage of the design. All later stages involve calculations in the adiabatic limit with the more simple code `transmission`. This should be kept in mind when interpreting calculations of the evolution of longitudinal kinetic energy along a particle trajectory.

**Table 4.2:** Modified parameters of the wire electrode compared to those of early drafts.

	old configuration	new configuration
radial spacing $l_1$	150 mm	150 mm
wire diameter $d_1$	0.5 mm	<b>0.3 mm</b>
radial spacing $l_2$	50 mm	<b>70 mm</b>
wire diameter $d_2$	0.15 mm	<b>0.2 mm</b>
$N_{\text{wires}}$ in the cylindrical part	1194	1200
module length $L$ in the cylindrical part	ca. 3 m	1.8 m

## 4.5 Estimation of tolerances for fabrication and mounting of the electrode system

Small imperfections in the production of the electrode system (*i. e.*, both the spectrometer vessel and the wire electrode) as well as related to the mounting of the wire modules inside the spectrometer will lead to deviations from the idealized electrode configuration of the simulated model. The following list contains the most important ones of those imperfections along with measures proposed to either avoid or counteract detrimental effects on the shape of the electric field.

1. *Self-loaded deformation of single (or several) wires in a module*, also called the “sag” of wires. The bending can be reduced either by cutting down on the length of the wires or increasing the mechanical tension. Also, reducing the weight (*i. e.*, effectively the diameter) of the wire helps to keep the sag small. The bending must be measured very precisely (and, if necessary, corrected) before the module is mounted inside the spectrometer (compare simulation results presented in section 4.5.1).
2. *Misplacement of wires within a module*, for example due to faulty shapes of combs or errors in the drilling of holes for the ceramics insulators. Since this effect cannot be corrected after a module is assembled, all parts need to undergo a stringent quality control and faulty ones must be removed from the production line.
3. *Misplacement of mounting points for the modules inside the vessel* (M10 bolts and rail system). A position measurement using a laser tracker system is necessary. Bolts exceeding the tolerances must be straightened manually. Residual misalignments are to be compensated for by the interlink between the bolts and the modules.
4. *Deformations of the vessel due to construction tolerances*. The mounting system should provide a certain degree of flexibility so as to at least partially compensate the imperfections of the vessel electrode. It is important to make sure that the two layers of the wire electrode – above all in the most critical part of the spectrometer, namely the cylindrical section close to the analyzing plane – form concentric shapes without any significant elliptic deviations that would lead to a distorted electric potential.

Unfortunately, none of these defects in general follows a rotational symmetry, which makes it clear that a numerical study through routines using full or partial rotational symmetry can only give a rough approximation. Nonetheless, some estimate on the magnitude of tolerances was needed for the construction process, and therefore efforts were taken to address at least the first and third item on the list (and to a limited extent also the fourth item). Still, the realization of the imperfections were not straightforward, and in some cases only a rather crude approximation to the expected real situation could be achieved. As an example, the problem of tolerance calculations for the self-loaded sag of wires (first item on the above list) shall now be investigated.

#### 4.5.1 Tolerance estimates regarding the bending of wires

Figure 4.6 illustrates a rather simplistic way of implementing the bending of wires in a fully rotational-symmetric model. The wires were divided into two equally long halves and the two new end points in the middle were shifted in radial direction, either outwards or inwards with respect to the ideal position. Both scenarios are indicated in the figure. Such calculations were carried out for various module rings in the spectrometer, using a simulation model without any mounting structures included (first stage in table 4.1). Here, the most relevant scenario concerning the central ring enclosing the analyzing plane is shown.

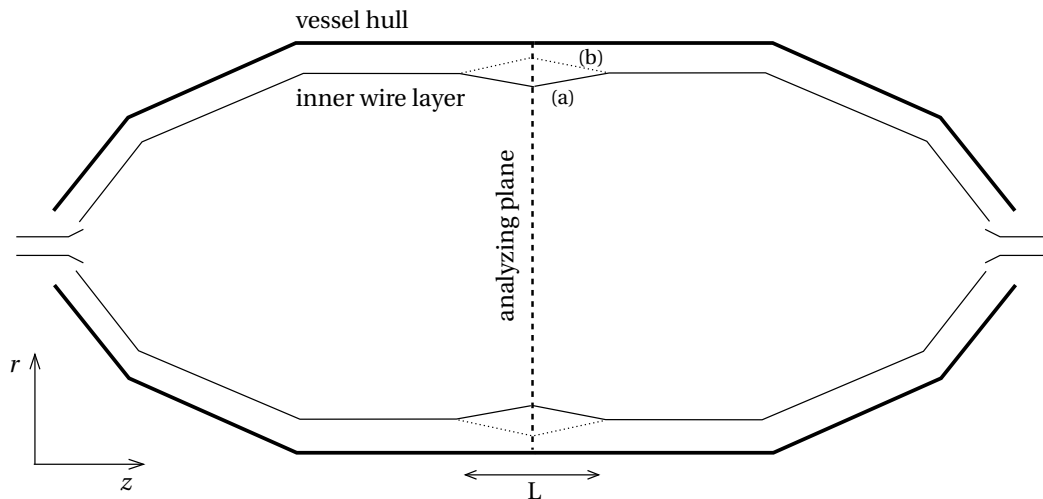


**Figure 4.6:** Sketch: modified geometry for tolerance calculations (dimensions not to scale). The sag of the wires is approximated by a discontinuous bend at the middle of the module of length  $L$ . The illustration shows the simulated geometry for a wire sag of the inner layer in the central module (outer wire layer not drawn). This crude rotational-symmetric model necessarily introduces unphysical properties contradictory to the behavior caused by the gravitational force, namely wires that are supposed to be bent sideways or even upwards in space. For example, a deflection of the wire pointing inwards (case (a) in the sketch) results in a downward-bending of the wires at the top of the spectrometer, but yields an upward-bending of the wires in the bottom section. The inverse holds for the case of outward-bending wires (b). Moreover, the model requires all of the wires to be deflected collectively in the same way, which leads to an overestimation of the effect. Nevertheless, in view of the high computational complexity of the problem, these simplifications were necessary in order to be able to assess the question of tolerance estimates at all.

As a consequence of the bending of the wires, the homogeneity of the electric potential in the analyzing plane as well as the evolution of the longitudinal kinetic energy are affected.<sup>18</sup> The

<sup>18</sup>In all calculations presented in section 4.5 the longitudinal kinetic energy was obtained from microscopic tracking calculations. These calculations were made before the overall revision of the electromagnetic design of the

effect is much more pronounced if the wires in the two layers are bent differently, with the extreme case that only one of the layers is affected by the bending at all. This can be intuitively understood by recalling the dependence of the electric screening factor (eq. (3.6)) on the radial distance  $l$  between the electrode layers: if the two layers are tilted in parallel, the distance  $l$  and thus also the screening factor  $S$  remain constant, but if the wires in one layer are tilted relative to the second layer the spacing  $l$  varies with the axial position  $z$ .

Such a case is visualized in figure 4.7, where a bending of the inner wire layer only is considered for the central ring of modules surrounding the analyzing plane. Bending of the wires in outward direction is indicated by a “+” sign, while the opposite bending is marked with a “-” sign. In the first case, the bending causes a slight retraction of the center point of the wires from the inner volume of the spectrometer, which results in a reduced retardation at the location of the analyzing plane ( $z = 0$ ) as compared to a position a few meters before (e. g., at  $z \approx -2.5$  m). For an electron that starts at the outer border of the transported magnetic flux tube, the longitudinal kinetic energy therefore assumes its minimum value long before the particle crosses the analyzing plane, and too early retardation occurs (compare section 4.2.2, in particular eq. (4.2)). For a bending of +1 mm the effect amounts to  $\delta E_{\parallel} \approx 215$  meV. Even for a bending of only +0.2 mm it is still present (see table 4.3).

**Table 4.3:** Results of first tolerance calculations for the sag of wires (bending of wires in the inner layer of the central module only, compare figure 4.7). Initially the geometry denoted as “first stage” in table 4.1 was used. The simulations were repeated later with more detailed computer models of the geometry (see text).

radial position $r$ of wire at $z = 0$	deviation relative to nominal radial position	“early retardation” effect $\delta E_{\parallel}$
4.7000 m	0.0 mm	—
4.7010 m	+1.0 mm	215 meV
4.7005 m	+0.5 mm	105 meV
4.7002 m	+0.2 mm	40 meV
4.6990 m	-1.0 mm	reflected at $z = -1.23$ m

The opposite case of an inward bending of the wires causes a stronger electrostatic retardation close to the analyzing plane as compared to the ideal scenario with completely straight wires.<sup>19</sup> Figure 4.7(a) includes also a case of inward bending of the wires (-1 mm), where the retardation is strengthened in such a way that the electron is physically reflected long before reaching the analyzing plane.

Next to these dramatic changes of the transmission properties, the influence of the wire sag on the homogeneity of the retardation potential appears to pose a rather less severe problem (see figure 4.7(b)). Only in extreme cases, such as a bending of the inner wire layer only by as much as -5 mm, an intolerable deterioration of the homogeneity of the electric potential is found.

Figure 4.8 demonstrates that the influence of the bending of the wires is not limited to the out-

---

main spectrometer. Thus, the former default magnetic field strength in the solenoids of the main spectrometer,  $B_{\text{solenoid}} = 3.5$  T, was used. At this field strength the maximum accepted starting radius inside the entrance solenoid corresponds to  $r_{\text{start,max}} = 41.7$  mm, and the maximum accepted starting angle is  $\theta_{\text{start,max}} \approx 50^\circ$ . To be conservative, all trajectory simulations were carried out for electrons with slightly larger values,  $r_{\text{start}} = 42$  mm and  $\theta_{\text{start}} = 51^\circ$ .

<sup>19</sup>This can be understood as follows: The electrostatic screening factor depends linearly on the spacing  $l$  between the two layers. If the wires are bent inwards, the spacing  $l$  at the location of the artificial “kink” in the wire is slightly larger than in the case without bending. Therefore, the more negative electric potential of the inner wire layer contributes with a slightly larger weight to the effective potential.

ermost border of the magnetic flux tube, but extends to large parts of the inner volume of the spectrometer. While the magnitude of the dip in longitudinal energy for an outward bending by 1 mm amounts to  $\delta E_{\parallel} \approx 215 \text{ meV}$  for electrons crossing the analyzing plane at a radius of  $r_{\text{ana,max}} = 4.54 \text{ m}$ , it is reduced to  $\delta E_{\parallel} \approx 43 \text{ meV}$  at  $r_{\text{ana}} = 3.19 \text{ m} = 0.7 \cdot r_{\text{ana,max}}$ .

The implementation of more realistic module lengths (in the cylindrical part: five segments with  $L = 1.8 \text{ m}$  each) leads to a minor amendment of the tolerance results. In this set of simulations, a simultaneous bending of the wires in all five rings in the cylindrical section of the spectrometer was considered. Instead of a dip of  $\delta E_{\parallel} \approx 215 \text{ meV}$ , a bending of the inner layer by +1 mm only results in  $\delta E_{\parallel} \approx 150 \text{ meV}$ . The amplitude of the dip for a bending of +0.2 mm is reduced by a similar factor; it amounts to 30 meV in the new simulations instead of the previous result of 40 meV. For a uniform bending of the wires in both layers by +1 mm, a value of  $\delta E_{\parallel} \approx 10 \text{ meV}$  is obtained.

One measure to cope with the problems related to the non-uniform wire sag in the two layers is to increase the radial spacing  $l_2$  between them. In this case, a given deviation  $\delta r$  in the bending is expected to have a smaller influence since it needs to be considered relative to the spacing  $l_2$ . This is illustrated by the following considerations: For either of the two layers, the wire sag can be expressed as a small variation  $\partial l$  of the distance parameter. Combining equations (3.4), (3.5) and (3.6), one obtains an estimate regarding the dependence of the effective retardation potential  $U_{\text{eff}}$  on  $l$ :

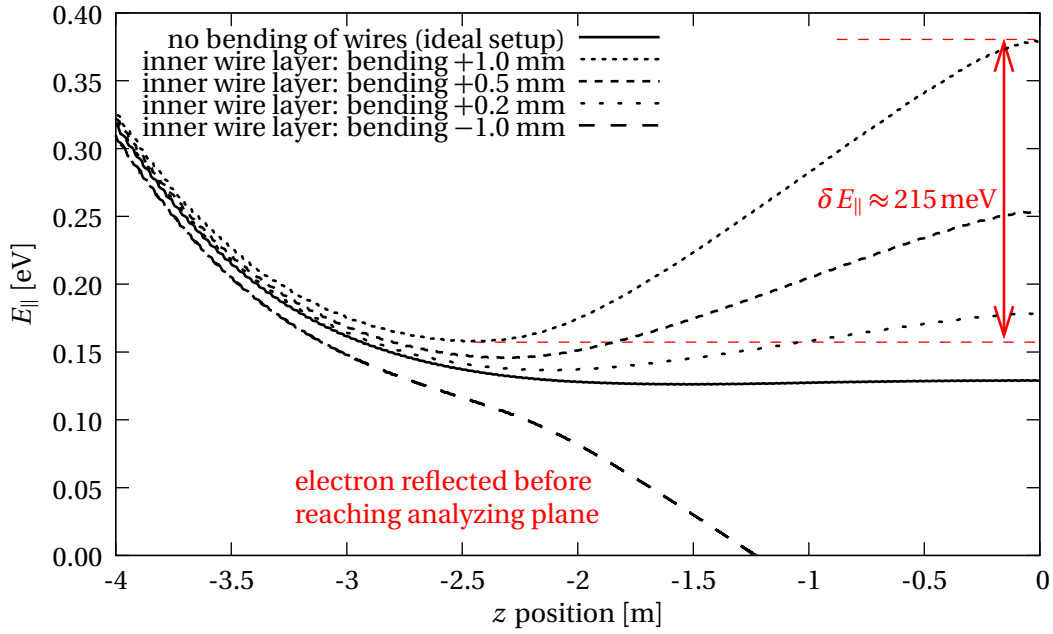
$$\begin{aligned} \frac{\partial U_{\text{eff}}}{\partial l} &= \frac{\partial}{\partial l} \left( U_{\text{grid}} + \frac{U_{\text{vessel}} - U_{\text{grid}}}{S} \right) \\ &= \frac{\partial}{\partial l} \left( \frac{U_{\text{vessel}} - U_{\text{grid}}}{S} \right) = \Delta U \frac{\partial}{\partial l} \frac{1}{S} \\ &= \Delta U \frac{\partial}{\partial l} \left( \frac{s \ln\left(\frac{s}{\pi d}\right)}{s \ln\left(\frac{s}{\pi d}\right) + 2\pi l} \right) \\ \Rightarrow \left| \frac{\partial U_{\text{eff}}}{\partial l} \right| &\propto \frac{1}{l^2} \quad \text{for } S \gg 1. \end{aligned} \quad (4.22)$$

The result indicates that  $U_{\text{eff}}$  can be stabilized against variations of  $l$  by increasing the distance parameter itself. For the next version of the simulation model, therefore,  $l_2$  was enlarged from 50 mm to 70 mm. This step includes also a change of the diameter of the wires in the outer layer from 0.5 mm to 0.3 mm, which was motivated by technical considerations:

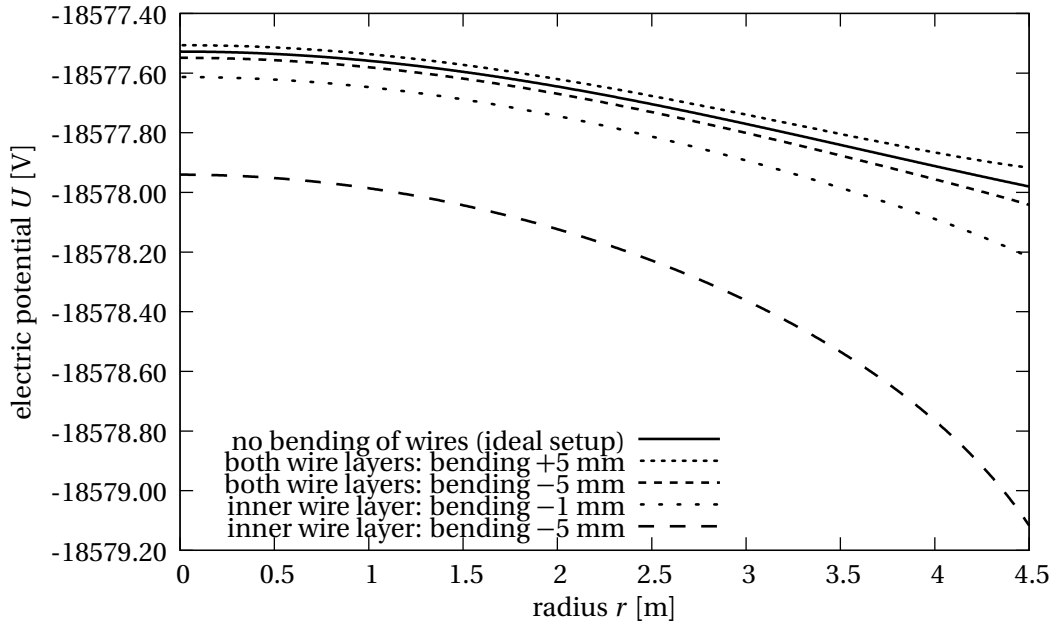
- The insulator capillaries are available off the shelf with drilled holes of 0.4 mm diameter only. Custom-made pieces with larger holes would be significantly more expensive. Therefore, the idea to mount the wires via insulating tubes does not work for a wire diameter of 0.5 mm.
- Furthermore, the  $\varnothing 0.5 \text{ mm}$  wires possess a considerable weight and would therefore require higher mechanical tension. Computer simulations investigating the structural mechanics of the module<sup>20</sup> showed that in this case the increased forces acting on the mounting structures would cause an inadmissible deformation. The option of reinforcing the mounting structures by using a larger material thickness is disfavored since the larger amount of material implies the risk of introducing more background. In addition, the weight of the individual modules should not be increased further.

Table 4.4 summarizes the results of the simulations using the updated values of  $l_2$ ,  $d_1$  and  $L$ . A marked difference to the previous results can be seen. A bending of the inner layer in all module rings of the cylindrical section by +0.2 mm now results in a dip in the longitudinal kinetic energy

<sup>20</sup>The simulations were done by H.-W. Ortjohann (Univ. Münster) using the ANSYS structural mechanics package.



(a) longitudinal kinetic energy  $E_{||}$

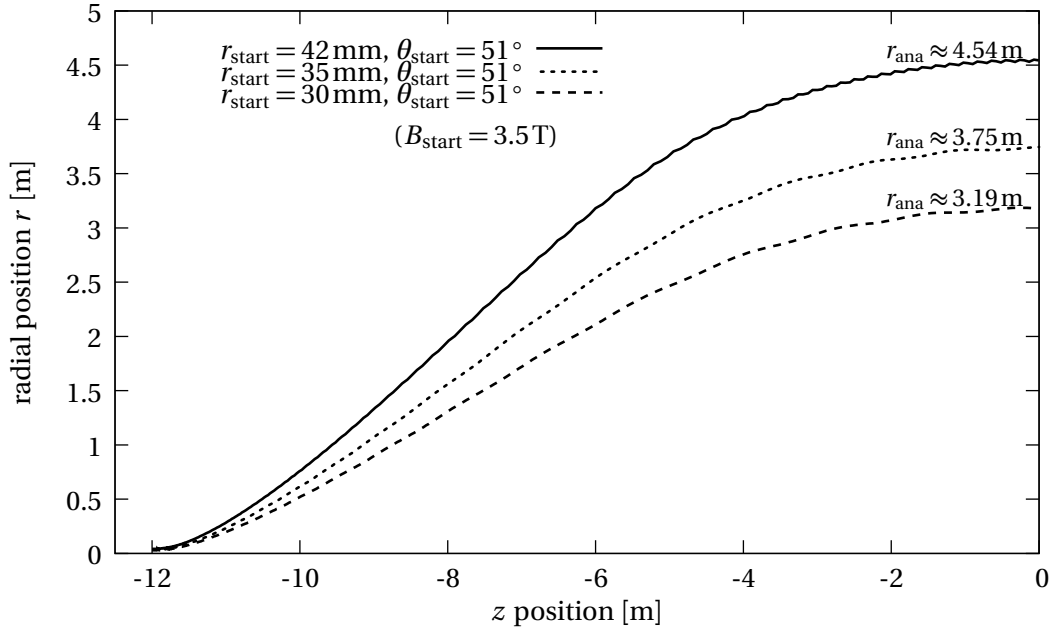


(b) potential depression  $\Delta U_{\text{ana}}$  in analyzing plane

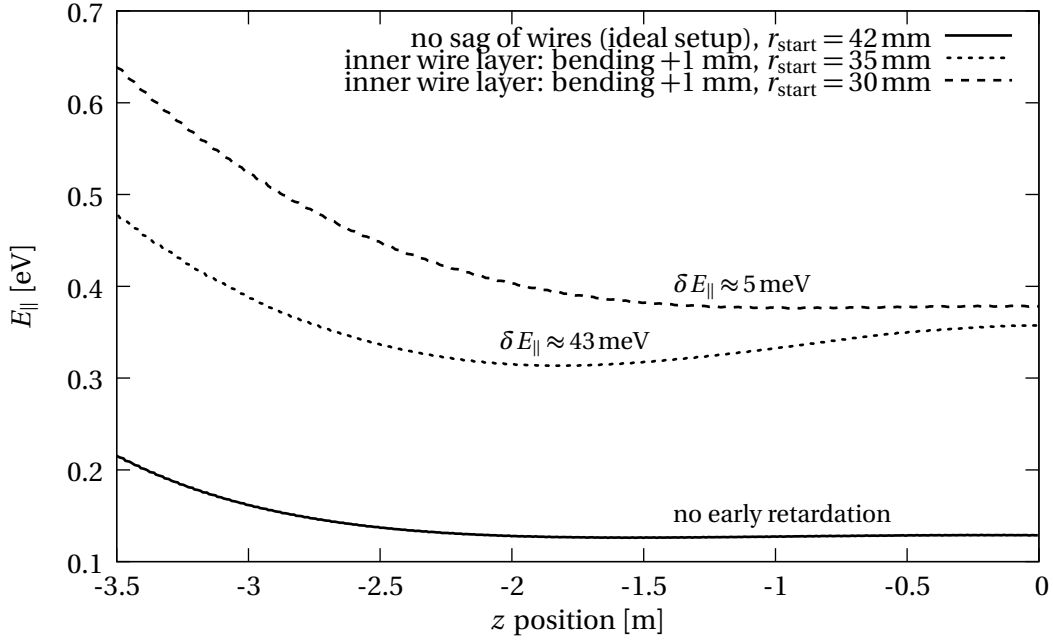
**Figure 4.7:** Tolerance estimate regarding the self-loaded deformation (sag) of wires in the central ring of modules. These calculations were done in the first phase of the implementation of the computer model and therefore do not yet involve any mounting structures. Furthermore, the length of the central wire modules is 4.47 m, which was later reduced to 1.80 m. (a) Effect on the longitudinal kinetic energy of electrons started at the outer border of the magnetic flux tube with  $E_{\text{start}} = 1$  eV,  $r_{\text{start}} = 42$  mm and  $\theta_{\text{start}} = 51^\circ$  ( $B_{\text{start}} = B_{\text{solenoid}} = 3.5$  T). (b) Effect on the homogeneity of the retardation potential at the analyzing plane.

of merely  $\delta E_{||} \approx 12$  meV, whereas in the old configuration the corresponding value (taking into account only a sag of the wires of the central module ring) was more than three times as large (compare table 4.3). Since the expected amplitude of the ripple on the high voltage supplied to

#### 4.5 Estimation of tolerances for fabrication and mounting of the electrode system



(a) electron trajectories from the entrance magnet ( $z = -12.0$  m) to the analyzing plane ( $z = 0$ )



(b) longitudinal kinetic energy  $E_{\parallel}$

**Figure 4.8:** Radial dependence of the impact of bent wires at the analyzing plane. The calculations for electrons with smaller starting radii show that the effect even persists further inside the volume of the spectrometer.

the wire electrode is of the order of 10 to 15 mV [FuG08], fixing the tolerance value for the sag of wires in the cylindrical part to  $\delta r = 0.2$  mm seems to be appropriate.

Shortly after the abovementioned modifications were implemented, the wire diameter  $d_2$  of the thin wires was raised from 0.15 mm to 0.2 mm, as the handling of the very thin wire turned out to be quite problematic during prototype testing. Since the four parameters  $d_1$ ,  $d_2$ ,  $l_2$  and  $L$  were

**Table 4.4:** Updated results of tolerance simulations for the sag of wires (bending of wires in the inner layer only for all module rings in the cylindrical part).

radial position $r$ of shifted wire endpoints	deviation relative to nominal radial position	“early retardation” effect $\delta E_{\parallel}$
4.6820 m	+2.0 mm	180 meV
4.6810 m	+1.0 mm	80 meV
4.6804 m	+0.4 mm	30 meV
4.6802 m	+0.2 mm	12 meV

modified in a close sequence of related steps, these can be subsumed under one major update of the simulation model (see table 4.2), which is termed the “second stage” in table 4.1.

The revised parameters lead to a change of the electric screening factor as well as of the geometrical coverage ratio compared to the values given in eq. (3.12):

$$\begin{aligned}
 \text{outer layer: } S_1 &\approx 14.6 \xrightarrow{d_1: 0.5\text{mm}\rightarrow 0.3\text{mm}} 12.5, & f_{gc,1} &\approx 1.2\%, \\
 \text{inner layer: } S_2 &\approx 4.2 \xrightarrow{d_2: 0.15\text{mm}\rightarrow 0.2\text{mm}} 5.8, & f_{gc,2} &\approx 0.8\%.
 \end{aligned}
 \tag{4.23}$$

In particular, the increase of the geometrical coverage  $f_{gc,2}$  for the inner wire layer from 0.6% to 0.8% should be noted, as it corresponds to the quantity most relevant for the background reduction.

The screening factor  $S_1$  for the outer layer is thus reduced by about 14%, whereas  $S_2$  for the inner layer is increased by roughly 38%. The net effect leads to a slightly more negative effective retardation potential in the cylindrical part:

$$\begin{aligned}
 U_{\text{eff},2} &\approx -18581.4\text{V} \\
 &= U_{\text{grid},2} + 18.6\text{V},
 \end{aligned}
 \tag{4.24}$$

*i. e.*,  $U_{\text{eff},2}$  is more strongly influenced by the potential  $U_{\text{grid},2}$  of the inner wire layer as in the design using the original wire parameters (compare eq. (3.16)).

#### 4.5.2 Tolerance estimates for the radial displacement of modules

Apart from the sag of wires within a module, the radial displacement of whole modules forms another point of concern. Such deviations from the ideal position can for example occur as a consequence of a non-perfect shape of the cylindrical part of the spectrometer vessel (a small degree of ellipticity is inevitable) or a variation in position and alignment of the M10 bolts. Furthermore, inaccuracies of the holding structure representing the link between the vessel hull and the module frames can contribute to positioning deviations.

Yet again, an accurate treatment of the problem would require simulations which do not rely on a strict rotational symmetry. Nevertheless, several attempts to tackle the question with the available simulation software were made, using different stages of the input model (*e. g.*, this work and references [Hug05, Kor06, Hug08]). Figure 4.9 shows a sketch of the simulated geometry. Initial investigations were concentrated on the three module rings closest to the analyzing plane (*i. e.*, the central ring and the adjacent ones in positive and negative axial direction). Later, similar calculations were done also for the sections located at larger distances from the analyzing plane.

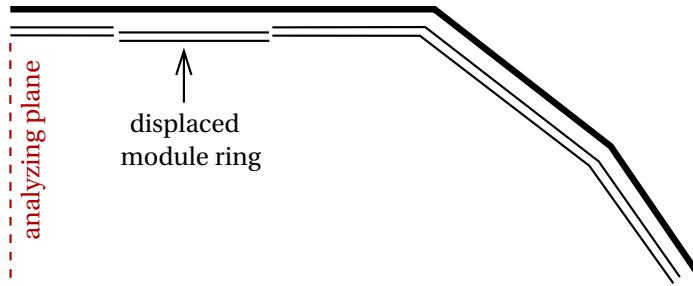


**Figure 4.9:** Sketch: modified geometry for tolerance calculations regarding the radial displacement of module belts (dimensions not to scale). In several sets of simulations, the radial positions of the endpoints of individual module rings were varied.

For the central ring, a tolerance value of about  $\pm 0.5$  mm was determined [Hug08]. As anticipated, the positioning requirements can be relaxed for the remote module rings, in particular for those in the conical sections of the spectrometer.

### 4.5.3 Tolerance estimates for the shape of the spectrometer vessel

In another study the influence of the shape of the spectrometer tank on the field homogeneity and transmission properties was investigated.<sup>21</sup> The configuration of the wire electrode was left unchanged. Keeping the absolute length of the vessel constant, the relative lengths of the cylindrical and the conical sections were varied (compare the sketch in figure 4.10). The effect thus leads to a small deviation in the opening angle of the large cone. The results of the simulations show that length deviations of the order of  $\delta L = 0.1$  m (either positive or negative) are not critical. Table 4.5 indicates that these tolerances were kept (with a large margin) during the construction of the spectrometer vessel.

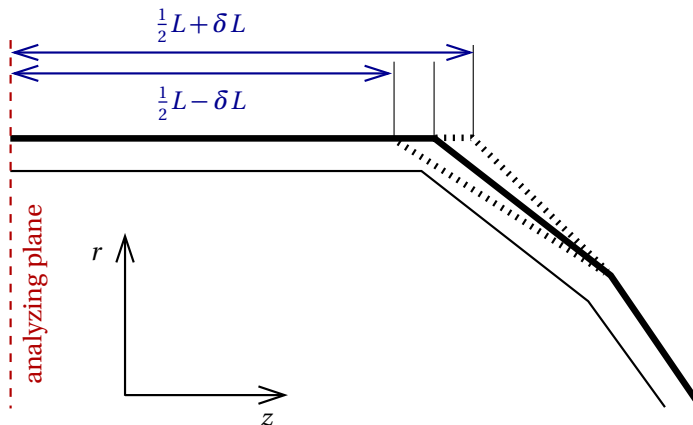


**Figure 4.10:** Sketch: modified geometry for tolerance calculations regarding the shape of the spectrometer vessel (dimensions not to scale). Starting from an ideal form with a total length of the cylindrical part of  $L = 9$  m, the  $z$ -coordinate of the junction between the cylinder and the large conical section was varied, while keeping the total length of the entire vessel unchanged.

### 4.5.4 Technical implications of the tolerance simulations

In spite of the abovementioned principal difficulties encountered during the attempt to incorporate deviations from the ideal shape of the wire electrode into the computer model, the calculations nevertheless deliver some valuable information regarding technical requirements.

- As a consequence of the bending simulations described in section 4.5.1, the mechanical tension of the wire needs to be sufficient to reduce the sag to a value specified by the tolerance estimate (*i. e.*,  $\delta r \approx 0.2$  mm for the most sensitive modules in the cylindrical part close

<sup>21</sup>The calculations were carried out in cooperation with K. Temming.

**Table 4.5:** Length of the main spectrometer vessel as measured with a laser tracker system [Gum08]. Compared to the reference length of 23280 mm the measured length is shorter by 52.5 mm, with the largest contribution stemming from the steep conical sections. The uncertainty of the laser tracker measurement is 0.1 mm.

reference length of the vessel (as contracted)	23280.0 mm
allowed tolerance (as contracted)	$\pm 100.0$ mm
measured deviation of length in cylinder and flat cones	-14.9 mm
measured deviation of length in steep cone (source side)	-18.3 mm
measured deviation of length in steep cone (detector side)	-19.3 mm
measured total length deviation	-52.5 mm

to the analyzing plane of the spectrometer). On the other hand, structural integrity both of the wire and of the mounting frames is a vital issue. The tension must not be too high, such as to ensure that

- a) no wire breaks during the full time scale of operation of the KATRIN experiment, and
- b) the comb-like mounting structures are not subject to mechanical deformation due to the collective forces exerted by the wires.

In particular, the modules must be able to withstand several baking cycles of the main spectrometer up to  $T = 350^\circ\text{C}$  without losing their position or even suffering a wire rupture. Therefore, careful and elaborate tests of wire and module integrity were carried out before starting the mass production [Geb07, Rei07]. These tests involve for example the temperature stability of an assembled module and the change of mechanical properties of the wires under stress and temperature cycling. The results suggest that a mechanical force of 10 N for the wires of the outer layer and 5 N for the wires of the inner layer is appropriate to fulfill the abovementioned criteria. The requirement on the wire sag thus brings about the need to both measure and adjust the mechanical tension of every single wire with high accuracy ( $\lesssim 0.1$  N). The measurement of the wire tension is carried out in an indirect way with a custom-made laser sensor by determining the oscillation frequency of the wire after mechanical excitation [Rei07, Pra09].

- The positioning tolerances require the careful inspection of the geometrical properties of each comb. Damaged or bent teeth must be detected prior to the assembly of the modules. Furthermore, the curvature radius of the comb and the positions of the centers of the holes in both layers are checked. After assembly, the geometry of each completed module is measured and documented, as well. All of the above tasks are carried out with the help of a fully automated three-axes coordinate measurement table [Jöh07, Pra09] which can either be equipped with a camera or with the abovementioned laser sensor, depending on the purpose of the measurement.

Furthermore, a mounting system which ensures a precise and stable positioning of the modules inside the tank is necessary. On the one hand, the mounting system must define the correct spacing of the modules with respect to the vessel hull. On the other hand, it is also responsible for keeping the modules in place and generating a smooth and continuous surface profile of the wire electrode without discontinuities or gaps either in radial or azimuthal direction. It is also quite important for the inner wire layer to form a quasi-perfect cylindrical shape, irrespective of deviations of the form of the vessel electrode. The third task of the mounting system is to establish electrical insulation between the vessel

#### 4.5 Estimation of tolerances for fabrication and mounting of the electrode system

electrode and the wire modules. A concept<sup>22</sup> qualifying for such a system is shown in figure 4.11. It consists of circular rails which are attached to the M10 bolts. The modules will be fixed to the rails with carriages that provide various degrees of freedom to adjust their position.

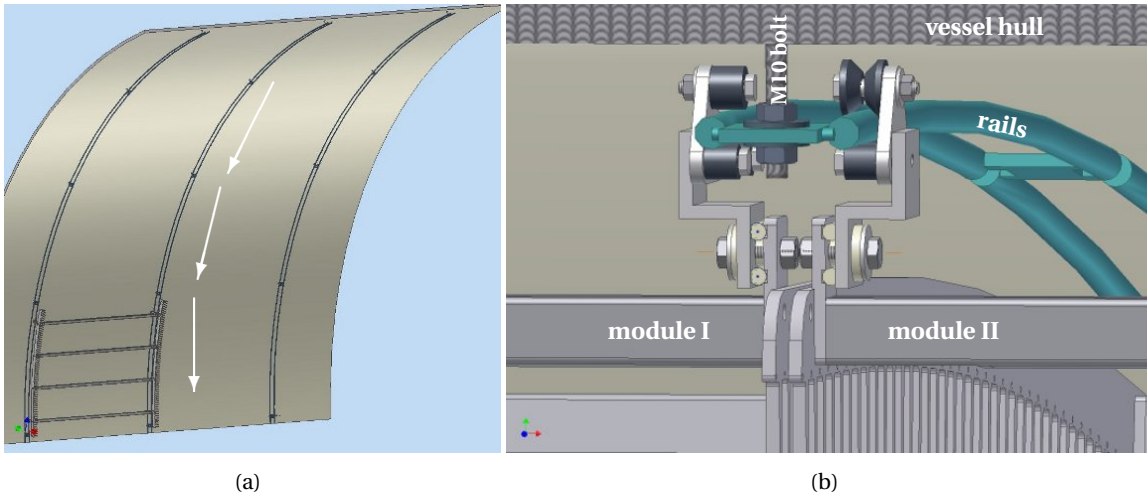


**Figure 4.11:** Rail system to mount the wire electrode modules. (a) One by one, the modules are attached to the circumferential rail system at the top and lowered to their intended position. (b) Each row of M10 bolts protruding from the vessel hull supports a set of rails which holds the ends of two adjacent rings of modules (labelled I and II in the picture). The adjustable fixing mechanism connecting the module with the rail system is capable of partially compensating manufacturing tolerances, while at the same time providing electrical insulation between the vessel electrode and the wire electrode modules.

<sup>22</sup>The rail system was developed at Forschungszentrum Karlsruhe (K. Müller *et al.*)

## 4.6 Measures to improve the homogeneity of the electric field

Even in the ideal case of vanishing imperfections regarding construction and mounting the homogeneity of the electric field would still be distorted by a number of effects which are inherent to the modular construction concept of the wire electrode:

1. The *C-shaped spacer rods* are placed on the same electric potential  $U_{\text{wire1}}$  as the outer wire layer. Their influence on the retardation potential within the spectrometer volume is, however, smoothed by the outer wire layer and additionally screened by the inner wire layer at the potential  $U_{\text{wire2}}$ . Variations caused by the rods can be sensed primarily in their local vicinity, but are negligible at the location of the flux tube. Dedicated studies [Glü06a] showed that the azimuthal variation of the electric potential at the analyzing plane is small inside the flux tube (of the order of a few meV at  $r \lesssim 4.5\text{m}$ ). In simulations using the fully rotational-symmetric code `e1cd3_2` these solid-metal rods cannot be implemented because they are arranged according to a discrete rotational symmetry. Also for the bulk part of the simulations using `e1cd3_3` the spacer rods were not included, since their discretization uses up a large number of electrode elements in the computation that could be better spent on other more critical details of the mounting structure (see for example the “compensation structures” introduced below).
2. Due to the *azimuthal segmentation* of the wire electrode a gap exists between two neighboring modules along the circumference. The last tooth in a module therefore braces the gap caused by the mounting frames (see figure 4.5(a)) in order to keep the wire pitch  $s$  constant along the full circumference, which allows better screening properties.
3. The modular design also implies the existence of gaps in axial direction. These are necessary to allow a mounting of the electrodes<sup>23</sup>, but they pose a principal problem since they allow the more positive electric potential of the spectrometer vessel to penetrate the inner volume. Furthermore, the gaps will be surrounded by two adjacent combs, which represent massive electrode parts and therefore form a marked difference compared to the rather uniform electric field generated by the wires in the center of each module ring. In the default configuration the comb-like structures share a common potential with the outer wire layer. Their influence is partially, but not fully screened by the wires of the inner layer, since the tips of the teeth protrude slightly further inwards than the radial position of the thin wires (compare figure 4.5(b)). Simulations have demonstrated that the combined effect of the axial gaps where no wires are present and the massive combs results in a significant distortion of the electric potential occurring at each joint between module rings. This is seen in the evolution of the longitudinal energy along an electron track (most pronounced at the outer border of the magnetic flux tube, but also further inside: see figure 4.13). In addition, the inhomogeneity of the retardation potential in the analyzing plane increases drastically. Both effects make a compensation of the influence of combs and gaps absolutely vital for the functioning of the main spectrometer. Two measures were investigated:
  - Placing the comb structures at an intermediate potential close to the equivalent potential. This would make the combs electrostatically “invisible”. Since both layers of wires are mounted via insulating capillaries, using a third electric potential would be difficult, but in principle it is technically feasible. There is, however, a strong physical argument against this method: if the potential of the wire layer is no longer sig-

<sup>23</sup>The cylinder consists of five module rings which will be placed on the same electric potential. In the conical parts, however, different electric potentials for the various rings of modules are envisioned; therefore, the inclusion of insulating gaps is also necessary from this point of view.

nificantly more negative than that of the mounting structures, the electric screening effect is almost entirely lost. This is particularly severe since the major fraction of the surface area of the combs is oriented perpendicularly to the magnetic field lines, such that any electrons emerging from the solid metal surface could leave it most easily.

- The second way of amending the distortions of the electric potential consists in the inclusion of additional electrode parts at the joint of two rings, placed at a separate potential more negative than that of the combs. An extensive series of simulations was carried out to find a suitable configuration. These investigations are described in sections 4.6.1 and 4.6.2.

#### 4.6.1 Simple model using full rotational symmetry

The first attempts to find a configuration with additional electrode parts that diminish the amount of inhomogeneity of the electric potential were pursued with a simulation model<sup>24</sup> using full rotational symmetry (third stage listed in table 4.1). Details of the geometry are shown in figure 4.12.

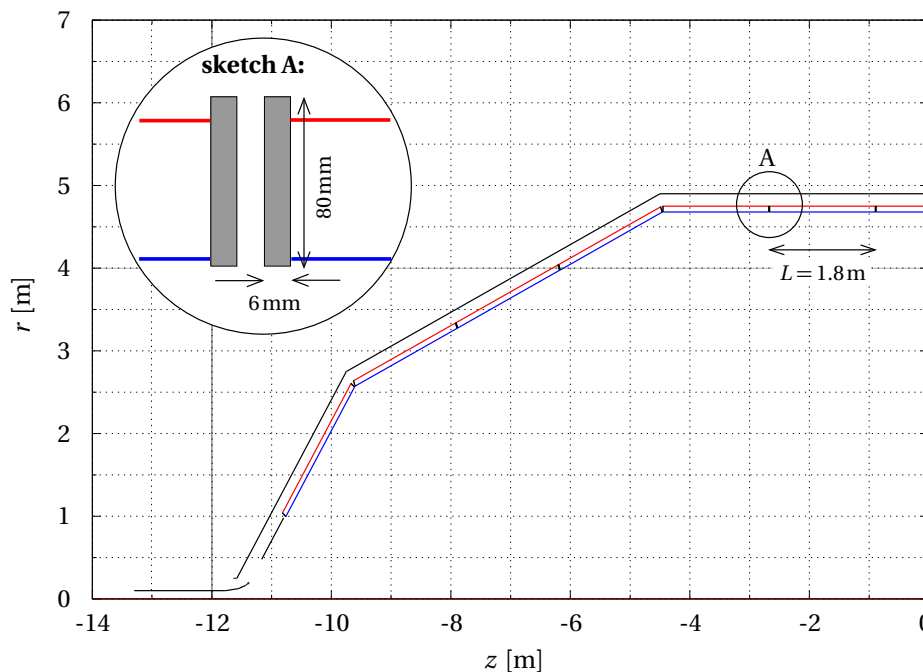


**Figure 4.12:** Wire electrode geometry with mounting structures using full rotational symmetry. The gap between two adjacent rings of modules is 10 mm, and the combs are implemented as solid “belts” with a width of 6 mm in  $z$ -direction and a radial extent of 80 mm.

In this version of the setup, the gaps in axial direction were assumed to be  $d_z = 10$  mm wide. Although the value was not fixed at the time the simulations were carried out, this number seemed to be a reasonable estimate. The combs were modelled as continuous hoops with rectangular cross section (6 mm  $\times$  80 mm) running along the full circumference of the vessel.

Figure 4.13 shows that in this configuration the potential depression in the analyzing plane is

<sup>24</sup>The generation of the model was greatly simplified by a program provided by N. Titov from INR, Troitsk.

increased<sup>25</sup> by more than a factor of 5 from  $\Delta U_{\text{ana}} \approx 0.45\text{V}$  without gaps and without mounting structures (compare figure 4.7(b)) to  $\Delta U_{\text{ana}} \approx 2.5\text{V}$ .

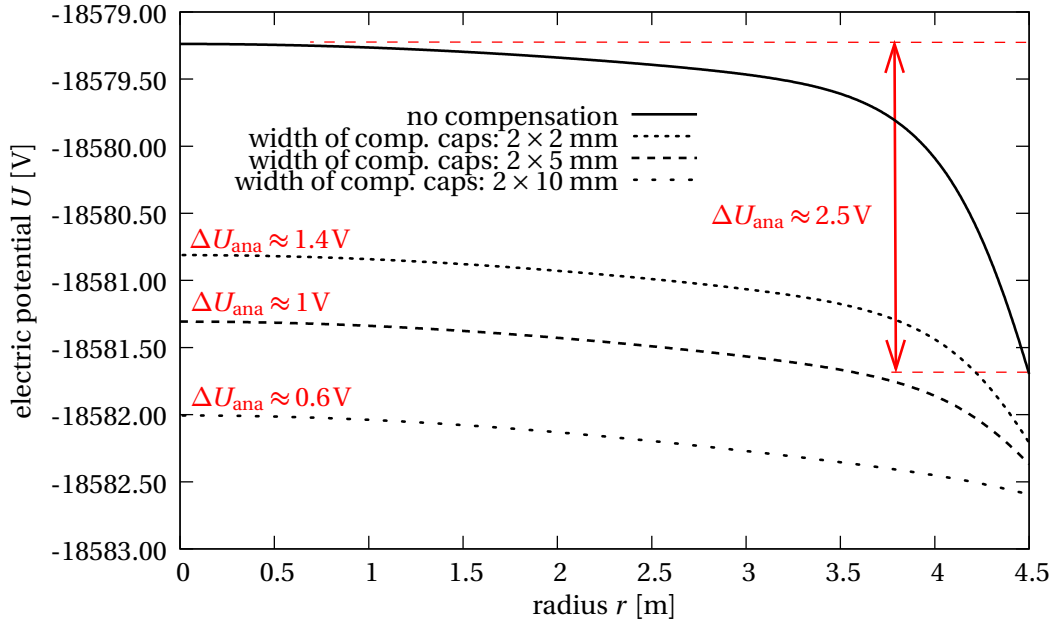


**Figure 4.13:** Inhomogeneity of electric potential in the analyzing plane: comb structures implemented using full rotational symmetry in all parts of the spectrometer, geometry according to figure 4.12. Without any compensating efforts, the potential depression in the analyzing plane increases to  $\Delta U_{\text{ana}} \approx 2.5\text{V}$  due to the inclusion of axial gaps between the modules and of the comb structures that are on the same electric potential as the wires of the outer layer. The potential depression can be reduced by adding compensating electrodes (see figure 4.14). The reduction factor depends on the width of the compensating belts.

Compensating structures can be implemented in a fully rotational-symmetric model as solid belts that run parallel to the combs at a radius  $r < r_{\text{comb}}$ . This concept is illustrated in figure 4.14. In general, the belts can be placed at an arbitrary potential  $U_{\text{belt}}$ . For technical reasons, however, it is practical to choose  $U_{\text{belt}} = U_{\text{wire}2}$ .

As demonstrated in figure 4.13, the potential inhomogeneity in the analyzing plane can be greatly reduced by the inclusion of belts at every junction between module rings in the spectrometer (cylinder and cones). For a belt width of  $2 \times 10\text{mm}$ , a value of  $\Delta U_{\text{ana}} \approx 0.6\text{V}$  is reached. Figure 4.15 shows the modulation of the longitudinal kinetic energy near the module joints which is caused by the more positive potential seen by the electrons when approaching the gaps. Analogously to the improvement of the homogeneity of the retardation potential, the amplitude of these modulations can be reduced by including the compensation belts, as shown in the figure for two different belt widths:  $w = 2 \times 2\text{mm}$  and  $2 \times 5\text{mm}$ . The latter configuration, for example, allows to suppress the “overshooting” of the longitudinal energy to a residual amount of  $\approx 2.45\text{eV}$ . The influence of the positive potential at the gaps between module rings is strongly damped when going to smaller radii (compare for example the curves for  $r_{\text{start}} = 42\text{mm}$  and  $r_{\text{start}} = 30\text{mm}$  in figure 4.15(a)). Nevertheless, the effect remains visible in a large fraction of the area of the analyzing plane. In principle, the positive excursions in  $E_{\parallel}$  separated by local minima are not harmful as

<sup>25</sup>Caution is due when comparing the two values of  $\Delta U_{\text{ana}}$  since the former was obtained with outdated values of the key parameters and the latter uses already the updated values; compare table 4.2. However, the main part of the increase in  $\Delta U_{\text{ana}}$  can safely be attributed to the inclusion of gaps and combs, rather than to the changed set of reference parameters, which are expected to have a greater influence on the absolute value of the retardation potential than on its radial inhomogeneity.

long as the global minimum is situated at the analyzing plane. At most, the introduction of local minima makes the transmission of electrons more prone to the phenomenon of too early retardation, which can be brought about by other influences (such as the abovementioned imperfections of the real electrode setup). However, the regions of slightly more positive potential can form local traps for low-energy electrons, which should be avoided.

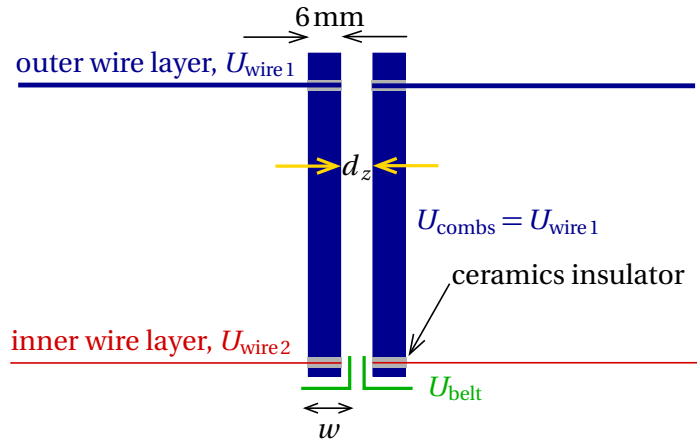


**Figure 4.14:** Sketch of compensating belts in the fully rotational-symmetric calculation. The width  $w$  of the belts was varied between 2 mm and 10 mm at either side of the gap between the modules. In the most general solution, the belts are mounted without electrical contact to the combs or wires, such that a separate potential  $U_{belt}$  can be applied.

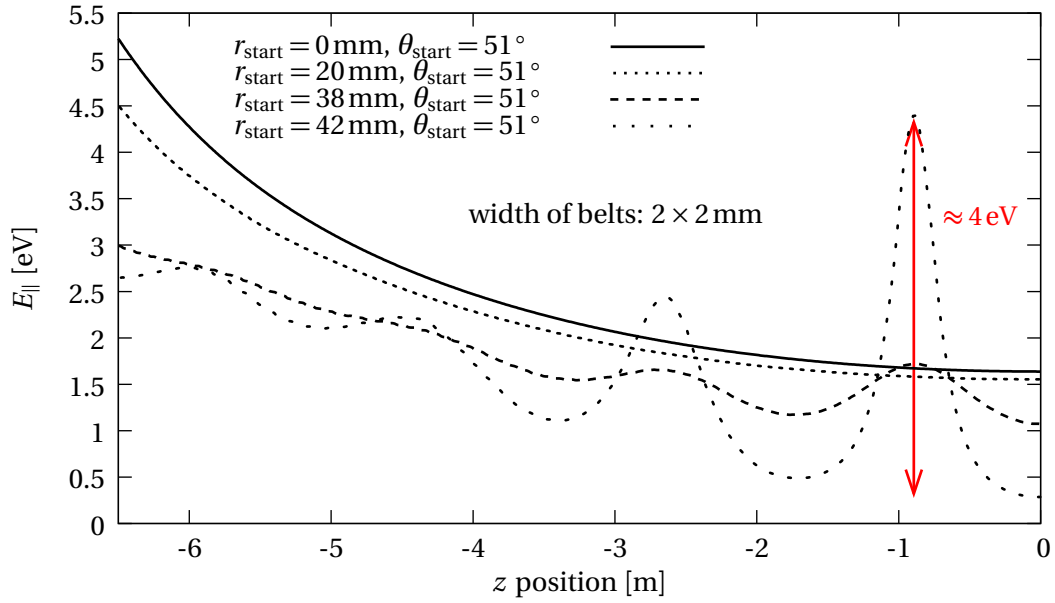
#### 4.6.2 Enhanced model using discrete rotational symmetry

The model used in the previous section tends to overestimate the influence of the mounting structures since the continuous hoop introduces more material than will be used in reality. In order to validate the results obtained before, the solid rings were step by step replaced by combs with more realistic “teeth” structures. This was only possible by porting the simulation model from `e1cd3_2` to the “3d-capable” code `e1cd3_3`. At first, only combs in the cylindrical part were used, but no mounting structures were included in the cones (fourth stage mentioned in table 4.1). Figure 4.16 shows a visualization of the basic tooth model used for the cylindrical part. It consists of a supporting ring segment that resembles the formerly used hoops (but incorporates much less material), a long cuboid representing the main part, and a small cuboid forming the tip of the tooth. This basic model is multiplied and rotated to form a comb-shaped structure. Due to the limited number of total elements available for a given amount of accessible computer memory, and because of the fact that only rectangular elements could be used, the model allows only quite a rough approximation of a real tooth. In particular the section close to the mounting point of the inner wires needs an adequate discretization.<sup>26</sup>

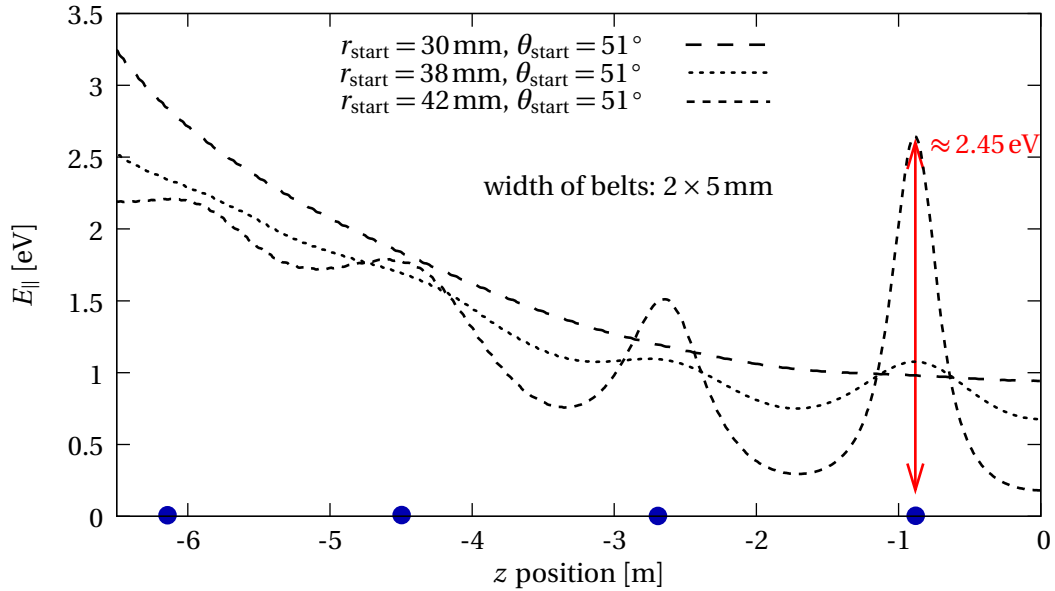
Applying the same “manual” modeling procedure to the tilted and scaled combs in the conical part is both complicated and error-prone. Therefore, the tooth-discretized combs in the conical parts were only implemented later, with the help of the automatic model builder `MainSpec`. In an intermediate step the old continuous hoops from the `e1cd3_2` setup were imported into what thus became a “hybrid model” (fifth stage in table 4.1). It provided enough flexibility to perform more detailed investigations of the compensation mechanism.

Figure 4.17 illustrates two basic possibilities to implement compensating structures in the `e1cd3_3` tooth model. The first studies were carried out using small caps (as seen in figure 4.17(a)).

<sup>26</sup>Presently, efforts are under way to improve the discretization of the teeth and to investigate its influence on the results of the computation (F. Glück, K. Hugenberg, H. Arlinghaus and S. Vöcking), which requires specific computational resources. The implementation of other shapes of elements, such as for example small triangular segments, could also help to enhance the model.



(a) small compensation caps



(b) medium-sized compensation caps

**Figure 4.15:** Comb structures implemented using full rotational symmetry in all parts of the spectrometer: longitudinal kinetic energy for different sizes of the compensation caps. The more positive potential penetrating through the axial gaps (positions marked by blue dots:  $z_{\text{gap},1} = -0.9$  m,  $z_{\text{gap},2} = -2.7$  m, transition between cylinder and cone at  $z_{\text{gap},3} = -4.5$  m, first gap in the conical part at  $z_{\text{gap},4} = -6.18$  m) causes several local rises in the longitudinal kinetic energy of the electrons. The amplitude of these variations diminishes for smaller radial positions inside the spectrometer. At the outer border of the flux tube the effect can be reduced by the inclusion of compensating bridges. The suppression factor increases with the width of the bridges.

They offer the advantage of introducing a smaller amount of additional material as compared to the belt-like structures discussed in the previous section. The downside of this version of the com-

compensation mechanism, however, is that it uses a large number of small, separate components<sup>27</sup>, and the technical difficulties regarding positioning and fixing of the caps form the main argument that led to abandoning this approach. The second possibility (figure 4.17(b)) uses similar structures as the belts in the e1cd3\_2 model. Continuous bridges allow a significant reduction of the number of parts compared to the use of caps. Two versions were tried:

- one rather broad bridge covering two rows of combs and the axial gap between them (fig. 4.17(b)), and
- each row of combs covered by a separate belt, leaving a small residual gap in  $z$ -direction (fig. 4.14).

The evolution of the potential depression  $\Delta U_{\text{ana}}$  in the analyzing plane for three different scenarios based on the “hybrid model” is presented in figure 4.18. It indicates that adding mounting structures also in the conical sections leads to a considerable change in the electrostatic potential even at the location of the analyzing plane. Interestingly, without the inclusion of any compensating caps  $\Delta U_{\text{ana}}$  remains the same in the “hybrid model” as in the fully rotational-symmetric model with continuous mounting structures in all parts of the spectrometer (stage three). However, the absolute value of the retardation potential changes slightly from about  $-18579.2\text{V}$  at  $r = 0$  in figure 4.13 to  $-18580.6\text{V}$  in figure 4.18. This indicates that the abovementioned effect of overestimating the influence of the combs is not too large.

Various models for the compensation using the “hybrid configuration” are compared in figs. 4.19 and 4.20. Both the width of the gap between adjacent rings in the cylinder and the width of the bridges were varied to check the influence of these two parameters on the potential depression in the analyzing plane and on the evolution of the longitudinal kinetic energy along electron trajectories. The impact on the width of the axial gap can best be seen by comparing the two scenarios without any compensation structures ( $d_z = 2\text{mm}$  (red curve in both figures) and  $d_z = 15\text{mm}$  (green curve)). The inhomogeneity of the retardation potential is changed by about  $0.35\text{V}$ , and marked differences occur as well in the plot of the longitudinal kinetic energy. For a spacing of  $d_z = 2\text{mm}$ , the positive “smoothing” effect on the retardation potential as well as on the longitudinal energy produced by a single compensating bridge of width  $w = 8\text{mm}$  (blue curve) is smaller than that of a more extended bridge with  $w = 14\text{mm}$  (cyan curve). Three observations are particularly relevant in view of a technical simplification of the setup:

- A satisfactory result can be obtained when including compensation structures only in the cylindrical part (as was the case in all of the simulations using e1cd3\_3 which are described in this section). This allows a significant reduction of the construction efforts.
- Furthermore, the effect of leaving out the last bridge at the junction between the conical parts and the cylinder on either side is rather small (black versus brown curve). The two cases exhibit a similar behavior of the longitudinal kinetic energy in the direct vicinity of the analyzing plane ( $|z| \lesssim 2.2\text{m}$ ) as well as at larger distances ( $|z| \gtrsim 5.5\text{m}$ ), but differ inbetween.
- The compensation of a  $15\text{mm}$  gap by two belts with  $w = 8\text{mm}$  (magenta curve) works just as well as that in the case of a smaller gap. Therefore, larger module gaps of the order of  $5$  to  $15\text{mm}$  allowing to relax some of the difficulties during the mounting of the modules are not principally precluded from the point of view of the simulation results.

From a technical point of view, an axial gap between the rings of  $d_z = 6\text{mm}$  seems feasible. Considering the simulation results, a width  $w = 20\text{mm}$  of the bridges is appropriate. The latter value

<sup>27</sup>To cover all teeth of the 10 rings of combs in the cylindrical part of the spectrometer,  $10 \cdot 1200$  caps in total would be needed.

#### 4 Design studies for the wire electrode of the KATRIN main spectrometer

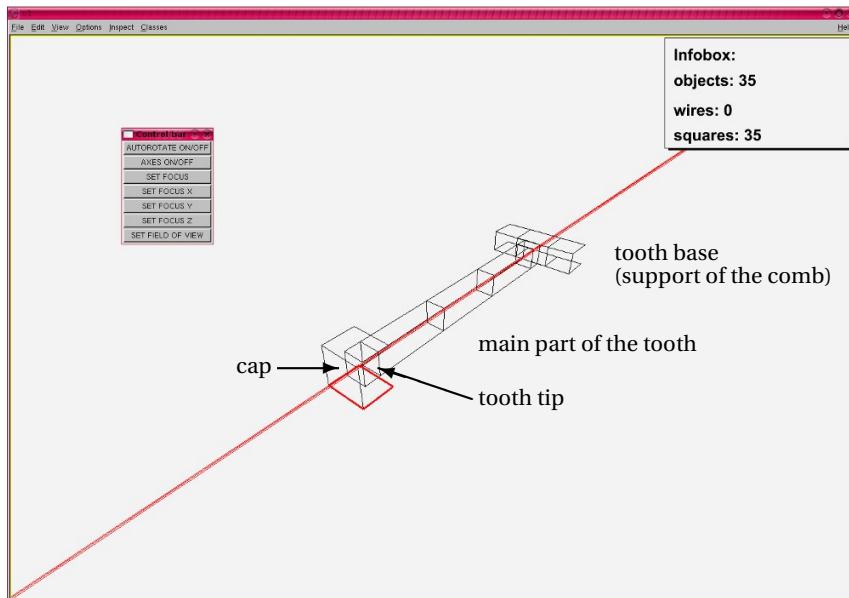
is composed as follows:

$$\begin{aligned} w &= 2 \cdot 6 \text{ mm} && \text{(thickness of 2 combs in axial direction)} \\ &+ 6 \text{ mm} && \text{(gap between rings in axial direction)} \\ &+ 2 \cdot 1 \text{ mm} && \text{(overhang at the edge of each comb)}. \end{aligned} \tag{4.25}$$

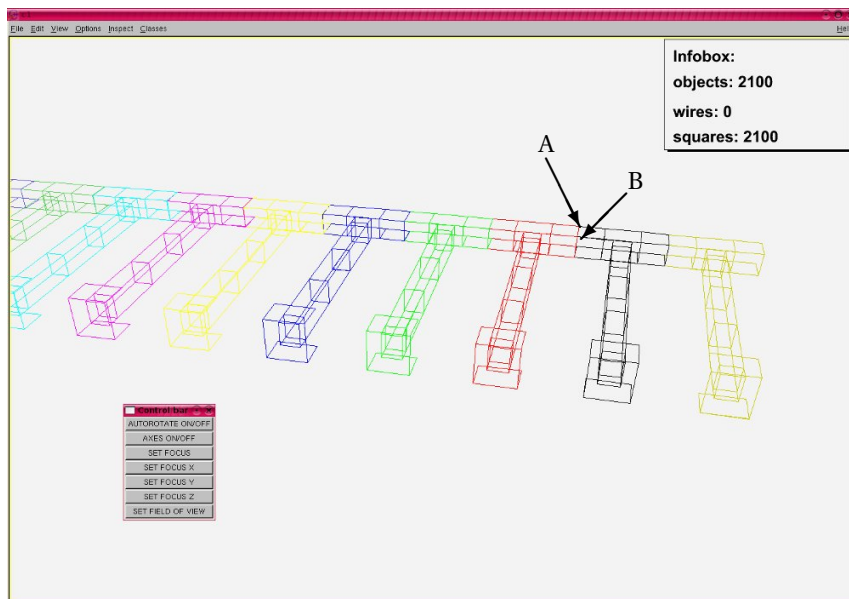
The single-belt solution is favored over the two-belt scenario because it reduces the number of parts to be mounted to a minimum.

Considering the results shown in figure 4.19, the inclusion of a compensating bridge at the interfaces between the conical and cylindrical parts is not urgently needed. Moreover, it would be technically quite difficult to mount. Therefore, it was decided to omit the last bridge. The abovementioned parameters represent the present stage of the design of the module joints in the cylindrical part (see figure 4.21).

#### 4.6 Measures to improve the homogeneity of the electric field



(a) basic tooth model



(b) comb structure created by multiplication and rotation of the basic tooth model

**Figure 4.16:** Implementation of mounting structures with discrete rotational symmetry. (a) Screenshot from an early version of the ROOTsim visualization program showing the simulation model of a single tooth belonging to the mounting structure. In total, about 30 rectangles are used to form a tooth; some additional parts make up a cap at the inner side of the tooth. (b) Excerpt of a comb structure created by multiplication and rotation of the tooth model depicted in (a). Since only rectangles can be used, a tiny gap is unavoidably introduced between two adjacent teeth after rotation. The model is built in such a way that the gap appears at the outer rim of the support structure (A), such that the rim facing towards the inner volume of the spectrometer forms a closed surface (B).

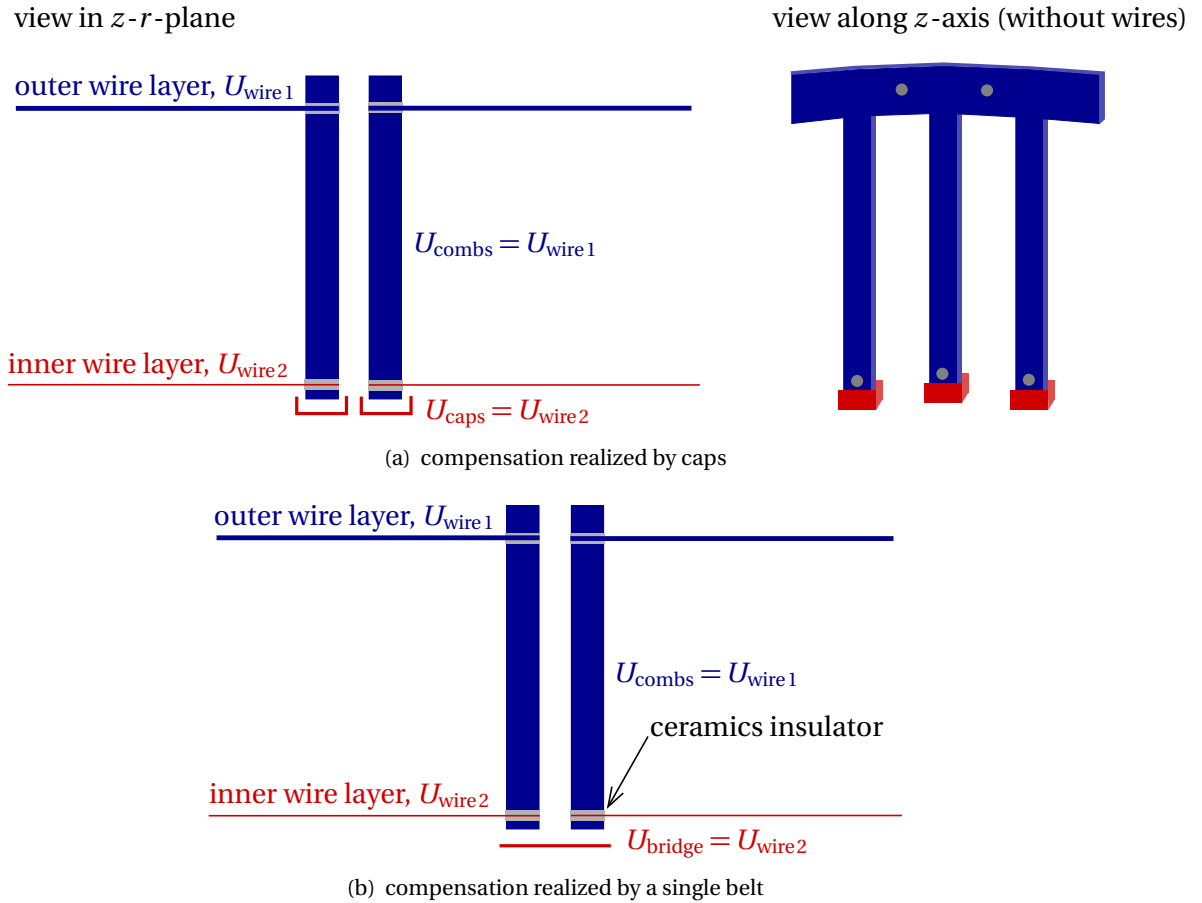


**Figure 4.17:** Compensation of electric potential inhomogeneities: different realizations. (a) Each tooth in the comb is covered by a small cap. Since all the caps would have to be mounted separately, this version is excluded due to the difficulties of its technical implementation. (b) A continuous belt made of sheet metal runs along the inner side of the combs, also covering the gap between the modules. In this realization only a few fixing points between comb and belt are necessary. The CAD drawing in figure 4.21(a) shows the technical realization of the version using such single belts.

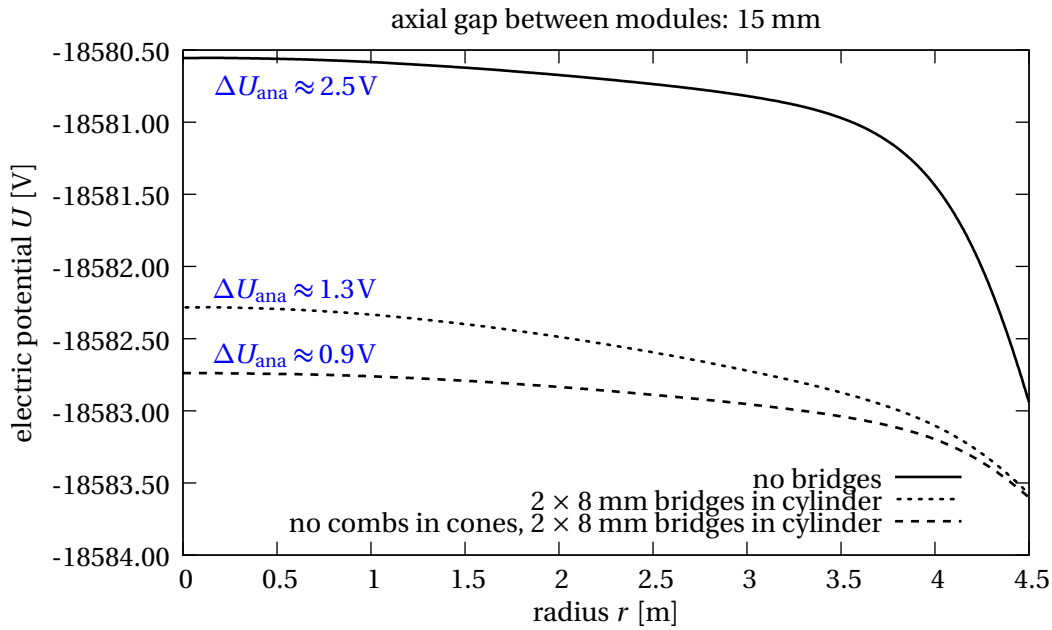


**Figure 4.18:** Potential depression in analyzing plane for different degrees of complexity of the input computer model. The “hybrid” model represented by the solid line includes combs with “teeth” structures in the cylindrical part and combs consisting of solid, fully rotational-symmetric belts in the conical parts. Without any compensative structures, the potential depression in the analyzing plane amounts to  $\Delta U_{\text{ana}} \approx 2.5\text{V}$ , similar to the value one obtained in figure 4.13. The dotted line stands for the same geometrical model, however with the inclusion of compensative bridges of 8 mm width covering each of the combs in the cylindrical part of the spectrometer. The dashed line, finally, results from a model with 8 mm bridges in the cylindrical section, but without any mounting structures included in the conical sections.

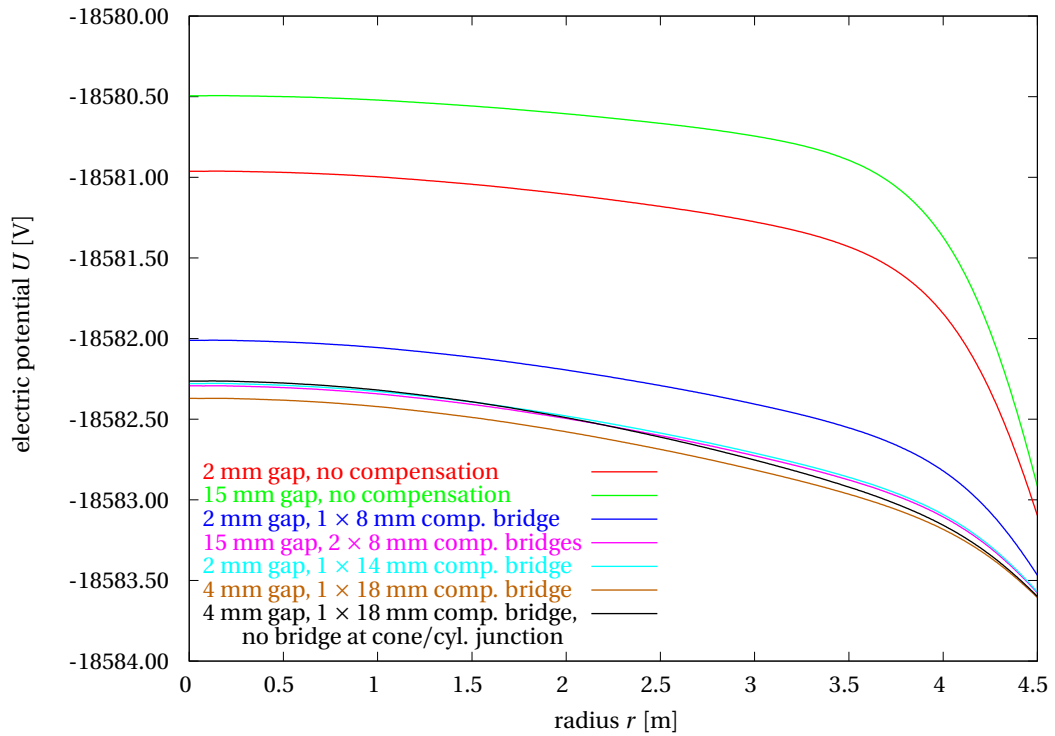


**Figure 4.19:** Influence of axial module spacing  $d_z$  and width of compensation structures  $w$  on potential depression in the analyzing plane. Without compensation,  $\Delta U_{\text{ana}}$  amounts to about 2.5V for a gap width of  $d_z = 15\text{ mm}$  and reduces to  $\Delta U_{\text{ana}} \approx 2.15\text{ V}$  for a smaller gap of  $d_z = 2\text{ mm}$ . Different geometries for the compensation structures were also tested, for example single belts spanning the whole gap ( $1 \times 8\text{ mm}$ ,  $1 \times 14\text{ mm}$ ,  $1 \times 18\text{ mm}$ ) or two belts placed directly at the location of the combs ( $2 \times 8\text{ mm}$ ).

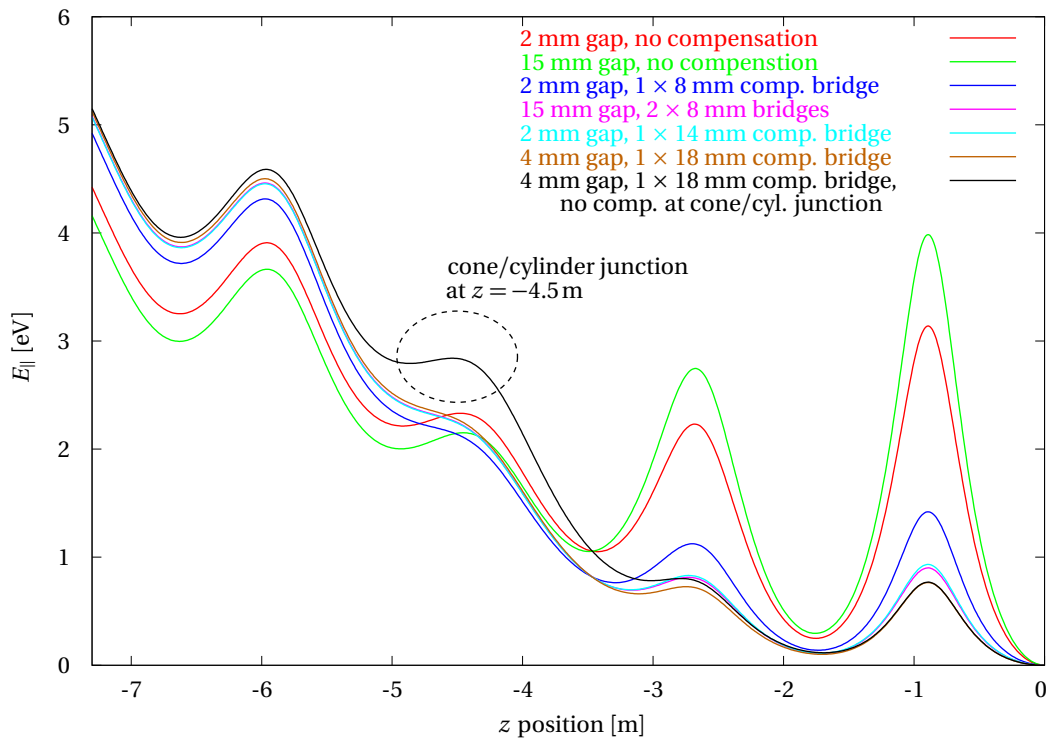
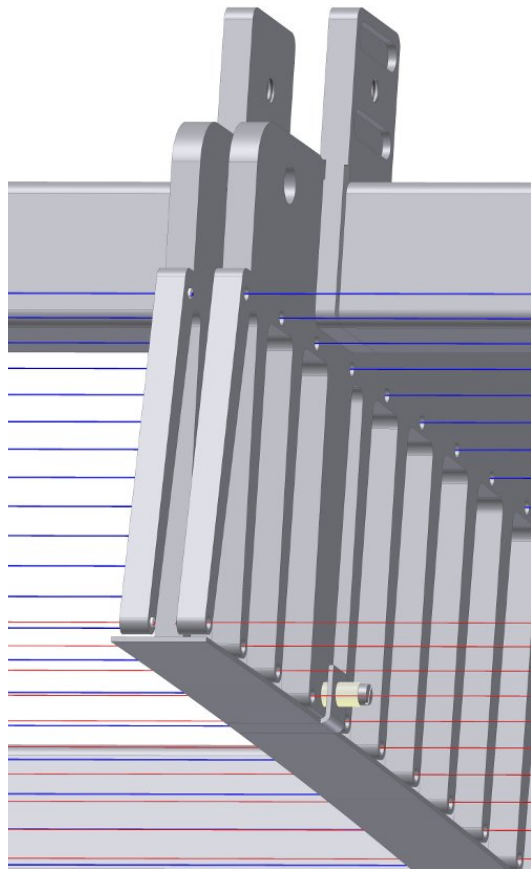
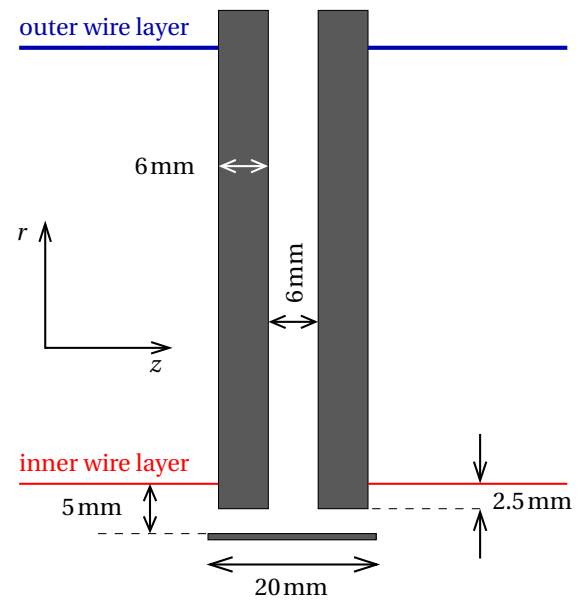


**Figure 4.20:** Influence of axial module spacing  $d_z$  and width of compensation structures  $w$  on longitudinal kinetic energy of electrons at the outer border of the flux tube.



(a) technical drawing of the axial joint between two module rings



(b) sketch indicating the measures of relevant parameters

**Figure 4.21:** Compensation of electric potential inhomogeneities realized by a single belt across the gap between two modules. (a) Technical drawing of the final design. The belt is fixed to the inward-facing side of one of the combs by screws. Small tubes made of ceramics provide insulation of the belt against the electric potential of the comb. (b) Measures of the final design. The axial gap between two adjacent module rings was fixed to 6 mm, which leads to a width of the compensation bridge of 20 mm.

## 4.7 Further design details obtained with a model using discrete rotational symmetry

### Arrangement of combs in the conical sections

Given the condition that both wire layers should be parallel to the vessel hull and keep equal distances to the vessel in all sections of the spectrometer, there are in general two ways of mounting the modules in the conical parts:

- The combs are perpendicular to the vessel hull in every point: the wires exit the teeth at an angle of  $90^\circ$ .
- The combs are perpendicular to the rotational axis of the vessel ( $z$ -axis): the wires are bent at the exit of the ceramic tubes and do not subtend a right angle with the surface of the comb.

The first option bears two fundamental disadvantages:

- In order to make the orientation of the teeth everywhere perpendicular to the vessel hull the combs would have to be bent in two directions (compare figure 4.22). This brings about large technical challenges regarding the fabrication of such components.
- Figure 4.22 also reveals that a significant gap between adjacent modules of the cylindrical and conical section exists at the outer boundary of the combs. Therefore, the screening efficiency is expected to be reduced.

Considering the second option instead (see figure 4.23), one finds different principal drawbacks:

- Wires in modules belonging to the cones are bent in a kink at the point of exiting from the insulator tubes. This abrupt curvature can be of concern both in view of stability of the wires against rupture and with regard to field emission due to increased electric field strength. An experimental test to check the high-voltage stability of the bent wires is described in reference [Zac09].
- If the distances  $l_1$  and  $l_2$  are supposed to be kept constant throughout all parts of the electrode (cylinder and cones) despite the tilt angle  $\alpha$  (see figure 4.23), the teeth have to be longer by a factor of  $1/\cos\alpha$ , which is particularly difficult to realize in the steep cone with  $\alpha \approx 55^\circ$ .

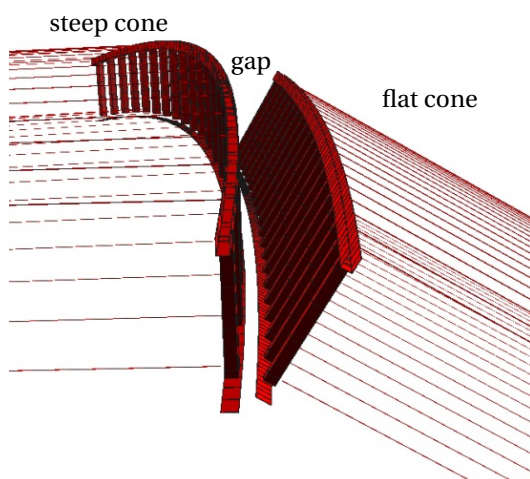


**Figure 4.22:** Simulation model: implementation of comb-like structures with teeth. The excerpt of the geometry shows the junction between the steep and the flat cone. If the wires are supposed to exit the teeth at a right angle, the shape of the comb becomes rather complicated: it is bent in two ways.

All things considered, the second mounting option with the combs aligned perpendicularly to the axis of the spectrometer was chosen. To solve the problem of the long teeth in the steep cone, the

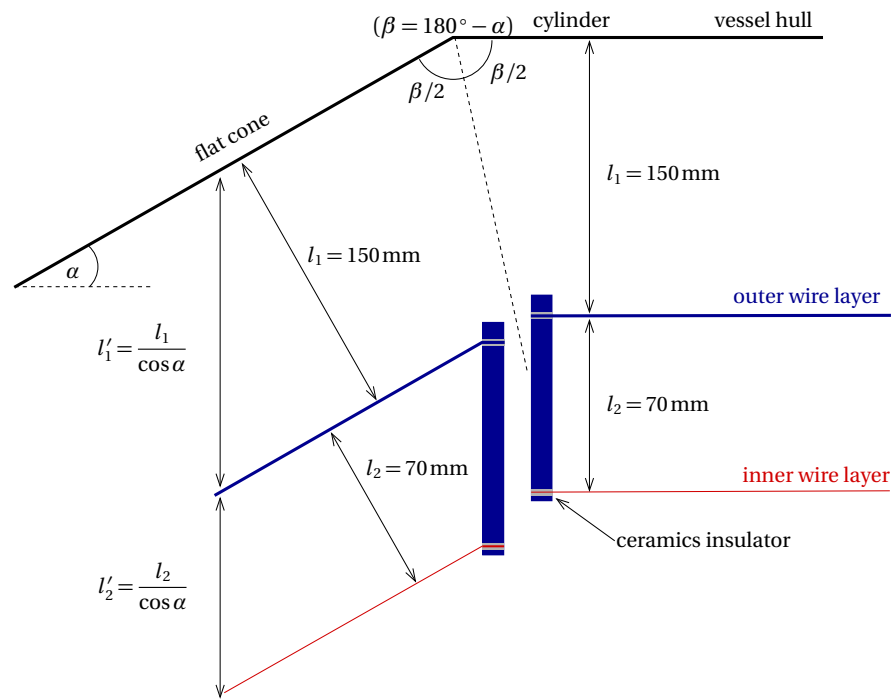


**Figure 4.23:** Schematic drawing: vertical mounting of combs in the conical parts of the spectrometer (dimensions not to scale). In this configuration the combs are only bent in one way (compare figure 4.22).

modules in this part will contain only one wire layer.

## 4.8 Overview of final parameters of the wire electrode system for the KATRIN main spectrometer

Table 4.6 summarizes the outcome of the latest design efforts, including the work that has been done in the scope of the diploma theses [Hug08] and [Zac09]. For reference, the individual sections of the electrode are numbered, starting with the number 02 at the source side and ending with 16 at the detector side (01 and 17 are reserved for the two ground electrodes, respectively). For an illustration see figure 4.25.

Adding to the computer-based conceptual studies described in this work, the design of the conical sections in particular has been optimized with the aim of suppressing Penning-type traps for charged particles which are located at the entrance and exit regions of the spectrometer (see the brief review of modifications in section 5.3).

**Table 4.6:** Summary of parameters of the inner electrode system for the main spectrometer. Numbering of the modules according to figure 4.25. The electric screening potential for both wire layers is given relative to the vessel potential of  $-18.4$  kV (outer layer:  $\Delta U_1 = U_{\text{vessel}} - U_{\text{grid},1}$ , inner layer:  $\Delta U_2 = U_{\text{vessel}} - U_{\text{grid},2}$ ).

section module ring number	steep cones		flat cones			cylinder
	02 & 16	03 & 15	04 & 14	05 & 13	06 & 12	07 – 11
modules per ring	4	10	20	20	20	20
wires per module and per layer	50	40	34	42	52	60
wire layers	1	1	2	2	2	2
wires per ring	200	400	1360	1680	2080	2400
el. screening pot. $\Delta U_1$ [V]	20	160	100	100	100	100
el. screening pot. $\Delta U_2$ [V]	—	—	200	200	200	200

The inner electrode of the main spectrometer thus consists of a total of 248 wire modules, plus two ground electrode cones and two conical shielding electrodes (“anti-Penning” electrodes). The central cylindrical section holds five rings of 20 modules each, the flat conical sections are divided into  $2 \times 3$  rings with the same azimuthal segmentation as the cylinder. Lastly, the steep cone encompasses  $2 \times 2$  rings with an azimuthal segmentation of 10 and 4 modules, respectively. All modules in the steep cones are equipped with only one wire layer ( $d = 0.2$  mm).

For the final stage of simulations (compare table 4.1) mounting structures in all parts of the spectrometer were included [Zac09] using the MainSpec geometry generator:

- Combs discretized with teeth are implemented in the cylindrical part and the flat conical sections 04 & 14 through 06 & 12.
- Since the modules in the steep conical sections 02 & 16 and 03 & 15 only have a single wire layer, combs are not necessary and belts with a simple rectangular cross section ( $6$  mm  $\times$   $40$  mm) are used instead.

The C-shaped spacer rods are not used in the standard configuration to save computational resources, but their influence has been shown to be marginal (see section 4.6). The resulting potential depression  $\Delta U_{\text{ana}}$  in the analyzing plane – and for completeness also the inhomogeneity  $\Delta B_{\text{ana}}$  of the magnetic field in the current coil configuration – are displayed in figure 4.24.

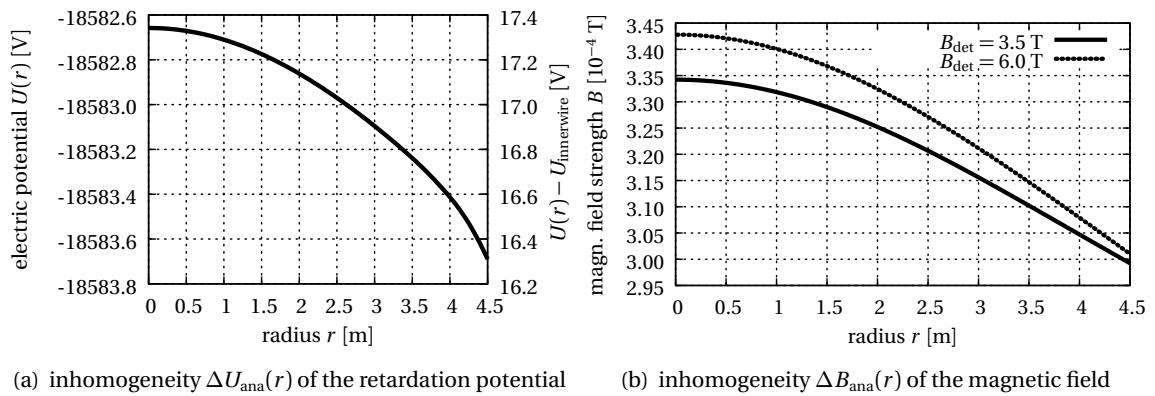


**Figure 4.24:** Inhomogeneities of electric potential and magnetic field in the analyzing plane of the main spectrometer for the finalized design of the wire electrode [Zac09]. (a) The potential depression at  $z = 0$  amounts to  $\Delta U_{\text{ana}}(r) \approx 1.03$  V. (b) The relative change of the magnetic field strength across the analyzing plane is  $\Delta B_{\text{ana}}(r) \approx 10.3\%$  for  $B_{\text{det}} = 3.5$  T (solid line) and  $\Delta B_{\text{ana}}(r) \approx 12.2\%$  for  $B_{\text{det}} = 6.0$  T (dotted line), respectively.

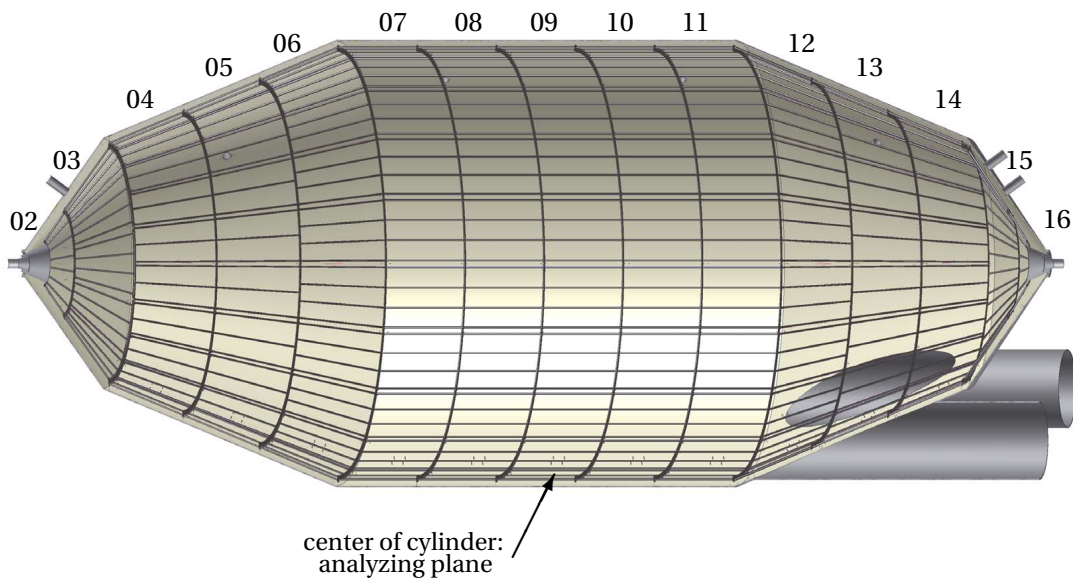


**Figure 4.25:** Cutaway drawing showing the modular setup of the inner electrode of the main spectrometer. The individual module rings are numbered (compare table 4.6).

## 4.9 Assembly of the modules and quality assurance procedures

In compliance with the stringent vacuum requirements mentioned in section 4.1, a large ultrasonic bath was developed and built [Tem07] to clean the parts for the wire electrode according to the ASTeC procedure adopted by KATRIN. Aside from the cleaning procedures, all steps of the module assembly are carried out inside a cleanroom, which was set up specifically for the construction of the wire electrode at the Institute of Nuclear Physics, University of Münster. This encompasses for example the quality assurance (QA) measurements of individual combs (compare section 4.5.4), the cutting of wires, their insertion into the comb structures and the mounting of the modules as well as the QA measurements of the mechanical wire tension (see figure 4.26) and the packing of the modules for their transportation to Karlsruhe.

The task of providing high voltage to the modules – and, more specifically, to each individual wire – is non-trivial (see [Pra09]). Since the wires of both layers are fixed using small insulating tubes, a mechanism to provide each layer with the corresponding electric potential is needed. This is achieved for every module by connecting all wires of one layer by a common connector in the form of a single wire running at the back side of the comb (outer layer) or the teeth (inner layer). The principle of electric interconnection of the wires is shown in figure 4.27. Interconnection of the modules is achieved by spacers establishing electrical contact across the module gaps in azimuthal and axial direction. In order to make sure that none of the modules remains incidentally unconnected, redundancy is provided. Furthermore, the electrostatic insulation between the two wire layers must be checked as a part of the comprehensive post-assembly (QA) measures.

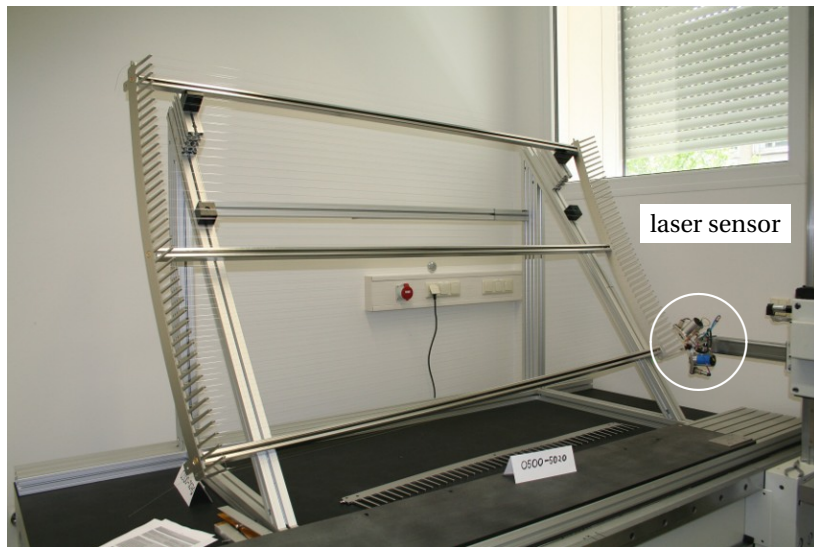
The most important aspects regarding QA (see, for example, [Rei07, Jöh07, Pra09]) have already been mentioned in the discussion of the tolerance estimates in section 4.5. Both the mass production of the modules [Hil10] as well as the careful control of the tolerances are particularly challenging because of the huge number of individual parts to be handled, including

- about 23500 pieces of wire (over 40km in total) for the screening grid, plus about 440 connecting wires,
- about 47000 capillaries (tubes) made of ceramics,
- about 440 combs and 930 C-shaped rods for the mounting structures, and
- many additional parts like screws, spacers and sheet metal strips for the compensation belts.

Documentation of the QA procedures and results in a database is required. For example, all of the insulator tubes together with the bent ends of the wires need to be inspected and photographed, in order to detect fissures or other damages that might later lead to a rupture of a wire or a capillary. Although most of the QA measurements are performed at Münster prior to, during and after assembly, some of the steps need to be repeated after transportation of the modules to Karlsruhe, shortly before they are finally installed inside the main spectrometer.



(a) assembly of a module for the flat conical part



(b) finished module for the flat conical part mounted on the measurement table for quality assurance procedures

**Figure 4.26:** Photographs: module assembly and quality assurance in the cleanroom at Münster University.

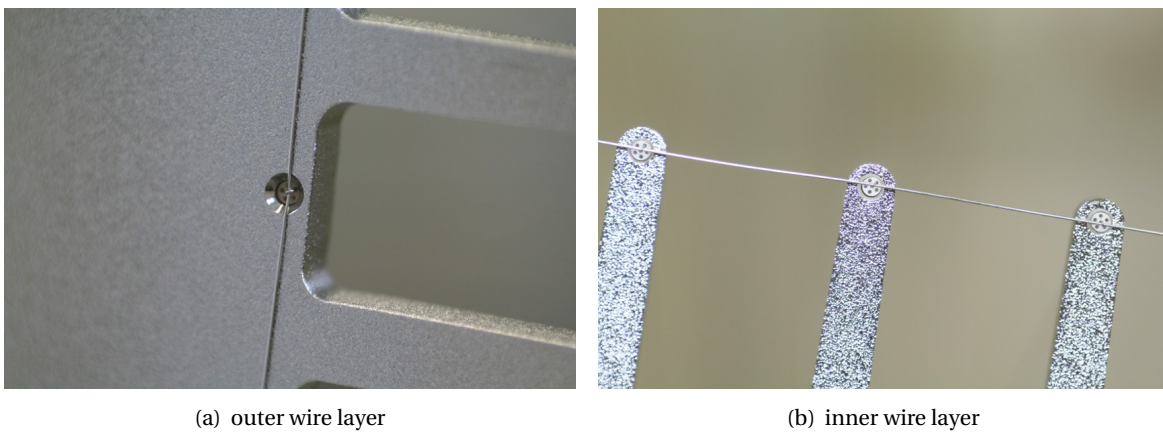


**Figure 4.27:** Photographs of connecting wires providing the electric potential to the grid wires in each layer. (a) The connecting wire in the outer layer is allowed to touch the comb as both are on equal electric potential. (b) The inner wire layer is placed on a different potential than the combs, therefore the connecting wire must be kept at an insulating distance to the solid material. This is achieved by making the insulator ceramics protrude slightly from the teeth.

## 4.10 Summary and status

### Summary of the design studies

As a result of extensive and intricate computer-based design studies, a technically realizable concept of a two-layer wire electrode system for the electrostatic screening of background electrons from the walls of the KATRIN main spectrometer was accomplished. This task required the coordination of electromagnetic design efforts including, for example, those presented in [Hug08], [Vöc08] and [Zac09], in close relation to the contributions described in this thesis.

This concept aims for a background suppression factor of the order of 10 – 100 (in addition to the magnetic screening effect intrinsic to the MAC-E filter) by limiting the geometrical coverage of the wire grid to about  $f_{gc} < 1\%$ . The electric screening also will allow to reduce part of the low-frequency noise on the retardation potential inside the analyzing volume of the main spectrometer.

Although modelled on the smaller inner electrode systems already in use at the Mainz MAC-E filter and the KATRIN pre-spectrometer, the two-layer system for the main spectrometer is significantly more complex. This is, on the one hand, reflected in the technical difficulties regarding several aspects of the construction of the electrode, but on the other hand also in the computational effort needed to model and calculate the electrostatic field of the main spectrometer including the details of the wire electrode and its mounting structures. The projected sensitivity of the KATRIN experiment requires a much higher overall precision of about 10 mV (corresponding to 1% of the energy resolution  $\Delta E$ ) as compared to the pre-spectrometer or the Mainz experiment.

Commercially available software can hardly be adapted to fulfill the needs arising from the highly disparate dimensions of the large spectrometer ( $\mathcal{O}(10\text{m})$ ) and the thin wires ( $\mathcal{O}(100\mu\text{m})$ ). Instead, tailor-made software based on the boundary element method were used. As the inclusion of an increasing level of detail became necessary in the course of the design studies described in this work, the development of new versions of the software was stimulated [Glü06a, Vöc08]. This chapter traces the evolution of the simulation model along with the gradual modifications of the physical concept of the electrode system. The interplay between technical and computational aspects is in fact characteristic of the design studies. One example is the estimate of tolerances which forms a major part of the investigations. Despite certain limitations defined by the necessity to rely on a full rotational symmetry, initial studies revealed a marked dependence of the electrostatic properties of the spectrometer on imperfections of the electrode setup such as a sag of the wires or a radial displacement of modules. This motivated the revision of several key parameters of the wire electrode design, namely the wire diameters in both layers and the radial spacing between the two layers. Moreover, the tolerances obtained from the computer simulations had a profound impact on the amount and depth of the required quality assurance procedures throughout construction and mounting of the modules [Geb07, Jöh07, Rei07, Pra09, Hil10].

Furthermore, the influence of realistic mounting structures on the electrostatic parameters of the main spectrometer was investigated. The inhomogeneity  $\Delta U_{\text{ana}}$  of the analyzing potential was found to be increased dramatically as a result of the axial gaps inbetween adjacent modules, and compensating structures were implemented into the modules of the cylindrical part in order to reduce this harmful effect. However, the unshielded surface area placed on  $U = -18.6\text{kV}$  introduced by these compensation bridges is still a point of concern, since these parts in turn can form sources of background electrons. The surface area of a single bridge can be estimated assuming a width of  $w = 20\text{mm}$  of the sheet-metal strip in axial direction and a radial position at least 5 mm

further inwards with respect to the thin wire layer (*i. e.*,  $r_{\text{bridge}} \approx 4.675 \text{ m}$ ):

$$\begin{aligned} A_{\text{bridge}} &= 2\pi \cdot r_{\text{bridge}} \cdot w \\ &\approx 0.59 \text{ m}^2. \end{aligned} \quad (4.26)$$

Thus, the total surface of the four bridges covering the gaps in the cylindrical part of the spectrometer amounts to

$$A_{\text{allbridges}} = 2.36 \text{ m}^2, \quad (4.27)$$

which represents about 0.36 % of the inner surface of the main spectrometer vessel and 0.85 % of the surface of the cylindrical part. This value is to be compared to the geometrical coverage factor of the wires defined in eq. (3.3). Inserting  $s \approx 25 \text{ mm}$  and  $d_2 = 0.2 \text{ mm}$  for the inner wire layer, one obtains

$$f_{\text{gc},2} = \frac{d_2}{s} \approx 0.8\%. \quad (4.28)$$

The comparatively large area of the belts might make a reinvestigation of the optimal width necessary. The geometry of the bridges, which defines the compensation, cannot be modified after the modules of the cylindrical part have been installed. Since the belts are connected to the same electric potential as inner wires, it will not be possible to later change the potential, either. Therefore, a timely and careful optimization of the design of the compensation structures is essential, and a high precision of the computation is required. Since the final design of the modules for the cylindrical part is almost complete, such studies need to be concluded in the very near future.

A major open question concerns the design of a small number of particular wire modules, namely the ones covering that part of the conical spectrometer section which is equipped with the three  $\varnothing 1700 \text{ mm}$  pump ports. Since the openings are placed in the downstream half of the spectrometer (*i. e.*, facing towards the detector), minor distortions of the electrostatic field are of no significant concern regarding the neutrino mass measurements. The aim is to make sure that none of the electrons which have successfully passed the analyzing plane are lost (*i. e.*, electrostatically reflected) in the downstream half of the spectrometer due to a more negative potential<sup>28</sup> compared to the analyzing potential, since this would affect the neutrino mass measurements. Presumably, a special module layout is needed for a coarse compensation of the effect. One of the possible solutions, for example, is the inclusion of a third wire layer in this small sample of modules.

### Hardware status

The main spectrometer vessel arrived at Forschungszentrum Karlsruhe in November 2006 and in the meantime has successfully passed first high-voltage, outbaking and vacuum tests. The vessel is presently being prepared for the installation of the wire electrode. A cleanroom has been set up to allow direct access to the interior of the spectrometer. Inside the vessel, a scaffolding and a flexible mounting platform (“intervention system”, shown in figure 4.28) were erected. These will be used both for the installation of the rail system and for the subsequent mounting of the modules, which is scheduled to start in spring 2009. As of February 2009, all of the modules belonging to the conical sections had been assembled at Münster, with a large fraction already transported to the main spectrometer site at Forschungszentrum Karlsruhe. In the next step the modules for the large cylindrical section will be produced (100 modules of the same type, plus spares). After completion of the installation, a comprehensive measurement program to investigate the electromagnetic properties of the main spectrometer and to study the background suppression achievable by the wire electrode system is going to be started.

<sup>28</sup>This could occur due to the fact that the electric screening factor  $S_1$  is increased by the larger distance between the vessel and the outer wire layer at the location of the pumping port holes, which means that the effective potential  $U_{\text{eff},1}$  would be more strongly influenced by the more negative potential  $U_{\text{wire},1} = U_{\text{vessel}} - \Delta U_1$  of the outer wire layer.



**Figure 4.28:** Scaffolding and working platform for the installation of the inner electrode system inside the main spectrometer vessel (June 2008). Photograph: FZK.

## 5 Penning traps in the KATRIN setup as a potential background source

In section 2.5, charged particles stored in electromagnetic traps<sup>1</sup> have already been listed among the background sources expected in the KATRIN experiment.

Within the approximately 70 m long solenoid chain of the setup, several sections can be identified in which strong magnetic fields and high electric potentials are simultaneously present (see figure 5.1). As will be discussed in detail in the first section of this chapter, which gives a general introduction to electrical discharge mechanisms and Penning traps, such regions can potentially host discharges which may cause background. However, the different trapping regions bear varying relevance with respect to their effect on the background in KATRIN.

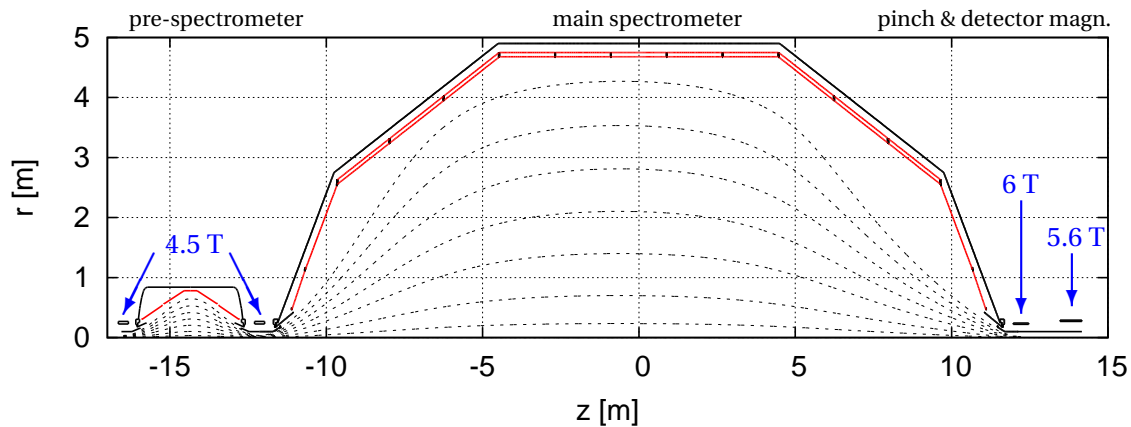


**Figure 5.1:** Overview of high-field regions in the KATRIN spectrometer and detector section. Dashed lines represent magnetic field lines. The air coil system of the main spectrometer has been omitted in this drawing.

High magnetic fields will be present throughout the source and transport sections, but only rather low electric potentials are applied.<sup>2</sup> The first occurrence of high magnetic fields combined with strong electric potentials is therefore at the entrance and exit regions of the pre-spectrometer. Indeed, strong discharges were observed during test measurements at the pre-spectrometer which led to the necessity of modifying the electrode configuration. Computer simulations carried out in the scope of this work in order to find an electrode configuration which solves the problem are described in section 5.2.

A very similar configuration exists at the entrance and exit regions of the main spectrometer. In

<sup>1</sup>In most configurations encountered within the KATRIN experiment, the geometry and other properties of such traps are analogous to those common in so-called Penning traps. This type of trap has been named after F. M. Penning, who also studied the mechanism of discharges present at low pressures in certain electrode configurations under the influence of magnetic fields (see Penning ionization gauge, section 5.1.3).

<sup>2</sup>It is planned to elevate the tritium source to a scanning potential of up to  $-1$  kV.

contrast to the discharges at the pre-spectrometer, which are expected to have little effect on the background rate measured at the final plane detector due to the lower electric potential, the traps in the main spectrometer can produce harmful effects. Section 5.3 briefly reviews the investigations of the trapping conditions and the draft of a set of additional electrodes to remove the Penning trap which were part of two diploma theses, [Hug08] and [Zac09].

Furthermore, another Penning trap is realized at the interface of the two spectrometers. Section 5.4 gives a detailed description of the trapping scenario and comments on its particular relevance to background concerns. A method to counteract the harmful influence of this trap is presented and discussed in chapter 6.

Lastly, strong magnetic fields occur also in the detector system. In the case that the option of post-accelerating the electrons by electric potentials up to  $-30\text{ kV}$  is used, discharges could pose a problem in the region of the post-acceleration electrode, which is, however, not treated in the scope of this work.

## 5.1 Discharge mechanisms

Various parameters, such as the pressure level and the composition of the residual gas in the system or the configuration of electromagnetic fields, can influence the discharge mechanisms which may lead to electrical breakdown in an evacuated system (see also the discussion in [Hug08], chapter 6). In the absence of magnetic fields, strong electric fields applied to electrodes in a vacuum system may lead either to a “Townsend discharge” or to a so-called “vacuum breakdown”, depending on the quality of the vacuum. If a strong magnetic field is applied in addition to the electric field, a “Penning discharge” with characteristics different from those in the previous two cases can occur.

### 5.1.1 Townsend discharge

This discharge mechanism is relevant mainly under poor vacuum conditions. Thus it does not play an important role at the ultra-high vacuum conditions achieved in the high electric field sections of the KATRIN experiment. However, the Penning discharge, which bears a great relevance for the KATRIN experiment, is to some extent related to the basic processes of the Townsend discharge.

Studies concerning this breakdown phenomenon have been carried out since the late 19th century<sup>3</sup>, but J. S. Townsend was the first to give a detailed account of the process (see for example [Tow10]), thus it was later named after him.

A formal description of the mechanism starts with a (small) initial number of electrons,  $N_0$ , which may emerge from the cathode as a result of radioactivity in the material or as secondaries due to environmental radiation impinging on the solid material from the outside.<sup>4</sup> These electrons are

---

<sup>3</sup>In 1889 already, F. Paschen [Pas89] found that for a given geometry of the electric field the critical potential difference or “sparking” potential  $U$  is a function of the product  $pd$  of the pressure  $p$  and the spacing  $d$  between the electrodes. The shape of the Paschen curve is specific to the type of gas present in the system and exhibits a minimum which is determined by two processes. If  $pd$  is small, the electric field strength may be large, but only a small number of collisions take place at low pressure. On the other hand, if  $pd$  is large, the electrons cannot gain high energies because they are not accelerated efficiently due to frequent collisions with the gas, and thus ionization will be somewhat suppressed.

<sup>4</sup>In his original works, Townsend irradiated the cathode with X-rays from an external tube to enhance the initial number of electrons and to facilitate the start of the discharge.

accelerated by the electric field from the cathode towards the anode, and at some point their energy will reach the ionization threshold of the residual gas. Then, a cascade of ionizations can be initiated: the ions created in the primary collisions of electrons with residual gas molecules are accelerated towards the cathode, where they create new electrons, which in turn are accelerated back towards the anode, and so on. The development of an avalanche amplification of charge carriers depends on several parameters (among them the shape of the electrode geometry as well as the composition and pressure of the residual gas), which define a critical value of the electric potential. Reaching this “ignition voltage” leads to a breakdown of the insulation provided by the vacuum, and a current flows between anode and cathode.

The first Townsend coefficient  $\alpha$  denotes the average number of electron-ion pairs produced per unit length by one electron (or negative ion). If the electrodes are assumed to be the parallel plates of a capacitor placed at a distance  $d$ , then the number of electrons flowing between cathode and anode can be expressed as

$$N_d^{(0)} = N_0 e^{\alpha d}. \quad (5.1)$$

The electrons liberated by positive ions hitting the cathode are included by introducing the second Townsend coefficient  $\gamma$ , defined as the average number of electrons created at the cathode surface per ion impact. The number of new electrons in the system after the first passage of the cycle is given by

$$N_d^{(1)} = N_0 \gamma (e^{\alpha d} - 1), \quad (5.2)$$

since  $N_0 (e^{\alpha d} - 1)$  is the number of positive ions reaching the cathode at the distance  $d$ .

However, the cycle continues with the  $N_d^{(1)}$  electrons being re-accelerated towards the anode, again amplifying the number of negative charge carriers by creating

$$N_d^{(2)} = N_0 \gamma (e^{\alpha d} - 1) e^{\alpha d} \quad (5.3)$$

new electrons on their way, and so on (compare [Ger93]).

Thus, the total number of negative charge carriers is given by a geometrical series:

$$\begin{aligned} N_{\text{tot}} &= N_d^{(0)} + N_d^{(1)} + N_d^{(2)} + \dots \\ &= N_0 e^{\alpha d} + N_0 \gamma (e^{\alpha d} - 1) e^{\alpha d} \\ &\quad + N_0 \gamma^2 (e^{\alpha d} - 1)^2 e^{\alpha d} + \dots \end{aligned} \quad (5.4)$$

If  $\gamma (e^{\alpha d} - 1) < 1$ , this series can be summed up to

$$N = N_0 \frac{e^{\alpha d}}{1 - \gamma (e^{\alpha d} - 1)}. \quad (5.5)$$

In this case the discharge will stop after some time. The discharge current is then proportional to the number of electrons given by equation (5.5). Because of the strong dependence of the ionization coefficient  $\alpha$  on the electron energy, the discharge current will rise quickly with the applied electric field strength.

On the other hand, the condition for a self-sustained or steady discharge can then be formulated as follows:

$$N_d^{(1)} \geq N_0 \quad \Rightarrow \quad \gamma (e^{\alpha d} - 1) \geq 1. \quad (5.6)$$

### 5.1.2 Vacuum breakdown

This term denotes the electric breakdown in the case of very good vacuum and without magnetic field. Instead of ionizing collisions with residual gas molecules, which do not play a major role in case the mean free path is much larger than the electrode spacing, the surface quality of the electrode material becomes the decisive factor for the ignition of a discharge.

Soon after the development of the quantum mechanical framework, a theoretical model of vacuum breakdown based on a solution of the Schrödinger equation for electrons tunneling through a potential barrier at the metal surface in the presence of strong electric fields was introduced by Fowler and Nordheim [Fow28]. According to this theory [Bas07, Dyk53], the field emission current density  $J$  is given by

$$J(E_{\text{surf}}) = C_1 \frac{(\beta E_{\text{surf}})^2}{\phi} \exp\left(-\frac{C_2 \phi^{\frac{3}{2}}}{\beta E_{\text{surf}}}\right), \quad (5.7)$$

where  $C_1$  and  $C_2$  are constants,  $\phi$  is the work function of the metal and  $E_{\text{surf}}$  represents the average electric field strength at the surface. The fact that locally enhanced electric field strengths  $\hat{E}$  might occur is taken into account by including the shape factor  $\beta = \hat{E}/E_{\text{surf}}$ .

While a perfectly smooth surface (*i. e.*,  $\beta = 1$ ) would allow to apply field strengths typically as high as about 1 GV/m, equation (5.7) indicates that in the case of microtips or other surface irregularities (*i. e.*,  $\beta \gg 1$ ) breakdown will necessarily occur at much lower field strengths which can be a factor of 100 to 1000 smaller<sup>5</sup> (compare [Ard56]).

Aside from a careful preparation of all cathode and anode surfaces before installation, it is also possible to condition the electrode system *in situ* by deliberately raising the applied high voltage above the breakdown threshold for a certain amount of time. The heat input in the electrodes due to the impact of ions and electrons created in the ionization avalanche can lead to an evaporation of small amounts of material and to a leveling of the surface irregularities, for example by sputtering. It has proven useful to interchange the polarity of the high voltage to obtain better results.

However, the same mechanism that is used in the conditioning procedure can also prove harmful during normal operations: if charged microparticles (for example from impurities of the electrode material) are present in the system, they will be accelerated towards the electrodes. Upon hitting the electrode surface, the microparticle can melt or even evaporate and cause a local overheating at the electrode surface. This results in a release of some amount of metal vapor which subsequently can lead to an ignition of a Townsend-like discharge. Typically, a combination of both mechanisms (field emission of electrons and microparticle evaporation) stands at the origin of vacuum breakdown.

### 5.1.3 Penning trap and Penning discharge

A large number of articles concerned with the mechanism of electric breakdown in the presence of crossed electric and magnetic fields discuss a typical setup consisting of a pair of coaxial cylindrical electrodes with an axial magnetic field (see figure 5.2).

Experimental studies (see, *e. g.*, [Har89]) show that the application of crossed electric and magnetic fields significantly reduces the breakdown voltage (defined by the onset of a discharge) as

<sup>5</sup>Special care needs to be taken when electrodes consisting of thin wires are involved. The small wire diameter will lead to a naturally enhanced electric field strength at the surface, which means that small defects on the wire surface can lead to field emission at even lower applied electric potentials. This has been taken into account in the quality assurance procedures for the wire electrode system of the KATRIN main spectrometer described in chapter 4.1.

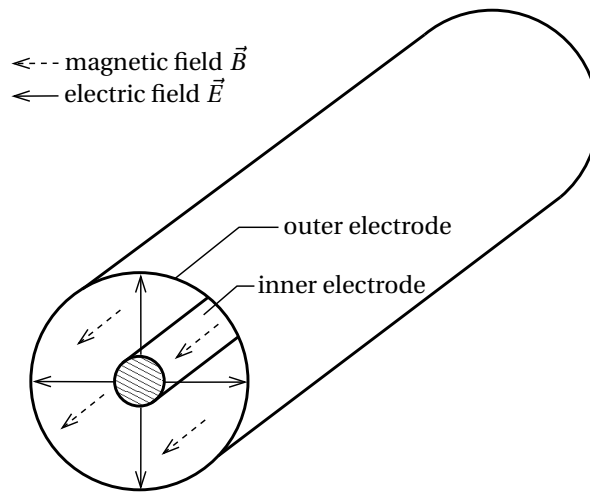


**Figure 5.2:** Cylindrical electrode setup with axial magnetic field.

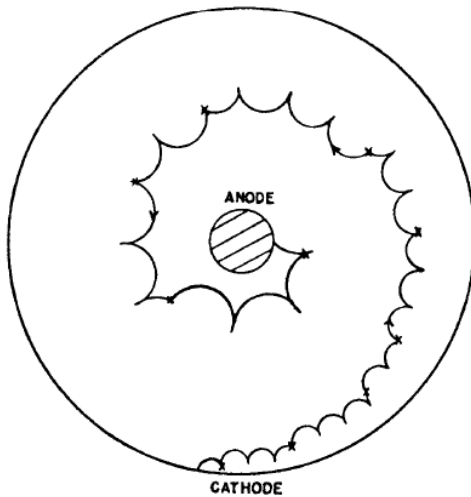


**Figure 5.3:** Sketch of an electron trajectory forming a hypocycloidal path in a system of coaxial cylindrical electrodes with axial magnetic field (taken from [Red58a]). The diagram shows a cross section (two-dimensional projection) of a cylindrical system like the one depicted in figure 5.2.

compared to the case without magnetic field. An explanation of this phenomenon can be found when considering the type of trajectory an electron will assume in such a field configuration. Unlike in the case without magnetic field, electrons released from the cathode cannot reach the anode on a straight line. Instead, they are forced on a more complicated trajectory describing a hypocycloidal path, as illustrated in figure 5.3. In this sketch, the electric field lines connect anode and cathode in radial direction, while the magnetic field lines run along the axis of the cylinders. The electron starts from the cathode surface and usually would go back to the cathode since the magnetic field bends the electron trajectory to a closed path. In this case, the electron is lost for any further ionization processes. However, energy loss due to collisions with gas molecules or – as pointed out in reference [Hae53] – also the presence of inhomogeneities<sup>6</sup> on the surface of the cathode can prevent the electrons from going back to the cathode. Supposed that the electron does not undergo any more inelastic collisions, it will perform a hypocycloidal motion created by a rolling circle [Som52, Red58a] of diameter  $D$  determined by the relative strength of the magnetic

<sup>6</sup>As first noted by Penning [Pen36], small imperfections of the cathode surface causing local deformations of the electric field can prohibit electrons from re-entering the cathode.

field,  $B$ :

$$D = 2 \frac{m}{e} \frac{E}{B^2}, \quad (5.8)$$

with the mass  $m$  and charge  $e$  of the electron and the electric field strength  $E = U/d$  defined by the applied voltage  $U$  and the gap size  $d$  between anode and cathode. In particular, one can show ([Har89], and references therein) that in a magnetic field exceeding a critical field strength  $B_{\text{crit}}$  defined by  $D$  and the gap spacing  $d$ , the electron will be trapped and can only reach the anode by suffering more ionizing collisions. In this scenario, a discharge of the Townsend type may be ignited, which can be described with the formalism discussed in the corresponding paragraph above, albeit with the distinction that this time some effective Townsend coefficients  $\tilde{\alpha}$  and  $\tilde{\gamma}$  need to be used. In the literature (see, e. g., [Hae53, Ble58]), the concept of “equivalent pressure” is introduced to incorporate the influence of transverse magnetic fields on the discharge mechanism as similar to a higher residual gas pressure. This concept is derived from the idea that both the prolonged path of the electron due to the influence of the magnetic field and a higher pressure would show the same effect of an increased number of ionizing collisions.

Figure 5.4 schematically presents the dependence of the breakdown voltage on the magnetic field strength.

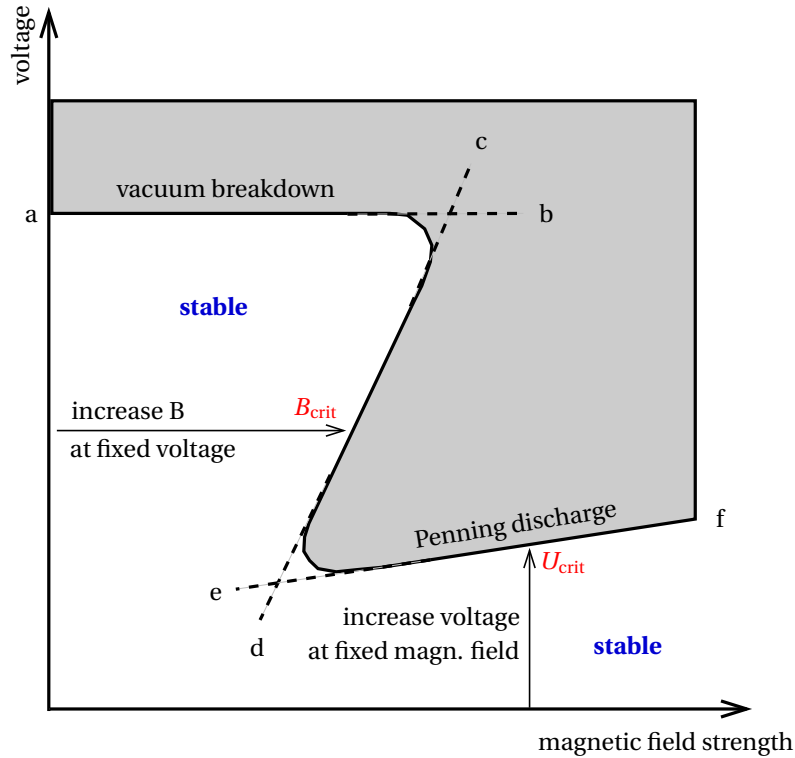


**Figure 5.4:** Breakdown voltage versus magnetic field: different characteristics for vacuum breakdown and Penning discharge (diagram adapted from [Har89]). For weak magnetic fields below the critical field strength  $B_{\text{crit}}$ , the breakdown voltage does not change significantly with the magnetic field (similar to vacuum breakdown, region a – b). Above the critical strength, however, the breakdown is initiated by the Penning discharge mechanism. Depending on the energy gained by the electrons in the accelerating electric field relative to the ionization potential of the residual gas, the breakdown characteristic follows either one of the curves c – d (large electron energy) or e – f (lower electron energy). Remarkably, the onset of a breakdown also depends on the order in which electric and magnetic fields are raised.

### Technical applications

Due to their superior sensitivity and wide dynamical range, so-called “cold cathode” (as opposed to “hot filament”) vacuum gauges exploiting the Penning discharge mechanism are today commonly used to measure residual gas pressures in ultra-high vacuum systems (see [Wil07]). The principle is based on the fact that the total ionization current  $I_{\text{tot}}$  sustained by both the current  $I_+$  of positive ions hitting the cathode and the current  $I_-$  of electrons accelerated towards the anode is a function of the pressure  $p$ :

$$I_{\text{total}} = I_+ + I_- = f(p). \quad (5.9)$$

It is the application of a transversal magnetic field that enables cold-cathode gauges to cover such a large range in pressure, since usually the discharge would be extinguished at pressures of  $p < 10^{-3} - 10^{-1}$  mbar due to the small particle density and the resulting long mean pathlengths for electrons. Various types of such pressure measurement instruments are known under the names Penning gauge [Pen36, Pen37], magnetron gauge [Red59], and inverted magnetron (or Redhead) gauge [Red58a, Red58b].

Other devices using the Penning effect for example include ion sources as well as UV light sources. Moreover, the discharge mechanism is employed in sputtering.

Aside from technical applications, trapping devices based on the Penning principle have become known for their broad range of utilizations in precision measurements. Such “Penning traps” are usually operated far below the breakdown conditions: instead of starting an avalanche of ionization processes, their purpose is merely to store a certain number of charged particles – or even a single one – for a suitable period of time to allow studies of some of their fundamental properties. H. G. Dehmelt, who built the first dedicated ion trap according to the mechanism investigated by Penning, eventually shared the 1989 Nobel Prize in physics with W. Paul for their development of the ion trap technique<sup>7</sup>. Two typical geometries of such traps are depicted in figure 5.5. The field configuration can be realized either by a hyperbolic or a cylindrical shape of the electrodes.<sup>8</sup> The motion of charged particles in the trap is confined in radial direction by the (homogeneous) magnetic field and in axial ( $z$ ) direction by the electric potential barrier, see figure 5.6. As a result of the combined magnetic and electric fields, the charged particle follows a complex trajectory determined by the cyclotron and magnetron motions overlaid with a harmonic axial oscillation, as sketched in figure 5.7.

<sup>7</sup>Further information is supplied on the web page

[http://nobelprize.org/nobel\\_prizes/physics/laureates/1989/](http://nobelprize.org/nobel_prizes/physics/laureates/1989/).

<sup>8</sup>The hyperbolic configuration represents the original form of the “classical” Penning trap, whereas the cylindrical version is an adaptation introduced by Malmberg and Driscoll [Mal80].

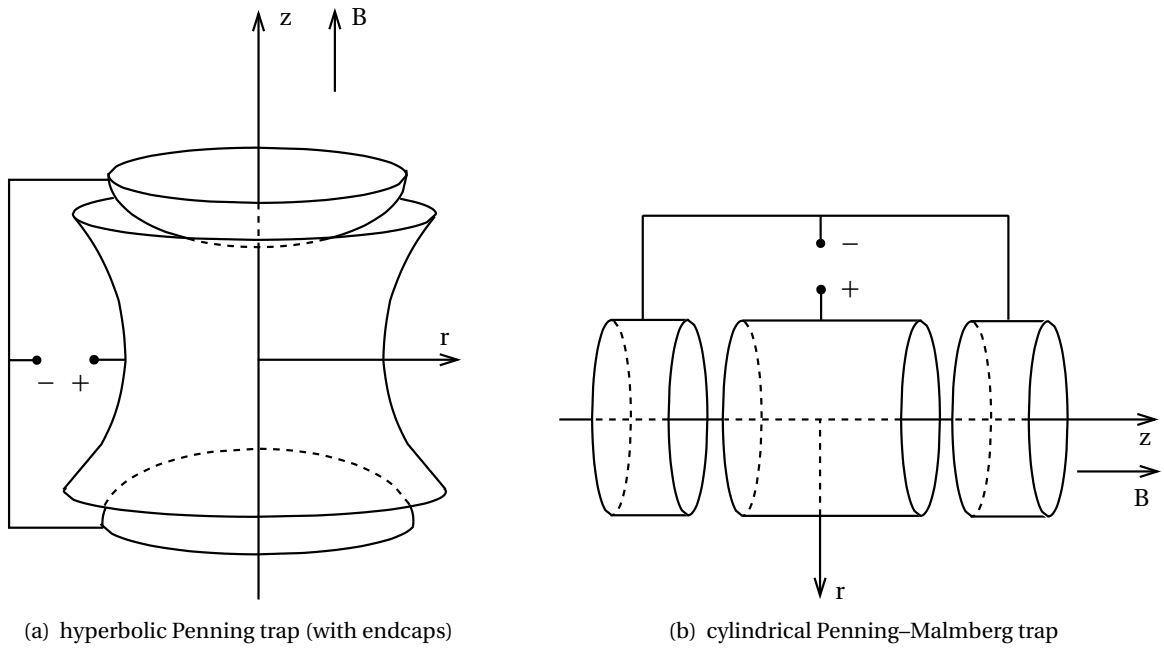


**Figure 5.5:** Two different realizations of a Penning trap. The polarity of the voltage is chosen such that the device will act as a trap for negatively charged particles. In (a), the hyperbolically shaped electrodes give rise to an electric quadrupole potential. In the cylindrical case (b) the dimensions of the electrodes can also be designed in a way that yields a potential in the central part of the trap similar to the one in configuration (a). A major difference between the two layouts is that in the hyperbolic geometry (a) the two endcap electrodes are directly connected by magnetic field lines, whereas in the case of a homogeneous magnetic field this will not be the case in configuration (b). In both cases, however, the potential along a magnetic field line inside the trap will have a shape as indicated in figure 5.6.

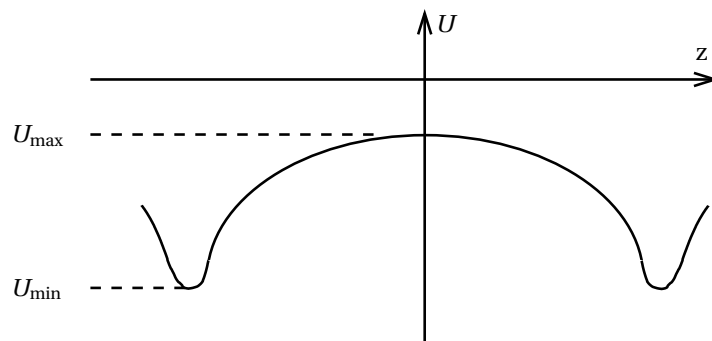


**Figure 5.6:** Schematic of electric potential distribution along a magnetic field line inside a Penning trap. For the polarity chosen in figure 5.5, the potential is more positive in the center of the trap and exhibits repulsive potential walls for negatively charged particles at both ends.

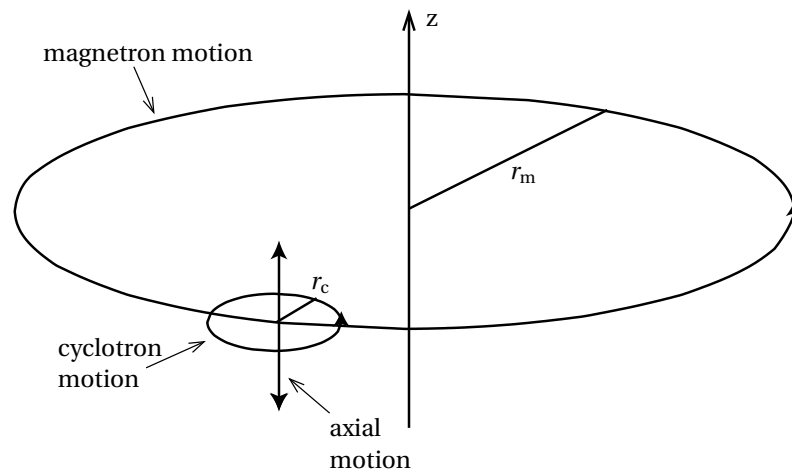


**Figure 5.7:** The motion of a charged particle in a Penning trap can be decomposed into three different components: the cyclotron motion (radius  $r_c$ ) and magnetron motion (radius  $r_m$ ) in radial direction and the harmonic oscillation in axial direction.

#### 5.1.4 Methods to counteract discharge problems due to particle traps

The following list contains a few suggestions on how to prevent the creation of traps for charged particles in the first place, or else on how to remove discharge conditions, where necessary.

- Optimized electromagnetic design. The electrode system should be shaped in such a way that the cathode surfaces run essentially parallel to the magnetic field lines. In any case, magnetic field lines crossing a cathode surface twice (which would create a local Penning trap) should be avoided.
- Careful machining of all electrode parts subject to high electric field strengths to avoid field emission. Mechanical and possibly also electro-polishing is mandatory.
- Good vacuum conditions help to increase the mean free path and thus to suppress ionizing processes.
- Application of an electric dipole field to drift out trapped particles by the  $\mathbf{E} \times \mathbf{B}$  drift motion that occurs in non-parallel electric and magnetic fields (compare eq. (2.45)).
- Compensation or decrease of the magnetic field strength inside the trapping region by applying an external field (*e. g.*, using an auxiliary coil).
- “Electron catcher”: Disturb or cut off trajectories of stored electrons,
  - by inserting solid material (*e. g.*, sheet metal, as described in reference [Har89]). This method requires a stationary installation, *i. e.*, the material permanently remains inside the system. It obviously does not work for KATRIN, where the trapping volume is formed by the beam opening that needs to stay clear of any material for the signal electrons to pass.
  - by inserting a stationary wire or pin-like obstacle connected to ground potential. The pin or wire should have a suitable length, covering at least the radius of the magnetic flux tube. This method not only works on the basis of pure geometrical shadowing (in which case it would be of limited effectiveness given the requirement that the pin should be quasi-massless), but rather exploits the fact that trapped electrons suffer a magnetron drift (according to eq. (2.45)) which accumulates over many reflection cycles and eventually makes them hit the pin or wire target.
  - by periodical intervention, *i. e.*, sweeping a grounded conductive wire through the magnetic flux tube, as envisaged for the trap between the two KATRIN spectrometers (see chapter 6). The sweeping device can be operated in short intervals or pauses between measurements and otherwise remains outside of the sensitive volume. It thus offers a more dynamical solution. Naturally, one would place such a system in a region of strong magnetic field, as this offers two advantages:
    1. the magnetic flux tube is strongly compressed and allows the dimensions of the scanning device to be small, and
    2. the Lorentz force can be exploited to move this wire scanner across the beam profile by feeding an electric current through it, thus requiring rather little external manipulation.

## 5.2 The Penning trap inside the pre-spectrometer

The pre-spectrometer arrived at Forschungszentrum Karlsruhe in autumn 2003 and thus was one of the first major components of the KATRIN setup available on site. It provides ideal conditions to validate several technological concepts which are intended to be used also at other places in the KATRIN experiment. For example, successful tests of the ultra-high vacuum concept and of the two superconducting magnets were performed, and the inner electrode system mentioned in section 3.3 was installed. In addition, a 64-pixel electron detector representing a scaled-down implementation of the Si-PIN technique to be used for the 148-pixel KATRIN final plane detector was installed and commissioned.

Figure 5.8 presents an overview of the pre-spectrometer setup. The magnetic field is generated by the two superconducting solenoids at the entrance and exit of the pre-spectrometer with a nominal central field strength of  $B_{\text{solenoid}} = 4.5\text{T}$  each. Separate electric potentials can be supplied to the vessel electrode and to the solid cones and the wire segments of the inner electrode.

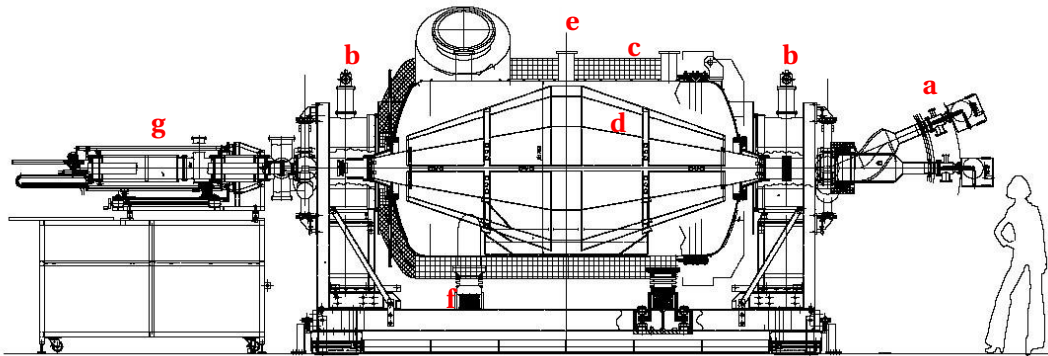


**Figure 5.8:** Setup used for stand-alone operation testing of the pre-spectrometer. The marked features are the following: (a) 2d-scanning electron gun calibration device, (b) superconducting solenoids, (c) vessel hull and thermal insulation, (d) inner electrode system, (e) central (analyzing) plane, (f) high voltage insulators separating the vessel from ground potential, (g) vacuum chamber for the 64-pixel electron detector.

During test measurements of the electromagnetic field configuration, severe problems were encountered when high electric potentials were employed in the presence of a magnetic field. Strong discharges were observed that prohibited further use of the 64-pixel Si-PIN diode detector system due to the risk of damaging it.<sup>9</sup> These discharges were characterized by a dramatic rise both in the pressure level and in the leakage current on the power supplies, usually accompanied by a breakdown of the applied high voltage. Early observations raised the suspicion that a Penning-like trap with a deep potential well was present in the pre-spectrometer setup, and that the discharges were caused by the accumulation of stored particles in this trap and by the corresponding chain of ionizations [Glü06b].

Several series of measurements were carried out to test this hypothesis and to investigate the characteristics of the presumed trap by using the pressure level and the leakage current as diagnostic tools. As an example, figure 5.9 shows an experimentally determined ignition curve (separate measurements were done using only one magnet or both). The critical potential or magnetic field strength causing an ignition of the discharge was found to depend on the order in which

<sup>9</sup>Several measurements were done using a micro channel plate or a single-pixel Si-PIN diode instead.

the fields are applied.<sup>10</sup> This observation is in accordance with the theoretical expectation for a Penning discharge (compare figure 5.4). The simultaneous rise of pressure and leakage current with increasing electric potential at a constant magnetic field strength (figure 5.10(a)), as well as the linear correlation between the two quantities (figure 5.10(b)), form additional evidence for a Penning discharge. A summary of a large number of test experiments and a comparison with results published in the literature, which led to the conclusion that a Penning trap must indeed be present in the pre-spectrometer, is given in refs. [Glü07a, Glü07d].

The following sections present a review of the computer simulations which were carried out in the scope of this work with the aim of locating the supposed Penning trap and finding a modified electrode configuration which allows to remove the trapping conditions.<sup>11</sup>

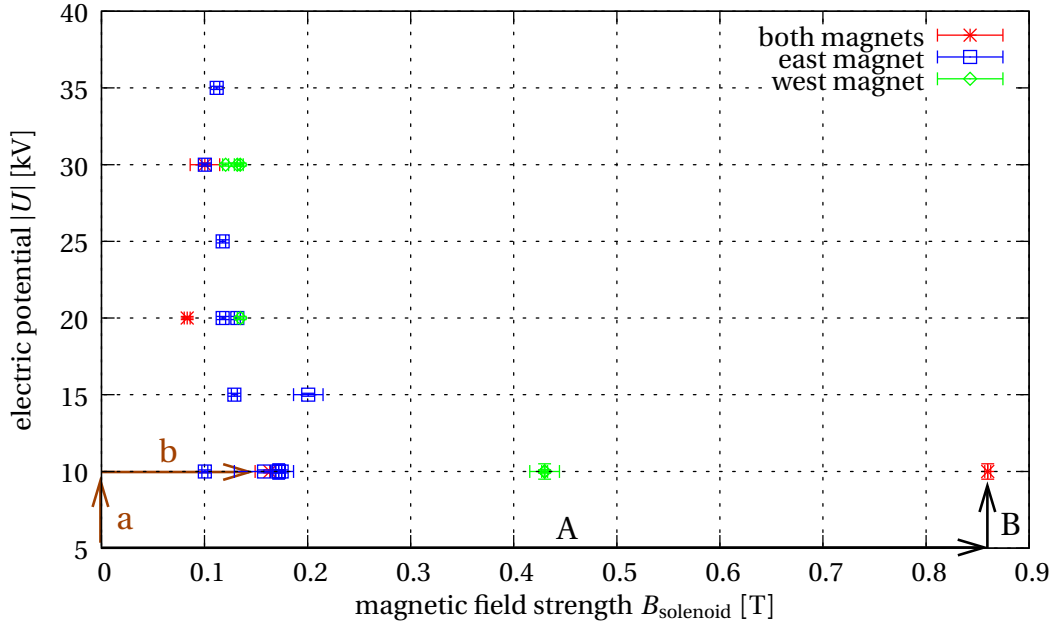


**Figure 5.9:** Experimentally determined ignition curve: start of strong discharges as a function of electric potential and magnetic field strength (compare ref. [Hug08], chapter 6.3). In all experiments shown here, breakdown occurred at magnetic field strengths much lower than the design value of  $B_{\text{solenoid}} = 4.5 \text{ T}$ . The onset of the discharge depends on the order in which the fields are applied. For example, if the magnetic field strength in the magnets is first increased from zero to  $B_{\text{solenoid}} = 0.86 \text{ T}$ , a subsequent increase of the electric potential (A – B) results in a discharge when reaching  $|U| = 10 \text{ kV}$ . On the other hand, if  $|U|$  is raised to  $10 \text{ kV}$  first and  $B_{\text{solenoid}}$  increased afterwards (a – b), the breakdown happens already at  $B_{\text{solenoid}} \approx 0.15 \text{ T}$ .

<sup>10</sup>See also the discussion of further measurements with the pre-spectrometer in reference [Hug08].

<sup>11</sup>Parts of section 5.2 have already been distributed among members of the KATRIN collaboration in the form of an internal report [Glü07b]. The simulations were carried out in collaboration with K. Hugenberg and F. Glück.

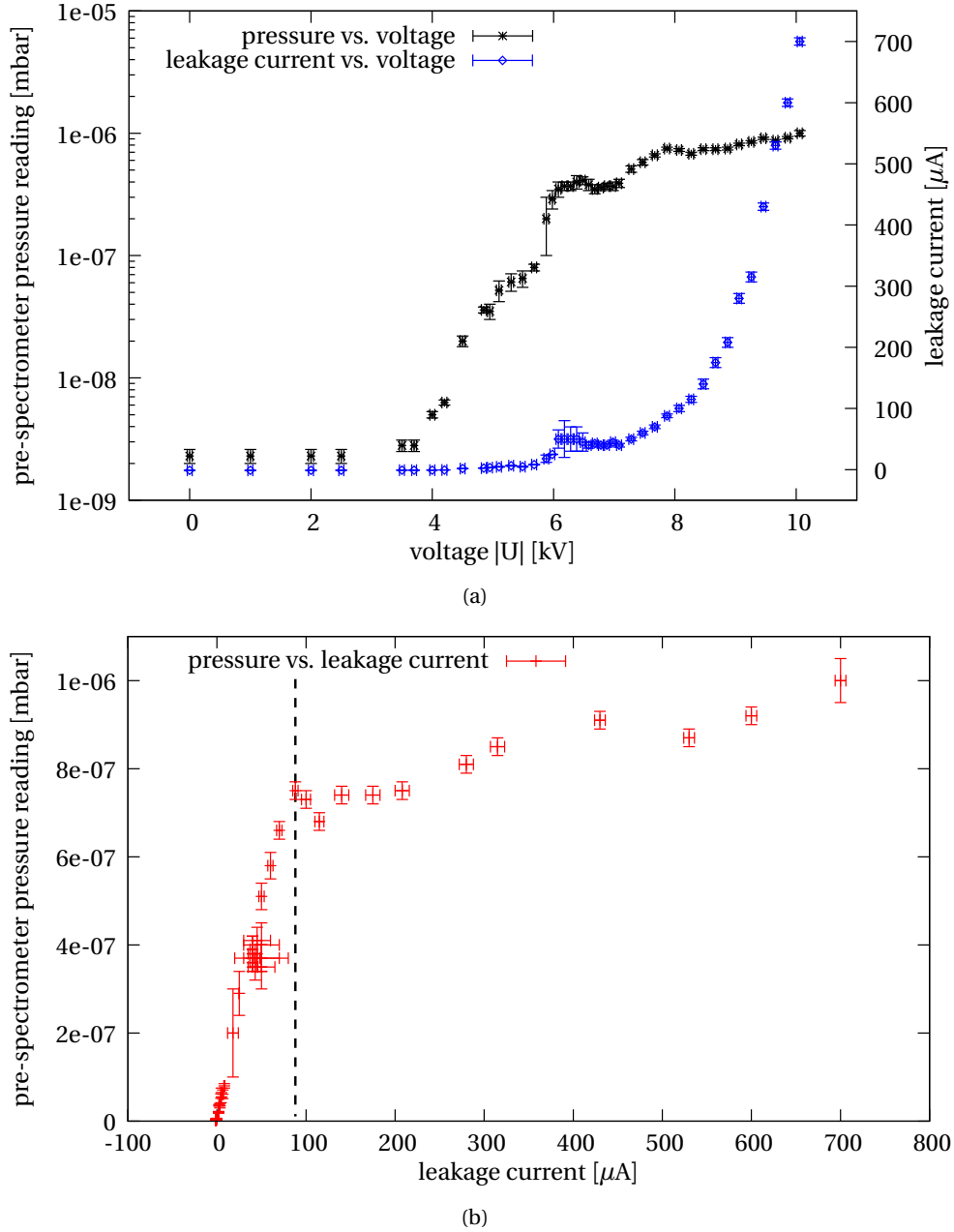


**Figure 5.10:** (a) The pressure inside the pre-spectrometer vessel (\*) as well as the leakage current of the high-voltage power supply ( $\diamond$ ) increase strongly with rising high voltage. For this measurement, all electrodes – vessel, cone and wire electrodes – were placed on equal potential. The magnetic field strength ( $B_{\text{solenoid}} \approx 0.86\text{ T}$  at the center of both solenoids, corresponding to a current of 30 A in both magnets) was not varied. Starting from zero, a potential of  $|U| = 10\text{ kV}$  was reached at  $I_{\text{leak}} \approx 700\ \mu\text{A}$  and kept constant after that until the onset of a strong discharge which lasted several minutes and is not included in this graph.

(b) A linear relationship is visible in the plot of pressure versus leakage current, which is typical of the Penning discharge. The slope changes at around  $I_{\text{leak}} = 90\ \mu\text{A}$  (dashed line), corresponding to a voltage setting of  $|U| \approx 8\text{ kV}$ . This might be due to local heating and evaporation of small amounts of material from the metal surfaces.

### 5.2.1 Location of the Penning trap

The design phase of the electrode system of the pre-spectrometer [Fla04] involved dedicated simulations searching for particle traps inside the sensitive volume.<sup>12</sup> Figure 5.11 shows some of the maps of the trapping volume for electrons generated with the program package *AdiPark*<sup>13</sup> at that time, along with the electrode configuration that was used for the simulations. Adiabatic trajectory calculations for electrons with starting energies of 10 eV, 100 eV and 1000 eV and various angles with respect to the magnetic field lines were performed. Electrons starting from the volume enclosed by the contour line  $n$  with a given energy  $E_{\text{start}}$  and an angle  $\theta_{\text{start}} \geq \theta_{n,\text{min}}$  specified for the corresponding line in figure 5.11 are trapped. Since the trapping volume examined here is defined by a magnetic mirror on the side facing the endcaps of the spectrometer and by an electrostatic barrier in the direction of the analyzing plane, electrons with higher starting energies are trapped more efficiently. The reason is that only those electrons starting in the low magnetic field close to  $B_{\text{min}}$  with a transversal kinetic energy at least equal to the energy resolution of the pre-spectrometer, which is about  $\Delta E_{\text{prespec}} \approx 85$  eV, can be magnetically trapped.<sup>14</sup> In [Fla04] it was thus argued that the detected traps will not be harmful for the operation of the pre-spectrometer since the majority of the electrons generated inside the trapping volume will possess a starting kinetic energy well below this threshold.

However, a second type of trap exists in the end cap sections of the pre-spectrometer, as was first realized in 2006 by F. Glück [Glü06b]. This trapping region was not detected in the original design studies in [Fla04], because the trapping scans were limited to the volume not shadowed by electrodes. Since this second kind of trap is situated “behind” the ground electrode, it did not show up in previous investigations.

The results of recent simulations, shown in figure 5.12, reveal the Penning-like trap which is formed at both sides of the symmetric spectrometer in the corner between the ground electrode and the solid-metal cones of the inner electrode. In this volume magnetic field lines connecting two parts of the cathode on negative high voltage are present, and inbetween those cathode surfaces the potential becomes significantly more positive due to the influence of the nearby ground electrode. Under these conditions electrons can be stored efficiently: they are guided along magnetic field lines and reflected when reaching the strongly negative potential at the two sides of the trap. These trapped electrons can start a discharge causing the observed breakdown of the high voltage and the increase of the leakage current as well as the surge in the pressure reading [Glü07a, Glü05b, Glü07d].

<sup>12</sup>The main focus lay on the trapping conditions for electrons. However, in the work described in the same reference [Fla04], it was realized that due to its higher magnetic field strength in the center and the larger diameter of the vessel as compared to the Mainz setup, the KATRIN pre-spectrometer also provides stable trapping conditions for positive ions.

<sup>13</sup>*AdiPark* was developed by Th. Thümmeler and is described in [Thü02]. It tracks the adiabatic motion of the so-called guiding center without considering the microscopic path of the cyclotron motion. This way, *AdiPark* is able to perform multi-electron trajectory calculations faster than other tracking tools that were previously used, like for example SIMION [Sim00]. In addition, it is capable of performing an automated search for trapping regions.

<sup>14</sup>According to eq. (2.22), the starting transversal kinetic energy  $E_{\perp,\text{start}}$  must fulfill the following condition in order to allow the particle to escape through the neck of the “magnetic bottle”:

$$\begin{aligned} E_{\perp,\text{start}} &< \Delta E = E_0 \cdot \frac{B_{\text{min}}}{B_{\text{max}}} \\ \Leftrightarrow E_{\perp,\text{magnet}} &= E_{\perp,\text{start}} \cdot \frac{B_{\text{max}}}{B_{\text{min}}} & (5.10) \\ &< E_0 \quad (i. e., E_{\parallel,\text{magnet}} > 0). \end{aligned}$$

Conversely, a starting transversal kinetic energy component equal to or larger than the energy resolution will lead to magnetic reflection of the particle.

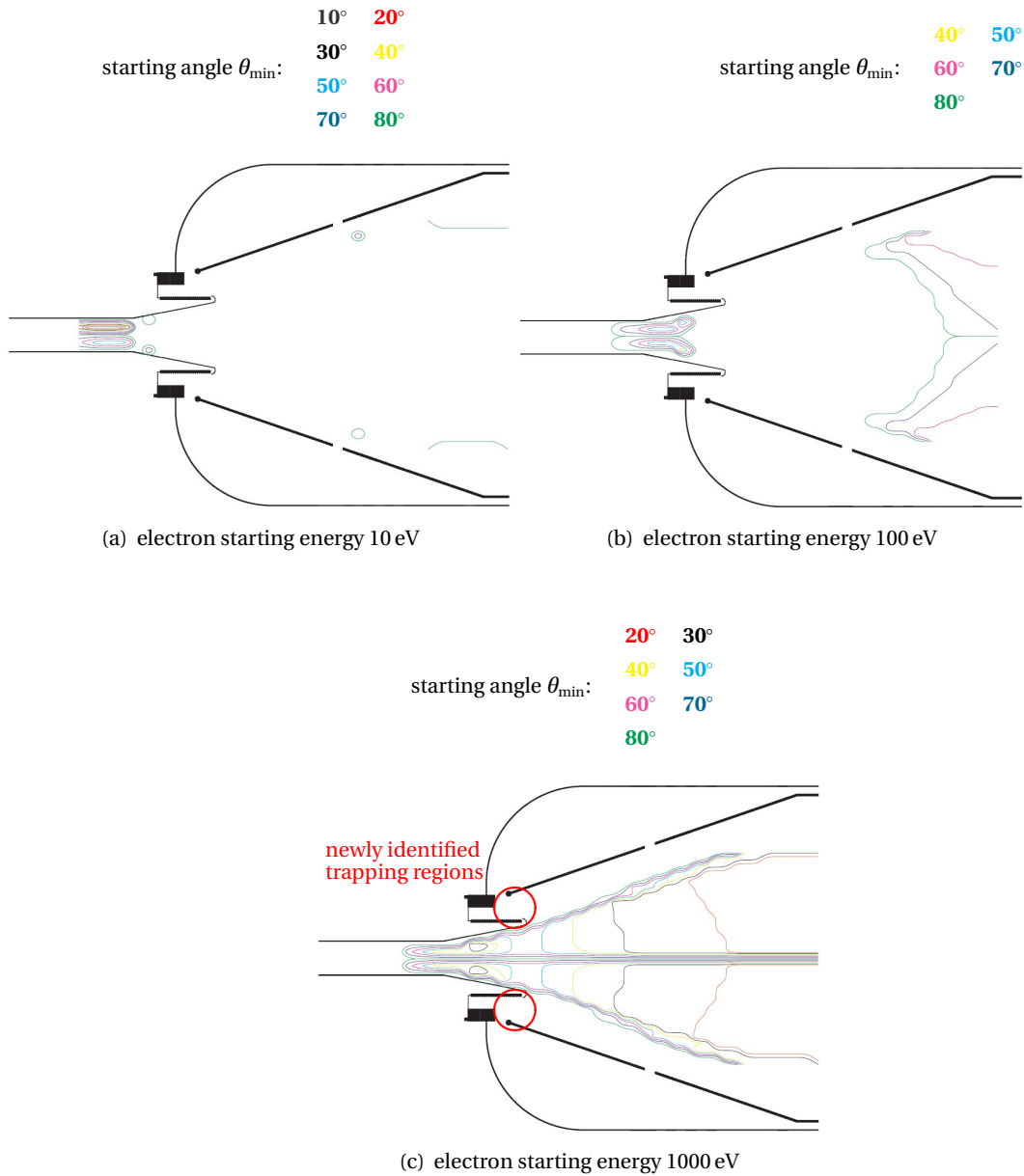
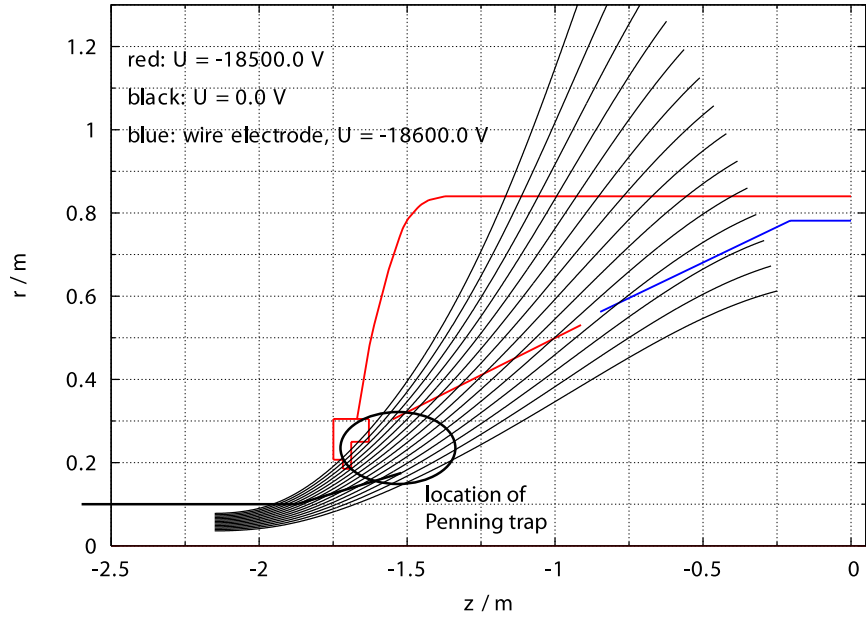
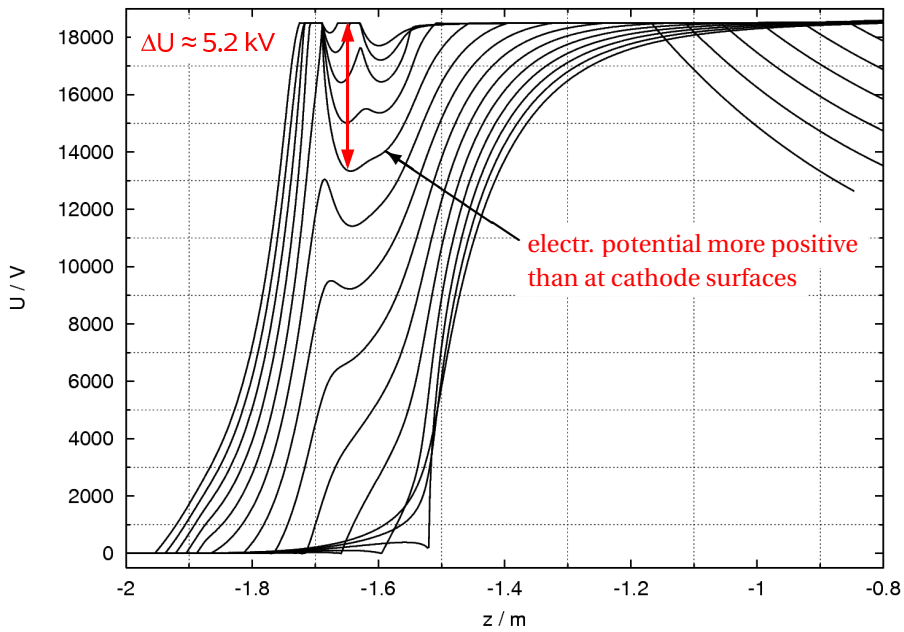


**Figure 5.11:** Trapping volume for electrons with different starting energies, taken from [Fla04]. A partially outdated electrode system of the KATRIN pre-spectrometer was used (in particular, the shape and position of the large insulator tube connected to the ground electrode was changed). The additional trapping regions found in recent simulations (see figure 5.12 for further details) are marked by red circles. The latter were not found previously because they are “shadowed” by the ground electrode.

5 Penning traps in the KATRIN setup as a potential background source



(a) previous electrode configuration of the pre-spectrometer with magnetic field lines



(b) electric potential along magnetic field lines

**Figure 5.12:** (a) Drawing of the original pre-spectrometer electrode configuration. Magnetic field lines are also indicated, some of which connect one part of the cathode at the solid-metal cone of the inner electrode to another part of the cathode situated at the flange of the pre-spectrometer. (b) Electric potential along magnetic field lines for the original pre-spectrometer setup ( $U_{\text{wire grid}} = -18.6\text{ kV}$ ,  $U_{\text{solid cones}} = U_{\text{vessel}} = -18.5\text{ kV}$ ). Without any additional shielding the Penning trap between cones and ground electrode has a depth of  $\Delta U \approx 5.2\text{ kV}$ . At the very right the electric potential along the magnetic field lines drops again, but this represents an artifact of the calculation since the magnetic field lines penetrate the vessel hull towards the outside of the spectrometer. For better readability, the electric potential is plotted with inverted sign.

### 5.2.2 Modification of the electrode system to remove the Penning trap in the cone region

Several possibilities to modify the existing electrode setup of the pre-spectrometer have been investigated. There are in principle two ways of building an additional electrode to remove the Penning trap in the cone region:

- a) The additional shielding electrode has a large diameter so as to cover most of the space in between the ground electrode and the solid-metal cones of the inner electrode. The best results are achieved for diameters larger than the  $\varnothing 500$  mm flanges at the end caps, which calls for a rather complex part that cannot be made out of a single piece (compare figure 5.13). This option is significantly more difficult to realize and is thus disfavored from the point of view of technical considerations.

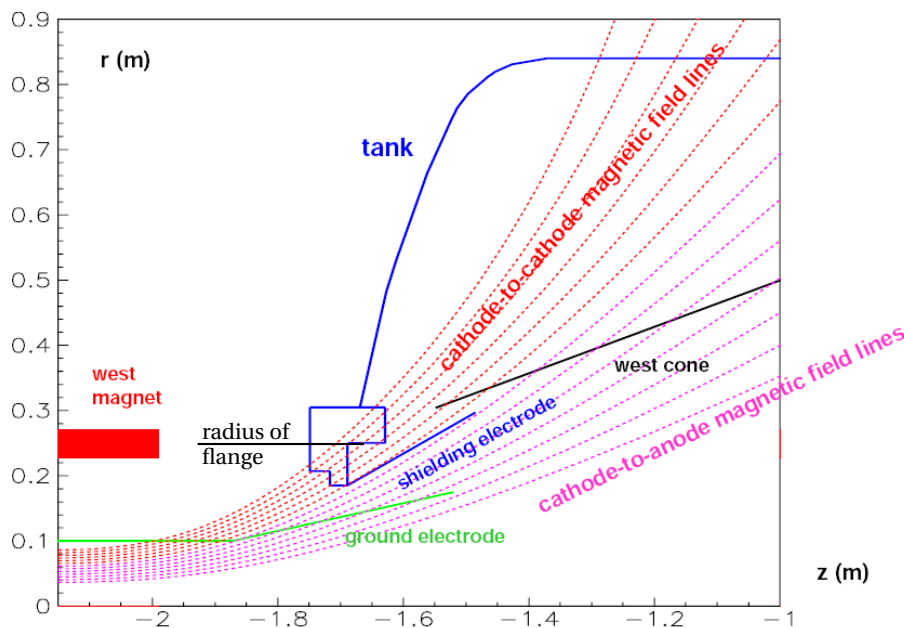


**Figure 5.13:** Shielding electrode with diameter exceeding the dimensions of the  $\varnothing 500$  mm flange (figure by F. Glück).

- b) The size of the additional shielding electrode does not exceed the dimensions of the flange. In this case, sufficient suppression of the Penning trap can only be obtained by simultaneously shortening the ground electrode in order to withdraw it a little further from the inner volume. This reduces the influence of the ground potential which is the cause for the Penning trap being created in the high potential region nearby. The drawback of this solution is that the shortened ground electrode leads to an earlier onset of the electrostatic retardation of electrons entering from the source side, and thus negatively influences the transmission properties (see detailed discussion in the following sections).

Due to technical constraints, the shielding electrode can only be supplied with a potential equal to that of the vessel electrode. The mounting mechanism does not provide the possibility to include an additional insulator.

Those configurations comprising a conical shielding electrode with a diameter exceeding the size of the  $\varnothing 500$  mm flange will not be described here. The risk of damaging sensitive parts of the existing inner electrode system during the mounting of the additional electrode was a strong ar-

gument for discarding the solution described in a). Instead, this section is focused on a setup including only structures that can be mounted directly via access through the  $\varnothing 500$  mm flange in one piece, accepting the necessity to replace the existing titanium ground cones. The new ground cones could be made out of stainless steel (which will also be much easier to work) to save considerable costs and construction time.<sup>15</sup>

### 5.2.3 Operational modes of the KATRIN pre-spectrometer

While simulations show that an additional correction electrode on vessel potential is suitable to essentially remove the Penning trap problem, they also indicate that the combination of an additional retarding electrode and a shortened ground electrode exacerbates the problem of too early retardation already existing in the previous configuration of the pre-spectrometer. One possibility to solve this problem is to set the solid-metal cones to a more positive potential. However, this in turn deepens the remaining Penning trap. In order to better understand this connection between the potential of the solid-metal cones and the depth of the Penning trap on one side and the transmission properties on the other side it is instructive to inspect the transmission properties of the pre-spectrometer in more detail.

#### General remarks on transmission properties of the pre-spectrometer

For electrons entering the pre-spectrometer on some outer magnetic field lines with very large angles the longitudinal component of the kinetic energy can become minimal at a position well before reaching the analysing plane of the pre-spectrometer. This problem has been known since 2004 and a cure was provided in the form of a separate high-voltage supply to set the solid conical parts of the inner electrode to a more positive potential than the tank and wires. Figure 5.14 shows the change in longitudinal energy for a voltage difference of  $U_{\text{solid cones}} - U_{\text{vessel}} = 500$  V. Figure 5.15 presents the influence of this voltage difference on the potential along the magnetic field lines. A secondary, more shallow but broader trap in the central volume of the spectrometer is visible.

In case it turns out later that such a shallow trap still causes a measurable increase of background, the option of connecting cones and tank to equal potential can be chosen. However, caution is due: in the standard configuration of the two MAC-E filters, the pre-spectrometer is set to a filter energy some  $\approx 200$  eV below the tritium endpoint. Thus, an early retardation on the scale visible in figure 5.14 may influence the measurements if it turned out to result in a significant broadening of the pre-spectrometer transmission function. For example, if the early retardation caused a deterioration of the energy resolution of the pre-spectrometer from its nominal value  $\Delta E_{\text{pre-spec}} \approx 85$  eV to a value in the range of 150 eV, a larger difference of the retardation potentials of the pre- and main spectrometer would have to be chosen in order to let a sufficient high-energy part of the tritium  $\beta$ -spectrum pass on to the main energy filter without any distortion. Therefore,

---

<sup>15</sup>The use of titanium was originally motivated by the aim of suppressing a minor source of background known from the former Mainz spectrometer: Some background was caused by X-ray photons which are produced by electrons hitting the ground electrode (anode). Subsequently emitted secondary photo- or Auger electrons from the central electrode can reach the detector with energies in the range of or above the expected tritium electron energies. This has been observed in the Mainz experiment in the form of a so-called "trans- $U_0$  peak". Reducing the X-ray energies by installing a ground electrode made of a lower  $Z$  material (*e.g.*, titanium) as compared to that of the central electrode would prohibit the emission of K-shell electrons and thus decrease the number and energy of secondary electrons which are liberated from the central electrode and may find their way to the detector. However, it was argued that the suppression of a minor background component at the pre-spectrometer is of less importance compared to the huge problems caused by the Penning trap.

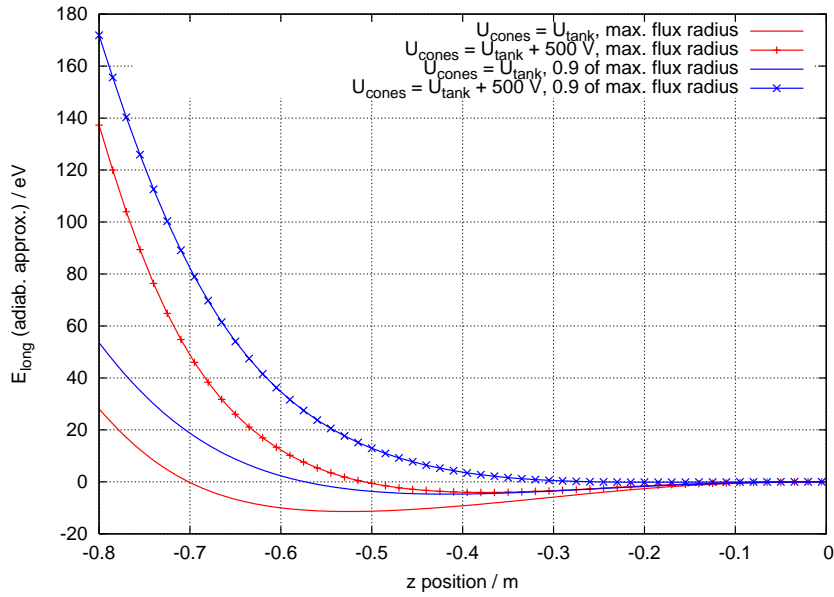


**Figure 5.14:** Longitudinal kinetic energy (in adiabatic approximation) for electrons with maximal admitted starting angle at the border of the flux tube (red) and at 0.9 of the outer flux tube (blue). By applying a more positive potential to the solid cones the early retardation problem can be reduced. – This calculation refers to the original setup of the pre-spectrometer ( $60^\circ$  maximum accepted starting angle).

it is necessary to check to which scale the inclusion of additional shielding electrodes enhances this negative effect on the transmission properties during the design studies of such electrodes.

### Relevance of background and transmission properties for various types of measurement

Before discussing the results of the design studies for the modified electrode setup, it is helpful to consider a list of various measurement modes of the pre-spectrometer and to outline the corresponding roles of background levels and transmission properties.

- (A) The pre-spectrometer will be used as a rather coarse energy pre-filter during normal operation for the neutrino mass measurement phases. The standard field configuration is slightly different from that in the present “stand-alone” test operation since the magnetic fields will change due to the stray fields from the large number of magnets of the full KATRIN setup.

As mentioned above, transmission characteristics are not a sensitive issue in the standard mode of operation, provided that the difference of the retardation potentials  $|U_{\text{pre-spec}} - U_{\text{main spec}}|$  is large enough to prevent a potential deterioration of the energy resolution of the pre-spectrometer due to the early retardation effect from affecting the analyzing interval of the main spectrometer. On the other hand, background caused by residual Penning traps (with depths of a few 100V) could be of concern if trapped particles were to introduce increased background rates also into the main spectrometer.

Hence, for this kind of measurement one would prefer to have the cone potential more negative than that of the vessel, so as to avoid the formation of large Penning traps in the central part of the pre-spectrometer (compare figure 5.15).

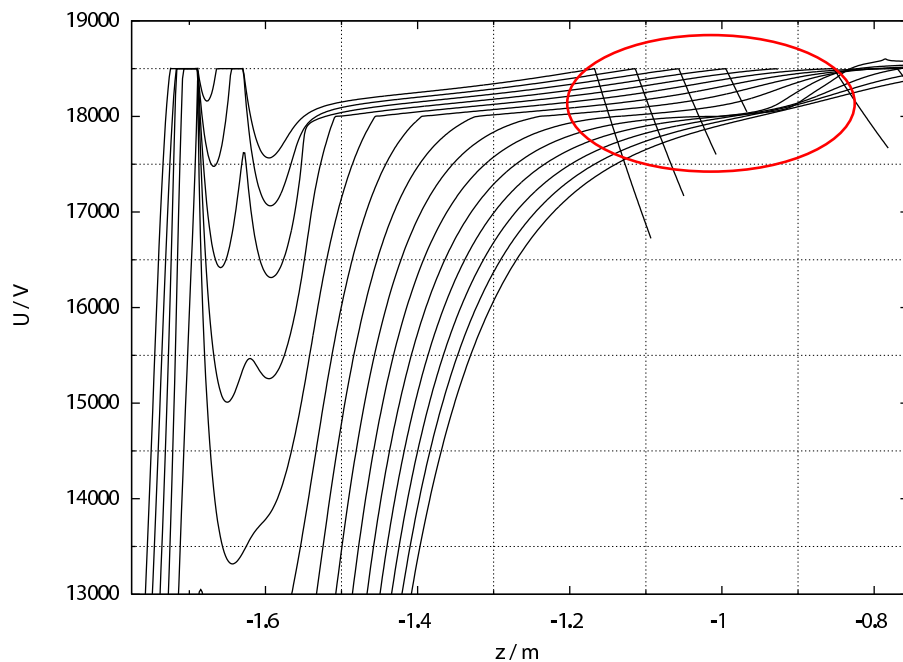


**Figure 5.15:** Electric potential along magnetic field lines for the original pre-spectrometer setup. Here, the cones are supplied with a 500 V more positive potential than the vessel:  $U_{\text{solid cones}} = -18.0$  kV,  $U_{\text{vessel}} = -18.5$  kV,  $U_{\text{wire grid}} = -18.6$  kV. The depth of the Penning trap near the ground electrode is left mainly unchanged, while a small "dip" at the transition between the cones and central wire grid appears around  $z \approx -1$  m. Again, the sudden drop of the potential in the upper right corner is caused by field lines penetrating the vessel wall.

- (A\*) This mode is similar to mode (A), but it will be used under test conditions. Therefore, the magnetic stray fields from the other magnets of the KATRIN setup are missing, and the magnetic flux is solely defined by the two pre-spectrometer magnets. This causes the spacing between the nominal magnetic flux of  $191 \text{ Tcm}^2$  and the ground electrode to change by a small amount. Furthermore, this configuration does not include a pinch magnet, and consequently electrons must be transmitted with angles up to  $\theta_{\text{solenoid}} = 90^\circ$  in the pre-spectrometer magnets.
- (B) This mode is similar to the standard mode (A) within the full KATRIN setup, yet here the transmission properties of the pre-spectrometer are optimized by putting the solid-metal cones to a more positive potential. This setting of the potentials is only allowed if the slightly deeper Penning trap does not influence the background rate.
- (B\*) Same as mode (B), but under test conditions (*i. e.*, using the two pre-spectrometer magnets only).

#### 5.2.4 Proposal for an additional pair of electrodes

Following detailed simulations, a proposal was worked out to modify the pre-spectrometer setup by adding conical electrodes in the end cap regions while at the same time shortening the ground cones by about 80 mm. As can be seen from figure 5.16 and 5.17, the additional electrodes have a diameter slightly smaller than 500 mm and extend about 250 mm along the  $z$  axis from the flange into the spectrometer. The dimensions have been chosen such that both ground and additional

electrode allow to transport the KATRIN reference flux with a reasonable safety margin (see table 5.1).

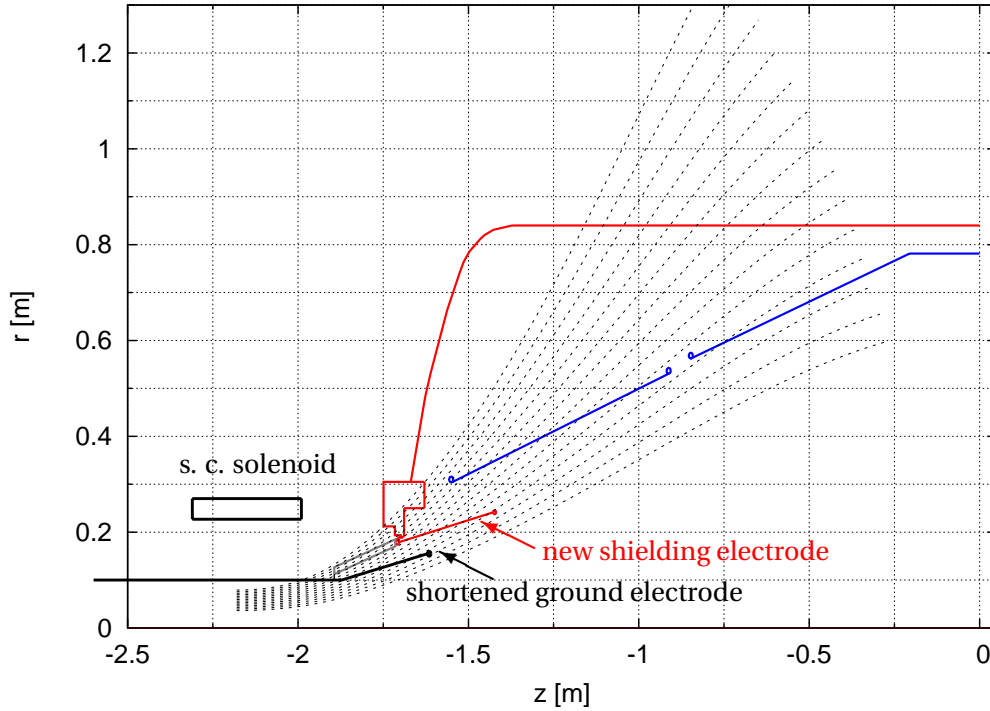


**Figure 5.16:** Modified pre-spectrometer electrode configuration with shortened ground electrode and additional screening electrode to remove the Penning trap in the entrance region. The grey lines indicate the position of the ceramics insulator. Note that in the “stand-alone” configuration the centers of the two solenoids are 4.30m apart. A close-up of the parts surrounding the ground electrode is shown in figure 5.17. For a detailed technical drawing see appendix B.1.

The effect of the additional electrode on the depth of the Penning trap is shown in figure 5.18. If all high-voltage electrodes are supplied with equal potential, the remaining trap is 210V deep. This value is small compared to the original setup without any shielding ( $\Delta U \approx 5.2\text{kV}$ , compare figure 5.12(b)). It is important to emphasize that the depth of the residual trap can be directly influenced via the potential of the cone electrodes and can even be removed completely by choosing a more negative potential for the cones (see details below).

**Table 5.1:** Distance in radial direction between ground electrode and  $191\text{Tcm}^2$  flux. Separate margin values for the source side and main spectrometer side are given. In the case of a symmetric setup with pre-spectrometer magnets only, both margins are of course equal. These numbers represent an estimate with some uncertainty due to the difference between simulated/nominal and actual magnetic field produced by the solenoids.

	PS magnets + CPS stray fields (“KATRIN beam line” setup, A & B)	PS magnets only (“stand-alone” setup, A* & B*)
margin source side	19.3 mm	26.4 mm
margin MS side	17.4 mm	26.4 mm

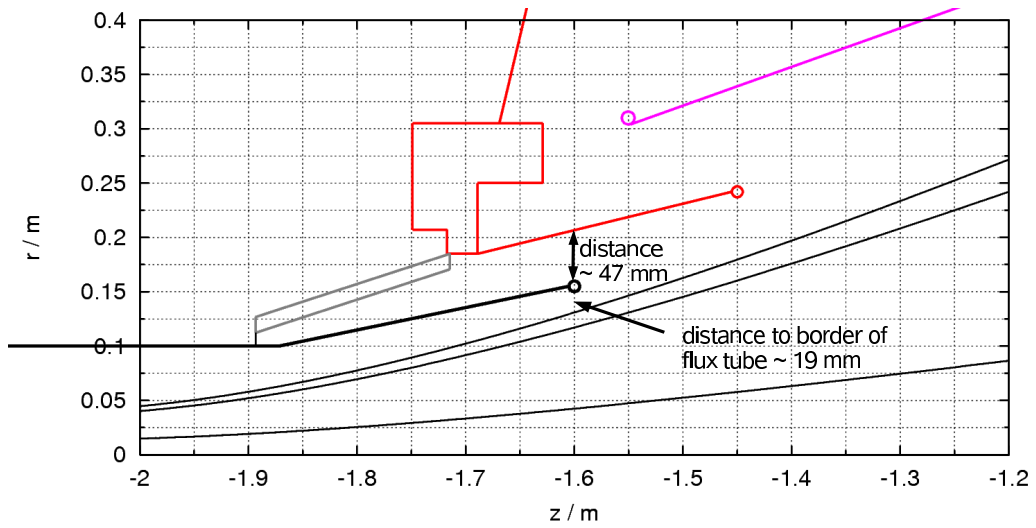


**Figure 5.17:** Close-up on the ground electrode region showing electron trajectories along field lines at  $\{0.33, 0.9, 1.0\} \times \text{max. flux radius}$ . Due to stray fields from the CPS section, the distance between flux tube border and ground electrode is a slightly different one on the source side ( $\approx 19.3 \text{ mm}$ ) as compared to the main spectrometer side ( $\approx 17.4 \text{ mm}$ , not shown here). Round parts ( $\varnothing 10 \text{ mm}$ ) are implemented at the end of ground and shielding electrodes to avoid field emission.

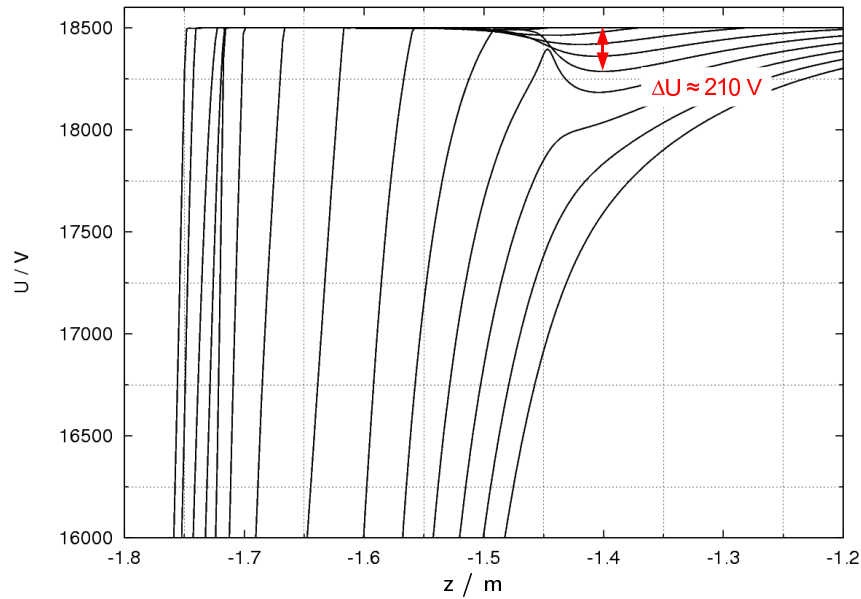


**Figure 5.18:** Electric potential along magnetic field lines for  $U_{\text{vessel}} = U_{\text{solid cones}} = U_{\text{wire grid}} = -18.5 \text{ kV}$ . A small Penning trap of depth  $\Delta U \approx 210 \text{ eV}$  remains.

### Neutrino mass measurement mode with complete avoidance of the Penning trap inside the pre-spectrometer (A)

In case it turns out to be necessary to remove even the shallow Penning trap remaining after installation of the additional electrode (figure 5.18) one can for example choose  $U_{\text{solid cones}} = -18.3 \text{ kV} = U_{\text{vessel}} - 400 \text{ V}$  and  $U_{\text{wire grid}} = -18.4 \text{ kV}$ . With a 400V more negative potential on the solid-metal cones as compared to the vessel potential, the modified setup allows to remove the Penning trap completely (figure 5.19(a)) without interfering with the transmission requirements

for normal neutrino mass measurements. Figure 5.19(b) presents the longitudinal energy of electrons started at the center of the pre-spectrometer solenoid with an angle of  $\theta_{\text{start}} = 60^\circ$  and an surplus energy of  $E_{\text{kin, ana}} = 200 \text{ eV}$ . Several starting radii corresponding to 0%, 30%, 90% and 100% of the maximum transported flux radius are shown.

### Test measurements with complete avoidance of the Penning trap inside the pre-spectrometer (A\*)

Unfortunately the neutrino mass measurement configuration (A) cannot be tested right after installing the proposed correction electrode since the full KATRIN magnet configuration is not yet available. The only way to test whether the discharges disappear by virtue of the shielding effect of the new electrodes is to use the configuration (A\*) with the two pre-spectrometer solenoids. Since the stray fields from the other magnets have no visible effect on the simulated potential along magnetic field lines and on the longitudinal kinetic energy, the graphs corresponding to those in figure 5.19 are not presented here.

### Test measurements (B\*) and neutrino mass measurements (B) with optimized transmission conditions

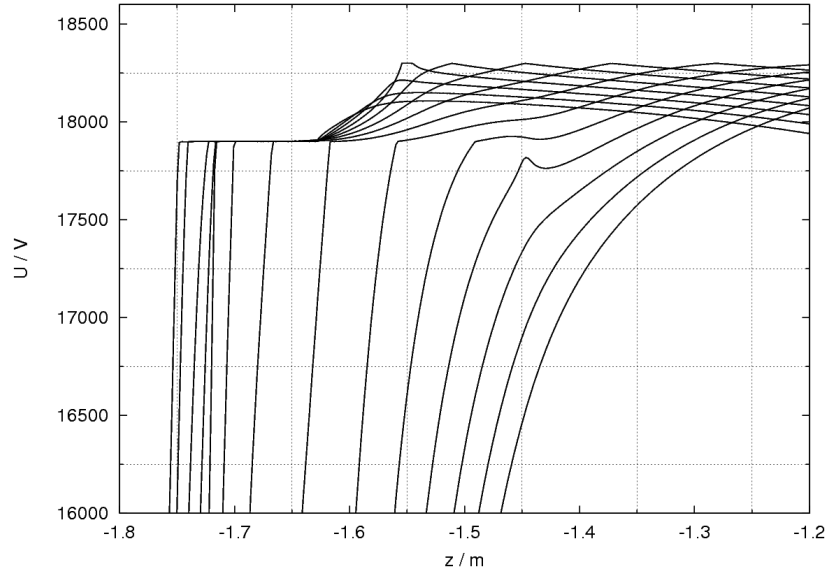
If measurements at the pre-spectrometer should confirm that a shallow residual Penning trap does not cause background, the neutrino mass measurements could be performed with the pre-spectrometer setting (B), which has less “too early retardation problems”, instead of using the more conservative configuration (A) of the electric potentials. Therefore, it is interesting to find out at which voltage setting of the solid-metal cone relative to the vessel the background induced by the Penning trap is starting to play a role. These investigations should be carried out already with the present pre-spectrometer setup (*i. e.*, only two solenoids). In the extreme case it might even be possible to avoid the problem of too early retardation completely. According to figure 5.20 (a), which shows the electric potential along the magnetic field lines for the mode (B\*), in this scenario a residual (secondary) Penning trap of 750V depth in the central part of the pre-spectrometer remains. This extreme case with optimized transmission properties will be achieved by choosing for example  $U_{\text{vessel}} = -18.5 \text{ kV}$ ,  $U_{\text{solid cones}} = -17.5 \text{ kV} = U_{\text{vessel}} + 1 \text{ kV}$  and  $U_{\text{wire grid}} = -18.5 \text{ kV}$ . For the simulation presented in figure 5.20 (b), electrons were started at the center of the pre-spectrometer solenoid with maximum starting angle and minimum surplus energy.<sup>16</sup>

Table 5.2 summarizes the findings of the simulations regarding the achievable residual trap depth for the different operational modes of the pre-spectrometer.

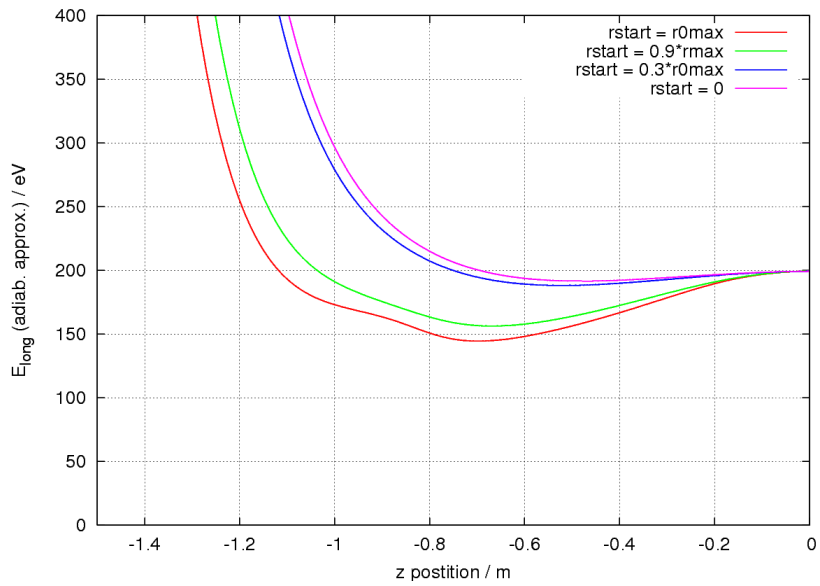
**Table 5.2:** Effectiveness of Penning trap removal for the modified electrode configuration in various simulated operational modes of the pre-spectrometer.

	$\nu$ mass meas. (A)	optimized transm. (B)	other tests
residual depth of Penning trap	0V	$\approx 750 \text{ V}$	$\approx 210 \text{ V}$
see figure	5.19	5.20	5.18

<sup>16</sup>Again, the simulation results for the operational mode (B) are very similar to that for (B\*) and hence are not shown here.

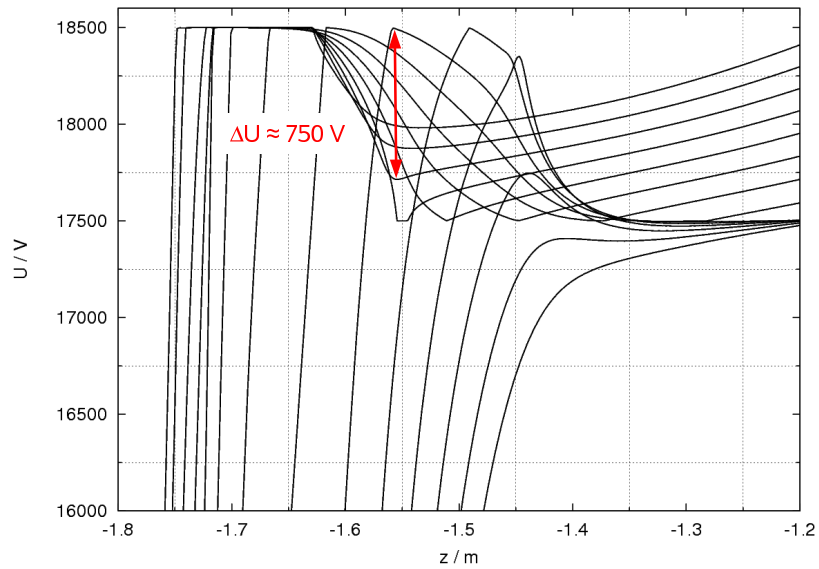


(a) electric potential along magnetic field lines

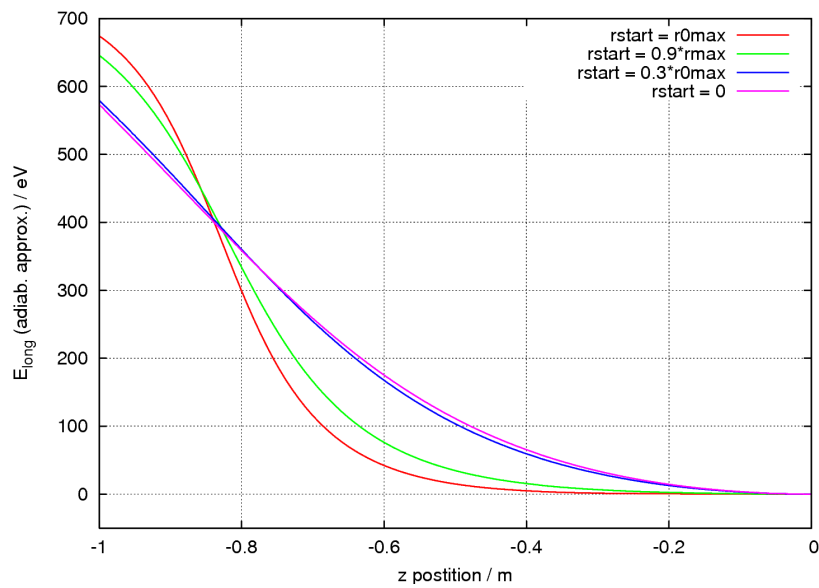


(b)  $E_{\parallel}$  calculated in adiabatic approximation

**Figure 5.19:** Electric potential along magnetic field lines and development of longitudinal kinetic energy of electrons for the “neutrino mass measurement mode” (A) of the pre-spectrometer.



(a) electric potential along magnetic field lines


 (b)  $E_{\parallel}$  calculated in adiabatic approximation

**Figure 5.20:** Electric potential along magnetic field lines and development of longitudinal kinetic energy of electrons for the “optimized transmission mode” (B) of the pre-spectrometer. (The field lines exhibiting a potential of exactly  $U = -17500\text{V}$  are irrelevant for the determination of the depth of the Penning trap since they first cross the solid cone electrodes and then penetrate the vacuum vessel.)

### 5.2.5 Electric field strength: original versus modified setup

Apart from the discharges due to the Penning trap, the original setup of the pre-spectrometer also exhibited some field emission problems that persisted even without magnetic fields. There are experimental clues that high electric field strengths at the flange region in combination with less carefully treated surfaces of some electrode parts in this area (foremostly welding seams) were the origin of these problems.

Since the additional electrode is attached to the flange its geometry can easily be conceived in such a way that it also covers the dangerous high-field region inside the flange (see figure 5.21). Of course, the end of the additional electrode should be equipped with a ring to keep the field strength as low as possible. It is evident that, in view of the overall high field strengths in the flange and ground electrode region, stringent requirements for the surface properties of the new parts need to be placed.

Table 5.3 as well as figures 5.22 and 5.23 give an overview of the calculated field strengths for the previous and the modified setup.

The electric field strength at the cathodes in the new design is about as large as in the previous design. Here, one could possibly benefit from using the additional electrode to cover parts of supposedly lower surface quality with new parts of very high surface quality. The margin for reducing the field strength at the cathode by increasing the diameter of the rounded part facing the insulator is very small due to the limited space inside the flange. A larger piece would leave only a very small spacing to the ground electrode and thus lead to an increase in field strength instead of a decrease.

The field strength at the anode is calculated to be 2.5 times higher with the new additional electrode than in the original configuration. Generally, high field strengths at the anode are expected to be less dangerous (*i. e.*, supposed to cause less discharges) than comparably high field strengths at cathodes because field emission of electrons will occur at cathode surfaces. It appears to be impossible to significantly decrease the field strength without cutting back on other important properties of the new setup.

**Table 5.3:** Electric field strength  $E$  in the original and in the modified setup (compare figures 5.22 and 5.23).

$r$ position [m]	$z$ position [m]	denotation	size of rounded tip	$E$ [kV/m]
<b>original setup</b>				
$\approx 0.203$	$\approx -1.530$	ground electr. (anode)	$\approx 30$ mm	530
$\approx 0.190$	$\approx -1.695$	corner of flange (cathode)	$\varnothing 0.6$ mm	1100
<b>modified setup</b>				
$\approx 0.155$	$\approx -1.610$	upper part of ground electr. tip (anode)	$\varnothing 6$ mm	1620
			$\varnothing 10$ mm	1350
			$\varnothing 20$ mm	1130
			$\varnothing 30$ mm	1120
$\approx 0.174$	$\approx -1.708$	lower part of ring-shaped tip of add. shielding (cathode) close to insulator	$\varnothing 4$ mm	990
			$\varnothing 6$ mm	970
			$\varnothing 10$ mm	1000
			$\varnothing 20$ mm	1000

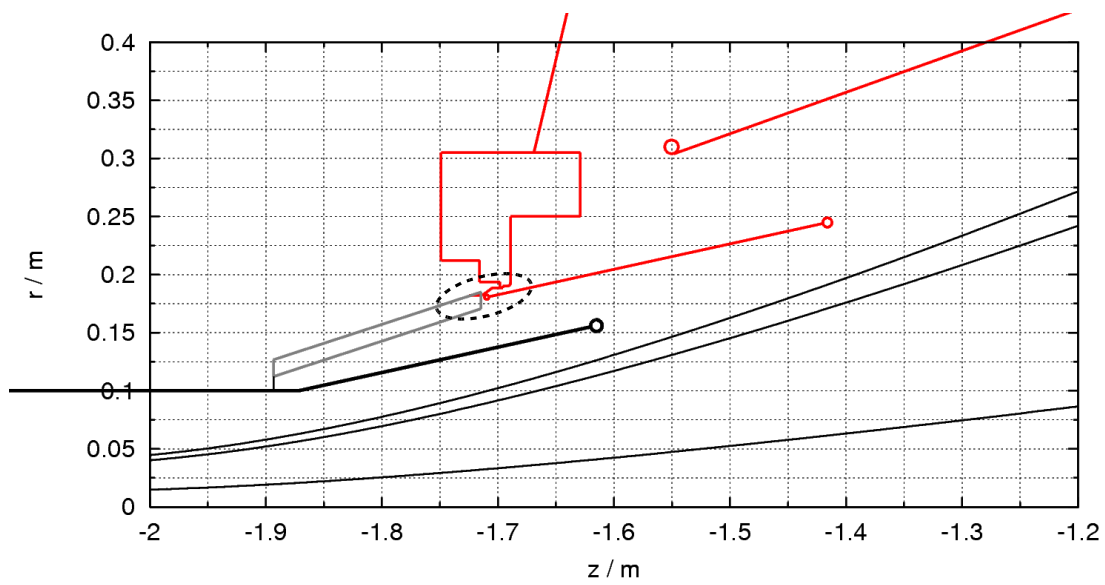


**Figure 5.21:** Modified setup with the shielding electrode now also covering the inner side of the flange next to the ceramic insulator.

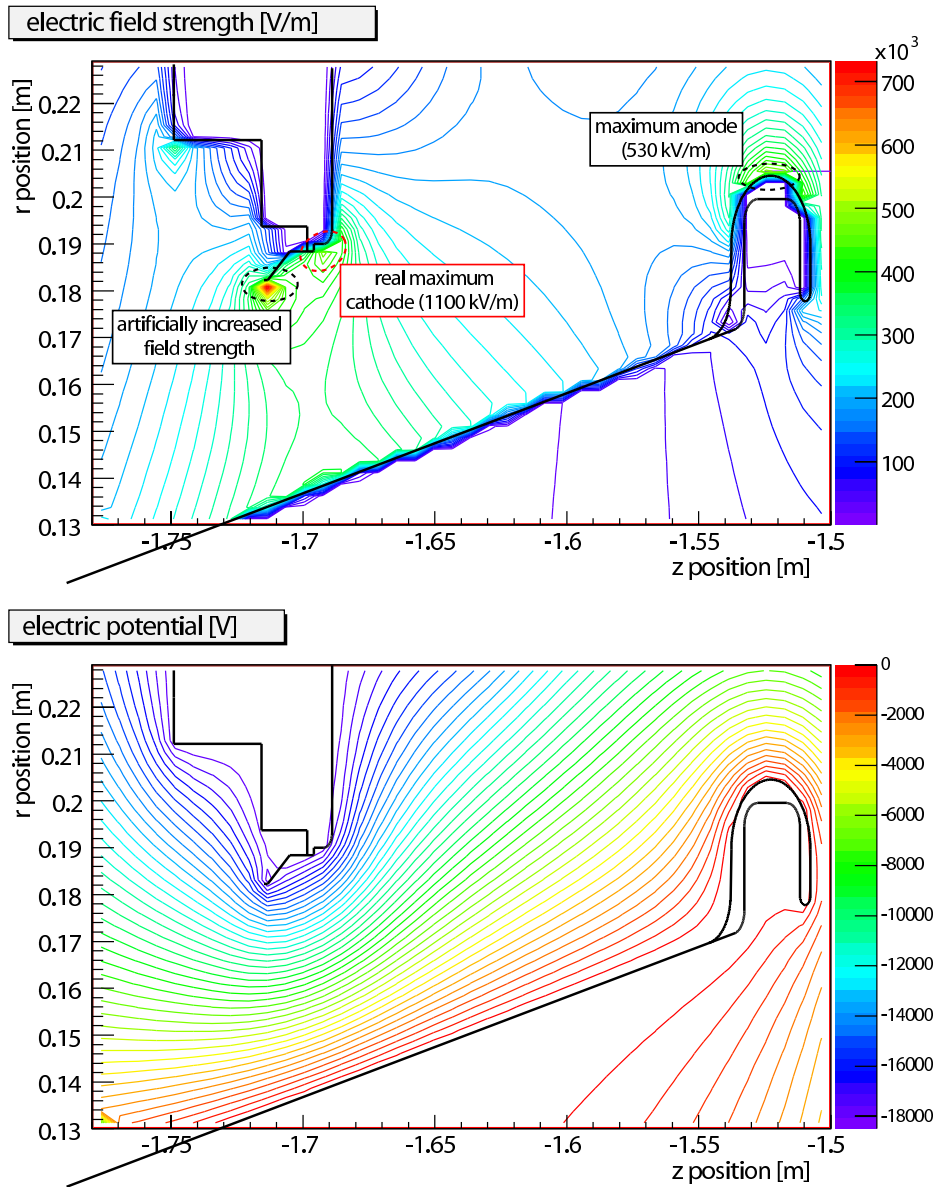


**Figure 5.22:** Map of electric field strength  $E$  (upper panel) and equipotential lines (lower panel) in the ground electrode and flange region of the original pre-spectrometer setup. The highest value at  $z \approx -1.71$  m,  $r \approx 0.18$  m is an artificial one since the electrode just ends in the simulation (in reality, it is shielded by the ceramic insulator which is not shown here, and the curvature radius is larger). In fact, the accuracy of the absolute values for  $E$  given in the plot is limited by the grid spacing used for the field scan (in this case,  $\Delta z = \Delta r = 1$  mm).

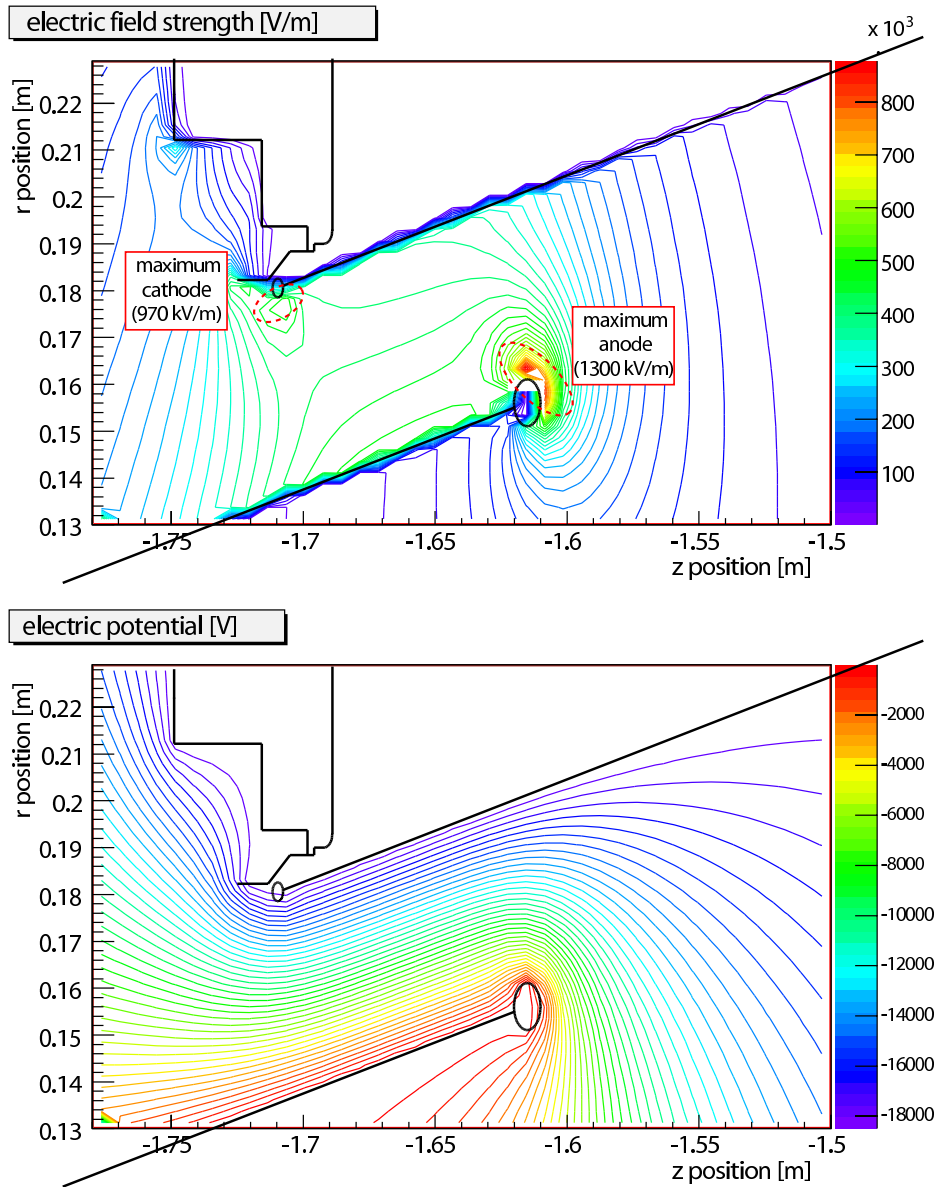


**Figure 5.23:** Map of electric field strength  $E$  (upper panel) and equipotential lines (lower panel) in the ground cone and flange region of the modified pre-spectrometer setup. The accuracy of the absolute values for  $E$  given in the plot is limited by the grid spacing used for the field scan (in this case,  $\Delta z = \Delta r = 1$  mm).

### 5.2.6 Behavior of the system after installation of the new electrodes

The design studies for the modified electrode system were finalized in March 2007 [Glü07b], and the construction of the four new pieces (two ground cones and two shielding electrodes, according to figure 5.21) was finished in that summer. Figure 5.24 shows photographs of the finished parts of the modified electrode setup before they were mounted inside the pre-spectrometer in September 2007. After the installation of the shielding electrodes, the strong discharge phenomena characterized by the increase of leakage current and pressure were no longer present. Therefore, it seems that these discharges were indeed related to the deep Penning trap that was previously present inside the pre-spectrometer and was effectively removed by the new electrode configuration. Background investigations using the Si-PIN detector could subsequently be started and are still ongoing. After the removal of the dominating discharges, other problems became visible. A strong background component is particularly puzzling, since it appears at high magnetic field (therefore, it was termed “high B-field background”) a certain time after the electric potential is elevated from zero to a few kV (see [Fra09, Hab09]). The origin of this background contribution is still unclear. It is suspected to be related to the electron traps confined on one side by the electrostatic potential of the analyzing plane and on the other side by the magnetic mirror, which are shown in figure 5.11, or to a small Penning trap at the ground electrode which was recently discovered in simulations by F. Fränkle (Forschungszentrum Karlsruhe). Although this background would not be visible directly at the KATRIN final plane detector because the pre-spectrometer is placed at a more positive potential with respect to the main spectrometer, it can still be harmful since it provides a feeding mechanism for the trap between the two spectrometers (cp. section 5.4).



(a) new ground electrode



(b) shielding electrode mounted on flange (with ceramics insulator)

**Figure 5.24:** Photographs showing the newly manufactured parts of the modified electrode system of the pre-spectrometer. All solid electrodes now consist of stainless steel (the previously used ground electrode was made of titanium).

### 5.3 The Penning trap inside the main spectrometer

The problem of increased background rates related to Penning discharges which was encountered at the pre-spectrometer revealed a sensitive issue to be considered also for the final design of the inner electrode system of the main spectrometer. Due to the similarities in the electromagnetic design of the two MAC-E filters the lessons learned from the smaller pre-spectrometer can mostly be transferred in a straightforward way to the huge main spectrometer. Indeed, computer simulations [Hug08] showed that the cone regions at both ends of the main spectrometer host deep Penning traps with  $\Delta U \approx 4.7\text{kV}$ . In view of the positive effect achieved at the pre-spectrometer through the installation of shielding electrodes, the KATRIN collaboration therefore decided to equip the main spectrometer entrance and exit regions with a similar pair of “anti Penning trap electrodes”. Extensive design studies analogous to those described in section 5.2 were carried out by K. Hugenberg and M. Zacher [Hug08, Zac09].

The design of the shielding electrode is strongly coupled to that of the ground electrode and that of the wire electrode modules in the steep cone (rings 02/16 in particular, to some extent also rings 03/15, compare fig. 4.25). An additional complication stems from the slightly asymmetric shape of the flux tube caused by the strong compensation fields of the air coils at the end of the main spectrometer facing the pinch magnet.<sup>17</sup> Since both  $B_{\text{det}} = 3.5\text{T}$  and  $B_{\text{det}} = 6\text{T}$  are still viable options for the magnetic field strength inside the detector solenoid, all calculations have to be done for these two configurations of the solenoid and air coil magnetic fields.

Figure 5.25 presents a preliminary technical concept prepared by S. Lichter (Forschungszentrum Karlsruhe), based on the outcome of the electromagnetic design studies [Zac08]. The results indicate that the most efficient suppression of the Penning trap is obtained with a large shielding electrode, which can only be mounted (or removed) through the  $\varnothing 500\text{mm}$  flange in several parts.

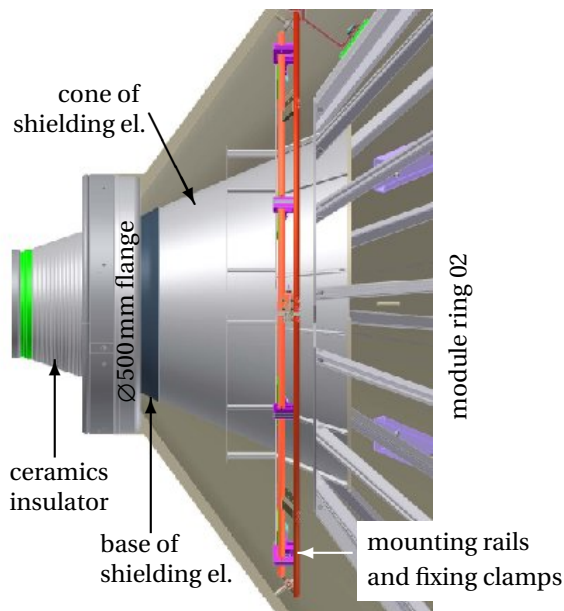


**Figure 5.25:** Preliminary design of the “anti Penning trap electrode” for the main spectrometer (picture taken from [Lic08]). The concept is similar to the shielding electrode already installed at the pre-spectrometer. However, the “anti Penning trap electrode” for the main spectrometer has considerably larger dimensions which pose a challenge regarding manufacturing and installation. In particular, its size in radial direction exceeds that of the  $\varnothing 500\text{mm}$  flange opening, which implies the necessity to construct and mount it in several pieces. The cone of the ground electrode is not visible in this drawing, as it is placed inside the cone of the shielding electrode.

<sup>17</sup>The ampere-turn values of the air coils are not mirror-symmetric with respect to the analyzing plane because of the need to compensate for the difference in the stray fields from neighboring solenoids at both sides of the main spectrometer. The exit side is strongly influenced by the magnetic fringe fields of the pinch and detector magnets.

## 5.4 The Penning trap between pre- and main spectrometer

Apart from introducing the characteristics of the Penning-like trap located between the KATRIN pre- and main spectrometer, this section essentially reviews the results obtained within the diploma thesis of K. Essig [Ess04]. In it, computer simulations were carried out in order to evaluate the possibility for such a large trapping region to start a potentially dangerous avalanche of ionization processes. This discussion forms the motivation for the experimental work described in the following chapter 6.

### 5.4.1 Trapping mechanisms and relevance for background concerns

The fact that a two-spectrometer combination gives rise to a deep trap for negatively charged particles has been realized already at an early stage of the design phase of the KATRIN experiment. Therefore, dedicated studies concerning the potential effects on the background rate (*i. e.*, the number of secondary electrons stemming from ionization processes that can reach the final plane detector) were launched and provisions were taken with the aim of preventing any detrimental effects on the neutrino mass measurement.

The trapping volume for negatively charged particles is defined in axial direction by the two negative potential barriers of the spectrometers and in radial direction by the strong magnetic field, as indicated in figure 5.26. The configuration is similar to the cylindrical Penning trap shown in figure 5.5(b), although details of the electromagnetic field geometry are slightly different.<sup>18</sup> The trajectory of a trapped electron, which performs many reflection cycles between the two spectrometers, is indicated in the figure as an example. Since trapping increases the path length of the electron by many orders of magnitude, the probability that the electron undergoes ionizing collisions with residual gas molecules rises accordingly. Both the secondary electrons and the positive ions emerging from these primary collisions have to be considered:

- The secondary electrons produced inside the trap can also remain trapped themselves. This is dangerous because
  - a) they are a source of more electrons and ions, and
  - b) they can contribute to the build-up of a significant space charge which might affect the measurements in a negative way.
- The positive ions (essentially  $H^+$  and  $H_2^+$ ) created in primary collisions inside the trap can be harmful in two ways:
  - a) Due to their positive electric charge, they can get accelerated into the main spectrometer and lead to ionization processes in the inner volume. Following [Ess04], the reaction probability  $P$  for ionizing collisions inside the main spectrometer can be estimated to be of the order of

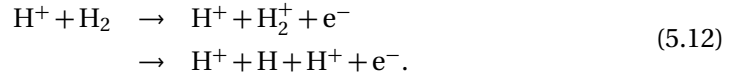
$$\begin{aligned} P &= l \cdot \sigma \cdot N \\ &\approx 1 \cdot 10^{-7}, \end{aligned} \tag{5.11}$$

where  $l \approx 2400$  cm denotes the total length of the main spectrometer,  $N \approx 3 \cdot 10^5$  cm<sup>-3</sup> is the particle number density at a residual gas pressure of  $p = 10^{-11}$  mbar and  $\sigma \approx 2 \cdot 10^{-16}$  cm<sup>2</sup> (taken from [Tab00]) gives the cross section for an ionizing reaction of the

---

<sup>18</sup>For example, an inhomogeneous instead of homogeneous magnetic field is present, and only parts of the electrode setup are cylindrical.

type



Electrons born in reactions like (5.12) may be magnetically guided and electrostatically accelerated towards the detector and registered as a significant background component.

- b) Since the positive ions are poorly confined by the magnetic field (particularly in the weak-field regions inside the main spectrometer volume), they can escape from the central magnetic flux tube and hit the electrode surfaces with considerable energy.<sup>19</sup> Upon impact, they can cause the emission of one or more electrons, with the multiplicity of the secondaries depending on the kinetic energy of the ion (compare the description of the Townsend effect in section 5.1.1, in particular eq. (5.2)). These electrons liberated from the electrodes have a small chance of reaching the sensitive flux tube via a radial drift or a multi-step process (see the discussion on backgrounds from the electrodes in chapter 3). Thus, they can also contribute to the background seen at the detector.

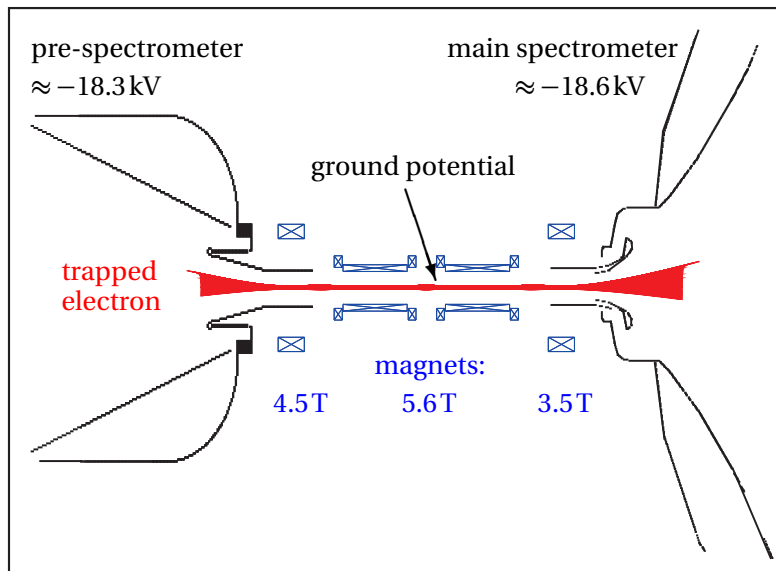


**Figure 5.26:** Trapping region at the junction of pre- and main spectrometer as of 2004 (taken from [Ess04]). The electrode systems of both spectrometers are drawn in black, whereas the magnet system – two transport magnets and two coils assigned to the pre- and main spectrometer, respectively – are shown in blue color. The red lines represent the trajectory of a stored electron inside the trapping region. The geometry of the trap resembles that of the cylindrical Penning trap (figure 5.5(b)) rather than that of the hyperbolic version (figure 5.5(a)).

The conditions for the development and length of the ionization chain depend on the initial potential energy at the location of the primary ionization and on the efficiency of energy loss processes of the trapped electrons, which will be discussed in the following paragraph.

<sup>19</sup>Ions originating from the region close to the ground electrode can gain energies up to 18.6 keV since they feel the full potential difference.

### Cooling processes

The two most relevant cooling mechanisms for electrons in the trap are the emission of synchrotron radiation and collisions with gas molecules. They lead to a significant and – as shown in [Ess04] – fast reduction of the number of secondary ionization processes by high-energy electrons. The cooling processes shall be briefly discussed in the following.

- Synchrotron radiation can in principle be generated from any of the three superimposed types of motion<sup>20</sup> performed by an electron in a Penning trap (see figure 5.7). The energy loss caused by synchrotron radiation from the cyclotron component of the motion by far dominates the losses due to the remaining two components<sup>21</sup>, the magnetron drift and harmonic axial oscillation, as was also discussed in [Ess04]. In particular, the power of synchrotron radiation  $P_{\text{synch},\perp}$  from the cyclotron motion is proportional to the square of the magnetic field strength. For a charge  $q$  accelerated on a circular orbit with the frequency  $\omega_{\text{cyc}} = \frac{qB}{\gamma m}$  one can express  $P_{\text{synch},\perp}$  in good approximation [Jac98] by

$$\begin{aligned} \dot{E}_{\text{kin},\perp} &= P_{\text{synch},\perp} = \frac{2}{3} \frac{q^2}{m^2 c^3} \gamma^2 \omega_{\text{cyc}}^2 |\mathbf{p}_{\perp}|^2 \\ &= \frac{2}{3} \frac{q^4}{m^4 c^3} B^2 |\mathbf{p}_{\perp}|^2. \end{aligned} \quad (5.13)$$

The rate of power dissipation can be measured in terms of the damping constant  $\Gamma$ , which is defined as

$$\Gamma = \frac{\dot{E}_{\text{kin},\perp}}{E_{\text{kin},\perp}}, \quad (5.14)$$

leading via eq. (5.13) and  $E_{\text{kin},\perp} = \frac{|\mathbf{p}_{\perp}|^2}{2m}$  to

$$\Gamma = \frac{4}{3} \frac{q^4}{m^3 c^3} B^2. \quad (5.15)$$

Simulations carried out by K. Essig to estimate the time needed by electrons with typical kinetic energies in the 10 keV range to lose all of their initial transversal energy (in the strong magnetic field of 5.6 T in the former transport section, see remarks in sec. 5.4.2) yield values of the order of well below one second (compare figure 5.27).

- Elastic scattering of electrons off residual gas molecules reshuffles part of the kinetic energy back into the transversal component of the motion, thus enabling the electrons to cool more efficiently by restarting the process of synchrotron radiation (see figure 5.27). For technical reasons these calculations were performed assuming a residual gas pressure of  $p = 10^{-10}$  mbar, with the synchrotron radiation increased by the same factor of 10 to preserve the scalability of the results. This means that the cooling time values obtained from the simulations should be increased by a factor of 10 in order to take into account a realistic pressure level of  $p = 10^{-11}$  mbar, as projected for KATRIN.

<sup>20</sup>To be more precise, the radiation caused by the axial motion inside the trap should be termed bremsstrahlung rather than synchrotron radiation, since the reflections of the electron in axial direction are caused by the electric potential barrier rather than by the magnetic field.

<sup>21</sup>The frequency of the magnetron motion is much smaller than that of the cyclotron motion; therefore the synchrotron energy losses from this component can be neglected. For the axial oscillation the radiation power  $P_{\parallel}$  depends on the loss (or gain) rate of longitudinal energy  $E_{\parallel}$  in the axial direction:  $P_{\parallel} \propto (dE_{\parallel}/dz)^2$ . Since in the KATRIN main spectrometer  $dE_{\parallel}/dz$  is rather small, the radiation power is also negligible compared to that from the cyclotron motion.

- Inelastic scattering leads to either excited or ionized gas molecules and thus takes away some of the electron energy. However, the secondary electrons produced in the ionization processes will add to the total number of electrons in the trap and, depending on the value of the electric potential they are born in, can contribute to the chain reaction of ionization.

This chain reaction is stopped when the kinetic energy of the electrons drops below the ionization energy  $E_i$  of the residual gas molecules (*e.g.*,  $E_i = 15.4$  eV for  $H_2$  molecules). Figure 5.28 shows simulation results for the location of ionizing events for 10 electrons started with 10 keV of kinetic energy, half of it in the form of transversal or cyclotron energy. 120 secondaries are produced in total, corresponding to an average secondary yield of 12 per primary particle. Considering that only about one out of ten of these secondary electrons is born in a strong negative electric potential (*i.e.*, with a kinetic energy of a few keV: compare fig. 5.28(b)), this reduces to about 1 high-energy secondary per primary particle on average, which is just on the verge of a self-sustained ionization avalanche.

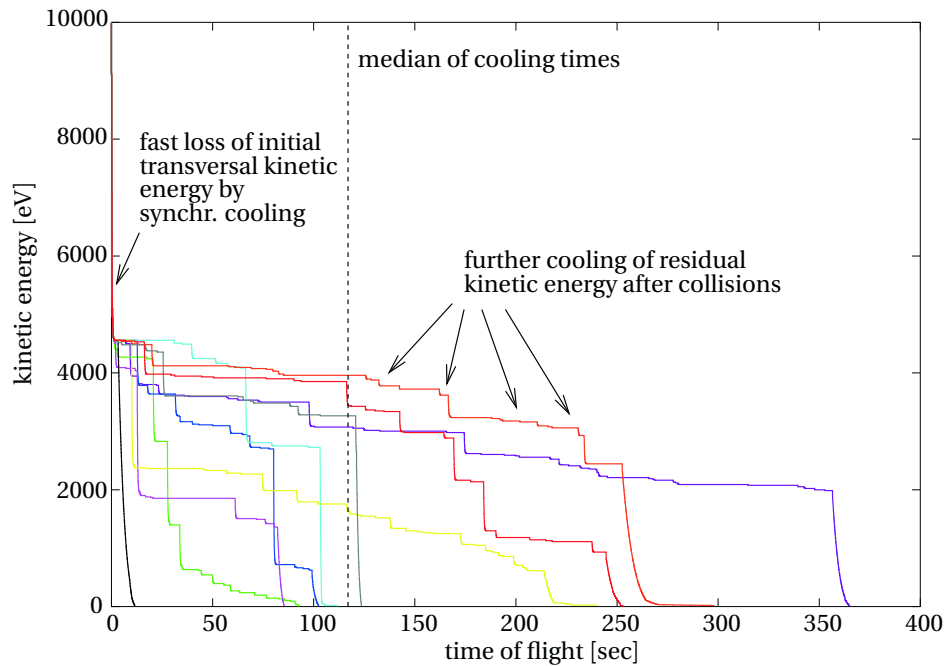
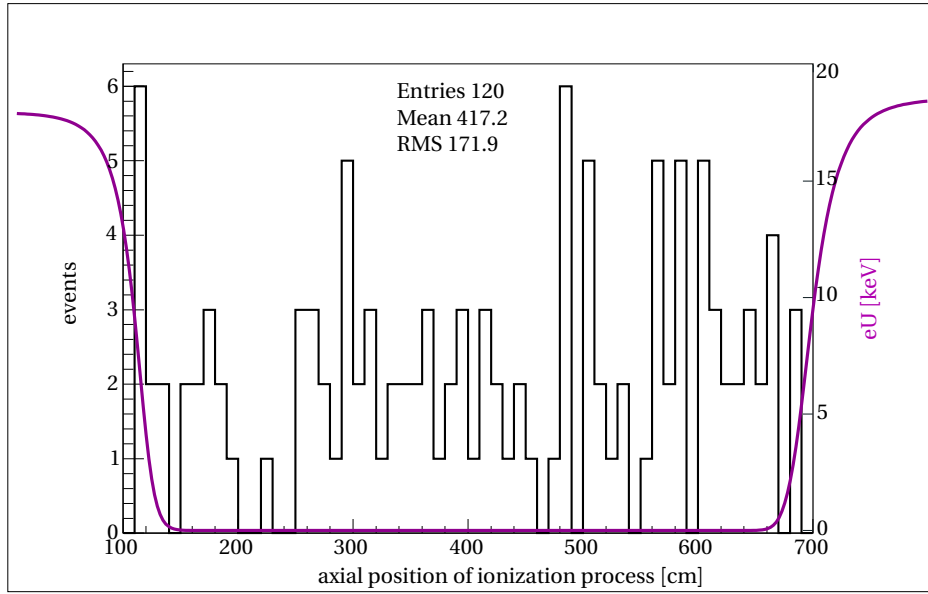
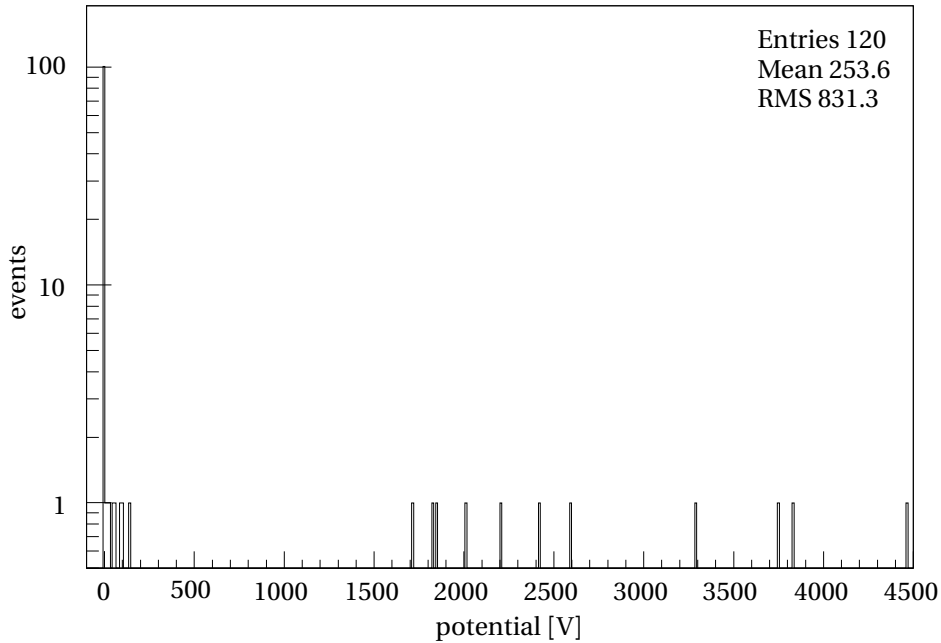


**Figure 5.27:** Simulated cooling times for 10 electrons starting with an initial kinetic energy of  $E_{\text{kin,start}} = 10$  keV and an angle of  $\theta_{\text{start}} = 45^\circ$  in a magnetic field of  $B_{\text{start}} = 4.5$  T (taken from [Ess04]). The median (dashed line) of the cooling time distribution for these conditions is 120 s. At smaller starting angles the total cooling time can be slightly larger, since more collisions are necessary to shuffle longitudinal into transversal energy which can be radiated by synchrotron emission. The simulation used as an input parameter a residual gas pressure equivalent to  $p = 10^{-10}$  mbar, *i.e.*, ten times higher than intended for the KATRIN spectrometer section. Therefore, all of the stated results need to be scaled up by a factor of 10, and thus typical cooling times at a pressure of  $p = 10^{-11}$  mbar would be in the range of  $\lesssim 1$  hour.



(a) distribution of ionization positions



(b) distribution of electric potentials at ionization positions

**Figure 5.28:** Simulation results: distribution of axial position and corresponding electric potential for ionizing collisions (both figures taken from [Ess04]). (a) Locations of ionizing collisions are approximately evenly distributed, therefore most secondary electrons are born in negligibly low electric potentials, as indicated by the purple line. However, some ionization processes do occur in the border regions of the simulated field map, where the slope of the electric potential is large and its absolute value is rapidly increasing in the direction of the two spectrometers. This can also be seen from the histogram in (b). The simulation, which was carried out for 10 electrons with the starting parameters  $E_{\text{start}} = 10 \text{ keV}$ ,  $\theta_{\text{start}} = 45^\circ$ , yields 120 secondary electrons, with about 10% of those born in the region of strong negative electric potential. This means each trapped primary particle produces on average 12 secondaries before cooling prevents any further ionizations, but only about one of them has enough kinetic energy to start a dangerous ionization chain. For lower starting angles  $\theta_{\text{start}}$  the absolute amount of secondary electrons becomes larger because the initial trapped electron takes a longer time to cool below the ionization threshold (compare figure 5.27); for larger starting angles the secondary yield is smaller.

### 5.4.2 Validity of the simulation results in view of the new KATRIN reference design

In 2007, the overall KATRIN design underwent an extensive revision. The modifications also affect the electromagnetic fields in the Penning trap region between the two spectrometers. The experimental configuration used for K. Essig's simulations, as shown in figure 5.26, is outdated in several aspects:

1. Important details of the actual shape of the electrode system are missing. The final design for the main spectrometer vessel and its inner electrodes was fixed after K. Essig's simulations had been concluded. The ground electrode and cone regions of both pre- and main spectrometer, which are of particular relevance for the trapping studies, have undergone design modifications as a consequence of the Penning trap studies described in sections 5.2 and 5.3.
2. The transport section, consisting of two large superconducting magnets, and the main spectrometer entrance magnet have been removed from the setup. The link between pre- and main spectrometer now consists of only one superconducting magnet and a beam tube on ground potential (see figure 5.29).

However, the design modifications do not remove the trapping conditions between the two spectrometers. On the contrary, they arguably even worsen the situation since the magnetic field strength  $B$  in the new concept is lowered by about 20% with respect to the original design, while at the same time the distance  $l$  an electron travels through the high magnetic field region is shortened considerably due to the removal of the large transport magnets. The power radiated away in the form of synchrotron light,  $P_{\text{synch}}$ , is proportional both to the length  $l$  and to the square of the magnetic field strength:  $P_{\text{synch}} \propto l \cdot B^2$ . Thus, both modifications cause a reduction of the synchrotron emission and the corresponding energy loss. As a result, the electrons tend to preserve an energy above the ionization threshold for a little longer than in the scenario of higher synchrotron emission investigated by K. Essig in her diploma thesis. Furthermore, the relative fraction of ionization events occurring in regions of high electric potential is increased significantly due to the reduction of the longitudinal trap dimension  $l$ .

Recently, the electron trapping and ionization processes have been re-investigated and earlier results were confirmed by new simulations done by F. Glück [Glü08]. Apart from the intention to check the previous results with the updated configuration of electromagnetic fields, a main motivation for this new study was to obtain a more confident statement regarding the probability of a self-sustained chain reaction to take place, which should be founded on much better statistics. In the case of K. Essig's calculations, only a small number of trapped electrons and their interactions could be simulated due to the fact that the simulation is quite demanding with respect to computational resources. Since at that time only a small number of CPUs was available, the statistics were necessarily limited. Therefore, it was not possible to conclusively determine whether a strong discharge could indeed build up inside the Penning trap. The argument that synchrotron radiation might be sufficient to prevent a dangerous multiplication of electrons in the trap was brought forward by E. W. Otten [Ott07].

A computation cluster<sup>22</sup>, which had in the meantime become available at Münster, allowed to significantly scale up the simulation to a total of about 300 CPU days. Instead of performing the full trajectory calculation for all secondary electrons created in the ionization chain, the compu-

<sup>22</sup>The GridIKP linux cluster at the Institute for Nuclear Physics at University of Münster, which presently comprises 60 nodes with a total of 138 CPU cores, was used for these calculations. Its primary function is to provide computational resources for the Worldwide LHC Computing Grid (see webpage <http://lcg.web.cern.ch/lcg/>).

tation was split into two separate tasks. First, trajectories of a large number of stored electrons with different starting parameters (*e. g.*, total starting energy and starting angle) were calculated. From these an energy spectrum of the secondary electrons was obtained. Next, the avalanche of ionizations was simulated in several steps. In each generation, the initial electrons were cooled down below the ionization threshold, and the ionization yield and thus also the number of electrons present in the system at the start of the subsequent step of the cascade was determined. Analogously to the earlier simulations, it was necessary to simultaneously increase the residual gas pressure and the intensity of the synchrotron radiation by a factor of  $10^5$  to  $10^6$  to facilitate the calculations.

The results [Glü08] show that, even when including synchrotron radiation as the most efficient cooling mechanism, a single primary electron with a starting kinetic energy of  $E_{\text{start}} = 18 \text{ keV}$  can produce an avalanche of ionizations with a huge ion yield of

$$N_{\text{ion}} \approx 10^8. \quad (5.16)$$

This is a strong argument calling for an active suppression of the number of high-energy electrons inside the trap. To illustrate the effect of the trapped electrons on the overall background rate in KATRIN, different filling mechanisms of the trap shall briefly be discussed.

- In [Ess04], two feeding processes were mentioned:
  - a) Electrons from the tritium source which pass the pre-spectrometer but do not possess enough energy to also pass the main spectrometer will be reflected and return towards the pre-spectrometer. However, these electrons can only be trapped between the two MAC-E filters if they undergo some energy loss processes (*e. g.*, non-adiabatic reflection, synchrotron emission and collisions with residual gas molecules). Otherwise, they pass the analyzing plane of the pre-spectrometer in reverse direction and go back towards the source. The new, more detailed simulations by F. Glück indicate that the number of trapped  $\beta$ -electrons will be small, and their contribution to the expected background rate therefore negligible.
  - b) The second process is of more concern: the normal spectrometer background (*i. e.*, secondary electrons from the solid high-voltage electrodes) from the two MAC-E filters can also provide trapped electrons. While electrons starting from the hull of the main spectrometer which make it into the inner flux tube have a low probability of getting trapped because they have a chance to pass the lower electrostatic potential of the pre-spectrometer, those electrons originating in the downstream half of the pre-spectrometer do not possess enough energy to escape from the trap by passing the analyzing plane of the main spectrometer. In view of the large ion yield per electron (eq. (5.16)) and the ionization probability inside the main spectrometer of the order of  $10^{-8} - 10^{-7}$  an amplification factor  $> 1$  and thus a self-sustained discharge due to this filling mechanism with high background rates at the final plane detector is possible.
- In case the origin of the “high B-field background” at the pre-spectrometer mentioned in section 5.2.6 cannot be found and eliminated until the start of the neutrino mass measurements, about  $10^3$  electrons per second will be emitted towards the trap between the spectrometers from the pre-spectrometer side, and many of these will end up being stored. According to eq. (5.16) this gives a total of  $N_{\text{ion,total}} \lesssim 10^{11}$  ions per second. A rough upper limit of the background signal to be expected at the KATRIN final plane detector from further ionization processes of the type (5.12) inside the main spectrometer can be estimated

using the corresponding ionization probability  $P$  (equation (5.11)):

$$\begin{aligned}
 N_{e^-, \text{backgrd}} &= N_{\text{ion, total}} \cdot P \\
 &\lesssim 10^{11} \frac{1}{\text{s}} \cdot 10^{-7} \\
 &= 10^4 \frac{1}{\text{s}}.
 \end{aligned} \tag{5.17}$$

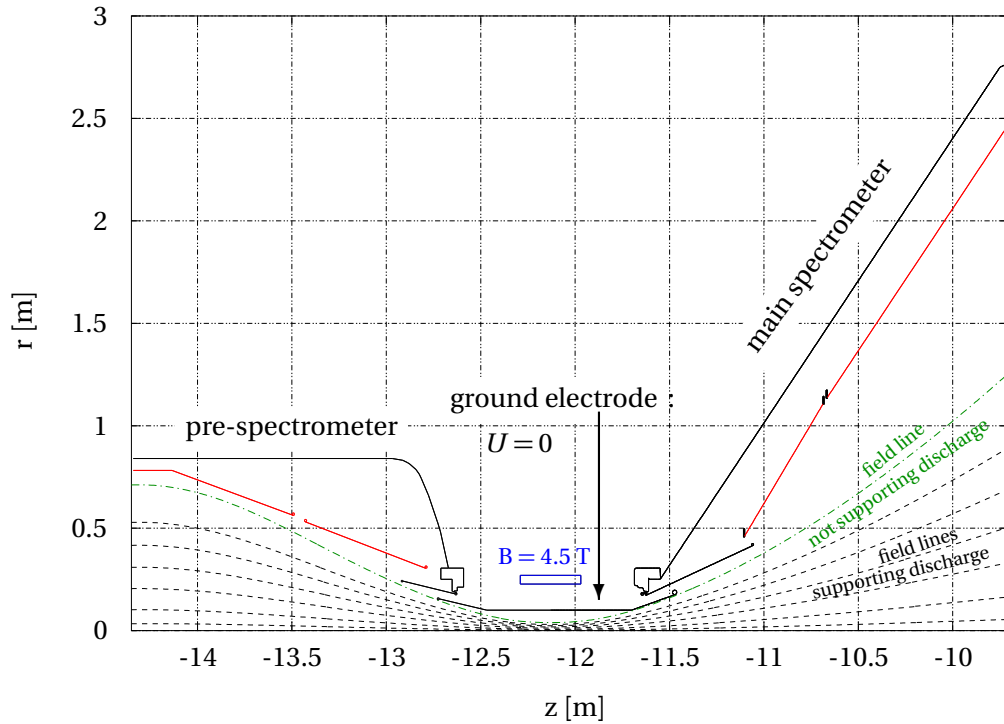
Such a background rate would of course be unacceptable for the neutrino mass measurements, and the problem may only be solved by turning off the high voltage of the pre-spectrometer or else by providing a very efficient mechanism to empty the trap.

### 5.4.3 Countermeasures

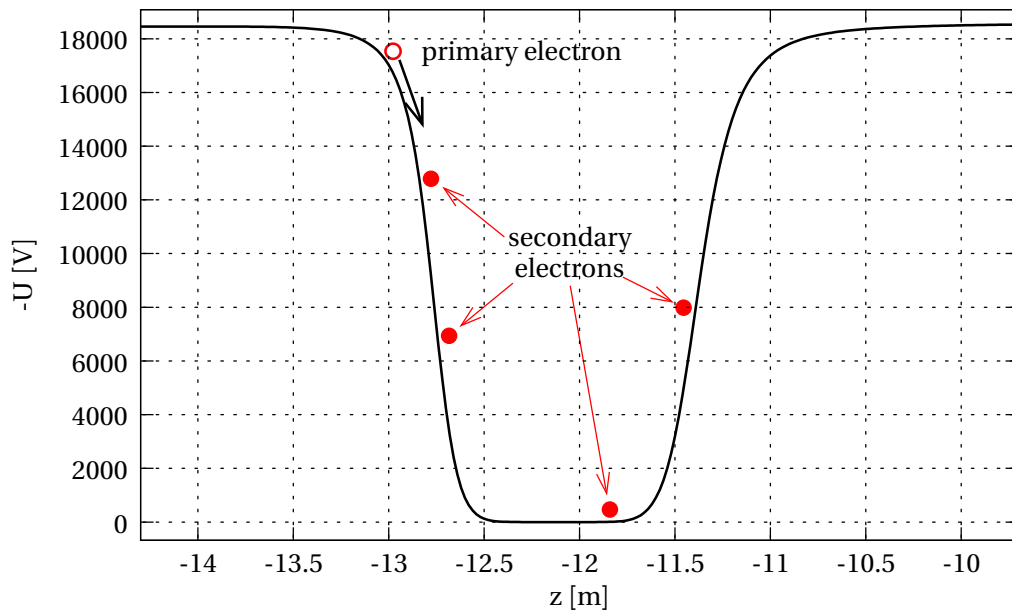
Some general methods to counteract Penning discharges have been outlined in section 5.1.4. In the following, they shall be evaluated in view of their applicability to the Penning trap between the two spectrometers.

- **General design optimization:** The first point mentioned in the list of countermeasures, the careful electromagnetic design that avoids Penning traps wherever possible, cannot be applied here since the trap between two successive spectrometers of MAC-E filter type is intrinsically present and cannot be completely avoided.
- **Surface quality:** Careful treatment of any electrode surfaces to lower the probability of electron emission – either by ion bombardment or by field emission – is mandatory for all parts of the pre- and main spectrometer electrode system. In addition, the screening grid electrode will help to suppress the flux of secondary electrons from the cathode surfaces into the sensitive spectrometer volume. Although this method might help to diminish the effects caused by positive ions emerging from the ionization chain inside the trap, it does not influence the trapping conditions, which need to be taken care of in the first place.
- **Removal of charged particles via drift motion induced by a strong electric dipole field:** This option has been investigated in K. Essig’s work by computer simulations using the separate conical parts of the pre-spectrometer inner electrode system to produce the electric dipole field. The results imply that very strong gradients of the electric potential in the transversal direction would be needed in order to overcome the accelerating effect of the axial gradient, which is very high in the entrance and exit regions of both spectrometers. Only potential differences of the order of  $U_{\text{dipole}} \approx 20 \text{ kV}$  showed a marked effect on the trapping characteristics. However, such potential differences are highly impractical.
- **Interception of trapped electrons:** At a very low residual gas pressure of  $10^{-11} \text{ mbar}$  as projected for KATRIN, the mean time between ionizations (about 1 minute) and the mean electron cooling time (of the order of 1 hour) are quite long (compare figure 5.27 and reference [Glü08]). By contrast, the magnetron time scale during which a trapped electron performs a full rotation around the axis is found in F. Glück’s simulations to be of the order of  $\tau_{\text{magnetron}} \approx 20 - 200 \mu\text{s}$ . This signifies that the time scale available for an intervening measure to empty the trap is sufficiently long. In particular, it opens up the possibility to prevent discharges by inserting either a stationary pin or a movable wire as an “electron catcher”.

Considering all options, the last method seems the most promising one with regard to removing trapped particles between the two KATRIN spectrometers effectively and reliably. Therefore, a setup to test a scanning wire device at the Mainz spectrometer was proposed already in the outlook of [Ess04]. Such a setup was now realized and experimentally tested, and the results are



(a) geometry of the trapping region in the  $r z$ -plane



(b) electric potential on the  $z$ -axis in the trapping region

**Figure 5.29:** (a) Close-up on the interface region between pre- and main spectrometer. The geometry has been updated to match the 2007 “KATRIN reference design” and also includes the newly introduced shielding electrodes for the pre- and main spectrometer (see sections 5.2 and 5.3). Dashed lines represent magnetic field lines supporting a Penning discharge; the dash-dotted line indicates a magnetic field line touching the ground electrode (anode) and therefore not supporting a Penning discharge. (b) Illustration of secondary electrons (●) arising from ionizing collisions of a primary electron (○) with the residual gas at different values of the electric potential.

discussed in chapter 6. The second possibility, namely that of a stationary electron catching pin, should also be investigated further.

## 5.5 Effects of Penning discharges in other experiments

It is noteworthy that several other past or ongoing experiments have been plagued by problems with Penning traps and discharges. In some cases, the discharges required significant modifications of the experimental setup in order to resolve the difficulties. The following list gives some examples:

- **The Mainz neutrino mass experiment.** Together with the Troitsk experiment, the Mainz group has established the MAC-E filter technique as the instrument of choice for direct neutrino mass searches based on precision tritium  $\beta$ -spectroscopy. In early phases of the experiment, strong discharges associated with a dramatic increase of background were observed, which were suspected to be related to deep Penning-like traps and eventually led to a revision of the system of high-voltage electrodes [Bor00]. In the course of the recent studies of the trapping scenarios at the KATRIN pre-spectrometer, a simulation-based search for Penning traps in the old configuration of the Mainz MAC-E filter was carried out [Hug08]. These investigations indeed revealed the existence of Penning traps with a depth of several kV, which can explain the observed high background rates.
- **The Troitsk neutrino mass experiment.** The Troitsk experiment also uses a high-resolution MAC-E type spectrometer of dimensions comparable to the one used in Mainz. In addition, the original setup also incorporated a second electrostatic filter upstream of the main energy filter, establishing a similarity to the KATRIN setup with its tandem spectrometers. However, this former configuration did not perform as anticipated. Like at Mainz, the inner electrode system of the Troitsk spectrometer had to be modified to cope with persistent discharge problems [Kaz07]. Furthermore, the combination of pre-filter and main spectrometer formed a Penning trap like the one expected to exist between the KATRIN pre- and main spectrometers. The fact that the low background rate necessary for neutrino mass measurements could not be reached at Troitsk with the pre-filter placed on high voltage, but only when the voltage of the pre-spectrometer was reduced to about  $-200$  V, confirms the suspicion that Penning discharges indeed were the source of the problems at Troitsk and calls for timely precautionary measures to be taken with respect to the KATRIN setup.
- Several **neutron decay spectrometers**, such as the running  $\alpha$ SPECT [Abe03, Glü05a, Bae08] and PERKEO [Schu07, Abe03] experiments as well as the planned Nab experiment [Ala07], are also faced with Penning traps existing in their experimental configurations. It is interesting to note that the neutron decay spectrometer PERKEO II did not encounter large discharges, albeit the fact that a deep Penning trap ( $\Delta U$  up to 30 kV in a magnetic field strength of  $B = 1$  T) is present in their setup. Furthermore, the residual gas pressure was as high as  $10^{-6}$  mbar. The absence of discharges may be attributed to the presence of several grids of screening wires in the central decay volume of the apparatus.  $\alpha$ SPECT has encountered problems with electric breakdown in the system, which are intended to be cured following the model of PERKEO II by installing wire electrodes to intercept the stored particles. The Nab group aims to prevent discharges by installing a swiping wire similar to the one constructed and tested for KATRIN (see chapter 6) in the trapping volume.
- **The Weak Interaction Trap for Charged particles (WITCH)** employs a MAC-E filter to determine the electron-neutrino angular correlation coefficient  $a$  in beta decay via a mea-

surement of nuclear recoil spectra. After problems assumed to be related both to field emission and to several Penning-like traps in the setup were encountered [Fri08, Coe07, Koz08], a number of measures along the lines sketched in section 5.1.4 were initiated:

- Parts of the electrode setup have been redesigned and remanufactured with special emphasis on the surface quality. In addition to removing problems caused by vacuum breakdown, the avoidance of field emission at the same time allows to reduce one of the potential mechanisms feeding the Penning traps.
- An improvement of the vacuum conditions will be achieved by implementing additional getter pumps (at present, the residual gas pressure is at a level of about  $p \approx 10^{-8}$  mbar).
- It is intended to lower the magnetic field strength at the location of one of the traps in order to make electron storage less efficient.
- In addition, the option of using a movable wire like the one tested for KATRIN to catch stored particles and prevent discharges is considered.

In conclusion, the experience gathered in other experiments clearly supports the view that active measures should be taken to either avoid Penning traps or arrange for a device to disturb the mechanism of particle storage and accumulation at KATRIN. One possible realization of such a device was investigated in the scope of this work, and the results are presented in the following chapter.

## 6 Experimental tests of a method to empty the Penning trap between pre- and main spectrometer

Starting from the more phenomenological considerations regarding the Penning trap between pre- and main spectrometer presented in section 5.4, this chapter gives an account of experimental tests of a method to periodically clean this trap by the use of a mechanical “scanning wire” device. These tests were carried out at the Mainz MAC-E filter during several measurement phases. The discussion begins with an introduction to the general intention and requirements for the test (section 6.1) and continues with a description of the experimental setup (section 6.2), before results of the different phases of measurement are presented (sections 6.3 and 6.4). The chapter closes with a review of the results and an outlook in section 6.5.

### 6.1 Aim and requirements of the experimental test

The aim of the investigation is twofold. First, the test of the trapping conditions should be performed before the final installation and commissioning of pre- and main spectrometer. Therefore, an experimental configuration substituting the combination of the two successive MAC-E filters needs to be found, and the characteristics of the resulting trap – such as occurrence and intensity of discharges – are to be investigated. The second part of the task comprises the construction, implementation and test of a device dedicated to intercepting and collecting the trapped particles.

The following essential parts are required:

- a mockup of the main spectrometer (magnets and electrode system, ultra-high vacuum),
- a device to emulate the pre-spectrometer electrode system (additional high-voltage electrode, ultra-high vacuum),
- electron sources with variable intensity for (optional) enhanced filling of the Penning trap,
- a mechanical “electron catcher”, implemented at the junction of the simulated “pre-spectrometer” and “main spectrometer”, and
- an electron detector.

The existing KATRIN pre-spectrometer would make an ideal starting point for a trapping experiment. To provide a second “spectrometer”, the so-called “test cylinder” (a cylindrical vacuum chamber with a diameter of 500mm and a length of 1.4m that was used as a testbed for the KATRIN ultra-high vacuum concept) might be equipped with an inner electrode system and attached to one end of the pre-spectrometer. However, within the time-frame allotted for the testing of the Penning trap between the two KATRIN spectrometers, the pre-spectrometer was not available for such studies due to a tight schedule of other vital test experiments. Therefore, an alternative setup at the Mainz MAC-E filter was conceived, which is described in detail in the following section.

## 6.2 Setup and field configurations at the Mainz MAC-E filter

In the simplest configuration, the KATRIN main spectrometer is represented by the MAC-E filter of the former Mainz neutrino mass experiment and the pre-spectrometer is simulated by a vacuum chamber containing an electrode on high voltage (in the following referred to as the “backplate” electrode). This chamber has to be attached to the Mainz spectrometer such that a Penning trap similar to that between the real KATRIN pre- and main spectrometer is formed: The two negative electric potentials of the backplate electrode and the MAC-E filter should enclose a region of more positive (or even ground) potential where a strong magnetic field is present. In addition, the setup should provide access for installation and operation of the mechanical device intended to clean the trap. Although the test experiment cannot be expected to fully reproduce the electromagnetic fields at KATRIN due to inevitable differences in the geometry of the setup, the electric potentials applied and the magnetic field strength should at least be comparable to those in the final KATRIN beam line. The solution that was realized at Mainz is presented in figure 6.1.

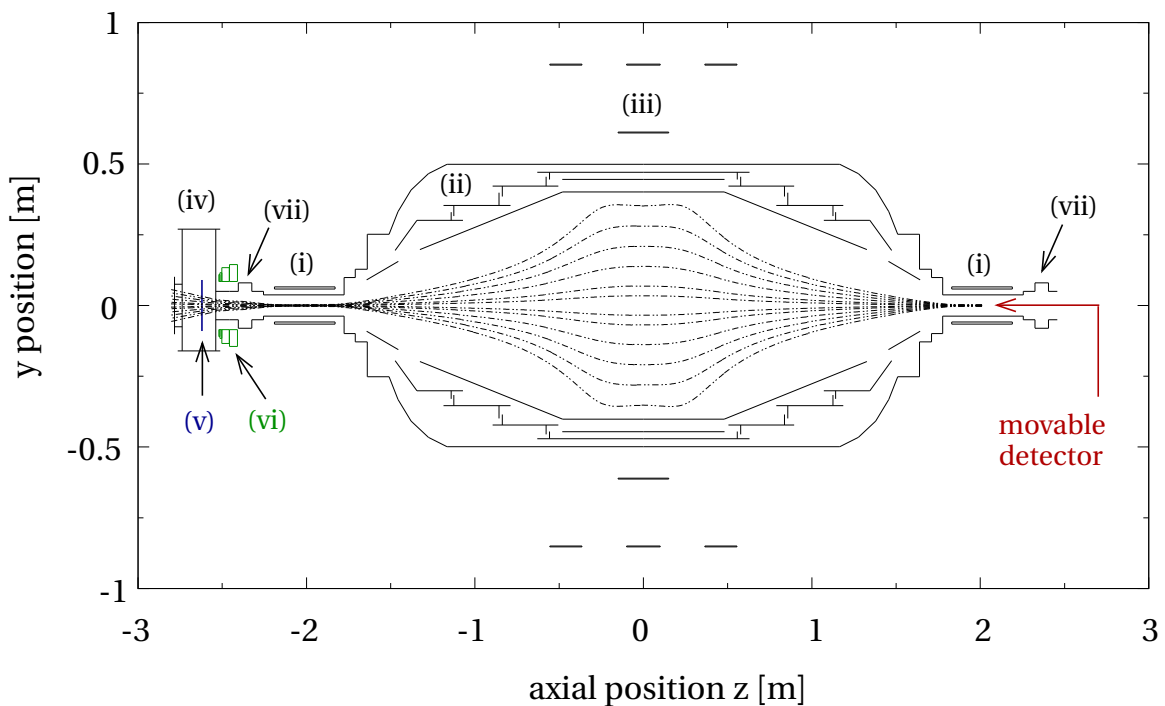


**Figure 6.1:** Setup used at the Mainz MAC-E filter for testing the trapping conditions between the KATRIN pre- and main spectrometer. (i) superconducting coils, (ii) electrode system consisting of vacuum tank at ground potential, solid and wire inner electrode systems on high voltage, (iii) field-shaping air coils, (iv) vacuum chamber housing both the wire scanner installation and (v) the backplate electrode, (vi) water-cooled additional coil for local enhancement of the magnetic field at the position of the wire scanner (not shown in this drawing), (vii) valves. The detector is situated on a movable sleigh close to the solenoid on the right-hand side. Magnetic field lines (settings corresponding to a resolving power of  $E/\Delta E \approx 2 \cdot 10^4$ ) are indicated as dashed curves.

### 6.2.1 Pre-spectrometer mockup: vacuum chamber and “backplate”

Figure 6.2(a) shows a side view of the vacuum chamber which was originally used to house parts of the condensed krypton calibration source (CKrS) for KATRIN during its tests at the Mainz MAC-E

filter [Ost09]. After the CKrS measurements at Mainz had been concluded, the vacuum chamber turned out to be the ideal container for the essential parts needed for the Penning trap test measurements. A cylinder of diameter  $\varnothing 200$  mm forms the central part of the chamber. Access is provided through various ports:

- A turbomolecular pump evacuates the chamber from the bottom port (DN 200 CF flange).<sup>1</sup>
- The opposing port on top of the chamber is equipped with a DN 200 CF lid containing two high-voltage feedthroughs on ceramics insulators that were used to hold and connect the electrode emulating the pre-spectrometer (see figures 6.2(b) and 6.2(c)). This way, the vacuum chamber itself can be kept on ground potential, while a variable (negative) electric potential is applied to the disc-shaped electrode.
- The right-hand side of the chamber has a DN 100 CF opening leading towards the spectrometer. A bellow with an inner diameter of 100 mm is situated between the flange and the gate valve next to the cryostat of the superconducting magnet.<sup>2</sup>
- In addition, the chamber possesses four DN 40 CF ports that usually serve as openings to couple the ablation and ellipsometry laser beams into the substrate region of the CKrS setup. In the Penning trap experiments, they are useful to provide optical access, for example for UV light producing photoelectrons off a target inside the chamber. These photoelectrons can contribute to filling the trap, as discussed in section 6.2.4 below.

Technical details of the electrode construction can be found in appendix B.2.

### Comparison between mockup and real KATRIN system

The model of the pre- and main spectrometer system described in the previous section cannot be an exact miniature copy of the final KATRIN setup – some concessions need to be made for the sake of technical feasibility. In particular, the realization chosen for the electrode emulating the pre-spectrometer forms a marked difference to the real field configuration at KATRIN. In the electromagnetic design of the KATRIN experiment, special emphasis was put on avoiding a direct connection between electrodes on high voltage and the detector via magnetic field lines in order to avoid discharges (see section 5.1, esp. 5.1.4). In other words, none of the magnetic field lines belonging to the nominal magnetic flux tube of  $\Phi = 191 \text{ T cm}^2$  touches or crosses cathode material. This rule is intended to reduce background by prohibiting the direct transport of charged particles from the electrodes to the detector. However, this concept has been deliberately violated in the test setup at Mainz by choosing the disc-shaped geometry of the backplate electrode, which is easy to realize within the pre-existing experimental setup.<sup>3</sup> It provides a special “feedback” mechanism that will significantly influence the behavior of the trap (and Penning discharge) in two ways, which are related to the mechanisms described in the previous chapter (see Townsend discharge, section 5.1.1):

- Electrons originating from the plate can leave it along the magnetic field lines crossing the electrode. They gain kinetic energy by running down the electric potential difference towards the region at ground potential. Ionizing collisions with residual gas will take place. If

<sup>1</sup>During most of the measurements done in 2007, the coldhead belonging to the CKrS setup was used as a cryo pump, allowing to reduce the pressure by almost an order of magnitude. However, the coldhead was no longer available for the 2008 measurements after the CKrS setup had been dismantled.

<sup>2</sup>In the photograph in figure 6.2(a) the bellow is covered by the copper windings of the water-cooled auxiliary magnet that is described in sections 6.2.2 and 6.2.3.

<sup>3</sup>It would have been technically more complicated to install a cylindrical electrode aligned with the central beam axis. Furthermore, the space inside the available vacuum chamber was limited, in particular since parts of the CKrS were still installed during the first measurement phase in 2007.

the trap height of the two potential walls is asymmetric (*i. e.*,  $|U_{\text{plate}}| < |U_{\text{spec}}|$ ), the electrons starting from the plate cannot gain enough energy to pass the electrostatic barrier formed by the analyzing plane of the spectrometer and will be reflected back towards the plate. Due to energy losses, some of the electrons will not be able to reach the surface of the plate: they enter the trapping volume between plate and analyzing plane and can cause many further ionization processes.

- The positive ions created in the trap can be accelerated towards the backplate and hit its surface with considerable energy. A subsequent release of electrons from the surface of the plate can lead to further amplification of the number of charged particles in the trap that would not be present, for example, in the case of a cylindrical electrode outside the Penning trap volume. Therefore, the discharge characteristics can be fundamentally different from those potentially present in the KATRIN setup. This point needs to be kept in mind when interpreting the results and attempting to transfer the conclusions drawn from experiments with the mockup to the KATRIN system.

### 6.2.2 Mechanical device to sweep a wire through the beam line: the “wire scanner”

The basic idea for a device to clean out the particle trap consists of a grounded wire periodically moved through the trapping region to collect stored charged particles. This “wire scanner” should fulfill the following requirements:

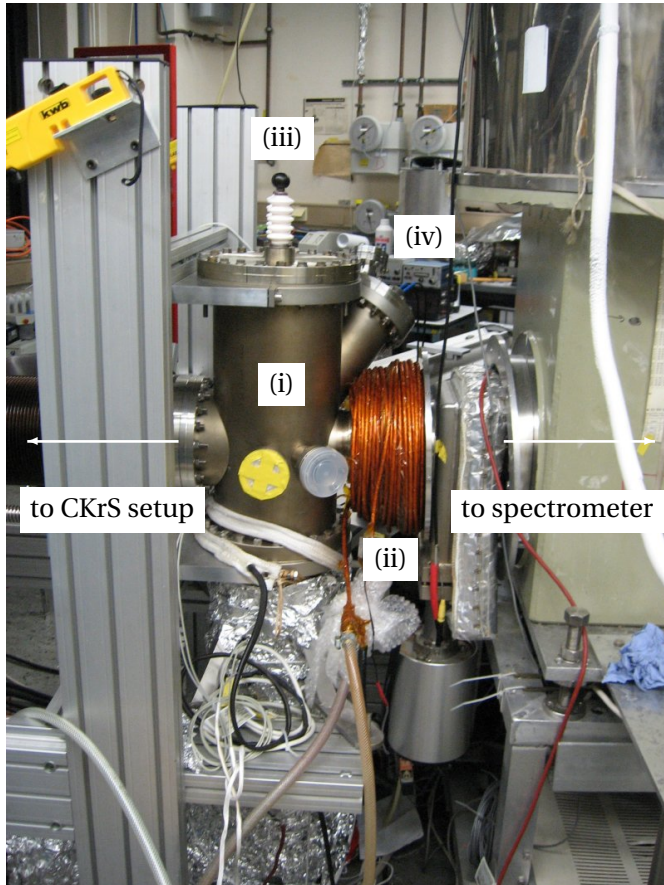
- The wire material should be conductive such as to allow the charged particles hitting its surface to flow off instead of accumulating on the surface (as would be the case for an insulating wire). Using a conductive wire also offers the opportunity to send an electric current through it, which provides a rather easy way to move it by virtue of the Lorentz force in the external magnetic field.
- The scanning motion should encompass the whole flux tube diameter in order to collect all trapped particles. Therefore, the device has to be installed inside a magnetic field of sufficient strength to compress the magnetic flux to a comparatively small diameter.
- The operating principle employed for the scanner should allow for easy handling, long-term stability of operation without intervention, and low maintenance requirements. Ultra-high vacuum compatibility is required. Therefore, the use of grease for the movable parts, for example, is prohibited.
- Flexibility and mechanical stability should be compatible with scanning rates of up to a few sweeps per second.
- Finally, the wire scanner should be of rather compact dimensions so as to be easily mountable in a tightly restricted space.

Three phases of measurements (one in the year 2007 and two successive phases in 2008) with different wire scanner designs were carried out. In all three phases, the same support structure was used – with only slight modifications – to hold the wire in place. Technical details of the holder arm are included in the appendix (section B.3).

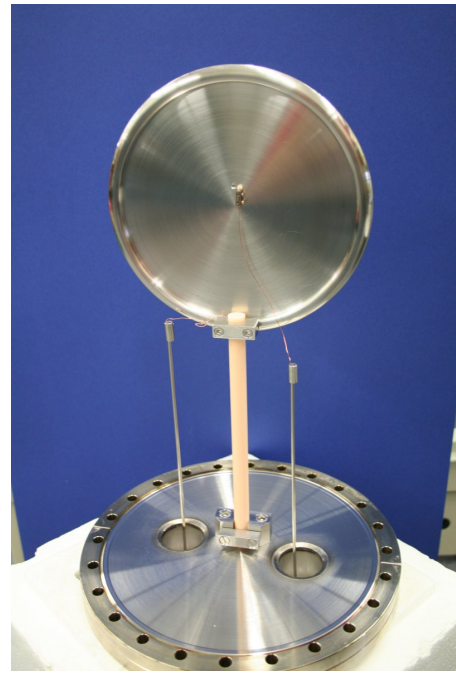
- **Phase I: 06/2007 – 07/2007**

A copper wire of diameter 0.4 mm equipped with springs at both ends was bent to an arc and placed in vertical position inside the 100CF bellow (see figure 6.3(a)). The scanning motion was stopped at either side by the wire hitting the walls of the tube. In the first measurement phase, this was problematic because the wire made electric contact with the

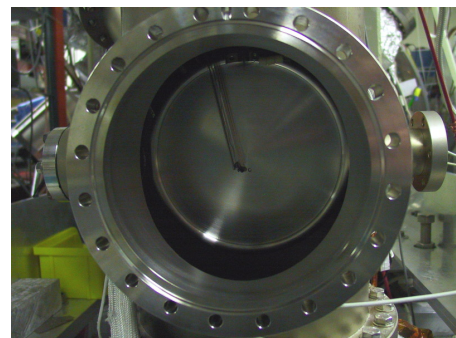
- (i) vacuum chamber housing disc-shaped electrode and wire scanner
- (ii) water-cooled auxiliary magnet
- (iii) HV feedthrough for disc-shaped electrode
- (iv) current feedthrough for wire scanner



(a)



(b)



(c)

**Figure 6.2:** Photographs of the test setup at the Mainz spectrometer. (a) Position of the vacuum chamber, with directions towards condensed krypton source (CKrS) setup and spectrometer indicated by arrows. (b) Front view of the disc-shaped high voltage electrode mounted on a DN 200 CF flange, with insulator and HV leads (shown in upside-down position). (c) Disc-shaped high voltage electrode inserted into the vacuum chamber, viewed from the backside through the open DN 150 CF flange (after removal of the CKrS setup).

surrounding material and a noise signal was induced on the detector under particular conditions (rectangular mode, see “types of wire scanner action” below).

- **Phase II: 02/2008 – 04/2008**

In the second version of the scanner, a larger wire diameter (copper, 1.4 mm) was used in order to enhance the mechanical stability. Miniature ball bearings and flat springs were added (see figures 6.3(b) and 6.4). The wire arc was still long enough to hit the walls of the surrounding DN 100 CF bellow at the turning points of the motion. Therefore, the walls of the bellow were covered with Kapton foil in order to avoid electric contact between the copper wire and the bellow.

- **Phase III: 04/2008**

The third version of the scanner was very similar to the mechanism used in phase II, but the wire was shortened in order to prevent it from hitting the inner side of the bellow. Stopping points of the wire motion were now defined by anchor-shaped parts attached to the bearings. The Kapton foil was removed (see figure 6.4(a)).

The photographs in figures 6.3(a) and 6.3(b) demonstrate the gain in mechanical stiffness of the copper loop from the first to the second version of the scanner and the resulting increased precision of positioning, particularly with respect to the center of the flux tube. A technical drawing of the last version of the scanning device can be found in appendix B.3.

In all three phases, the current signal driving the wire was provided by the output of a function generator (Tektronix FG 502 or AFG 3102) amplified by a bipolar operational amplifier (Kepeco BOP 20-20M). A schematic drawing of the electronics is shown in figure 6.5.

Since the fringe fields of the superconducting magnets provide only a rather weak magnetic field at the location of the wire scanner, an auxiliary water-cooled coil was installed, which helps to shape the magnetic flux tube which connects the backplate and the detector. This is necessary because of the rather large distance between the backplate electrode and the superconducting solenoid, which cannot be reduced due to spatial constraints (a valve and a small bellow define a minimum distance to the solenoid). Furthermore, the enhanced magnetic field facilitates the motion of the wire scanner and allows it to be operated at electrical currents low enough to avoid resistive heating of the wire<sup>4</sup> or the bearings (typically 1 – 5 A).

### Types of wire scanner action

In principle the wire scanner can be driven by an arbitrarily shaped signal provided by the function generator. In practice, however, four basic forms of wire scanner action were used:

- **Rectangular mode:** The wire scanner receives a bipolar rectangular signal from the function generator. This signal is characterized by the peak-to-peak amplitude  $A_{\text{rect}}$  and the period  $T_{\text{rect}}$  (or by a frequency  $f_{\text{rect}} = 1/T_{\text{rect}}$ , respectively). At both edges of the signal, the wire performs a quick motion across the beam profile and then rests outside of the beam at maximum displacement for the duration of half a period. This way, it spends only a very brief time inside the trapping region. Such a mode would be optimal for the neutrino mass runs at KATRIN because it allows normal data-taking during most of the time with only a short interval cut out due to the action of the wire scanner.
- **Sine wave mode:** The function generator feeds a sine wave of peak-to-peak amplitude  $A_{\text{sine}}$  and frequency  $f_{\text{sine}}$  to the wire scanner. The resulting motion is of a very different character compared to the rectangular case: in the sine wave mode, the wire scanner stays inside the magnetic flux tube for a prolonged time, and thus the collection of charged particles in the trapping region can be more efficient. Furthermore, the sine wave involves much less electronic noise than the rectangular pulse which is made up of high-frequency signals. However, the sine mode would be unfavorable for KATRIN because of the large ratio of dead time (*i. e.*, wire scanner inside the magnetic flux tube) to live time (*i. e.*, wire scanner safely outside of the magnetic flux tube) and the difficult separation between the two.

---

<sup>4</sup>The resistance of a copper wire of length  $L \approx 0.15$  m and diameter  $d = 0.4$  mm is  $R \approx 20$  m $\Omega$ . The thicker wire with diameter  $d = 1.4$  mm has a 12 times lower resistance of  $R \approx 1.7$  m $\Omega$ . The resistance of the cabling is thus non-negligible. For the wire scanners of phase II and III, the bearings were the most sensitive parts with respect to heating as they would lose their flexibility.

- **No current:** With no current applied, the wire scanner is drawn into a position close to the center of the beam by virtue of the spring load. The exact position of the wire scanner at rest depends on the mechanical stiffness (small bends) of the scanner and thus varies for the different versions of the wire scanner.<sup>5</sup>
- **Constant (dc) current:** The wire can also be driven out of the flux tube permanently by applying a constant current. Especially for the second and third measurement phases the positive and negative signal amplitudes needed for the wire to reach maximum displacement are not equal ( $A_{dc}^- \neq A_{dc}^+$ ) because of the asymmetric spring load of the holders.

The signal amplitudes  $A_{rect}$ ,  $A_{sine}$  and  $A_{dc}^\pm$  necessary to produce a sufficient current for the wire scanner to reach the spatial limits of its operating range depend on the magnetic field strength at the location of the wire scanner. Suitable values have been determined for various magnetic field settings via optical inspection of the scanning motion (with open vacuum chamber) before the start of the actual measurements.

In some measurements the timing of the wire scanner was recorded on a separate channel of the data acquisition system. Figure 6.6 shows the phase relation between the trigger output of the function generator used for the timing signal and the sine wave that was fed to the wire scanner. For the interpretation of the measurements it is important to note that the wire scanner reaches the center of the beam twice, at  $t_{start} + 1/4 T_{trig}$  and  $t_{start} + 3/4 T_{trig}$  after the trigger pulse. Here,  $t_{start}$  denotes the start signal given by the trigger and  $T_{trig}$  denotes the trigger period (compare annotations in figure 6.6). In the case of rectangular pulses, however, the phase relation between trigger signal and wire scanner motion is trivial (the short time delay between both is defined by the inertia of the wire itself).

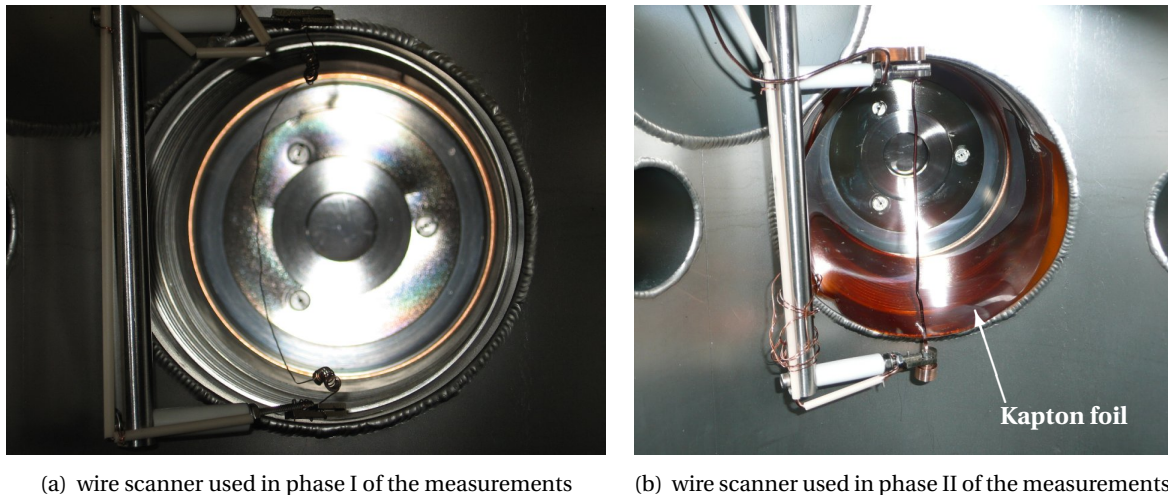
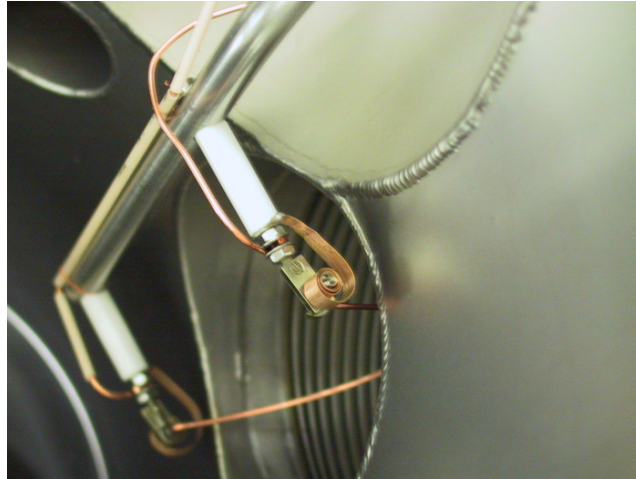
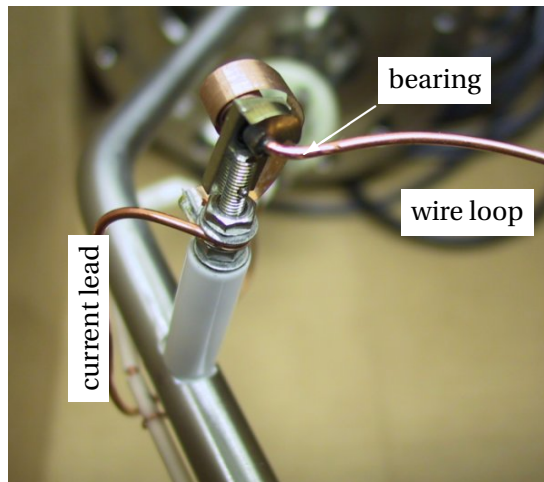


**Figure 6.3:** Photographs showing two stages of technical realizations of the “scanning wire mechanism” to empty the Penning trap. The pictures were taken from the rear side of the vacuum chamber serving as “pre-spectrometer mockup”. The line of sight coincides with the central beam axis. In the background of each picture, the bellow connecting vacuum chamber and spectrometer and the closed gate valve towards the spectrometer are visible. As a common feature, both “scanning wire” solutions involve springs to facilitate the motion of the wire and provide an electric current via insulated leads, although they differ in the details of mechanical construction.

<sup>5</sup>After the first phase of the measurements was finished, it turned out that the shape of the wire had been altered under the stress of many cycles. The “zero position” was not the same as at the start of the measurements. This condition improved in the next measurement phase, where a more stable wire was used.



(a) wire scanner (phase III) viewed from above



(b) close-up on flat spring and bearing

**Figure 6.4:** Details of the wire scanner mounting as used in phase III of the measurements. The shortened copper wire can be seen in (a); the Kapton foil visible in figure 6.3(b) has been removed. The close-up view in (b) shows the flat spring, a bearing equipped with an anchor-shaped stopper, and one of the current leads.

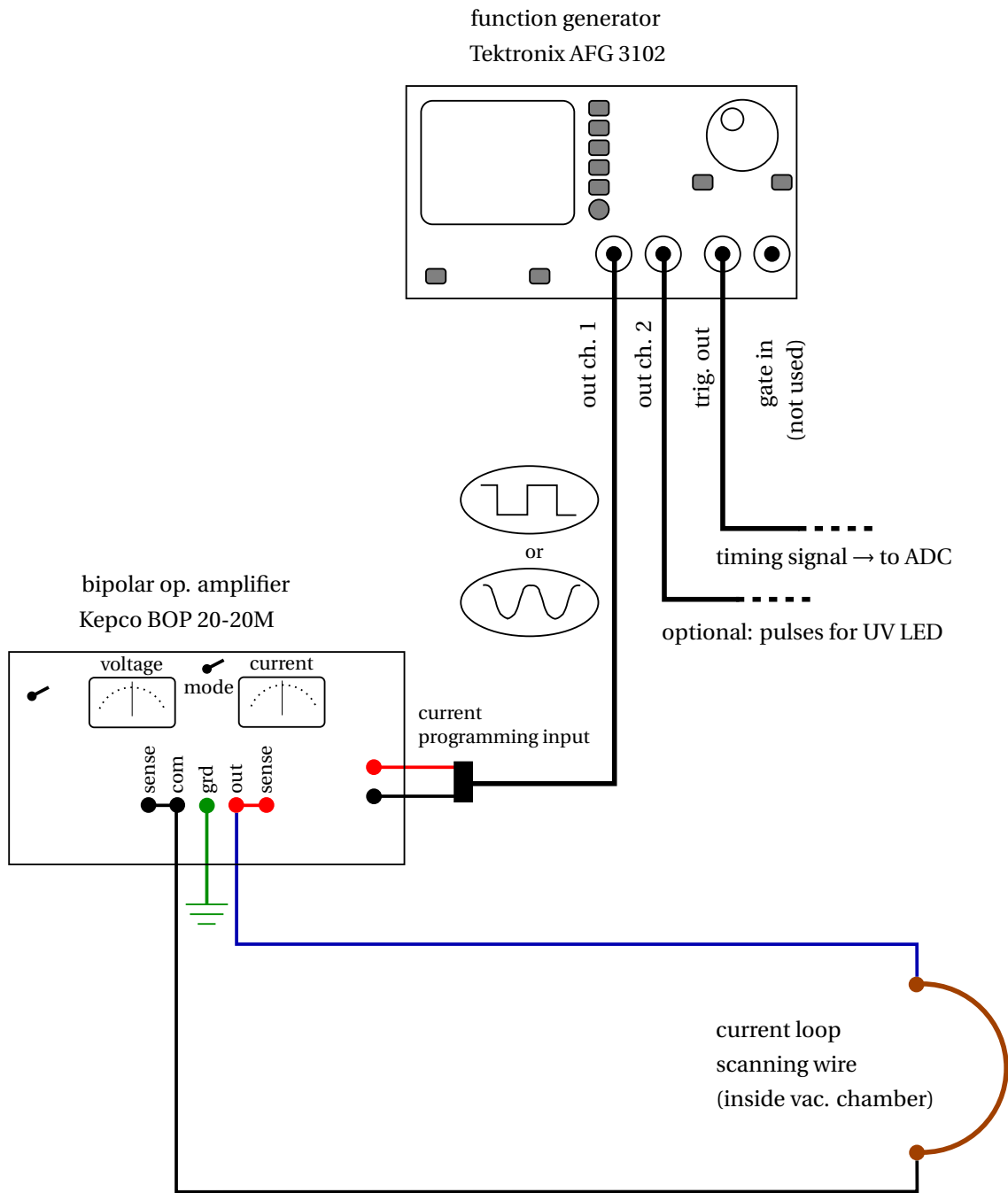


**Figure 6.5:** Schematic drawing: Electronics for operating the wire scanner. The shape of the current pulse is defined by choosing a waveform at the function generator (for measurements in 2008: Tektronix AFG 3102, for 2007: Tektronix FG 502), which is turned into a correspondingly modulated current by a bipolar operational amplifier (BOP 20-20M). Typical waveforms are bipolar rectangular pulses of varying width or sine waves with different frequencies. The current amplitudes sufficient to make the wire move are in the range between  $\pm 1$  A (thin copper wire) and  $\pm 5$  A (thicker copper wire), and the settings depend on the magnetic field strength at the location of the current loop.

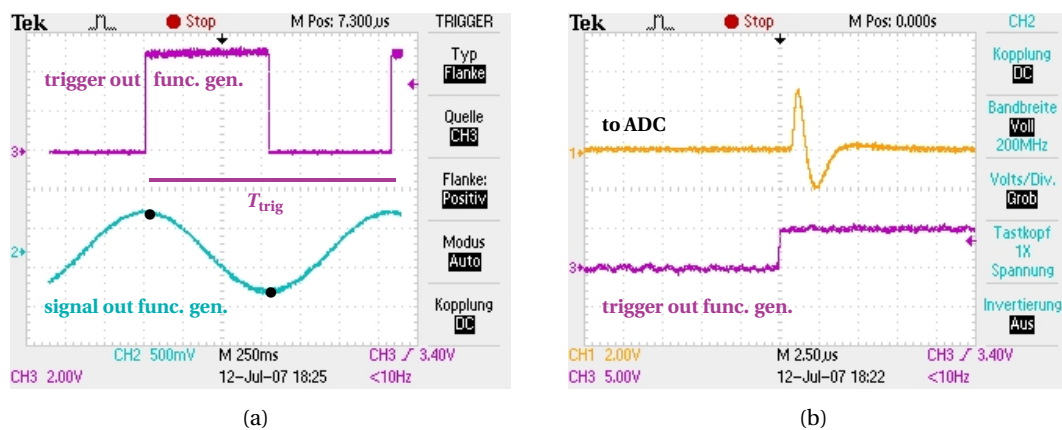


**Figure 6.6:** Trigger timing for wire scanner measurements. (a) Scope screenshot illustrating the phase relationship between sine wave output (lower curve) and TTL trigger output (upper curve) of the Tektronix FG 502 function generator. Bullets ( $\bullet$ ) indicate the approximate time of maximum displacement (either side) of the wire scanner. The central position with zero displacement is reached at about  $1/4$  and  $3/4$  of the trigger period  $T_{\text{trig}}$ . (b) Before passing it to the ADC, the trigger signal (lower curve) was processed by a gate and delay generator, a constant fraction discriminator, and a spectroscopy amplifier (upper curve) to adapt it to the data acquisition system.

### 6.2.3 Configuration of electric and magnetic fields

#### Magnet configuration

The magnet system of the Mainz MAC-E filter consists of two superconducting solenoids and two sets of auxiliary air coils for the purpose of

- (a) tuning (lowering) the magnetic field strength in the analyzing plane of the spectrometer in order to achieve the desired energy resolution, and
- (b) adjusting the position (and shape) of the magnetic flux tube by compensating for misalignments of the detector relative to the central axis of the spectrometer, and for the Earth's magnetic field. (Note: these are neither shown in figure 6.1 nor included in table 6.1.)

In order to clarify which of the two separate sets of coils is meant, the notation “additional air coils” (or short, “air coils”) for the former and “xy-compensation coils” for the latter will be adopted in the following.

Table 6.1 outlines some characteristic parameters of the magnets. The electric current settings are taken from reference [Thü07], where studies to improve the energy resolution of the Mainz spectrometer (in view of its later use as a monitor spectrometer for KATRIN) by tuning the magnetic field settings are described. Since the energy resolution of a MAC-E filter is solely determined by the ratio of minimum and maximum magnetic field strength,  $B_{\min}/B_{\max}$ , the resolution can in practice be chosen simply by changing the electric current through one of the central air coils. If air coil number 2 (compare table 6.1) is supplied with a current of  $I_{\text{aircoil}2} = -8.8\text{A}$ , the magnetic field strength in the analyzing plane is attenuated to a value of  $B_{\text{ana}} = 3.09 \cdot 10^{-4}\text{T}$  (see figure 6.7), while a current of  $I_{\text{aircoil}2} = -3.0\text{A}$  gives rise to a slightly higher magnetic field strength of  $B_{\text{ana}} = 5.05 \cdot 10^{-4}\text{T}$  [Thü07]. Together with the field strength of  $B_{\max} = 6.014\text{T}$  at the center of each solenoid for current settings of  $I_{\text{sol.A}} = I_{\text{sol.B}} = 50\text{A}$ , these settings result in an energy resolution of 0.96 eV (or 1.55 eV, respectively) for electrons with energies of 18.6 keV.

**Table 6.1:** Magnetic field configuration of the Mainz spectrometer (xy-compensation coils omitted).

magnet / type	axial position of magn. center	inner radius	length	typical current setting <sup>*)</sup>
solenoid A	+2.01 m	0.058 m	0.36 m	50 A
solenoid B	-2.01 m	0.058 m	0.36 m	50 A
air coil 1	-0.46 m	0.85 m	0.19 m	-19 A
air coil 2	0.0 m	0.85 m	0.20 m	<b>-8.8 A</b> (-3.0 A)
air coil 3	+0.46 m	0.85 m	0.19 m	-19 A
air coil 4	0.0 m	0.61 m	0.30 m	+5 A
aux. water-cooled coil	-2.465 m	0.085 m	0.11 m	[0 A, 120 A]

<sup>\*)</sup> The current settings for the solenoids and air coils 1 – 4 given here correspond to an energy resolution of **0.96 eV** (or 1.55 eV) at electron energies of 18.6 keV (see [Thü07] for details). The current in the auxiliary water-cooled coil was varied between 0 A and about 120 A.

The current settings for the xy-compensation coils are related to the alignment of the detector and have to be determined empirically. In particular, they usually need to be revised after changes of the apparatus have been made, for example after a new alignment of either the electron source or the detector has been chosen. The values of the two independent currents, from now on labelled  $I_{\text{comp.1}}$  and  $I_{\text{comp.2}}$ , will therefore be indicated separately for each of the measurements described

in this chapter. The xy-coils are also a tool to deliberately deform the magnetic flux tube in such a way that it touches the solid electrodes, which can be useful for investigations of background and electron transport phenomena.

The latest addition to the magnet system is the water-cooled auxiliary coil wound around the bellow connecting the cylindrical vacuum chamber with the spectrometer. It was installed particularly for the tests of the wire scanner. The mechanical setup is simple; it consists of a long copper tube wound into a coil body of compact dimensions that is supported by a frame made of aluminium. Figure 6.8 shows the measured local contribution of the coil to the overall magnetic field for varying electric currents.

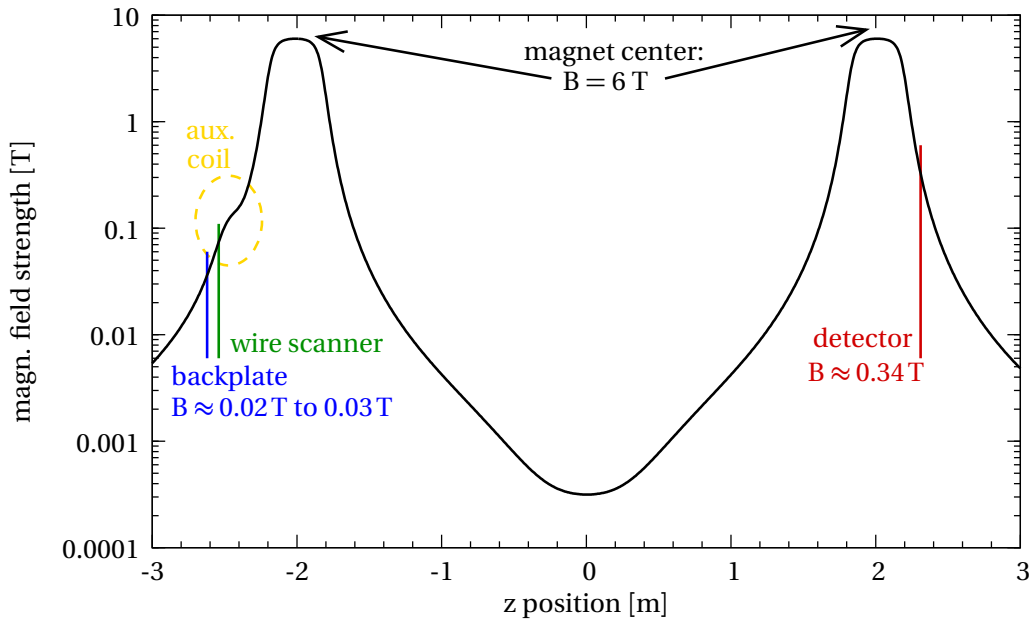


**Figure 6.7:** Simulated magnetic field strength on the  $z$  axis of the experimental setup. Settings for the magnet currents are the ones given in table 6.1 for an energy resolution setting of 1.55 eV at 18.6 keV. The influence of the auxiliary water-cooled coil (current: 100 A) is seen around  $z = -2.5$  m.

### Electrode configuration

Figure 6.1 shows the electrode setup of the Mainz spectrometer. The vacuum vessel is connected to ground potential, while the inner electrodes are provided with a negative high voltage. Apart from a set of cylindrical and conical sheet-metal electrodes, the Mainz spectrometer in its configuration “V” is also equipped with two wire electrodes which are briefly described in section 3.2: one is cylindrical and only covers the central part of the spectrometer surrounding the analyzing plane, the other one additionally possesses conical segments to provide almost a full coverage of the solid high-voltage electrodes. For the measurements presented in this work, however, all inner high-voltage electrodes were supplied with the same potential  $U_0$  (*i. e.*, no screening voltage was applied to the wire grids). Simulations show that in this configuration the radial variation of the retardation potential at the analyzing plane is small (see figure 6.9).

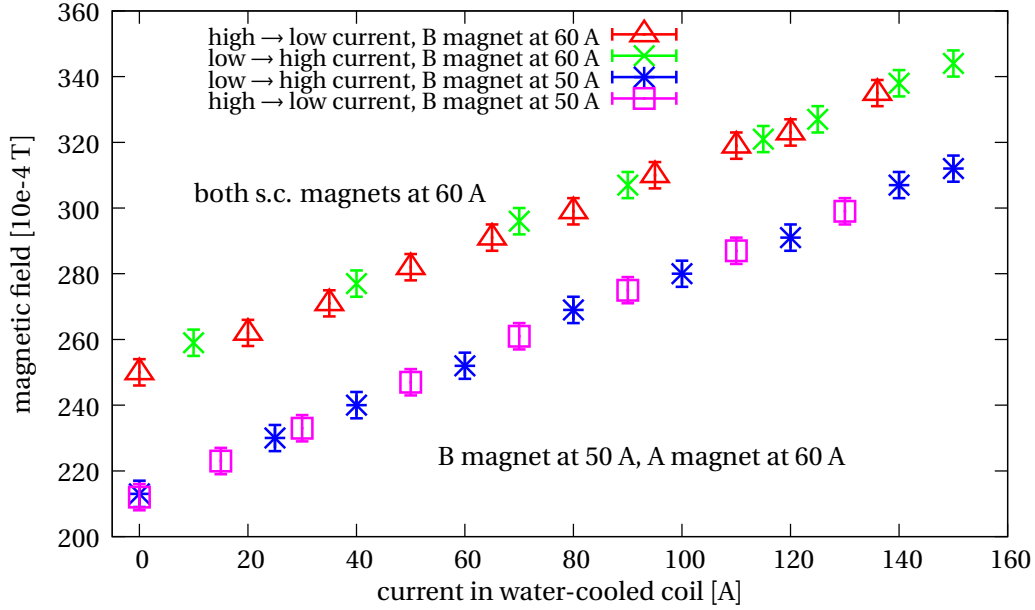


**Figure 6.8:** Influence of the additional water-cooled coil on the magnetic field strength at the center of the vacuum chamber, close to the position of the high-voltage backplate. The magnetic field strength was measured with a gaussmeter for various settings of the electric current in the water-cooled auxiliary coil ( $\times$  and  $*$ : increasing current;  $\Delta$  and  $\square$ : decreasing current). The upper two curves were measured with both superconducting magnets running at a current of 60 A, whereas for the lower two curves the current in magnet B (*i. e.*, the one closest to the wire scanner) was reduced to 50 A. The latter value was used for the Penning trap experiments described in this chapter.

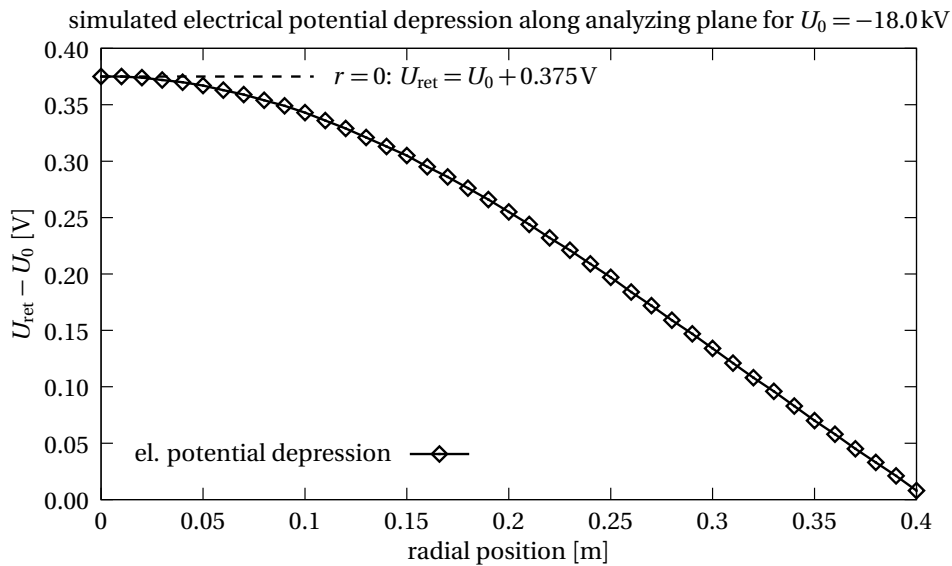


**Figure 6.9:** Simulated electric potential depression in the analyzing plane (*i. e.*, at  $z = 0$ ) of the Mainz spectrometer. A common potential of  $U_0 = -18.0$  kV was applied both to the solid and the wire electrodes. At any given radial position  $r < r_{\text{electrode}}$  the retardation potential  $U_{\text{ret}}(r)$  is slightly more positive than the potential supplied to the electrodes.

## 6.2.4 Methods of filling the trap

For the test measurements it would be desirable to have filling mechanisms with variable rates of electron injection in order to be able to study the characteristics of the Penning trap under varying conditions. Some artificial filling mechanisms that were explored for this purpose in addition to the “natural” background are described in the following.

### **Secondary electrons from electrodes originating from radioactive impurities, atmospheric muons, or environmental gamma radiation**

Electrons emerging from any electrode surface on high voltage can feed the trap. This comprises the retardation electrodes inside the MAC-E filter as well as the disc-shaped backplate electrode representing the mockup of the pre-spectrometer. As a “natural” or “given” background, this mechanism is permanently present. In contrast to various other methods described below, it cannot be switched on or off deliberately, and the possibilities to turn down the injection rate by external manipulation are limited.<sup>6</sup> The more “direct” contribution from the backplate deserves some extra consideration. Electrons can be liberated for example by atmospheric muons or environmental  $\gamma$ -rays hitting the plate, or by intrinsic radioactive impurities. Field emission from surface irregularities of the plate may also play a role, but it can be suppressed by suitable high-voltage conditioning. Due to the magnetic field lines crossing the plate electrons can be guided directly into the trap. This is the fundamental difference to electrons generated by the same mechanisms from the spectrometer electrodes: because of the magnetic screening effect they cannot enter the flux tube on a straight path. Drift motions perpendicular to the magnetic field lines are necessary in order to allow those electrons to reach the inner volume of the spectrometer, and eventually find their way into the trapping region.<sup>7</sup>

### **Thermionic emission from a hot filament mounted on the backplate**

A thermionic electron source was realized in a very simple manner. Figure 6.10 shows the filament attached to the front face of the backplate, a little off the center of the disc. The filament was heated by a variable current  $I_{\text{filament}} \leq 0.2\text{A}$  supplied by a battery. The current had to be controlled remotely because the whole system was on high voltage. Electrons from the filament were accelerated by the negative potential of the plate and magnetically guided towards the spectrometer. However, the thermionic method proved to be unfavorable as an electron source for the trapping measurements because of its large intensity. Furthermore, photons from the glowing filament might scatter onto the Si PIN photodiode used as electron detector (see section 6.2.5) and disturb the measurement. For these reasons the filament was switched on only for some initial tests, but was not used for the studies described in sections 6.3 to 6.4.

---

<sup>6</sup>In the case of the background coming from the spectrometer electrodes, the screening wire grid principally provides a handle on the rate of electrons penetrating the inner volume from the outside. However, as explained above, this option was disabled by choosing to use a common electric potential for all inner electrodes of the Mainz spectrometer. For the electrons originating from the backplate no such suppression mechanism exists.

<sup>7</sup>Investigations of the secondary yield from  $\gamma$ -irradiation of a metal surface were carried out in the work described in [Scha01]. A correlation between the flux of atmospheric muons traversing the Mainz MAC-E filter and secondary electrons observed at the detector was found in [Schw04], and a recent investigation of the muon-related electron yield from metal surfaces on high voltage was carried out in [Arl09].

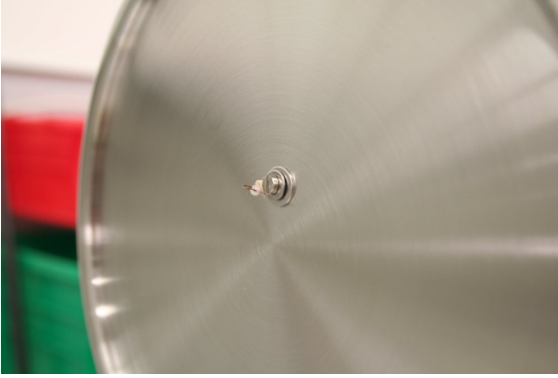


**Figure 6.10:** Close-up on the central region of the backplate electrode with the filament for thermionic production of electrons.

### Photoelectrons from UV light irradiating the backplate

One of the windows in the vacuum chamber housing the high-voltage electrode (backplate) was used to irradiate the electrode with UV light in order to generate photoelectrons (see figures 6.2 and 6.11). Only photons with an energy in excess of about 4.4 eV [Pic92a] are able to eject electrons from a stainless steel plate via the photoelectric effect. Two types of UV light sources with sufficiently short wavelength were investigated in this work:

- A Nd:YAG laser (type Quantel Brilliant [Qua08]) with a main wavelength of  $\lambda = 1064$  nm was equipped with a frequency-quadrupling module, reducing the emitted wavelength to  $\lambda_{4\omega} = 266$  nm. This pulsed laser system<sup>8</sup> proved to be too powerful to generate photoelectrons in a controllable manner. The nominal energy output per pulse is 360 mJ at  $\lambda = 1064$  nm or 40 mJ at  $\lambda_{4\omega} = 266$  nm, and the built-in attenuator was not sufficient to reduce the output power level to a practical value. An insertion of additional attenuators was technically difficult to realize.
- Instead, deep-ultraviolet light emitting diodes (deep-UV LEDs, Seoul Semiconductor, types T9B25C and T9B26C [Seo06b, Seo06a]), that were introduced to commercial markets a few years ago, were employed to produce controllable amounts of photoelectrons.<sup>9</sup> Figure 6.11 illustrates this method. The major advantage of this particular technique is that the flux of photoelectrons can be easily adjusted over a wide range by choosing a pulsed UV emission with variable settings of
  - a) the pulse width  $\tau$  of the UV emission,
  - b) the repetition rate  $f$  of the UV emission (or, equivalently, time interval  $\Delta t$  between successive pulses), and of
  - c) the current  $I_{\text{LED}}$  through the UV LED (tunable via the applied voltage  $U_{\text{LED}}$ ).

The photoelectron flux is constrained by the limited optical power of the LED which is of the order of  $P_{\text{opt}} \lesssim 400 \mu\text{W}$  and the duty cycle<sup>10</sup> allowed for long-term operation. Typical values used in the studies presented here are

$$\tau = (0.5 - 40) \mu\text{s}, \quad \Delta t = (0.1 - 1) \text{ms}, \quad I_{\text{LED}} \lesssim 100 \text{mA}. \quad (6.1)$$

<sup>8</sup>repetition rate 10 Hz, pulse width 5 ns

<sup>9</sup>For a detailed discussion on the production of photoelectrons from stainless steel using a deep-UV light emitting diode see chapter 7.

<sup>10</sup>According to the data sheet [Seo06a] a pulsed forward current of 100 mA is acceptable for a duty cycle of 1% at a repetition rate of 1 kHz.

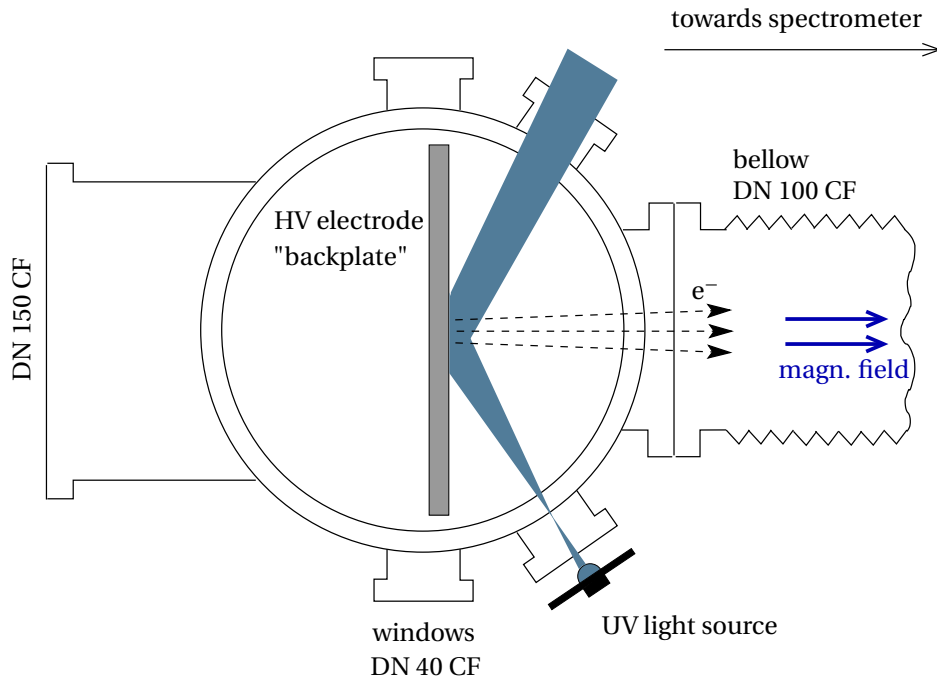


**Figure 6.11:** Sketch of the irradiation of the backplate with UV light from a UV LED. The schematic diagram (dimensions are not to scale) shows the top view of the vacuum chamber housing the disc-shaped high voltage electrode of diameter  $D = 180\text{mm}$  and thickness  $d = 10\text{mm}$ . The chamber is attached to the spectrometer via a bellow, indicated on the right-hand side of the drawing. Two of the four windows are made of UV-transparent material (sapphire and Suprasil<sup>®</sup>, respectively) and thus allow to shine UV light from an external light source onto the electrode disc. Photoelectrons created at the stainless steel cathode will be accelerated by the strong electric field and guided by the magnetic field through the bellow towards the spectrometer.

### Secondary electrons from X-ray bombardment of parts of the electrode system

A mobile X-ray source<sup>11</sup> equipped with a narrow lead collimator was employed to irradiate selected parts of the electrodes in order to produce secondary electrons. The beam was directed for example at the central section of the spectrometer or through the backplate. For calibration purposes the X-rays were also targeted directly at the detector chamber.

Since measurements with natural background and photoelectrons from UV light were successful, no systematic studies with secondary electrons from X-rays as the main trap-filling mechanism were carried out and the X-ray method was merely used to adjust and calibrate the apparatus (*e. g.*, to find suitable settings for the air coil currents).

## 6.2.5 Electron detection, data acquisition, and high-voltage system

### Detector and data acquisition

For the experiments described in this chapter the multi-segment detector originally installed at the Mainz spectrometer (see, for example, [Thü07]) was replaced by a windowless, single-pixel silicon PIN photodiode of type S3590-06 (Hamamatsu Photonics). The diode offers a sensitive area of  $9 \times 9\text{mm}^2$ . Some of its characteristics are listed in table C.1 in the appendix. The detec-

<sup>11</sup>Smiths Heimann Hi-Ray 7 casing with X-ray tube type Svetlana 0.32BPM 35-160 (tungsten anode), maximum operating voltage 140kV at 1 mA.

tor was installed on a movable sleigh, allowing to adjust its position along the beam axis of the experiment. During normal measurements the detector was situated in a magnetic field of about 0.34 T, at a distance of about 300 mm from the center of the second spectrometer solenoid (compare figure 6.7). For the second part of the 2008 measurement phase, however, the detector sleigh was modified in order to allow a positioning of the detector closer to the magnet center, at about 240 mm distance, in a higher magnetic field of about 0.94 T.

The signal from the PIN diode was fed to a charge-sensitive pre-amplifier [Schr90] and a spectroscopy amplifier before being digitized and recorded. For the measurement phases in 2007 and 2008, different data acquisition (DAQ) systems were employed. In 2007, the parts of the existing DAQ of the Mainz neutrino mass experiment comprising an peak-sensitive analog-to-digital converter (ADC)<sup>12</sup> were used. However, the limited timing resolution of this ADC system and the associated software made it desirable to arrange for a faster and more flexible DAQ. In the 2008 measurement phase, a Flash-ADC (FADC) system<sup>13</sup>, which measured the pre-amplifier signals directly, was installed in parallel to the existing DAQ. This allowed to use the slower ADC system for standard applications of Penning trap and wire scanner measurements and the faster FADC system for spectroscopy measurements with short-pulsed UV photoelectron generation that are much more demanding in terms of time resolution. The latter application is not a subject of this chapter, but will be treated in chapter 7.

The pre-amplifier signals recorded with the Flash-ADC DAQ system were first digitally filtered, typically with lower and upper filter cutoff frequencies of 1 kHz and 1 MHz, respectively, and subsequently differentiated. A more detailed documentation of the signal processing and physics analysis of these FADC data can be found in [Arl09, Str09].

### Flux tube considerations

The diameter of the magnetic flux tube  $\Phi$  transporting electrons directly from the source on to the detector of a given size is governed solely by the ratio of magnetic fields at the detector ( $B_{\text{det}}$ ) and at the source ( $B_{\text{source}}$ ). For a circular active area of the detector with radius  $r_{\text{det}}$  the radius of the imaged flux tube at the source,  $r_{\text{source}}$ , can be calculated as follows:

$$\Phi_{\text{det}} = \Phi_{\text{source}} \quad (6.2)$$

$$\Leftrightarrow \frac{B_{\text{det}}}{B_{\text{source}}} = \frac{r_{\text{source}}^2}{r_{\text{det}}^2} \quad (6.3)$$

$$\Rightarrow r_{\text{source}} \leq r_{\text{det}} \cdot \sqrt{\frac{B_{\text{det}}}{B_{\text{source}}}}. \quad (6.4)$$

Some reference values for the maximum diameter of an on-axis, circular electron source which is projected onto a detection area with radius  $r_{\text{det}} = 4.5$  mm are listed in table 6.2. The effective source size depends on the current setting of the auxiliary coil as well as on the axial position of the detector,  $z_{\text{det}}$ .

This effective source size on the backplate  $A_{\text{source}}^{\text{backplate}} = \pi r_{\text{source}}^2$  can for example be compared to the area of the spot illuminated by the UV LED,  $A_{\text{UV-light}}^{\text{backplate}}$ . The latter can be estimated using the distance between the LED and the opening angle of the divergent beam:  $A_{\text{UV-light}}^{\text{backplate}} \approx 2 \text{ cm}^2$ , while  $A_{\text{source}}^{\text{backplate}} \approx 10 \text{ cm}^2$  for  $B_{\text{source}} = 0.021 \text{ T}$  and  $B_{\text{det}} = 0.34 \text{ T}$ . With good alignment of the UV LED,

<sup>12</sup>CAMAC Quad 8k ADC type Ortec AD413A [Ort08]

<sup>13</sup>SIS3301-105: 8-channel, 14 bit VME-based FADC system with 100 MHz sampling rate [Str08]

**Table 6.2:** Diameter of detectable magnetic flux tube at the position of the backplate (“source”) for different detector positions.

$z_{\text{det}}$ [m]	$B_{\text{det}}$ [T]	$I_{\text{aux.coil}}$ [A]	$B_{\text{source}}$ [T]	$2r_{\text{source}}$ [mm]	used in
2.31	0.34	0	0.021	36.2	2007, 2008
2.31	0.34	100	0.027	32.0	2007, 2008
2.24	0.94	0	0.021	60.2	2008 (second part)
2.24	0.94	100	0.027	53.1	2008 (second part)

therefore, all photoelectrons from the UV irradiation of the backplate were created inside the flux tube leading towards the detector.

### High-voltage system

Figure 6.12 shows a schematic overview of the high-voltage supply and measurement chain for the disc-shaped electrode and the spectrometer electrode system. The “backplate” was connected to a Knürr-Heinzinger PNC5 30000-5 power supply. To match the 20 V measurement range of the Fluke 8508A precision digital voltmeter, the backplate voltage was divided by a Julie Research Labs high-voltage divider (type KV-50) with a ratio of  $M_{\text{JRL}} = 1 : 5000$  and measured on one of the two inputs of the voltmeter. The second input was used for measurement of the spectrometer voltage. All high-voltage electrodes of the Mainz spectrometer were supplied with a single voltage provided by a F.u.G. HCN 140M 35000 power supply and scaled down for measurement by the KATRIN precision high-voltage divider (ratio  $M_{\text{KATRIN}} = 1 : 1972.5$ ), developed in [Thü07]. Thus, the high voltage settings  $U_{\text{plate}}$  for the backplate or  $U_{\text{spec}}$  for the spectrometer for a readout value  $U_{\text{DVM,readout1}}$  (or  $U_{\text{DVM,readout2}}$ , resp.) of the digital voltmeter are obtained by multiplying the readout value with the divider ratio  $M$ :

$$\begin{aligned} U_{\text{plate}} &= M_{\text{JRL}} \cdot U_{\text{DVM,readout1}} \\ U_{\text{spec}} &= M_{\text{KATRIN}} \cdot U_{\text{DVM,readout2}}. \end{aligned} \quad (6.5)$$

The ratios for the two dividers used in the measurements are listed in table 6.3.

**Table 6.3:** Divider ratio  $M$  of the JRL KV-50 high-voltage divider [Zbo07] and the KATRIN high-voltage divider [Thü07, Thü08]. The error of the JRL divider ratio corresponds to an uncertainty of 30 ppm. The uncertainty of the divider ratio for the KATRIN divider has been estimated to be 5 ppm since the last calibration at PTB<sup>14</sup> took place in as far back as November 2006.

year	JRL KV-50 1:5000 connector	KATRIN precision high-voltage divider 1:1972 connector
2007	1:(5000.10(15)) measured	1:(1972.49(1)) extrapolated since last calibration (2006)
2008	— no measurement available	1:(1972.50(1)) extrapolated since last calibration (2006)

<sup>14</sup>Physikalisch-Technische Bundesanstalt, Braunschweig, Germany

**Remark on high-voltage stability and precision of measurement**

The high-precision equipment listed above was used at the Mainz spectrometer for tests of the precision high-voltage divider, the condensed krypton calibration source (CKrS) and the rubidium-krypton source (RbKrS). Compared to the ppm-level stability and precision requirements regarding the retardation potential of the KATRIN main spectrometer, the requirements for the Penning trap experiments described in this chapter are modest. In principle, the potentials applied to the backplate and to the spectrometer do not need to be known to a precision better than about  $5 \cdot 10^{-5}$ . However, the voltage stability as well as the absolute calibration does play a role for the photoelectron studies presented in chapter 7, for which the same high-voltage equipment was used.

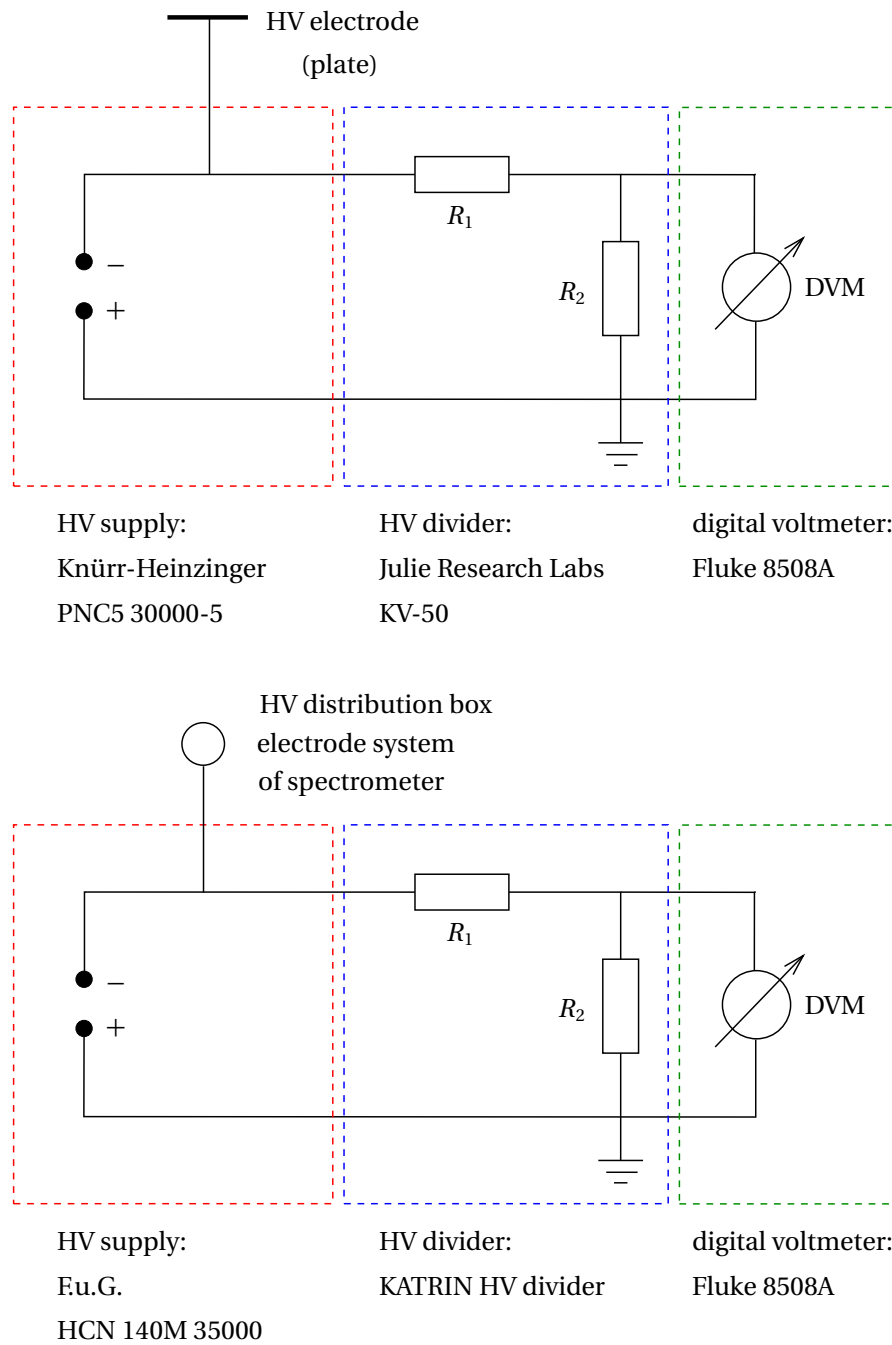


**Figure 6.12:** Schematic diagram: HV supply and measurement chain for the disc-shaped HV electrode used as a mockup of the pre-spectrometer (upper panel) and for the spectrometer (lower panel). In both cases the high voltage was scaled down to a range  $\leq 10\text{V}$  by a voltage divider and measured with a precision digital voltmeter. Only one voltmeter was necessary since the Fluke 8508A possesses two inputs (front and rear).

## 6.3 First measurement phase: proof of principle

The first measurement phase in 2007 showed that in the modified experimental setup at the Mainz spectrometer using the backplate on high voltage a deep Penning trap is indeed created, which manifests itself in an increase and destabilization of the detected background rate (section 6.3.1). Furthermore, it was possible to establish a positive influence of the wire scanner motion on the count rate (sections 6.3.2 and 6.3.3). Different modes of the wire scanner action were tested. The results can therefore be regarded as a proof of principle for the wire scanner mechanism.

### 6.3.1 Increased background rate caused by backplate on high voltage

Before describing more detailed investigations of the wire scanner and its influence, some general characteristics of the trapping system formed by the backplate and the spectrometer shall be pointed out. The most important one is the experimental finding that indeed strong discharges can be initiated in such a system, indicating that a trap has been filled. Without the regulating influence of the wire scanner, frequent and violent bursts in count rate were observed that often led to an automatic shutdown of the detector power supply due to an excess current.

Figure 6.13 shows a comparison of the count rate and the energy distribution measured for

- the background from the spectrometer only (spectrometer on high voltage, backplate at zero potential: figs. 6.13(a) and 6.13(b)), and for
- an increased background with both spectrometer and backplate on negative high voltage (but  $U_{\text{plate}} = -18600\text{V} \approx U_{\text{spec}} + 2\text{V}$  slightly more positive, such that no direct transmission of electrons through the spectrometer is expected: figs. 6.13(c) and 6.13(d)).

In both cases, the wire scanner was turned out of the flux tube by applying a constant current. The fact that with the plate on high voltage the count rate is significantly larger than when no voltage is applied to it indicates that a trap has been filled which leads to an increased detection rate. In addition, the observed strong fluctuations of the count rate support this interpretation. While only the typical spectrometer background consisting of a small number of 18.6 keV electrons is visible in figure 6.13(b), the additional background caused by the backplate leads to a pronounced pile-up effect due to the short time differences between successive events (the timing resolution of the DAQ system is about  $50\mu\text{s}$ ). Therefore, electron peaks at twice and even three times the nominal electron energy (around 37 and 56 keV, respectively) become visible in figure 6.13(d), which correspond to 2 and 3 coincident electrons counted as one event. A possible explanation for this enhanced background rate with the plate on more positive high voltage than the spectrometer is discussed in section 6.4.1 (see p. 194).

### 6.3.2 Characteristics of the Penning effect without extra filling of the trap

One specific series of measurements was dedicated to an investigation of the background level of electrons from the plate with a potential  $U_{\text{plate}}$  more positive than the filter potential  $U_{\text{spec}}$  of the spectrometer:

$$\begin{aligned} U_{\text{plate}} &= -15000.41\text{V} \\ &\approx U_{\text{spec}} + 12.5\text{V} \end{aligned} \tag{6.6}$$

This potential difference of the order of 10 V means the trap is rather symmetric, with about the same electric potential at both sides. Even if the slight radial depression of the retardation potential in the analyzing plane of the spectrometer (about 0.375 V at  $U_0 = -18\text{kV}$ , see figure 6.9)

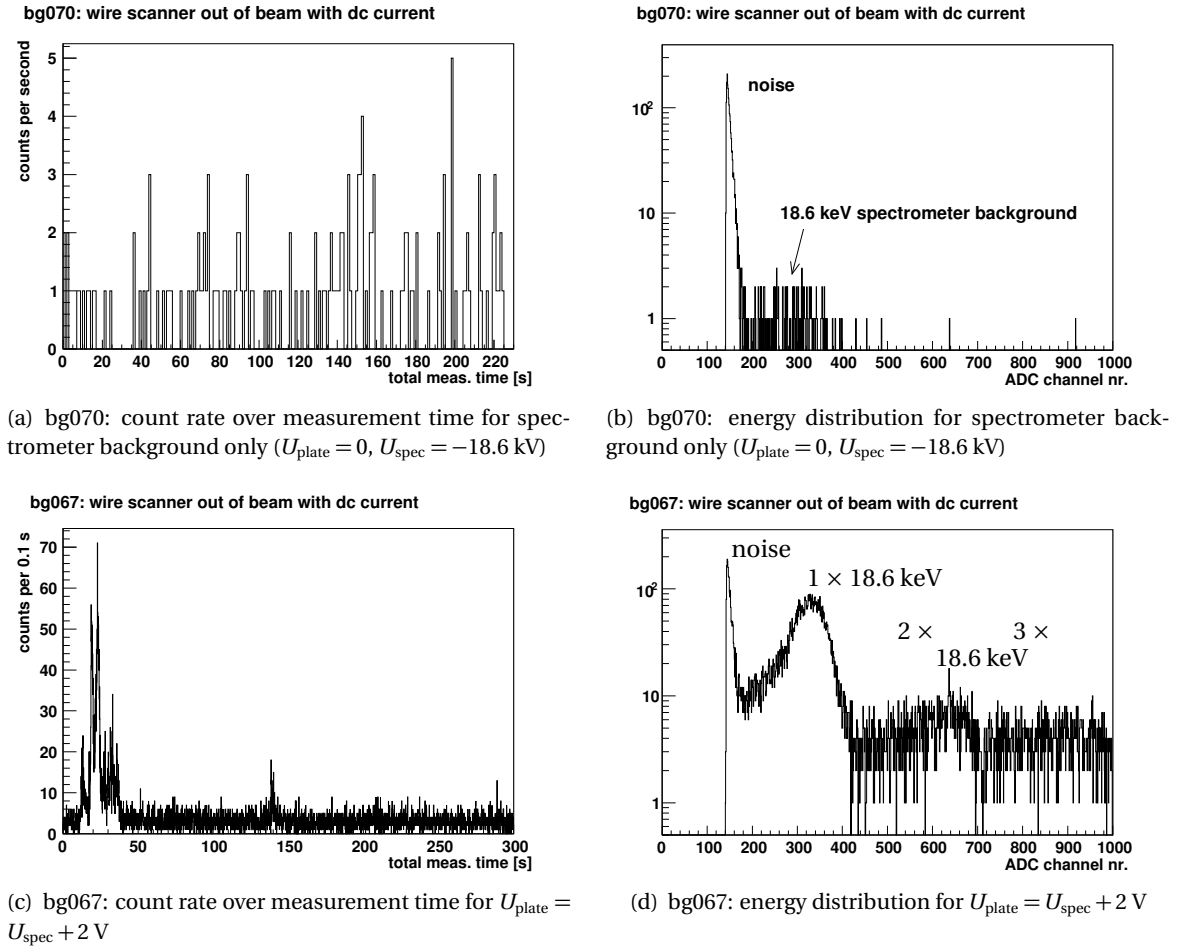


**Figure 6.13:** Count rate without and with high voltage on the backplate. In both cases the wire scanner was switched to one wall by applying a constant current; no extra feeding mechanism of the trap was active. (a) and (b): Backplate at zero potential leads to a count rate of about  $0.7 \frac{1}{\text{s}}$  after the noise cut, corresponding to the background originating from the spectrometer. (c) and (d): Count rate evolution and energy spectrum for a 300 s measurement with the plate potential about 2 V more positive than that of the spectrometer. Strong fluctuations of the count rate on top of a generally elevated level of 25 to  $35 \frac{1}{\text{s}}$  are visible. (Note the difference in the ordinate scale for (a) and (c).)

or measurement uncertainties of the relative voltage between spectrometer and plate are considered, one would expect that with these settings the bulk of electrons starting from the backplate will not be able to pass the retardation barrier directly. However, if the energy distribution of electrons starting from the plate possesses a pronounced tail towards higher energies ( $E \gtrsim 12.5$  eV), some electrons would be able to pass the electrostatic filter without contributing to the filling of the trap between the two negative potentials.

No additional electrons were injected (filament on the plate and UV light source both switched off). The residual gas pressure inside the spectrometer vessel was  $p_{\text{spec}} = 1.2 \cdot 10^{-9}$  mbar.<sup>15</sup> The magnetic field settings are summarized in table 6.4.

The wire scanner was driven by a sine wave (function generator Tektronix FG 502) with the fre-

<sup>15</sup>With the spectrometer vessel sealed by closed valves at both ends, the pressure was about an order of magnitude lower. Both the additional vacuum chamber housing backplate and wire scanner as well as the detector chamber had a considerably worse residual gas pressure with  $p_{\text{plate}} \approx 5.5 \cdot 10^{-9}$  mbar and  $p_{\text{det}} \approx 2.5 \cdot 10^{-8}$  mbar, respectively.

**Table 6.4:** Magnetic field configuration for the measurement of the influence of the scanner frequency on the count rate.

magnet	current [A]
s.c. solenoids A and B	50
aux. water-cooled coil	100
air coils 1 / 2 / 3 / 4	-19 / -8.8 / -19 / +5 ( $\Rightarrow \frac{\Delta E}{E} = \frac{1}{20000}$ )
xy-compensation coil 1	55
xy-compensation coil 2	20

quency being tuned in several steps from zero (scanner not moving at all) to 0.9 Hz. For the interpretation of the results it is important to note that the output frequency of the function generator corresponds to half the frequency of the actual wire scanner motion since the wire performs one forward and one backward sweep per period.

Table 6.5 gives an overview of the counts<sup>16</sup> measured in the 15 keV peak region (*i.e.*, summed over ADC1 channels no. 181 – 343) within a period of 600 s. Faster repetition rates of the scanner motion lead to significantly decreased count rates. In turn, the highest count rates are measured for a stopped wire scanner which is driven out of the beam range by applying a dc current. Figure 6.14 illustrates this dependency.

Figures 6.15 to 6.17 show the time structure of the 600 s runs.<sup>17</sup> Comparing the energy spectra for the “burst state” and the “quiet state” (see figure 6.18), one finds that the burst mainly increases the count rate within the signal window around 15 keV, but also produces some entries at higher channel numbers.

### Summary of observations

The following list presents results and conclusions from the measurements described above.

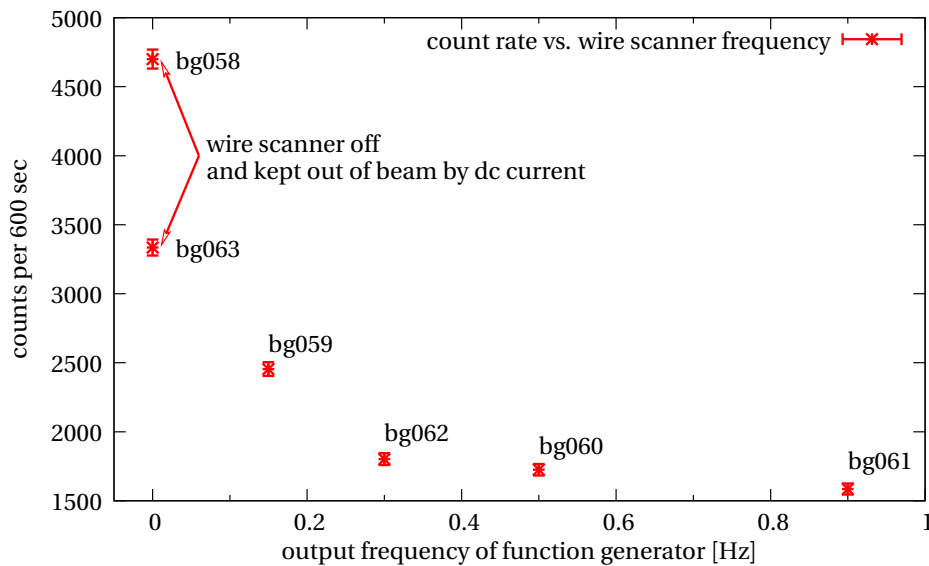
- The count rate is highest when the wire is driven completely out of the beam by a constant current. Similarly high rates occur when the wire is not provided with any current, that is, it is placed at an undefined position close to the axis.
- The number of total counts in the single-electron background peak decreases with increasing wire scanner frequency.
- The observed number of bursts as well as their duration and amplitude decrease with rising wire scanner frequency. A sine wave frequency of  $f = 0.5$  Hz or 0.9 Hz seems to be suitable to remove the bursts efficiently, whereas at 0.3 Hz some are still visible.
- Between bursts the count rate drops to a constant value of about  $2 - 8 \frac{1}{s}$  (above noise). This “background rate” is independent of the scanning frequency of the wire.
- The time between two successive bursts seems to be of the order of 20 – 100 s. The flare duration usually appears to be smaller than 5 – 10 s, but can be as long as  $\approx 30 - 40$  s in total,

<sup>16</sup>The numbers are meant to provide a rough estimate of the influence of the wire scanner only. In order to obtain more precise values of the count rate, the events showing up in the higher-order peaks (compare figure 6.13(d)) would have to be considered, as well, which was not done here.

<sup>17</sup>Due to a combination of dead time effects and a conversion process in the data analysis and processing chain, the differential times recorded for single events do not add up to a total measurement time of 600 s, but a little less than that.

**Table 6.5:** Sum of counts in the 15 keV peak (channels 181 – 343) as a function of the frequency of the wire scanner motion. No artificial filling mechanism was employed.

run #	output frequency of function generator [Hz]	count rate in peak per 600 s	comments
bg058	0	$4700 \pm 69$	wire to wall with dc current (1st measurement)
bg063	0	$3335 \pm 58$	wire to wall with dc current (2nd measurement)
bg059	0.15	$2454 \pm 50$	
bg062	0.30	$1802 \pm 42$	
bg060	0.50	$1725 \pm 42$	
bg061	0.90	$1585 \pm 40$	
bg064	0	$2182 \pm 47$	no current applied: undefined position
bg065	0	$4489 \pm 67$	no current applied: undefined position

**Figure 6.14:** Counts in background peak at 15 keV as a function of the frequency of the wire scanner motion. The difference in counts observed in the first (bg058) and second (bg063) measurement with dc current can be explained by frequent bursts in the count rate, see time spectra in figures 6.15 and 6.16.

disregarding the fact that longer bursts usually exhibit a considerable sub-structure.

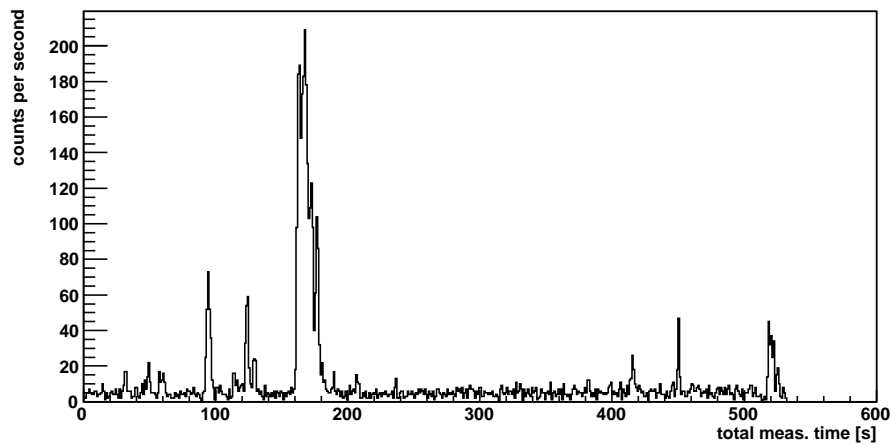
Thus, the underlying idea of the wire scanner has been demonstrated to work successfully by these first measurements. As expected, the action of the scanner helps to remove bursts in the count rate which are probably associated with the filling of the Penning trap. However, even under the influence of the sweeping motion the residual background rate is elevated with respect to the usual level without the plate on high voltage. This indicates that there is a continuous flow of electrons which is not related to the more irregular surges in the rate caused by the trap. The

increase of the rate during bursts is typically of the order of  $10 - 200 \frac{1}{s}$  when the wire scanner is either inactive or used with a slow sine motion only. For medium frequencies of the sine wave (about  $0.15 - 0.5 \text{ Hz}$ ) it amounts to about  $5 - 60 \frac{1}{s}$ . In contrast, the continuous or “pedestal” background exhibits a rate of  $2 - 8 \frac{1}{s}$ . It could be due to normal (not trapped) secondary electrons from the plate caused by cosmic rays or environmental gamma radiation. Remarkably, the pedestal background rate detected in this set of measurements is thus lower than the one observed with a smaller potential difference  $|U_{\text{spec}}| - |U_{\text{plate}}| \approx 2 \text{ V}$  in the run shown in figure 6.13(c). This might be a sign of higher-energetic electrons from the plate leaking through the energy filter at very small differences of the electric potentials of plate and spectrometer.

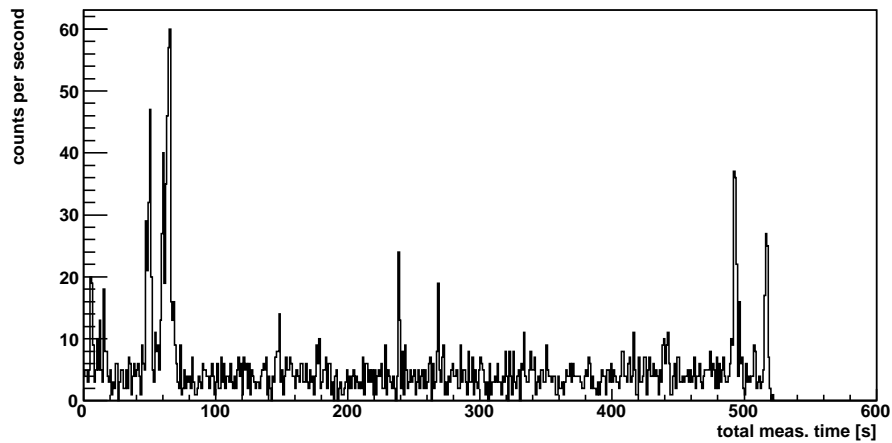
**Remark on electronic noise induced by the wire scanner in the rectangular mode**

A strong noise signal was detected during operation of the wire scanner with rectangular pulses. Part of the noise was still present when the valve between wire scanner and the spectrometer was closed. Therefore, it was concluded that the signal was produced to a large extent by the fast switching of the bipolar operational amplifier, with the current leads acting as antennae. Another source of excess noise could be related to the electric contact between the current loop and the walls of the surrounding bellow. Due to these problems the rectangular mode of the wire scanner was seldom used in the first measurement phase. In the subsequent phases, coaxial cables were used which provide better screening. Furthermore, the electric contact between the wire and the casing was avoided by a Kapton lining of the surrounding metal walls. Both measures helped to remove the initial problems, and the rectangular mode of operation was frequently used in the second and third phases in 2008.

bg058: wire scanner moved out of beam with dc current



bg059: wire scanner active, sine wave,  $f = 0.15$  Hz



bg062: wire scanner active, sine wave,  $f = 0.3$  Hz

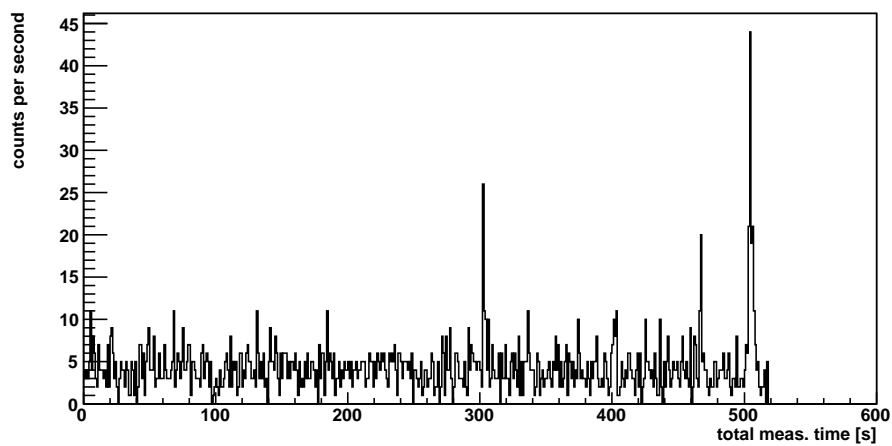


**Figure 6.15:** Count rate for varying sweeping speeds of the wire scanner (part 1): wire scanner removed from the beam by a dc current (top panel, run bg058), wire scanner driven by sinusoidals with frequencies  $f = 0.15$  Hz (central panel, run bg059) and  $f = 0.3$  Hz (bottom panel, run bg062). (Note the changing ordinate scale.) To cut out detector noise, events in all ADC channels below channel 180 (compare figure 6.18) have been discarded.

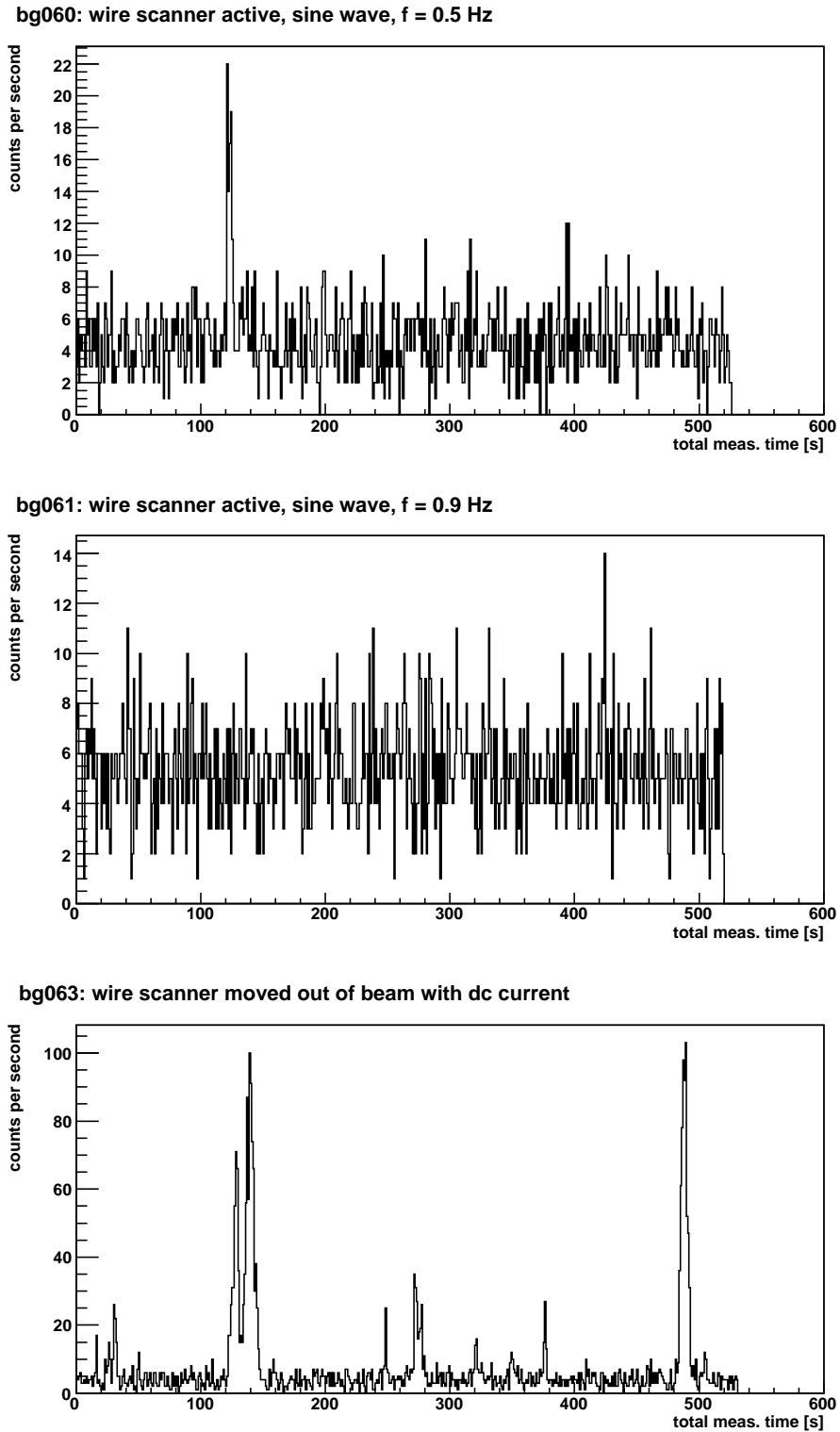
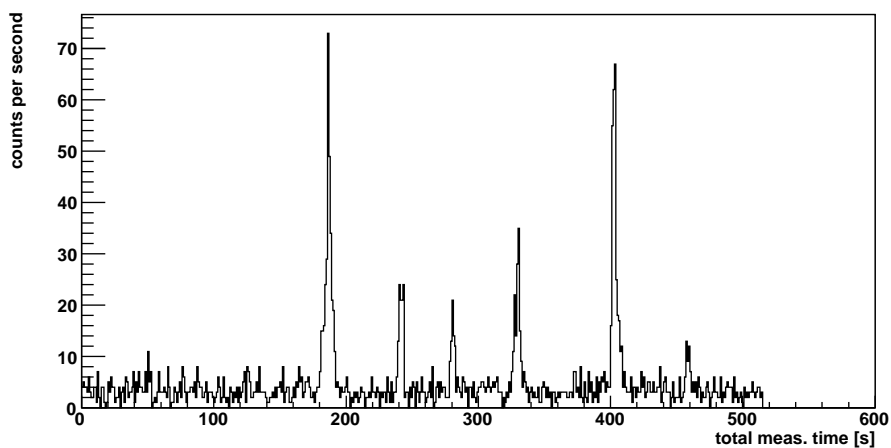


**Figure 6.16:** Count rate for varying sweeping speeds of the wire scanner (part 2): wire scanner driven by sinusoidals with frequencies  $f = 0.5$  Hz (top panel, run bg060) and  $f = 0.9$  Hz (center panel, run bg061), wire scanner removed from the beam by a dc current (bottom panel, run bg063). To cut out detector noise, events in all ADC channels below channel 180 (compare figure 6.18) have been discarded.

bg064: wire scanner without current (undef. position)



bg065: wire scanner without current (undef. position)

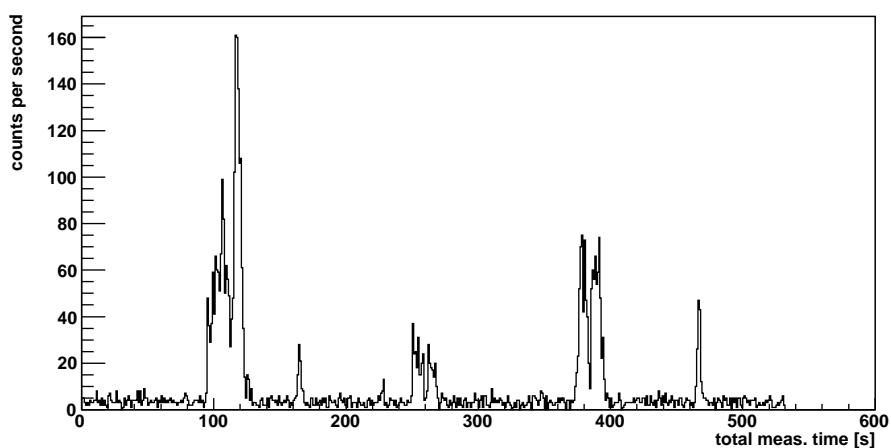


**Figure 6.17:** Count rate for runs bg064 and bg065 with the wire scanner stopped at an undefined position close to the center of the beam (see figure 6.3(a)) without any driving current. To cut out detector noise, events in all ADC channels below channel 180 (compare figure 6.18) have been discarded. Two successive runs of 600 s each were recorded in order to investigate the time scale of the variability. The ‘bursts’ are similar to the ones observed when the wire is driven out of the beam by a constant current and appear with a time constant of some minutes.

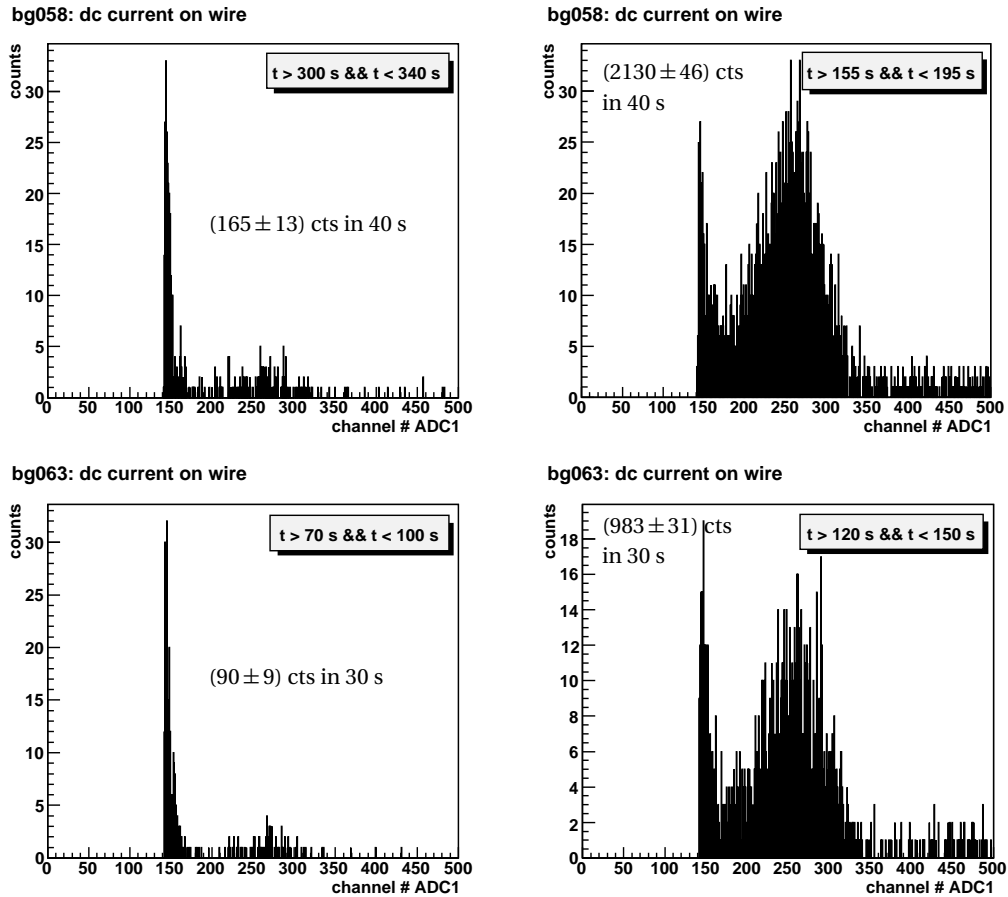


**Figure 6.18:** Energy distribution: comparison between quiet (left panel) and burst state (right panel). The two plots in the top row were generated for run “bg058”, the ones in the bottom row for “bg063”. In each, a period without bursts and an equally long one with strong bursts was selected. The number of events (evaluated in the energy window between channel number 180 and 350) is printed onto each histogram. The burst mode generates a large number of additional entries in the single-electron background peak and in the “multiple electron region” at channel numbers larger than 350.

### 6.3.3 Characteristics of the Penning effect with injection of photoelectrons

A new set of measurements similar to those described in the previous section was carried out, but this time additional electrons were injected into the trap by using the UV LED to create photoelectrons at the surface of the backplate. A pulse width of  $\tau = 12\ \mu\text{s}$  and a pulsing frequency of  $f_{\text{LED}} = 1\ \text{kHz}$  of the LED were employed. The magnetic field settings were the same as for the previous measurements (compare table 6.4). Again, direct transmission of electrons from the backplate through the spectrometer was prohibited by the high voltage settings:

$$\begin{aligned} U_{\text{plate}} &= -14988.88\ \text{V} \\ &\approx U_{\text{spec}} + 9.05\ \text{V}. \end{aligned} \tag{6.7}$$

Figures 6.19 and 6.20 present the evolution of the count rate over a measurement time of 100 s each for different operational modes of the wire scanner, analogous to the results shown in figures 6.15 to 6.17 for the measurement with “natural” feeding of the trap only.

Like in the previous measurements, the influence of the wire scanner in the sine mode results in a significant reduction of the overall rate (compare overview in table 6.6). There are several marked differences to the case without artificial injection of photoelectrons:

- No particularly strong bursts are observed. They rather stand back against an overall increase in the count rate due to the additional filling of the trap with photoelectrons created with the UV LED.
- Moreover, the wire scanner motion is seen as a direct modulation of the count rate, which was not the case at the much lower count rate in the previous investigations. When the scanner is driven out of the sensitive volume by applying a dc current, the rate exhibits a high degree of fluctuation (figure 6.20). The average rate of  $(1.1 - 1.4) \cdot 10^3\ \frac{1}{\text{s}}$  (see table 6.6) is about a factor of 200 higher than with the UV LED switched off. Interestingly, this average count rate roughly corresponds to the filling rate obtained with the UV LED (compare the remarks further below), but the peak rates observed are higher than the filling rate.
- This time, the current-free wire, which is stopped at a position close to the center of the beam, results in the lowest count rate of all runs. It is significantly smaller than in the case of the sine wave operation. This important observation will be picked up again in the final discussion (section 6.5).

The latter observation could be explained by the lack of reproducibility of the position of the wire scanner after the current is switched off. As can be seen in figure 6.3(a), the wire scanner model used in this first phase of the experiments had a rather flexible shape. Due to a deformation of the springs, in some cases it settled into a position tilted by a few degrees with respect to the beam axis. However, it was noticed that this “off position” changed during long-term operation of the scanner. Therefore, it is possible that the “off position” of the wire in the measurements with injection of photoelectrons was closer to the central beam axis – and the effect on the count rate thus more pronounced – than in the measurement with the UV LED switched off.

By using pulsed photoelectrons it was also possible to further investigate the question whether the majority of the events seen at the detector stems from trapped electrons or those passing the spectrometer directly by virtue of a small surplus energy with respect to the filter setting. Figure 6.21 shows the timing differences between successive events for two measurements, (a) with the wire scanner operated in a slow sinewave mode ( $f = 0.1\ \text{Hz}$ ) and (b) with the wire scanner driven out of the beam by applying a constant current. In both cases, the distribution of arrival time differences shows no correlation to the timing of the UV pulses. It is fundamentally different from

**Table 6.6:** Sum of counts in the 15 keV peak (channels 181 – 343) as a function of the frequency of the wire scanner motion. Photoelectrons were artificially filled into the trap by using the pulsed UV LED with a repetition rate of 1 kHz and a pulse width of 12  $\mu$ s.

run #	output frequency of function generator [Hz]	counts in peak per 100 s	comment
di010	0.1	$43150 \pm 208$	
di011	0.5	$8483 \pm 92$	
di016	0	$110849 \pm 333$	wire to wall with dc current (1st measurement)
di017	0	$142568 \pm 378$	wire to wall with dc current (2nd measurement)
di009	0	$747 \pm 27$	no current applied: undefined position close to the center of the beam

the case of directly transmitted electrons which is presented in figure 6.22(b), and its shape rather resembles that of a pure noise spectrum (figure 6.22(a)).

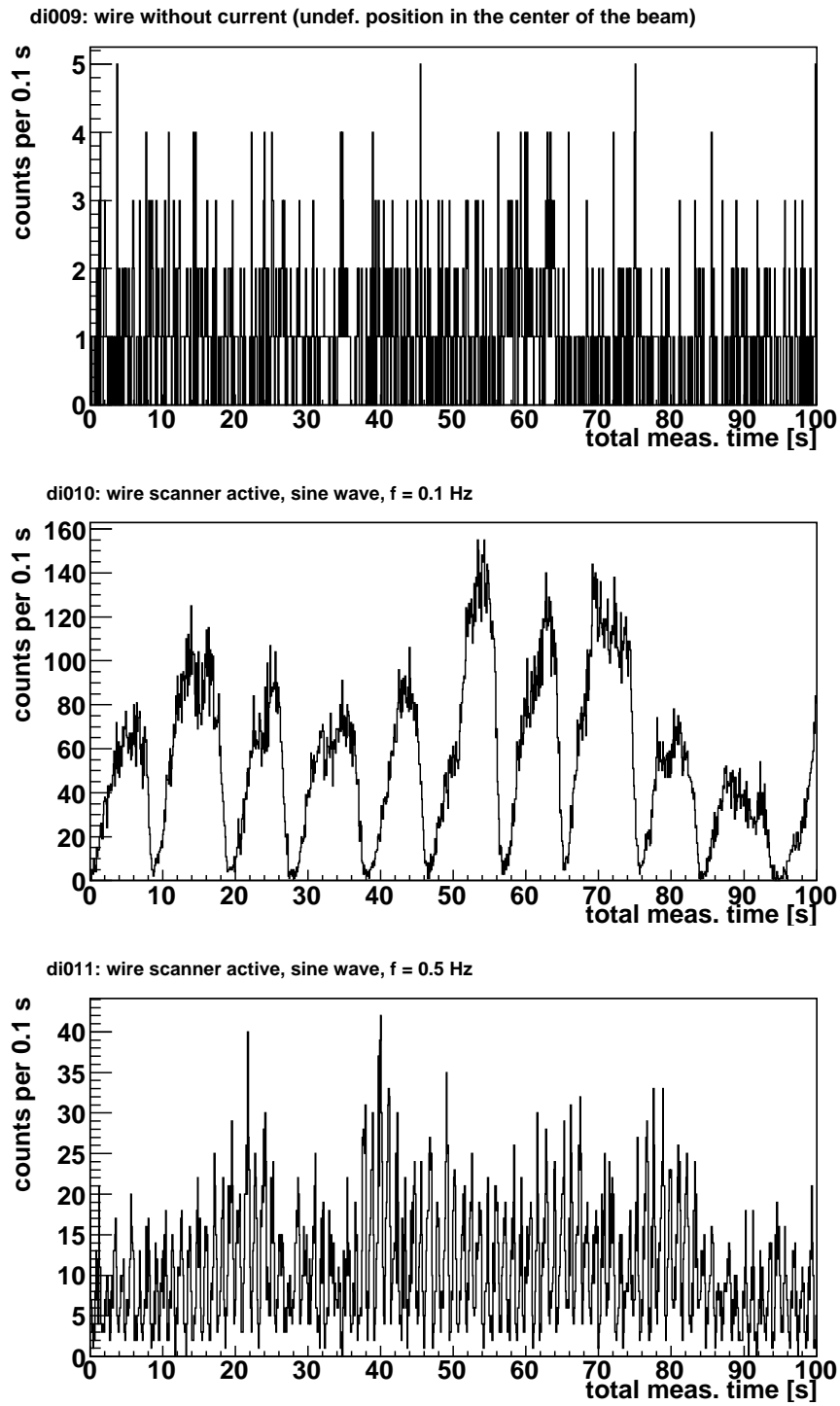
It is difficult to determine the rate of photoelectrons feeding the trap. A simple estimate can be obtained by setting the filter energy threshold of the spectrometer lower than the maximum kinetic energy achievable for a photoelectron starting from the backplate:  $qU_{\text{spec}} < qU_{\text{plate}}$ . Figure 6.23 shows a series of measurements where the potentials to the plate and the spectrometer were successively applied. The first plot, figure 6.23(a), represents the pure detector noise over a short measurement interval of 100 s. The corresponding spectrum of time differences, which was already presented in figure 6.22, demonstrates that no significant amount of UV light reaches the detector: if the measurement of photoelectrons were contaminated with UV photons, a series of peaks corresponding to the repetition rate of the UV LED should show up in the time differences. Even with the plate elevated to a potential of  $U_{\text{plate}} = -15$  kV (figure 6.23(b)), only a very small amount of photoelectrons is detected due to the fact that they pass the spectrometer ( $U_{\text{spec}} = 0$ ) with huge surplus energies. These cause strong losses resulting from non-adiabatic effects (compare the detailed discussion in [Thü07]). Figures 6.23(c) and 6.23(d), finally, show that a large number of photoelectrons is indeed detected when  $U_{\text{plate}}$  is set to a potential 150 V more negative than  $U_{\text{spec}}$ . The energy spectrum exhibits multiple peaks, since the timing resolution is not sufficient to separate all events. Therefore, some of the electrons appear at two, three, or even four times the energy corresponding to the potential setting of the plate. The rate (above noise) averages at about  $1.1 \cdot 10^3 \frac{1}{\text{s}}$ , which means that a mean value of slightly more than one photoelectron per UV light pulse reaches the detector.<sup>18</sup> This number needs to be corrected for the multiplicity of the events showing up in the higher-order peaks: To obtain the rate shown in figure 6.23(d) each detected event was counted as one electron, but in fact all events in the second peak should be counted twice, those in the third peak have a weight of three etc. Applying this correction raises the average rate from  $1.1 \cdot 10^3 \frac{1}{\text{s}}$  to about  $1.4 \cdot 10^3 \frac{1}{\text{s}}$ , which can be assumed as the mean filling rate of photoelectrons injected into the trap when the retardation potential inside the spectrometer does not permit a direct passage of the electrons. It is important to note that this value of the filling rate is lower than the maximum rate detected during the trapping measurements (figure 6.20): among the highly fluctuating values, rates up to  $(3.5 - 4) \cdot 10^3 \frac{1}{\text{s}}$  (without taking into account the weight of the multiple peaks). Again, this observation gives evidence for an accumulation (and

<sup>18</sup>For further discussion of the photoelectron spectra exhibiting multiple peaks see chapter 7.

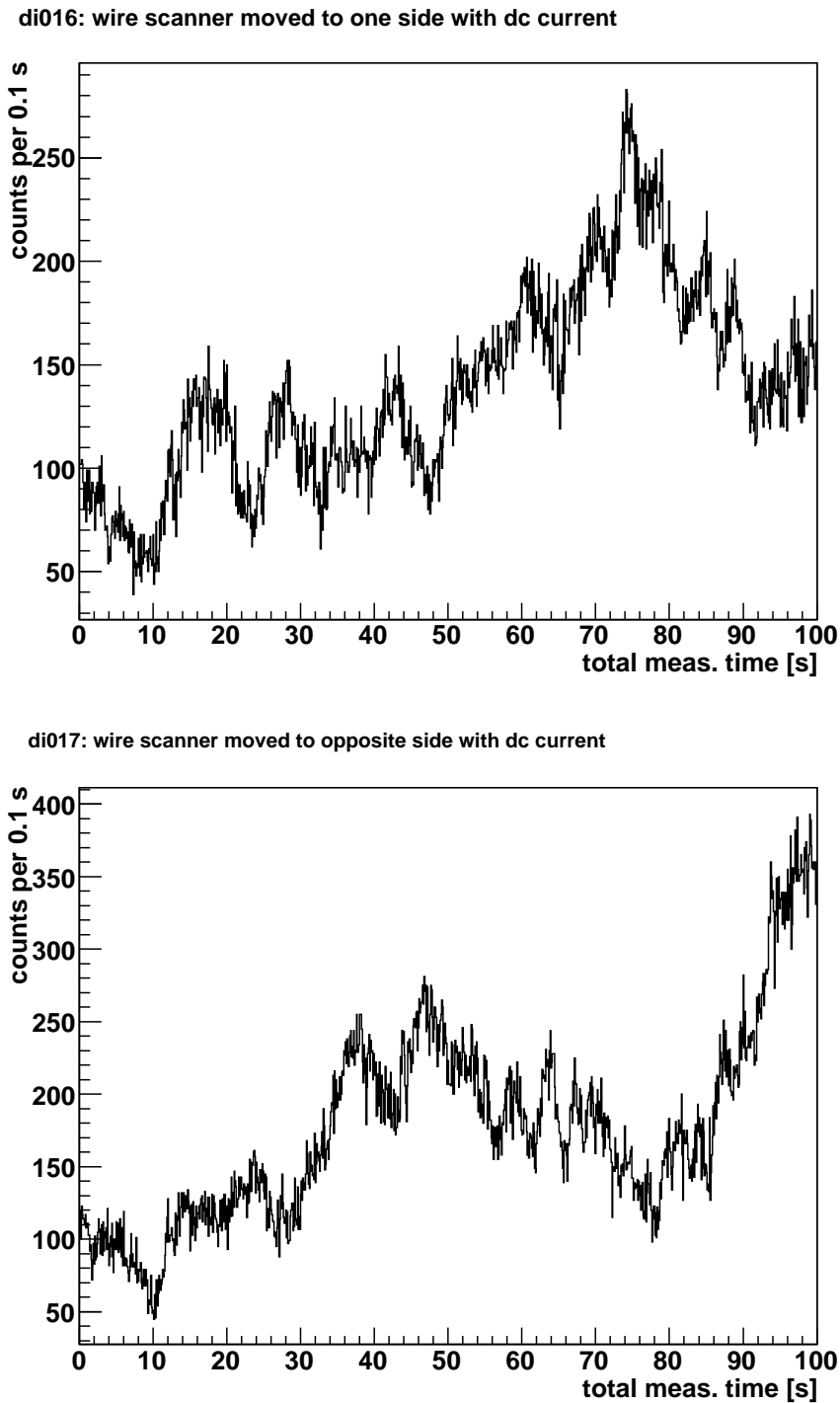
possibly also multiplication) of electrons inside the Penning trap, although in this case no strong discharges were observed.

In summary, the wire scanner proved to be a valuable instrument to counteract increased background rates which were shown to be related to trapping effects. A residual rate stemming from other sources could not be influenced by the scanner. Moreover, a reproducible and reliable method of filling the trap by photoelectron production off the backplate electrode was established.

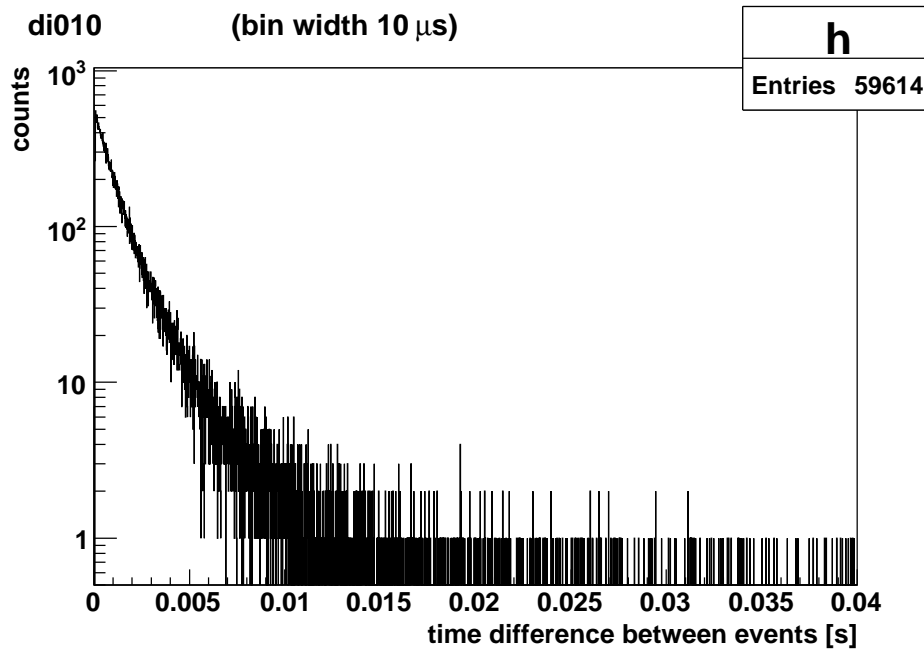
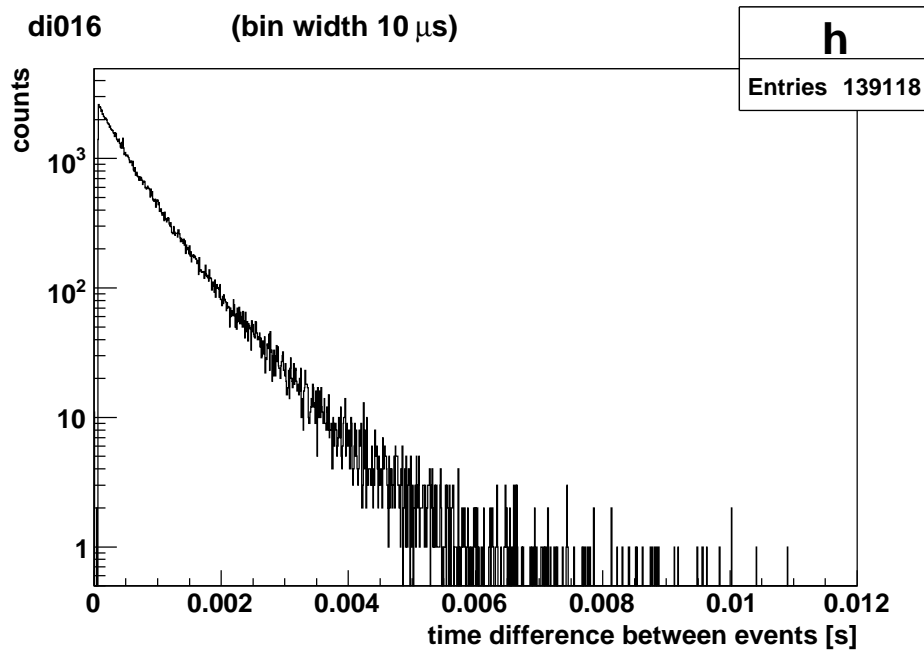
Although the mechanical construction of the scanning wire used in this first phase of measurements was operated many hours a day over a period of several weeks, some deficits of the setup were revealed (*e. g.*, lack of mechanical stiffness of the wire, noise problems in the rectangular mode of operation). Therefore, it was decided to resume the measurements after these initial problems were fixed. To achieve this aim, a redesign of the concept of the wire scanner was necessary. The results obtained with the modified setup in the second and third measurement phases are given in the next section.



**Figure 6.19:** Count rate (after noise cut) for varying sweeping speeds of the wire scanner, with UV photoelectrons as filling mechanism (runs di009, di010 and di011). Voltage setting:  $U_{\text{plate}} = -14988.88 \text{ V} \approx U_{\text{spec}} + 9.05 \text{ V}$ . The maxima and minima of the count rate observed for  $f = 0.1$  Hz and  $0.5$  Hz correspond to the outer and inner position of the wire, respectively.

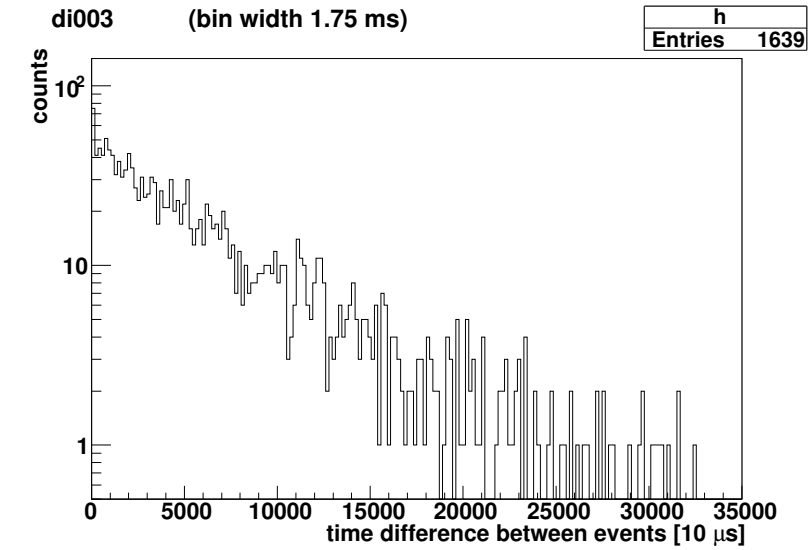


**Figure 6.20:** Count rate (after noise cut) with UV photoelectrons as filling mechanism in runs di016 and di017. Voltage setting:  $U_{\text{plate}} = -14988.88 \text{ V} \approx U_{\text{spec}} + 9.05 \text{ V}$ . The wire scanner was moved out of the beam with a dc current (first to one side for 100 s of measurement, then to the opposite side). High count rates of the order of  $1 \cdot 10^3 \frac{1}{\text{s}}$  to  $3.5 \cdot 10^3 \frac{1}{\text{s}}$  were observed. The timing of the events is not correlated to the time of UV emission at the LED (see figure 6.21).

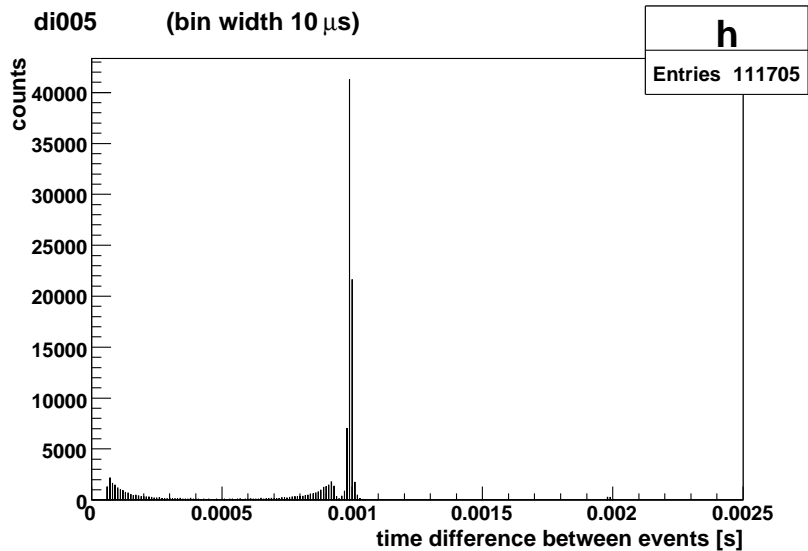
(a) run di010: wire scanner active, sine wave,  $f = 0.1$  Hz

(b) run di016: wire scanner kept out of the beam with a dc current

**Figure 6.21:** The spectrum of timing differences between successive events (after the noise cut) does not show a clear peak at the time difference between two pulses of the UV LED, as it is seen when the spectrometer is in transmission (figure 6.22(b)). This confirms that at  $U_{\text{plate}} \approx U_{\text{spec}} + 9.05$  V photoelectrons from the backplate do not pass through the spectrometer directly (as it would be expected for  $U_{\text{plate}}$  more negative than  $U_{\text{spec}}$ ). The electrons rather seem to get trapped and thus lose their timing correlation to the UV LED pulses.



(a) run di003:  $U_{\text{plate}} = U_{\text{spec}} = 0$



(b) run di005:  $U_{\text{plate}} = -15 \text{ kV}$ ,  $U_{\text{spec}} = -14.85 \text{ kV}$

**Figure 6.22:** Time difference between successive events for runs di003 and di005. (a) Noise signal without any voltage applied to either spectrometer or backplate. Measurement time 100 s, UV LED settings  $f = 1 \text{ kHz}$ ,  $\tau = 12 \mu\text{s}$ . No peak at the expected time difference  $\Delta t = 1 \text{ ms}$  corresponding to the kHz pulsing of the UV photons is seen. (b) In comparison, the photoelectron signal with a fully transmitting spectrometer ( $|U_{\text{spec}}| \approx |U_{\text{plate}}| - 150 \text{ V}$ ) shows a pronounced peak at  $\Delta t = 1 \text{ ms}$ . Peaks at integer multiples of  $\Delta t$  (e. g., at 2 ms and 3 ms) are also present, but they are strongly suppressed. In addition to the total rate shown in figure 6.23(d), this further supports the estimate that in this measurement the average number of photoelectrons detected per UV light pulse is close to one.

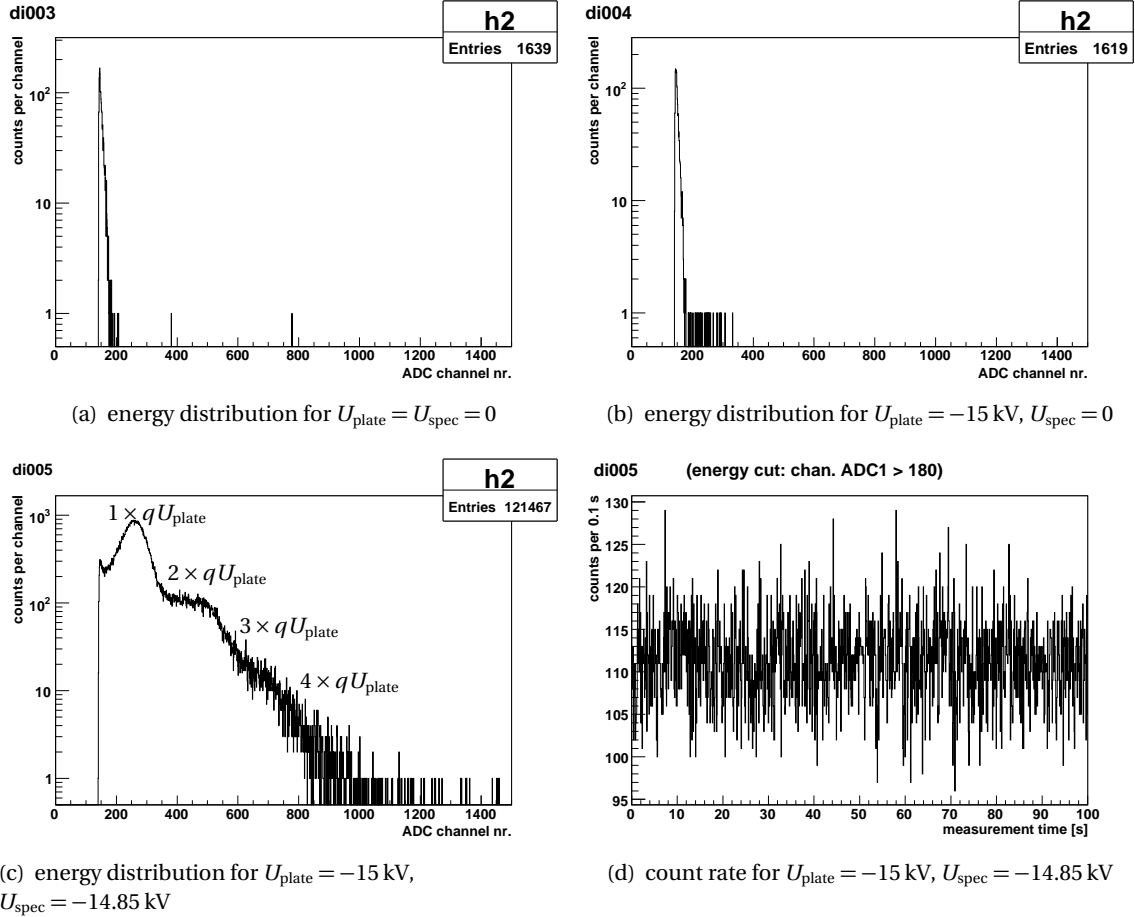


**Figure 6.23:** Irradiation of the backplate with pulsed UV light (pulse width  $\tau = 12 \mu\text{s}$ , repetition rate 1 kHz). (a) Noise signal without any voltage applied either to the backplate electrode or to the spectrometer. No significant photon signal from the UV LED can be seen (compare figure 6.22(a)). (b) Only the plate was supplied with high voltage. Therefore, electrons entering the spectrometer with energies of  $\sim 15 \text{ keV}$  see no retardation potential at all and suffer large transmission losses due to non-adiabaticity. (c) At  $U_{\text{spec}} = -14.85 \text{ kV}$  and  $U_{\text{plate}} = -15 \text{ kV}$ , electrons pass the filter with only about  $150 \text{ eV}$  of excess kinetic energy. Therefore, transmission losses are smaller than in (b). (d) The mean rate of photoelectrons reaching the detector corresponding to the settings in (c) is  $\approx 1.1 \cdot 10^3 \frac{1}{\text{s}}$ . This indicates that, on average, a little more than one photoelectron per UV light pulse is detected.

## 6.4 Second and third measurement phases: ignition and specific quenching of Penning discharges

After the first successful tests in 2007, the investigations were continued with a modified wire scanner device in 2008.<sup>19</sup> The aim was

1. to gather more systematic information on the relation between the discharges, which were frequently observed under varying conditions already in the 2007 phase, and the action of the wire scanner, and
2. to establish a fully and reliably working wire scanner prototype.

### 6.4.1 Observations from the second measurement phase

During this phase, the residual gas pressure inside the spectrometer vessel was about  $p_{\text{spec}} \approx (5 - 7) \cdot 10^{-10}$  mbar. Typical values for the backplate vacuum chamber and the detector chamber were  $p_{\text{backplate}} \approx 4.5 \cdot 10^{-9}$  mbar and  $p_{\text{det}} \approx 1.8 \cdot 10^{-8}$  mbar, respectively.

The electric potential difference between backplate and spectrometer was of the order of a few hundred volts, which corresponds to the nominal setting of pre- and main spectrometer during neutrino mass runs at KATRIN. Thus, the potential difference was much larger than the one used in the measurements described in sections 6.3.2 and 6.3.3. The spectrometer was set to high energy resolution,  $\frac{\Delta E}{E} = \frac{1}{20000}$  ( $\Delta E = 0.96$  eV at  $E = 18.6$  keV), The xy-correction coils were operated at the current setting  $I_{\text{comp.1}} = 20$  A,  $I_{\text{comp.2}} = 0$ , since at these settings the count rate of photoelectrons from the backplate was maximal.

Unfortunately, the trigger of the wire scanner motion was not logged during this series of measurements.<sup>20</sup>

The following list contains some of the observations that were made during this phase. In view of the large number of individual measurements, some of which were done to check the reproducibility of earlier runs, not all of them can be treated in detail here. Therefore, a description of the runs that are being referred to in the following can be found in appendix D.

- Strong discharges were seen when all of the following conditions were met:
  - asymmetric trap potentials with the backplate some hundred volts more positive than the spectrometer potential, typically  $U_{\text{plate}} = U_{\text{spec}} + 0.5$  kV
  - injection of photoelectrons into the trap, and
  - wire scanner active in rectangular mode, with about one sweep every 10 seconds.

The discharge usually starts after several minutes of constantly low count rate with a small increase which can be influenced by the wire scanner motion. However, the intensity of the discharge rises further, and the rectangular mode of the wire scanner is no longer sufficient to suppress it (compare figures 6.24 and 6.25). This state is typically reached on a time scale of about 15 to 25 minutes into the measurement (depending also on the history of previous measurements, in particular on that of the wire scanner operation).

- Due to practical reasons most of the runs were limited to 30 minutes of measurement time. In some cases the discharge would not start during this time, which indicates that the time scale of the discharge could be longer than 30 minutes.

<sup>19</sup>Regarding the changes made to the experimental setup, please refer to the overview given in section 6.2.2.

<sup>20</sup>The correlation between wire scanner motion in rectangular mode and decrease in count rate can, however, clearly be seen in a measurement from phase III shown in figure 6.30.

- There are several ways of reacting to a starting discharge:
  - a) Stop the filling mechanism by switching off the UV LED and in addition turn the rectangular wire scanner motion with large intervals into a fast sine wave motion with a slow crossing of the beam. The discharge subsides and the count rate stabilizes to the pre-discharge level after some minutes (see runs di018 and di019 in figures 6.24 and 6.25).
  - b) Switch to a more efficient wire scanner motion, *i. e.*, a fast sine wave, *without* turning off the UV LED. This was done for example in run di062 (not pictured, but see appendix D for a description), where the fast sine wave scanning motion was sufficient to prevent a detector shutdown and stabilize the count rate despite the continued feeding of the trap.<sup>21</sup> Remarkably, keeping the rectangular motion of the wire scanner and merely increasing its frequency (*e. g.*, from 0.1 Hz to 1 Hz) did not help to suppress or extinguish discharges.
  - c) Neither stop the filling mechanism nor switch the wire scanner to a more efficient sweeping motion. In such cases a dramatic surge in the count rate usually resulted in a safety shutdown of the detector, following a shutdown of both plate and spectrometer high voltages due to the intervention of an interlock system<sup>22</sup> of the power supplies (see for example run di064, appendix D).
- In particular, some runs were carried out without additional filling of the trap with photoelectrons, during which the discharge did not ignite. Possibly the time constants were too long to be observed in half an hour of measurement. In addition, the number of measurements was limited and thus the smallness of the sample does not permit to draw well-founded conclusions.
- In several attempts, no runs were found where a significant discharge would start while the wire scanner was active in sine mode (for example run di029, appendix D). This indicates that the wire scanner in sine mode prevents discharges from occurring, or at least increases their ignition time scale.
- The question whether the trap was filled with charged particles at all was investigated by abruptly lowering the potential barrier on the spectrometer some time after the artificial filling mechanism by photoelectron injection (UV LED) was turned off (see run di066, figure 6.26). The count rate instantly rises and stays at an elevated level for several minutes. The motion of the wire scanner is clearly seen as a modulation of the count rate, which indicates that the excess counts are indeed related to the region between the backplate and the scanner. Nevertheless, the long time constant of the slow decay of the rate is remarkable: even 5 minutes after emptying the trap through the spectrometer, the rate is still at an elevated level of about  $(15 - 20) \frac{1}{s}$ . It is possible that the discharge in the trap ignites only when the potential at the plate is more positive than that of the spectrometer, but once ignited, it is stable even with  $U_{\text{plate}}$  more negative than  $U_{\text{spec}}$ . The energy spectrum in figure 6.26(b) exhibits multiple peaks up to very high orders. This structure might be caused by positive ions which stem from ionizing processes of the trapped electrons. The ions impinging on the backplate can liberate many electrons per impact.

<sup>21</sup>Further examples of similar runs, although done without using artificial methods of filling electrons into the trap, are documented among the measurements of the third phase below.

<sup>22</sup>The pressure gauge at the spectrometer vessel provides two trigger outputs which can be used as an interlock signal. The interlock is triggered as soon as a certain pre-set pressure limit is exceeded. Usually, these triggers were set to pressure levels of  $p_{\text{spec, trig1}} = 6.5 \cdot 10^{-9}$  mbar for the plate high-voltage supply and  $p_{\text{spec, trig2}} = 9.5 \cdot 10^{-9}$  mbar for the spectrometer high-voltage supply.

**Possible explanation of the electron signal seen with  $U_{\text{plate}}$  more positive than  $U_{\text{spec}}$**

If the backplate is placed at an electric potential which is several hundred volts more positive than the retardation potential of the spectrometer, as in the measurements described in this section, the observed electron signal is not self-explanatory. It cannot be caused by simple transmission of electrons starting at the plate to the detector, as these clearly lack the energy necessary to pass the analyzing plane of the MAC-E filter. For the same reason, they also cannot come directly from the trapping region. A possible explanation is that positive ions created in the discharge inside the trap can enter the spectrometer, where they may generate a signal of secondary electrons at the detector in two ways:

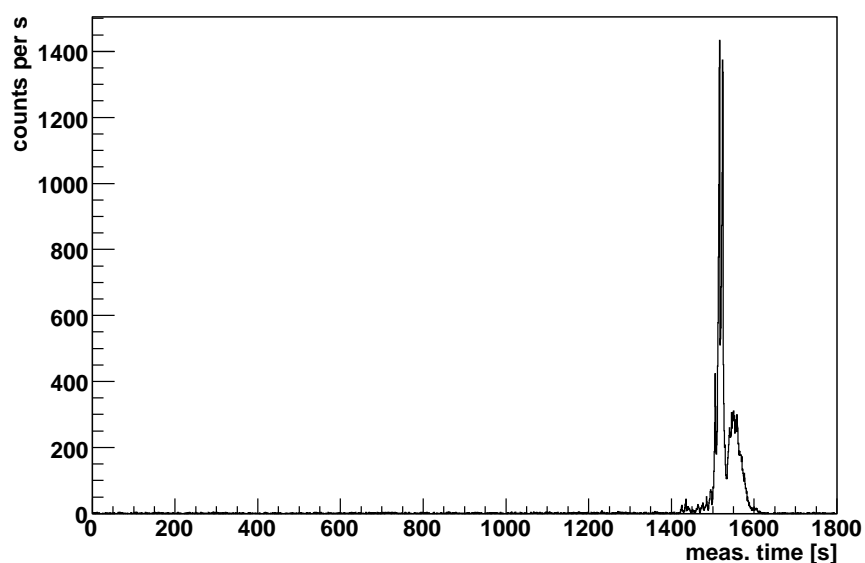
1. They undergo ionizing collisions with the residual gas, and part of the secondary electrons move on towards the detector.
2. They hit a cathode surface and there induce the emission of secondary electrons.

In both cases, however, the rate of detected electrons is expected to be significantly smaller than the production rate of positive ions: In the first scenario, the collision rate is small due to the good vacuum conditions. In the second case, the transfer of electrons from the cathode surfaces towards the detector must take place perpendicularly to the magnetic field lines and is thus suppressed by the magnetic screening effect discussed before.

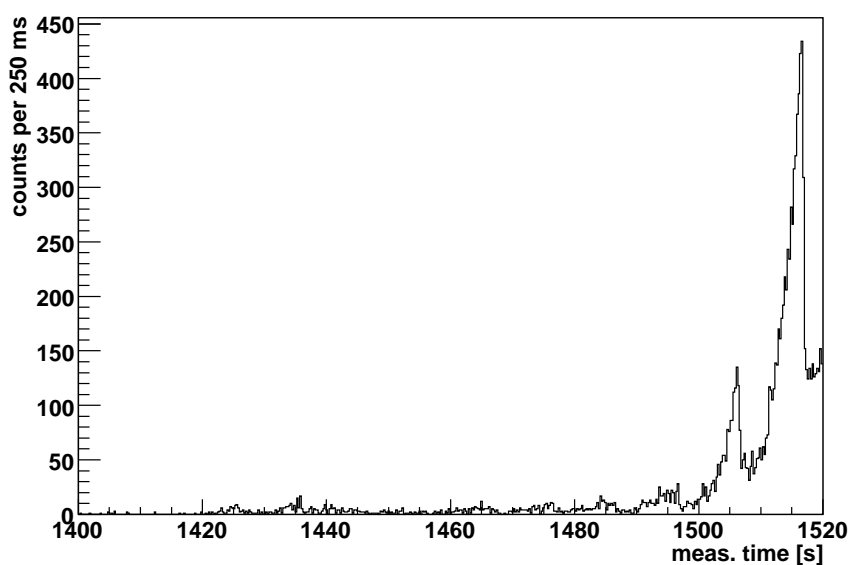
The wire electrodes installed at the Mainz spectrometer might prove useful in deciding which of the two processes dominates. In case the ion impact on the electrodes gives the larger contribution, a significant reduction due to a negative screening potential on the wires should be seen. The first process, on the other hand, is not affected by the grid potential.

Likewise, the signal from the first mechanism should increase if a magnetic field configuration with magnetic field lines directly linking parts of the electrodes with the detector is chosen. Enhancing the second type of process by increasing the residual gas pressure is more ambiguous, because it will also cause a stronger discharge apart from increasing the collision rate of ions and gas molecules inside the spectrometer.

Due to time constraints, however, such tests could not be carried out in the scope of the measurements described in this chapter.

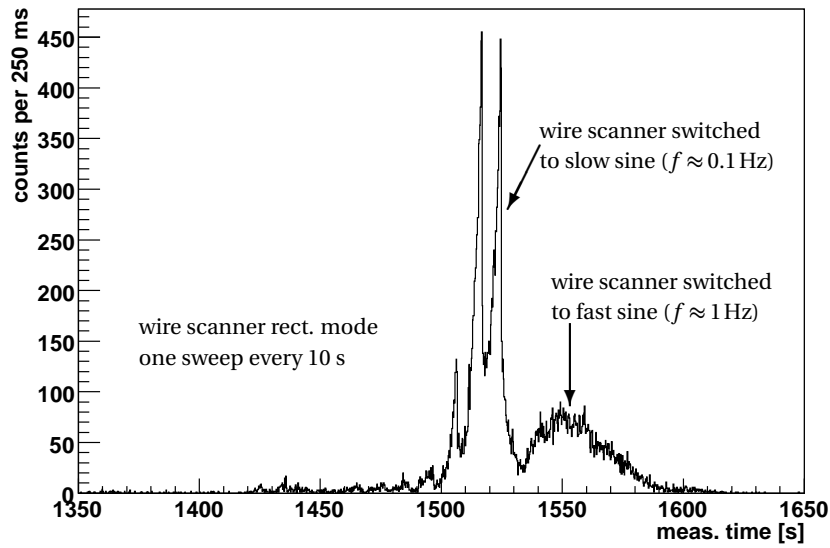


(a) count rate over full 1800 s measurement time

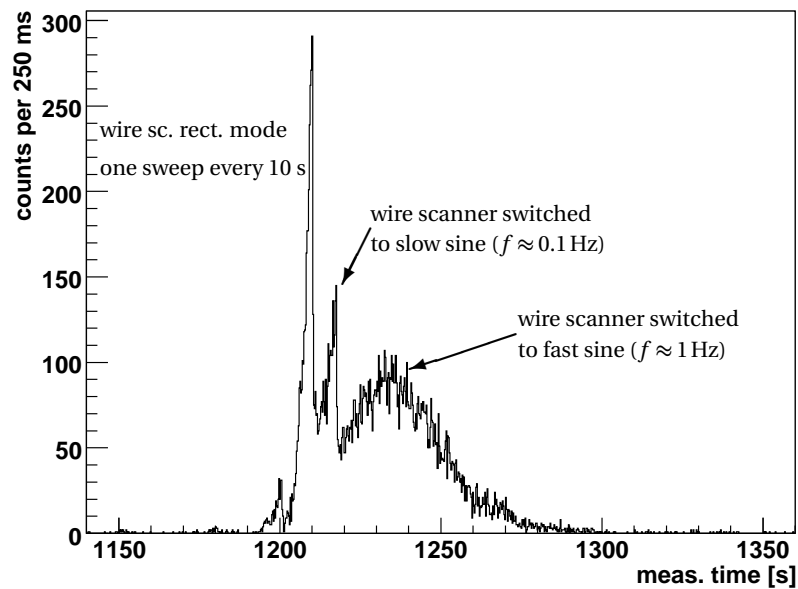


(b) close-up on the start of the discharge

**Figure 6.24:** Run di018: discharge ignition due to the Penning effect with wire scanner in rectangular motion (about one sweep every 10 seconds). (a) Evolution of count rate during the full measurement interval of 30 minutes. (b) Influence of the rectangular sweeps of the wire scanner at an early stage of the ignition. The main part of the discharge in this run is shown in figure 6.25(a).

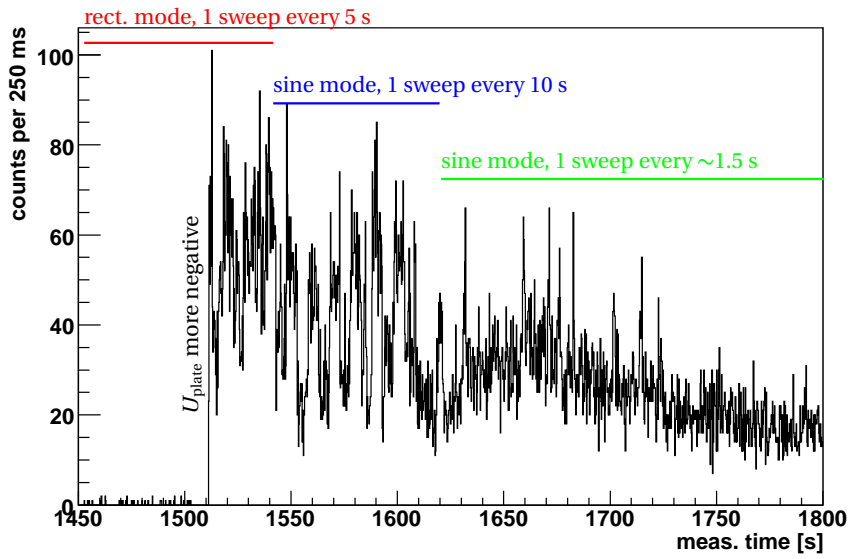


(a) run di018



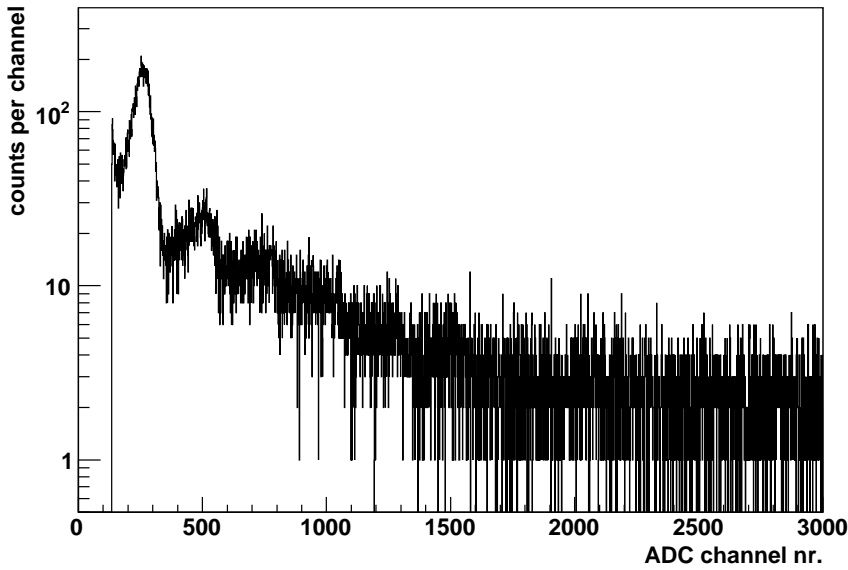
(b) run di019

**Figure 6.25:** Runs di018 and di019: evolution and specific quenching of discharges in two successive runs. In both cases the positive influence of the rectangular sweeps of the wire scanner is seen during the first moments of the starting discharge, but each decrease in count rate is of limited duration. Between two sweeps of the wire the count rate quickly recovers and eventually rises to even higher levels. The discharge is quenched successfully only by switching the wire scanner to a smoother and faster sine wave motion. In these two cases the artificial feeding mechanism was turned off simultaneously, which can have contributed to the quenching. However, the positive effect was also seen in other measurements (*e. g.*, run di062, appendix D) where the feeding mechanism was not turned off.



(a) close-up on start of particle release

energy ( $t > 1510$  s)



(b) energy spectrum for  $t > 1510$  s

**Figure 6.26:** Run di066: release of trapped particles through the spectrometer. (a) The run was started with  $U_{\text{plate}} = -17.5 \text{ kV} = U_{\text{spec}} + 0.5 \text{ kV}$  and the trap was fed by photoelectron production with the UV LED. The wire scanner was active in rectangular pulse mode, with one sweep every 10 s. At  $t_{\text{meas}} = 1470 \text{ s}$ , the UV LED was switched off. Up to this point, no discharge occurred. At  $t_{\text{meas}} = 1510 \text{ s}$ , the potential on the plate was quickly ramped to a more negative value than that of the spectrometer ( $U_{\text{plate}} = -18.11 \text{ kV}$ ). The prompt increase in count rate to over  $300 \frac{1}{\text{s}}$  indicates the release of a large number of particles from the trap that had not been able to pass the potential barrier inside the spectrometer before. After  $t = 1510 \text{ s}$ , the influence of the wire scanner is visible as a modulation of the count rate. (b) The energy spectrum for  $t > 1510 \text{ s}$  exhibits a broad structure with multiple peaks up to high orders, which may be due to positive ions hitting the backplate electrode.

### 6.4.2 Results of the third measurement phase

The measurements were resumed after minor modifications of the wire scanner. In contrast to the second measurement phase the investigations were done without feeding any electrons into the trap from artificial sources. Like in phase II, asymmetric trap potentials with the backplate voltage a few hundred volts more positive than that of the spectrometer were used. The spectrometer was set to an intermediate energy resolution of  $\frac{\Delta E}{E} = \frac{1}{12000}$  ( $\Delta E = 1.55 \text{ eV}$  at  $E = 18.6 \text{ kV}$ ). In the meantime, the detector position had been altered and therefore new current settings for the xy-correction coils were used:  $I_{\text{comp.1}} = 40 \text{ A}$ , and  $I_{\text{comp.2}} = 22 \text{ A}$ . The residual gas pressure in the spectrometer vessel was higher than in the previous measurement phase ( $p_{\text{spec}} \lesssim 1 \cdot 10^{-9} \text{ mbar}$ ), owing to the fact that the peripheral systems (backplate vacuum chamber and detector chamber) had been opened without properly baking them afterwards.

#### Discharge behavior with wire scanner in rectangular or sinewave mode

The potentials were set as follows:  $U_{\text{plate}} = -17.538 \text{ kV}$ ,  $U_{\text{spec}} = -17.893 \text{ kV} = U_{\text{plate}} - 0.355 \text{ kV}$ . Runs with a typical duration of the order of 10 minutes were carried out in order to check the time-variation of the count rate, particularly with respect to the occurrence of discharges and a potential influence of the wire scanner motion. In several runs, the wire scanner was operated first with rectangular pulses, *i. e.*, crossing the beam quickly and resting outside of the beam for a certain time span determined by the frequency setting of the function generator.<sup>23</sup>

Figure 6.27 presents the count rate as a function of measurement time for run “sc033” starting with a rectangular wire scanner motion of  $f = 0.3 \text{ Hz}$ . Over the first 4 minutes the count rate is stable at a few counts per second (above noise). During that time the energy spectrum resembles that of normal spectrometer background (figure 6.28). However, at about  $t_{\text{meas}} = 245 \text{ s}$  the count rate starts to rise significantly. The close-up in figure 6.29 shows that the wire scanner motion (indicated in the figure by markers for each trigger signal) cuts down on the count rate with every sweep, but the effect is not a lasting one. About 19 s after the first notable increase above background level (*i. e.*, at  $t_{\text{meas}} \approx 264 \text{ s}$ ), the count rate reaches  $9 \cdot 10^3 \frac{1}{\text{s}}$  in between two wire sweeps. The peak is reached at  $t_{\text{meas}} \approx 270 \text{ s}$  (figure 6.30).<sup>24</sup> It appears that the rate would keep on increasing and could no longer be controlled by a wire scanner moving in rectangular pulses. Therefore, the scanner motion was switched to sine operation, at first with the same frequency as the rectangular pulse before, and shortly afterwards to  $f = 0.5 \text{ Hz}$ . This way, the wire motion is smoothed out in time and it is able to disturb the trapping conditions with a longer duty cycle. The timeline of the three successive intervals of wire scanner settings is listed in table 6.7. Around  $t_{\text{meas}} \approx 350 \text{ s}$ , a low count rate level similar to that at the start of measurement is reached, and the run is stopped after a total time of 520 s.

In an earlier run (“sc032”, not depicted here) the discharge showed a very similar behavior; it started about 140 s into the run while the scanner was moving with a 0.3 Hz rectangular motion,

<sup>23</sup>Due to a mishap, the second channel of the arbitrary function generator AFG 3102 was broken halfway through the second measurement phase, and therefore the older model FG 502 had to be used to drive the wire scanner for the investigations discussed below. The frequency setting of the FG 502 in the low-frequency range is not as accurate as that of the AFG 3102, such that for example a setpoint of  $f = 0.3 \text{ Hz}$  corresponded rather to one full cycle completed in two seconds (0.5 Hz). This bears little relevance for the outcome of the measurements, but should be kept in mind when interpreting the results.

<sup>24</sup>The measured rate of  $\dot{n} \approx 1.5 \cdot 10^4 \frac{1}{\text{s}}$  needs to be corrected for dead time effects: there is some truncation of the true rate  $\dot{N}$  due to the limited data rate of the DAQ system. Assuming the rate is uniform over a short period of time around the peak value, a dead time of  $\tau_d \approx 50 \mu\text{s}$  leads to a significant correction and the true rate can be estimated as being four times the measured value:  $\dot{N} = \frac{\dot{n}}{1 - \dot{n}\tau_d} \approx \frac{1.5 \cdot 10^4 \frac{1}{\text{s}}}{1 - 1.5 \cdot 10^4 \frac{1}{\text{s}} \cdot 50 \mu\text{s}} = 4\dot{n}$ .

and was completely extinguished by fast sine wave sweeping motions ( $f_{\text{func.gen.}} \approx 0.5 \text{ Hz}$ ), just as in the case shown in figure 6.30.

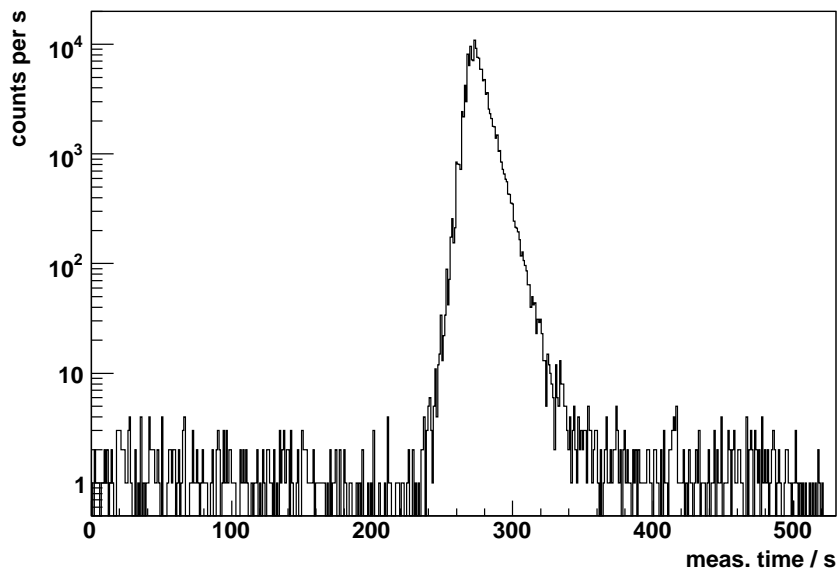


**Figure 6.27:** Run sc033: count rate during the complete 520 s run (after noise cut). After a quiet initial period with count rates of the order of few counts per second, during which the wire scanner is active in rectangular mode, a strong discharge starts at  $t_{\text{meas}} \approx 245 \text{ s}$ . The build-up of the discharge during the interval [245 s, 265 s] is documented in figure 6.29; the interval [250 s, 320 s] is presented in figure 6.30. The increase of count rate is stopped and even turned into a decrease after the wire scanner is switched into sine mode at  $t \approx 272 \text{ s}$  (compare table 6.7).

before discharge ( $t_{\text{meas}} < 235 \text{ s}$ )

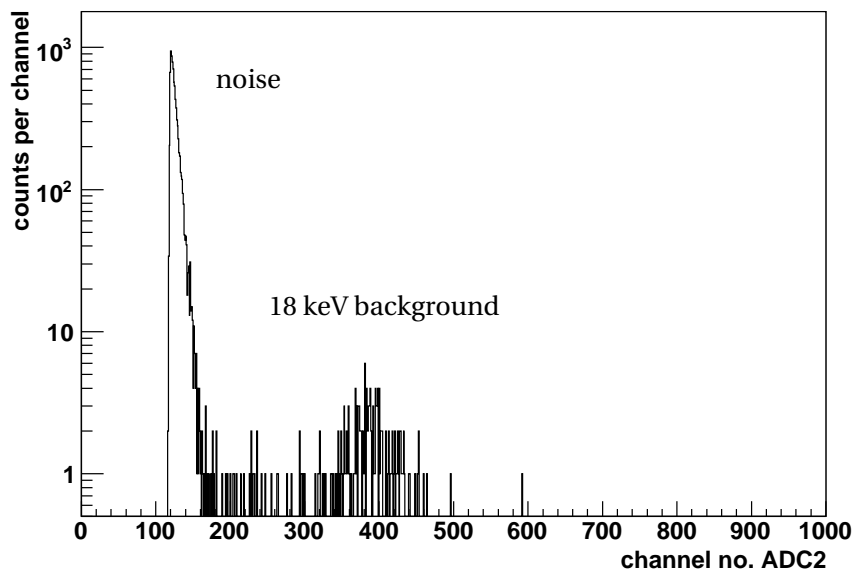


**Figure 6.28:** Run sc033: energy spectrum before onset of discharge. The 18 keV background peak contains about 200 counts for 234 seconds of measurement.

**Table 6.7:** Overview of different measurement intervals in run sc033.

meas. time interval	wire scanner motion	label in fig. 6.30
0 – 272 s	rectangular, $f \approx 0.3$ Hz	(a)
272 s – 277 s	sine wave, $f \approx 0.3$ Hz	(b)
277 s – end of run	sine wave, $f \approx 0.5$ Hz	(c)

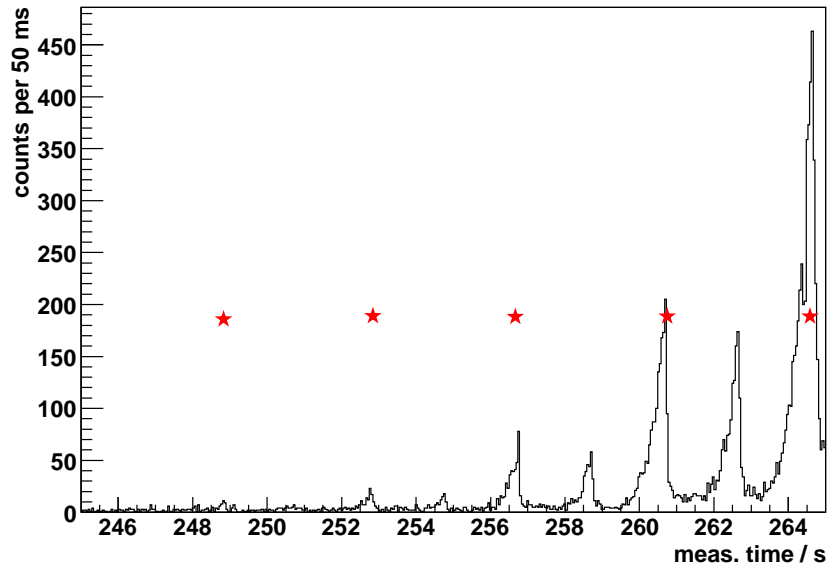


**Figure 6.29:** Run sc033: build-up of the count rate at the start of the discharge (bin width 0.05 s). The trigger signal for the rectangular pulse driving the wire scanner motion is indicated by red markers (★). Each trigger signal stands for a sweep of the wire in one direction; the backward sweeps are located inbetween two trigger signals and are therefore not shown here.

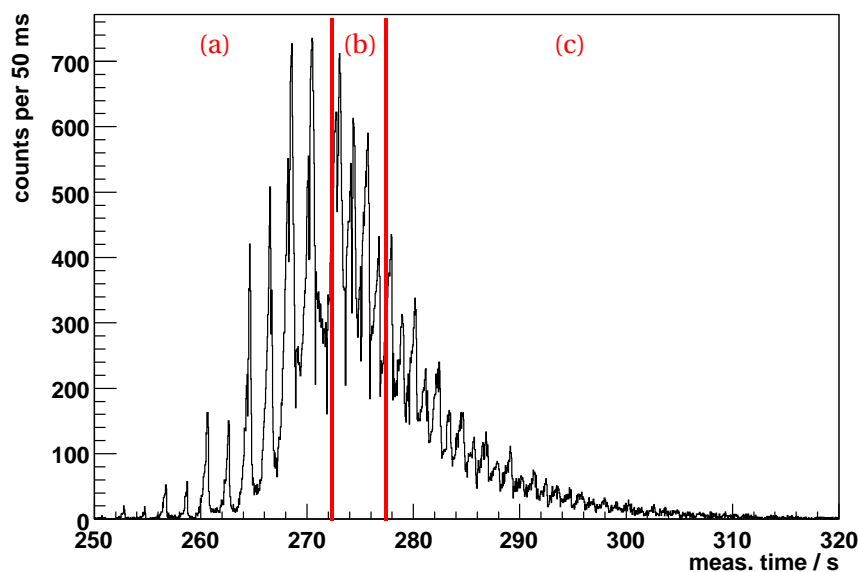


**Figure 6.30:** Run sc033: influence of wire scanner motion on count rate (after noise cut). The labels (a), (b) and (c) mark intervals with different wire scanner settings, see table 6.7.

#### Discharge behavior with wire scanner removed from the beam by a constant current

Figure 6.31 shows a measurement where the wire was kept out of the beam from the start by applying a constant current of  $I_{\text{wire}} = 5.5\text{A}$ . High voltage settings were the same as in the measurements documented in the previous paragraph. After only about 6.5 s, the count rate started

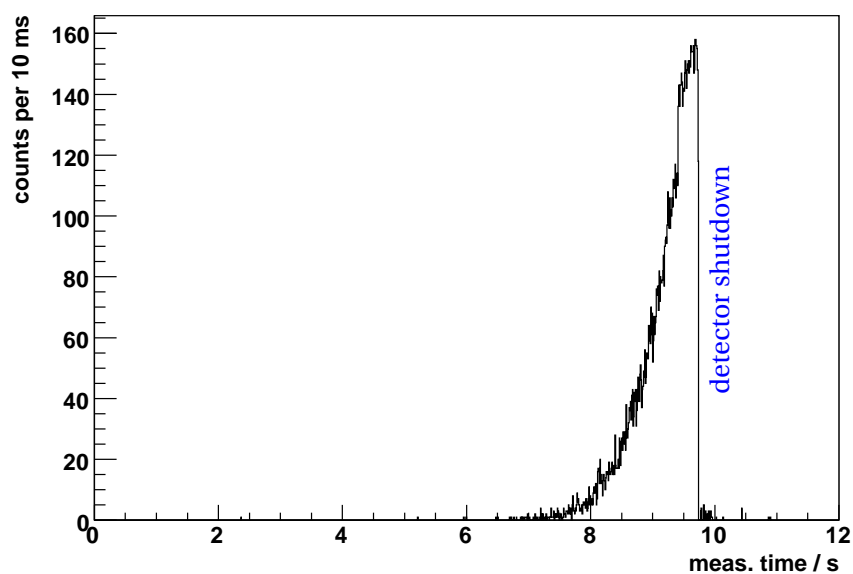


**Figure 6.31:** Run sc034: build-up of discharge without intervention of the wire scanner. After a quick rise of the count rate to about  $1.6 \cdot 10^4 \frac{1}{\text{s}}$  (limited by the data rate accepted by the DAQ system) the detector was automatically shut down at  $t_{\text{meas}} \approx 9.75\text{ s}$ .

to increase dramatically, reaching a level of about  $1.6 \cdot 10^4 \frac{1}{s}$  (uncorrected for dead time) within approximately 3 s. The detector was then automatically shut down for safety reasons. Without wire scanner, the behavior was thus fundamentally different from the previous case (runs “sc032” and “sc033”) where the wire scanner motion showed a clearly stabilizing effect. Not only was the discharge not halted or even stopped at a certain point, but the time scale of the onset of the discharge was significantly shorter than with the wire scanner active. This last observation might be related to the measurement history: the system had been used for a series of successive discharge tests previous to run “sc034”. However, drawing definitive conclusions from these observations is difficult, owing to the circumstance that (due to time constraints) this last experiment in particular could not be repeated within the same series of measurements after shutdown and recovery of the detector.

### Test of a stationary pin as electron catcher

While the scanning wire was removed from the setup during a maintenance period between measurement phases II and III, a stationary wire was inserted in its place (see figure 6.32).

This was meant as a test [Bon08] to see whether an immobile wire would be sufficient to stabilize the measurement conditions by virtue of the magnetron drift of trapped electrons (compare discussion in section 6.5) for two other projects, namely the study of pulsed photoelectron production presented in chapter 7, and an investigation of the correlation between atmospheric muons crossing the backplate and background electrons seen on the detector [Arl09]. A positive effect of the pin on the experimental conditions was observed, as the occurrence of bursts in the background count rate was significantly reduced (in amplitude as well as in frequency). Under the conditions discussed in section 6.3.3 the immobile wire scanner stopped at the center of the beam provided the largest suppression of the count rate variations (with additional filling the trap with photoelectrons). These preliminary findings, which are based on a smaller sample of measurements than the studies regarding the movable wire scanner, is certainly encouraging with respect to further, more comprehensive studies.



**Figure 6.32:** Stationary wire (no scanning mechanism provided) tested between the second and third wire scanner measurement phase at Mainz.

### Results of the second and third measurement phases

In conclusion, the second and third measurement phases have revealed more specific details regarding the influence of the wire scanner action on the ignition of Penning discharges in the system. It has been successfully shown that the operation of the wire scanner is suitable to prevent or significantly delay the onset of discharges, and to quench them after they already were initiated. However, the wire needs to spend a significant amount of time close to the center of the beam, which can for example be achieved by choosing a fast sine wave operation (*i. e.*,  $f = 0.5$  Hz or higher). In the extreme case, the electron catcher may possibly also be implemented as an immobile wire. In contrast, driving the scanner by rectangular pulses of for example a 10 second

time interval is in general not sufficient to prevent the eventual initiation of a discharge, at least under the experimental conditions of the test setup at the Mainz spectrometer with a residual gas pressure in the  $10^{-9}$  mbar region.

## 6.5 Discussion of results and application to KATRIN

The Penning trap between the two KATRIN spectrometers and the build-up of Penning-type discharges are indeed a problem regarding the background level seen at the detector. This assessment is founded on theoretical arguments supported by detailed computer simulations [Ess04, Glü08] as well as on experience gained at early stages of the Troitsk experiment which had a similar configuration using a pre- and a main spectrometer.

One option to avoid increased background due to this Penning trap consists in operating the pre-spectrometer at zero or very low negative electric potential<sup>25</sup>, thereby essentially removing the trapping conditions between the two spectrometers. From the point of view of neutrino mass sensitivity, switching off the high voltage of the pre-spectrometer does not pose a severe problem since the precision electron energy spectroscopy is achieved solely by the main spectrometer. However, this option does not represent an ideal solution, as the functionality of the pre-spectrometer as a coarse energy filter rejecting the largest part of the  $\beta$ -electrons, which was intended to suppress background due to ionizing collisions inside the main spectrometer, would be lost.<sup>26</sup>

A different approach, which was already proposed in 2003/2004 [Ess04] but could be experimentally tested only now, is to face the trapping conditions and to prevent their harmful effects by actively removing stored particles from the trap before the ignition of a Penning discharge can lead to a serious increase of the background rate. The concept of an “electron catcher” in the form of a movable wire installed inside the beam line was realized and successfully tested in this work in a Penning trap environment comparable to that in the KATRIN experiment.

At the test setup using the Mainz MAC-E filter as a main spectrometer and an additional high-voltage electrode inside an adjacent vacuum chamber as a pre-spectrometer mockup, the ignition of Penning-type discharges was observed under various conditions. The trapping characteristics were found to depend on the amount of electrons being injected into the Penning trap, but frequently discharges also occurred without employing any extra feeding mechanism.

Several successive prototype versions of a scanning electron catcher compatible with operation in an ultrahigh-vacuum environment and in strong magnetic fields were developed, with gradual refinements of the concept with every step. The latest versions have been operated reliably during long-term tests at the Mainz spectrometer, and thereby the operational principle based on a current loop in a magnetic field moved across the beam by virtue of the Lorentz force is approved for the intended application.

In particular, the following experimental findings allowed to establish a proof of principle of the proposed electron catcher:

1. The moving wire helps to reduce the background which arises from the Penning trap. The suppression factor of bursts in the count rate and of small discharges depends on the type of motion of the wire and on the frequency with which it passes the center of the beam.

<sup>25</sup>This is indeed how the problem was eventually solved at the Troitsk experiment.

<sup>26</sup>Recent calculations by F. Glück [Glü08] indicate that the background component caused by the large unfiltered flux of  $\beta$ -electrons entering the main spectrometer if the pre-spectrometer potential is turned off is of no major concern.

2. A sinusoidal motion of the wire scanner can prevent or significantly delay discharges inside the trap.
3. If the wire is driven by a rectangular motion of a frequency of the order of 1/10 s to 1/s, it can dampen discharges in their initial phase, but not prevent strong ignitions.
4. Once a discharge has ignited, it can be extinguished by switching on the wire scanner with a fast sine wave motion of a frequency of the order of 1/s.
5. Positioning the wire in the center of the beam reduces the probability of bursts or discharges to occur.

Since the test setup at Mainz differs in some aspects from that of the final KATRIN beam line, a transfer of specific results, like for example ignition time scales and optimal swiping speeds and intervals of the wire scanner, is difficult. The most important differences are listed in the following.

- The Mainz spectrometer offers very good vacuum conditions in the  $10^{-10}$  mbar region, but due to peripheral systems which were used for the test measurements the pressure was usually increased to a few times  $10^{-9}$  mbar. In the KATRIN spectrometer section, however, the residual gas pressure will be about two orders of magnitude lower. Since the mean time between ionization events,  $\tau_{\text{ionization}}$ , is inversely proportional to the residual gas pressure, the discharge behavior observed at Mainz cannot be directly compared to that expected at KATRIN. This affects the ignition time scale as well as the strength of discharges.
- The differences in the electromagnetic field configuration were already mentioned in section 6.2.1. The most prominent discrepancy is related to the planar high-voltage plate, which covers the cross section of the transported magnetic flux and is oriented perpendicularly to the magnetic field lines. The influence of the feedback mechanism related to an amplification of charge carriers due to the impact of positive ions on the plate will not be present in the KATRIN configuration.

Furthermore, the feeding rates due to atmospheric muons or environmental radioactivity at KATRIN will also be different from those at the test setup.

- In addition, the magnetron time scale<sup>27</sup>  $\tau_{\text{magnetron}}$  characteristic of the Mainz setup is expected to be different from that in the KATRIN setup. The ratio of the magnetron time scale to the ionization time scale is of fundamental importance for the efficient collection of trapped charges on an immobile pin: Without the capability of scanning the wire across the beam profile, the only possibility to extract the stored electrons from the trap is for them to hit the wire by virtue of the magnetron rotation, which takes many cycles of the axial motion of the trapped particle to complete one turn. The build-up of an ionization chain and a discharge can only be avoided if for all trapped particles the ionization probability along this integrated path of many axial oscillations is small enough. This can be expressed as

$$\frac{\tau_{\text{magnetron}}}{\tau_{\text{ionization}}} \ll 1. \quad (6.8)$$

Indeed, simulations [Glü08, Glü09b] show that for the test setup at Mainz  $\tau_{\text{magnetron}}$  is typically one or even two orders of magnitude lower than that obtained for the trapping region between the two KATRIN spectrometers:

$$\tau_{\text{magnetron, Mainz}} \approx 1 \mu\text{s}, \quad \tau_{\text{magnetron, KATRIN}} \approx 20 - 200 \mu\text{s} \quad (6.9)$$

---

<sup>27</sup> $\tau_{\text{magnetron}}$  is defined here as the time needed for a trapped electron to perform a full rotation around the axis due to the magnetron drift motion. An expression for the magnetron drift velocity is given in eq. (2.45).

At KATRIN, with a residual gas pressure of  $p = 10^{-11}$  mbar, the mean time between ionizing collisions is of the order of one minute. Therefore, the relation (6.8) should be fulfilled. Considering the higher pressure level of the test setup at Mainz mentioned above, one obtains a ratio of  $\tau_{\text{magnetron}}/\tau_{\text{ionization}}$  which is of roughly the same order as in the KATRIN case (due to an approximate cancellation of the two similar factors in the nominator and denominator in the relation 6.8).

Despite these dissimilarities, it is still possible to give a recommendation for a “discharge prevention device” for KATRIN based on the experience from the test measurements. The two mentioned options of a stationary pin and a movable wire shall be discussed.

**a) Stationary pin**

In view of the technical effort needed to provide a well-defined motion of the scanner in an ultrahigh vacuum environment and considering the large number of cycles a scanning wire would have to perform reliably during the full five years of data taking planned for the KATRIN experiment, the installation of a stationary wire seems an attractive alternative.

For this option to be realizable within KATRIN, a manipulator system allowing to insert and to fully withdraw the pin from the beam is necessary. During the time the pin is inserted the data of the detector pixels “shadowed” by the stationary pin have to be discarded in order to avoid a contamination of the signal with scattered electrons, which forms one of the disadvantages of this concept.  $\beta$ -electrons see an effective width of the stationary pin which corresponds to the pin diameter plus two times the cyclotron radius, thus at least 13 out of 148 detector pixels would be affected (yielding a loss fraction of 9 %).

Moreover, it remains to be clarified whether all trapped particles exhibit a magnetron drift motion satisfying the relation (6.8). It is still possible that some electrons with particular starting conditions do not undergo a significant magnetron drift at all and would therefore not be efficiently eliminated by a stationary pin. Therefore, although preliminary experimental studies at Mainz look promising, further detailed investigations are necessary in order to confirm the usability of this alternative concept of an electron catcher for the trapping section between the two KATRIN spectrometers.<sup>28</sup>

**b) Movable (scanning) wire**

In contrast to the case of the stationary pin, the magnetron motion is not a limiting factor for the functioning of the wire scanner, as the latter actively collects the trapped electrons across the full flux tube instead of passively waiting for them to hit the wire. For the movable wire, the requirement in eq. (6.8) can be reformulated as

$$\Delta t_{\text{out}} \ll \tau_{\text{ionization}}, \tag{6.10}$$

where  $\Delta t_{\text{out}}$  denotes the time span the wire spends outside of the flux tube, *i. e.*, during which it does not remove electrons from the trap.

The wire scanner can also be moved out of the beam permanently, if necessary, by applying a constant current. Therefore, it would permit an unhindered transport of the full flux of  $\beta$ -electrons. The disturbance caused by a periodic scanning motion of the wire can probably be kept at a tolerable level: The excellent vacuum conditions at KATRIN presumably allow to reduce the sweeps of the wire from a frequency of typically  $\mathcal{O}(1/\text{s})$  (experimentally determined at the Mainz setup with inferior vacuum conditions) to  $\mathcal{O}(1/100 \text{ s}) - \mathcal{O}(1/10 \text{ s})$ . However, it is not possible to give a concise estimate of the required scanning frequencies

---

<sup>28</sup>Further insight and experience may be gained through the installation of a grid of stationary wires, which is planned for the KATRIN pre-spectrometer [Glü09b].

without a robust knowledge of the actual filling rate of the trap between the two KATRIN spectrometers (compare the discussion in section 5.4.2). Suitable scanning frequencies will have to be determined experimentally at the completed KATRIN setup.

A scanning electron catcher has the advantage that the loss of usable data is not defined by geometry alone, but for the case of the good vacuum conditions at KATRIN ( $\tau_{\text{ionization}} = \mathcal{O}(1 \text{ min})$ ) probably more by the duty factor of the scanning. For example, a one-second sweep across the beam every 100 seconds corresponds only to a loss of 1 % of the data.<sup>29</sup>

Considering these arguments, it can be concluded that with the scanning wire tested at Mainz the prototype of a “discharge prevention device” suitable for the use at KATRIN has been developed. The stationary pin might be a viable option, but until its effectiveness is ultimately established the scanning wire provides a proven solution. Lastly, it should be mentioned that the wire scanner stopped at its central position may also act as a stationary pin. However, this option requires a reliable and precise method to bring the wire to the center of the beam in a controlled manner, which proved to be difficult for the first prototypes tested at Mainz, but was already improved on with the more advanced versions.

---

<sup>29</sup>Within the slow scanning motion, one could even consider to accept those electrons which pass outside of the “shadow” of the wire scanner.

## 7 Tests of a UV LED-based photoelectron source

In addition to the testing of the scanning wire mechanism to empty the trap between the two KATRIN spectrometers, the measurement time at the Mainz MAC-E filter was used to investigate a novel method of fast-pulsed production of photoelectrons with a narrow energy distribution. Experimental studies showed that it is even possible to select particular starting angle intervals of the electrons by choosing a particular segmented photocathode geometry and a specific configuration of the electric and magnetic fields surrounding the electron source.

Section 7.1 presents arguments why such a photoelectron source would greatly facilitate the initial test measurements and calibration runs of the KATRIN main spectrometer after its commissioning. In particular, the possibility to operate and characterize the MAC-E filter in a time-of-flight measurement mode is highly promising.

Section 7.2 briefly discusses the options of light sources suitable to produce the short and well-defined pulses of ultraviolet light necessary to realize the proposed photoelectron gun with the abovementioned characteristics. A motivation for using light emitting diodes in the UV range is given. These LEDs were employed in test measurements described in the two subsequent sections. The superior timing properties of the photoelectron pulses and the narrow energy smearing are demonstrated in section 7.3, where an integrated energy scan and a high-resolution time-of-flight spectrum measured with the Mainz MAC-E filter are presented. Section 7.4 introduces a prototype concept of a pulsed photoelectron gun offering the additional feature of angular selectivity and presents first experimental results yielding a successful proof of principle.

Finally, section 7.5 reviews what has been achieved so far and outlines further improvements of the concept of an angular-defined pulsed photoelectron gun envisioned for future studies.

### 7.1 Motivation

Important measurements to characterize the electromagnetic properties of the main spectrometer have to be carried out [Wei07] after the installation of the vital components and before the start of the neutrino mass measurements. The main required components are listed in the following:

- **The vacuum vessel of the main spectrometer** has already been installed in the dedicated spectrometer hall at the KATRIN site in November 2006. Among other tests, a complete bakeout cycle and a check of the ultrahigh vacuum capability of the vessel as well as a first high-voltage test were performed. After the implementation of the mounting rails, the vessel will be ready for the installation of the **inner electrode system**, which is planned to start in spring 2009.
- **Two superconducting magnets** will be needed for the EMD test measurements. In the default configuration, the existing magnets of the pre-spectrometer will be used, since the pinch magnet and the detector magnet are expected to be available at only a later time.

- **The air coil systems** (low-field coils to tune the field homogeneity and the energy resolution of the main spectrometer and the Earth field compensation system) are required for the tests, as well as
- **a segmented electron detector.** While the 64-pixel PIN diode presently installed at the pre-spectrometer could be employed for first tests of the functioning of the individual components, the complex 148-pixel detector system which will be used for the neutrino mass measurements is needed for the calibration runs: As discussed in section 4.2.1, the transmission function of the main spectrometer must be determined for each pixel of the detector, which corresponds to a specific segment of the cross section of the flux tube in the analyzing plane.
- Furthermore, an **electron source** fulfilling several requirements is essential:
  - It should deliver stable and sufficiently high rates of electrons.
  - The energy spread of the electrons has to be small compared to the energy resolution  $\Delta E_{\text{spec}}$  of the main spectrometer ( $\Delta E_{\text{source}} \approx 0.2 - 0.3 \text{ eV}$ ).
  - Since simulations for the electromagnetic design of the main spectrometer show that electrons with large transversal kinetic energies in the outer regions of the flux tube are most critical with respect to the transmission condition, the electron source should be able to provide electrons with large starting angles.
  - A two-dimensional positioning system is required in order to scan the full area of the flux tube.

A fully automated control (and monitoring) of all the components as well as a data acquisition system connected to a database are needed as well.

Due to the considerable maintenance and running costs, extensive calibration measurements are not only time consuming but also rather expensive. Therefore, it is essential to minimize the time needed for commissioning and calibration runs. Electron sources capable of delivering high count rates for the test of the transmission function are one idea to speed up the measurements. In this case, the limiting factor is the rate sustainable by the electron detector and the data acquisition system. However, it is also possible to increase the amount of information that can be drawn from a single measurement by using the non-integrating time-of-flight operational mode of the MAC-E filter, which was originally proposed and tested in a pilot study at the Mainz neutrino mass experiment [Bon99].

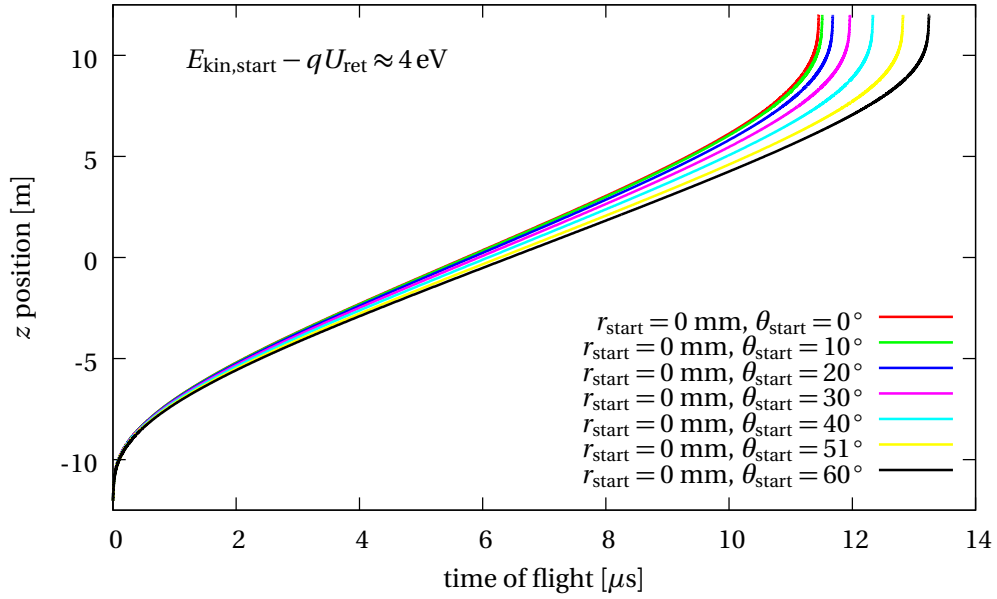
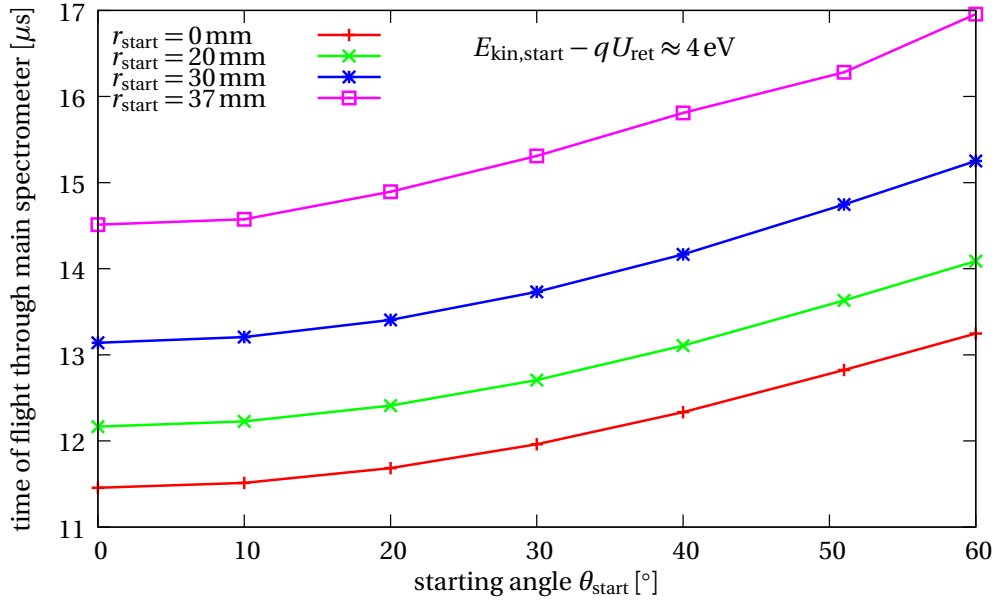
### 7.1.1 Time-of-flight simulations for the KATRIN main spectrometer

Time-of-flight simulations for the KATRIN main spectrometer were carried out using the microscopic trajectory routine described in section 4.3.3. The time needed for an electron with a given starting kinetic energy  $E_{\text{kin, start}} = (E_{\parallel})_{\text{start}} + (E_{\perp})_{\text{start}}$  to pass the MAC-E filter is expected to be a monotonous function of the starting angle  $\theta_{\text{start}}$  and of the radius  $r_{\text{start}}$ :

- The angle  $\theta_{\text{start}}$  defines the ratio of longitudinal and transversal kinetic energy. For a fixed value of the total kinetic energy the electrons with larger starting angles will have a lower longitudinal velocity component  $v_{\parallel}$  in the long drift region of high electric potential inside the MAC-E filter and hence need a longer time of flight as compared to low-angle electrons.
- The radius  $r_{\text{start}}$  influences the path length of the electron through the spectrometer. Due to the curvature of the outer magnetic field lines, electrons passing along the border of the flux tube have to cover a larger distance and their time of flight is thus longer than that of electrons which travel on the axis of the spectrometer.

- In addition, both  $r_{\text{start}}$  and  $\theta_{\text{start}}$  (via the cyclotron radius  $\rho_{\text{cyc}}$ , to be discussed below) determine at which radial position  $r_{\text{ana}}$  the electrons pass the analyzing plane, *i. e.*, which analysis potential they see, since  $U_{\text{ana}}(r) \neq \text{const.}$  (compare figure 4.24(a)).

This is confirmed by the simulation results presented in figure 7.1. On-axis electrons with surplus energies of about 4 eV and maximum starting angle  $\theta_{\text{start}} = 60^\circ$  take about  $1.8 \mu\text{s}$  longer to travel the distance of 24 m from the entrance to the exit of the spectrometer than electrons which are emitted parallel to the magnetic field lines (figure 7.1(a)). For various starting radii  $r \leq r_{\text{start, max}} = 37 \text{ mm}$  similar results were found. These are summarized in figure 7.1(b). With the expected timing resolution of the KATRIN final plane detector of  $\Delta t_{\text{detector}} \approx 100 \text{ ns}$  it should thus be feasible to distinguish electrons belonging to different starting angle intervals (in a radial segment with finite size) with the time-of-flight method. Using a calibration source with isotropic emission and well-known energy distribution (like the condensed krypton source [Ost09]) in a chopped mode by pulsing the applied electric potential would allow to record the angular information of the electrons due to their time of flight and thus to measure a full transmission function pixel by pixel without the need to step the retardation potential. This would clearly help to speed up the calibration procedure considerably, and further investigations should be conducted to work out the details of this promising method.


 (a) axial position as a function of elapsed time of flight since start of the trajectory at  $z = -12 \text{ m}$ 


(b)

**Figure 7.1:** (a) Relationship between axial ( $z$ ) position along a trajectory and the time of flight elapsed since the start if the trajectory for different starting angles  $\theta_{\text{start}}$  between  $0^\circ$  and the maximum accepted starting angle  $\theta_{\text{start,max}} = 60^\circ$  at a given surplus energy of  $E_{\text{kin,start}} - qU_{\text{ret}} \approx 4 \text{ eV}$ . The slope of the curves reflects the fact that the electron velocity is largest in the entrance and exit regions, and much lower in the long central part where the retardation is strongest. As an example, the plot shows the results of simulations for electrons started on-axis. The shapes of the curves for starting radii  $r_{\text{start}} \neq 0$  look similar; these are therefore not included here. Instead, (b) illustrates the evolution of the total time of flight needed for a full passage of the main spectrometer as a function of both starting radius  $r_{\text{start}}$  and starting angle  $\theta_{\text{start}}$  for a fixed surplus energy.

### 7.1.2 Details of the transmission function and proposal of an enhanced time-of-flight mode

The time-of-flight analysis proposed by the authors of reference [Bon99] assumes the distribution of the retardation potential to be flat in axial direction, *i. e.*,  $U(z) = \text{const.} = U_L$  in a drift region with length  $L$  and zero outside of this region. Hence,  $v_{\parallel}$  is also assumed to be constant over most of the distance along  $z$ . According to figure 7.1(a), this approximation is generally justified for a typical MAC-E filter with a steep gradient of the electric potential in the endcap regions. The drift time is dominated by the long central part where the retardation potential is close to its maximum and  $v_{\parallel}$  is at its minimum. The time needed to pass the spectrometer can thus be approximated<sup>1</sup> by

$$t_L = \frac{L}{v_{\parallel, \text{ana}}} = \frac{L}{\sqrt{2E_{\parallel, \text{ana}}/m}}, \quad (7.1)$$

where  $v_{\parallel, \text{ana}}$  and  $E_{\parallel, \text{ana}}$  denote the velocity and longitudinal kinetic energy of the electrons close to the analyzing plane, respectively. This simplifies the formal treatment of the problem; however, all information on the actual evolution of the potential  $U(z)$  along the trajectory of the electron is lost on principle.

It is possible to go one step further and extend the concept to a so-called second order time-of-flight mode of the MAC-E filter [Wei07, Val07, Wei08]. The correlation between the time of flight and the longitudinal kinetic energy, which is largely determined by the electric retardation potential along the flight path of the particle, will lead to small deviations from eq. (7.1) and thus can be exploited to measure the integrated electric potential along the trajectory. Once the nominal time of flight for a given setting of the high voltages is known (either by experiment or through simulations, or ideally both), precision time-of-flight measurements for different starting angles and radial positions (*i. e.*, for different trajectories) can serve as an uncomplicated diagnostic tool of the properties of the spectrometer. An example is illustrated in figure 7.2, in which the approximation of eq. (7.1) holds for the default situation (solid line), but not for the hypothetical faulty setting (dashed line).

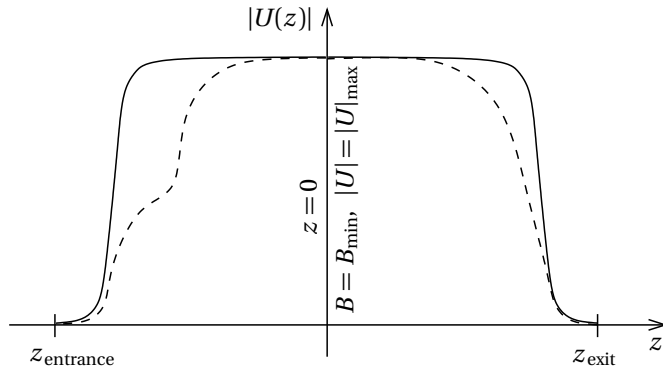


**Figure 7.2:** Sketch of electric potential along a magnetic field line inside a MAC-E filter: The solid curve shows the nominal evolution of  $U(z)$ , while the dashed line represents a faulty setting. Since in both cases the maximum retardation occurs at the same axial position (in particular, at the same minimum magnetic field  $B_{\text{min}}$ ), they would yield identical widths of the transmission function and thus be indistinguishable in standard tests.

Likewise, this enhanced time-of-flight method may be used to disentangle various effects which might influence the measured transmission function in a similar way. For example, a broadened (or otherwise deformed) measured transmission function might arise from a convolution of the nominal (sharp and narrow) transmission function with an energy smearing of a calibration source (compare figure 7.3). Since the energy distributions of the calibration sources are known

<sup>1</sup>It is sufficient to illustrate the relevant arguments in the non-relativistic limit, as a full relativistic treatment would only yield minor corrections.

## 7 Tests of a UVLED-based photoelectron source

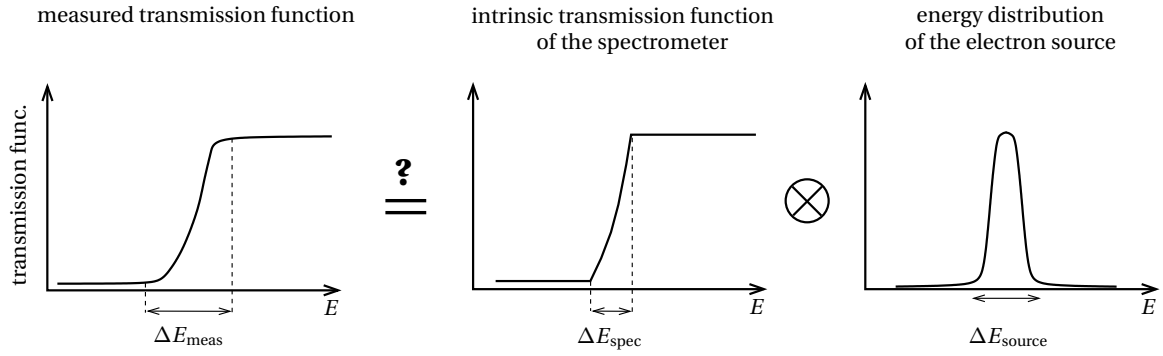


**Figure 7.3:** Schematic drawing: broadening and smearing of the transmission function due to an energy spread at the electron source.

to a certain level (but not with ultimate precision), a part of the intrinsic energy spread might remain undetected. On the other hand, a similar observed shape of the transmission function may as well be caused by other influences which are not related to the electron source, but rather to the properties of the spectrometer. As an example, figure 7.4 shows the broadened transmission function<sup>2</sup> resulting from the effect of too early retardation of the electrons inside the main spectrometer, which was introduced in section 4.2.2. The simulated transmission function was obtained by calculating various electron trajectories with starting angles equispaced in  $\cos \theta$  to find the minimum amount of starting kinetic energy  $E_{\text{kin}}$  needed to pass the analyzing plane. It is interesting to study in what way time-of-flight measurements might help to disentangle the two classes of distortions of the transmission function. To this end, time-of-flight simulations for electrons with and without early retardation were carried out. As displayed in figure 7.5(a), the effect caused by an exaggerated sag of the wires in the inner layer (compare section 4.5.1) amounts to a dip in the longitudinal kinetic energy of  $\delta E_{\parallel} \approx 10 \text{ eV}$ . Therefore, the influence on the time of flight through the main spectrometer is also huge: for the deformed potential distribution, the simulated time of flight from the entrance to the exit solenoid is about  $15.7 \mu\text{s}$  shorter than that for undisturbed transmission (see figure 7.5(b)). Although in both cases the minimum surplus energy reached is similar (below  $10 \text{ meV}$ ), the early retardation leads to a reacceleration of the electron seen as an increase of the longitudinal kinetic energy at  $z \gtrsim -3.8 \text{ m}$ . Even though this demonstrative example uses an unrealistically large amount of  $\delta E_{\parallel}$ , the time-of-flight method should in principle be sensitive to much more subtle effects. The simulations indicate that a distinction between a scenario similar to that in figure 7.3 and early retardation as shown in figure 7.5 on the basis of time-of-flight measurements may be feasible.

Related to the trajectory simulations to study the transmission function, further interesting de-

<sup>2</sup>Instead of the normalized transmission function  $T(E, qU_0)$ , the unnormalized expression  $1 - \cos(\theta_{\text{start}})$  (compare eqs. (2.27) and (2.28) in section 2.2) is plotted as a function of the kinetic energy  $E_{\text{kin}}$  of the electrons. The magnetic field settings in the KATRIN reference design of 2007,

$$\begin{aligned} B_{\text{pinch}} &= 6 \text{ T} \quad \text{and} \\ B_{\text{spec, entrance}} &= B_{\text{start}} = 4.5 \text{ T}, \end{aligned} \quad (7.2)$$

yield the following value of the maximum accepted polar angle for electrons starting inside the entrance solenoid:

$$\begin{aligned} \theta_{\text{start, max}} &= \arcsin \left( \sqrt{\frac{B_{\text{start}}}{B_{\text{pinch}}}} \right) = 60^\circ \\ \Rightarrow 1 - \cos \theta_{\text{start, max}} &= 0.5. \end{aligned} \quad (7.3)$$

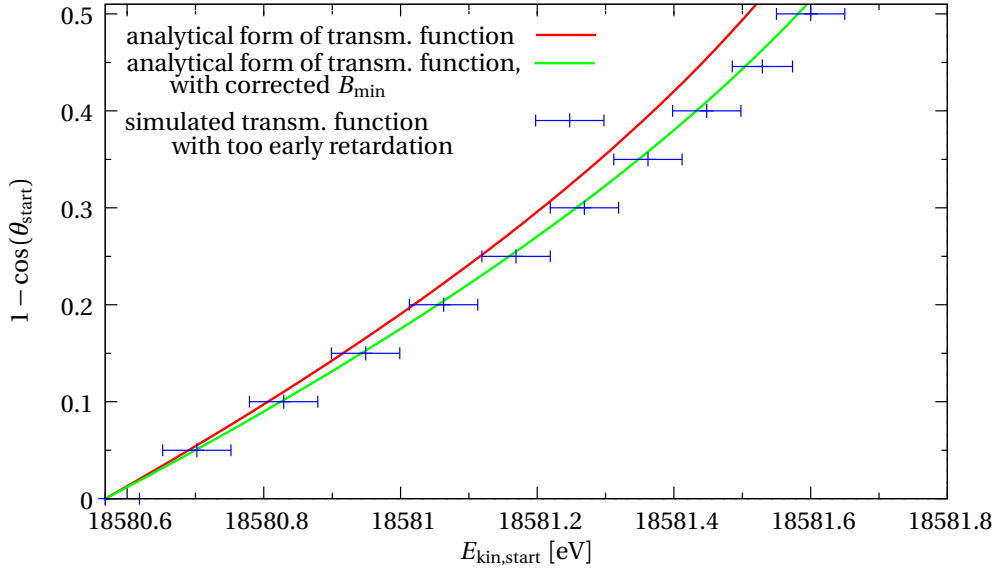


**Figure 7.4:** Comparison between simulated transmission function and analytical shape for a single value of the starting radius ( $r_{\text{start}} = 30$  mm). The red curve denotes the analytic shape of the transmission function (energy resolution  $\Delta E = 0.93$  eV) without too early retardation. The simulation data (blue) obtained from microscopic trajectory calculations exhibit a broadening with respect to the nominal shape of the transmission function. It can be explained (green curve) by taking into account the slightly higher magnetic field at the location of the minimum in the longitudinal kinetic energy (figure 7.5). The error bars attached to the simulation data reflect the uncertainty due to the influence of different azimuthal angles (figure 7.6).

tails regarding the influence of the inhomogeneity of the retardation potential  $\Delta U_{\text{ana}}(r)$  should be mentioned, which were not considered before. Two interrelated ones are illustrated in the following:

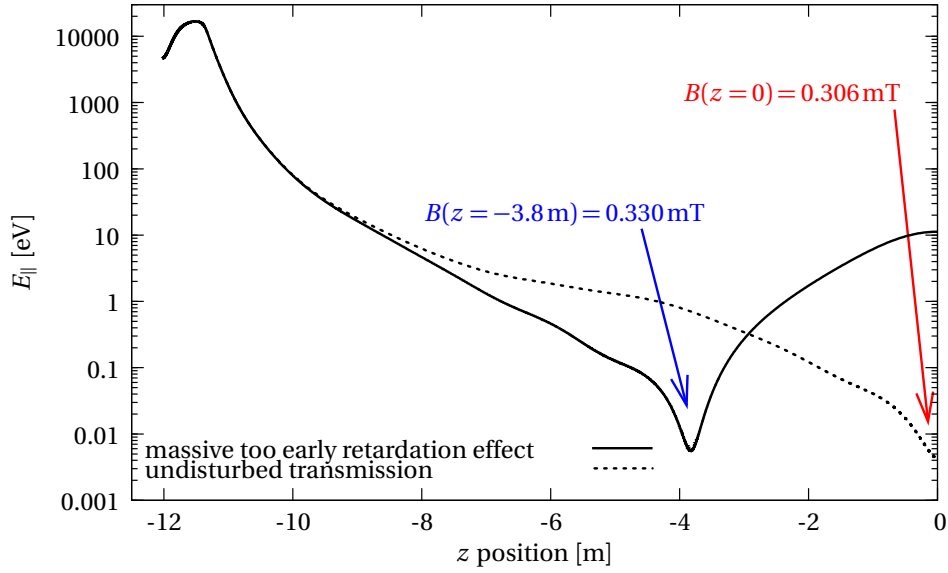
- Gyrating motion with cyclotron radius  $\varrho_{\text{cyc}}$  (figure 7.6(a)): in particular in the weak magnetic field at the analyzing plane, the electrons probe an extended region with varying retardation potential.
- In addition to the polar angle  $\theta$  which defines the ratio  $E_{\parallel}/E_{\perp}$ , the azimuthal angle  $\varphi$  also influences the radial position at which the electron passes the energy filter. The enveloping curve of the electron impact points on the analyzing plane for all angles  $\varphi$  covers an area with a diameter of  $4\varrho_{\text{cyc}}$  (figure 7.6(b)).

For the electrode configuration of the main spectrometer chosen for this example, both effects are particularly pronounced because this version of the simulation model does not include compensative structures to reduce the inhomogeneity of the analyzing potential. Hence,  $\Delta U_{\text{ana}}(r) \approx 2.5$  V was quite large. The gradient in the outer regions of the flux tube is largest, with a change in the electric potential of  $\approx 2$  V over the last 0.5 m. The following estimate shows that this can lead to a noticeable variation of the retardation potential along a cyclotron loop of the electron.

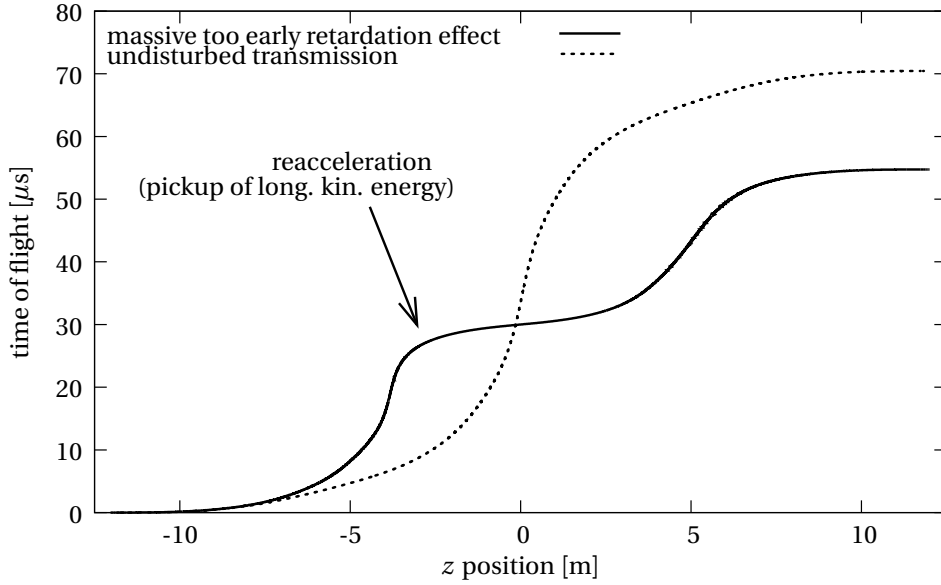
For a given amount of energy  $E_{\perp}$  in the cyclotron component of the motion and a given magnetic field strength  $B$ , the cyclotron radius  $\varrho_{\text{cyc}}$  can be estimated by

$$\varrho_{\text{cyc}} \approx 1 \text{ m} \cdot \frac{\sqrt{E_{\perp} [\text{keV}]}}{B [\text{Gauss}]} = 0.1 \text{ m} \cdot \frac{\sqrt{E_{\perp} [\text{keV}]}}{B [\text{mT}]} \quad (7.4)$$

Thus, for an electron passing the analyzing plane of the main spectrometer at  $B_{\text{ana}} \approx 0.3$  mT with a



(a) longitudinal kinetic energy



(b) time of flight

**Figure 7.5:** Evolution of longitudinal kinetic energy (a) and time of flight (b) for simulated electron trajectories with and without too early retardation. For the same starting conditions (high starting angle, path along the outer border of the magnetic flux tube), the electron reaches the exit of the main spectrometer about  $15.7 \mu\text{s}$  earlier in the scenario with too early retardation (solid line) as compared to the case without too early retardation (dashed line). This can be explained as follows: Both electron trajectories were simulated with a small amount of surplus energy that barely allows them to pass the analyzing plane ( $E_{\parallel} \approx 5 \text{ meV}$  at  $z = 0$ ). With too early retardation this requires a higher starting kinetic energy of the electron as for the default case, which translates in an overall shorter time of flight.

maximum transversal kinetic energy corresponding to the energy resolution,  $(E_{\perp})_{\text{ana, max}} = \Delta E = 0.93 \text{ eV}$ , the cyclotron radius is

$$\rho_{\text{cyc, ana}} \approx 0.01 \text{ m}, \quad (7.5)$$

and the variation of the retardation potential across a length of  $4\rho_{\text{cyc}}$  at the outer border of the

flux tube amounts to about 160mV. The effect of this variation on the transmission function of the main spectrometer should be further investigated. In the case of the study presented in figure 7.5, the uncertainty in the energy needed for transmission caused by disregarding different angles  $\varphi$  is reflected in the error bars of the simulated data. As demonstrated in figure 7.7, the inhomogeneity of  $U_{\text{ana}}$  can even lead to a  $\varphi$ -dependent violation of the transmission condition for electrons with very low surplus energies, which are most strongly affected by the variations of the retardation potential.

In contrast to the polar angle  $\theta$ , there is no way of controlling (or even restricting) the azimuthal emission angle  $\varphi$  in a calibration electron source. Furthermore, the relation between  $\varphi_{\text{start}}$  and  $\varphi_{\text{ana}}$  is non-trivial and unknown, which makes it difficult to exploit the connection between  $\varphi_{\text{start}}$  and the time of flight determined by the calculations. Nevertheless, the simulation results are useful in two ways:

- a) In combination with the calculations presented in figure 7.1 they allow to set a coarse scale for the timing resolution of the detection system required for time-of-flight measurements at the KATRIN main spectrometer. In view of the simulation studies a precision of the timing information in the range of about 100 ns seems to be a reasonable specification.
- b) The strong influence of the uncontrollable phase angle on the transmission of low-energy electrons, which are of greatest interest for KATRIN, supports the arguments for compensating measures to increase the homogeneity of  $U_{\text{ana}}(r)$  (compare section 4.6).

In conclusion, the simulation studies presented in this section underline the potential of time-of-flight studies at the KATRIN main spectrometer as a sensitive probe of subtle transmission variations. In order to carry out such time-of-flight measurements, electron sources with fast pulsing capabilities are required. The next sections explore the attractive possibility of realizing such a source on the basis of photoelectron production.

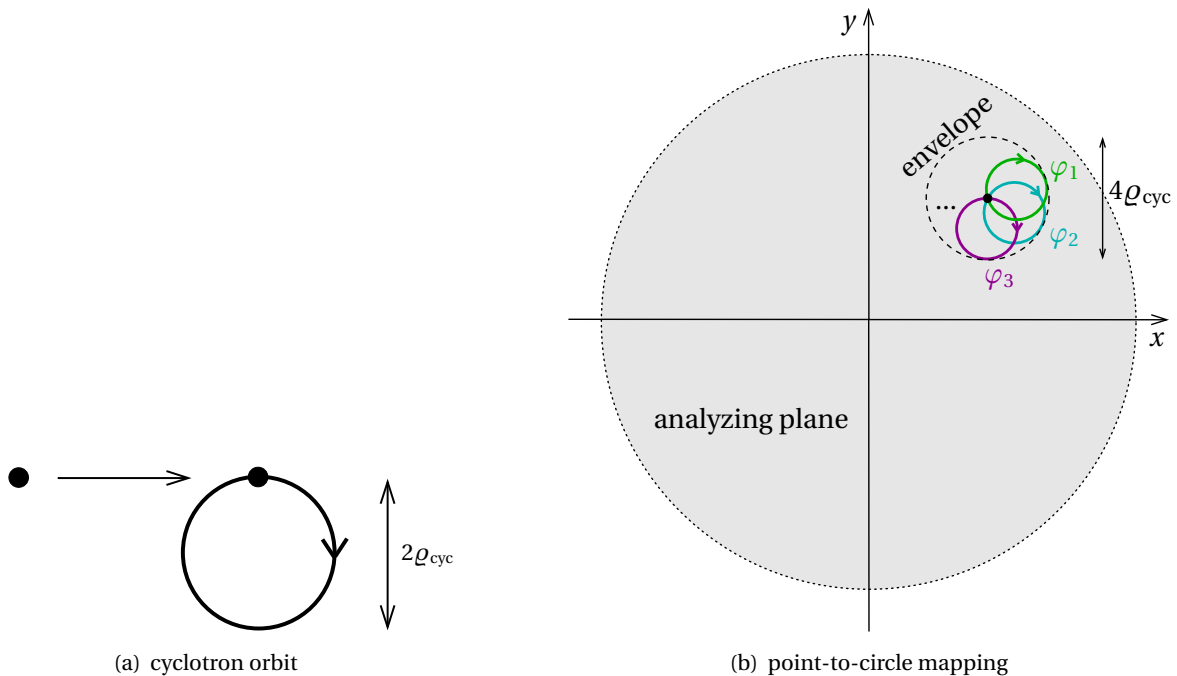
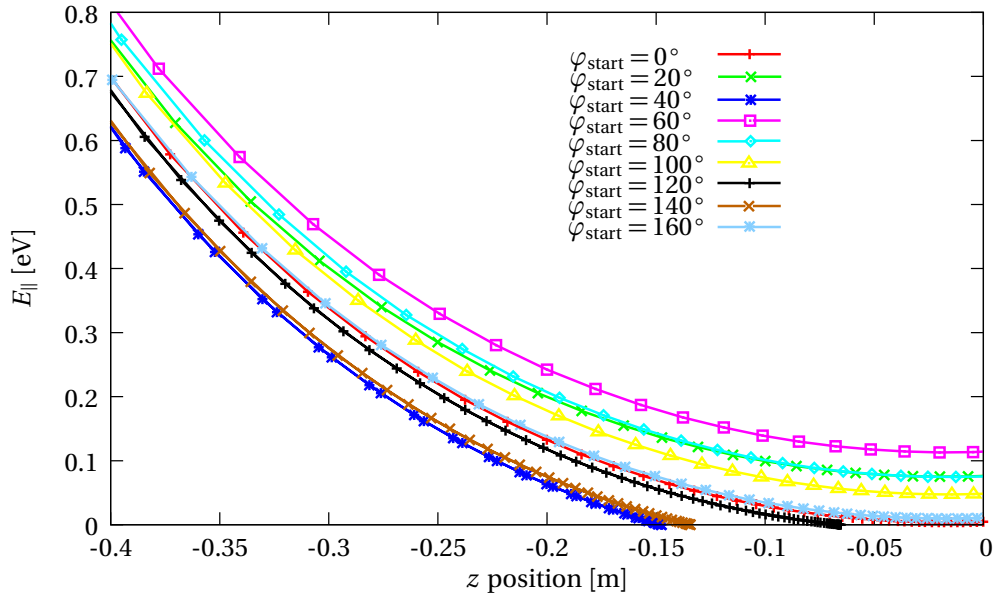
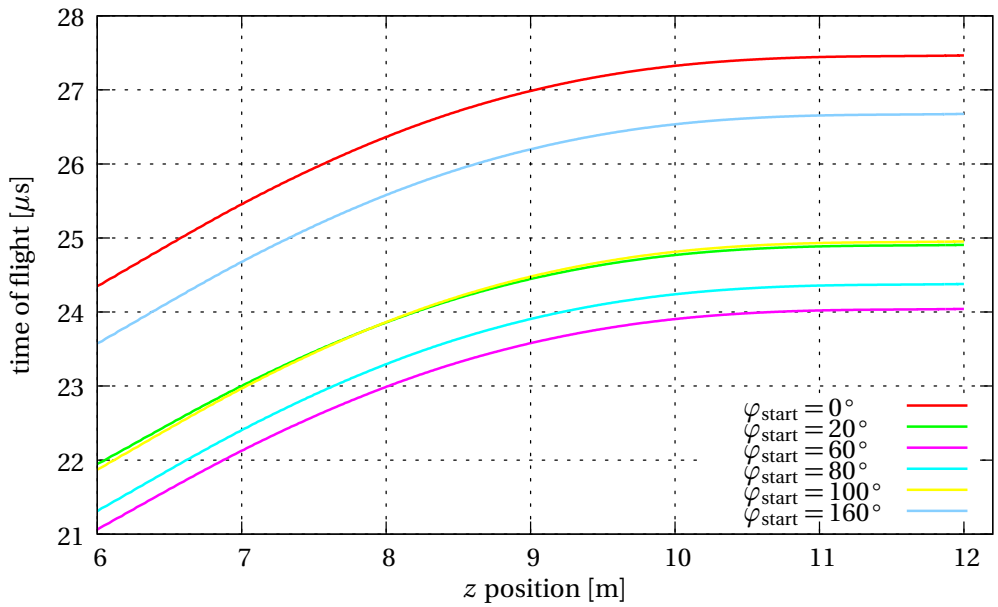


**Figure 7.6:** Cyclotron motion and point-to-circle mapping. Depending on the amount of cyclotron energy  $E_{\perp} = \sin^2 \theta \cdot E_{\text{kin}}$  and the azimuthal angle  $\varphi$ , a starting point  $(r_{\text{start}}, z_{\text{start}})$  is mapped onto an extended circular area with diameter  $4\rho_{\text{cyc}}$  at the analyzing plane.

## 7 Tests of a UVLED-based photoelectron source



(a)



(b)

**Figure 7.7:** Influence of the cyclotron motion on transmission properties of the main spectrometer. Electron trajectories at the outermost border of the transmitted flux tube were simulated with a fixed starting kinetic energy of  $E_{\text{kin,start}} = 18583.32 \text{ eV}$ , a polar angle of  $\theta_{\text{start}} = 53.13^\circ$  with respect to the magnetic field lines and varying azimuthal angles (*i. e.*, phases) between  $\varphi_{\text{start}} = 0^\circ$  and  $\varphi_{\text{start}} = 160^\circ$ . (a) The longitudinal kinetic energy close to the analyzing plane is influenced by the local variations of the retardation potential probed by the different angles  $\varphi$ . Some electrons are even reflected (*i. e.*, their longitudinal kinetic energy is used up completely:  $E_{\parallel} = 0$ ) shortly before reaching the analyzing plane. (b) The differences in the longitudinal kinetic energy of the order of  $\gtrsim 100 \text{ meV}$  at the analyzing plane translate into differences in the time of flight of up to  $3.5 \mu\text{s}$  at the exit of the main spectrometer ( $z = 12 \text{ m}$ ).

## 7.2 Suitable light sources for fast-pulsed photoelectron production

Before discussing possible technical realizations of a fast-pulsed photoelectron gun, it is expedient to compile a list of requirements regarding a suitable light source. The following points are essential:

1. The spectral width  $\Delta\lambda$  of the emitted light should be sufficiently small in order to provide quasi-monoenergetic photoelectrons (after acceleration to  $qU_{\text{source}} \approx E_{\text{photoel.}} \approx 18\text{keV}$ :  $\Delta E_{\text{photoel.}} \ll \Delta E_{\text{spec}}$ , for example  $\Delta E_{\text{photoel.}}/E_{\text{photoel.}} \approx 10^{-5}$ ).
2. The light source should be capable of emitting short pulses with small rise and fall times in order to yield well-defined intervals  $\Delta t_{\text{emis}}^{e^-}$  of photoelectron production. According to the simulations presented in the previous section, the pulse width  $\tau$  should be of the order of 100 ns or below.
3. To achieve good statistics even at comparatively low photoelectron yields, high repetition rates  $f$  are necessary, for example in the range of a few kHz. The resulting duty cycles which are to be sustained by the light source, also in long-term operation, are of the order of

$$f \cdot \tau = 10^4 \frac{1}{\text{s}} \cdot 10^{-7} \text{ s} = 0.1\%. \quad (7.6)$$

4. A smoothly variable intensity over a relatively wide range is also desirable.

For electrons to be liberated from the surface of the cathode through the photoelectric effect, the photon energy  $E_{\text{photon}}$  is required to exceed the work function  $\Phi$  of the cathode material:

$$\begin{aligned} E_{\text{kin, start}}^{e^-} &= E_{\text{photon}} - \Phi \\ \Rightarrow E_{\text{photon}} &\gtrsim \Phi \quad \text{for } E_{\text{kin, start}}^{e^-} \gtrsim 0. \end{aligned} \quad (7.7)$$

If  $\Phi$  and  $E_{\text{photon}}$  are chosen such that only photons from the high-energy part of the distribution can cause photoemission, the energy spread of the photoelectrons will be reduced accordingly. Since measured work function values of most elements are centered around 3.5 eV with a spreading of about  $\pm 1.5\text{eV}$  ([Höl79], cited in [Zan88], and compare table 7.1), this requirement restricts the suitable light sources to the regime of ultraviolet (short: UV) light for most available photocathode materials. As an example, a photon energy of  $E = 5\text{eV}$  corresponds to a wavelength of  $\lambda = \frac{hc}{E} \approx 248\text{nm}$ . Only a few elements possess work functions accessible via visible light, *e. g.* caesium with  $\Phi_{\text{Cs}} = 2.14\text{eV}$  [Wea81]. However, the utilization of such materials is often unfavorable from the technical point of view, for example due to considerations regarding vacuum compatibility, workability of the material, or stability of the work function against spatial inhomogeneities and temporal variations (oxidation when exposed to air).

Commercially available UV light sources like deuterium lamps or Xe/HgXe arc lamps are commonly used for standard applications in photoelectron production. They provide high stability and intensity, but usually their emission covers a wide spectrum of wavelengths between 160 nm and 450 – 2000 nm (which would thus have to be restricted by filters), and short pulsing is not readily achievable. In recent years, narrow-band laser devices operating at wavelengths down to  $\gtrsim 220\text{nm}$  were developed<sup>3</sup>. With output power levels of typically  $< 100 - 200\text{mW}$ , they offer repetition rates of only about 0 – 20 Hz and pulse lengths in excess of 20 – 120  $\mu\text{s}$ . Thus, they are not suitable for the use in a fast-pulsed photoelectron source. Q-switched laser systems delivering

<sup>3</sup>HeAg- and HeCu-lasers provide output wavelengths of  $\lambda_{\text{HeAg}} = 224.3\text{nm}$  and  $\lambda_{\text{HeCu}} = 248.6\text{nm}$ , respectively [Pho07].

**Table 7.1:** Work function values for selected metals gathered from various references, as listed in the last column. Some references do not give error bars for the measurements. There are notable differences in the values obtained by photoelectric or contact potential measurements, as well as between different crystalline orientations of monocrystals and for polycrystalline samples. The discrepancy between the work function of gold obtained with the contact potential difference method (1 and 2) is attributed [Hub66] to a contamination of the gold sample with mercury in those experiments using mercury diffusion pumps.

No.	material (cryst. direction)	method / remarks	$\Phi$ [eV]	reference
1	Au	contact potential diff.	$5.22 \pm 0.05$	[Hub66]
2	Au	contact potential diff.	$4.83 \pm 0.02$	[And59]
3	Au (polycryst.)	photoelectric	$5.1 \pm 0.1$	[Eas70]
4	Au (100)	photoelectric	5.47	[Wea81]
5	Au (110)	photoelectric	5.37	[Wea81]
6	Au (111)	photoelectric	5.31	[Wea81]
7	Au	after exposure to air	4.2	[Sav95]
8	Ag (110)	photoelectric	$4.14 \pm 0.04$	[Che82]
9	Ag (100)	photoelectric	$4.22 \pm 0.04$	[Che82]
10	Ag (111)	photoelectric	$4.46 \pm 0.02$	[Che82]
11	Ag (polycryst.)	photoelectric	$4.0 \pm 0.15$	[Eas70]
12	Cu (polycryst.)	photoelectric	$4.65 \pm 0.05$	[Eas70]
13	Cu (100)	photoelectric	4.59	[Wea81]
14	Cu (110)	photoelectric	4.48	[Wea81]
15	Cu (111)	photoelectric	4.94	[Wea81]
16	Cu (112)	photoelectric	4.53	[Wea81]
17	Cr (polycryst.)	photoelectric	$4.5 \pm 0.15$	[Eas70]
18	Fe (polycryst.)	photoelectric	$4.5 \pm 0.15$	[Eas70]
19	Ni (polycryst.)	photoelectric	$5.15 \pm 0.1$	[Eas70]
20	stainless steel 1.4429 DIN, 316LN AISI/SAE		$4.4 \pm 0.2$	[Pic92a]
21	stainless steel 302 AISI/SAE	photoelectric clean surface	4.75	[Wal99]
22	stainless steel 302 AISI/SAE	photoelectric varying grades of oxygen contamination	4.35 – 4.55	[Wal99]

short pulses of  $\approx 10$  ns duration operate at higher wavelengths of about 355 nm [Coh07]. It is also possible to use frequency-multiplying modules in combination with standard-technology lasers at higher wavelengths, for example a frequency-quadrupled Nd:YAG laser (output wavelength  $\lambda_{4\omega} = \frac{1}{4} \cdot 1064 \text{ nm} = 266 \text{ nm}$ ), however with standard repetition rates of  $\mathcal{O}(10 \text{ Hz})$ . Aside from the low rates, such (high-power) laser systems are disfavored because they are rather expensive, immobile and require particular safety installations in the laboratory.

By contrast, light emitting diodes (LEDs) operating in the deep-UV domain are advantageous due to their versatility and ease of use, albeit offering only a fraction of the optical output power as well

as inferior spectral and beam profile characteristics compared to laser systems. LEDs in this spectral range are still under development, and first devices have only become commercially available in the last few years.<sup>4</sup> Suitable materials for deep-ultraviolet emission in the range between about  $\lambda = 230$  nm and 280 nm are alloys like AlGaN and InAlGaN [Hir02]. Wavelengths down to 247 nm at a pulsed output power of  $\lesssim 10$  mW have been achieved [Bil05, Den07]. The major advantage of such LEDs resides in the possibility to easily achieve short pulses ( $\tau \lesssim 25$  ns with rise times of a few ns only, see for example [Gas05, Sha03]) at high repetition rates of the order of 1 – 10 kHz. The pulse width and rate as well as the light intensity can be tuned easily by controlling the signal shape and the amplitude of the driving voltage (*i. e.*, of the forward current).

The emission of UV LEDs is not strictly monochromatic. Table 7.2 summarizes the spectral data of the LEDs employed in this work, and further technical details can be found in appendix C.2. The full width of the emission at a central wavelength of  $\lambda_{\text{central}} = 265$  nm is about  $\Delta\lambda = 36$  nm, which corresponds to an energy spread of  $\Delta E_{\text{photon}} = 0.62$  eV (see table 7.2). The usable energy range is slightly reduced by the abovementioned cutoff at the low-energy end of the interval due to the work function of the photocathode material, *e. g.*, for stainless steel:  $E_{\text{photon}} \geq \Phi_{\text{stainless steel}} = (4.4 \pm 0.2)$  eV [Pic92a]. However, the remaining energy interval still has a width of about 0.5 eV. If the full width at half maximum (FWHM) instead of the total width is used to determine the upper limit of the photon energy range (compare table 7.2) and the lower bound is determined by the work function, the energy spread after cutoff reduces to about 0.41 eV.<sup>5</sup>

**Table 7.2:** Wavelength range and corresponding photon energies covered by UV light emitting diodes of type T9B25C and T9B26C, based on spectra measured with a grating spectrograph (figure C.3).

LED type	T9B25C		T9B26C	
	$\lambda$ [nm]	E [eV]	$\lambda$ [nm]	E [eV]
lower limit	245	5.06	252	4.92
central value	257	<b>4.82</b>	265	<b>4.68</b>
upper limit	276	4.49	288	4.30
full width	31	0.57	36	0.62
FWHM	13.8	<b>0.26</b>	15.3	<b>0.27</b>

Considering the overall characteristics, UV LEDs stand out as ideal light sources for fast-pulsed photoelectron production. Of the abovementioned options they represent the only class of light sources which “out of the box” fulfill all points of the list of requirements. Yet, although their qualities look promising on paper, they need to be verified experimentally. Since UV LEDs of the types T9B26C [Seo06a] (and later also T9B25C [Seo06b]) were already used to provide photoelectrons for the studies of the wire scanner mechanism (chapter 6), it was straightforward to carry out further tests regarding timing properties and energy distribution of the photoelectrons, which are presented in the next section.

<sup>4</sup>The prospects of possible applications comprise different fields, such as (bio-)medical applications, chemical processing, high-density optical storage, etc.

<sup>5</sup>These considerations only take into account the intrinsic energy spread due to the light emission spectrum, but not other influences like the uncertainty and possible inhomogeneities of the work function values.

### 7.3 Pulsed photoelectron production from a stainless steel cathode

The following sections report on investigations of photoelectron pulses carried out at the Mainz MAC-E filter. Parts of the equipment installed for the Penning trap studies described in chapter 6 were reused for these measurements. The essential piece is a simple photoelectron source consisting of a UV LED illuminating the stainless steel plate that served as a high-voltage electrode for tests of the wire scanner (figure 6.11). Section 7.3.1 presents several measurements demonstrating that these LEDs qualify as light sources for a fast-pulsed photoelectron gun which can be used for the MAC-E-ToF mode. In particular, the possibility to produce single or few photoelectrons per pulse at high repetition rates was studied, which allows to achieve sufficient statistics while keeping the pile-up ratio low.

With this photoelectron emitter an integrated energy spectrum (section 7.3.2) and a time-of-flight spectrum (section 7.3.3) of photoelectrons created in short pulses were measured.

#### 7.3.1 Timing properties, photoelectron yield and photoelectron multiplicities

Figure 7.8 shows a typical energy spectrum taken with the Flash-ADC system at a given surplus energy setting of the photoelectrons. A structure of clearly separated and equidistant multiple peaks is visible above the noise band. They indicate a pile-up effect where two or more electrons of the energy  $E_0 = qU_{\text{source}} = 18 \text{ keV}$  each are detected simultaneously, *i. e.*, within the timing

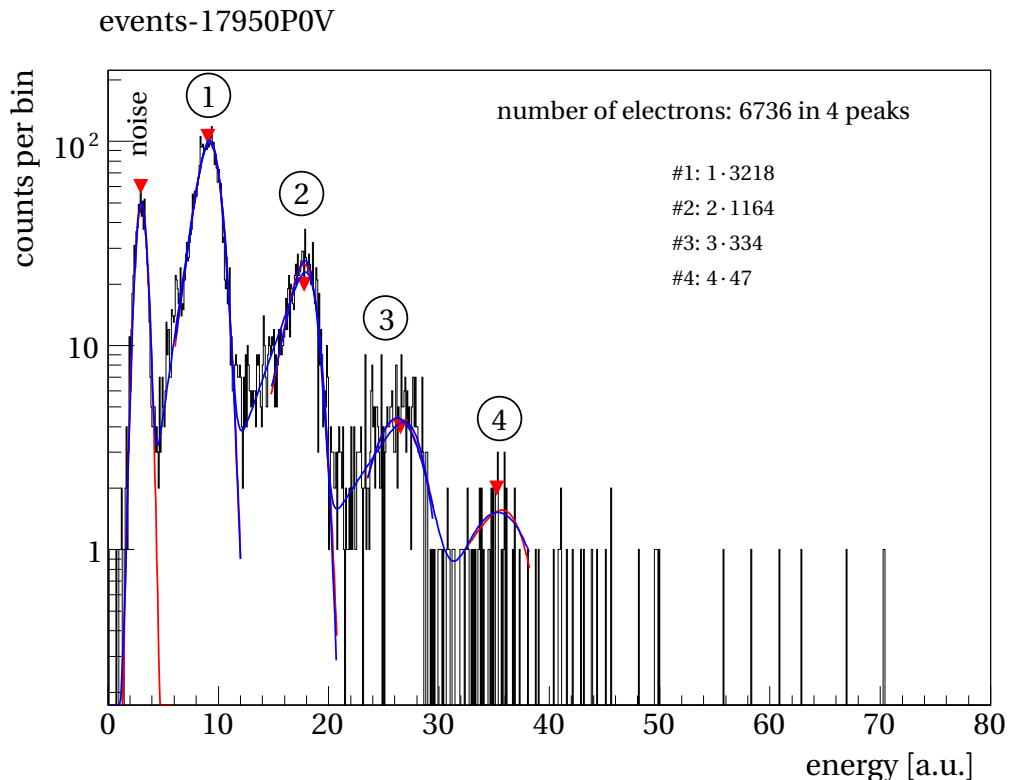


**Figure 7.8:** Energy distribution at a fixed setting of kinetic surplus energy of the photoelectrons (here:  $qU_{\text{surplus}} = q(U_{\text{source}} - U_{\text{spec}}) = 57 \text{ eV}$ ). Operating parameters of the UV LED: repetition rate  $f_{\text{LED}} = 1 \text{ kHz}$ , pulse width  $\tau = 200 \text{ ns}$ , voltage setting at the function generator  $U_{\text{AFG}} = 10 \text{ V}$ .

resolution of the data acquisition and analysis chain.<sup>6</sup> This pile-up gives rise to events appearing at integer multiples  $n > 0$  of  $E_0$ .

One aim of the test measurements was to study the timing characteristics, especially in view of the number of coincidentally detected electrons. The probability  $P(n)$  to find  $n$  coincident electrons was determined as a function of pulse width  $\tau$  for fixed operational voltage  $U_{\text{LED}}$  and repetition rate  $f_{\text{LED}}$ . In addition, the dependence of the detected photoelectron rate on the UV light intensity was studied by varying  $U_{\text{LED}}$  in the range between 5.8 V and 7.6 V at constant  $\tau$  and  $f_{\text{LED}}$ .

The spectrometer was set to a constant retardation potential of  $U_{\text{spec}} = -17.966$  kV at an energy resolution of  $\Delta E = 1.5$  eV, and the photocathode was supplied with a slightly more negative voltage of  $U_{\text{source}} = U_{\text{spec}} - 15.7$  V so that the created photoelectrons could be transmitted with a moderate surplus energy. The auxiliary water-cooled coil was turned off, and the xy-compensation coils were powered by currents of  $I_{\text{comp},1} = 32$  A and  $I_{\text{comp},2} = 40$  A, respectively.

The magnetic field strength was  $B_{\text{det}} \approx 0.34$  T at the location of the detector and  $B_{\text{source}} \approx 0.02$  T at the source. At these settings the transported magnetic flux covered an area of about  $10 \text{ cm}^2$  on the photocathode (see table 6.2), which is significantly larger than the area actually illuminated by the UV LED ( $\approx 2 \text{ cm}^2$ ). It can therefore be assumed that for a careful alignment of the UV LED all photoelectrons were imaged onto the detector.

During this measurement, the Flash-ADC system was operated with a sampling length of  $2^{14} = 16384$  channels per buffer and a sampling rate of  $f_{\text{sampling}} = 100$  MHz, *i. e.*, the width of each channel is 10 ns. One buffer therefore covers a measurement time of

$$t_{\text{buffer}} = 2^{14} \cdot 10 \text{ ns} = 163.84 \mu\text{s}. \quad (7.8)$$

Since in this measurement the UV LED delivered one photoelectron pulse per millisecond ( $f_{\text{LED}} = 1$  kHz,  $\tau \ll t_{\text{buffer}}$ ), one buffer started after the trigger signal only contained one photoelectron pulse.

If  $N_{\text{peaks}}$  is the number of peaks visible in the spectrum,  $N_{\text{entries},n}$  is the number of entries in the peak with order  $n$  ( $n = 1, \dots, N_{\text{peak}}$ ) and  $N_{\text{buffers}}$  is the number of recorded Flash-ADC-buffers, the total number of photoelectrons detected per UV light pulse is given by

$$N_{\text{electrons/pulse}} \stackrel{\wedge}{=} \frac{N_{\text{electrons}}}{N_{\text{buffers}}} = \frac{1}{N_{\text{buffers}}} \sum_{n=1}^{N_{\text{peaks}}} (n \cdot N_{\text{entries},n}). \quad (7.9)$$

### Dependence of photoelectron count rate on the pulse width of the UV LED

The photoelectron count rate was measured for varying widths of the UV light pulses. Starting with a large pulse width of  $\tau = 40 \mu\text{s}$  at  $f_{\text{LED}} = 1$  kHz, the count rate of photoelectrons arriving at the detector was high; therefore, a medium operating voltage  $U_{\text{LED}} = 6.6$  V was chosen. A step-wise reduction of the pulse width led to a linear decrease in the count rate (see figure 7.9(a)). Pulse widths of several  $10 \mu\text{s}$  resulted in an average of 10 to 40 photoelectrons per UV light pulse, whereas at  $\tau = 5 \mu\text{s}$ , the number of photoelectrons detected per pulse averaged at about 2.6. Going to even shorter pulses, the intensity of the UV light was increased by raising the operating voltage from 6.6 V to 7.6 V (see figure 7.9(b)). The relation between pulse length and count rate was still fairly linear, albeit with a different slope. The irregularity seen at  $\tau = 100$  ns stems from a repositioning of the UV LED, which resulted in a shift of the irradiated spot on the photocathode.

<sup>6</sup>It was determined in [Str09] that 68.3% of the signals occurring with a time difference of  $\Delta t = (760 \pm 20)$  ns were counted as separate events.

This sensitivity of the count rate with regard to the point of incidence of the UV light on the electrode can be explained by taking into account that not the full surface of the disc is imaged onto the detector (compare table 6.2). A significant misalignment of the LED can thus result in a loss of photoelectrons.

Figure 7.10 presents the number of single photoelectrons per pulse relative to the total photoelectron yield per pulse as a function of  $\tau$ . This ratio contains information on the pile-up effect. Using the notation introduced in eq. (7.9), the ratio  $\epsilon_{\text{single}}$  is obtained by counting the entries in the first peak and dividing this number ( $N_{\text{entries},1}/\text{pulse}$ ) by the weighted sum of the entries in all peaks ( $N_{\text{electrons}}/\text{pulse}$ ):

$$\begin{aligned}\epsilon_{\text{single}} &= \frac{N_{\text{entries},1}/\text{pulse}}{N_{\text{electrons}}/\text{pulse}} \\ &= \frac{N_{\text{entries},1}}{\sum_{n=1}^{N_{\text{peaks}}} (n \cdot N_{\text{entries},n})}.\end{aligned}\quad (7.10)$$

One particular advantage of the UV LEDs consists in the possibility to achieve sufficiently high count rates while keeping the pile-up low by choosing an appropriate pulse width and intensity of the UV light. This is an important feature, as for the second-order time-of-flight mode a high ratio  $\epsilon_{\text{single}}$  is an essential prerequisite. For small duty cycles ( $\tau \cdot f_{\text{LED}} \ll 1$ ) the total count rate  $R_{\text{tot}}$  integrated over many pulses can be estimated as

$$R_{\text{total}} \approx f_{\text{LED}} \cdot N_{\text{electrons}}/\text{pulse}.\quad (7.11)$$

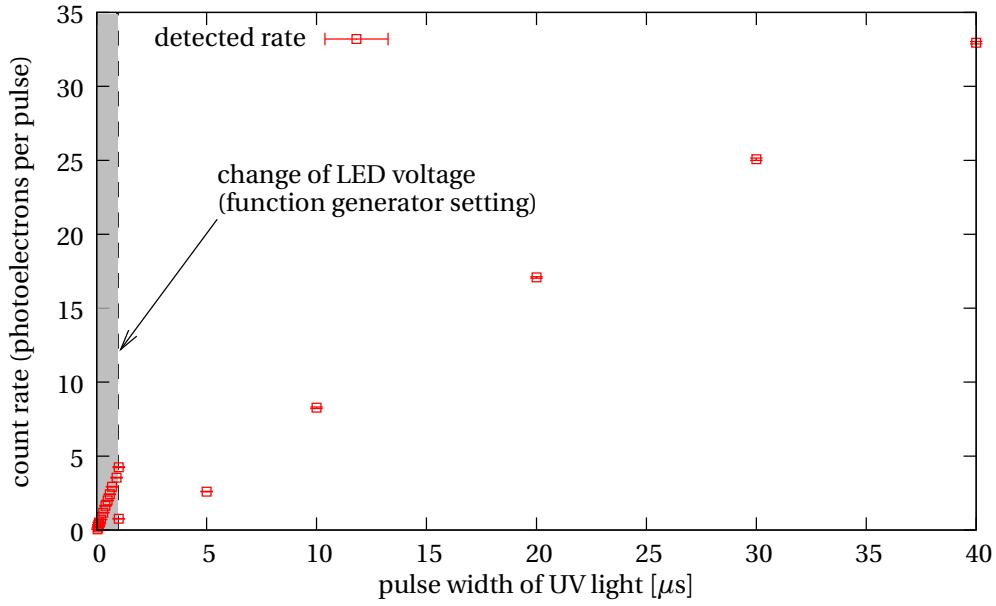
Within certain limits, the total detection rate can be scaled by varying the duty cycle via the repetition rate  $f_{\text{LED}}$  at constant  $\tau$  and  $U_{\text{LED}}$  without changing the pile-up ratio.

Examples of UV LED settings and the corresponding values of  $\epsilon_{\text{single}}$  are compiled in table 7.3. For a pulse width of  $\tau = 200$  ns at a high LED voltage, a total count rate of about 700 photoelectrons per second was detected, with about half of these contained in the single-electron peak. Using very short pulses, *e. g.*,  $\tau = 40$  ns, even a single-electron ratio  $\epsilon_{\text{single}}$  of 1 can be reached.

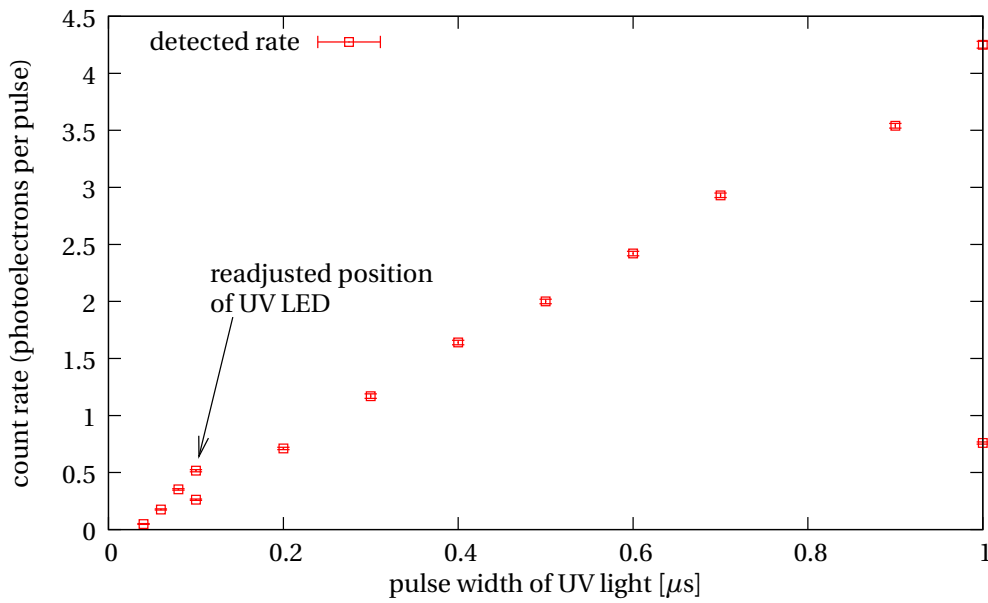
Figure 7.11(a) presents the measured probability to detect  $n = 1, \dots, 10$  coincident photoelectrons for varying pulse widths  $\tau$ . With increasing  $\tau$  (between  $\tau = 40$  ns and  $\tau = 1000$  ns) the average multiplicity is shifted towards higher values of  $n$ . The measured probabilities  $P(n)$  are in reasonable agreement with Poisson statistics (figure 7.11(b)).

**Table 7.3:** Ratio  $\epsilon_{\text{single}}$  and mean total detection rate  $R_{\text{total}}$  achievable for various settings of the UV LED.

	$\tau = 40$ ns	$\tau = 200$ ns	$\tau = 20$ $\mu$ s
$\epsilon_{\text{single}}$	1	$0.50 \pm 0.01$	$0.369 \pm 0.002$
$N_{\text{electrons}}/\text{pulse}$	$0.049 \pm 0.003$	$0.711 \pm 0.010$	$17.08 \pm 0.05$
$U_{\text{LED}}$ [V]	7.6	7.6	6.6
$f_{\text{LED}}$ [kHz]	1	1	1
$R_{\text{total}}$ [1/s]	50	700	17000

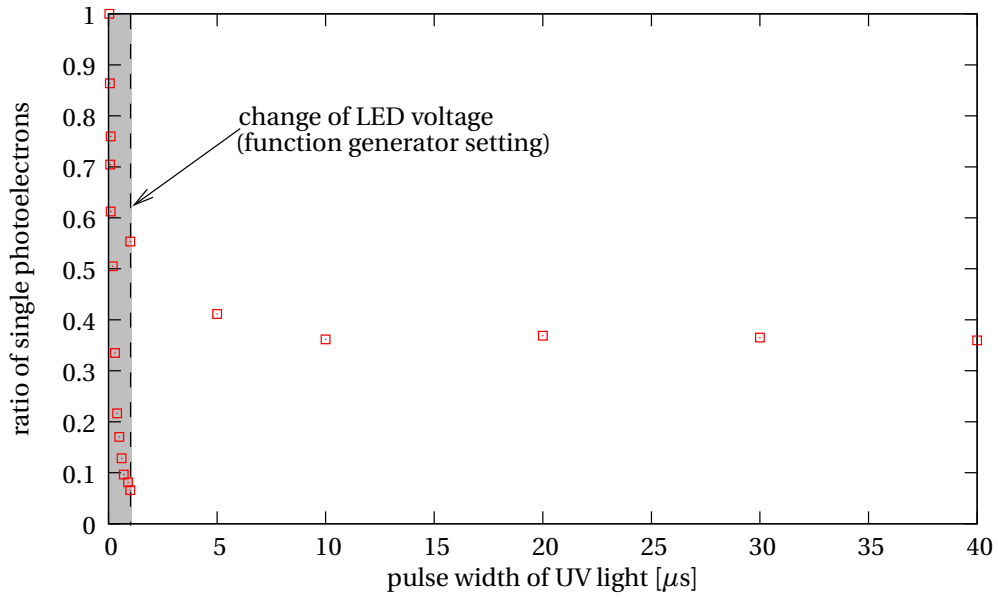


(a) full range of pulse widths:  $\tau_{\min} = 40 \text{ ns}$  to  $\tau_{\max} = 40 \mu\text{s}$

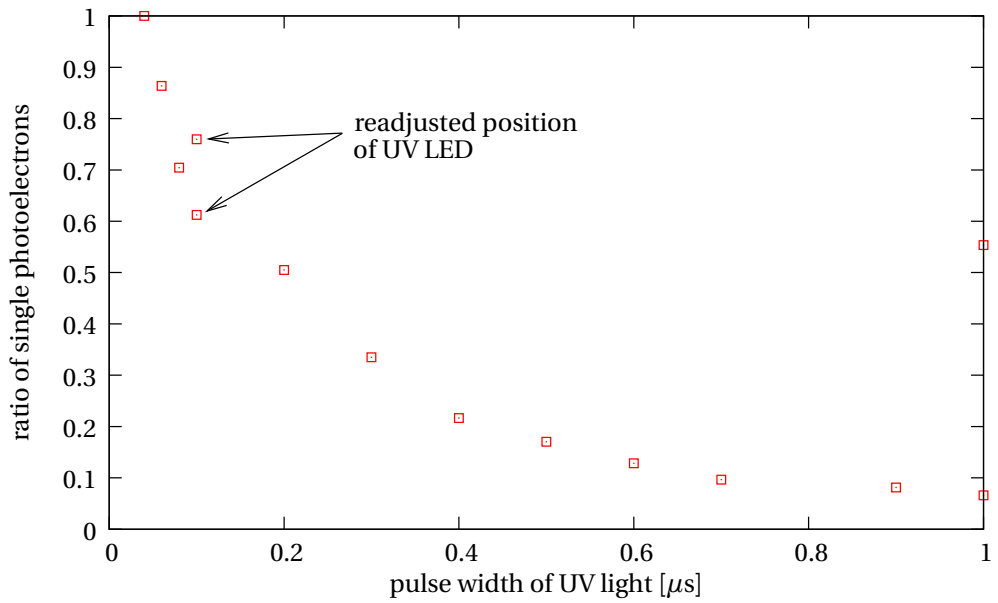


(b) small pulse widths only:  $\tau \leq 1 \mu\text{s}$

**Figure 7.9:** Dependence of the photoelectron count rate on the pulse width  $\tau$  of the UV light. Pulse widths between  $\tau_{\min} = 40 \text{ ns}$  and  $\tau_{\max} = 40 \mu\text{s}$  were investigated. For small pulse widths  $\tau \leq 1 \mu\text{s}$  (gray-shaded area) a higher intensity of the UV light was used: the driving voltage was set to  $U_{\text{LED}} = 7.6 \text{ V}$  instead of  $U_{\text{LED}} = 6.6 \text{ V}$  for larger pulse widths. The repetition frequency of the LED was  $f_{\text{LED}} = 1 \text{ kHz}$ .



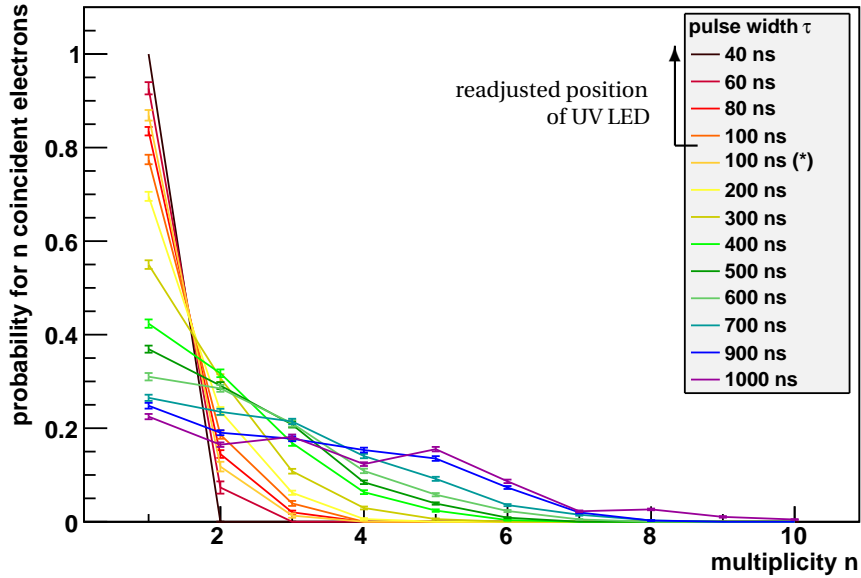
(a) full range of pulse widths:  $\tau_{\min} = 40 \text{ ns}$  to  $\tau_{\max} = 40 \mu\text{s}$



(b) small pulse widths only:  $\tau \leq 1 \mu\text{s}$

**Figure 7.10:** Relative fraction of single photoelectrons detected per pulse as a function of the pulse width  $\tau$  of the UV light. Pulse widths between  $\tau_{\min} = 40 \text{ ns}$  and  $\tau_{\max} = 40 \mu\text{s}$  were investigated. For small pulse widths (gray-shaded area,  $\tau \leq 1 \mu\text{s}$ ) a higher intensity of the UV light was used: the driving voltage was set to  $U_{\text{LED}} = 7.6 \text{ V}$  instead of  $U_{\text{LED}} = 6.6 \text{ V}$  for larger pulse widths. The repetition frequency of the LED was  $f_{\text{LED}} = 1 \text{ kHz}$ . The largest relative fraction of single photoelectrons per pulse compared to the total number of photoelectrons per pulse is obtained at the smallest values of  $\tau$ .

(a) multiplicity distributions



(b) comparison with Poisson distribution

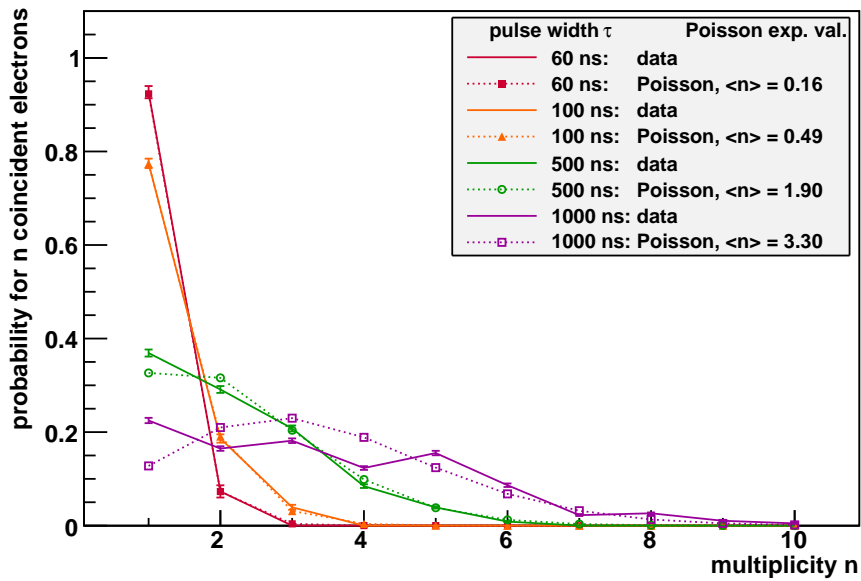


**Figure 7.11:** Measured multiplicity distributions for various pulse widths (a) and comparison with calculated distributions according to Poisson statistics (b).

### Dependence of photoelectron count rate on the driving voltage of the UV LED

In order to tune the detected rate of photoelectrons, it is also possible to vary the intensity of the light emitted by the LED by changing the operating voltage, while keeping the other operational parameters ( $f$  and  $\tau$ ) constant.

The optical power output of a LED increases with the forward current  $I_F$ , which is given by

$$I_F = \frac{U_{AFG} - U_{LED}}{R} \quad (7.12)$$

for the driving circuit of the LED depicted in figure 7.12. The relation is approximately (although not strictly) linear (a typical diagram for the UV LEDs employed in this measurement is included in figure C.1 in the appendix).

Figure 7.13 presents the measured number of photoelectrons per pulse for various voltage settings  $U_{LED}$  at fixed pulse width  $\tau = 40\mu s$  and repetition rate  $f_{LED} = 1\text{ kHz}$ . For low operating voltages about 1 photoelectron per light pulse is detected on average, whereas at higher operating voltages several tens of photoelectrons per pulse reach the detector.

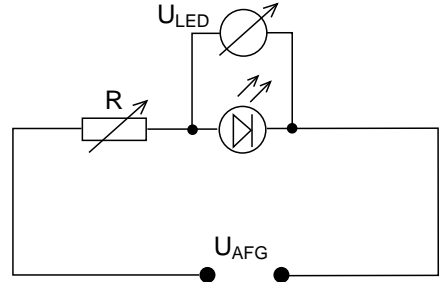


**Figure 7.12:** Driving circuit of the UV LED. A series resistor  $R$  protects the diode against thermal damage due to excess currents. In most of the measurements,  $R = 90\Omega$  was used.

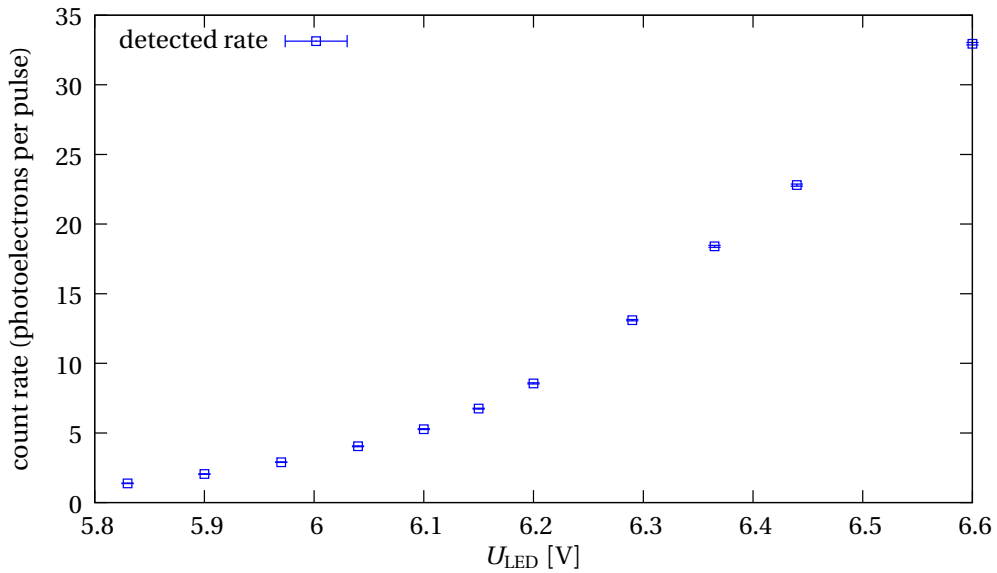


**Figure 7.13:** Dependence of the photoelectron count rate on the operating voltage in the range between  $U_{LED} = 5.8\text{V}$  and  $6.6\text{V}$  (further measurement points up to  $U_{LED} = 7.6\text{V}$  are not included in the graph). Measurement with fixed pulse width  $\tau = 40\mu s$  and repetition rate  $f_{LED} = 1\text{ kHz}$  at a surplus energy of  $q(U_{source} - U_{spec}) \approx 15.7\text{ eV}$ .

### Overview of the results

In summary, the investigations of the timing properties of photoelectron pulses generated with a fast-pulsed UV LED demonstrate the following key qualities:

1. The operating parameters  $f$ ,  $\tau$  and  $U$  of the UV LED in pulsed mode can be varied over a wide range, turning the LED-based photoelectron source into a multipurpose device.<sup>7</sup>
2. Photoelectron rates of several  $10^4 \frac{1}{s}$  have been achieved. This would allow to carry out calibration measurements of the transmission function at the main spectrometer in the normal mode (*i. e.*, without the additional time-of-flight option), where high electron rates are necessary.
3. The emission time interval  $\Delta t_{\text{emis}}^{e^-}$  of the photoelectrons, which can be controlled by tuning the pulse width  $\tau$  of the LED, is sufficiently well defined for the purpose of using this electron source in a pulsed time-of-flight measurement. In particular, the UV LEDs used in the measurements can deliver pulses which fulfill the following requirements:

- $\Delta t_{\text{emis}}^{e^-} \ll \text{ToF}$

The photoelectron pulses are short compared to the overall time of flight (ToF) through the spectrometer. This holds for the Mainz MAC-E filter with ToF values of a few  $\mu\text{s}$  or below (see section 7.3.3), and thus necessarily also for the much longer KATRIN main spectrometer with ToF values of up to several  $10 \mu\text{s}$  (compare sections 7.1.1 and 7.1.2).

- $\Delta t_{\text{emis}}^{e^-} \ll \delta\text{ToF}$

The photoelectron pulses are also short compared to the expected *differences* in the time of flight ( $\delta\text{ToF}$ ) which are intended to be resolved in the second-order MAC-E-ToF mode introduced in section 7.1.2 (compare simulations for the KATRIN main spectrometer, figures 7.5 and 7.7(b)).

- $\Delta t_{\text{emis}}^{e^-} \lesssim \Delta t_{\text{DAQ, analysis}}$

The pulse widths are comparable to the timing resolution  $\Delta t_{\text{DAQ, analysis}}$  of the DAQ system and the data analysis methods (for further details see reference [Str09]).

Furthermore,  $\Delta t_{\text{DAQ, analysis}}$  is required to be smaller than ToF and  $\delta\text{ToF}$ .<sup>8</sup>

It is possible to choose  $f$ ,  $\tau$  and  $U$  such that only – or at least predominantly – single photoelectrons per pulse are obtained (figure 7.10(b)), although the overall detection rate of photoelectrons in this case may be low (figure 7.9(b)). This high fraction  $\varepsilon_{\text{single}}$  is important to take full advantage of the good timing resolution of a fast DAQ system in the ToF measurement mode.

<sup>7</sup>Aside from fast pulsing with duty cycles of the order of  $10^{-5} - 10^{-2}$  as mostly used in the experimental work described in this thesis, high duty cycles (*e. g.*, 50%) or continuous operation are possible, as well. In any application, attention should be devoted to the maximum thermal load sustainable by the LED, and the forward current should be limited according to the duty factor (compare datasheets [Seo06b, Seo06a]).

<sup>8</sup>For the test measurements at Mainz  $\Delta t_{\text{DAQ, analysis}}$  was determined to be about 60 ns (gaussian width  $\sigma$  of the measured distribution).

### 7.3.2 Energy scan of photoelectrons at 18 keV

In further measurements the energy distribution of the photoelectrons was investigated. To obtain the energy spectrum, the photocathode was set to  $U_{\text{source}} = -18.0\text{ kV}$  and the retardation potential of the spectrometer was varied between  $U_{\text{spec}} = U_{\text{source}} - 4\text{ V}$  and approximately  $U_{\text{source}} + 410\text{ V}$ . The following settings of the UV LED were used: rate  $f = 1\text{ kHz}$ , pulse width  $\tau = 200\text{ ns}$ , driving voltage  $U_{\text{LED}} = 7.6\text{ V}$ . The energy scan contains about 30 points with a measurement time of about 10–12 s each (the exact value was determined by counting the number of recorded buffers, which was typically of the order of  $N_{\text{buffers}} \lesssim 10000$ ). Two principal methods of analysis can be applied to these data:

- a) evaluation of the total number of photoelectrons detected (per UV light pulse) as a function of the surplus energy  $E_{\text{surplus}} = q(U_{\text{source}} - U_{\text{spec}})$  (*integrated energy spectrum*, presented in this section),
- b) determination of the mean time of flight of the photoelectrons as a function of the surplus energy (*time-of-flight spectrum*, see next section 7.3.3).

The integrated energy spectrum shall be discussed first.

One channel of the Flash-ADC was used to record the pre-amplified signals of the electron detector. In the analysis software, these signals were later digitally filtered and differentiated. The peaks in the differentiated data were fitted. Subsequently, energy and timing information were extracted from the parameters of the fit.<sup>9</sup>

Figure 7.8 contains an energy spectrum resulting from the analysis of the processed pre-amplifier pulses for one measurement point. For each of these individual spectra, the ROOT<sup>10</sup> PeakSearch algorithm was employed to find the position of the peaks (triangle symbols ▼ in figure 7.8). They were first fitted one by one with a function consisting of an exponential rise convolved with a Gaussian (red curves). After that, pairs of two adjacent peaks were fitted together in order to find the position of the minimum separating them (blue curves). This way the limits  $E_{\text{min}}^n$  and  $E_{\text{max}}^n$  for the summation of events in the peak of order  $n$  were determined. In case of overlapping peaks, the peak positions at higher orders were extrapolated from the position and width of the first peaks.<sup>11</sup> A means to control the quality of the peak analysis is to plot the position of the peak maxima determined by the fit as a function of peak order. Such a plot is shown in figure 7.14.

With this information from the fitting procedure the number of detected photoelectrons per pulse was determined according to eq. (7.9). This quantity is plotted as a function of surplus energy in figure 7.15. Due to the high-pass character of the MAC-E filter, the spectrum is an integrated one, *i. e.*, all electrons with energies  $E_{\parallel} > qU_{\text{spec}}$  can pass the electrostatic filter.

In the following the uncertainties of the energy determination and electron counting method shall be discussed.

- *Uncertainty of the surplus energy determination*

Two major contributions are expected:

- a) High-voltage stability and relative calibration.

The error bars for the surplus energy values  $E_{\text{surplus}} = q(U_{\text{source}} - U_{\text{spec}})$  shown in figure 7.15 only reflect the short-term stability of the two voltages  $U_{\text{source}}$  and  $U_{\text{spec}}$  during the scan, which was monitored with a high-stability precision voltmeter. A further systematic uncertainty, however, arises from the fact that the divider ratios of the two

<sup>9</sup>A comprehensive overview of the signal processing and analysis chain is given in [Arl09, Str09].

<sup>10</sup>ROOT: An Object Oriented Data Analysis Framework [ROOT]

<sup>11</sup>See [Str09] for further details.

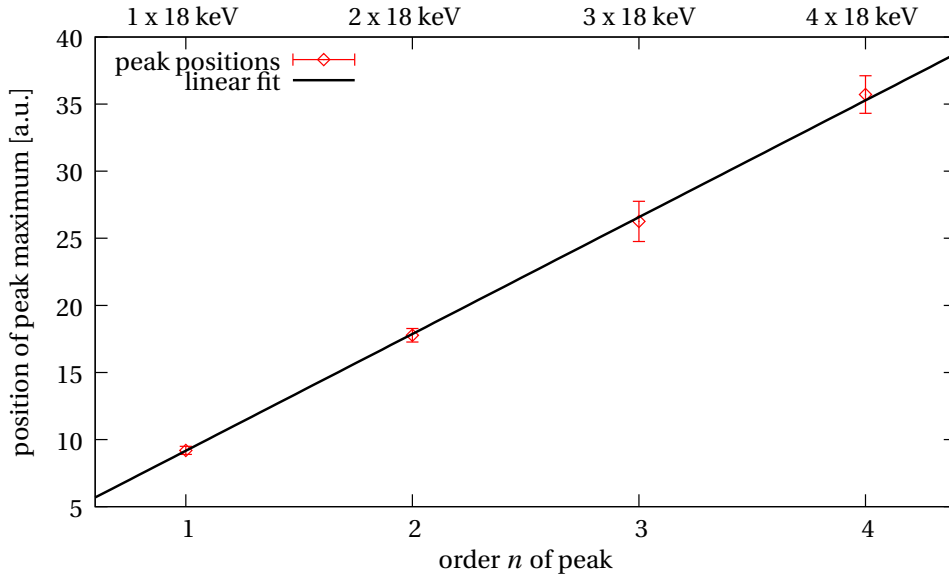


**Figure 7.14:** Multiple peaks in energy spectrum: linear relation between peak position and peak order. A linear fit of the data with the function  $f(x) = a + bx$  yields the fit parameters  $a = 0.46 \pm 0.17$  and  $b = 8.70 \pm 0.11$ .

high-voltage dividers are only known to a limited accuracy, which affects the determination of the two voltages relative to each other. This uncertainty is not included in the graph, but should be regarded as a constant offset to the value of the surplus energy of a magnitude of  $\Delta E_{\text{surplus}} \approx 1.1$  eV. The shift is dominated by the uncertainty of the JRL divider ratio (compare table 6.3).

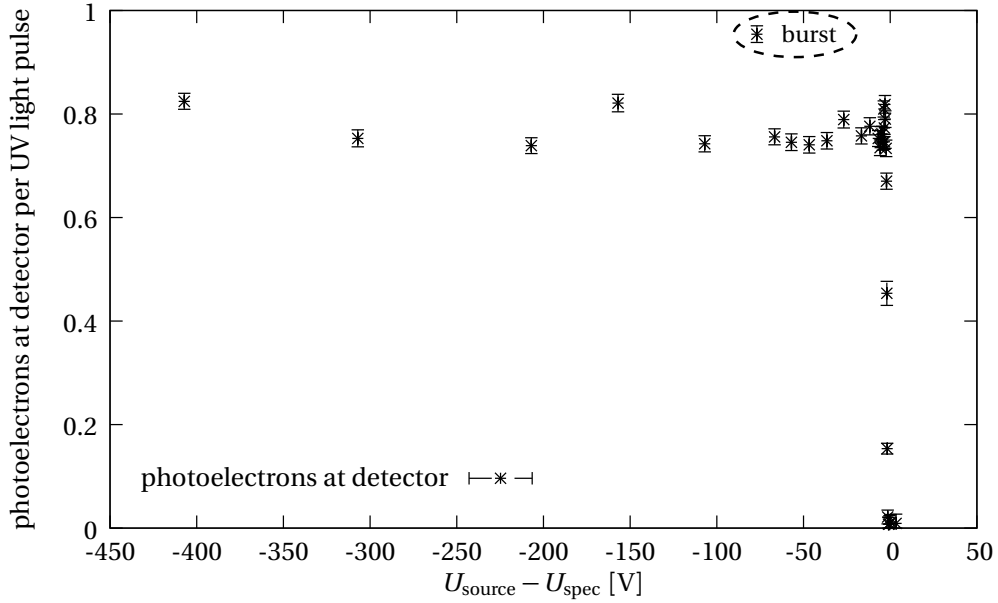
b) Work function values.

The kinetic energy of the electrons analyzed by the electrostatic filter is influenced by the difference  $\Phi_{\text{source}} - \Phi_{\text{spec}}$  of the work functions of source and spectrometer (compare, for example, the extensive discussion in [Ost09]). Although both the photocathode and the retardation electrodes of the spectrometer consist of stainless steel, it is plausible that their respective work functions are not exactly the same (different grades of material were used, and further effects due to the machining and a potential oxygen contamination of the surfaces are expected). It is difficult to determine the size of the contribution, yet a shift of the order of a few 100 meV seems to be a reasonable assumption.<sup>12</sup>

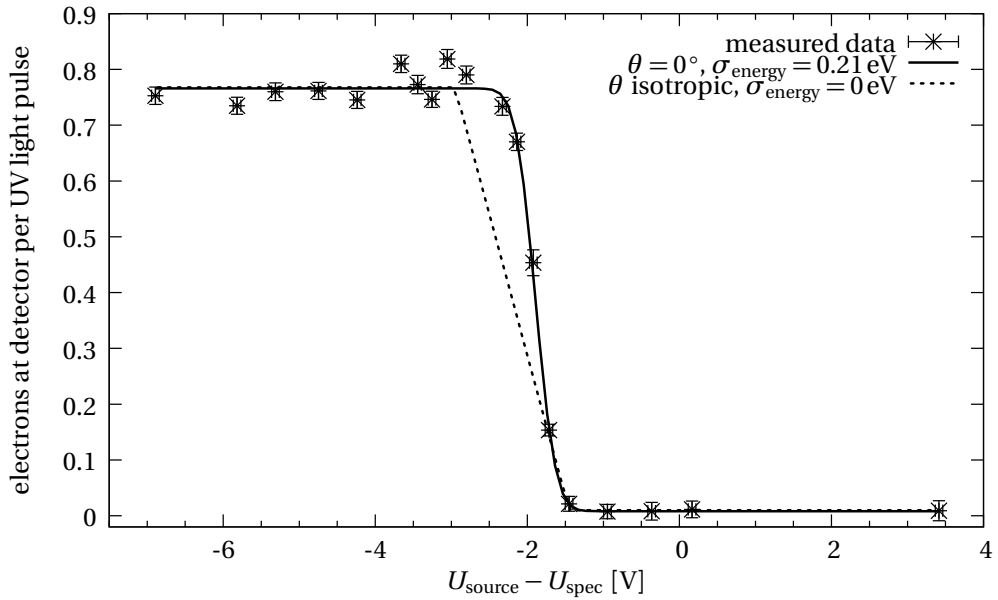
A combination of these two contributions may well explain the shifted onset of the transmission observed in the measurement (fig. 7.15(b)). The transmission edge, where electrons start to pass the electrostatic filter, is located at a surplus energy of  $q(U_{\text{source}} - U_{\text{spec}}) \approx 1.5$  eV. This observation is consistent with the slightly larger values found in the measurements with the fiber-coupled photoelectron gun described in section 7.4, where different photocathode materials were used. However, it cannot be excluded that further uncertainties play a role which have up to now remained undetected.

<sup>12</sup>Measured values of  $\Phi_{\text{stainless steel}}$  found in the literature vary over a range between 4.35 eV and 4.75 eV (cf. table 7.1).

## 7 Tests of a UVLED-based photoelectron source



(a) full range of surplus energies ( $qU_{\text{source}} - qU_{\text{spec}} = E_{\text{surplus}} \lesssim 410 \text{ eV}$ )



(b) small surplus energies ( $qU_{\text{source}} - qU_{\text{spec}} = E_{\text{surplus}} \lesssim 7 \text{ eV}$ )

**Figure 7.15:** (a) Integrated energy spectrum of photoelectrons at  $U_{\text{source}} = -18 \text{ kV}$ . (b) Close-up on low surplus energies. A fit assuming a gaussian energy spread  $\sigma_{\text{energy}}$  of the photoelectrons with a vanishing starting angle distribution (solid line) and the expected analytical transmission curve for an isotropically emitting, but monoenergetic photoelectron source at a spectrometer energy resolution of  $\Delta E_{\text{spec}} = 1.5 \text{ eV}$  (dashed line) are included. The former yields a good agreement with the data for  $\sigma_{\text{energy}} = 0.21 \text{ eV}$ .

- *Uncertainty of the number of detected photoelectrons per UV pulse*

The total uncertainty of the number of photoelectrons per UV pulse is obtained by quadratically adding the statistical and systematical uncertainties:

$$\sigma_{\text{tot}} = \sqrt{\sigma_{\text{stat}}^2 + \sigma_{\text{sys}}^2}, \quad (7.13)$$

with the statistical uncertainty

$$\sigma_{\text{stat}} = \frac{\Delta N_{\text{electrons}}}{N_{\text{buffers}}} = \frac{\sqrt{N_{\text{electrons}}}}{N_{\text{buffers}}} \quad (7.14)$$

and the systematical uncertainty due to the analysis method of the peaks given by

$$\sigma_{\text{syst}} = \frac{1}{N_{\text{buffers}}} \cdot \sqrt{\sum_{n=1}^{N_{\text{peaks}}} (n \cdot \Delta N_{\text{entries}, n})^2}. \quad (7.15)$$

The latter uncertainty arises from the method of determining the total number of photoelectrons according to eq. (7.9). For example, the choice of binning of the photoelectron energy slightly influences the number of entries attributed to each of the multiple peaks in the energy spectrum (see figure 7.8). This gives individual uncertainties  $\Delta N_{\text{entries}, n}$ , which need to be taken into account according to their weight  $n$ . In the case of the measurement presented in figure 7.15, a typical value of the systematic error is 120 counts divided by  $N_{\text{buffers}}$ , while the statistical error is usually slightly lower (but of the same order).

### Interpretation of the integrated energy spectrum

Figure 7.15 shows that, for the given operational parameters of the UV LED, at full transmission ( $qU_{\text{source}} \gg qU_{\text{spec}}$ ) the total rate of detected photoelectrons averages at about 0.8 per pulse. A considerable fluctuation of the count rate is observed, in particular at low surplus energies around  $E_{\text{surplus}} \approx 2 - 3 \text{ eV}$ . A further burst occurs at  $E_{\text{surplus}} \approx 80 \text{ eV}$ . During the measurement, the wire scanner was installed, but inactive. This means that the wire was located close to – yet probably not exactly at – the center of the beam line. It is likely that minor, short-lived discharges from the Penning trap discussed in chapter 6 played a significant role. The fluctuating count rate is reminiscent of the behavior observed during the wire scanner test measurements (compare section 6.3.2). It is also possible that the “bump” at low surplus energies is an indication of formerly stored electrons spilling out of the Penning trap as soon as the energy barrier formed by the retardation potential is lowered (this fits the direction of the energy scan seen in figure 7.15, which was performed starting from  $U_{\text{source}} - U_{\text{spec}} > 0$  and proceeding towards  $U_{\text{source}} - U_{\text{spec}} < 0$ .) In future measurements it would be worthwhile to check for this effect by reversing the direction of the energy scan.

In order to interpret the observed width of the rise in the integrated energy spectrum from zero to 0.8 photoelectrons per pulse, the individual contributions due to the transmission function of the spectrometer and the energy spread associated with the process of photoelectron production must be disentangled. Two general scenarios have to be distinguished:

1. The angular distribution of the photoelectrons fills up the entire forward solid angle and the spectral width is thus expected to reflect the full spectrometer energy resolution  $\Delta E_{\text{spec}} = 1.5 \text{ eV}$  used for the measurement. In this case the measured width, which is indeed comparable to this value of  $\Delta E_{\text{spec}} = 1.5 \text{ eV}$ , would leave no room for any additional spread in the work function  $\Phi$  or a finite width of the photon energy  $E_{\text{photon}}$ . Considering the arguments presented in section 7.2, this case representing a “perfectly monoenergetic” photoelectron source is unlikely.
2. In the alternative scenario, the angular distribution of the photoelectrons is confined to small angles. Hence, the transmission function of the spectrometer only gives a minor contribution to the observed spectral width, which in this case is determined by the inhomogeneity of the work function of the photocathode, the spread of the photon energy (FWHM

## 7 Tests of a UV LED-based photoelectron source

= 0.27 eV for the 265 nm LED), potential energy losses of the electrons inside the photocathode and by the ripple of the high-voltage power supplies ( $\mathcal{O}(100\text{ mV})$ ).

Due to the immediate and strong forward acceleration in the high electric field at the cathode, it is expected that the photoelectrons gain only a small amount of transverse energy as compared to the longitudinal component. Therefore, they can obtain only small starting angles

$$\theta_{\text{start,max}} = \arctan \left( \sqrt{\frac{(E_{\perp})_{\text{start,max}}}{E_{\parallel}}} \right) \approx \arctan \left( \sqrt{\frac{0.5\text{ eV}}{18\text{ keV}}} \right) \approx 0.3^{\circ}, \quad (7.16)$$

assuming a maximum initial transversal energy of  $(E_{\perp})_{\text{start,max}} \approx 0.5\text{ eV}$  (estimated from the work function and photon energy values given in tables 7.1 and 7.2). Consequently, the angular distribution reached inside the strong magnetic field does not encompass the full forward solid angle<sup>13</sup>, thus ruling out the first of the two abovementioned cases.

The two scenarios are compared in figure 7.15(b), from which it can be seen that the theoretical curve for the case of isotropic emission without intrinsic energy spread of the photoelectrons (dashed line) does not match the measured data, while the model with mono-angular emission along the normal of the photocathode ( $\theta = 0^{\circ}$ ) and a small energy spread (solid line) is in good agreement with the measurement. Fitting the measured data in the range between  $U_{\text{source}} - U_{\text{spec}} = -8\text{ V}$  and  $4\text{ V}$  with a complementary Gauss error function  $\text{erfc}$  (thus respecting the integrating character of the MAC-E filter) with the fit parameters

$a$	amplitude,
$\sigma_{\text{energy}}$	gaussian width,
$E_0$	position, and
$b$	background (offset)

yields

$$\sigma_{\text{energy}} = (0.207 \pm 0.017)\text{ eV}. \quad (7.17)$$

The fit result allows to set an upper limit on the width of the energy smearing of

$$\sigma_{\text{energy}} < 0.24\text{ eV} \quad (95\% \text{ C.L.}), \quad (7.18)$$

which corresponds to a full width at half maximum of  $\Delta E_{\text{energy}}^{\text{fwhm}} < 0.57\text{ eV}$ .

<sup>13</sup>Based on the estimated upper limit of starting angles  $\theta_{\text{start,max}}$  obtained in eq. (7.16), the adiabatic transformation when going from the weak magnetic field  $B_{\text{start}} \approx 0.02\text{ T}$  at the location of the photocathode to the high magnetic field  $B_{\text{magnet}} \approx 6\text{ T}$  inside the entrance solenoid of the spectrometer can only produce a maximum angle of  $\theta_{\text{magnet,max}} = \arcsin \left( \sin \theta_{\text{start,max}} \cdot \sqrt{B_{\text{magnet}}/B_{\text{start}}} \right) \approx 5^{\circ}$ , which is indeed far from filling the full forward solid angle.

### 7.3.3 Time-of-flight measurement of photoelectrons at 18 keV

Taking advantage of the good timing resolution of the Flash-ADC data acquisition system, the time of flight (ToF) for photoelectrons passing the retardation filter at different surplus energies was determined analyzing data from the same measurement that was used to obtain the integrated energy spectrum.

The start signal for the ToF measurement was provided by the trigger output of the function generator powering the UV LED. After being processed by a gate and delay unit and a spectroscopy amplifier, this control signal was recorded on the second channel of the Flash-ADC card. The starting point was then determined by the zero point of the bipolar control signal.

To obtain the ToF spectrum, a histogram of the arrival times was generated for each measurement point and the mean of the distribution was determined. Some examples are shown in figure 7.16. At large surplus energies above the filter threshold the distribution can be described by a Gaussian (figure 7.16(a)), since for small pulse widths of the UV LED ( $\tau \lesssim 250\text{--}300\text{ ns}$ ) the systematic effects introduced by the timing resolution of the measurement method dominate (compare [Str09]). For small surplus energies, however, the arrival time distribution exhibits additional features related to physical origins rather than to systematic effects. A broadening of the distribution and a tail towards higher arrival times (see figure 7.16(b)) are observed for decreasing surplus energy. They are to a large extent caused by the spread of the photoelectron energies, which is mainly due to two effects. First, as seen in section 7.2, the light from the UV LED is not strictly monochromatic. Second, the work function of the cathode material is not spatially uniform. The extended spot of UV light on the surface of the photocathode therefore encompasses local inhomogeneities, and photoelectrons with slightly varying energies are generated.

Figure 7.17 shows the full width at half maximum (FWHM) of the arrival time distribution as a function of  $E_{\text{surplus}}$ . Between surplus energies of about 410 eV and 15 eV, the width remains constant and the shape of the curve is essentially Gaussian. For lower surplus energies, however, the spread in the kinetic energy translates into a spread of the arrival times of more than a microsecond.

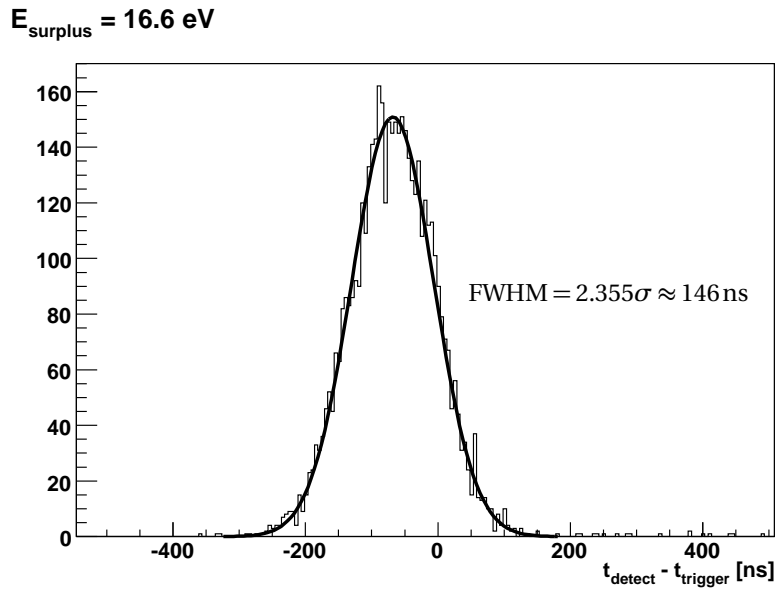
Figure 7.18(a) presents the time-of-flight spectrum for photoelectrons over a wide range of surplus energies. Electrons with  $E_{\text{surplus}} \approx 410\text{ eV}$  reach the detector about 220 ns after the UV light pulse irradiated the photocathode, whereas electrons with small energies of  $E_{\text{surplus}} \approx 1.7\text{ eV}$  arrive after a mean time of flight of about 4  $\mu\text{s}$ .

The absolute scale of the time of flight was fixed using calculated values, which are also included in the plot. These allow to correct for a systematic offset due to processing and propagation times, which partly shifted the uncorrected values into the unphysical negative range (compare for example 7.16(a)). The time of flight for electrons starting with a specific kinetic energy  $E_{\text{kin}}$  was calculated by numerical integration according to the relation

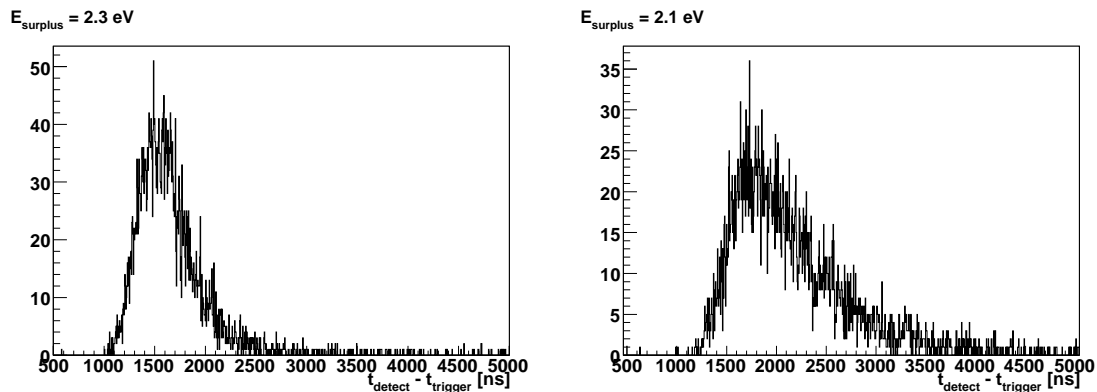
$$t_{\text{arrival}} - t_{\text{start}} = \int_{z_{\text{start}}}^{z_{\text{stop}}} \frac{dz}{v(z)}, \quad (7.19)$$

where  $dz$  is a line element along the  $z$  axis, and the velocity  $v$  of the particle is given by

$$\begin{aligned} v(z) &= c \beta(z) = c \sqrt{1 - \frac{1}{\gamma^2(z)}} \\ &= c \sqrt{1 - \frac{1}{\left(\frac{E_{\text{kin}}(z)}{m_0 c^2} + 1\right)^2}} = c \sqrt{1 - \frac{1}{\left(\frac{q(U_{\text{source}} - U(z))}{m_0 c^2} + 1\right)^2}}. \end{aligned} \quad (7.20)$$



(a) The arrival time distribution obtained for large surplus energies, like for example 16.6 eV, can be described by a Gaussian function (here: mean  $t_0 = (-68.1 \pm 0.9)$  ns and standard deviation  $\sigma = (62.0 \pm 0.7)$  ns).



(b) The arrival time distribution for smaller surplus energies, for example 2.3 eV and 2.1 eV, can no longer be fitted with a simple Gaussian function. With decreasing surplus energy, the distribution broadens and develops a tail towards larger arrival times.

**Figure 7.16:** Arrival time distribution of photoelectrons at different surplus energies.

The axial distribution of the electric potential,  $U(z)$ , is calculated using a detailed computer model of the electrode configuration. In the relations (7.19) and (7.20) it is assumed that the velocity of the electron is parallel to the magnetic field lines and thus defined by the gain of the kinetic energy  $E_{\text{kin}}$  in the electric potential  $U(z)$ . This assumption reflects the expectation discussed in the previous section that the photoelectrons are emitted from the cathode with a negligible amount of transverse energy (compare eq. (7.16)).

As can be seen in figure 7.18(a), calculated time-of-flight values and measured data are in good agreement over a range of 400 V.

However, discrepancies between the theoretical curve for a single value of  $E_{\text{kin}} = qU_{\text{source}}$  and the experimental data become visible when considering the smallest surplus energies in detail (figure 7.18(b)). These point to the finite energy distribution of the photoelectrons, which has so far

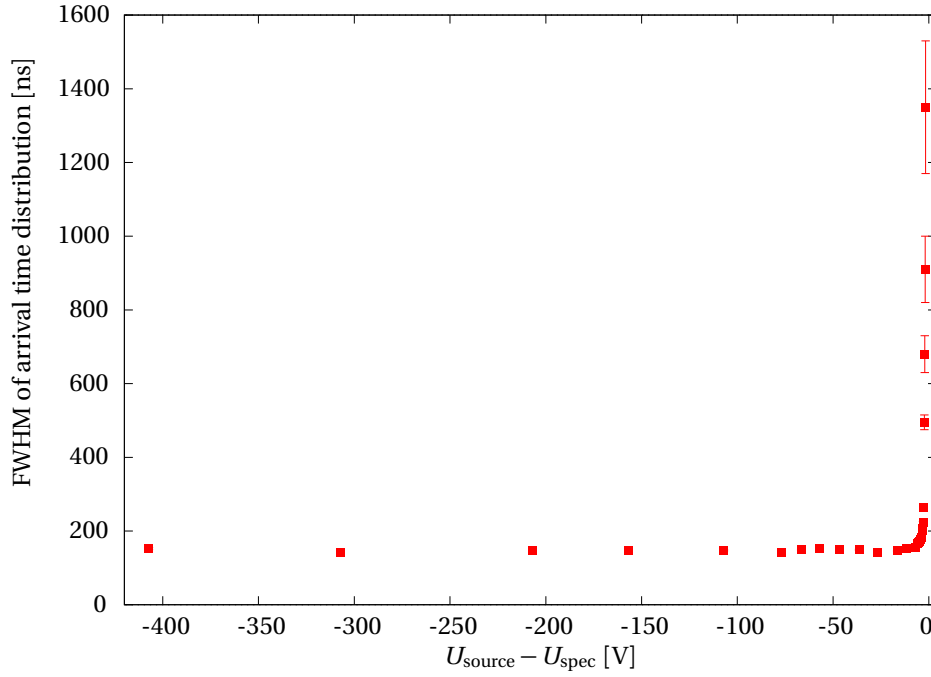
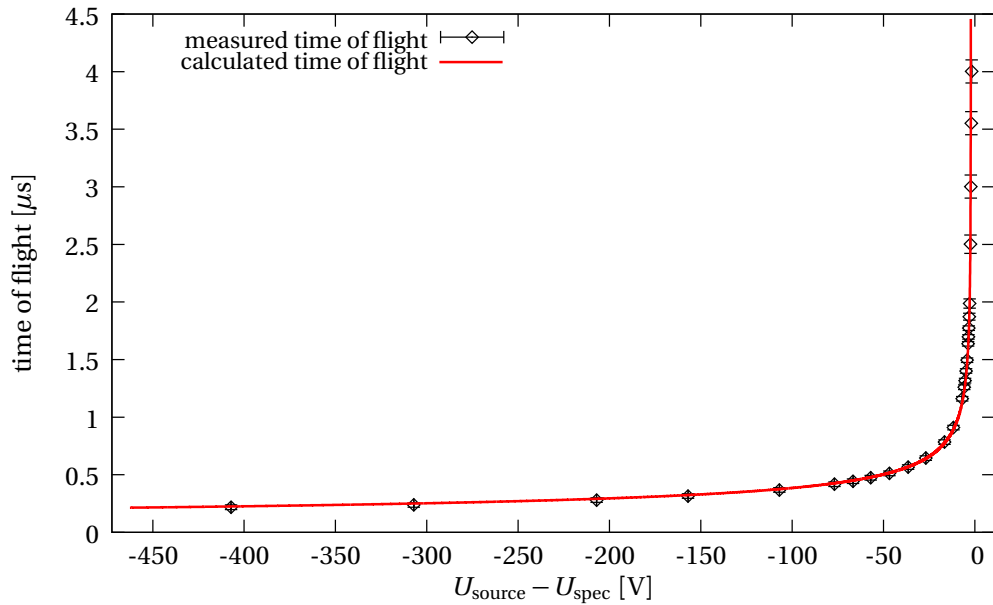


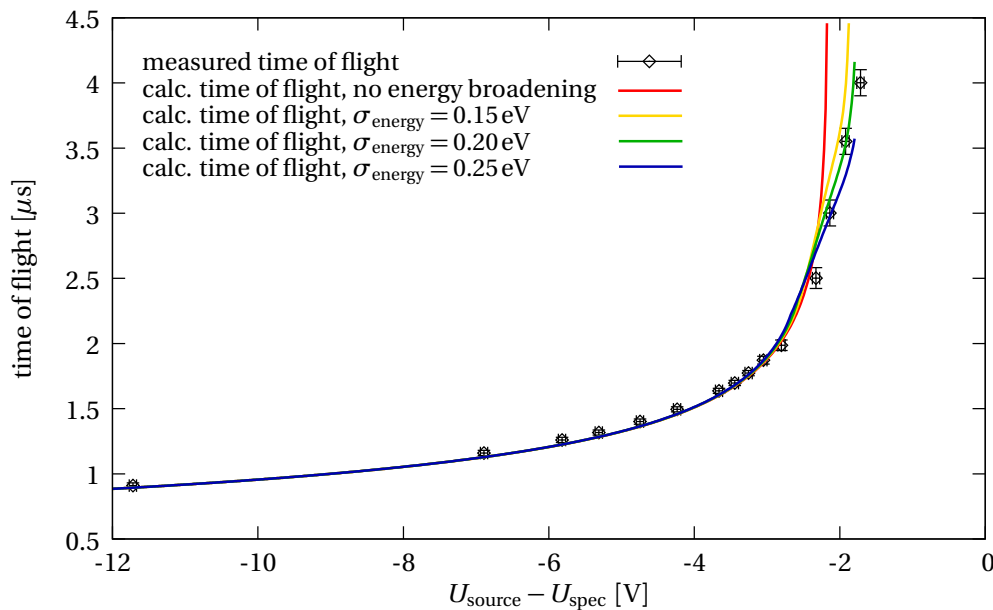
**Figure 7.17:** FWHM of arrival time distribution of photoelectrons at different surplus energies. At high surplus energies the width is constant at about  $\text{FWHM} \approx 180$  ns (for comparison: the start time  $t_{\text{emis}}^{-}$  of the photoelectrons has an uncertainty corresponding to the width of the UV light pulse:  $\Delta t_{\text{emis}}^{-} \approx \tau = 200$  ns).

been neglected in the calculation. It can be incorporated in form of a gaussian distribution of the starting kinetic energies with a width  $\sigma_{\text{energy}}$  (three different calculation results are shown along with the monoenergetic model in figure 7.18(b)). A spread of the starting energies of  $\sigma_{\text{energy}} \approx 0.2 - 0.25$  eV is suitable to describe the measured time-of-flight data, which is in good agreement with the earlier results obtained from the integrated energy spectrum (eq. (7.18)).

Figure 7.19 illustrates that the ToF spectrum ( $\times$ ) contains additional information where the normal transmission curve ( $\diamond$ ) has reached its saturation (at medium and large surplus energies), or hides away small details in the rising part (at low surplus energies).



(a) full range of surplus energies

(b) small surplus energies ( $qU_{\text{source}} - qU_{\text{spec}} = E_{\text{surplus}} \lesssim 12 \text{ eV}$ )

**Figure 7.18:** Time-of-flight spectrum of photoelectrons measured with the Mainz MAC-E filter at an energy resolution of  $\Delta E = 1.5 \text{ eV}$ . Short UV light pulses (duration: 200 ns, repetition rate: 1 kHz) were used for photoelectron production off a planar cathode which was placed at an electric potential of  $-18.0 \text{ kV}$ . (a) Comparison between the measured mean values of the arrival time distribution ( $\diamond$ ) and simulation results (solid red line) over a wide range of surplus energies. (b) Close-up on the region of small surplus energies. At the largest time-of-flight values, corrections due to an energy smearing of the photoelectrons become relevant. Several calculations for varying widths of a gaussian broadening of the surplus energy are shown. A good agreement between data and calculation is achieved for a broadening around  $\sigma_{\text{energy}} = 0.20 - 0.25 \text{ eV}$ .

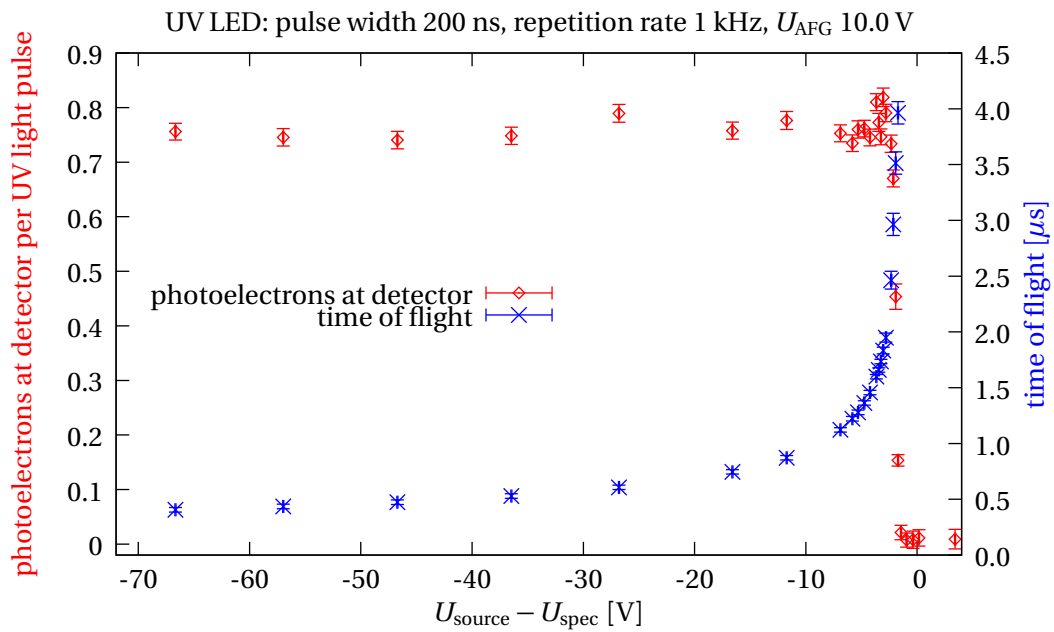


**Figure 7.19:** Comparison of integrated energy spectrum and time-of-flight (ToF) spectrum of photoelectrons, obtained with different analyses of the same measurement data. Surpassing the integrating quality of the energy scan, the ToF spectrum allows to draw further information from the measurement: it shows an evolution even in regions of medium and high surplus energies ( $U_{\text{source}} - U_{\text{spec}} < -3\text{V}$ ) where the integrated scan remains essentially flat.

## 7.4 Prototype studies of a pulsed photoelectron source with angular selectivity

In order to motivate the idea of an angular-defined photoelectron source introduced in this section, it is helpful to first consider the photoelectron gun installed at the present stand-alone setup of the KATRIN pre-spectrometer (compare figure 5.8), which is used for measurements to test the electromagnetic design. Figure 7.20 illustrates the basic principle of the device. A rounded quartz tip of about  $\varnothing 2$  mm is coated with a thin film of gold. The tip is placed on negative high voltage and surrounded by a hemispherical casing (also on high voltage) which helps to shape the electric field. A broadband deuterium lamp illuminates the gold film from the backside through the UV-transparent quartz substrate, such that photoelectrons are created at the front of the tip and are accelerated into the pre-spectrometer after passing a focusing ground electrode.

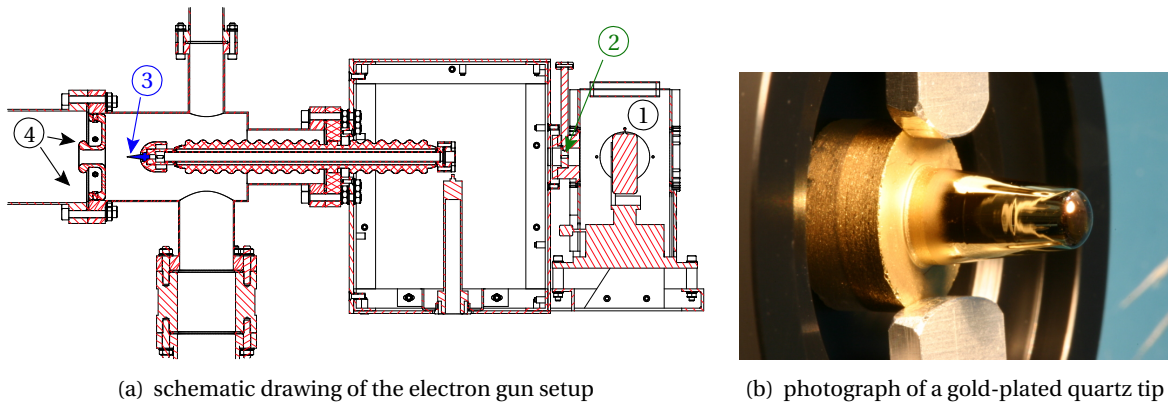


**Figure 7.20:** Electron gun for tests of the KATRIN pre-spectrometer. The technical drawing in (a) outlines the central parts of the device: (1) the UV light source, (2) a shutter system allowing to select varying aperture diameters or to block the UV light, (3) the ceramics insulator holding the quartz tip covered with a thin gold layer (see photograph in (b)) which is attached to a hemispherical guard electrode, and (4) the annular ground electrode acting as a beam collimator before the electrons enter the spectrometer magnet (not depicted here).

Theoretical and experimental studies of the transmissive emission of photoelectrons from gold thin films are abundant in the literature (see, for example, [Jia98] and references therein). The angular distribution of photoelectrons from backside-illuminated, planar thin films made of gold was investigated in reference [Pei01]. The authors found experimentally that the angular emission spectrum is described quite well by a theoretical curve derived from a three-step model<sup>14</sup> and can be approximated by a simple cosine function for incident photon energies  $E_{\text{photon}}$  only slightly higher than the work function  $\Phi$  of the metal film.

However, microscopic trajectory calculations carried out in order to better understand the emission characteristics of the pre-spectrometer electron gun showed that for a suitable configuration of electric and magnetic fields the angular emission profile at the surface of the metal film

<sup>14</sup>In this model, originally conceived by Berglund and Spicer [Ber64a, Ber64b] and treated in several articles in the compendium [Scha03], the process of photoemission is decomposed into three stages: 1) optical excitation of electrons within the metal, 2) scattering inside the solid and propagation to the surface, and 3) release of the electron into the vacuum. In this simplified approach, the electron excitation energy  $E_i$  inside the solid and the work function  $\Phi$  together with the electron angle  $\varphi$  prior to emission are sufficient to derive the angle  $\theta$  under which the electron will be ejected with respect to the surface normal:  $\cos^2 \theta = \cos^2 \varphi + \sin^2 \varphi \frac{\Phi}{E_i}$ . According to [Pei01], the angular distribution is obtained by integrating over all excitation energies up to the vacuum level.

becomes irrelevant.<sup>15</sup> Instead, the location of the emitting spot on the surface of the tip – more precisely: the radial distance of the point of photoemission with respect to the symmetry axis of the tip – defines the angle  $\theta$  and thus the relative amount of transversal kinetic energy at the start of the trajectory.

The salient points are that the electric and magnetic fields at the location of the tip must be non-parallel, and that the strength of the magnetic field  $B_{\text{egun}}$  at the tip is low compared to the maximum magnetic field  $B_{\text{max}}$ . The third prerequisite is that a strong electrostatic acceleration of the electrons takes place in the early phase of the motion, which can be realized by a round photocathode tip on high voltage to achieve a suitable shape and strength of the electric field. In this case, the motion will be non-adiabatic at the start of the trajectory, and therefore the transformation relation according to eq. (2.22) is not valid in the initial phase.

In the specific case of the pre-spectrometer, the electron gun is placed at a distance of about 1.3 m from the center of the entrance solenoid. The magnetic field at the tip is thus small, since only the fringe fields of the superconducting solenoids contribute:

$$B_{\text{egun}} \approx \frac{1}{100} B_{\text{solenoid}} \quad (7.21)$$

(with  $B_{\text{max}} = B_{\text{solenoid}}$ ).

In the local environment of the tip, the magnetic field can be assumed to be quasi-homogeneous, whereas the electric field lines diverge radially due to the hemispherical shape of the tip (see figure 7.21).

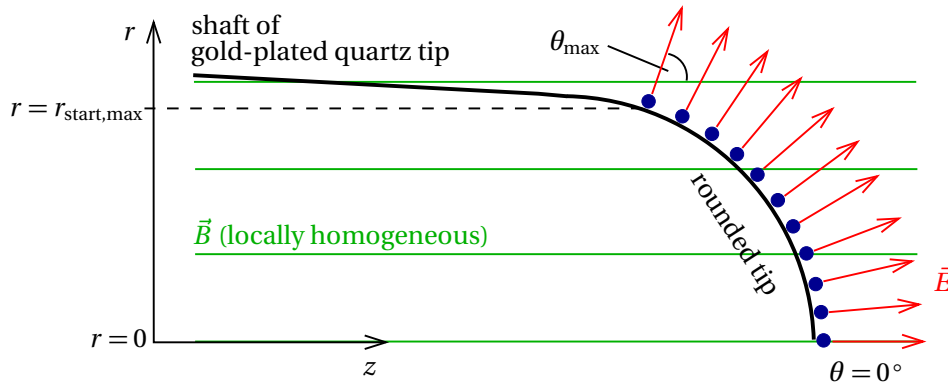


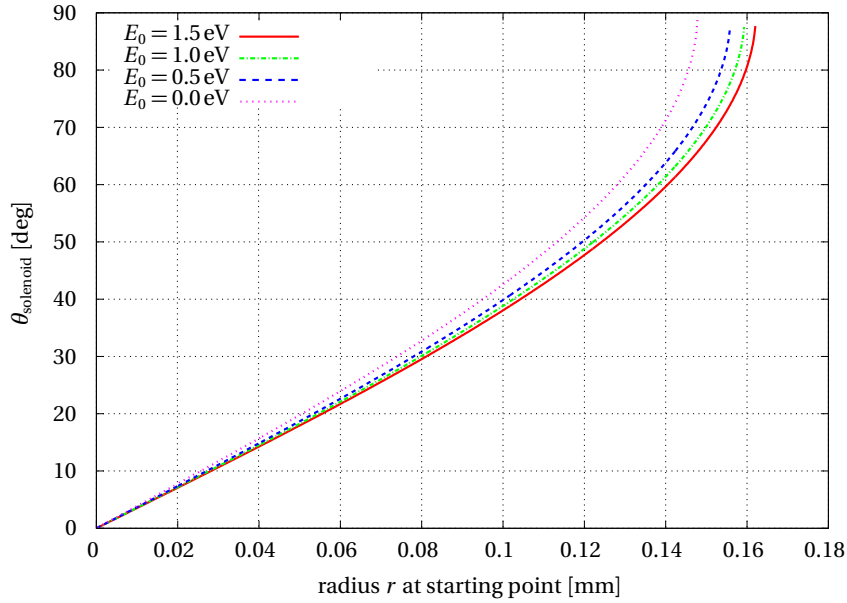
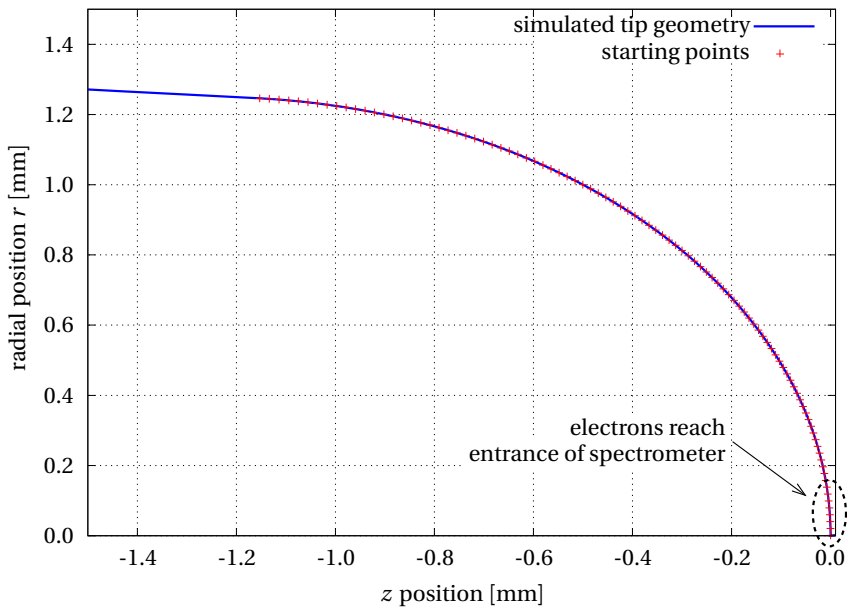
**Figure 7.21:** Sketch illustrating the relation between starting angle and radial position on the tip of the electron gun.

Independently of the angle  $\theta$  between the electron momentum and the magnetic field lines at the start of the trajectory, the electrons gain a certain amount of initial transversal kinetic energy by non-adiabatic acceleration in the strong electric field. In the early phase of the motion, they follow the electric field lines rather than the magnetic field lines. After a very short distance the electrons leave the region of strongest acceleration. The magnetic field then takes over and subsequently the electrons are guided adiabatically along the magnetic field lines. Due to the specific geometry of the fields, those electrons starting at a larger radial distance from the tip will “attach” to the magnetic field lines with a larger angle  $\angle(\mathbf{B}, \mathbf{p})$  than those emitted close to the axis, where  $\mathbf{E}$  and  $\mathbf{B}$  are essentially parallel. As they travel from the low magnetic field into a region with higher

<sup>15</sup>These calculations were carried out in cooperation with K. Hugenberg and are presented in detail in her diploma thesis [Hug08].

magnetic field strength, the initial amount of transversal kinetic energy is amplified according to eq. (2.22), which has regained its validity in the advanced stages of the electron trajectory. Hence, by virtue of the magnetic gradient force (eq. (2.19)), the angle  $\theta$  is increased. In view of the large ratio  $B_{\text{solenoid}}/B_{\text{egun}}$ , even very small starting angles  $\theta_{\text{start}}$  – and therefore small starting radii  $r_{\text{start}}$  – are sufficient to yield large angles  $\theta_{\text{solenoid}}$  at the center of the entrance solenoid of the pre-spectrometer.

This is seen in the simulation results [Hug08] presented in figure 7.22. Electrons originating from a very small region restricted to  $r_{\text{start}} \leq r_{\text{start,max}} \approx 160 \mu\text{m}$  reach large angles up to  $\theta_{\text{solenoid}} \lesssim 90^\circ$ . All electrons starting at larger radii on the tip are magnetically reflected before entering the pre-spectrometer. Variations of the starting kinetic energy of the electrons, which are determined by the difference between the maximum photon energy delivered by the deuterium lamp ( $E_{\text{photon}} \lesssim 6.7 \text{ eV}$ ) and the work function of the gold film ( $\Phi_{\text{gold}} \approx 5 \text{ eV}$ ), have only little influence on the results.


 (a)  $\theta_{\text{solenoid}}$  as a function of starting radial position for various starting energies  $E_0$ 


(b) starting coordinates for trajectory calculations of electrons emitted from the tip

**Figure 7.22:** Angular emission characteristics of the pre-spectrometer electron gun as a function of the starting radius (both figures taken from [Hug08]).  $\theta_{\text{solenoid}}$  denotes the angle  $\angle(\mathbf{B}, \mathbf{p})$  in the high magnetic field inside the pre-spectrometer entrance solenoid.  $\theta_{\text{solenoid}} = 90^\circ$  is the critical value of the angle with regard to reflection due to the magnetic mirror effect. (a) Dependence of  $\theta_{\text{solenoid}}$  on the radial position of the starting point along the contour of the tip of the electron gun. Four discrete values of the starting energy  $E_0$  between 0 and 1.5 eV were used. The simulation was carried out for typical values of magnetic field ( $B_{\text{solenoid}} = 0.283$  T) and electric potential ( $U_{\text{egun}} = -1$  kV) employed during initial test measurements to determine the transmission function of the pre-spectrometer. (b) Starting positions of calculated electron trajectories (red crosses) marked on top of a close-up on the tip geometry (blue line). Only electrons originating from the encircled region reach the entrance magnet; all others are magnetically reflected.

### 7.4.1 Mechanical construction of the fiber-coupled photoelectron gun

The principle of non-adiabatic acceleration explained above can be exploited to conceive an angular-defined photoelectron gun. The basic idea is to selectively illuminate small areas on a metal tip in order to generate localized photoemission of electrons from discrete spots ( $r_{\text{inner}}^k \leq r \leq r_{\text{outer}}^k$ ) which correspond to discrete intervals of angles ( $\theta_{\text{lower}}^k \leq \theta \leq \theta_{\text{upper}}^k$ ). Here,  $k$  denotes the index of the individual spots of photoemission. The relative width of such an interval  $[\theta_{\text{lower}}^k, \theta_{\text{upper}}^k]$  depends on the spatial extent of the irradiated area, whereas the central angle in each interval is determined by the position of the spot. For a first experimental test of a prototype, it would be sufficient to arrange for a small number of distinct emission areas. However, for a more elaborate device a large number of closely packed emission regions should be envisioned.

Figure 7.23 compares two different methods to achieve spatially confined photoemission, which are based on reflective versus transmissive illumination of a metal surface. In the following, these two possibilities will be evaluated with regard to their application in a simple prototype setup.

In the first case, a beam of UV light with a small cross section is directed from the side onto the bulk-metal surface. The beam needs to be focused to a spot with a diameter of the order of  $20 - 100 \mu\text{m}$  on the tip in order to arrange for a small number of separate spots on the small available area. Obviously, a better angular resolution can be achieved for smaller spot sizes. Furthermore, the required precision for the positioning of the spot on the tip is of the order of  $10 \mu\text{m}$ . Reproducible positioning to selected coordinates is also an issue. UV laser systems of an appropriate wavelength might fulfill these requirements. Considering the experimental constraints (among others, the limited space, the ultrahigh vacuum environment and the necessary precautions associated with the operation of a UV laser), the technical implementation of such a micro-focus system seems rather challenging.

The second method uses UV-transparent optical fibers to guide the UV light from the source through drills in the bulk metal to the tip. The ends of the fibers are cut and polished to match the local shape of the tip, and subsequently are covered with a thin metal film (for example by vapor coating). In this case the diameter of the light-guiding core of the fiber and the minimum possible spacing of the fibers determines the size and position of the illuminated spots on the tip. Since the fibers are fixed, reproducible measurements should be easier to achieve than in the aforementioned solution. Either a separate LED for each fiber could be used or a single LED might supply all fibers sequentially by means of some “multiplexing” unit.

For the purpose of a simple proof of principle, the second method seemed to be most suitable. A prototype of an electron gun offering at least rudimentary angular selectivity was built and tested at the Mainz MAC-E filter. The same vacuum chamber that housed the wire scanner and the disc-shaped extra electrode in the measurements described in chapter 6 was employed as a container for the new photoelectron gun. Figure 7.24 shows photographs of the prototype setup. It comprises the following basic components:

- A photocathode tip. The geometry was modelled on that of the pre-spectrometer electron gun, but since the backside illumination made the need for quartz glass obsolete, the new tip was made of aluminium. To connect the tip with the flange of the vacuum chamber its support structure is equipped with a 30 kV insulator and a high-voltage feedthrough.
- A hemispherical casing and an annular ground electrode provide additional shaping of the electric field.
- Three UV-transparent fibers are embedded into the metal tip. Step-index UV fibers with a core diameter of  $98 \mu\text{m}$  and an outer diameter of  $245 \mu\text{m}$  supplied by the company j-fiber GmbH were chosen [Leo08]. The ends of the fibers were coated with thin metal films (see

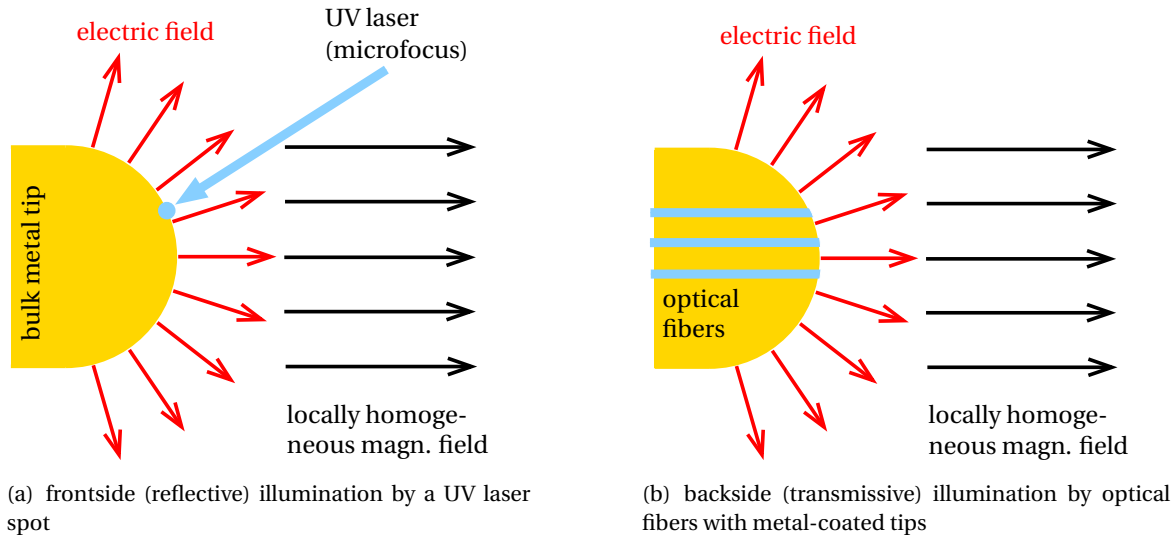


**Figure 7.23:** Two options of illuminating the photocathode in an angular-selective electron gun with a ball-shaped metal tip. (a) A small spot on the surface of the bulk metal is irradiated by a well-collimated beam, for example using a micro-focused UV laser. (b) UV-transparent optical fibers are employed to guide the light through the bulk-metal electrode. The fibers are cut and polished at the surface of the tip. Their ends are coated with a thin metal film, which is illuminated from the backside.

table 7.4). Silver and copper were used in successive measurement periods. The work function of both materials is lower than the photon energy supplied by the UV LEDs (compare tables 7.1 and 7.2:  $\Phi_{\text{Ag, polycryst.}} = (4.0 \pm 0.15) \text{ eV}$  and  $\Phi_{\text{Cu, polycryst.}} = (4.65 \pm 0.05) \text{ eV}$ , both values according to [Eas70]). In addition, they can be easily applied in well-defined quantities by the vaporization method. Since silver rapidly oxidizes when exposed to air and its work function is thus expected to change in a rather undefined manner, it is difficult to determine the energy of the photoelectrons. One way to avoid this problem is to handle and transport the film and the assembled electron gun setup in an enclosure filled with inert gas. Another possibility is to use a different cathode material, for example copper, which is much less sensitive to this problem.<sup>16</sup> Two opposite side faces of the aluminium tip (“shafts”, compare sketch of the tip geometry in fig. 7.21) were coated with gold and chromium films, respectively. This opened up the possibility to compare the photoelectron spectra measured with the fibers with a spectrum of undefined angular emission by irradiating the shafts of the tip through the windows of the vacuum chamber.

- A single UV LED was mounted on a positioning device (micrometer screw) to allow the selective illumination of specific fibers. The by now well-characterized LEDs of the types T9B26C (central wavelength  $\lambda_{\text{central}} = 265 \text{ nm}$ ) and T9B25C ( $\lambda_{\text{central}} = 255 \text{ nm}$ ) were employed. In order to facilitate the interfacing of the LED emission with the optical fiber, these LEDs are equipped with a simple ball lens. Nevertheless, the manual coupling of the UV light beam into the fiber is rather difficult and clearly forms one of the disadvantages of the method. According to manufacturers, the radial extent of the focal region achievable with the ball lens is about 1.5–2 mm at a typical focal length of 15–20 mm [SET08]. Considering that the core diameter of the fiber is about 20 times smaller than the width of the focused

<sup>16</sup>Regarding stability against oxidation, gold would be the obvious choice. However, the work function of a polycrystalline gold film seems to have only a marginal overlap with the photon energy obtainable with the UV LEDs (compare table 7.2). Therefore, gold was only applied to one of the side shafts of the tip, and not to the fibers. Indeed, no conclusive photoelectron signal from the gold surface was observed (compare remark at the end of section 7.4.2).

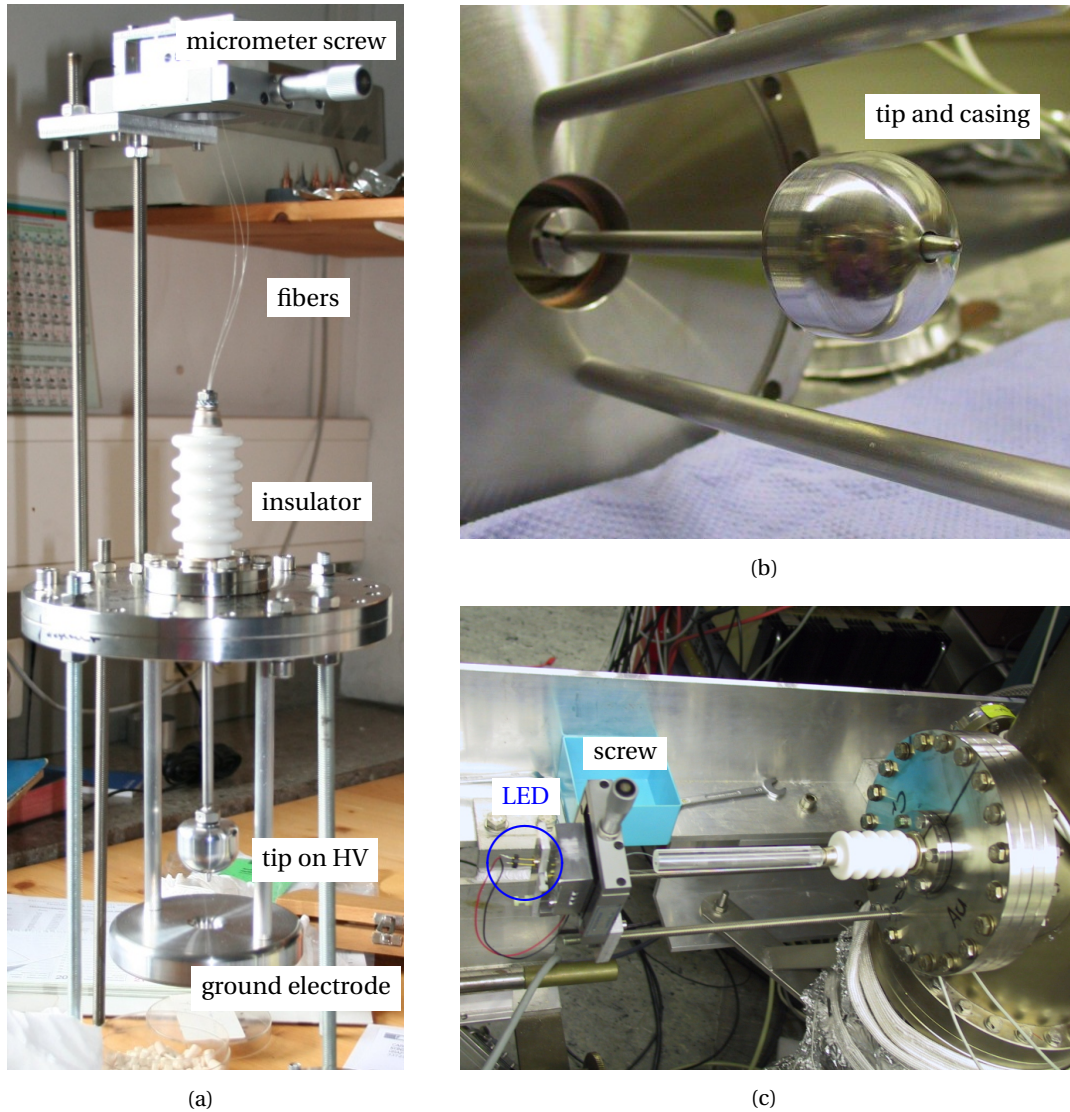


**Figure 7.24:** Prototype of a fiber-coupled photoelectron gun. The photographs show (a) the assembled setup with support structure, (b) a close-up on the tip, and (c) the photoelectron gun mounted at the Mainz spectrometer.

beam at its minimum extent, the losses due to the mismatch are large. In general, it would be desirable to find a better way of matching the UV LED and the fiber in order to maximize the light yield at the tip.<sup>17</sup>

Technical drawings with further details regarding the construction are included in appendix B.4. Table 7.5 and figures 7.25 and 7.26 illustrate the positioning and mounting of the three equidistant fibers. Unfortunately, the outermost fiber (# 3, see fig. 7.26) broke already before the electron gun could be tested at Mainz. Therefore, only one inner and one outer fiber could be used for the measurements. The centers of the two working fibers are placed  $80\ \mu\text{m}$  and  $170\ \mu\text{m}$  relative to the symmetry axis of the tip, respectively. This rather large spacing is due to the thickness of the fibers. Because of the large diameter of both coating and core of the fibers, only a very crude angular resolution of the source can be expected. In addition to the position of the emitting spots

<sup>17</sup>Commercial solutions to this problem of light collection and coupling into a fiber are available.

**Table 7.4:** Materials used for vapor-metalization of the fibers and shafts of the tip in the electron gun setup. (All work function values according to [Eas70].)

	1 <sup>st</sup> meas. period	2 <sup>nd</sup> meas. period
material covering fibers	<b>Ag</b> , $\Phi = (4.0 \pm 0.15) \text{ eV}$ (might be oxidized)	<b>Cu</b> , $\Phi = (4.65 \pm 0.05) \text{ eV}$
quantity [ $\mu\text{g}/\text{cm}^2$ ]	30 – 35	20 – 30
material on shafts of tip	<b>Cr</b> , $\Phi = (4.5 \pm 0.15) \text{ eV}$ <b>Au</b> , $\Phi = (5.1 \pm 0.1) \text{ eV}$	

**Table 7.5:** Fiber-coupled photoelectron gun: radial parameters of fiber positions. All positions are measured relative to the center of the  $\varnothing 2.8 \text{ mm}$  aluminium tip (compare figures 7.25 and 7.26). The mechanical preparation of the tip allows a positioning accuracy of about  $\pm 20 \mu\text{m}$  (construction tolerance), which determines the uncertainty to be applied to all values listed in the table. The outermost fiber # 3 could not be used, therefore the relevant parameters of fibers # 1 and # 2 are highlighted in bold font.

fiber	# 1	# 2	# 3
comment	'outer fiber'	'inner fiber'	broken (not used)
center of fiber	170 $\mu\text{m}$	80 $\mu\text{m}$	330 $\mu\text{m}$
innermost position covered by core	<b>121 <math>\mu\text{m}</math></b>	<b>31 <math>\mu\text{m}</math></b>	281 $\mu\text{m}$
outermost position covered by core	<b>219 <math>\mu\text{m}</math></b>	<b>129 <math>\mu\text{m}</math></b>	379 $\mu\text{m}$

on the tip, the uncertainty of the positioning of the entire electron gun with respect to the central axis of the spectrometer is critical for the success of the measurement. The mounting structures holding the tip are mechanically stiff, but nevertheless a small deviation of the assembled system from its ideal position cannot be completely avoided.

The simulations of the pre-spectrometer electron gun presented in figure 7.22 can only be used to obtain a rough estimate of the angular emission of the two fibers, since the configuration of electric and magnetic fields at the test setup in Mainz is different from that used in the simulation. The magnetic field ratio used for the prototype measurements of the fiber-coupled electron gun is

$$\frac{B_{\text{egun}}}{B_{\text{solenoid}}} \approx \frac{0.03 \text{ T}}{6 \text{ T}} = \frac{1}{200}, \quad (7.22)$$

and an acceleration voltage of  $-18 \text{ kV}$  was applied. In order to achieve a detailed understanding of the experimental results, a new set of simulations is thus necessary, which is presently in preparation in the scope of the diploma thesis of H. Hein [Hei09]. The observation of different shapes of the transmission curve for the inner and the outer fiber could already be considered as an experimental hint that the principle idea works.

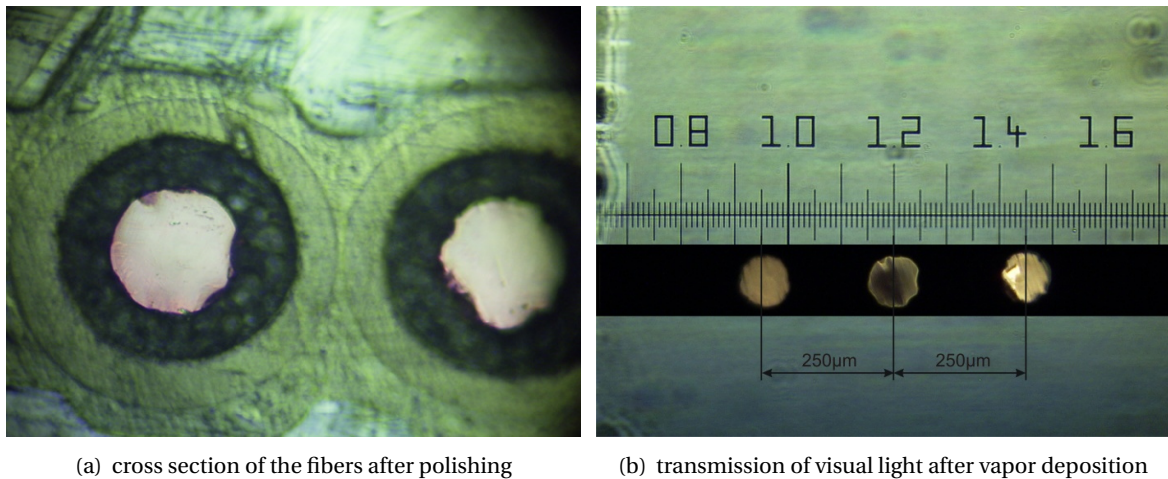


**Figure 7.25:** Photographs of fiber feedthroughs in the tip of the photoelectron gun prototype, as viewed through an optical microscope. (a) The fiber consists of three layers: the silica core (illuminated), the cladding (dark) and the outer coating (greenish color). In total, the fiber diameter amounts to about  $245\ \mu\text{m}$ . The fibers are mounted closely spaced in diamond-shaped holes and fixed with glue. During polishing, some small pieces at the edge of the fiber have come off, but the central surface remains flat and smooth enough to avoid field emission due to microtips. (b) Transmission test of the fibers with visible light, after polishing and vapor-metalization of the fiber ends. The fiber cores are  $98\ \mu\text{m}$  in diameter, and their centers are  $250\ \mu\text{m}$  apart. (Pictures by H. Baumeister and W. Hassenmeier.)

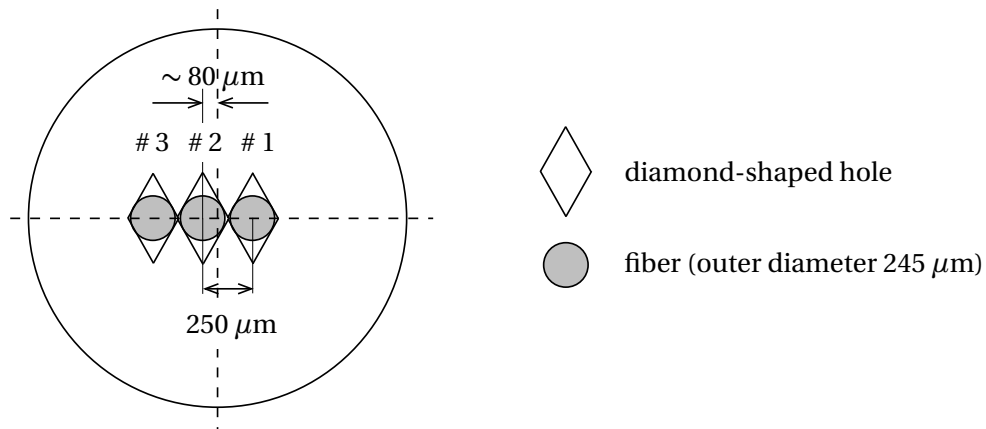


**Figure 7.26:** Sketch: tip of the fiber-coupled electron gun. The cross section of the tip is shown, including the outlines of the three fibers implanted closely spaced into the bulk of the tip. The fibers are glued into diamond-shaped openings. The center of fiber # 2 is offset by  $(80 \pm 20)\ \mu\text{m}$  with respect to the center of the tip, and fibers # 1 and # 3 are placed symmetrically around fiber # 2. During tests of the setup before shipment to Mainz, fiber # 3 was broken and could no longer be used. In the description of the measurements below, fibers # 1 and # 2 will be labelled 'outer fiber' and 'inner fiber', respectively.

### 7.4.2 Measurement of integrated energy spectra: comparison between outer and inner fiber

Both for silver and copper as metal plating on the tips of the fibers photoelectrons from transmissive irradiation with UV light from the UV LEDs were successfully detected. The Mainz MAC-E filter allowed to measure high-resolution energy spectra of the photoelectrons. Typical experimental settings and vacuum conditions<sup>18</sup> for the spectroscopy runs are listed in table 7.6. Figure 7.27 shows two energy scans for each of the two functioning fibers. The high voltage of the electron gun was set to  $U_{\text{source}} = -18053\text{V}$  and the spectrometer voltage was ramped in steps from  $U_{\text{source}} - 10\text{V}$  to  $U_{\text{source}} + 15\text{V}$ .

The results of the five runs presented in this section (2 · 2 runs with fibers, one for the chromium layer at the shaft) are confirmed by a large number of further measurements under varying experimental conditions, which are however not included here. For example, spectroscopy measurements were carried out using silver instead of copper as a metal coating material, with varying resolution settings of the spectrometer and with the two available LEDs of different central wavelengths.

**Table 7.6:** Settings and parameters for the energy scans with the fiber-coupled photoelectron gun.

spectrometer resolution	$\Delta E = 1.5\text{eV}$ at $E = 18\text{keV}$
pressure levels	$p_{\text{spec}} = 1.0 \cdot 10^{-8}\text{mbar}$ $p_{\text{egun}} = 2.5 \cdot 10^{-7}\text{mbar}$ $p_{\text{detector}} = 2.6 \cdot 10^{-8}\text{mbar}$
water-cooled auxiliary coil	$I_{\text{aux.coil}} = 100\text{A}$
xy-compensation coils	$I_{\text{comp.1}} = 30\text{A}$ , $I_{\text{comp.2}} = 22\text{A}$
wire scanner	moved out of the beam by constant current, $I_{\text{wire}} = 3.5\text{A}$
UV LED	pulse width $\tau = 10\mu\text{s}$ repetition rate $f = 2\text{kHz}$ voltage setting at function generator $U_{\text{AFG}} = 6\text{V}$ (7V)

During the first scan with the outer fiber (run egunsc38), a strong discharge occurred, which was probably related to the fact that the wire scanner was inactive and switched out of the beam by a dc current. As a consequence, the high voltage on the electron gun was automatically shut down upon reaching the current limit of the power supply. The measurement was repeated (run egunsc39) after resetting the high voltage supply. Both runs are included in figure 7.27; however, all points after the onset of the discharge are left out in run egunsc38 (therefore, the measurement points at higher surplus energies are missing).

A measurement interval of 30 s for each step of the spectrometer voltage was chosen for the inner fiber, whereas the interval had to be doubled to 60 s per step for the outer fiber, which exhibited a significantly lower detection rate of photoelectrons. In addition, the voltage setting of the LED was increased from  $U_{\text{AFG}} = 6\text{V}$  (inner fiber) to 7V (outer fiber). In figure 7.27 all count rates are

<sup>18</sup>With the electron gun installed, the residual gas pressure in the setup was significantly higher than during the wire scanner measurements. This is partly due to the fact that, by the end of the second measurement phase, the system had been opened already several times without proper baking. Before the particular measurement described here, the pumps had only been running for a relatively short time and the overall pressure levels were still falling. In addition, the prototype setup of the electron gun was not suitable to achieve good ultrahigh vacuum conditions, for example because the fibers were fixed to the tip using glue.

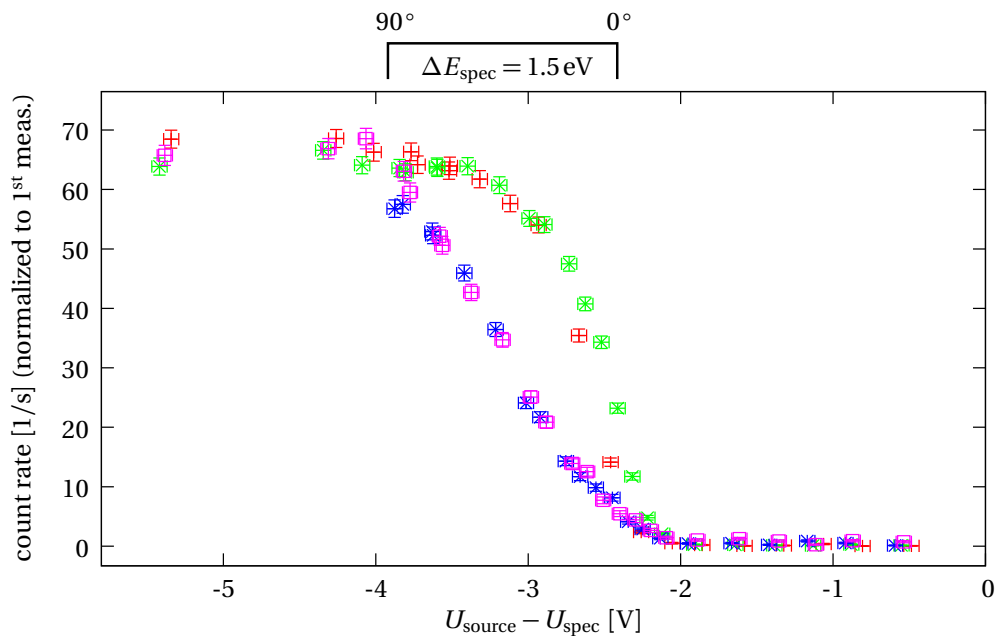
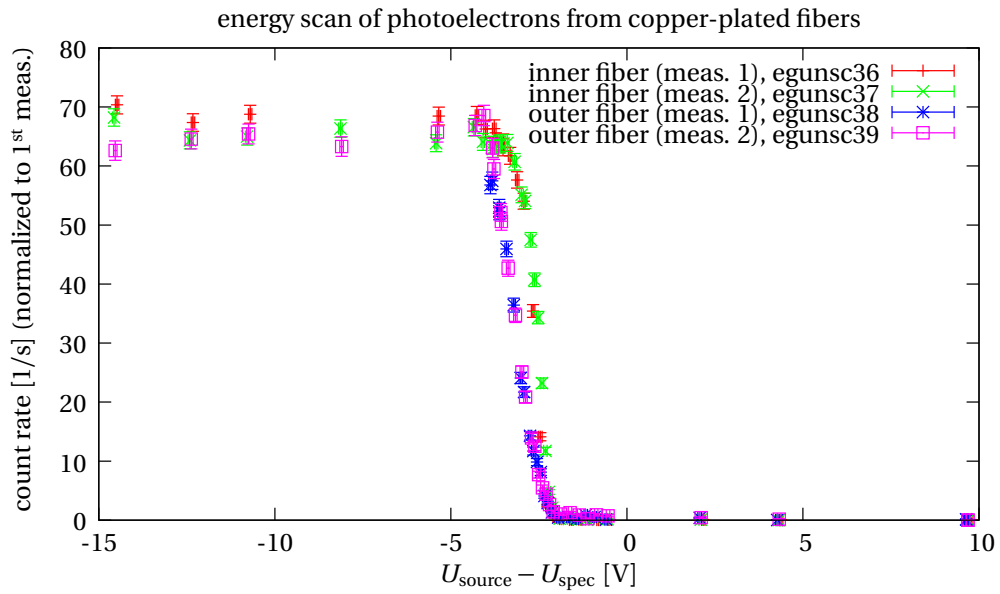


**Figure 7.27:** Measurement of integrated electron energy spectra with the prototype of an angular-selective photoelectron gun. The two scans using the inner fiber (+, ×) exhibit a marked difference in the shape of the integrated energy spectrum as compared to the two scans for the outer fiber (\*, □). The width of the measured transmission curves is slightly larger than the nominal energy resolution  $\Delta E_{\text{spec}}$  of the spectrometer, which is indicated in (b) for comparison. The labels “0°” and “90°” mark the surplus energies at which electrons with minimum and maximum angle starting from an isotropically emitting source are expected to be able to pass the MAC-E filter. (Caution: the angular scale is not linear in  $\theta$ , but rather in  $\cos(\theta)$ ). The rise in the transmission curves measured for the inner fiber is significantly steeper than for the outer fiber, which yields a proof of principle confirming the idea of selecting particular intervals of starting angles.

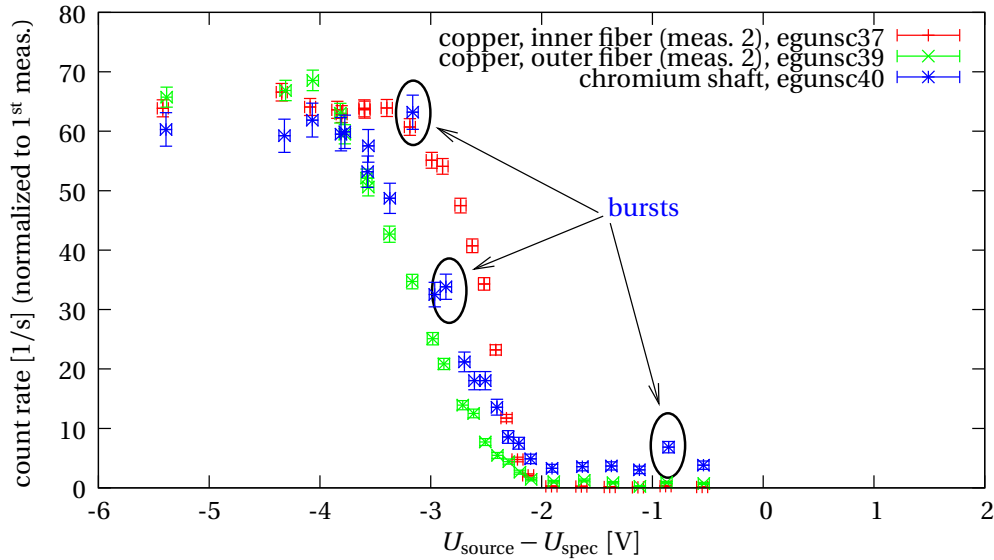


**Figure 7.28:** Comparison of integrated electron energy spectra for photoelectrons from chromium (shaft of the tip, 255 nm LED  $*$ ) and copper (two fibers,  $+$  and  $\times$ , 265 nm LED).

approximately normalized to match the region of high surplus energies of the first scan, egunsc36. The following scaling factors were applied:

egunsc36	egunsc37	egunsc38	egunsc39
$\times 1$	$\times 0.97$	$\times 2.28$	$\times 2.60$

The marked difference in the count rates between the two fibers might be attributed to the fact that the coupling of the UV light into the fibers was done manually using the micrometer screw (compare figure 7.24). Thus, it is possible that the efficiency of the coupling was higher in the case of the inner fiber. However, a similar suppression of the rate for the outer fiber was observed in all measurements, and it could not be amended by many attempts to adjust the optical link. Therefore, the reduced rate rather seems to be due to other effects:

- a) The lower photoelectron yield might originate from a lower transfer efficiency of the outer fiber as compared to the inner fiber. Possible reasons are a higher reflectance at the entrance of the fiber or a larger attenuation factor during transfer to the tip.
- b) The lower count rate of photoelectrons at the detector could be related to the magnetic reflection of electrons with high starting angles, which is expected to effect the outer fiber in a much more pronounced way than the inner fiber. Taking the simulations presented in figure 7.22 as a guide, one would expect fewer electrons from the outer fiber to be transmitted because of the larger starting radii (the values given in table 7.5 are to be compared with the calculated spot of emission, which in the case of the simulations for the pre-spectrometer had a radial extent of only  $160\ \mu\text{m}$ ). However, as stated before, new simulations adapted to the particular geometry of the prototype electron gun used for these measurements are necessary to confirm this interpretation.

The latter scenario fits in with the general observation that the shapes of the transmission curves for the two fibers are indeed different. In particular, the initial rise in count rate when going from lower to higher surplus energies is significantly steeper for the inner fiber as compared to the outer fiber. In both cases the total width of the transmission curve is comparable to, but slightly larger than, the energy resolution of the spectrometer. The individual angular distribution asso-

ciated with each of the fibers as well as the common intrinsic energy spread of the photoelectrons (determined in sections 7.3.2 and 7.3.3), are expected to contribute to the total width. A comparison with the integrated energy spectrum obtained for photoelectrons from the chromium-plated shaft of the tip (figure 7.28), taken with the 255 nm LED with slightly higher photon energies, shows that the shapes of the measured transmission curves for the outer fiber and the shaft are similar. The spectrum of photoelectrons from chromium is slightly shifted with respect to all spectra measured for photoelectrons from copper, which might be attributed to a combination of the difference in the work functions and the photon energies. Notably, the count rate of the chromium photoelectrons was much lower than in the measurements using the fibers; hence the corresponding statistical uncertainty in the normalized spectrum is comparatively large. It is noteworthy that the chromium photoelectron spectrum exhibits a number of burst-like rises in the count rate which were not observed in the runs with the fibers.

A detailed analysis of the energy spectra obtained from the fibers still needs to be done (compare [Hei09]). Using the estimate of the energy spread derived from the measurements with the planar front-illuminated photocathode presented in the previous sections, it should be possible to deduce the actual intervals of angular emission for the two fibers. Likewise, future simulations may help to understand the angular emission from the chromium surfaces.

### Remarks on photoelectron production from a gold film

In the first measurement phase a photoelectron signal from the gold-coated shaft of the tip was seen, which could however not be confirmed after the electron gun had been refurbished and reinstalled for the second measurement period. A conclusive explanation for this has not yet been found. It is suspected that aging effects of the UV LED might play a role. According to recent updates of the LED specifications issued by the manufacturers, the guaranteed lifetime of the UV LEDs – in particular in the deep-UV range – can be as low as about 150 hours [Las06]. Details on the effects of the aging process on the characteristics of the LEDs are unfortunately not known, and they seem to be a topic of current research and development efforts. It can only be speculated, therefore, that the intensity or even the wavelength of the emitted light might change considerably (or be subject to fluctuations) when a UV diode approaches the end of its lifetime, which could have led to the observed discrepancies.

## 7.5 Evaluation of results and outlook

### 7.5.1 Summary of simulation studies for time-of-flight measurements at the KATRIN main spectrometer and experimental tests of a fast-pulsed photoelectron source at the Mainz spectrometer

Trajectory calculations show that part of the allowed starting conditions for electrons are critical with respect to fulfilling the transmission condition or causing harmful effects such as early retardation. For example, as was seen in chapter 4, the radius at which the electrons cross the analyzing plane is important. Those electrons passing along magnetic field lines at the outer border of the flux tube are subject to local variations of the electrostatic potential caused by the modular structure of the wire electrode. Furthermore, due to the radial potential depression the retardation potential at the analyzing plane is more negative for large radii than on-axis. In order to investigate key characteristics of the MAC-E filter, such as the broadening of the transmission function due to radial inhomogeneities of the electrostatic retardation potential and the magnetic field, an electron source with a two-dimensional manipulator system<sup>19</sup> is necessary which allows to cover the full extent of the transported magnetic flux tube by scanning a spatially well-confined electron beam in small steps in both directions perpendicular to the symmetry axis  $z$ .

Likewise, electrons with high starting angles, which possess a large fraction of their kinetic energy in the cyclotron component of the motion, need to be considered carefully. It would thus be desirable to have a calibration electron source with the additional feature of angular selectivity, which permits to specifically select electrons with large starting angles for detailed investigations of their transmission behavior.

In order to check for all potentially harmful deviations of the real transmission function from the analytical shape, some of which were identified in the course of this work (compare chapter 4), extensive calibration measurements will have to be carried out. The advantages of operating the main spectrometer during parts of the test runs in a time-of-flight mode were pointed out in section 7.1. Due to the about 20 m long region with a strong negative electric potential inside the KATRIN main spectrometer, electrons with low surplus energies need comparatively large flight times of the order of several  $10 \mu\text{s}$  to pass it. However, the timing resolution necessary to perform a detailed characterization of the MAC-E filter by measuring time-of-flight *differences* is of the order of a few 100 ns. This requirement has to be met by the calibration electron source, by the detector electronics and by the data acquisition and analysis chain.

The experimental studies described in this chapter have successfully demonstrated that short-pulsed photoelectron production fulfilling the abovementioned timing demands is feasible by using commercially available light emitting diodes with emission in the deep-ultraviolet range (sections 7.2 and 7.3). These LEDs deliver photon energies sufficient to liberate electrons from the surface of various materials, for example from stainless steel, silver or copper. The major advantage of this method is that fast pulsing can be achieved simply by an appropriate modulation of the operating voltage  $U_{\text{LED}}$  of the LED. The test measurements using a stainless steel photocathode showed that usable photoelectron detection rates are achievable at pulse widths of  $\tau_{\text{LED}} \gtrsim 40 \text{ ns}$  and repetition rates of  $f_{\text{LED}} = 1 - 10 \text{ kHz}$ . By choosing a suitable set of operating parameters  $U_{\text{LED}}$ ,  $f_{\text{LED}}$  and  $\tau_{\text{LED}}$ , the multiplicity of photoelectrons detected per pulse can be tuned, and even single photoelectrons per pulse can be produced (section 7.3.1). Using light pulses of 200 ns duration a high-resolution time-of-flight spectrum was measured (see section 7.3.3) which

<sup>19</sup>Such a scanning mechanism is in use at the pre-spectrometer electron gun and could possibly be applied to other calibration sources, as well.

exposes low-energy details of the photoelectron energy that are more difficult to discern in the usual integrated energy scan (compare section 7.3.2). This successful measurement at the Mainz spectrometer confirms that the proposed method is indeed suitable to provide electron pulses for time-of-flight studies at a MAC-E filter.

It is even possible to use short photoelectron pulses in combination with an additional selection of restricted intervals of angular emission (section 7.4). Compared to the timing qualities, however, this second feature of the photoelectron gun requires more technical consideration. Different variants of a setup exploiting non-adiabatic acceleration in non-parallel electric and magnetic fields are possible, one of which was realized in a prototype electron gun with discrete spots of emission on a thin metal film illuminated from the back side through thin optical fibers. Even though the test setup only consisted of two working fibers, a clear hint at different angular emission profiles obtained from the two illuminated spots on the tip was seen: The two fibers exhibit differing shapes of the integrated energy spectrum measured with the Mainz MAC-E filter. The prototype tests thus yield a proof of principle of the method.

Table 7.7 contains a comparison of important characteristics of the condensed krypton calibration source (CKrS), which represents the standard calibration source for the electromagnetic design tests of the KATRIN main spectrometer, and a potential UV LED-based photoelectron source that may be developed on the basis of the test measurements described in this work. The table shows that these two sources have different properties which complement each other well. In this compilation the fast pulsing is treated as a basic feature of the UV LED-based electron gun, whereas the angular selectivity forms an additional option.

Some clear advantages of the CKrS are pointed out in the table: Firstly, the energy of the conversion electrons is well-defined and highly stable. The  $K_{32}$  line possesses a natural width (Lorentz shape:  $\Gamma = 2.7$  eV) which is larger than the energy resolution of the KATRIN main spectrometer, but which on the other hand is well determined. Furthermore, the angular distribution of the conversion electrons delivered by the CKrS is naturally a rather wide one: it resembles the isotropic distribution obtained with the gaseous tritium source in the neutrino mass measurements, which – as pointed out above – is of particular relevance in view of the large-angle electrons needed for the tests of the electromagnetic design. Thus, the angular emission characteristics of the CKrS contrasts with those of simple photoelectron sources<sup>20</sup>: It was demonstrated that the setup using a plane cathode disc only emits electrons at very small angles with respect to the normal of the cathode, and simulations [Hug08] show that also the rounded tip employed at the pre-spectrometer photoelectron gun delivers only a comparatively small relative number of electrons at large angles. Therefore it is appealing to further develop the idea of the angular-defined photoelectron gun presented in the previous sections, which represents the only one of the mentioned concepts that in principle allows full control over the angular emission. However, judging from the results of the first prototype tests of the fiber-based electron gun, it is clear that further conceptual and experimental investigations are necessary in order to understand and control the characteristic properties of this electron gun on a level that permits its use as a reliable calibration source for KATRIN. First ideas to improve and possibly simplify the concept are presented in section 7.5.2.

Another advantage of conversion electron sources like the CKrS over photoelectron-based sources

---

<sup>20</sup>It is important to emphasize that the restricted angular emission of the simple photoelectron sources discussed here is due to the fact that the electrons are created with low initial kinetic energy and thus must be accelerated by applying a strong electric field quasi-parallel to the magnetic field, which leads to a preferential gain of longitudinal instead of transverse energy. On the other hand, electrons from atomic/nuclear standards, such as the conversion electrons from  $^{83m}\text{Kr}$ , are produced with multi-keV energies and hence do not need to be post-accelerated to the same extent as the low-energy photoelectrons created by UV irradiation of metals.

is the stability of the count rate which can be achieved and maintained both on short and long time scales. Here, a fundamental problem exists on the side of the photoelectron sources because their strong negative accelerating potential necessarily forms a Penning trap together with the retardation potential of the spectrometer and the intermediary magnetic field. Count rate instabilities possibly related to this effect have been observed at the pre-spectrometer and in the prototype test measurements presented in this work (compare section 7.4.2). This problem has to be solved in view of an application as high-precision and high-stability electron sources.

For the purpose of time-of-flight studies, a source-related energy spread smaller than the spectrometer resolution is desirable. According to first test measurements the UV LED-based photoelectron source looks promising in this regard: for the plane photocathode disc made of stainless steel an energy distribution which can be described by a gaussian broadening of  $\sigma_{\text{energy}} < 0.24 \text{ eV}$  was determined, with room for potential further improvements (*e. g.*, better matching of photocathode work function and photon energy of the UV light, better spatial and temporal stability of the work function, etc.).

The aforementioned capability to easily achieve short photoelectron pulses at high repetition rates, as well as the possibility to obtain single photoelectrons per pulse, are arguments in favor of the photoelectron gun. The tests of the timing characteristics presented in section 7.3 encourage an upgrade of the present pre-spectrometer electron gun by replacing the deuterium UV lamp with a UV LED (provided that the photon energy is high enough to produce photoelectrons off a gold film) in order to profit from the pulsing capability.

Although the krypton source can also be operated in a pulsed mode by applying a fast-chopped bias voltage, this involves a somewhat larger technical effort. At the former Mainz neutrino mass experiment, the feasibility of  $2.5 \mu\text{s}$  pulses with a rise/fall time of 200 ns and a duty factor of 50% was demonstrated [Bon99].<sup>21</sup>

In summary, it seems to be worthwhile to further pursue both options of the CKrS conversion electron source and photoelectron sources to be used for a calibration of the main spectrometer, as they offer complementing characteristics which the KATRIN experiment could benefit from.

---

<sup>21</sup>With suitable high voltage switches, faster chopping (down to switching times of  $\gtrsim 50 \text{ ns}$  at 50% duty cycle [Sta09]) can be envisioned.

**Table 7.7:** Comparison of properties of the condensed krypton calibration source (CKrS) and the UV LED-based photoelectron gun (without or with optional angular selectivity by implementing fibers).

	CKrS	UV LED-based electron gun
electron source	conversion electrons from $^{83m}\text{Kr}$	photoelectrons
energy spread	natural line width ( $K_{32}$ ): $\Gamma = 2.7 \text{ eV}$ (well studied) [Ost09]	$\Delta E$ of order $(0.2 - 0.5) \text{ eV}$ , nearly gaussian width ( $\sigma < 0.24 \text{ eV}$ ), seems improvable by matching work fcn. $\Phi$ and UV-wavelength $\lambda$
energy stability	line position highly stable and reproducible ( $\sim 1 \text{ ppm/month}$ ) [Ost09]	in principle easy to control via measurement of $U_{\text{source}} - U_{\text{spec}}$ , but stability of work fcn. still to be investigated
fast-pulsing capability	achievable by chopping $U_{\text{source}}$ (proven at Mainz $\nu$ -mass experiment: $\tau = 2.5 \mu\text{s}$ , rise time $0.2 \mu\text{s}$ , $f = 0.4 \text{ MHz}$ ), requires some effort	simple implementation by fast pulsing of UV LED, $\tau \gtrsim 40 \text{ ns}$ , $f = (1 - 10) \text{ kHz}$ achieved
coverage of full magn. flux	2-dim. scanning device necessary	2-dim. scanning device necessary
angular emission characteristics	isotropic (without HV at source), similar to $T_2$ source	angular selectivity possible (first proof of principle done, but further studies required); present pre-spectrum. $e^-$ gun: few electrons with large angles (but these are particularly important for main spectrum. tests) planar photocathode: only small angles angular-selective $e^-$ gun: freely tunable via tip geometry and fields
spatial emission profile	extended (diameter of substrate)	<ul style="list-style-type: none"> <li>extended (diameter of irradiated spot on planar photocathode), or</li> <li>confined (diameter of fiber cores: <math>\approx (25 - 100) \mu\text{m}</math>)</li> </ul>
count rate	<p><math>\sim 10^3</math> to <math>10^4 \frac{1}{\text{s}}</math> feasible</p> <p>stable on relative level of <math>10^{-3}</math></p>	<p>single electrons per pulse achievable, present experimental upper limit of rate <math>\lesssim 5 e^-/\mu\text{s}</math> in pulsed mode with duty cycle 1% from planar photocathode (<i>i. e.</i>, average of <math>5 \cdot 10^4 \frac{1}{\text{s}}</math>); lower rates when using optical fibers; variable rates easily achievable stability to be proven (non-trivial due to trapped particles, see text)</p>

### 7.5.2 Improvements envisioned for an upgraded design of an angular-selective photoelectron gun

On the part of modeling, efforts to achieve a better understanding of the emission characteristics of the fiber-coupled electron source by detailed computer simulations are under way [Hei09]. The aim of these calculations is to obtain an optimized electromagnetic design for such a photoelectron source with better angular definition (maybe even offering the possibility to select individual angles). There are several ways in which the mechanical concept could be improved or simplified. Some appealing strategies will be presented in the following.

#### Strategies to improve the present concept

Count rate and reliability of the optical coupling mechanism are listed among the technical aspects of the device that need to be improved on, in particular when viewed in the light of the requirements for a potential application as a calibration source for the main spectrometer. Calibration measurements to determine the pixel-resolved transmission function of the main spectrometer and the energy loss function of the WGTS are time-consuming and therefore quite costly. A high electron rate would largely facilitate such measurements.<sup>22</sup> Since the original concept of the prototype tested at Mainz was by far not optimized with respect to the count rate, a gain in emittance is to be expected for an upgraded source. Potential points to improve on include the intensity of the UV light source (using several LEDs instead of just one low-power device), efficiency of light collection into the fiber, operation in a higher initial magnetic field to reduce the loss of high-angle electrons due to the magnetic mirror effect, etc. Smaller fiber diameters could be used (*e. g.*, so-called “high power small core” (HPSC) fibers available with core diameters of down to 10 or 25  $\mu\text{m}$ ). In order to take full advantage of the compact core, however, the dimensions of the outer cladding and coating layers would have to be reduced accordingly. On the other hand, a smaller core diameter also implies a reduced transfer capacity of the fiber, *i. e.*, the light yield at the tip will be lower. Reaching the required positioning accuracy with the fiber-coupled solution is difficult due to the large tolerances of the machining and preparation of the parts. Furthermore, it is not easy to scale up the approach significantly beyond 3 - 5 separate angular intervals, since a corresponding increase of the number of fibers would be required, which might pose technical problems.

#### Options for alternative concepts

In view of the abovementioned difficulties to be overcome when attempting to improve the present concept, it is reasonable to also explore other options. One such idea was recently proposed by Ch. Weinheimer [Wei08]. Instead of the rounded tip holding several small fibers to create localized emission regions with varying starting angles, it is also possible to use a simple planar cathode surface and tune the amount of initial transverse kinetic energy by choosing a suitable ratio of the accelerating electric field and the crossing magnetic field. In the KATRIN setup, both the strength and the alignment of the magnetic field will be fixed (foremostly by the stray fields of the strong superconducting magnets). The strong decrease of the magnetic field strength with increasing distance from the high-field solenoids is in fact favorable for this concept, because a large ratio of the field strengths  $B_{\text{magnet}}/B_{\text{e-gun}}$  is required for the principle of this electron gun

<sup>22</sup>The efficiency of numerical techniques to perform the deconvolution of the response function to obtain the energy loss function relies on good statistics, as can be seen from the discussion of simulated energy loss spectra in [Wol08].

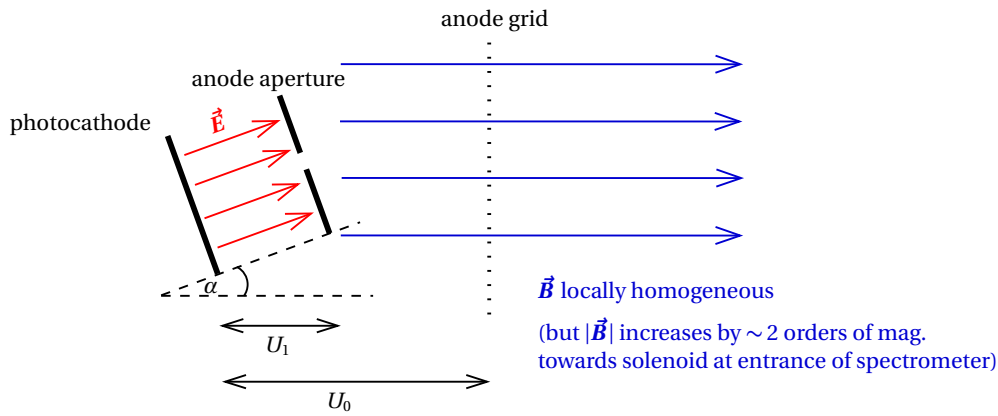


**Figure 7.29:** Alternative concept of an angular-selective electron gun using a planar capacitor. The electric field  $\vec{E}$  between the two electrodes of the capacitor is tilted by an angle  $\alpha \neq 0$  relative to the direction of the magnetic field  $\vec{B}$ . The ratio  $E_{\perp}/E_{\parallel}$  of transverse and longitudinal kinetic energy reached after the acceleration is completed can be tuned by choosing appropriate electric potential differences between the photocathode and the anode aperture ( $U_1$ ) and between the photocathode and the remote anode grid ( $U_0$ ). The UV light is guided to the emitting spot of the photocathode by an optical fiber (not shown). An enhanced version of this concept uses a staged capacitor with two apertures and three voltage differences  $U_0$ ,  $U_1$  and  $U_2$ .

to work.<sup>23</sup> The magnitude and the direction of the accelerating electric field in principle can be varied in a simple capacitor setup using a solid cathode and an anode with an opening to let the photoelectrons pass (see figure 7.29). A third electrode, included in the figure in the form of an anode grid, defines the final kinetic energy of the electrons. In a real setup, the grounded vacuum tube of the beam line may replace the anode grid. UV-transparent fibers offer sufficient flexibility to transport the UV light from an external source to the cathode surface.

There are two basic ways of selecting specific values of the transverse energy (and thus specific angles):

- The angle of rotation between the axis of the planar capacitor and the magnetic field is variable. This is technically challenging, since a manipulator mechanism allowing finetuning of the rotation angle in an ultrahigh vacuum environment is required.
- A fixed angle of rotation is implemented (for example,  $\alpha = 10^\circ$  or  $20^\circ$ ). In this case, the relative amount of transverse energy achievable at the onset of the adiabatic motion is selected by choosing a suitable ratio of the accelerating voltages  $U_0$  and  $U_1$ .

Detailed simulation studies investigating a setup using a planar capacitor (figure 7.29) are presently under way [Hei09], with promising initial results. First experimental tests of the new concept at the Mainz MAC-E filter are scheduled for spring 2009.

<sup>23</sup>First simulations indicate that an amount of  $E_{\perp} \approx 100 - 200$  eV in the initial (non-adiabatic) phase of the motion can be reached. The additional energy in the transverse component necessary to fill the full forward solid angle (in the high magnetic field at the center of the magnet) at electron energies of around 18.6 keV has to be achieved by adiabatic transformation due to the gradient of the magnetic field.

## 8 Conclusions and outlook

After making its debut into physics almost 80 years ago as an unseen “ghost particle” postulated by Pauli to solve an apparent paradox in the field of  $\beta$ -radioactivity, the neutrino soon began to occupy an area of research in its own right. Even today, with large efforts undertaken both in the theoretical and experimental sections of neutrino physics, the neutrino has preserved parts of its mysterious character, with many questions still to be answered. Among these, the absolute scale of neutrino masses ranges as one of particular interest, since it bears considerable relevance for particle physics, astrophysics, and cosmology. Although many indirect leads hint at a small, but non-vanishing neutrino mass (in contrast to a long-standing belief), an indisputable positive detection of a neutrino mass signal by a laboratory experiment is still pending and eagerly anticipated from many sides.

One method of direct neutrino mass determination consists in the precise study of the kinematics of weak decays, for example tritium  $\beta$ -decay. Even a tiny non-zero neutrino mass will leave an imprint on the shape of the  $\beta$ -spectrum that is most pronounced in the high-energy part close to the endpoint. However, this signal can only be detected with high-resolution electron spectrometers which, at the same time, provide a very low background level. In the KATRIN experiment, which is presently being set up at Forschungszentrum Karlsruhe, Germany, the technology of an electrostatic retardation filter with magnetic adiabatic collimation (“MAC-E filter”) will be used. This type of spectrometer allowed previous experiments at Mainz (Germany) and Troitsk (Russia) to set an upper limit of  $m(\nu_e) < 2 \text{ eV}/c^2$  [PDG08]. In order to improve the sensitivity on  $m(\nu_e)$  by an order of magnitude with KATRIN [KAT04], a much more luminous windowless gaseous tritium source and a very large main spectrometer (with a length of 23.3m and a diameter of 10m) achieving an energy resolution of 0.93 eV at electron energies around the tritium endpoint of  $E_0 \approx 18.6 \text{ keV}$  will be needed, among other requirements. To eliminate the bulk part of the low-energy electrons, a smaller pre-spectrometer is included upstream of the main energy filter.

Considering that the influence of systematic uncertainties related to inelastic collisions between  $\beta$ -particles and tritium molecules inside the source increases with the width  $E_0 - E$  of the analyzing energy window below the endpoint, it is advisable to keep this interval as small as possible. Unfortunately, the count rate drops approximately as  $(E_0 - E)^3$  when decreasing the size of the analyzing interval. Thus, it is important to prevent the minute signal from being concealed by background. Several potential background sources in the KATRIN setup have been identified, which can in general be grouped into spectrometer-related and detector-related contributions. The latter can be minimized by an appropriate design of the detector section, in particular by a careful selection of materials, by implementing a passive as well as an active shielding system, and lastly by shifting the region of interest to a more favorable energy range via post-acceleration of the electrons. Detailed studies concerning the intrinsic detector background are presented in [Schw04] and [Leb09].

In the first part of this thesis, various spectrometer-related background sources and methods for their suppression were investigated. Experience obtained at the conceptually very similar neutrino mass experiments at Mainz and Troitsk shows that a major contribution is caused by secondary electrons created at the surface of the solid retardation electrodes by interactions of atmo-

spheric muons or through environmental radioactivity. Moreover, a two-spectrometer system like the one at KATRIN unavoidably forms a Penning trap for electrons. Such a trapping region was found to give rise to a severe increase of background in the Troitsk setup, which also contained two successive spectrometers. Likewise, Penning traps may exist inside a MAC-E filter, which in the case of the KATRIN pre-spectrometer has led to the occurrence of strong discharges interfering with the test measurements. The following outlines the discussion of the abovementioned topics in this work:

- Chapters 3 and 4 discuss the concept of background reduction in MAC-E filters by means of an inner wire electrode placed on a negative electric potential with respect to the solid electrodes. The design of a complex double-layer wire electrode for the KATRIN main spectrometer is worked out and optimized in several steps on the basis of detailed computer simulations. The calculations also allow to give estimates for the tolerances to be met during manufacturing, assembly and mounting of the electrode parts.
- A phenomenological introduction to different mechanisms of electric discharges in vacuum in connection with particle traps is given in chapter 5. The specific characteristics of three major trapping regions in the KATRIN setup (entrance/exit regions both of the pre- and main spectrometers as well as the section between the two MAC-E filters) are elucidated. In particular, the conceptual design of a set of additional electrodes for the pre-spectrometer to remedy the observed discharge problems is presented, and consequences for the analogous design of the main spectrometer electrode system are pointed out. In a general overview methods to counteract discharges are collected and evaluated in view of their applicability to KATRIN, including a proposed active measure (compare [Ess04]) to empty the Penning trap between the two KATRIN spectrometers by swiping a metallic wire through the trapping region in periodic intervals. Experimental tests demonstrating the viability of this method were carried out in the scope of this work, and they are reported on in chapter 6.

The second part of this work picks up another topic related to the properties of MAC-E filters. To accomplish the projected gain in sensitivity on the observable  $m^2(v_e)$  of two orders of magnitude with respect to KATRIN's predecessor experiments, it is essential to achieve a detailed understanding of the characteristics of the main spectrometer, and to control and reduce the spectrometer-related systematic uncertainties. Among these, the transmission characteristics of the main spectrometer are of particular importance. The transmission function has to be known to high accuracy, as it enters into the analysis of the measured  $\beta$ -spectrum. The radial variation of the electric potential and the magnetic field strength in the analyzing plane of the spectrometer have a profound influence on the shape of the transmission function. They can be computed from an approximative simulation model, but nevertheless a direct measurement of the transmission function for each individual pixel of the KATRIN final plane detector is indispensable to confirm the simulation results. To this end, quasi-monoenergetic and stable calibration sources delivering electrons with energies around 18.6 keV are required. Since from the point of view of the electromagnetic design tests electrons with a large ratio of cyclotron energy over longitudinal energy are of particular interest, the calibration sources should be able to provide electrons with large angles. As a further prerequisite, the electron detection rate should be high enough to allow a full calibration measurement in a limited period of time with sufficient statistics. The standard calibration source for the main spectrometer, based on 17.8 keV conversion electrons from  $^{83\text{m}}\text{Kr}$ , fulfills these requirements.

- As described in chapter 7 of this work, it may be possible to obtain an alternative calibration source based on the creation of photoelectrons with light emitting diodes (LEDs) in

the UV range illuminating a cathode on high voltage. Aside from delivering electrons with a very narrow energy spread at appropriate count rates, such photoelectron sources have the additional advantage of superior timing capabilities. The latter are essential for a proposed time-of-flight operational mode of the MAC-E filter, which might significantly facilitate (and speed up) the calibration measurements at the KATRIN main spectrometer. Simulations regarding time-of-flight values expected for various starting parameters of electrons passing the main spectrometer are also presented in this chapter. These define the timing requirements which both the calibration electron source and the detection and data acquisition system should satisfy.

Lastly, chapter 7 also contains the basic principle as well as a successful first experimental test of a UV LED-based photoelectron source with the additional feature of angular definition, which might in further studies be developed into a powerful calibration tool for KATRIN.

A summary of the results presented in the individual sections of this work is given in the following.

## Design of a wire electrode system to reduce the secondary electron background in the KATRIN main spectrometer

Screening wire electrodes have previously been built for the Mainz MAC-E filter and for the KATRIN pre-spectrometer [Mül02, Fla04]. Both spectrometers are of comparable size (length  $\approx 4$  m, diameter  $\approx 1 - 2$  m), and thus the mechanical concept of the wire electrode systems is similar. At Mainz, an overall<sup>1</sup> background suppression by a factor of about 10 was achieved when applying typical screening potentials  $\Delta U = U_{\text{solid}} - U_{\text{grid}}$  of the order of 100 – 200 V (compare section 3.2). Conceivably, new challenges have to be met when transferring the concept to the KATRIN main spectrometer with its inner diameter of 9.8 m, its length of 23.3 m and a 650 m<sup>2</sup> surface of solid electrodes on high voltage to be screened by wires. The aim of maintaining a background level  $\mathcal{O}(10^{-2} \frac{1}{s})$  (or, if possible, even lower) with the large KATRIN main spectrometer calls for a very small geometric coverage  $f_{\text{gc}}$ , defined as the ratio of the wire diameter  $d$  over the wire spacing  $s$ . In order to reconcile this demand with other, opposing requirements (for example the need to keep the electric field strength at the surface of the wires low in order to avoid field emission and the aim of achieving a large electrical screening factor  $S$ : see discussion in section 3.4), the wire electrode for the KATRIN main spectrometer must be conceived as a double-layer system. This solution with two separate screening voltages  $\Delta U_1$  and  $\Delta U_2$  also makes a novel mechanical design necessary.

The first conceptual ideas of a wire electrode for the KATRIN main spectrometer were pinned down in 2004 [Val04]. Since then, comprehensive computer-based design studies were carried out in order to continually improve both the simulation model and the physical properties of the electrode system. Leading contributions were elaborated in the scope of this thesis, in close collaboration with the diploma theses of K. Hugenberg [Hug08], S. Vöcking [Vöc08] and M. Zacher [Zac09]. In the process, several stringent requirements regarding technical as well as physical aspects had to be respected, like for example high-voltage and ultrahigh vacuum compatibility, homogeneity of the electrostatic potential, avoidance of particle traps, transmission properties and energy resolution of the spectrometer. Driven by the growing complexity of the computer model, the simulation software had to be adapted and the development of new programs (F. Glück, S. Vöcking) was stimulated. The new software was in parts tested in the framework of this thesis.

---

<sup>1</sup>As seen in figure 3.4, the suppression factor can be larger for specific parts of the spectrometer and under certain experimental conditions.

The two layers of the wire electrode will be mounted on a large number of separate frames (“modules”) with two adjacent comb-like structures and spacer rods in between. In this work a computer model incorporating the details of the combs (“teeth”) was generated. Important insight on the relation between mechanical parameters of the electrode design (*e. g.*, the width of axial gaps between module rings) and the electrostatic properties – in particular regarding the inhomogeneity of the electric potential in the analyzing plane – was gained, and methods to amend these problems were worked out. This way, an interplay between mechanical design and engineering aspects on one side and the concerns of the electromagnetic design on the other side was established.

Furthermore, the computer simulations also revealed that the electrostatic properties of the main spectrometer are quite sensitive to mechanical tolerances related to the fabrication and preparation of electrode parts, as well as to the construction of the modules and to the accuracy of their placement inside the vessel. Despite the fact that most of these effects lead to deviations from the strictly rotational-symmetric computer model and therefore in principle cannot be modelled accurately with the available tools and computational resources, it was possible to at least obtain estimates on the required accuracy. An important point concerns the sag of wires under their own weight, which is expected to produce the most pronounced effect for the wires close to the analyzing plane. Simulation results show that the maximum allowed value for a deviation from a straight line amounts to about 0.2 mm. On the part of module assembly, this result necessitates a careful adjustment and control of the mechanical wire tension. The same tolerance in principle applies for the relative radial position of the two wire layers in the modules close to the analyzing plane. This calls for high-precision cutting of the comb-like mounting structures and for an equally accurate positioning of the holes for the fixing points of the wires. Likewise, the quality assurance procedures must be capable of reliably resolving defects on this scale. Generally, these criteria can be relaxed when considering modules further away from the critical region around the analyzing plane.

Once completed, the inner electrode system for the KATRIN main spectrometer will consist of 248 individual wire modules, plus several solid-metal parts (ground and “anti Penning trap” electrodes). The manufacturing of the modules at the Institute of Nuclear Physics of Münster University is ongoing, and presently about 60% of the modules have been assembled. The installation of the wire electrode into the main spectrometer vessel is scheduled to start in spring 2009.

## Investigation of background caused by Penning traps in the KATRIN setup

### Modification of the electrode system of the pre-spectrometer

Test experiments carried out at the pre-spectrometer suffered from severe discharge problems, in a way that prohibited to use the sensitive electron detector (64-pixel PIN diode) foreseen for these measurements. By computer simulations and a detailed experimental program it was possible to trace back these problems to a deep Penning trap ( $\Delta U \approx 5.2$  kV) located in the symmetric entrance and exit regions of the pre-spectrometer. In the course of this work a new set of additional electrodes was designed which allows cut off most of the trapping volume. The computer simulations showed that, in order to achieve the best suppression of the trap, the ground electrodes of the pre-spectrometer had to be shortened, as well.

After the installation of the new electrodes, the strong discharges vanished, and measurements with the electron detector are now feasible. Yet, some problems with increased background rates above a certain critical magnetic field strength  $B_{\text{crit}} \approx B_{\text{max}}/2$  persist, which may be related to a recently discovered smaller Penning trap at the ground electrode [Fra09]. The background in-

vestigations at the pre-spectrometer are still ongoing. The results bear particular relevance for the design of a similar pair of “anti Penning trap” shielding electrodes for the main spectrometer, which was worked out in [Hug08] and [Zac09].

### **Test of an electron catcher to empty the Penning trap between pre- and main spectrometer**

The system of two successive spectrometers of MAC-E filter type included in the KATRIN beam line was simulated by a test setup at the spectrometer of the former Mainz neutrino mass experiment. The aim of this investigation was to examine the characteristics of the resulting Penning trap for electrons and thereby to create a testbed for an active mechanism to empty the trap in periodic intervals. Using different filling methods the behavior of the trap was studied under various conditions, yielding a marked increase in the background rate as well as frequent bursts and even strong discharges associated with an increase of the pressure reading in the vacuum system.

A total of three measurement phases to test the influence of an “electron catcher” in the form of a current loop moved across the trapping volume by virtue of the Lorentz force were carried out in 2007 and 2008. In each of the phases, modifications of the device were made to further improve its mechanical properties. This process finally resulted in a stable prototype of the wire scanner which was reliably operated under ultrahigh vacuum conditions in an environment very similar to that in the real KATRIN setup.

The wire scanner proved capable of influencing the background rate observed at the test setup in a positive way, with a notable dependence on the type and frequency of the motion performed by the wire. While a rectangular motion was usually not sufficient to prevent the onset of discharges, a sinusoidal motion with a frequency of the order of 1 Hz was found to significantly delay the onset of discharges or dampen and even extinguish them once they had been ignited. Under certain conditions it was observed that the wire left immobile at the center of the beam would lead to reduction of the count rate. This behavior may be explained by considering the magnetron drift motion, which contributes to emptying the trap by making stored electrons hit the wire after a certain number of axial oscillations. Whether such a stationary wire (or a pin covering at least the radius of the transported magnetic flux tube) might be suitable for preventing discharges at KATRIN remains to be clarified. Furthermore, the main disadvantage of the stationary wire, namely the considerable loss of data due to the permanent “shadowing” of at least 9% of the detector pixels, would have to be overcome (for example by withdrawing the pin from the beam to allow certain undisturbed measurement intervals).

A direct transfer of the observations made at the test setup in Mainz – in particular those regarding ignition time scales and swiping frequencies of the wire – to the KATRIN setup is not possible because of several important differences (*e. g.*, the residual gas pressure at Mainz was about two orders of magnitude higher than that projected for KATRIN, and the test setup contained an additional feedback mechanism due to the high-voltage electrode linked by magnetic field lines with the detector, which will not be present in the KATRIN experiment). Nevertheless, the positive results from Mainz offer encouraging perspectives for a usage of the wire scanner mechanism at KATRIN. The operational parameters (frequency and type of the scanner action) will need to be found experimentally once the KATRIN setup is completed.

## Test of a UV LED-based fast-pulsed photoelectron source for time-of-flight studies

Trajectory simulations were carried out in order to get a handle on the time-of-flight values to be expected for the KATRIN main spectrometer (section 7.1.1) and in addition to possibly establish a relationship between time-of-flight values and details of the transmission properties of the MAC-E filter (section 7.1.2). Typical values for intermediate and low surplus electron energies are of the order of several  $10\ \mu\text{s}$ , but the aim of

1. running the spectrometer in a non-integrating bandpass mode (“first order MAC-E-ToF mode”) and
2. performing diagnostics of spectrometer properties (“second order MAC-E-ToF mode”)

requires a timing resolution of the order of a few 100 ns. Pulsing of an electron source can be achieved either by chopping the bias potential or by switching the electron creation on and off. The latter can be achieved for photoelectron production in a very simple manner by using modern UV LEDs (commercially available only since a few years) as light sources and by modulating the LED operating voltage in an appropriate manner (*e. g.*, with a function generator). These LEDs emit in the deep-ultraviolet range ( $\lambda_{\text{central}} = 265\ \text{nm}$  and  $255\ \text{nm}$ , respectively: photon energies around  $E_{\text{photon}} \approx 4.7\ \text{eV}$ ), which permits to use easily workable and ultra-high vacuum compatible photocathode materials, such as stainless steel (work function  $\Phi_{\text{stainless steel}} \approx 4.4\ \text{eV}$ ).

Using the same experimental setup at the Mainz spectrometer as for the wire scanner test measurements, the timing characteristics of such photoelectron pulses was studied. Short light pulses of width  $\tau = 40\ \text{ns}$  to  $\tau = 40\ \mu\text{s}$  were created, resulting in a wide dynamic range of the detected photoelectron rate between single photoelectrons per pulse and up to 5 photoelectrons per  $\mu\text{s}$  (section 7.3.1). Typically, pulse repetition rates of 1 – 10 kHz were employed. Maximizing the fraction  $\varepsilon_{\text{single}}$  of single electrons per pulse is important to keep the pile-up ratio low, and it forms an essential feature needed for the second order MAC-E-ToF mode. The measurements demonstrated that it is indeed possible to achieve  $\varepsilon_{\text{single}} \approx 1$  with such a UV LED-based photoelectron source. The combination of the three operational parameters  $f$  (repetition frequency),  $\tau$  (pulse width) and  $U_{\text{LED}}$  (driving voltage) of the LED, which can be chosen separately, allow this electron source to reach a high degree of versatility.

The energy distribution of the photoelectrons was determined in two ways (sections 7.3.2 and 7.3.3), with both methods yielding consistent values of an energy smearing assumed to be of gaussian shape.

- a) From the fit in the integral energy spectrum an upper limit of the gaussian width was obtained:

$$\sigma_{\text{energy}} < 0.24\ \text{eV} \quad (95\% \text{ C.L.}), \quad (8.1)$$

with a best-fit value of  $\sigma_{\text{energy}} = (0.21 \pm 0.02)\ \text{eV}$ . Herein, it was assumed that the photoelectrons are emitted from the cathode without picking up a significant amount of transversal kinetic energy, which corresponds to the expectation for the case of strong electrostatic acceleration in the forward direction and quasi-collinear electric and magnetic fields that was realized in the test setup. The assumption of nearly mono-angular emission can be justified by comparing the alternative case of monoenergetic, but isotropic electron emission with the measured data, which strongly disfavors the latter case.

- b) A similar value was found in an analysis of the time-of-flight spectrum also taken at the Mainz MAC-E filter. The measured time-of-flight values are in very good agreement with calculated values over a large range of surplus energies of the electrons with respect to the

filter energy ( $E_{\text{surplus}} \lesssim 400 \text{ eV}$ ). For the very lowest values ( $E_{\text{surplus}} \lesssim 4 \text{ eV}$ ) an energy spread of gaussian width  $\sigma_{\text{energy}} \approx 0.20 - 0.25 \text{ eV}$  folded into the calculation was necessary to describe the measured data.

Although this narrow energy spread in itself makes such a photoelectron source an attractive option for the characterization of the KATRIN main spectrometer, it should be emphasized that there seems to be room for further improvement of  $\sigma_{\text{energy}}$ , for example by better matching the work function of the photocathode and the photon energy of the LED and by reducing the high-frequency noise of the retardation voltage.

## Prototype studies of a photoelectron source with angular selectivity

In contrast to the aforementioned emission of photoelectrons from a plane cathode which is confined to very small angles of emission, it is also possible to devise an electron source offering full control of the angle. More explicitly, such a source permits to tune the ratio of transverse over longitudinal energy up to the point where  $\theta \lesssim 90^\circ$  inside the maximum magnetic field is reached. This can be achieved by using a particular geometry of the photocathode and of the electric and magnetic fields at the location of the source. In fact, the concept is especially suited for the application at a MAC-E filter, since it expressly makes use of the adiabatic transformation  $E_{\parallel} \rightarrow E_{\perp}$  when going from a weak magnetic field into a stronger one, which can be realized in a straightforward manner by placing the source in the stray field of an entrance solenoid of a MAC-E-type spectrometer.

Based on earlier simulation results [Hug08] regarding the emission characteristics of the electron gun used at the KATRIN pre-spectrometer, a prototype of such an angular-selective photoelectron source was developed (section 7.4.1) and successfully tested at the Mainz spectrometer in the course of this work (section 7.4.2). The basic concept consists of a locally homogeneous magnetic field and a hemispherical tip creating a radial electric field. The selective illumination of small regions at different radii on the tip yields different starting angles of the photoelectrons with respect to the magnetic field lines, thus defining the initial amount of transverse (or cyclotron) energy. Even though only two such emission spots with rather broad intervals of starting angles were implemented in the prototype, clearly distinct shapes of the transmission curve for the two cases were observed.

Since a scaling of the above concept to a larger number of emission regions with finer granularity of the angular definition is not trivial, an alternative approach is presently under investigation ([Hei09], see section 7.5.2), with promising initial results. A first experimental verification of the new concept at the Mainz MAC-E filter is envisaged for spring 2009.

By combining fast pulsing with angular selectivity a powerful calibration tool for KATRIN may thus be obtained.



## A Electric screening factor of a single-layer cylindrical wire electrode

In order to find a mathematical expression for the electric screening factor  $S$  – as defined by equations (3.4) and (3.5) – of a cylindrical electrode configuration consisting of a solid electrode and a single-layer wire grid, it is helpful to first consider a planar electrode geometry.<sup>1</sup> In this model a (solid) sheet electrode extends infinitely in the  $xz$ -plane at  $y = -l$ . The region with  $y < -l$  is filled with solid metal and therefore the electric field vanishes in this domain. A grid of equidistant, parallel wires of diameter  $d$  with a spacing  $s$  in the  $x$ -direction is located at  $y = 0$  (see figure A.1).

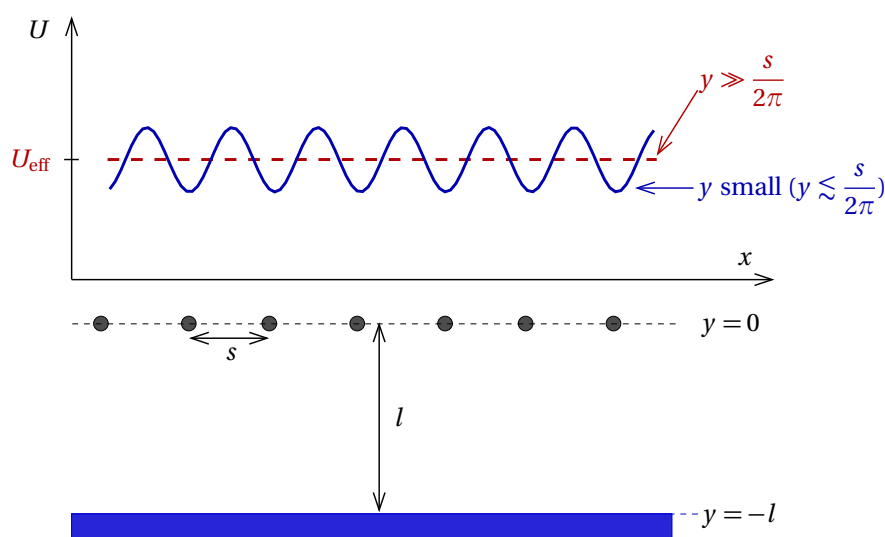


**Figure A.1:** Schematic illustration: Influence of the wire grid on the electric potential  $U$  at large and small distances for the case of a planar electrode system.

We assume that  $l > s/2$ . The wires have infinite extent in the  $z$ -direction and are assumed to be very thin ( $\pi d \ll s$ ), such that the charge distribution of a wire can be approximated by a linear charge density  $\lambda$ . What is the resulting electric potential of this configuration at fieldpoints with  $y > s/2$ , if a potential  $U_{\text{sheet}}$  is applied to the sheet electrode and  $U_{\text{grid}} \neq U_{\text{sheet}}$  is applied to the wire grid? The solution can be found by superimposing the potentials  $\phi_{\text{sheet}}$  and  $\phi_{\text{grid}}$  arising at a given field point  $(x, y, z)$  from the charge distribution on the plate and on the wire, respectively. The two components can be calculated separately:

- If the distance  $l$  between grid and sheet is sufficiently large compared to the wire pitch  $s$ , the surface charge density  $\sigma$  on the sheet can be assumed to be constant. The electric potential  $\phi_{\text{sheet}}$  at a field point  $(x, y, z)$  due to a given charge density on the plate is then

<sup>1</sup>The line of argument presented here follows that of reference [Glü05d].

only a function of  $y$ :

$$\phi_{\text{sheet}}(y) = C_1 - \frac{\sigma}{2\epsilon_0} |y + l|, \quad (\text{A.1})$$

with an arbitrary constant  $C_1$  (SI units are employed throughout the text).

- The potential  $\phi_{\text{grid}}$  due to the linear charge distribution on the large number of wires exhibits a dependence both on  $x$  and on  $y$ . Due to the translational symmetry, it is invariant in  $z$ -direction and can be shown [Blu94, Rea98, Glü05d] to take the following form:

$$\phi_{\text{grid}}(x, y) = C_2 - \frac{\lambda}{4\pi\epsilon_0} \ln \left[ 2 \left( \cosh \left( \frac{2\pi y}{s} \right) - \cos \left( \frac{2\pi x}{s} \right) \right) \right], \quad (\text{A.2})$$

where the second term in the square brackets reflects the periodic variation due to the influence of the wires. ( $C_2$  is another constant.)

Using the decomposition  $\cosh(k) = \frac{1}{2}(e^k + e^{-k})$ , one finds that the fluctuating term is washed out at large distances due to an exponential damping with a characteristic length  $s/(2\pi)$  that is solely determined by the spacing of the wires:

$$\phi_{\text{grid}}(x, y) \propto \exp \left( -\frac{2\pi y}{s} \right) \cos \left( \frac{2\pi x}{s} \right). \quad (\text{A.3})$$

For example, for a pitch of  $s = 25$  mm the amplitude of the fluctuating term decays to half of its maximum value at a distance of  $y_{1/2} \approx 3$  mm, and to 1% at  $y_{1/100} \approx 18$  mm.

Neglecting the fluctuating term at sufficiently large distances from the grid (*i. e.*,  $2\pi y/s \gg 1$ ), the expression for the field at a remote point can be rewritten as

$$\phi_{\text{grid}}^{\text{far}} \approx C_2 - \frac{\lambda}{s} \frac{|y|}{2\epsilon_0}. \quad (\text{A.4})$$

A comparison of eqs. (A.1) and (A.4) shows that the remote grid potential appears just like that of a sheet electrode with an equivalent charge density  $\sigma_{\text{grid, equiv}} = \lambda/s$ .

Combining eqs. (A.1) and (A.2), the total potential  $\phi$  resulting from the superposition of the potentials of the metal sheet and the wire grid is obtained:

$$\phi(x, y) = C - \frac{\sigma}{2\epsilon_0} |y + l| - \frac{\lambda}{4\pi\epsilon_0} \ln [2f(x, y)], \quad (\text{A.5})$$

with

$$f(x, y) = \cosh \left( \frac{2\pi y}{s} \right) - \cos \left( \frac{2\pi x}{s} \right). \quad (\text{A.6})$$

The remaining unknown quantities,  $\sigma$ ,  $\lambda$  and  $C$ , can be calculated by exploiting the boundary conditions:

- The electric field in the region of solid metal ( $y < -l$ ) is zero.
- The potential on the surface of the solid metal equals  $U_{\text{sheet}}$ .
- The potential on the surface of the wires (*i. e.*, for  $x^2 + y^2 = (d/2)^2$ ) is  $U_{\text{grid}}$ .

One then finds:

$$\begin{aligned} \sigma &= -\frac{\lambda}{s}, \\ C &= U_{\text{sheet}} + \frac{\lambda l}{2\epsilon_0 s}, \quad \text{and} \\ \lambda &= \frac{\epsilon_0 s (U_{\text{grid}} - U_{\text{sheet}})}{l} \frac{1}{1 + \frac{s}{2\pi l} \ln \left( \frac{s}{\pi d} \right)}. \end{aligned} \quad (\text{A.7})$$

With these ingredients the potential in points far from the grid (*i. e.*, at  $2\pi y/s \gg 1$ ) can be expressed via the potentials  $U_{\text{grid}}$  and  $U_{\text{sheet}}$ :

$$\begin{aligned}\phi_{\text{total}}^{\text{far}} &\approx U_{\text{grid}} + \frac{U_{\text{sheet}} - U_{\text{grid}}}{S} \\ &\equiv U_{\text{grid}} + \delta U,\end{aligned}\tag{A.8}$$

where  $S$  is given by

$$S = 1 + \frac{2\pi l}{s \ln\left(\frac{s}{\pi d}\right)}.\tag{A.9}$$

The relations found above for a planar geometry can be applied in good approximation to a cylindrical electrode with large radius  $R \gg l$ , such that the curvature of the cylinder becomes locally negligible. The screening factor obtained from computer simulations for various parameters  $d$ ,  $l$ , and  $s$  agrees with the analytical results on a level of a few percent (see, for example, reference [Val04] and compare table A.1). In one of these studies the simulated geometry consisted of a solid outer cylinder of length  $L = 20\text{m}$  and radius  $R = 0.85\text{m}$  on ground potential ( $U_{\text{vessel}} = 0$ ), and an inner cylindrical wire electrode with radius  $R - l = 0.80\text{m}$  and wire spacing  $s = 20\text{mm}$ , which was placed on a potential  $U_{\text{grid}} = 100\text{V}$ . The computed effective potential  $U_{\text{eff}}$  inside the cylinder was used to determine a numerical screening factor according to the relation

$$S_{\text{numer}} = \frac{U_{\text{grid}} - U_{\text{vessel}}}{U_{\text{grid}} - U_{\text{eff}}},\tag{A.10}$$

which was compared to the value obtained from the analytical formula for planar electrodes (eq. A.9). The relative deviation

$$\chi = \frac{S_{\text{analyt}} - S_{\text{numer}}}{S_{\text{analyt}}}\tag{A.11}$$

becomes smaller for decreasing wire diameter  $d$ .

Figure A.2 shows the simulated radial dependence of the potential for the abovementioned example of a long cylinder. Inbetween the solid electrode and the grid the potential rises linearly. Only at field points very close to the wire the linear behavior is distorted. When reaching the position of a wire the potential becomes equal to  $U_{\text{grid}} = 100\text{V}$ . However, proceeding towards the center of the cylinder the potential quickly reaches the value of the effective potential  $U_{\text{eff}}$  and remains constant further on. According to eq. (A.9), the effective potential for fixed  $s$  and  $l$  depends on the wire diameter  $d$ . This is seen in the graph; the larger the wire diameter, the smaller the difference  $U_{\text{grid}} - U_{\text{eff}}$ .

$d / \mu\text{m}$	2000	200	20
$U_{\text{eff}} [\text{V}]$	92.744	81.463	72.526
$S_{\text{numer}}$	13.782	5.395	3.640
$S_{\text{analyt}}$	14.566	5.539	3.726
rel. deviation $\chi$	5.4 %	2.6 %	2.3 %

**Table A.1:** Analytical and numerical electric screening factors for a long cylindrical electrode setup (table adapted from [Val04]). The relative deviation is of the order of a few percent, most of which can be attributed to the different geometry of cylindrical and planar electrodes (numerical influences, such as finite discretization elements of the electrodes, are small compared to the deviations).

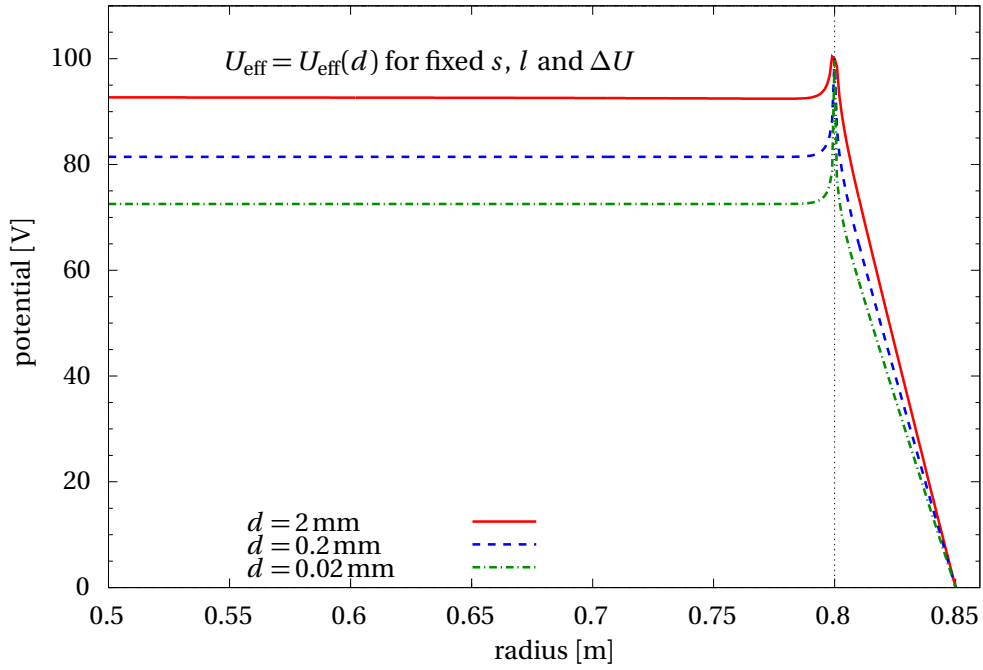


**Figure A.2:** Radial dependence of the electric potential for a long cylindrical screening electrode with varying wire diameter  $d$  (figure taken from [Val04]). The solid outer cylinder with radius  $R = 0.85\text{ m}$  was on ground potential, while the wire electrode with radius  $R - l = 0.80\text{ m}$  was put to a potential of  $100\text{ V}$ . The spacing between the wires was  $s = 20\text{ mm}$ .

#### Electric field strength at the surface of the wire

With the prerequisites obtained above the electric field strength  $E_{\text{wire}}$  at the surface of a wire in the grid can be calculated:

$$\begin{aligned}
 E_{\text{wire}} &= \frac{\lambda}{\pi d \epsilon_0} \\
 &= \frac{U_{\text{grid}} - U_{\text{sheet}}}{l} \frac{s}{\pi d} \underbrace{\frac{1}{1 + \frac{s}{2\pi l} \ln\left(\frac{s}{\pi d}\right)}}_{(\star)}. \tag{A.12}
 \end{aligned}$$

In many cases the factor marked with  $(\star)$  is close to 1 and can therefore be neglected. For example, for a single-layer electrode with the parameters  $d = 0.2\text{ mm}$ ,  $s = 25\text{ mm}$  and  $l = 200\text{ mm}$ ,  $(\star)$  takes the value 0.93.

## B Technical drawings

This appendix contains a set of construction drawings related to devices that are described in this work:

- A new set of ground and additional shielding electrodes conceived for the purpose of reducing the depth of the Penning trap present in the entrance and exit regions of the KATRIN pre-spectrometer (B.1). The simulation work dedicated to finding an optimal electrode geometry is reported on in section 5.2.
- The disc-shaped stainless steel plate that was used to emulate the high voltage electrode of the pre-spectrometer in the test setup at the Mainz spectrometer (section B.2). These measurements were carried out in order to study the characteristics of the Penning trap that is formed in the electromagnetic field configuration defined by the successive KATRIN pre- and main spectrometers. They are described in chapter 6.
- A wire scanner (section B.3).
- The prototype of a fiber-coupled photoelectron source (section B.4).

### B.1 Pre-spectrometer shielding electrode

Figure B.1 shows a detailed construction drawing for the newly introduced shielding electrodes and the modified configuration of the ground electrodes for the KATRIN pre-spectrometer. The drawing was provided by H. Hucker (Institut für Kernphysik, Forschungszentrum Karlsruhe). Note that the new pair of ground electrodes now installed in the pre-spectrometer was constructed from stainless steel rather than titanium, the material that was used for the previous set of ground electrodes.

B Technical drawings

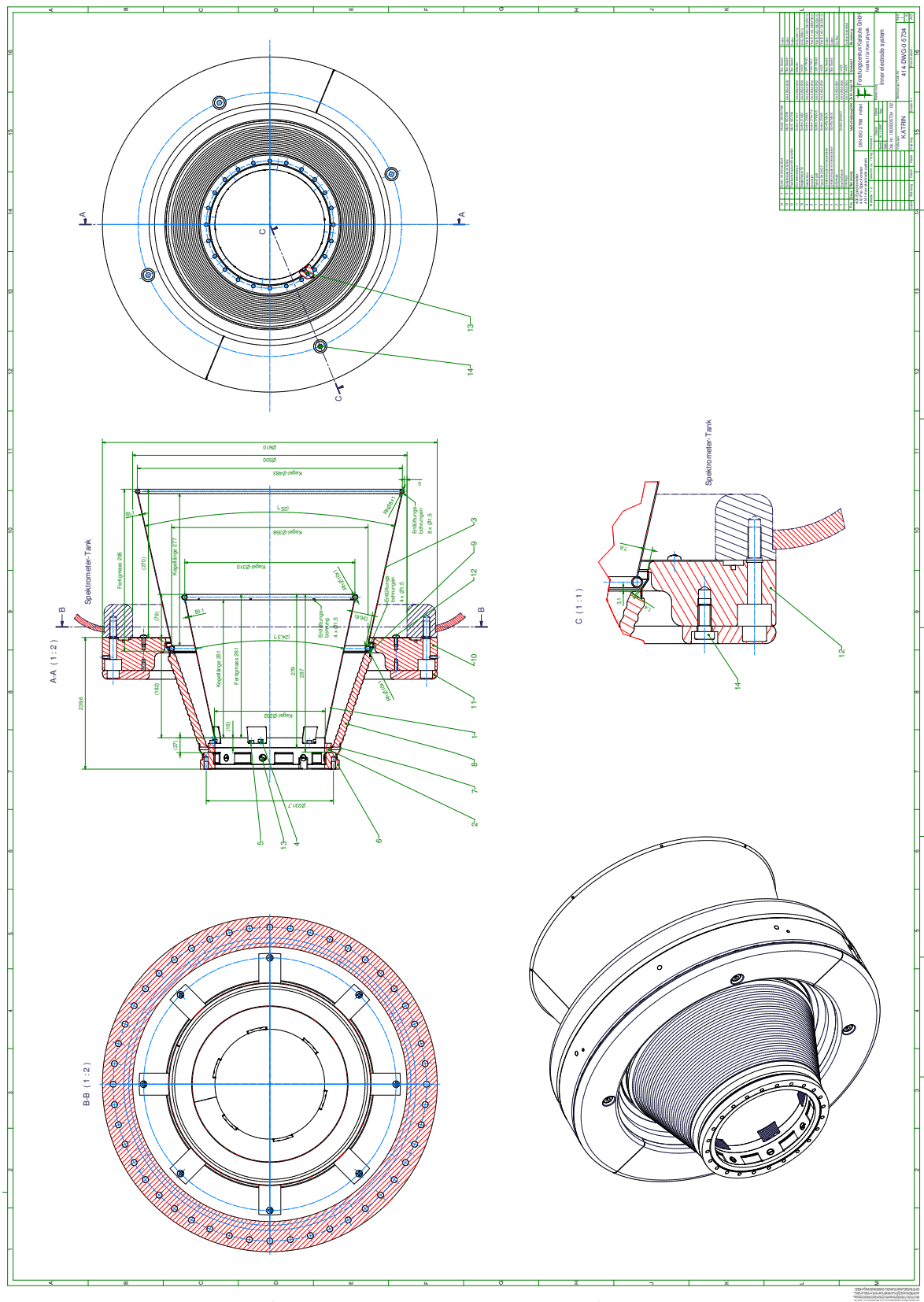


**Figure B.1:** CAD drawing of the modified ground electrode and additional shielding electrode for the pre-spectrometer (H. Hucker, FZK).

## B.2 Disc-shaped high voltage electrode for Penning trap experiments at Mainz

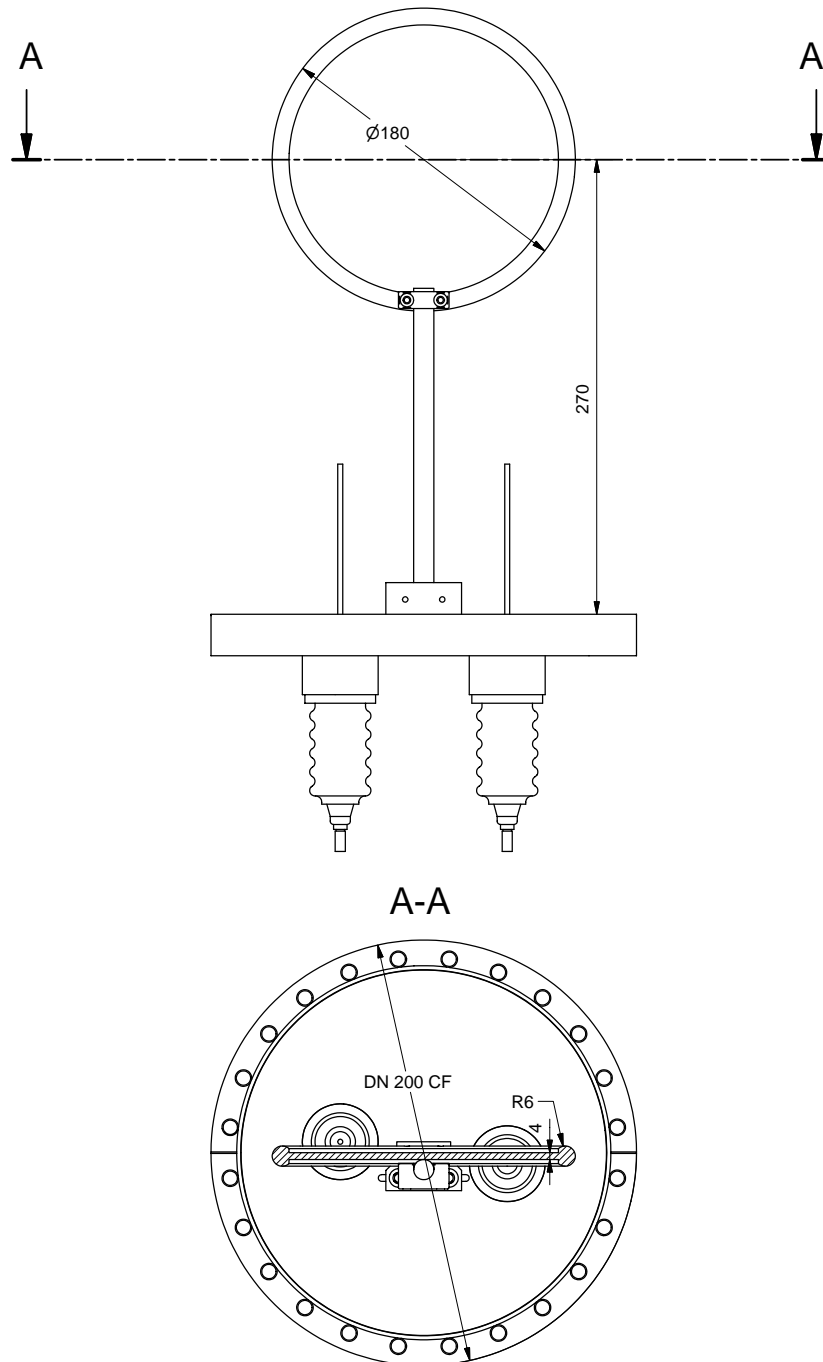


**Figure B.2:** High-voltage electrode for Penning trap experiments at Mainz (construction by H.-W. Ortjohann, U. Münster).

### B.3 Scanning wire device to disturb the trapping conditions of charged particles

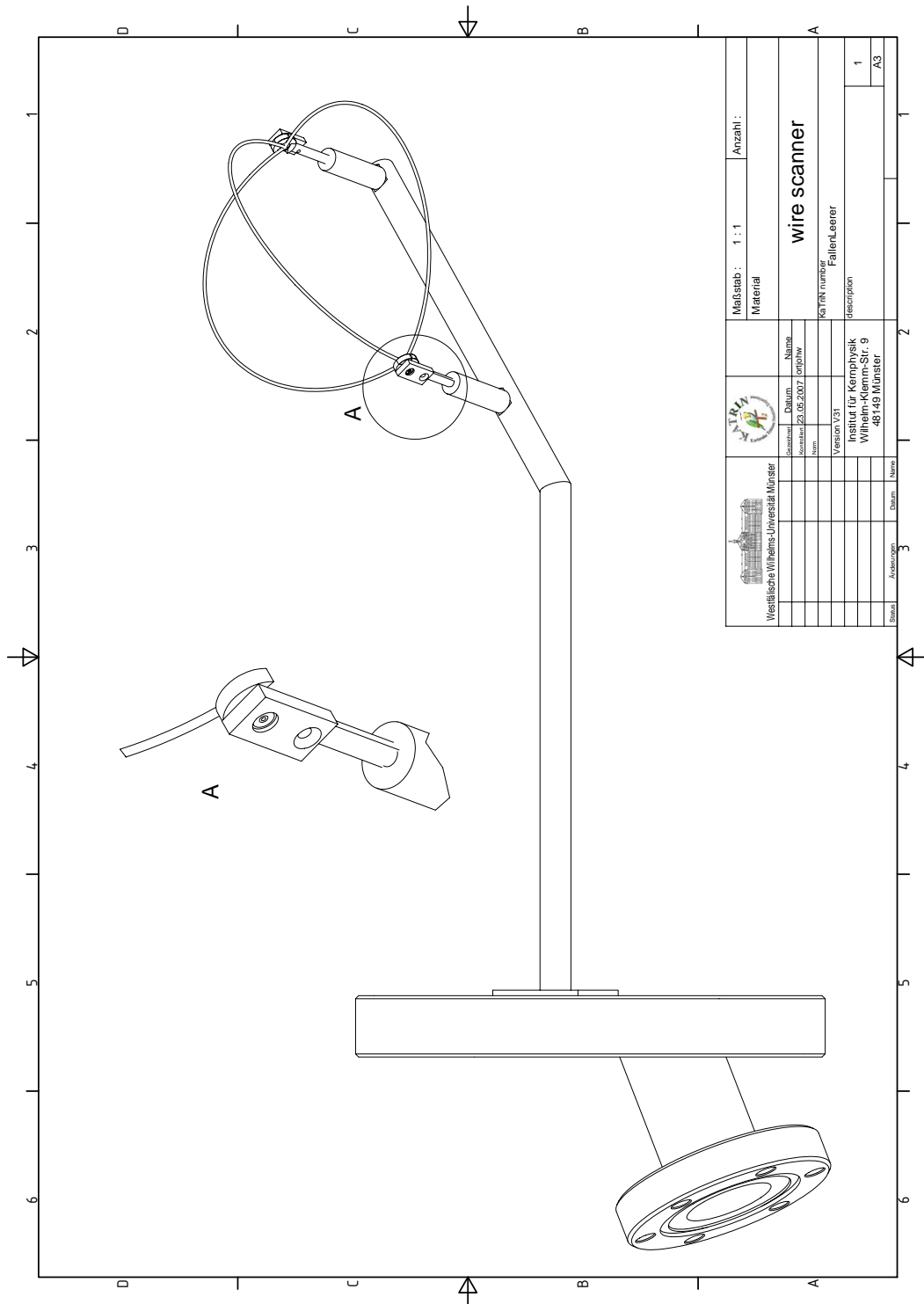


**Figure B.3:** Holding structure of “wire scanner” device for Penning trap measurements at Mainz (H.-W. Ortjohann, U. Münster). Three different positions – left outer, middle, and right outer position – of the wire are shown.

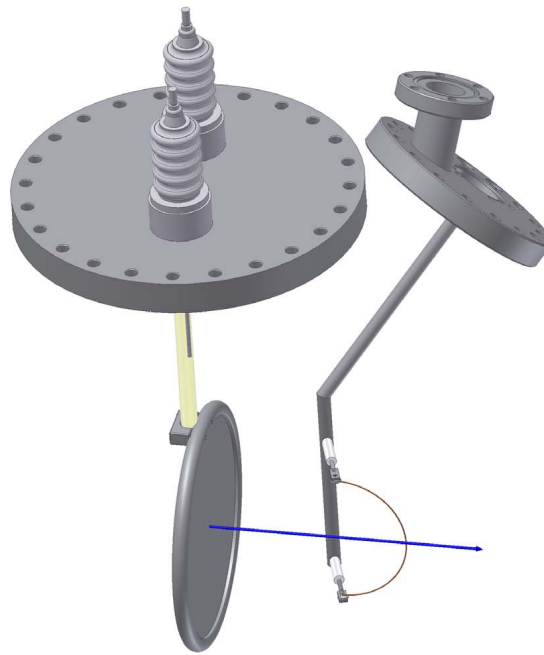


**Figure B.4:** Wire scanner (in the currentless central position) together with the disc-shaped high-voltage electrode (H.-W. Ortjohann, U. Münster). The blue arrow indicates the direction towards the Mainz spectrometer.

## B.4 Prototype of a fiber-coupled photoelectron source

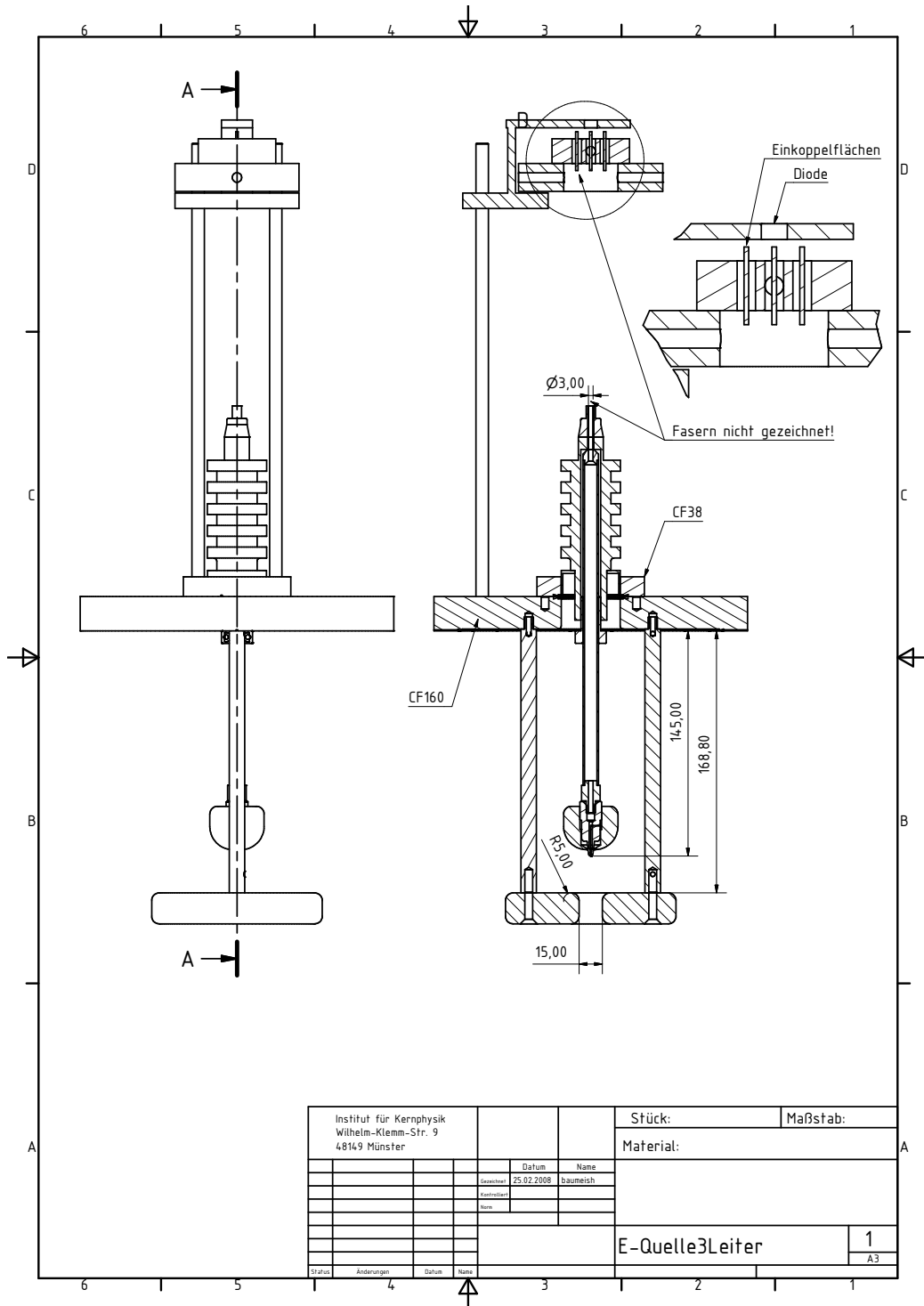


**Figure B.5:** Technical drawing of the photoelectron source with UV light guided towards the tip at the bottom by three optical fibers (H. Baumeister, U. Münster). From top to bottom: LED holder and mechanical gear allowing to couple the light into one of the three optical fibers, supporting rod, high-voltage insulator and fiber feedthrough mounted on a CF 160 flange, the tip including the hemispherical housing just above the annular focusing electrode, which is suspended by a support structure. The fibers are not shown.

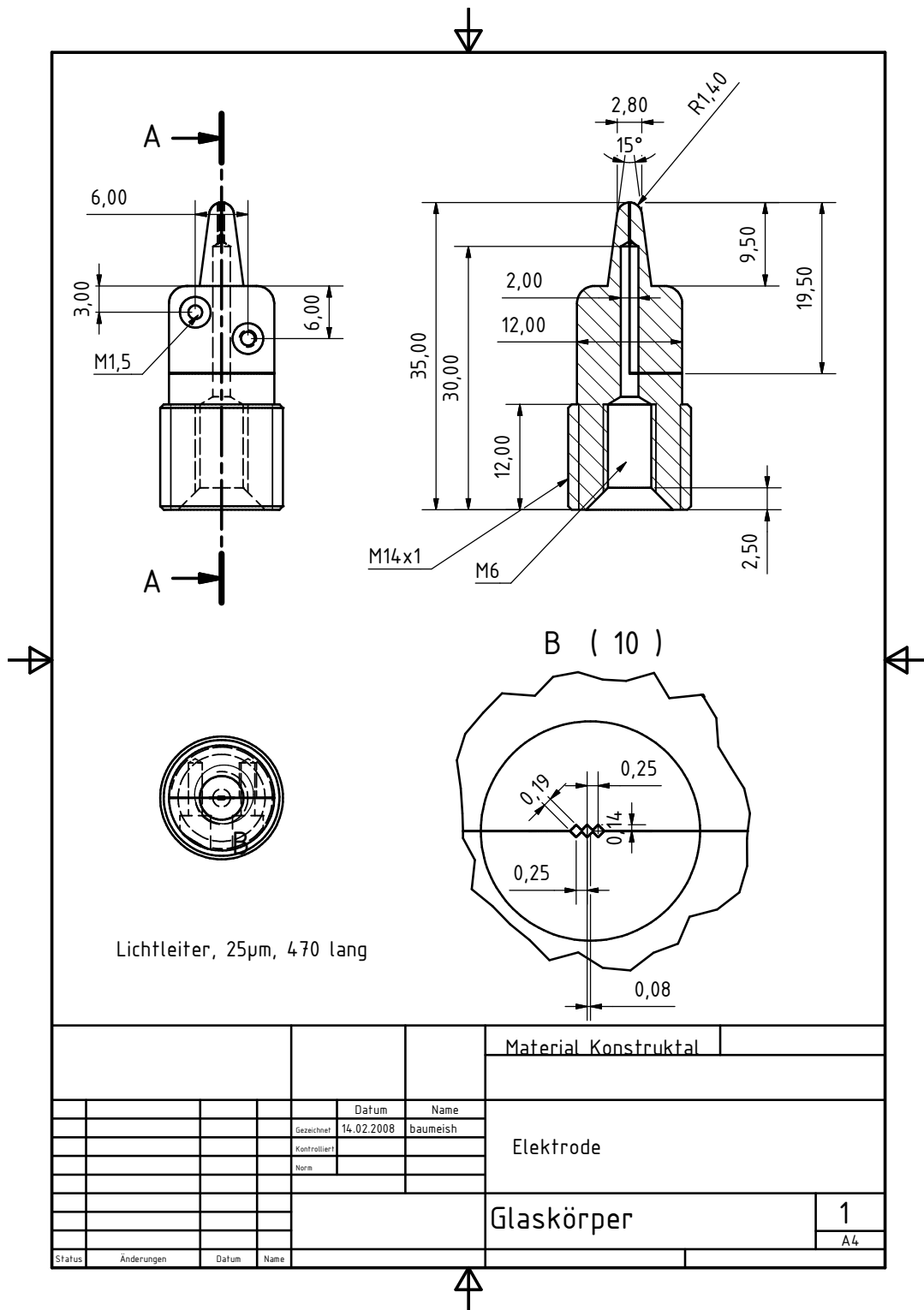


**Figure B.6:** Technical drawing of the tip of the photoelectron source with UV light guided towards the photo-emissive spots by three optical fibers (H. Baumeister, U. Münster). The drawing shows a detailed close-up on the tip with the positions of the diamond-shaped holes into which the fibers are glued.



# C Technical data of the electron detector and the UV LEDs used for measurements at the Mainz MAC-E filter

## C.1 Silicon PIN diode Hamamatsu S3590-06

Table C.1 presents characteristics of the Hamamatsu Si PIN diode (type S3590-06). Two of these diodes were employed as electron detectors in the measurements at the Mainz spectrometer which are described in chapters 6 and 7 of this work. The first diode was used during all of the 2007 measurements; it was replaced by the second one in 2008.

**Table C.1:** Technical data of Si PIN diode S3590-06. All information according to the manufacturer's data sheet [Ham06].

manufacturer	Hamamatsu Photonics, Solid State Division
type	Si PIN photodiode, windowless
active volume	9 mm × 9 mm × 0.5 mm
sensitivity to UV light	ca. 10% at $\lambda = 260$ nm
max. reverse voltage	$V_R^{\max} = 150$ V
dark current	8 nA (typ.), 30 nA (max.) at $V_R = 100$ V
recomm. operating temperature	$-20^\circ\text{C}$ to $+60^\circ\text{C}$ for better noise reduction the diode was usually operated at lower temperatures (cooled with LN <sub>2</sub> )

## C.2 UV LED 265 nm and 255 nm

Table C.2 summarizes technical data and operational parameters of deep ultraviolet light emitting diodes (UV LEDs) of the types T9B25C and T9B26C which were used to produce photoelectrons for test measurements at the Mainz MAC-E filter.

Figure C.1 presents the relative optical output power for the 265 nm LED as a function of the forward current. In order to achieve a higher optical power output in the pulsed mode, the diodes were operated with much larger forward currents (up to  $I_F \approx 100$  mA) during the measurements at Mainz.

The wavelength characteristics of both LEDs – as published by the manufacturer – are shown in figure C.2. A measurement extending to longer wavelengths, which was carried out by H. Hein in the course of his diploma thesis, reveals a second group of peaks in the range of visible light

(figure C.3). However, the emission in the visible band is strongly suppressed with respect to the ultraviolet radiation. At the same forward current of  $I_F \approx 11.7$  mA the 265 nm LED has a higher output power than the 255 nm LED.

**Table C.2:** Technical data of UV LEDs of the types T9B26C and T9B25C. All information according to the manufacturer's data sheets [Seo06a, Seo06b].

supplier	Roithner Lasertechnik, Vienna/Austria	
manufacturer	Seoul Semiconductor Co., Ltd.	
type	<b>T9B26C</b> with ball lens	<b>T9B25C</b> with ball lens
viewing angle $2\theta_{1/2}$	10°	10°
emitted wavelength $\lambda$	(265 ± 10) nm	$\lambda = (255 \pm 10)$ nm
spectrum half width $\Delta\lambda_{\text{half}}$	15 nm	15 nm
optical power output $P_{\text{opt}}$	301 – 400 $\mu$ W	101 – 150 $\mu$ W
dc forward current $I_F$	20 mA	20 mA
forward peak pulse current	100 mA	100 mA
	(duty cycle 1%, frequency 1 kHz)	
forward voltage $U_F$	6.5 V (typ.), 7.5 V (max.)	7.3 V (typ.), 7.8* V (max.)
		(*: active cooling required)
operating temperature $T$	–30°C to +50°C	–30°C to +50°C

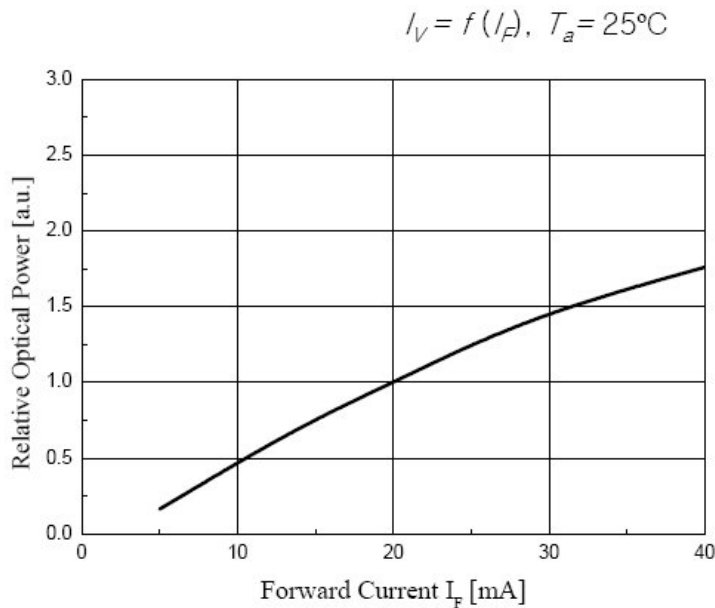


**Figure C.1:** Relative optical power output of a UV LED of type T9B26C as a function of the forward current  $I_F$  (diagram taken from [Seo06a]). For continuous operation, currents up to 20 mA are recommended. However, up to five times larger currents were used in pulsed operation for the measurements at Mainz.

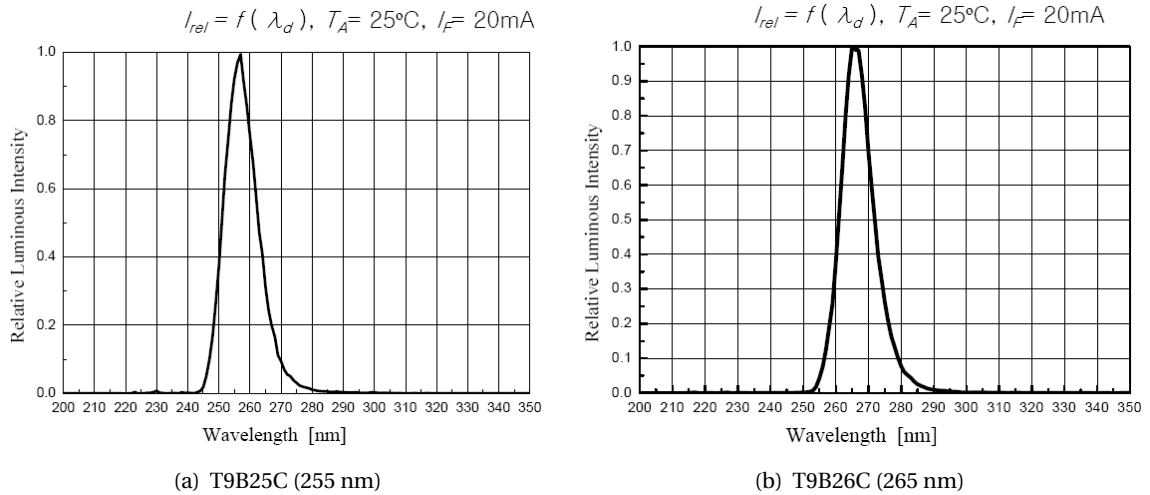


**Figure C.2:** Wavelength characteristics of the UV LEDs type T9B25C and T9B26C (taken from [Seo06b, Seo06a]). According to the manufacturer, the peak wavelengths of the diodes are  $\lambda_{\text{peak}} = (255 \pm 10) \text{ nm}$  and  $\lambda_{\text{peak}} = (265 \pm 10) \text{ nm}$ , respectively, with a spectrum half width of  $\Delta\lambda_{\text{half}} = 15 \text{ nm}$ .

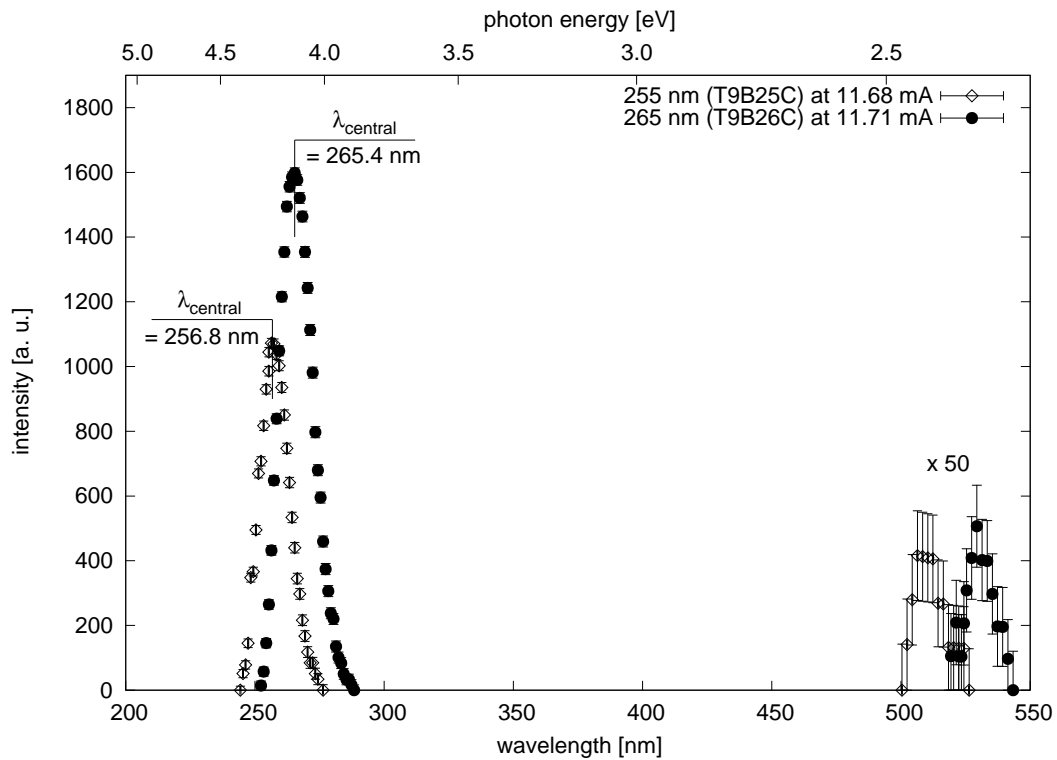


**Figure C.3:** Spectra of deep-UV LEDs of the types T9B25C ( $\diamond$ ) and T9B26C ( $\bullet$ ), recorded with a grating spectrograph and a silicon PIN diode [Hei09]. In addition to the ultraviolet peak, a less intense emission component of visible light is present in both spectra. The measured characteristics of the UV emission (central wavelengths of  $\lambda_{\text{central}} \approx 257 \text{ nm}$  and  $265 \text{ nm}$ , full width of the emission  $31 \text{ nm}$  and  $36 \text{ nm}$ , respectively) generally comply with the specifications of the manufacturer.



## D Run descriptions from the second measurement phase of testing a device to empty the Penning trap between pre- and main spectrometer

The list below contains a short summary of some of the runs conducted during the second measurement phase (2008) at the test setup at Mainz (see section 6.4.1).

- **Run bg004:** background run
  - $U_{\text{plate}} = -17.5 \text{ kV}$ ,  $U_{\text{spec}} = -18 \text{ kV}$
  - UV LED off
  - wire scanner off (*i. e.*, close to center of beam)
  - after noise cut: 1950 cts in 3416 s  $\Rightarrow \approx 0.56 \frac{1}{\text{s}}$ ,  
no significant bursts or discharges seen in close to one hour of measurement time
- **Run di018:** strong discharge (see figure 6.24)
  - $U_{\text{plate}} = -17.5 \text{ kV}$ ,  $U_{\text{spec}} = -18 \text{ kV}$
  - UV LED:  $f_{\text{LED}} = 1 \text{ kHz}$ ,  $\tau = 40 \mu\text{s}$ ,  $U_{\text{func.gen.}} = 3.9 \text{ V}$   
( $\Rightarrow$  with  $|U_{\text{spec}}| < |U_{\text{plate}}|$ : 360 counts per second at detector above noise)
  - wire scanner active in sine wave mode with  $f_{\text{func.gen.}} = 1 \text{ Hz}$ ;  
at  $t_{\text{meas}} = 530 \text{ s}$  switched to rectangular mode with one sweep every 10 seconds
  - at  $t_{\text{meas}} \approx 1420 \text{ s}$ : first notable increase in count rate observed  
wire scanner in rectangular mode causes periodic reduction of count rate (see fig. 6.24(b)), but general level increasing, up to  $\approx 2 \cdot 10^3 \frac{1}{\text{s}}$
  - at  $t_{\text{meas}} = 1525 \text{ s}$ : turn off UV LED and switch wire scanner first to slow sine wave mode ( $f_{\text{func.gen.}} \approx 0.1 \text{ Hz}$ ), then to fast sine wave mode ( $f_{\text{func.gen.}} \approx 1 \text{ Hz}$ )
  - discharge slowly subsides and count rate returns to pre-discharge value after approximately 100 s (see figure 6.25(a))
- **Run di019:** strong discharge (see figure 6.25(b))
  - high voltage and UV LED settings: same as di018
  - wire scanner active in sine wave mode with  $f_{\text{func.gen.}} = 1 \text{ Hz}$ ;  
at  $t_{\text{meas}} = 750 \text{ s}$  switched to rectangular mode with one sweep every 10 seconds
  - at  $t_{\text{meas}} \approx 1150 \text{ s}$ : first notable increase in count rate observed  
wire scanner in rectangular mode causes periodic reduction of count rate, but general level keeps increasing, up to  $\approx 1.2 \cdot 10^3 \frac{1}{\text{s}}$
  - at  $t_{\text{meas}} = 1218 \text{ s}$ : turn off UV LED and switch wire scanner first to slow sine wave mode ( $f_{\text{func.gen.}} \approx 0.1 \text{ Hz}$ ), then to fast sine wave mode ( $f_{\text{func.gen.}} \approx 1 \text{ Hz}$ )
  - discharge slowly subsides and count rate returns to pre-discharge value after approximately 90 s

## D Run descriptions (phase II of wire scanner measurements)

- **Runs di024, di026:** no discharge
  - $U_{\text{spec}} = -15 \text{ kV}$ ,  $U_{\text{plate}} = -14 \text{ kV}$
  - UV LED settings for di024:  $f_{\text{LED}} = 0.5 \text{ kHz}$ ,  $\tau = 40 \mu\text{s}$ ,  $U_{\text{func.gen.}} = 3.5 \text{ V}$
  - UV LED settings for di026:  $f_{\text{LED}} = 1 \text{ kHz}$ ,  $\tau = 40 \mu\text{s}$ ,  $U_{\text{func.gen.}} = 3.9 \text{ V}$
  - wire scanner active in fast sine wave mode ( $f_{\text{func.gen.}} \approx 1 \text{ Hz}$ ) from start of measurement on
  - in both runs no discharge observed during 1800 s of measurement
- **Run di029:** no discharge
  - $U_{\text{spec}} = -15 \text{ kV}$ ,  $U_{\text{plate}} = -14.5 \text{ kV}$
  - UV LED:  $f_{\text{LED}} = 1 \text{ kHz}$ ,  $\tau = 40 \mu\text{s}$ ,  $U_{\text{func.gen.}} = 3.9 \text{ V}$
  - wire scanner active in fast sine wave mode ( $f_{\text{func.gen.}} \approx 1 \text{ Hz}$ ) from start of measurement on
  - no discharge observed during 1800 s of measurement
- **Run di062:** strong discharge without detector shutdown
  - $U_{\text{spec}} = -18 \text{ kV}$ ,  $U_{\text{plate}} = -17.5 \text{ kV}$
  - UV LED:  $f_{\text{LED}} = 1 \text{ kHz}$ ,  $\tau = 40 \mu\text{s}$ ,  $U_{\text{func.gen.}} = 3.9 \text{ V}$
  - wire scanner active in rectangular mode, one sweep every 10 s
  - at  $t_{\text{meas}} \approx 560 \text{ s}$ : first increase in count rate
  - at  $t_{\text{meas}} \approx 570 \text{ s}$ : wire scanner switched to slow sine mode ( $f_{\text{func.gen.}} = 0.1 \text{ Hz}$ ), but UV LED not switched off
  - count rate stabilized after few seconds
  - at  $t_{\text{meas}} \approx 820 \text{ s}$ : returned wire scanner to rectangular mode, one sweep every 10 s
  - at  $t_{\text{meas}} \approx 1570 \text{ s}$ : increase in count rate
  - at  $t_{\text{meas}} \approx 1658 \text{ s}$ : wire scanner switched to fast sine mode ( $f_{\text{func.gen.}} = 1 \text{ Hz}$ )
  - slow decrease of count rate without detector shutdown
- **Run di064:** strong discharge leading to detector shutdown
  - $U_{\text{spec}} = -18 \text{ kV}$ ,  $U_{\text{plate}} = -17.5 \text{ kV}$
  - UV LED:  $f_{\text{LED}} = 1 \text{ kHz}$ ,  $\tau = 40 \mu\text{s}$ ,  $U_{\text{func.gen.}} = 3.9 \text{ V}$
  - wire scanner active in sine mode ( $f_{\text{func.gen.}} = 1 \text{ Hz}$ ); switched to rectangular mode (one sweep every 10 s) at  $t_{\text{meas}} \approx 300 \text{ s}$
  - after some smaller rises in count rate starting at about  $t_{\text{meas}} \approx 900 \text{ s}$ , count rate increases dramatically at  $t_{\text{meas}} \approx 1380 \text{ s}$
  - wire scanner not switched to sine motion and UV LED not switched off
  - pressure-induced shutdown of spectrometer and plate high voltages (interlock), detector safety shutdown at  $t_{\text{meas}} = 1465 \text{ s}$
- **Run di066:** release of trapped particles through the spectrometer (see figure 6.26)
  - at start of measurement:  $U_{\text{spec}} = -18 \text{ kV}$ ,  $U_{\text{plate}} = -17.5 \text{ kV}$
  - UV LED:  $f_{\text{LED}} = 1 \text{ kHz}$ ,  $\tau = 40 \mu\text{s}$ ,  $U_{\text{func.gen.}} = 3.9 \text{ V}$
  - wire scanner active in rectangular mode, one sweep every 5 s
  - at  $t_{\text{meas}} = 1470 \text{ s}$ : UV LED turned off
  - at  $t_{\text{meas}} = 1510 \text{ s}$ :  $U_{\text{plate}}$  ramped from  $-17.5 \text{ kV}$  to  $-18.11 \text{ kV}$ 
    - prompt increase in count rate, up to  $\gtrsim 300 \frac{1}{\text{s}}$

- wire scanner switched to slow sine mode ( $t_{\text{meas}} \approx 1540$  s) and subsequently to fast sine mode ( $t_{\text{meas}} \approx 1610$  s)
- temporary influence of the scanning motion on the count rate visible; general

*D Run descriptions (phase II of wire scanner measurements)*

# E Operation and control of UV LEDs

## E.1 First measurement phase (2007)

In the first phase of measurements to investigate the Penning trap characteristics at the Mainz spectrometer, the UV LED used for filling the trap with photoelectrons was integrated into a control box. Figure E.1 shows a photograph of the casing with opened lid. The box contains a constant current source (circuitry see figure E.2) which protects the LED by providing a constant current corresponding to the design value<sup>1</sup> of  $I_{LED} \lesssim 20\text{ mA}$  for an input voltage of 12 V. To operate the LED in pulsed mode, the box is equipped with a TTL gate input via a BNC connector (see figure E.1).

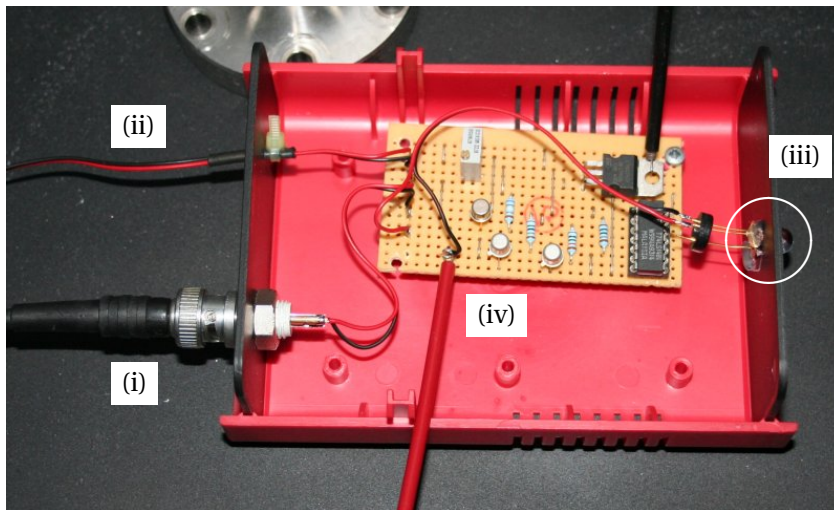


**Figure E.1:** Photograph of the control box containing the UV LED.

(i) BNC connector for TTL gate pulse, (ii) cables for 12 V supply, (iii) LED with hemispherical lens glued into casing, (iv) constant current circuitry.

## E.2 Second and third measurement phases (2008)

In later phases of the experiment, the LED was controlled in a more direct manner via a custom-made connector without any dedicated current stabilization. However, a variable series resistor was employed to protect the diode and at the same time allow a higher dynamical range of the driving current – and thus the output power – of the LED. According to the data sheet [Seo06a, Seo06b], the LEDs can be operated with higher currents in pulsed mode, for example with  $I_{LED} = 100\text{ mA}$  at a pulse width of  $10\mu\text{s}$  and a repetition rate of 1 kHz. Figure E.3 illustrates the direct powering of UV LEDs.

<sup>1</sup>taken from the product information in [Seo06a, Seo06b]

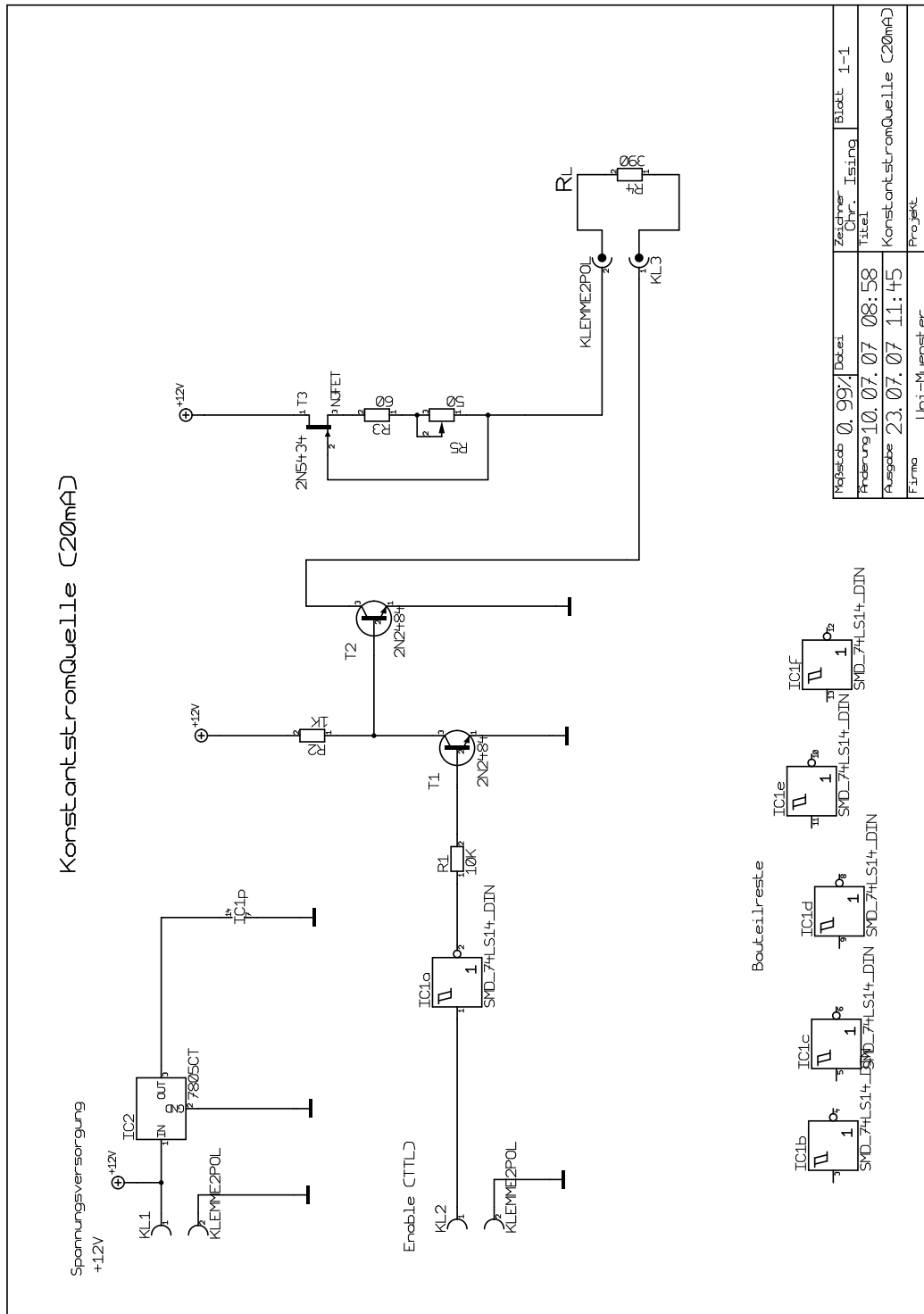
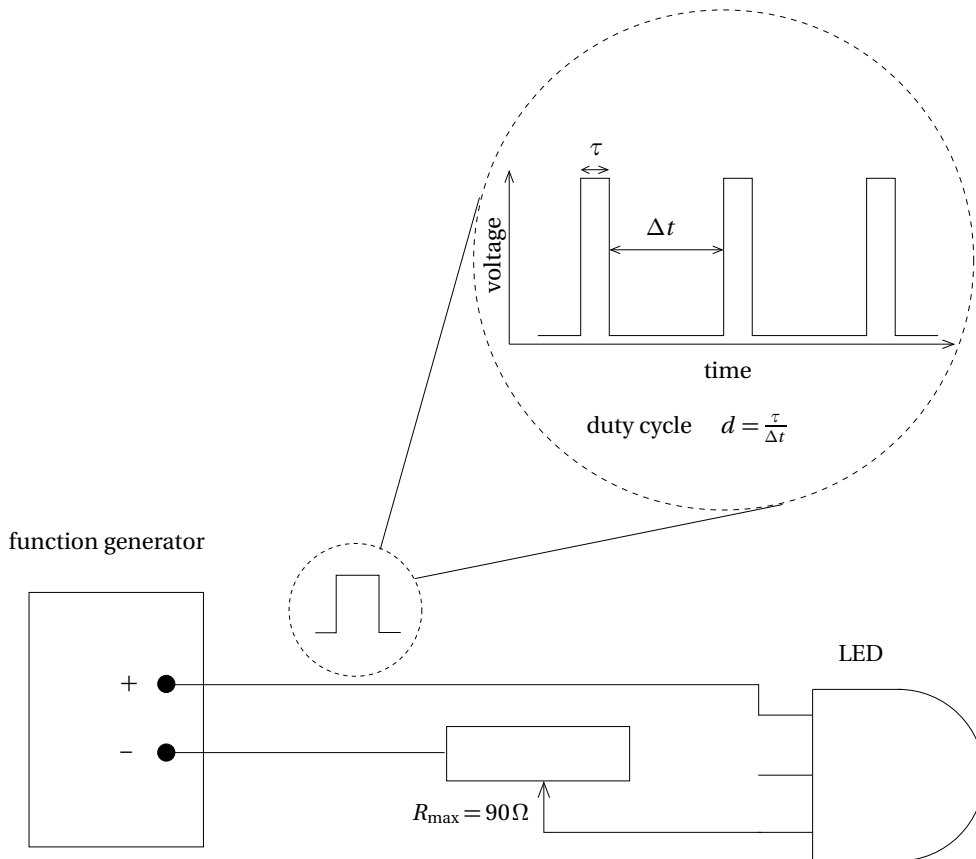


Figure E.2: Circuit diagram for control box of UV LED (Chr. Ising).



**Figure E.3:** Direct operation of UV LEDs. A pulsed positive voltage from a function generator is supplied to two of the three pins of the LED via a custom-made connector. The third pin is not used. The duty cycle  $d$  is defined as the ratio of the pulse width,  $\tau$ , and the time interval between two successive pulses,  $\Delta t$ . Typical values for the operation of UV LEDs in the measurements described in this work are  $d \approx 0.01\%$  (for large operating voltages) and  $d \approx 5\%$  (for low operating voltages).



# F Measurement of the photoelectron current and determination of the quantum efficiency

During the test experiments regarding the production of short photoelectron pulses carried out at Mainz (see chapter 7), the current of photoelectrons and the quantum efficiency of a UV LED with a peak wavelength of  $\lambda_{\text{peak}} = 265 \text{ nm}$  irradiating a stainless steel plate were measured. The results are presented in the following two sections.

## F.1 Measurement of the current of photoelectrons

Figure F.1 shows a sketch of the experimental setup used to determine the current of photoelectrons liberated from the stainless steel electrode by irradiation with UV light from the LED type T9B26C. The relative arrangement of LED and photocathode can be seen in figure 6.11. The LED was powered by periodic pulses with a frequency of 1 kHz, and a lock-in amplifier (Princeton Applied Research, Model 126) set to this frequency was employed to measure the current via the ground cable of the voltage supply to the cathode. To allow the electrons to leave the cathode and thus provide a measurable current, a small negative potential of  $U_{\text{cathode}} = -30 \text{ V}$  was applied to it.

- At first, the response of the lock-in amplifier needed to be calibrated to account for the fact that rectangular pulses rather than a sinusoidal signal were fed into it. The correction factor was determined by feeding 1 kHz pulses with an amplitude  $U_{\text{AFG, meas.}} = 3.9 \text{ V}$  and a width of  $\tau = 50 \mu\text{s}$  from the Tektronix AFG 3102 function generator into the lock-in amplifier. An attenuator (1:300) in front of the lock-in input was used:

$$U_{\text{lock-in, input}} = \frac{1}{300} \cdot U_{\text{AFG, meas.}} = 13 \text{ mV}. \quad (\text{F.1})$$

At the output of the lock-in amplifier the measured signal amplitude was  $U_{\text{lock-in, output}} = 2 \text{ mV}$ . Thus, the experimentally determined correction factor  $f_{\text{lock-in}}^{\text{rect}}$  amounts to

$$f_{\text{lock-in}}^{\text{rect}} = \frac{U_{\text{lock-in, output}}}{U_{\text{lock-in, input}}} = \frac{2 \text{ mV}}{13 \text{ mV}}. \quad (\text{F.2})$$

- In a second step, the current of photoelectrons flowing off the plate was measured. Table F.1 lists the results obtained for different voltages (*i. e.*, forward currents) driving the UV LED. Here,  $U_{90\Omega}$  denotes the voltage drop across the protective series resistor  $R_{90\Omega}$  of the LED, and  $I_{\text{LED}}$  is the forward current of the LED derived from  $I_{\text{LED}} = \frac{U_{90\Omega}}{R_{90\Omega}}$ . The photoelectron current  $I_{\text{photoel.}}$  is obtained from  $U_{\text{lock-in, output}}$  and  $f_{\text{lock-in}}^{\text{rect}}$  via the relation

$$I_{\text{photoel.}} = \frac{|U_{\text{lock-in, output}}|}{f_{\text{lock-in}}^{\text{rect}} \cdot R_{\text{lock-in}}}, \quad (\text{F.3})$$

where  $R_{\text{lock-in}} = 100 \text{ M}\Omega$  is the internal resistance of the lock-in amplifier.

**Table F.1:** Photocurrent measurement. The function generator settings are presented on the left-hand side, whereas the right-hand side contains measured values of UV LED voltage and forward current as well as the readings of the lock-in amplifier and the result of converting this reading into a photoelectron current. The fact that the ratio of currents  $I_{LED}$  for the two measurements I and II is not the same as the ratio of lock-in responses  $U_{lock-in,output}^{photoel.}$  reflects the nonlinear dependence of the optical output power of the UV LED on the forward current (see figure C.1).

no.	AFG settings			measured values			
	$U$ [V]	$f$ [kHz]	$\tau$ [ $\mu$ s]	$U_{90\Omega}$ [V]	$I_{LED}$ [mA]	$U_{lock-in,output}^{photoel.}$ [ $\mu$ V]	$I_{photoel.}$ [pA]
I	4.0	1	50	$0.59 \pm 0.01$	$6.6 \pm 0.1$	$-12 \pm 1$	$0.78 \pm 0.07$
II	10	1	50	$4.60 \pm 0.06$	$51.1 \pm 0.7$	$-60 \pm 5$	$3.9 \pm 0.3$

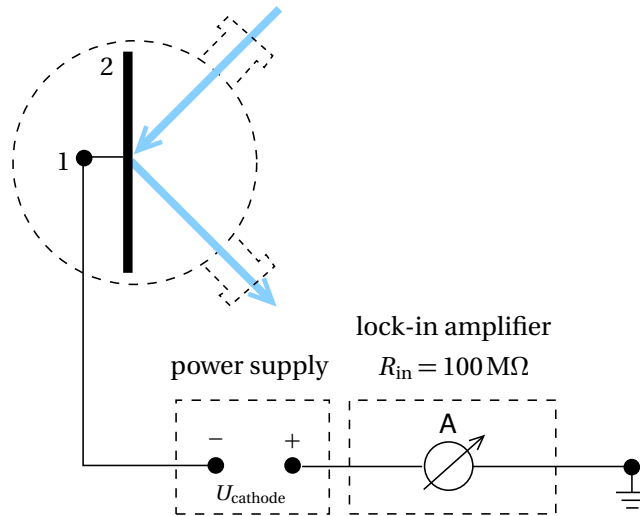


**Figure F.1:** Schematic diagram of the setup for the measurement of the current of photoelectrons. With a voltage of  $U_{cathode} = -30V$  applied to the cathode, the current was monitored via the ground cable with a lock-in amplifier. (1) marks the feedthrough port used to apply high voltage to the electrode, and (2) symbolizes the cathode plate. The bold arrows indicate the UV light irradiating the cathode through windows in the vacuum chamber.

**Remark:** Due to its load-dependence and an additional miscalibration of the actual output of the function generator voltage as compared to the displayed value, the setpoint values of  $U_{AFG}$  given in the tables are only meant to serve as a rough guidance as to what settings were used. For the interpretation of the data, the measured values of  $U_{AFG, meas.}$  and  $U_{90\Omega}$  are relevant since they provide a much better accuracy.

## F.2 Determination of the quantum efficiency

In addition to the current measurement described in the previous section, a direct measurement of the UV photon signal was carried out with a Si-PIN photodiode (Hamamatsu S3590-06). This type of diode provides a large sensitive area ( $9\text{ mm} \times 9\text{ mm}$ ) and a relative detection efficiency of about  $\epsilon_{UV-light} \approx 10\%$  for UV light in this wavelength regime [Ham06], which means that, on average, only one UV photon out of 10 is detected. For this measurement, the UV LED and the Si-PIN diode were placed face-to-face (outside of the vacuum chamber) in a very short distance

**Table E.2:** Measurement of UV light intensity. The function generator settings are presented on the left-hand side, whereas the right-hand side contains measured values of UV LED voltage and forward current as well as the readings of the lock-in amplifier and the current generated in the Si-PIN photodiode by the UV light.

AFG settings			measured values			
$U$ [V]	$f$ [kHz]	$\tau$ [ $\mu$ s]	$U_{90\Omega}$ [V]	$I_{LED}$ [mA]	$U_{lock-in,output}^{UV\ light}$ [ $\mu$ V]	$I_{Si-PIN}$ [pA]
4.0	1	50	$0.52 \pm 0.01$	$5.8 \pm 0.1$	$-600 \pm 50$	$39 \pm 3.2$

in order to make sure that the full UV photon flux hits the detector. Figure E.2 illustrates the setup. The settings for the UV light pulses are listed in table E.2. As in the measurement of the photoelectron current, the UV LED was again fed with rectangular pulses. Analogously to eq. (E.3), the current generated in the Si-PIN diode was measured with the lock-in amplifier:

$$I_{Si-PIN} = \frac{|U_{lock-in,output}|}{f_{lock-in}^{rect} \cdot R_{lock-in}}. \quad (E.4)$$

The quantum efficiency  $\eta$ , defined as the ratio of photoelectron yield and UV light input, can be determined<sup>1</sup> as follows:

$$\begin{aligned} \eta &= \frac{\# e^-}{\# \gamma_{UV}} = \frac{\# e^- / \Delta t}{\# \gamma_{UV} / \Delta t} \\ &= \frac{I_{photoel.}}{I_{Si-PIN} / \epsilon_{UV-light}} \cdot \frac{1}{T_{window}} \\ &= \frac{0.78 \text{ pA}}{39 \text{ pA} / 0.1} \cdot \underbrace{\frac{5.8 \text{ mA}}{6.6 \text{ mA}}}_{\text{LED currents}} \cdot \frac{1}{0.92} \\ &\approx 2 \cdot 10^{-3}. \end{aligned} \quad (E.5)$$

The transmission efficiency  $T_{window}$  of the 10mm Suprasil<sup>®</sup> window used in the experiment is about 92% in the corresponding wavelength range [Her06].

### Discussion of experimental uncertainties

In order to find a reliable estimate of the experimental error for the quantum efficiency value determined in eq. (E.5), a number of systematic effects need to be considered.

- Conceivably, the largest contribution stems from the uncertainty  $\delta \epsilon_{UV\ light}$  of the UV detection efficiency. The value taken from the data sheet [Ham06] represents a rather coarse estimate, since the diagram provided by the manufacturer does not include sufficient detail.
- We observed a saturation effect of the current measured with the UV-illuminated Si-PIN photodiode for large photon fluxes. Therefore, the voltage supplied to the UV LED by the function generator was limited to about  $U_{AFG} \lesssim 4.5\text{V}$ . However, it is possible that a small saturation effect occurred already at the lower voltages ( $U_{AFG} \approx 3.9\text{V}$ ) used for the actual measurements. In this case, the detected light signal would be too small and thus the effect would result in a lowering of the measured value of the quantum efficiency.

<sup>1</sup>The UV light pulses and the photoelectron current from the cathode both originate from the same (rectangular) signal shape. Therefore, the same calibration factor  $f_{lock-in}^{rect}$  applies for both quantities and thus cancels in the calculation of the quantum efficiency.

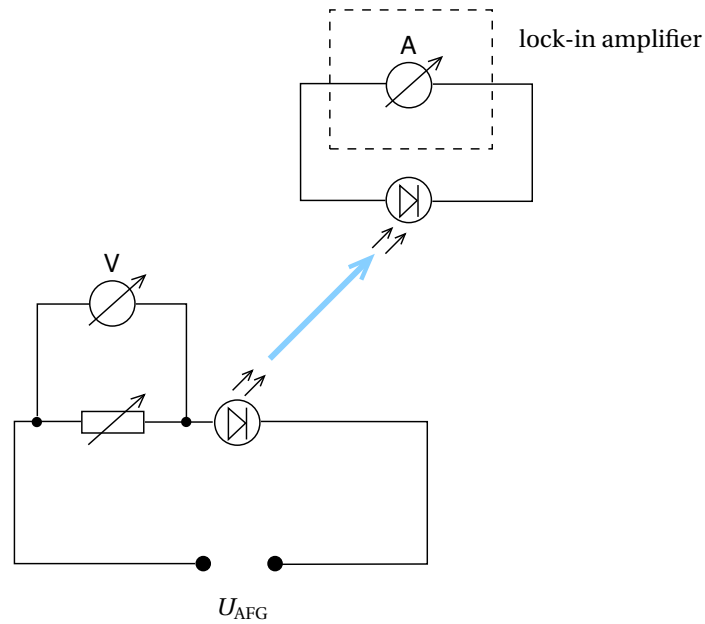


**Figure E.2:** Schematic diagram of the setup for measurement of the UV light intensity. A function generator provides the voltage supplied to the UV LED via a variable series resistor (in this case:  $R_{\text{variable}} = 90\Omega$ ). The bold arrow indicates the UV light illuminating the Si-PIN photodiode. The signal induced in the photodiode is measured with a lock-in amplifier.

- A comparison of the values listed in tables E1 and E2 reveals that the settings of the supplied voltage  $U_{90\Omega}$  – and, as a consequence, of the forward current  $I_{LED}$  – were not exactly equal for the measurement of the photon intensity and of the photoelectric current from the electrode ( $I_{LED} = 5.8\text{mA}$  and  $6.6\text{mA}$ , respectively). Due to the dependence of the LED output power on the forward current (compare figure C.1 in appendix C), a shift in the UV light intensity between the two measurements is to be expected, which favors a smaller value of the quantum efficiency. A linear approximation of the dependence was respected in the calculation in eq. (E.5).
- The reflectance of the cathode surface was not taken into account. Certainly, the number of photons absorbed by the stainless steel surface is smaller than the total number of impinging photons. The reflectance value of the stainless steel plate for UV light is not precisely known. Therefore, eq. (E.5) represents a quantum yield defined as the number of photoelectrons per *incident* photon rather than per *absorbed* photon.

In conclusion, an accuracy of the presented result for the quantum efficiency to a level of not better than about 50% seems to be a fair estimate. The result should rather be considered as an upper limit, as most of the experimental uncertainties listed above cause a reduction of the value of  $\eta$ .

# List of Figures

1.1	Beta spectrum of Radium E . . . . .	2
1.2	Current status of neutrino oscillation parameters . . . . .	7
1.3	Hierarchical neutrino mass scenarios . . . . .	8
1.4	Neutrino masses and neutrino energy density . . . . .	11
1.5	Power spectrum of matter distribution in the Universe . . . . .	13
1.6	Computer simulations: neutrino mass and structure formation . . . . .	14
1.7	Neutrino burst from the supernova SN 1987A . . . . .	16
1.8	Comparison of the neutrino mass observables $m_{ee}^{\nu}$ and $m(\nu_e)$ . . . . .	18
2.1	Tritium $\beta$ -spectrum . . . . .	23
2.2	Schematic view of an electrostatic spectrometer with magnetic adiabatic collimation (MAC-E filter) . . . . .	25
2.3	Transmission function of a MAC-E filter . . . . .	29
2.4	Characteristics of a MAC-E filter . . . . .	30
2.5	Overview of the KATRIN experiment . . . . .	31
2.6	Schematic view of the tritium-related parts of the KATRIN setup . . . . .	33
2.7	Photograph of the KATRIN main spectrometer vessel . . . . .	35
2.8	Photograph of the KATRIN pre-spectrometer . . . . .	36
2.9	Pixel layout of the KATRIN final plane detector . . . . .	37
2.10	Optimized distribution of measurement points . . . . .	41
2.11	Statistical uncertainty as a function of the measuring interval below $E_0$ . . . . .	41
2.12	KATRIN final plane detector: general layout including detector magnet, shields and post-acceleration electrode . . . . .	42
3.1	Schematic: principle of background suppression by electrostatic screening with a wire grid . . . . .	48
3.2	Photograph showing the wire electrode of the “Mainz IV” setup . . . . .	50
3.3	Background reduction by screening wire grids at the Mainz MAC-E filter: dependence on screening potential . . . . .	51
3.4	X-ray-induced background at the Mainz spectrometer . . . . .	51
3.5	Photograph showing the wire electrode system of the pre-spectrometer . . . . .	52
3.6	Two-layer wire electrode concept for the main spectrometer in an early design stage . . . . .	55
3.7	Schematic illustration: parameters of a double-layer wire electrode . . . . .	56
4.1	Influence of field inhomogeneities on the shape of the transmission function . . . . .	63
4.2	Transmission function without pixelization of the detector . . . . .	64
4.3	Definition of input parameters for e1cd3_3 . . . . .	71
4.4	Drawing of a wire electrode module from the cylindrical part of the main spectrometer . . . . .	77
4.5	Realization of a mechanism to mount the wire electrode via comb-like structures . . . . .	78
4.6	Sketch: modified geometry for tolerance calculations regarding the sag of wires . . . . .	81
4.7	Tolerance estimate regarding the self-loaded deformation (sag) of wires . . . . .	84

## List of Figures

4.8	Radial dependence of the impact of bent wires at the analyzing plane . . . . .	85
4.9	Sketch: modified geometry for tolerance calculations regarding the radial displacement of module belts . . . . .	87
4.10	Sketch: modified geometry for tolerance calculations regarding the shape of the spectrometer vessel. . . . .	87
4.11	Rail system to mount the wire electrode modules . . . . .	89
4.12	Wire electrode geometry with mounting structures using full rotational symmetry .	91
4.13	Comb structures implemented using full rotational symmetry in all parts of the spectrometer: inhomogeneity of the electric potential in the analyzing plane . . . . .	92
4.14	Sketch of compensating bridges in the fully rotational-symmetric calculation . . . . .	93
4.15	Comb structures implemented using full rotational symmetry in all parts of the spectrometer: longitudinal kinetic energy for different sizes of the compensation caps . . . . .	94
4.16	Details of the wire electrode: implementation of mounting structures with discrete rotational symmetry . . . . .	97
4.17	Compensation of electric potential inhomogeneities: different realizations . . . . .	98
4.18	Potential depression in analyzing plane for different input computer models . . . . .	99
4.19	Influence of axial module spacing and different compensation structures on potential depression in the analyzing plane . . . . .	100
4.20	Influence of axial module spacing and different compensation structures on longitudinal kinetic energy of electrons . . . . .	101
4.21	Compensation of electric potential inhomogeneities . . . . .	102
4.22	Simulation model: implementation of comb-like structures with teeth . . . . .	103
4.23	Schematic drawing: vertical mounting of combs in the conical parts of the spectrometer . . . . .	104
4.24	Inhomogeneities of electric potential and magnetic field in the analyzing plane of the main spectrometer . . . . .	106
4.25	Modular setup of the inner electrode for the main spectrometer . . . . .	106
4.26	Photographs: module assembly and quality assurance in the clean room at Münster	108
4.27	Photograph: electric connection of the wires . . . . .	109
4.28	Scaffolding inside the main spectrometer vessel . . . . .	112
5.1	Overview of high-field regions in the KATRIN spectrometer and detector section . . .	113
5.2	Cylindrical electrode setup with axial magnetic field . . . . .	117
5.3	Example of an electron trajectory in a system of coaxial cylindrical electrodes with axial magnetic field . . . . .	117
5.4	Breakdown voltage versus magnetic field . . . . .	118
5.5	Two different realizations of a Penning trap . . . . .	120
5.6	Electric potential along a magnetic field line inside a Penning trap . . . . .	120
5.7	Motion of a charge particle in a Penning trap . . . . .	121
5.8	Setup used for stand-alone operation testing of the pre-spectrometer . . . . .	123
5.9	Ignition of Penning discharges as a function of magnetic field strength and applied high voltage. . . . .	124
5.10	Pressure reading and leakage current at the pre-spectrometer as a function of applied high voltage during a discharge. . . . .	125
5.11	Trapping volume for electrons inside the pre-spectrometer . . . . .	127
5.12	Drawing of the original pre-spectrometer electrode configuration and location of the deep Penning trap. . . . .	128
5.13	Alternative draft of pre-spectrometer shielding electrode. . . . .	129

5.14	Original electrode configuration of the pre-spectrometer: longitudinal kinetic energy for electrons with maximal admitted starting angle. . . . .	131
5.15	Original electrode configuration of the pre-spectrometer: electric potential along magnetic field lines. . . . .	132
5.16	Modified pre-spectrometer electrode configuration with shortened ground electrode and additional screening electrode . . . . .	133
5.17	Close-up on the pre-spectrometer ground electrode region shown together with some electron trajectories. . . . .	134
5.18	Electric potential along magnetic field lines with additional shielding electrode. . . . .	134
5.19	Penning traps and long. kinetic energy for the neutrino mass measurement mode . . . . .	136
5.20	Penning traps and long. kinetic energy for optimized transmission conditions . . . . .	137
5.21	Pre-spectrometer electrode system optimized to prevent field emission close to the ceramics insulator at the flange. . . . .	139
5.22	Map of electric field strength and equipotential lines for the original configuration of the pre-spectrometer electrodes. . . . .	140
5.23	Map of electric field strength and equipotential lines for the modified configuration of the pre-spectrometer electrodes. . . . .	141
5.24	New parts of the modified electrode system of the pre-spectrometer . . . . .	142
5.25	“Anti Penning trap electrode” for the main spectrometer . . . . .	143
5.26	Trapping region at the junction of pre- and main spectrometer . . . . .	145
5.27	Simulated electron cooling times in the trap between pre- and main spectrometer . . . . .	147
5.28	Distribution of axial position and corresponding electric potential for ionizing collisions. . . . .	148
5.29	Close-up on the interface region between pre- and main spectrometer . . . . .	152
6.1	Setup used at the Mainz MAC-E filter for testing the trapping conditions between the KATRIN pre- and main spectrometer . . . . .	156
6.2	Photographs of the test setup at the Mainz spectrometer . . . . .	159
6.3	Photographs of two technical realizations of the scanning wire . . . . .	161
6.4	Details of the wire scanner mounting . . . . .	162
6.5	Schematic drawing: Electronics for operating the wire scanner . . . . .	163
6.6	Trigger timing for wire scanner measurements . . . . .	164
6.7	Simulated magnetic field strength on the $z$ axis of the Mainz MAC-E filter . . . . .	166
6.8	Influence of the additional water-cooled coil on the magnetic field strength . . . . .	167
6.9	Simulated electric potential depression in the analyzing plane of the Mainz spectrometer . . . . .	167
6.10	Photograph of backplate electrode: close-up on filament . . . . .	169
6.11	Sketch of the irradiation of the backplate with UV light . . . . .	170
6.12	Schematic diagram: HV supply and measurement . . . . .	174
6.13	Count rate without and with high voltage on the backplate . . . . .	176
6.14	Counts in background peak at 15keV as a function of the frequency of the wire scanner motion . . . . .	178
6.15	Count rate for varying sweeping speeds of the wire scanner (part 1) . . . . .	180
6.16	Count rate for varying sweeping speeds of the wire scanner (part 2) . . . . .	181
6.17	Count rate for varying sweeping speeds of the wire scanner (part 3) . . . . .	182
6.18	Energy distribution: comparison between burst and quiescent state . . . . .	183
6.19	Count rate for varying sweeping speeds of the wire scanner, with UV photoelectrons as filling mechanism . . . . .	187
6.20	Count rate for stopped wire scanner, with UV photoelectrons as filling mechanism . . . . .	188

## List of Figures

6.21	Spectrum of timing differences for trapping measurements with injection of photoelectrons . . . . .	189
6.22	Time difference between successive events: noise signal compared to photoelectron signal . . . . .	190
6.23	Irradiation of the backplate with pulsed UV light . . . . .	191
6.24	Run di018: discharge ignition due to the Penning effect with wire scanner in rectangular motion . . . . .	195
6.25	Runs di018 and di019: examples of evolution and specific quenching of discharges . . . . .	196
6.26	Run di066: release of trapped particles . . . . .	197
6.27	Run sc033: count rate during complete run . . . . .	199
6.28	Run sc033: energy spectrum before onset of discharge . . . . .	199
6.29	Run sc033: build-up of count rate at the start of the discharge . . . . .	200
6.30	Run sc033: influence of wire scanner motion on count rate . . . . .	201
6.31	Run sc034: build-up of discharge and detector shutdown . . . . .	201
6.32	Stationary wire . . . . .	202
7.1	Axial position vs time of flight for different starting angles . . . . .	210
7.2	Sketch of electric potential along a magnetic field line inside a MAC-E filter . . . . .	211
7.3	Schematic drawing: broadening of the transmission function due to an energy spread at the electron source . . . . .	212
7.4	Comparison between simulated transmission function and analytical shape with and without too early retardation . . . . .	213
7.5	Evolution of $E_{\parallel}$ and time of flight for simulated electron trajectories with and without too early retardation . . . . .	214
7.6	Cyclotron motion and point-to-circle mapping . . . . .	215
7.7	Influence of cyclotron motion on transmission properties of the main spectrometer . . . . .	216
7.8	Energy distribution at a fixed setting of kinetic surplus energy of the photoelectrons . . . . .	220
7.9	Dependence of photoelectron count rate on pulse width of UV light . . . . .	223
7.10	Relative fraction of single photoelectrons detected per pulse as a function of the pulse width of UV light . . . . .	224
7.11	Measured multiplicity distribution of photoelectrons per pulse and comparison with Poisson statistics . . . . .	225
7.12	Driving circuit of the UV LED . . . . .	226
7.13	Dependence of photoelectron count rate on operating voltage $U_{\text{LED}}$ . . . . .	226
7.14	Multiple peaks in energy spectrum . . . . .	229
7.15	Integrated energy spectrum of photoelectrons . . . . .	230
7.16	Arrival time distribution of photoelectrons at different surplus energies . . . . .	234
7.17	Width of arrival time distribution of photoelectrons at different surplus energies . . . . .	235
7.18	Time-of-flight spectrum of photoelectrons measured with the Mainz MAC-E filter . . . . .	236
7.19	Comparison of integrated energy spectrum and time-of-flight spectrum of photoelectrons . . . . .	237
7.20	Electron gun for tests of the KATRIN pre-spectrometer . . . . .	238
7.21	Sketch illustrating the relation between starting angle and radial position on the tip of the electron gun . . . . .	239
7.22	Radial dependence of the angular emission characteristics of the pre-spectrometer electron gun . . . . .	241
7.23	Two options of illuminating the photocathode in an angular-selective electron gun . . . . .	243
7.24	Prototype of a fiber-coupled photoelectron gun . . . . .	244
7.25	Photographs of fiber feedthroughs in the tip of the photoelectron gun prototype . . . . .	246

7.26	Sketch: tip of the fiber-coupled electron gun . . . . .	246
7.27	Measurement of integrated electron energy spectra with the prototype of an angular-selective photoelectron gun . . . . .	248
7.28	Comparison of integrated electron energy spectra for chromium (shaft of the tip, 255 nm LED) and copper (two fibers, 265 nm LED) . . . . .	249
7.29	Alternative concept of an angular-selective electron gun using a planar capacitor . .	256
A.1	Electric potential for a planar electrode system . . . . .	265
A.2	Radial dependence of the electr. potential for a long cyl. screening electrode . . . . .	268
B.1	Technical drawing: modified ground electrode and additional shielding electrode for the pre-spectrometer. . . . .	270
B.2	High-voltage electrode for Penning trap experiments at Mainz . . . . .	271
B.3	Holding structure of “wire scanner” device for measurements at Mainz . . . . .	272
B.4	Wire scanner and disc-shaped high-voltage electrode . . . . .	273
B.5	Technical drawing: photoelectron source with fiber coupling to UV LED . . . . .	274
B.6	Technical drawing: photoelectron source with fiber coupling to UV LED . . . . .	275
C.1	Output power of UV LED type T9B26C as a function of forward current . . . . .	278
C.2	Wavelength characteristics of the UV LEDs type T9B25C and T9B26C . . . . .	279
C.3	Measured spectra of the UV LEDs T9B25C and T9B26C. . . . .	279
E.1	Photograph of the control box containing the UV LED. . . . .	285
E.2	Circuit diagram for control box of UV LED . . . . .	286
E.3	Operation of UV LEDs . . . . .	287
F.1	Schematic diagram: measurement of the current of photoelectrons . . . . .	290
F.2	Schematic diagram: measurement of the UV light intensity . . . . .	292

*List of Figures*

# List of Tables

1.1	The 12 fundamental fermions of the Standard Model . . . . .	4
1.2	Key parameters of the Concordance Model of cosmology . . . . .	10
2.1	Characteristics of the main spectrometer vessel . . . . .	34
3.1	Parameters of the wire electrode for the KATRIN main spectrometer in an early design stage . . . . .	54
3.2	Electric potentials assigned to different parts of the electrode system in an early design stage . . . . .	54
3.3	Comparison of geometrical coverage $f_{gc}$ and electrostatic screening factor $S$ for the wire electrodes of the Mainz MAC-E filter, the KATRIN pre-spectrometer and the KATRIN main spectrometer . . . . .	59
4.1	Progressive stages of the computer model of the wire electrode for the main spectrometer . . . . .	79
4.2	Modified parameters of the wire electrode . . . . .	80
4.3	Results of first tolerance simulations for the sag of wires . . . . .	82
4.4	Updated results of tolerance simulations for the sag of wires . . . . .	86
4.5	Measured length of the main spectrometer vessel . . . . .	88
4.6	Summary of parameters of the inner electrode system for the main spectrometer . . . . .	105
5.1	Spacing between ground electrode and border of magnetic flux tube inside the pre-spectrometer for various magnetic field configurations. . . . .	133
5.2	Effectiveness of Penning trap removal for the modified electrode configuration of the pre-spectrometer. . . . .	135
5.3	Electric field strength values in the original and in the modified setup of the pre-spectrometer. . . . .	138
6.1	Magnetic field configuration of the Mainz spectrometer . . . . .	165
6.2	Diameter of detectable magnetic flux tube at the position of the backplate . . . . .	172
6.3	Divider ratio of the JRL KV-50 high-voltage divider and the KATRIN high-voltage divider . . . . .	172
6.4	Magnetic field configuration for the measurement of the influence of the scanner frequency on the count rate . . . . .	177
6.5	Counts (no extra filling) as a function of wire scanner frequency . . . . .	178
6.6	Counts as a function of wire scanner frequency, with artificial filling of the trap with photoelectrons . . . . .	185
6.7	Overview of different measurement intervals in run sc033 . . . . .	200
7.1	Work function values for selected metals . . . . .	218
7.2	Photon energies covered by UV LED types T9B25C and T9B26C . . . . .	219
7.3	Ratio $\epsilon_{\text{single}}$ achievable for various settings of the UV LED . . . . .	222
7.4	Materials used for vapor-metalization of the tip of the photoelectron gun . . . . .	245

*List of Tables*

7.5	Fiber-coupled photoelectron gun: parameters of fiber positions . . . . .	245
7.6	Settings and parameters for the energy scans with the fiber-coupled photoelectron gun . . . . .	247
7.7	Comparison of properties of the condensed krypton calibration source (CKrS) and the UV LED-based photoelectron source . . . . .	254
A.1	Electric screening factor for a long cylindrical electrode . . . . .	267
C.1	Technical data of Si PIN diode S3590-06 . . . . .	277
C.2	Technical data of UV LEDs of the types T9B26C and T9B25C . . . . .	278
E1	Photocurrent measurement. . . . .	290
E2	Measurement of UV light intensity. . . . .	291

# Bibliography

- [Aba95] S. Abachi *et al.* (D0 collaboration), *Search for High Mass Top Quark Production in  $p\bar{p}$  Collisions at  $\sqrt{s} = 1.8$  TeV*, Phys. Rev. Lett. **74** (1995) 2422
- [Abe95] F. Abe *et al.* (CDF collaboration), *Observation of Top Quark Production in  $p\bar{p}$  Collisions with the Collider Detector at Fermilab*, Phys. Rev. Lett. **74** (1995) 2626
- [Abe03] H. Abele and D. Mund (eds.), proceedings of the workshop *Quark-Mixing, CKM-Unitarity*, Mattes Verlag, Heidelberg, 2003, and available online at [arXiv:hep-ph/0312124v1](http://arxiv.org/abs/hep-ph/0312124v1)
- [Aha07] B. Aharmim *et al.* (SNO collaboration), *Determination of the  $\nu_e$  and total  $^8\text{B}$  solar neutrino fluxes with the Sudbury Neutrino Observatory Phase I Data Set*, Phys. Rev. **C 75** (2007) 045502
- [Ahm02] Q. R. Ahmad *et al.* (SNO collaboration), *Direct Evidence for Neutrino Flavor Transformation from Neutral-Current Interactions in the Sudbury Neutrino Observatory*, Phys. Rev. Lett. **89** (2002) 011301
- [Ahm04] S. N. Ahmed *et al.* (SNO collaboration), *Measurement of the Total Active  $^8\text{B}$  Solar Neutrino Flux at the Sudbury Neutrino Observatory with Enhanced Neutral Current Sensitivity*, Phys. Rev. Lett. **92** (2004) 181301
- [Ahn06] M. H. Ahn *et al.* (K2K collaboration), *Measurement of Neutrino Oscillation by the K2K Experiment*, Phys. Rev. **D 74** (2006) 072003
- [Ala07] R. Alarcon *et al.*, *Precise Measurement of the Neutron Beta Decay Parameters “a” and “b”* (proposal for the Nab experiment), 2007, available online at [http://nab.phys.virginia.edu/nab\\_proposal.pdf](http://nab.phys.virginia.edu/nab_proposal.pdf)
- [Alc03] J. L. Alcaraz Auni3n and E. Torro3 Pastor, *Background study: Radial motion of electrons in a spectrometer*, student research project, Johannes Gutenberg-Universit3t Mainz, 2003
- [Ale88] E. N. Alexeyev, L. N. Alexeyeva, I. V. Krivosheina and V. I. Volchenko, *Detection of the neutrino signal from SN 1987A in the LMC using the INR Baksan underground scintillation telescope*, Phys. Lett. **B 205** (1988) 209
- [All42] J. S. Allen, *Experimental Evidence for the Existence of a Neutrino*, Phys. Rev. **61** (1942) 692
- [And59] P. A. Anderson, *Work Function of Gold*, Phys. Rev. **115** (1959) 553
- [Ara05] T. Araki *et al.* (KamLAND collaboration), *Measurement of Neutrino Oscillation with KamLAND: Evidence of Spectral Distortion*, Phys. Rev. Lett. **94** (2005) 081801
- [Ard56] M. von Ardenne, *Tabellen der Elektronenphysik, Ionenphysik und 3bermikroskopie, II. Band · Randgebiete und Hilfsgebiete*, VEB Deutscher Verlag der Wissenschaften, Berlin, 1956
- [Arl09] H. Arlinghaus, *Investigation of the muon-induced secondary electron background in the KATRIN experiment*, diploma thesis in preparation, Westf3lische Wilhelms-Universit3t M3nster

## Bibliography

- [Ash04] Y. Ashie *et al.* (Super-Kamiokande collaboration), *Evidence for an Oscillatory Signature in Atmospheric Neutrino Oscillations*, Phys. Rev. Lett. **93** (2004) 101801
- [Ash05] Y. Ashie *et al.* (Super-Kamiokande collaboration), *Measurement of atmospheric neutrino oscillation parameters by Super-Kamiokande I*, Phys. Rev. **D 71** (2005) 112005
- [Ass96] K. Assamagan *et al.*, *Upper limit of the muon-neutrino mass and charged-pion mass from momentum analysis of a surface muon beam*, Phys. Rev. **D 53** (1996) 6065
- [Bae10] O. von Baeyer und O. Hahn, Phys. Z. **11** (1910) 488
- [Bae11] O. von Baeyer, O. Hahn und L. Meitner, Phys. Z. **12** (1911) 273
- [Bae08] S. Baeßler *et al.*, *First measurements with the neutron decay spectrometer aSPECT*, Eur. Phys. J. **A 38** (2008) 17
- [Bah68] J. N. Bahcall, N. A. Bahcall, G. Shaviv, *Present Status of the Theoretical Predictions for the  $^{37}\text{Cl}$  Solar-Neutrino Experiment*, Phys. Rev. Lett. **20** (1968) 1209
- [Bah01] J. N. Bahcall, M. H. Pinsonneault, and S. Basu, *Solar Models: Current Epoch and Time Dependences, Neutrinos, and Helioseismological Properties*, Astrophys. J. **555** (2001) 990
- [Bah05] J. N. Bahcall, homepage, <http://www.sns.ias.edu/~jnb/> (last updated 2005)
- [Bar98] R. Barate *et al.* (ALEPH collaboration), *An upper limit on the tau neutrino mass from three- and five-prong tau decays*, Eur. Phys. J. **C 2** (1998) 395
- [Bas07] M. Bastani Nejad *et al.*, *Evidence for Fowler-Nordheim behaviour in RF breakdown*, proceedings of the 2007 Particle Accelerator Conference (PAC07) 2499, available online at <http://epaper.kek.jp/p07>
- [Bea80] G. Beamson, H. Q. Porter and D. W. Turner, *The collimating and magnifying properties of a superconducting field photoelectron spectrometer*, J. Phys. **E 13** (1980) 64; corrigendum: G. Beamson, H. Q. Porter and D. W. Turner, J. Phys. **E 14** (1981) 256
- [Bea81] G. Beamson, H. Q. Porter and D. W. Turner, *Photoelectron spectromicroscopy*, Nature **290** (1981) 556
- [Ben09] S. Benning, diploma thesis in preparation, Westfälische Wilhelms-Universität Münster
- [Ber64a] C. N. Berglund and W. E. Spicer, *Photoemission Studies of Copper and Silver: Theory*, Phys. Rev. **136** (1964) A1030
- [Ber64b] C. N. Berglund and W. E. Spicer, *Photoemission Studies of Copper and Silver: Experiment*, Phys. Rev. **136** (1964) A1044
- [Bil05] Y. Bilenko *et al.*, *10 Milliwatt Pulse Operation of 265 nm AlGaIn Light Emitting Diodes*, Jpn. J. Appl. Phys. **44** (2005) L98
- [Ble58] H. A. Blevin and S. C. Haydon, *The Townsend ionization coefficients in crossed electric and magnetic fields*, Aust. J. Phys. **11** (1958) 18; *The electrical breakdown of gases in the presence of crossed electric and magnetic fields*, Z. Phys. **151** (1958) 340
- [Blu94] W. Blum and L. Rolandi, *Particle Detection with Drift Chambers*, Springer-Verlag, Berlin, 1994
- [Bog06] L. N. Bogdanova, M. G. Gavrillov, V. N. Kornoukhov and A. S. Starostin, *Cosmic muon flux at shallow depths underground*, arXiv:nucl-ex/0601019v1
- [Bon99] J. Bonn, L. Bornschein, B. Degen, E. W. Otten, Ch. Weinheimer, *A high resolution electrostatic time-of-flight spectrometer with adiabatic magnetic collimation*, Nucl. Instr. Meth. **A 421** (1999) 256

- [Bon08] J. Bonn, private communication, 2008
- [Bor00] B. Bornschein, *Untersuchung systematischer Effekte und erste Tritiummessungen mit dem verbesserten Mainzer Neutrinomassenexperiment*, dissertation, Johannes Gutenberg-Universität Mainz, 2000
- [Cha14] J. Chadwick, *Distribution in intensity in the magnetic spectrum of the  $\beta$ -rays of radium*, Verh. Dtsch. Phys. Ges. (Germany) **16** (1914) 383
- [Cha32] J. Chadwick, *Possible Existence of a Neutron*, Nature **129** (1932) 312
- [Che82] M. Chelvayohan and C. H. B. Mee, *Work function measurements on (110), (100) and (111) surfaces of silver*, J. Phys. C **15** (1982) 2305
- [Coe07] S. Coeck, *Search for non Standard Model physics in nuclear  $\beta$ -decay with the WITCH experiment*, dissertation, Katholieke Universiteit Leuven, 2007
- [Coh07] Coherent, Inc., *Matrix 355 solid state Q-switched laser* (data sheet), 2007, <http://www.coherent.com/Lasers/>
- [Cra38] H. R. Crane and J. Halpern, *New Experimental Evidence for the Existence of a Neutrino*, Phys. Rev. **53** (1938) 789
- [CPO08] CPO Ltd., Charged Particle Optics programs website, <http://www.electronoptics.com>
- [Cra39] H. R. Crane and J. Halpern, *Further Experiments on the Recoil of the Nucleus in Beta-Decay*, Phys. Rev. **56** (1939) 232
- [Cra48] H. R. Crane, *The Energy and Momentum Relations in the Beta-Decay, and the Search for the Neutrino*, Rev. Mod. Phys. **20** (1948) 278
- [Cru63] D. R. Cruise, *A numerical method for the determination of an electric field about a complicated boundary*, J. Appl. Phys. **34** (1963) 3477
- [Cub99] D. Cubric, B. Lencova, F. H. Read, and J. Zlamal, *Comparison of FDM, FEM and BEM for electrostatic charged particle optics*, Nucl. Instr. Meth. **A 427** (1999) 357
- [Dan62] G. Danby *et al.*, *Observation of High-Energy Neutrino Reactions and the Existence of Two Kinds of Neutrinos*, Phys. Rev. Lett. **9** (1962) 36
- [Dav68] R. Davis, Jr., D. S. Harmer and K. C. Hoffman, *Search for Neutrinos from the Sun*, Phys. Rev. Lett. **20** (1968) 1205
- [Den07] J. Deng *et al.*, *247 nm Ultra-Violet Light Emitting Diodes*, Jpn. J. Appl. Phys. **46** (2007) L263
- [Dos06] N. Doss *et al.*, *Molecular effects in investigations of tritium molecule beta decay endpoint experiments*, Phys. Rev. C **73** (2006) 025502
- [Dun07] J. A. Dunmore, *Pixelation-Dependence of Transmission Function*, KATRIN internal document, 2007  
KATRIN BSCW, 40 Detector, 2 Design, Documents describing setup and subsystems, Review of Detector Design Summer 07, Design documents
- [Dun09] J. Dunkley *et al.*, *Five-Year Wilkinson Microwave Anisotropy Probe Observations: Likelihoods and Parameters from the WMAP Data*, Astrophys. J. Supplement Series **180** (2009) 306
- [Dyk53] W. P. Dyke and J. K. Trolan, *Field Emission: Large Current Densities, Space Charge, and the Vacuum Arc*, Phys. Rev. **89** (1953) 799

## Bibliography

- [Eas70] D. E. Eastman, *Photoelectric Work Functions of Transition, Rare-Earth, and Noble Metals*, Phys. Rev. **B 2** (1970) 1, and further references cited therein
- [Eic09] F. Eichelhardt, *Measurement of the Tritium Pumping Properties of a 4.2 K Argon Condensate for the Cryogenic Pumping Section of KATRIN*, dissertation, Universität Karlsruhe (TH), 2009;  
F. Eichelhardt, B. Bornschein, L. Bornschein, O. Kazachenko N. Kernert and M. Sturm, *First tritium results of the KATRIN test experiment TRAP*, Fusion Sci. Technol. **54** (2008) 615
- [Ell27] C. D. Ellis and W. A. Wooster, *The Average Energy of Disintegration of Radium E*, Proc. R. Soc. **A 117** (1927) 109
- [Ell87] S. R. Elliott, A. A. Hahn, and M. K. Moe, *Direct evidence for two-neutrino double-beta decay in  $^{82}\text{Se}$* , Phys. Rev. Lett. **59** (1987) 2020
- [Ess04] K. Essig, *Untersuchungen zur Penningfalle zwischen den Spektrometern des KATRIN-Experiments*, diploma thesis, Rheinische Friedrich-Wilhelms-Universität Bonn, 2004
- [Fer34] E. Fermi, *Versuch einer Theorie der  $\beta$ -Strahlen*, Z. Phys. **88** (1934) 161
- [Fey58] R. P. Feynman and M. Gell-Mann, *Theory of the Fermi Interaction*, Phys. Rev. **109** (1958) 193
- [Fix02] D. J. Fixsen and J. C. Mather, *The Spectral Results of the Far-Infrared Absolute Spectrophotometer Instrument on COBE*, Astrophys. J. **581** (2002) 817
- [Fla04] B. Flatt, *Voruntersuchungen zu den Spektrometern des KATRIN Experiments*, dissertation, Johannes Gutenberg-Universität Mainz, 2004
- [Fow28] R. H. Fowler and L. Nordheim, *Electron emission in intense electric fields*, Proc. Royal Soc. London **A 119** (1928) 173
- [Fra09] F. Fränkle and F. Glück, private communication, 2009
- [Fri08] P. Friedag, *Bahnverfolgungssimulationen für das WITCH-Experiment*, diploma thesis, Westfälische Wilhelms-Universität Münster, 2008
- [FuG08] M. Prall and Th. Thümmeler, communication with companies Fu.G. Elektronik GmbH and Iseg Spezialelektronik GmbH, 2008
- [Fuk98a] Y. Fukuda *et al.* (Super-Kamiokande Collaboration), *Measurement of a small atmospheric  $\nu_\mu/\nu_e$  ratio*, Phys. Lett **B 433** (1998) 9
- [Fuk98b] Y. Fukuda *et al.* (Super-Kamiokande Collaboration), *Study of the atmospheric neutrino flux in the multi-GeV energy range*, Phys. Lett **B 436** (1998) 33
- [Fur39] W. H. Furry, *On Transition Probabilities in Double Beta-Disintegration*, Phys. Rev. **56** (1939) 1184
- [Gar51] M. W. Garrett, *Axially Symmetric Systems for Generating and Measuring Magnetic Fields. Part I*, J. Appl. Phys. **22** (1951) 1091
- [Gas05] R. Gaska and J. Zhang, *Deep-UV LEDs: Physics, Performance and Applications*, Device and Process Technologies for Microelectronics, MEMS, and Photonics IV, Proceedings of SPIE Vol. **6037** (2005) 603706
- [Geb07] A. Gebel, *Entwicklung und Aufbau eines Prototypmoduls für die Drahtelektrode des KATRIN Hauptspektrometers*, diploma thesis, Westfälische Wilhelms-Universität Münster, 2007
- [Ger93] Ch. Gerthsen and H. Vogel, *Physik*, 17<sup>th</sup> revised ed., Springer-Verlag, Berlin, 1993

- [Glü05a] F. Glück *et al.*, *The neutron decay retardation spectrometer aSPECT: Electromagnetic design and systematic effects*, Eur. Phys. J. **A 23** (2005) 135
- [Glü05b] F. Glück, *Electrical breakdown in high vacuum and magnetic field*, presentation at the 8<sup>th</sup> KATRIN collaboration meeting, Münster, March 2005  
KATRIN BSCW, 95 General Meetings and Review Panels, 1 Collaboration Meetings, 8. Collaboration Meeting, Mon\_21Mar05, C1, FGlueck\_C1\_1.ppt
- [Glü05c] F. Glück, *Background theory: radial motion of electrons from spectrometer electrodes into the fluxtube*, KATRIN internal note, 2005  
KATRIN BSCW, 25 EMD, 51 Background, background\_theory\_Glueck.pdf;  
F. Glück, to be published
- [Glü05d] F. Glück, *The electric shielding factor of the wire electrode*, KATRIN internal note, 2005  
KATRIN BSCW, 25 EMD, 8 Programs, electric fields, electric\_shielding\_factor.pdf;  
F. Glück, to be published
- [Glü06a] F. Glück, *New electric field calculation program for wire electrodes with support structure*, presentation at the 10<sup>th</sup> KATRIN collaboration meeting, Bad Liebenzell, March 2006  
KATRIN BSCW, 95 General Meetings and Review Panels, 1 Collaboration Meetings, 10. Collaboration Meeting, Parallel Session - A2, 95-TRP-4031-A2-FGlueck.ppt;  
F. Glück, private communication, March 2006
- [Glü06b] F. Glück, *Penning traps in the pre-spectrometer*, presentation at a meeting of the KATRIN Electromagnetic Design (EMD) group, Fulda, December 2006  
KATRIN BSCW, 25 EMD, 9 Task meetings, 11-12-06 Fulda, FGlueck\_Penningtraps.ppt
- [Glü07a] F. Glück, L. Bornschein, F. Fränkle, F. Habermehl, K. Hugenberg, M. Leber and K. Valerius, *Penning discharge experiments with the KATRIN pre-spectrometer*, KATRIN internal report, 2007  
KATRIN BSCW, 25 EMD, 3 Pre-spectrometer, Penning Trap Investigations, Penning\_experiments\_with\_pre-spectrometer.pdf;  
F. Glück, *Penning discharge in the KATRIN pre-spectrometer*, presentation at the particle physics spring meeting of the German Physical Society (Deutsche Physikalische Gesellschaft, DPG), Freiburg, 2008
- [Glü07b] F. Glück, K. Hugenberg, K. Valerius and Ch. Weinheimer, *Simulations of a pair of additional electrodes to shield the Penning trap at the cone regions of the KATRIN pre-spectrometer*, KATRIN internal report, 2007  
KATRIN BSCW, 25 EMD, 3 Pre-spectrometer, Penning Trap Investigations, report-simulations-addelectrode.pdf
- [Glü07c] F. Glück, *Background electrons in MAC-E filters*, presentation at the particle physics spring meeting of the German Physical Society (Deutsche Physikalische Gesellschaft, DPG), Freiburg, 2008
- [Glü07d] F. Glück, *The Penning discharge*, KATRIN internal report, 2007  
KATRIN BSCW, 25 EMD, 3 Pre-spectrometer, Penning Trap Investigations, The\_Penning\_discharge\_(F\_Glueck).pdf
- [Glü08] F. Glück, *Background at the KATRIN final plane detector and the pre-spectrometer potential*, presentation at the 15<sup>th</sup> KATRIN collaboration meeting, Karlsruhe, 2008  
KATRIN BSCW, 95 General Meetings and Review Panels, 1 Collaboration Meetings, 15. Collaboration Meeting, Session - B1, 95-TRP-4518-B1-FGlueck.ppt
- [Glü09a] F. Glück, to be published

## Bibliography

- [Glü09b] F. Glück, private communication, 2009
- [Goe35] M. Goeppert-Mayer, *Double Beta-Disintegration*, Phys. Rev. **48** (1935) 512
- [Gol58] M. Goldhaber, L. Grodzins, and A. W. Sunyar, *Helicity of Neutrinos*, Phys. Rev. **109** (1958) 1015
- [Gum08] R. Gumbsheimer, *Main spectrometer overview*, presentation at the 15<sup>th</sup> KATRIN collaboration meeting, Karlsruhe, 2008  
KATRIN BSCW, 5 General Meetings and Review Panels, 1 Collaboration Meetings, 15. Collaboration Meeting, Session - 3, 95-TRP-4510-S3-RGumbsheimer.ppt
- [Hab09] F. Habermehl, dissertation in preparation, Universität Karlsruhe (TH)
- [Hae53] R. Haefel, *Die Zündspannung von Gasentladungen unter dem Einfluß eines transversalen Magnetfeldes im Druckbereich von 10 bis 10<sup>-8</sup> Torr*, Acta Physica Austriaca **7** (1953) 52
- [Ham06] Hamamatsu Photonics K. K., data sheet *Si PIN photodiode S3590 series*, 2006, <http://www.hamamatsu.com>
- [Ham50] D. R. Hamilton and L. Gross, *An Electrostatic Beta-Spectrograph*, Rev. Sci. Instrum. **21** (1950) 912
- [Ham53] D. R. Hamilton, W. P. Alford and L. Gross, *Upper Limits on the Neutrino Mass from the Tritium Beta Spectrum*, Phys. Rev. **92** (1953) 1521
- [Han05] S. Hannestad, *Neutrino Masses and the Dark Energy Equation of State: Relaxing the Cosmological Neutrino Mass Bound*, Phys. Rev. Lett. **95** 221301 (2005)
- [Har89] M. Hara *et al.*, *Influence of transverse magnetic field on breakdown characteristics of vacuum, gaseous helium at low temperature and liquid helium*, Cryogenics **29** (1989) 448
- [Har76] E. Harting and F. H. Read, *Electrostatic Lenses*, Elsevier, Amsterdam, 1976
- [Hau08] T. Haugbølle, homepage, <http://www.phys.au.dk/~haugboel/projects.shtml>
- [Hei09] H. Hein, diploma thesis in preparation, Westfälische Wilhelms-Universität Münster
- [Her06] Heraeus Quarzglas GmbH & Co. KG, *Product Information Suprasil<sup>®</sup> 3001 and 3002*, 2006, available online at <http://www.heraeus-quarzglas.de>
- [Her77] S. W. Herb *et al.*, *Observation of a Dimuon Resonance at 9.5 GeV in 400-GeV Proton-Nucleus Collisions*, Phys. Rev. Lett. **39** (1977) 252
- [Hey04] K. Heyde, *Basic Ideas and Concepts in Nuclear Physics*, third edition, Institute of Physics Publishing, Bristol and Philadelphia, 2004
- [Hil10] B. Hillen, dissertation in preparation, Westfälische Wilhelms-Universität Münster
- [Hir02] H. Hirayama *et al.*, *Efficient 230–280 nm emission from high-Al-content AlGaIn-based multi-quantum wells*, Appl. Phys. Lett. **80** (2002) 37
- [Höl79] J. Hölzl and F. K. Schulte, *Work Function of Metals*, in: Springer Tracts in Modern Physics, Vol. 85 – Solid Surface Physics (ed. G. Höhler), Springer-Verlag, Berlin, 1979
- [Hsu76] T. Hsu and J. L. Hirshfield, *Electrostatic energy analyzer using a nonuniform axial magnetic field*, Rev. Sci. Instrum. **47** (1976) 236
- [Hu98] W. Hu, D. J. Eisenstein, M. Tegmark, *Weighing Neutrinos with Galaxy Surveys*, Phys. Rev. Lett. **80** (1998) 5255

- [Hub66] E. E. Huber, *The effect of mercury contamination on the work function of gold*, Appl. Phys. Lett **8** (1966) 169
- [Hug05] K. Hugenberg and A. Möller, *Untersuchung des Einflusses von Ungenauigkeiten beim Einbau der Drahtelektrode auf die Feldhomogenität und die Elektronenbahnen*, student research project, Westfälische Wilhelms-Universität Münster, 2005
- [Hug08] K. Hugenberg, *Design of the electrode system for the KATRIN main spectrometer*, diploma thesis, Westfälische Wilhelms-Universität Münster, 2008
- [Jac98] J. D. Jackson, *Classical Electrodynamics*, 3<sup>rd</sup> edition, John Wiley & Sons, Inc., 1998
- [Jia98] X. Jiang, C. N. Berglund, A. E. Bell, and W. A. Mackie, *Photoemission from gold thin films for application in multiphotocathode arrays for electron beam lithography*, J. Vac. Sci. Technol. **B 16** (1998) 3374
- [Jöh07] R. Jöhren, *Entwicklung eines automatischen Messsystems zur Qualitätskontrolle des Elektrodensystems für das KATRIN Hauptspektrometer*, diploma thesis, Westfälische Wilhelms-Universität Münster, 2007
- [Kas08] J. Kaspar, *Am/Co photoelectron source for energy scale monitoring of the KATRIN neutrino experiment*, dissertation, Czech Technical University in Prague, 2008
- [KAT01] The KATRIN collaboration (A. Osipowicz *et al.*), *Letter of Intent – KATRIN: A next generation tritium beta decay experiment with sub-eV sensitivity for the electron neutrino mass*, 2001, arXiv:hep-ex/0109033v1
- [KAT04] The KATRIN collaboration (J. Angrik *et al.*), *KATRIN Design Report 2004*, FZKA Scientific Report 7090, 2005, available online at <http://bibliothek.fzk.de/zb/berichte/FZKA7090.pdf>
- [Kau02] W. Kaufmann, *Die elektromagnetische Masse des Elektrons*, Phys. Zeitschr. **4** (1902) 54
- [Kaz07] O. Kazachenko, private communication, Jan. 2007
- [Kla01] H. V. Klapdor-Kleingrothaus *et al.*, *Latest Results from the Heidelberg-Moscow Double-Beta-Decay Experiment*, Eur. Phys. J. **A 12** (2001) 147; pre-print arXiv:hep-ph/0103062v1
- [Kla04] H. V. Klapdor-Kleingrothaus, I. V. Krivosheina, A. Dietz and O. Chkvorets, *Search for neutrinoless double beta decay with enriched <sup>76</sup>Ge in Gran Sasso 1999–2003*, Phys. Lett. **B 586** (2004) 198
- [Kla06] H. V. Klapdor-Kleingrothaus and I. V. Krivosheina, *The evidence for the observation of  $0\nu\beta\beta$  decay: the identification of  $0\nu\beta\beta$  events from the full spectra*, Mod. Phys. Lett. **A 21** (2006) 1547
- [Kno00] H. E. Knoepfel, *Magnetic fields: A comprehensive theoretical treatise for practical use*, John Wiley & Sons, Inc., 2000
- [Kob72] M. Kobayashi and T. Maskawa, *CP-violation in the renormalizable theory of weak interaction*, Prog. Theor. Phys. **49** (1973) 652
- [Kod01] K. Kodama *et al.* (DONUT collaboration), *Observation of tau neutrino interactions*, Phys. Lett. **B 504** (2001) 218
- [Kom09] E. Komatsu *et al.*, *Five-Year Wilkinson Microwave Anisotropy Probe Observations: Cosmological Interpretation*, Astrophys. J. Supplement Series **180** (2009) 330
- [Kor06] S. Korsten and S. Tacke, *Elektromagnetische Feldberechnungen und Bahnberechnungen für das KATRIN-Hauptspektrometer*, student research project, Westfälische Wilhelms-Universität Münster, 2006

## Bibliography

- [Koz08] V. Yu. Kozlov *et al.*, *The WITCH experiment: Acquiring the first recoil ion spectrum*, Nucl. Instr. Meth. **B 266** (2008) 4515
- [Kra05] Ch. Kraus, B. Bornschein, L. Bornschein, J. Bonn, B. Flatt, A. Kovalik, B. Ostrick, E. W. Otten, J. P. Schall, Th. Thümmler, Ch. Weinheimer, *Final results from phase II of the Mainz neutrino mass search in tritium  $\beta$  decay*, Eur. Phys. J. **C 40** (2005) 447
- [Kri89] J. Kristian *et al.*, *Submillisecond optical pulsar in supernova 1987A*, Nature **338** (1989) 234
- [Kri08] J. R. Kristiansen and Ø. Elgarøy, *Cosmological implications of the KATRIN experiment*, JCAP **01** (2008) 007
- [Kru83] P. Kruit and F. H. Read, *Magnetic field paralleliser for  $2\pi$  electron-spectrometer and electron-image magnifier*, J. Phys. **E 16** (1983) 313
- [Las06] Laser2000 GmbH, *Deep UV Semiconductor LEDs and Lasers, 250 nm to 280 nm*, data sheet for light-emitting diodes procurable from the company Photon Systems, 2006, <http://www.laser2000.de>
- [Leb08] M. L. Leber, *Improved simulations and measurements of the “room” background*, presentation at the 15<sup>th</sup> KATRIN collaboration meeting, Karlsruhe, 2008  
KATRIN BSCW, 5 General Meetings and Review Panels, 1 Collaboration Meetings, 15. Collaboration Meeting, Session - C3, 95-TRP-4552-C3-MLeber.pdf
- [Leb09] M. L. Leber, *The Karlsruhe Tritium Neutrino experiment detector system and related backgrounds*, dissertation in preparation, University of Washington, Seattle;  
M. L. Leber, T. H. Burritt, J. A. Dunmore, P. J. Doe, J. A. Formaggio, R. G. H. Robertson, M. Steidl, B. A. VanDevender, B. L. Wall, and J. F. Wilkerson, *Background simulations and detector design for the KATRIN experiment*, IEEE Nuclear Science Symposium Conference Record (2007) 2105
- [Lei36] A. I. Leipunski, *Determination of the energy distribution of recoil atoms during  $\beta$  decay and the existence of the neutrino*, Proc. Camb. Phil. Soc. **32** (1936) 301
- [Leo08] j-fiber GmbH Jena (LEONI Group), product information for step-index high-OH fibers, <http://www.j-fiber.de/>
- [Les06] J. Lesgourgues and S. Pastor, *Massive neutrinos and cosmology*, Phys. Rep. **429** (2006) 307
- [Lew08] R. J. Lewis, H. H. Telle, B. Bornschein, O. Kazachenko, N. Kernert, and M. Sturm, *Dynamic Raman spectroscopy of hydrogen isotopomer mixtures in-line at TILO*, Laser Phys. Lett. **5** (2008) 522
- [Lic08] S. Lichter, *Anti Penning Electrode*, presentation at the 15<sup>th</sup> KATRIN collaboration meeting, Karlsruhe, 2008  
KATRIN BSCW, 5 General Meetings and Review Panels, 1 Collaboration Meetings, 15. Collaboration Meeting, Session - C1, 95-TRP-4539-C1-SLichter.ppt
- [Lob85] V. M. Lobashev and P. E. Spivak, *A method for measuring the electron antineutrino rest mass*, Nucl. Instr. Meth. **A 240** (1985) 305
- [Lob03] V. M. Lobashev, *The search for the neutrino mass by direct method in the tritium beta-decay and perspectives of study it in the project KATRIN*, Nucl. Phys. **A 719** (2003) C153
- [Lor02] T. J. Loredo and D.Q. Lamb, *Bayesian analysis of neutrinos observed from supernova SN 1987A*, Phys. Rev. **D 65** (2002) 063002

- [Maj37] E. Majorana, *Teoria simmetrica dell'elettrone e del positrone (Symmetrical theory of the electron and positron)*, Nuovo Cimento **14** (1937) 171
- [Mak62] Z. Maki, M. Nakagawa and S. Sakata, *Remarks on the Unified Model of Elementary Particles*, Prog. Theor. Phys. **28** (1962) 870
- [Mal80] J. H. Malmberg and C. F. Driscoll, *Long-Time Containment of a Pure Electron Plasma*, Phys. Rev. Lett. **44** (1980) 654
- [Mei22] L. Meitner, *Über die Entstehung der  $\beta$ -Strahl-Spektren radioaktiver Substanzen*, Z. Phys. **9** (1922) 131;  
L. Meitner, *Über den Zusammenhang zwischen  $\beta$ - und  $\gamma$ -Strahlen*, Z. Phys. **9** (1922) 145;  
L. Meitner, *Über die  $\beta$ -Strahl-Spektren und ihren Zusammenhang mit der  $\gamma$ -Strahlung*, Z. Phys. **11** (1922) 35
- [Mei30] L. Meitner und W. Orthmann, *Über eine absolute Bestimmung der Energie der primären  $\beta$ -Strahlung von Radium E*, Z. Phys. **60** (1930) 143
- [Mik86] S. Mikheyev and A. Yu. Smirnov, *Resonant amplification of  $\nu$  oscillations in matter and solar-neutrino spectroscopy*, Nuovo Cimento **C9** (1986) 17
- [Mon06] A. Monfardini *et al.*, *The Microcalorimeter Arrays for a Rhenium Experiment (MARE): a next-generation calorimetric neutrino mass experiment*, Nucl. Instr. Meth. **A 559** (2006) 346; for a detailed proposal see F. Gatti *et al.*, *MARE – Microcalorimeter Arrays for a Rhenium Experiment*, 2006, available online at <http://mare.dfm.uninsubria.it>
- [Mül02] B. Müller, *Umbau des Mainzer Neutrinomassenexperimentes und Untergrunduntersuchungen im Hinblick auf KATRIN*, diploma thesis, Johannes Gutenberg-Universität Mainz, 2002
- [Nag06] Sz. Nagy *et al.*, *On the Q-value of the tritium  $\beta$ -decay*, Europhys. Lett. **74** (2006) 404
- [Nor61] T. G. Northrop, *The Guiding Center Approximation to Charged Particle Motion*, Annals of Physics **15** (1961) 79
- [Nor63] T. G. Northrop, *The Adiabatic Motion of Charged Particles*, John Wiley & Sons, Inc., New York, 1963
- [Ort08] Ortec (Advanced Measurement Technology, Inc.), product information for AD413A digitizer, website <http://www.ortec-online.com/electronics/adc/ad413a.htm>
- [Ost09] B. Ostrick, *Eine kondensierte  $^{83m}\text{Kr}$ -Kalibrationsquelle für KATRIN*, dissertation, Westfälische Wilhelms-Universität Münster, 2009
- [Ott07] E. W. Otten, *On trapping and discharge conditions*, KATRIN internal memo, June 2007 KATRIN BSCW, 25 EMD, 51 Background, *On\_trapping\_and\_discharge\_conditions.doc*
- [Ott08] E. W. Otten and C. Weinheimer, *Neutrino mass limit from tritium  $\beta$  decay*, Rep. Prog. Phys. **71** (2008) 086201
- [Pai86] A. Pais, *Inward Bound – Of Matter and Forces in the Physical World*, Oxford University Press, Oxford, 1986 (reprinted 2002)
- [Pas89] F. Paschen, *Ueber die zum Funkenübergang in Luft, Wasserstoff und Kohlensäure bei verschiedenen Drucken erforderliche Potentialdifferenz*, Annalen der Physik **273** (1889) 69
- [Pau30] W. Pauli, letter to a local meeting on radioactivity at Tübingen, Germany (dated Dec. 4, 1930), original German version reprinted in: R. Kronig and V. Weisskopf (eds.), *Wolfgang Pauli, Collected Scientific Papers*, Vol. 2, Interscience, New York (1964) 1316;

## Bibliography

- for an English translation see, *e. g.*, Physics Today, 09/1978
- [PDG08] C. Amsler *et al.* (Particle Data Group), *Review of Particle Physics*, Phys. Lett. **B 667** (2008) 1, available online at <http://pdg.lbl.gov>
- [Pei01] Z. Pei and C. N. Berglund, *Angular Distribution of Photoemission from Gold Thin Films*, Jpn. J. Appl. Phys. **41** (2001) L52
- [Pen36] F. M. Penning, *Die Glimmentladung bei niedrigem Druck zwischen koaxialen Zylindern in einem axialen Magnetfeld*, Physica **III** (1936) 873
- [Pen37] F. M. Penning, *Ein neues Manometer für niedrige Gasdrucke, insbesondere zwischen  $10^{-3}$  und  $10^{-5}$  mm*, Physica **IV** (1937) 71
- [Pen65] A. A. Penzias and R. W. Wilson, *A Measurement of Excess Antenna Temperature at 4080 Mc/s*, Astrophys. J. **142** (1965) 419
- [Per75] M. L. Perl *et al.*, *Evidence for Anomalous Lepton Production in  $e^+e^-$  Annihilation*, Phys. Rev. Lett. **35** (1975) 1489
- [Pho07] Photon Systems, *Deep UV Laser 224 and 248 nm* (data sheet, revision 2), 2007, <http://www.photonsystems.com>
- [Pic92a] A. Picard *et al.*, *A solenoid retarding spectrometer with high resolution and transmission for keV electrons*, Nucl. Instr. Meth. **B 63** (1992) 345
- [Pic92b] A. Picard *et al.*, *Precision measurement of the conversion electron spectrum of  $^{83m}\text{Kr}$  with a solenoid retarding spectrometer*, Z. Phys. **A 342** (1992) 71
- [Pon47] B. Pontecorvo, *The neutrino and the recoil of nuclei in beta disintegrations*, Rep. Prog. Phys. **11** (1947) 32
- [Pon67] B. Pontecorvo, Zh. Eksp. Teor. Fiz. **53** (1967) 1717 [Sov. Phys. JETP **26** (1968) 984]
- [Pra09] M. Prall, dissertation in preparation, Westfälische Wilhelms-Universität Münster
- [Qua08] Quantel, industrial and scientific laser website, <http://www.quantel-laser.com/industrial-scientific-lasers/uk/>, 2008
- [Rea71] F. H. Read, A. Adams and J. R. Soto-Montiel, *Electrostatic cylinder lenses I: Two element lenses*, J. Phys. **E 4** (1971) 625
- [Rea98] F. H. Read, N. J. Bowring, P. D. Bullivant, and R. R. A. Ward, *Penetration of electrostatic fields and potentials through meshes, grids, or gauzes*, Rev. Sci. Instrum. **69** (1998) 2000
- [Rea99] F. H. Read, N. J. Bowring, P. D. Bullivant, and R. R. A. Ward, *Short- and long-range penetration of fields and potentials through meshes, grids or gauzes*, Nucl. Instr. Meth. **A 427** (1999) 363
- [Red58a] P. A. Redhead, *The Townsend discharge in a coaxial diode with axial magnetic field*, Canad. J. Phys. **36** (1958) 255
- [Red58b] J. P. Hobson and P. A. Redhead, *Operation of an inverted-magnetron gauge in the pressure range  $10^{-3}$  to  $10^{-12}$  mm. Hg*, Canad. J. Phys. **36** (1958) 271
- [Red59] P. A. Redhead, *The magnetron gauge: a cold-cathode vacuum gauge*, Canad. J. Phys. **37** (1959) 1260
- [Rei59] R. Reines and C. L. Cowan, *Free Antineutrino Absorption Cross Section. I. Measurement of the Free Antineutrino Absorption Cross Section by Protons*, Phys. Rev. **113** (1959) 273
- [Rei96] F. Reines, *The neutrino: from poltergeist to particle* (Nobel lecture 1995), Rev. Mod. Phys. **68** (1996) 317

- [Rei07] M. Reinhardt, *Entwicklung eines Lasersensors und Materialcharakterisierung für die Drahtelektroden des KATRIN Hauptspektrometers*, diploma thesis, Westfälische Wilhelms-Universität Münster, 2007
- [Ren82] A. Renau, F. H. Read and J. N. H. Brunt, *The charge-density method of solving electrostatic problems with and without the inclusion of space-charge*, J. Phys. E **15** (1982) 347
- [ROOT] ROOT System homepage: <http://root.cern.ch/>
- [Rut08] E. Rutherford and H. Geiger, *The charge and nature of the  $\alpha$ -particle*, Proc. Roy. Soc. A **81** (1908) 162
- [Rut14] E. Rutherford and E. N. da C. Andrade, *The Wave-Length of the Soft  $\gamma$  Rays from Radium B*, Phil. Mag. **27** (1914) 854
- [Sak58] J. J. Sakurai, *Mass reversal and weak interactions*, Nuovo Cimento **7** (1958) 649;  
J. J. Sakurai, *Rest Mass of the Neutrino*, Phys. Rev. Lett. **1** (1958) 40
- [San03] S. Sánchez Majos, *Study of background suppression in MAC-E filters*, diploma thesis, Johannes Gutenberg-Universität Mainz, 2003
- [Sav95] G. F. Saville, P. M. Platzman, G. Brandes, R. Ruel, and R. L. Willett, *Feasibility study of photocathode electron projection lithography*, J. Vac. Sci. Technol. **B 13** (1995) 2184
- [Schr90] M. Schrader, *Rauschoptimierung eines landungsempfindlichen Vorverstärkers für Halbleiterdetektoren und digitale Filterung des analogen Ausgangssignals*, diploma thesis, Johannes Gutenberg-Universität Mainz, 1990
- [Scha01] J.-P. Schall, *Untersuchungen zu Untergrundprozessen am Mainzer Neutrinomassenexperiment*, diploma thesis, Johannes Gutenberg-Universität Mainz, 2001
- [Scha09] J.-P. Schall, F. Schwamm *et al.*, *Background in MAC-E filters from the electrodes*, in preparation
- [Scha03] W. Schattke and M. A. Van Hove (eds.), *Solid-State Photoemission and Related Methods – Theory and Experiment*, Wiley-VCH, Weinheim, 2003
- [Schm08] U. Schmitt, *Entwicklung eines Monitordetektors für das KATRIN-Experiment*, dissertation, Universität Karlsruhe (TH), 2008
- [Schu07] M. Schumann *et al.*, *Measurement of the Neutrino Asymmetry Parameter B in Neutron Decay*, Phys. Rev. Lett. **99** (2007) 191803
- [Schw04] F. Schwamm, *Untergrunduntersuchungen für das KATRIN Experiment*, dissertation, Universität Karlsruhe (TH), 2004
- [SET08] Sensor Electronic Technology, Inc., *Technical Data on UVTOP series of UV LEDs*, 2008, <http://www.s-et.com/products/uvtop.html>
- [Seo06a] Seoul Semiconductor Co., Ltd., *Specification document for UVLED model series T9B26\** (Rev. 2.0), 2006, <http://www.biouvledstore.com>
- [Seo06b] Seoul Semiconductor Co., Ltd., *Specification document for UVLED model series T9B25\** (Rev. 1.0), 2006, <http://www.biouvledstore.com>
- [Ser07] P. Serra, R. Bean, A. De La Macorra, A. Melchiorri, *Massive neutrinos and dark energy*, Nucl. Phys. Proc. Suppl. **168** (2007) 31
- [Sha03] M. Shatalov *et al.*, *Time-resolved electroluminescence of AlGaIn-based light-emitting diodes with emission at 285 nm*, Appl. Phys. Lett. **82** (2003) 167

## Bibliography

- [Sim00] D. A. Dahl, *Simion 3D Version 7 User's Manual*, Idaho National Engineering and Environmental Laboratory, ID 83415, 2000;  
information available online at <http://www.simion.com/>
- [Sis04] M. Sisti *et al.*, *New limits from the Milano neutrino mass experiment with thermal microcalorimeters*, Nucl. Instr. Meth **A 520** (2004) 125
- [Som52] J. M. Somerville, *Sparking Potentials in a Transverse Magnetic Field*, Proc. Phys. Soc. London **B 65** (1952) 620
- [Sta09] S. Stahl (Stahl Electronics), private communication, 2009  
preliminary data sheet high voltage switch HVS-1000
- [Str09] S. Streubel, *Aufbau eines PET-Demonstrations-Experimentes und Anwendung von dessen FADC-basiertem Datenaufnahmesystem für Photoelektronenspektroskopie*, diploma thesis, Westfälische Wilhelms-Universität Münster, 2009
- [Str08] Struck Innovative Systeme GmbH, product information for SIS3301 digitizer at website <http://www.struck.de/sis3301.htm>
- [Sud58] E. C. G. Sudarshan and R. E. Marshak, *Chirality Invariance and the Universal Fermi Interaction*, Phys. Rev. **109** (1958) 1860
- [Tab00] T. Tabata and T. Shirai, *Analytic cross sections for collisions of  $H^+$ ,  $H_2^+$ ,  $H_3^+$ ,  $H$ ,  $H_2$  and  $H^-$  with hydrogen molecules*, Atomic Data and Nuclear Data Tables **76** (2000) 1
- [Teg04a] M. Tegmark *et al.*, *The three-dimensional power spectrum of galaxies from the Sloan Digital Sky Survey*, Astrophys. J. **606** (2004) 702
- [Teg04b] M. Tegmark, *Neutrino masses and other parameters from cosmological observations*, presentation at the 129<sup>th</sup> Nobel Symposium ("Neutrino Physics"), 2004,  
URL: <http://nobelprize.org/nobelprizefoundation/symposia/physics/ns129/>
- [Tem07] K. Temming, *Aufbau einer vollautomatischen Ultraschallreinigungsanlage für die Drahtelektrode des KATRIN-Hauptspektrometers*, diploma thesis, Westfälische Wilhelms-Universität Münster, 2007
- [Tow10] J. S. Townsend, *The theory of ionization of gases by collision*, Constable & Company Ltd., London, 1910
- [Thü02] Th. Thümmler, *Entwicklung von Methoden zur Untergrundreduzierung am Mainzer Tritium- $\beta$ -Spektrometer*, diploma thesis, Johannes Gutenberg-Universität Mainz, 2002
- [Thü03] Th. Thümmler, B. Flatt and Ch. Weinheimer, *Violation of adiabaticity in the transport magnets of the KATRIN experiment*, KATRIN internal report, 2003  
KATRIN BSCW, 25 EMD, 2 Electron transport to pre-spectrometer, 25-ME-2001-1.pdf
- [Thü07] Th. Thümmler, *Präzisionsüberwachung und Kalibration der Hochspannung für das KATRIN-Experiment*, dissertation, Westfälische Wilhelms-Universität Münster, 2007
- [Thü08] Th. Thümmler, private communication, 2008
- [Val04] K. Valerius, *Elektromagnetisches Design für das Hauptspektrometer des KATRIN Experiments*, diploma thesis, Rheinische Friedrich-Wilhelms-Universität Bonn, 2004
- [Val07] K. Valerius and Ch. Weinheimer, *Transmission function simulations for the main spectrometer*, presentation at the 12<sup>th</sup> KATRIN collaboration meeting, Karlsruhe, 2007  
KATRIN BSCW, 95 General Meetings and Review Panels, 1 Collaboration Meetings, 12. Collaboration Meeting, Session - B2, 95-TRP-4226-B2-KValerius.pdf

- [Vöc08] S. Vöcking, *Implementierung der Multipole Boundary Element Methode für das KATRIN-Experiment*, diploma thesis, Westfälische Wilhelms-Universität Münster, 2008
- [Wal99] S. G. Walton *et al.*, *Low energy, ion-induced electron and ion emission from stainless steel: The effect of oxygen coverage and the implications for discharge modeling*, J. Appl. Phys. **85** (1999) 1832
- [Wea81] R. C. Weast and M. J. Astle (eds.), *CRC Handbook of Chemistry and Physics*, 62<sup>nd</sup> edition, CRC Press, Inc., Boca Raton, 1981, and further references cited therein
- [Wei03] Ch. Weinheimer, *Laboratory Limits on Neutrino Masses*, in: G. Altarelli and K. Winter (Eds.), *Neutrino Mass*, Springer, 2003
- [Wei07] Ch. Weinheimer, *Requirements for the main spectrometer EMD tests*, presentation at the 13<sup>th</sup> KATRIN collaboration meeting, Karlsruhe, 2007  
KATRIN BSCW, 95 General Meetings and Review Panels, 1 Collaboration Meetings, 13. Collaboration Meeting, Session - 3, 95-TRP-4310-S3-CWeinheimer.pdf
- [Wei08] Ch. Weinheimer, M. Beck, J. Bonn, H. Hein, K. Hugenberg, S. Streubel and K. Valerius, *An angular-defined electron gun for KATRIN*, presentation at the 15<sup>th</sup> KATRIN collaboration meeting, Karlsruhe, 2008  
KATRIN BSCW, 95 General Meetings and Review Panels, 1 Collaboration Meetings, 15. Collaboration Meeting, Session - C2, 95-TRP-4543-C2-CWeinheimer.pdf
- [Wil07] S. Wilfert, *Grundlagenuntersuchungen zur Entwicklung eines langzeitstabilen Kaltkathoden-Ionisationsmanometers vom inversen Magnetron-Typ*, dissertation, Otto-von-Guericke-Universität Magdeburg, 2007
- [Wol78] L. Wolfenstein, *Neutrino oscillations in matter*, Phys. Rev. **D 17** (1978) 2369, and *Neutrino oscillations and stellar collapse*, Phys. Rev. **D 20** (1979) 2634
- [Wol08] I. Wolff, *Entfaltung der Energieverlustfunktion beim KATRIN Experiment*, diploma thesis, Westfälische Wilhelms-Universität Münster, 2008
- [Wu57] C. S. Wu, E. Ambler, R. W. Hayward, D. D. Hoppes, and R. P. Hudson, *Experimental Test of Parity Conservation in Beta Decay*, Phys. Rev. **105** (1957) 1413
- [Zac08] M. Zacher, K. Hugenberg and Ch. Weinheimer, *Overview of the steep cone design for the inner wire electrode for the main spectrometer*, KATRIN internal report, 2008  
KATRIN BSCW, 25 EMD, 5 Main spectrometer, steep\_cone\_design.pdf
- [Zac09] M. Zacher, *Electromagnetic design and field emission tests for the wire electrode of the KATRIN main spectrometer*, diploma thesis in preparation, Westfälische Wilhelms-Universität Münster, 2009
- [Zan88] A. Zangwill, *Physics at Surfaces*, Cambridge University Press, Cambridge, 1988
- [Zbo07] M. Zbořil, private communication, 2007
- [Zbo10] M. Zbořil, dissertation in preparation, Westfälische Wilhelms-Universität Münster
- [Zub04] K. Zuber, *Neutrino Physics*, Institute of Physics Publishing, Bristol and Philadelphia, 2004

## *Bibliography*

# Danksagung

An dieser Stelle gebührt mein Dank all jenen, die zum Gelingen dieser Dissertation beigetragen haben.

Herr Prof. Dr. Christian Weinheimer hat mir ein spannendes und vielseitiges Dissertationsprojekt anvertraut, bei dem er mir stets mit Rat und Tat zur Seite stand – egal, ob es mal bei den Simulationsaufgaben nicht weiter gehen wollte oder ob Probleme im Labor auftraten. Ich bin ihm auch dankbar für die Möglichkeit, meinen fachlichen Horizont durch den Besuch von Tagungen, Konferenzen und Workshops zu erweitern, worauf er als Betreuer meiner Arbeit stets besonderen Wert legte.

Meinem Zweitgutachter Herrn Prof. Dr. Johannes P. Wessels danke ich dafür, dass er seine formale Rolle als Mentor nicht nur auf dem Papier wahrnahm, sondern durch viele wertvolle Ratschläge und Ermutigungen ausfüllte.

Dass ich mich von Anfang an in der neuen Umgebung in Münster trotz der teils anstrengenden wöchentlichen Pendelei so wohl gefühlt habe, ist der tollen Atmosphäre in der Arbeitsgruppe und dem gesamten Umfeld am Institut für Kernphysik geschuldet. Hierzu haben vor allem meine Bürokollegen (in wechselnder Besetzung – u.a. Thomas, Karen, Michael, Alexander, Irina und Kim) beigetragen.

Helmut Baumeister und Hans-Werner Ortjohann waren immer geduldige und kompetente Ansprechpartner für jegliche technischen Fragestellungen. Ich möchte auch die großartige Arbeit der Werkstätten – Feinmechanik und Elektronik – erwähnen. Für alle organisatorischen Belange war dank Michaela Erdmann, Uta Mayer und Christina Kösters stets bestens gesorgt.

Für die Unterstützung bei meinen auswärtigen Tätigkeiten am Forschungszentrum Karlsruhe und am Institut für Physik der Uni Mainz bin ich vielen Kollegen zu Dank verpflichtet. Dies sind u.a. Prof. Dr. Guido Drexlin, Dr. Lutz Bornschein, Florian Fränkle, Dr. Ferenc Glück, Florian Habermehl, Dr. Klaus Schlösser und Dr. Thomas Thümmel für Karlsruhe, sowie Prof. Dr. Ernst-Wilhelm Otten, Dr. Bea Ostrick, Marta Ubieto-Diaz und besonders Dr. Jochen Bonn in Mainz.

Auch den Münsteranern, die bei den Messungen in Mainz vor Ort (im Keller) so tatkräftig mitgeholfen haben, möchte ich für ihren unermüdlichen Einsatz danken: Allen voran Dr. Marcus Beck und Miroslav Zbořil, außerdem Henrik Arlinghaus, Hendrik Hein und Sebastian Streubel – und natürlich unserem zuverlässigen „Elvis“. :-)

Bereits in Münster haben viele dazu beigetragen, die Messungen in Mainz vorzubereiten und dadurch zum Erfolg zu bringen. Hier möchte ich u.a. Helmut Baumeister und Hans-Werner Ortjohann, Dr. Volker Hannen, Alexander Gebel, Daniel Hampf, Frank Hochschulz, sowie Roland Berendes und Wladimir Buglak stellvertretend für die Elektronikwerkstatt und Georg Bourichter stellvertretend für die Feinmechanische Werkstatt nennen.

Neben dem experimentellen Teil möchte ich auch auf den Simulationsteil der Arbeit eingehen, der unzweifelhaft stark durch Ferenc geprägt ist. Ihm bin ich nicht nur für die zur Verfügung gestellten Computerprogramme, sondern auch für seine immerwährende Hilfs- und Diskussionsbereitschaft und die vielen Erklärungen sehr dankbar. Bei jeglichen Computerproblemen konnte ich mich jederzeit auf Torges Hilfe verlassen. Ebenso haben Matthias Prall, Dr. Nikita Titov und Sebastian Vöcking zur Weiterentwicklung des Simulationspaketes beigetragen. Vielen Dank dafür!

Beim Korrekturlesen der Arbeit haben insbesondere Marcus, Karen und Volker mir sehr geholfen. Sie waren auch in den schwierigsten Phasen immer für mich da. Vielen Dank für's Zuhören, gut Zureden, für die wohltuenden kulturellen Ausflüge (besonders an Karen) und die Nervennahrung (besonders an Marcus).

Zum Schluss, aber nicht zuletzt, möchte ich mich bei meiner Familie, insbesondere meinen Eltern Martha und Matthias Valerius, und bei meinem Freund Torge Szczepanek ganz besonders für die andauernde liebevolle Unterstützung und ihren Rückhalt während meines gesamten Studiums bedanken. Ihr habt es während dieser ganzen Zeit bestimmt nicht immer leicht mit mir gehabt! :-)



# Lebenslauf

## **Persönliche Daten**

Name	Kathrin Martha Valerius
Geburtsdatum	19.04.1980
Geburtsort	Wittlich
Eltern	Matthias Valerius und Martha Valerius, geb. Baden
Staatsangehörigkeit	deutsch
Familienstand	ledig

## **Schulausbildung und Studium**

1986–1990	Humbrecht-Grundschule Hupperath
1990–1999	Peter Wust-Gymnasium Wittlich
21.06.1999	Allgemeine Hochschulreife
10/1999–12/2004	Studium der Physik an der Rheinischen Friedrich-Wilhelms-Universität Bonn
04.04.2002	Diplom-Vorprüfung
02/2004–12/2004	Diplomarbeit in Physik: „Elektromagnetisches Design für das Hauptspektrometer des KATRIN Experiments“
20.12.2004	Diplomprüfung

## **Promotionsstudium**

01/2005	Beginn der Dissertation am Institut für Kernphysik der Westfälischen Wilhelms-Universität Münster unter der Betreuung von Prof. Dr. Christian Weinheimer
---------	---

## **Berufliche Tätigkeit**

10/2003–12/2004	Studentische Hilfskraft am Helmholtz-Institut für Strahlen- und Kernphysik der Rheinischen Friedrich-Wilhelms-Universität Bonn
01/2005–03/2009	Wissenschaftliche Mitarbeiterin am Institut für Kernphysik der Westfälischen Wilhelms-Universität Münster

Münster, den 20.02.2009